20th Sensors and Their Applications colocated with 5th International Conference of Fibre Optic and Photonic Sensors for Industrial and Safety Applications (OFSIS)

Organized by
Institute of Measurement and Control (InstMC) (UK)
University of Limerick (Ireland)

Cooperating Organization
China Instrument and Control Society (CIS) (China)
The Optical Fibre Sensors Committee (OFSC) of China Optical Engineering Society (China)
Institute of Physics (UK and Ireland)

Kenneth Grattan and Elfed Lewis
Editors

11th – 14th August 2024
Limerick, Ireland

ISBN: 978-1-911620-84-6

Introduction

Welcome to the University of Limerick, Ireland and to the twentieth edition of the Sensors and Their Applications Conference co-located with the 5th edition of the International Conference of Fibre Optic and Photonic Sensors for Industrial and Safety Applications (OFSIS). Following the successful series of events since 1983 held mainly in UK Ireland, the University of Limerick retains the privilege to host and organize the 2024 meeting.

Sensors are ubiquitous today. Whether in our homes or stores, in our cars, in the aeroplanes that we travel in or most evidently in our smartphones – they are an increasingly important presence in our modern world. Sensors and sensor systems underpin the Internet of Things (IoT) which focuses on configuration, control and networking via the Internet of devices or 'Things' that are traditionally not associated with the Internet. The excellent measurements that modern sensor systems provide enable us not only to observe the world around us, but (at least in part) to control our environment and without high quality measurement tools, we cannot create the control systems we need – we require good measurement for the control systems that are built to exploit the advanced sensor systems developed.

The field is global and worth an estimated $200 billion annually – and more when both software and hardware aspects of the field are considered. 'Smart sensors' are an increasing share of that market and with the development of Artificial Intelligence and Machine Learning tools, will continue to develop and to offer more to the user and the consumer.

This Conference builds on the heritage of the successful series of 'Sensors & their Applications' Conferences, first held in 1983 and reflects the changing landscape since then. It is organized by the Institute of Measurement & Control (InstMC), with the support of the Institute of Physics (IoP), the China Instrument & Control Society (CIS), the Optical Fibre Sensors Committee (OFSC) of China Optical Engineering Society, and incorporating the 5th International Conference for Fibre-optic and Photonic Sensors for Industrial and Safety Applications (OFSIS). The Conference aims to bring both researchers and instrument developers and users together from across the world to discuss the latest developments in and directions for the field.

The Conference includes original, high-quality contributions from all relevant fields of the highly topical and multi-disciplinary subject of measurement, sensors, and associated instrumentation. The conference will cover practical developments of sensors and sensor systems 'in the field' as well as a wide range of application areas, with an emphasis on both applied and theoretical aspects.

Conference Committees

Conference General Co- Chairs (Sensors and Their Applications, 2024)

Kenneth Grattan, London City University (UK)
Elfed Lewis, University of Limerick (Ireland)

Conference General Chair (International Conference of Fibre Optic and Photonic Sensors for Industrial and Safety Applications)

Tongyu Liu, Qilu Technology, University Shandong and Micro-sensor Photonics Ltd.

International Organising Team

Steff Smith, Chief Executive, Institute of Measurement and Control, London, UK.
Kenneth Grattan, London City University, London, UK.
Tongyu Liu, Qilu Technology, University Shandong and Micro-sensor Photonics Ltd.
Huimin (Stephanie) Shan, China Instrument and Control Society (CIS), Beijing, China.
Zihai Liu, Harbin Engineering University(HEU), Harbin, China.
Chunying Guan, Harbin Engineering University (HEU), Harbin, China.
Andy Augousti, Kingston University, London, UK.
Hairul Azhar Abdul Rashid, Multimedia University, Malaysia
Olga Korostynska, Oslo Metropolitan University, Oslo, Norway.
Adam Drobot, OpenTechWorks, USA
Elfed Lewis, University of Limerick (Ireland)

Conference Management

Deborah Tudge, Plassey Campus Life (UL)
Megan Tuite, Plassey Campus Life (UL)
Fiona Bynane-Power, Plassey Campus Life (UL)
Kellie Ryan, Plassey Campus Life (UL)

Technical Local Organising Team

Muhammad Mahmood Ali, Atlantic Technological University (Ireland)
Gerard Dooly, University of Limerick (Ireland)
Colin Fitzpatrick, University of Limerick (Ireland)
Gabriel Leen, University of Limerick (Ireland)
Sean McGrath, University of Limerick (Ireland)
Sanober Farheen Memon, University of Limerick (Ireland)
Thomas Newe, University of Limerick (Ireland)
Eoin O'Connell, University of Limerick, Ireland
Sinead O'Keeffe, University of Limerick (Ireland)
Julia Semenova, Technical University Dublin (Ireland)
Tofail Syed, University of Limerick (Ireland)
Joseph Walsh, Munster Technological University (Ireland)

Administrative Local Organising Committee

Emily Spencer, University of Limerick (Ireland)
Caroline Dalton, University of Limerick (Ireland)

Sensors and Their Applications 2024 Format

The Conference is organised to include five plenary sessions, one special invited session and a number of invited and regular submission papers. The latter two categories are scheduled to operate in two parallel sessions whereas the plenaries and special invited sessions are to be held in a single venue.

This year's plenary speakers are
Professor Guofa Wang, Academician of China Engineering Academy, China Coal Technology Engineering Group, China.
Prof. K.T.V. Grattan, City University of London, London, UK.
Prof. Dr. Yu Fang, Academician of the Chinese Academy of Sciences and Shaanxi Normal University, Xi'An, China.
Professor Dasheng Jiang, Wuhan Technology University, Wuhan, China.
Professor Jiachen Wang, Vice-president, China University of Mining and Technology Beijing, China.

The special invited talk is by **Dr Lars Hildebrandt** of Nanonoplus Systems, Germany

The outline schedule of the conference is included below

SENSORS AND THEIR APPLICATIONS OUTLINE SCHEDULE AND AGENDA OF SESSIONS

Sunday	**18.30-19.30 Registration, Reception and Welcome**	
Monday	**09.00 – 09.40 Opening Session and Remarks**	
	09.40 – 11.10 Plenary Session 1 (two plenary talks)	
	11.10 – 11.30 Coffee	
	11.30 - 12.40 Industrial Sensing 1	**11.30 - 12.40 Spectroscopy**
	12.40 – 13.30 Lunch	
	13.30 - 15.20 Industrial Sensing 2	**13.30 - 15.20 Optical Fibre Sensors 1**
	15.20 – 16.00 Coffee	
	16.00 – 16.45 Plenary Session 2 (one plenary talk)	
	16.50 – 18.05 Biomedical Sensors 1	**16.50 – 18.05 Photonic Sensors**
	19.50 – Late. Barbeque	

Tuesday	**09.15 – 10.00 Plenary Session 3 (one plenary talk)**	
	10.05 – 11.15 Biomedical Sensors 2	**10.05 – 11.50 Optical Fibre Sensors 2**
	11.15 – 11.30 Coffee	
	11.30 – 13.20 Biomedical Sensors 3	**11.30 – 13.20 Optical Fibre Sensors 3**
	13.10 – 14.00 Lunch	
	14.00 – 14.45 Plenary Session 4 (one plenary talk)	
	14.50 – 16.00 Biomedical Sensors 4	**14.50 – 16.00 Microwave and Photonic Sensors**
	16.00 – 16.20 Coffee	
	16.20 – 18.10 Industrial Sensing 3	**16.20 – 18.10 Environmental Sensing**
	19.30 – Late. Dinner	

Wednesday	**09.30 – 10.30 Applications**	**09.30 – 10.30 Emerging Sensor Strategies**
	10.30 – 11.00 Coffee	
	11.00 – 12.10 Applications (Contd.)	**11.00 – 12.10 Emerging Sensor Strategies (Contd.)**
	12.20 – 12.45 Closing Remarks	

Proceedings Publications

Table of Content

12 A SIGNAL PROCESSING METHOD TO IMPROVE THE DETECTION ACCURACY OF CO GAS CONCENTRATION IN TDLAS DETECTION

Yingshuai Li[1], Guangdi Mao[2], Qiaofeng Yi[2], Jie Hu[2], Hongmin Zhang[2], **Yanong Ning**[2], **Tongyu Liu**[1]

[1]Laser Institute,Qilu University of Technology (Shandong Academy of Sciences), Jinan, China, [2]Shandong Micro-sensor Photonics Co. Ltd, Jinan, China

15 Ultrahigh-Resolution Whispering Gallery Mode Thermometer based on Silica-Microsphere

Jiaxing Gao[1,2], **Wei Jin**[1,2], Shanshan Li[1,2], **Yu Zhang**[1,2], **Yifan Qin**[1,2], **Zhihai Liu**[1,2]

[1]Key Laboratory of In-Fiber Integrated Optics, Ministry of Education, Harbin Engineering University, Harbin, China, [2]Key Laboratory of Photonic Materials and Device Physics for Oceanic Applications, Ministry of Industry and Information Technology of China, Harbin Engineering University, China.

17 STRAIN MEASUREMENT WITH A HIGH SENSITIVITY BASED ON AN OPTOELECTRONIC OSCILLATOR INCORPORATING CHIRPED FIBER BRAGG GRATINGS

Professor Yunxin Wang[1], Qiming Su[1], **Jing Zhang**[1], Professor Dayong Wang[1], Associate professor Jie Zhao[1], Yu Zhang[1]

[1]School of Physics and Optoelectronic Engineering, Beijing University of Technology, Beijing, China

18 BESSEL GAUSSIAN BEAM CHIP BASED ON METASURFACE

Professor Yiyang Xie[1], **Bo Wu**[1], Chen Xu[1], Baolu Guan[1], Weiling Guo[1]

[1]A.key Laboratory Of Optoelectronics Technology, Ministry Of Education, Beijing University Of Technology, Beijing, China

19 ULTRASENSITIVE VISUALIZED ARTIFICIAL OLFACTORY SYSTEM

Xincun Dou[1]

[1]Center of Materials Science and Optoelectronics Engineering, University of Chinese Academy of Sciences, Beijing, China

20 SOLID ROCKET MOTOR INTEGRITY HEALTH MONITORING BASED ON HIGH PERFORMANCE FEMTOSECOND GRATING ARRAY

Lecturer Yunshan Zhang[1], **Prof. Dayong Wang**[1,2], Associate Professor Jie Zhao[1,2], Professor Yunxin Wang[1,2], Lecturer Jing Zhang[1], Yu Zhang[1]

[1]School of Physics and Optoelectronic Engineering, Beijing University Of Technology, Beijing, China, [2]Engineering Research Center of Precision Measurement Technology and Instruments, Beijing, China

21 MICROWAVE PHOTONIC CHAOTIC RADAR WITH FREQUENCY UP/DOWN CONVERSION CAPABILITY

Yu Zhang[1,2], Prof. Jie Zhao[1,2], Professor Yunxin Wang[1,2], Lecturer Jing Zhang[1], Professor Dayong Wang[1,2]

[1]School of Physics and Optoelectronic Engineering, Beijing University of Technology, , China, [2]Engineering Research Center of Precision Measurement Technology and Instruments, , China

23 Effect of film forming quality on the performance of PbSe detector
YANYAN ZHENG[1]

[1]Hanwei Electronics Group Corporation, Zhengzhou, China

24 MICROWAVE PHOTONIC FILTERING FOR FIBRE OPTIC INTERFEROMETER SENSORS
Miss Wenjing Li[1], Miss Zhuqing Yu[1], Dr Xiansheng Tang[1], Dr Zhaowei Wang[1], Prof Jiasheng Ni[1], **Wei Zhang**[1], Prof Kenneth Grattan[2]

[1]Qilu University of Technology (Shandong Academy of Sciences), Jinan, China, [2]City,University of London, London, United Kingdom

25 DESIGN AND SIMUATION OF A SAW GAS SENSOR FOR DETECTION OF METHANE AND NITRIC OXIDES
Eric Wickens[1]

[1]Munster Technological University, Cork, Ireland

28 ULTRASENSITIVE LONG-PERIOD FIBER GRATING REFRACTIVE SENSOR WITH MICROCAVITIES
Shan Gao[1], **Prof. Jinhui Shi**[1], **Chunying Guan**[1]

[1]Harbin Engineering University, Harbin, China

29 DUAL PARAMETRIC SENSORS BASED ON MULTI-CORE FIBER
Chunying Guan[1], **Prof. Jinhui Shi**[1], **Jing Yang**[1]

[1]Harbin Engineering University, Harbin, China

30 COVALENT/NON-COVALENT RECOGNITION STRATEGIES FOR VISUALIZED SENSING OF TRACE ORGANIC AMINES
Dr. Yuan Liu[1]

[1]Xinjiang Institute Of Physics And Chemistry, Chinese Academy Of Sciences, Urumqi, China

31 VERTICAL CAVITY SURFACE EMITTING LASERS WITH SIO2/ZNS DIELECTRIC DISTRIBUTED BRAGG REFLECTOR
Professor Yiyang Xie[1], Xiaodong Yan, Bo Wu, Baolu Guan, Weiling Guo

[1]key Laboratory Of Optoelectronics Technology, Ministry Of Education, Beijing University Of Technology, Beijing, China

33 HIGH-PERFORMANCE VISUALIZED SENSING MATERIALS: FROM SINGLE MODE TO TRIPE MODE
Baiyi Zu[1]

[1]Center of Materials Science and Optoelectronics Engineering, University of Chinese Academy of Sciences, Beijing, China

34 PEAK WAVELENGTH TRACKING FOR ENHANCED MEASUREMENT SENSITIVITY AND RANGE
IN AN FIBRE OPTIC INTERFEROMETRIC SENSOR

Zhuqing Yu[1], Wenjing Li[1], Dr Duo Chen[1], Dr Jiasheng Ni[1], **Wei Zhang**[1], Kenneth Grattan[2]

[1]Qilu University of Technology (Shandong Academy of Sciences), Jinan, China, [2]City, University of London, London, United Kingdom

35 PEDIATRIC CONSULTATIONS: A MULTI-SENSORY MONITOR FOR OPTIMAL ENGAGEMENT AND DIAGNOSIS

Ifunanya Barbara Onyekwelu[1], Marit Skårsmoen[1], Andreas Andersen Kjernlie[1], Morten Ødegård[1], **Olga Korostynska**[1], Professor Olga Korostynska[1], Professor Peyman Mirtaheri[1]

[1]Oslo Metropolitan University, Oslo, Norway

36 SPECIFIC AND SENSITIVE DETECTION WITH NUCLEIC ACID SENSORS

LUYAN YANG[1]

[1]Center Of Materials Science And Optoelectronics Engineering, University Of Chinese Academy Of Sciences, Beijing, China

37 Sensing the Cyber-Physical: Extended Reality in Smart Manufacturing

Mr Adam Dooley[1], Mr. Denis Moore[1], Mr William O'Brien[1], Mr Mihai Penica[1], Dr Sean McGrath[1], Professor Eoin O'Connell[1]

[1]University Of Limerick, Castletroy, Ireland

38 A DISTURBANCE LOCALIZATION METHOD BASED ON REGION SEGMENTATION AND FNLM ALGORITHM FOR Φ-OTDR

None Wei Shen, None Chengyong Hu, None Ziyi Wei, None Yi Huang, None Chuanlu Deng, **Tingyun Wang**[1], None Qi Zhang, None Sujuan Huang, None Xiaobei Zhang, Wei Shen

[1]Key Laboratory of Specialty Fiber Optics and Optical Access Networks, Shanghai, Baoshan

39 CYBER RANGES – REAL WORLD SKILLS DEVELOPMENT FOR OT & IT CYBERSECURITY EDUCATION

George O Mahony[1], Paudie Walsh[2], Killian Sanceo[3], Dean Brennan[1], Muzaffar Rao[2], Thomas Newe[2], Donna O'Shea[1]

[1]Dept. Computer Science, Munster Technological University, Cork, Ireland, [2]Dept. Electronic & Computer Engineering, University of Limerick, Limerick, Ireland, [3]Airbus Defense and Space Cyber, , France

40 OPTICAL FIBER-BASED SENSOR USING THE LOCALIZED SURFACE PLASMON RESONANCE EFFECT

V.R. Anand[a], Abhijnan Bhat[b], Baljit Singh[b,c], Zhe Wang[a], Zhuochen Wang[a], Anuradha Rout[a], Rayhan Habib Jibon[a], Furong Tian[b,d], **Yuliya Semenova[a]***

[a] Photonics Research Centre, School of Electrical and Electronic Engineering, Technological University Dublin, Grangegorman, Dublin 7, Ireland

[b] School of Food Science & Environmental Health, Technological University Dublin (TU Dublin), Grangegorman, Dublin, D07 ADY7, Ireland

[c] MiCRA Biodiagnostics Technology Gateway, Technological University Dublin (TU Dublin), Dublin, D24 FKT9, Ireland

[d] Nanolab Research Centre, FOCAS Research Institute, Technological University Dublin (TU Dublin), Camden Row, D08 CKP1 Dublin, Ireland

41 A REVIEW OF UNCOOLED THERMAL IMAGER SPECIFICATIONS AND THEIR INFLUENCE ON IMAGER PERFORMANCE

Juan Coetzer[1*], Prof. Joseph Walsh[1]

[1]IMaR Research Centre, Munster Technological University, Tralee, Ireland

42 LEVERAGING DEEP LEARNING FOR RECONSTRUCTION OF CANCER CELLS FROM 3D IR THERMOGRAPHY FOR FASTER CANCER DIAGNOSIS

Suzad Mohammad[1,2], **Dr. Charlie O'Mahony**[1], Dr. Sadia Sharmin[2], Dr. Fahmida Gulshan[3], Dr. Syed A. M. Tofail[1]

[1]Department of Physics, University of Limerick, Limerick, Ireland, [2]Department of Computer Science and Engineering, Bangladesh University of Engineering and Technology, Dhaka, Bangladesh, [3]Department of Materials and Metallurgical Engineering, Bangladesh University of Engineering and Technology, Dhaka, Bangladesh

43 USE OF DEEP LEARNING TECHNIQUES TO CLASSIFY ACOUSTIC EMISSION DATA FROM KNEE JOINTS

Ivan Vatolik[1], Dr Gordon Hunter[1], Dr Nicola Swann[2], Dr Michael Everington[1], Dr Olena Lanets[1,3], Dr Solomiia Liaskovska[1,3], Chinnedu Mbachu[1], Professor Andy Augousti[1]

[1]Kingston University London, [2]University of Surrey, [3]Lviv Polytechnic National University,

44 Utilising Instrumentation to Monitor the Construction of a Large Underground Shaft in Ireland

Ronan Royston, Dr. Ronan Royston, Dr. Declan Phillips

[1]Ward And Burke Construction Ltd. & University Of Limerick, Castletroy, Ireland

45 Laser Structure Based on a Fiber Ring and Peanut-Shaped Whisper Gallery Mode Microresonator

Anuradha Rout[1], Zhe Wang[1], Zhouchen Wang[1], Rayhan Habib Jibon[1], Anand V.R[1], **Yiming Shen Shen**[1], Yuliya Semenova[1]

[1]Technological University Dublin, Grangegorman Lower, Dublin 7, D07 H6K8, Ireland

46 Development of an optical fibre-based plasmonic sensor for specific detection of target biomolecules

Saumyakanti Khatua[1], Ms. Payel Ghosh, Dr. Praneeth NVS, Dr. Gayatri Joshi, Dr. Sharmistha Dutta Choudhury, Prof. Arup Lal Charkraborty, Prof. Sai VV Raghavendra

[1]Indian Institute Of Technology Gandhinagar, Gandhinagar, India

47 RADIO FREQUENCY DIRECTION SENSING ENABLED BY BROADSIDE COUPLED SPLIT RING RESONANTORS

Xiaoguang Zhao[1], Dr. Zhenci Sun[1], Prof. Rui You[2], Dr. Jiahao Zhao[1]

[1]Tsinghua University, Beijing, China, [2]Beijing Information Science and Technology University, Beijing, China

48 MONITORING OF COMPOSITE PRESSURE VESSELS USING SURFACE-APPLIED DISTRIBUTED FIBRE OPTIC SENSORS

Christos Karapanagiotis[1], Marcus Schukar[1], Mathias Breithaupt[1], Katerina Krebber[1]

[1]Bundesanstalt für Materialforschung und -prüfung (BAM), Berlin, Germany

49 PIEZOELECTRIC ENERGY HARVESTING AND SELF-POWERED PRESSURE SENSING WITH HEN EGG WHITE LYSOZYME

Krittish Roy[1], Dr. Charlie O'Mahony[1], Mr. Hema Dinesh Barnana[1], Dr. Sarah Markham[1], Dr. Ehtsham Ul Haque[1], Dr. Syed A. M. Tofail[1]

[1]Department of Physics and Bernal Institute, University Of Limerick, Castletroy, Limerick, Ireland

50 Challenges in Adapting Fiber Optic Sensors for Biomedical Applications

Sahar Karimian[1,2], Dr Muhammad Mahmood Ali[1,2], Dr Dineshbabu Duraibabu[1,2], Dr Waqas Saleem[3], Dr Marion McAfee[1,2], Dr Elfed Lewis[4]

[1]Centre for Mathematical Modelling and Intelligent Systems for Health and Environment (MISHE), Atlantic Technological University, Sligo, Ireland, [2]Department of Mechatronic Engineering, Faculty of Engineering and Design, Atlantic Technological University, Sligo, Ireland, [3]Technological University Dublin, Dublin, Ireland, [4]Optical Fibre Sensors Research Centre, University of Limerick, Limerick, Ireland

51 SENSORS AND ACTUATORS FROM BIODIELECTRICS

Hema Dinesh Barnana[1], Dr Charlie O'Mahony[1], Dr Krittish Roy[1], Dr Ehtsham ul Haq[1], Prof Tofail Syed A.M.[1]

[1]University Of Limerick, Limerick, Ireland

52 GAMIFIED ORTHOSIS FOR MUSCLE REHABILITATION:
ESCAPE SPLINT

Azadeh Hajian[1], Faten Aboalkhair[1], Firdowsa Cige[1], **Prof Olga Korostynska**[1], Morten Ødegård[1], Anne-Marthe Sanders[2]

[1]Oslomet - Storbyuniversitetet, Oslo, Norway, [2]Department of Occupational Therapy, Sunnaas Rehabilitation Hospital, Nesodden, Europe

53 Robust On-Hand Robot-3D Camera Calibration Using Gradient Descent in Noisy Sensor Environments

Evgenii Dushkin[1], Niall O' Mahony[1], Juan Wian Coetzer[1], Anshul Awasthi[1], Prof. Joseph Walsh[1]

[1]Munster Technological University, Tralee, Ireland

54 AUTONOMOUS TEXTILE SORTING USING HYPERSPECTRAL IMAGING

Jessica Lo Faro[a], Olena Lanets[a,b], Solomiia Liaskovska[a,b], Andy T. Augousti[a],* and Olga Duran[a]

[a]Kingston University, London, United Kingdom

[b] Department of Technical Mechanics and Dynamics of Machines, Lviv Polytechnic National University, Lviv, S. Bandery Street 12 Ukraine

55 PIEZOELECTRICITY IN UNPOLED HYDROXYAPATITE CERAMICS

Reena Rasheed[1], Mr Hema Dinesh Bernana[1], Dr Chalie O' Mahony[1], Professor Tofail Syed. A.M.[1], Dr Ehtsham Ul-Haq[1]
[1]University Of Limerick, Castletroy, Ireland

56 Stem Effect Correction Using Machine Learning Technique in Radioluminescence Sensors

H.T. Zubair[1], Dr. Tan Yi Fei[1], Mr. Azmi Basaif[1], Dr. Adebiyi Oresegun[1], Ms. Chuah Kai Wei[3], Ms. Nor HafizahIshak[3], Dr. HM Zin[3], Dr. HA Abdul Rashid[2], Dr. DA Bradley[4]

[1]Faculty of Computing and Informatics, Multimedia University, Jalan Multimedia, Malaysia [2]Fibre Optics Research Centre, Faculty of Engineering, Multimedia University, Jalan Multimedia, Malaysia, [3]Advanced Medical and Dental Institute, Universiti Sains Malaysia (USM), Bertam, 13200, Kepala Batas, Malaysia, [4]Centre for Applied Physics and Radiation Technologies, Sunway University, 46150, Malaysia

58 AN OPTICAL FIBRE SENSOR PROBE FOR OXYGEN MEASUREMENT IN HYPOXIC TUMOURS DURING RADIOTHERAPY TREATMENT

Dr. Sanober Farheen Memon[1], Dr. Carla McDonnell[2], Professor Kevin M. Prise[2], Professor Elfed Lewis[1]

[1]Optical Fibre Sensors Research Centre, University of Limerick, Limerick, Ireland, [2]Patrick G. Johnston Centre for Cancer Research, Queen's University Belfast, Belfast, United Kingdom

60 ONLINE MONITORING AND FAULT DIAGNOSIS SYSTEM FOR FILLING PIPELINE LEAKAGE BASED ON DISTRIBUTED FIBER OPTIC ACOUSTIC SENSING TECHNOLOGY

Guangxian Jin[1]

[1]Shandong Micro-sensor Photonics Ltd., Jinan, China

61 AN EVALUATION OF MODELLING OF PROPAGATION USING COMSOL FOR A SINGLEMODE-MULTIMODE-SINGLEMODE STRUCTURE

Thomas Freir[1], Dr. Arun Kumar Mallik[2], Prof. Yuliya Semenova[1], Prof. Gerald Farrell[1]

[1]Photonics Research Centre, Technological University Dublin, Dublin, Ireland, [2]Tyndall National Institute, Cork, Ireland

62 Application of Low-Power Fiber Optic Demodulation Technology Based on VCSEL Laser and Wireless Monitoring of Coal Mine Roof

Zegong Wu[1], **Lu Cao**[2], Shijie Deng[3], Shoutao Wang[2], Lilei Zhang[1], Guangxian Jin[2], Yanong Ning[2], Tongyu Liu[2]

[1]Laser Institute, Qilu University of Technology (Shandong Academy of Sciences), Jinan, China, [2]Shandong Micro-sensor Photonics Ltd, Jinan, China, [3]Guilin University of Electronic Technology, Guilin, China

63 CHARACTERISATION OF THE FBGS INFINITYSCAN® , A CODE-DIVISION MULTIPLEXING INTERROGATOR FOR PRECISION AND DYNAMIC SCANNING

Prof. Steffen Lochmann

65 THREE-DIMENSIONAL DETECTION OF BURIED DEFECTS USING INFRARED FLASH THERMOGRAPHY: ANALYTICAL FRAMEWORK, SIMULATION AND EXPERIMENTAL VALIDATION

Charlie O'Mahony, Aladin Mani, Joanna Bauer, Christophe Silien, Syed A. M. Tofail

66 On-Site Rapid Detection of Ethidium Bromide Using Ultramicroelectrode Sensors
Marcello Valente[1], Dr. Ian Seymour[1], Mr. Md Ridwan Adib[1], Mr. Tarun Narayan[1], Prof. Valentina Alessandria[2], Prof. Luca Cocolin[2], Prof. Kieran G Meade[3,4], Dr. Alan O'Riordan[1]

[1]Tyndall, Cork, Munster, [2]DISAFA., University of Turin, , Grugliasco, Piemonte, [3]UCD School of Agriculture and Food Science, University College Dublin, , Belfield, D04 V1W8, Dublin, , Dublin, [4]UCD Conway Institute of Biomolecular and Biomedical Research, University College Dublin, , Belfield, D04 V1W8, Dublin, , Dublin

68 Bent optical microfibre sensor and its application for nanonewton force measurement
Qiang Wu[1]

[1]Northumbria University, United Kingdom, Newcastle Upon Tyne, United Kingdom

69 Advancement of Low-power Microwave Sensors for Non-invasive Lactate Monitoring
Alex Mason[1]

[1]Norwegian University Of Life Sciences, Aas, Norway

70 A MULTIMODAL ADAPTIVE DETECTION ALGORITHM FOR OPTICAL FIBER MEMS FABRY-PEROT SENSOR
Jiqiang Wang[1], Zhen Li[1], Lu Cao[2], Lin Zhao[1], Jiqiang Wang[1]

[1]Laser Institute,Qilu University of Technology (Shandong Academy of Sciences), JiNan, China, [2]Shandong Micro-sensor Photonics Ltd, JiNan, China

73 An intelligent optical fiber device integrating sensing, storage, and computing functions
Yiran Feng[1], **Zhihai Liu**[1], Yu Zhang[1], Siying Cheng[1], Xiang Li[1], Yaru Li[1], Wei Jin[1]
[1]Harbin Engineering University, Harbin, China

78 Innovative MIR LASER-, LED- and PD-cascade technologies for sensing
Dr Lars Hildebrandt

79 DEVELOPMENT OF CHINA'S SMART MINES AND UNDERGROUND SPATIOTEMPORAL PERCEPTION DETECTION TECHNOLOGY
Guofa WANG

[1]China Coal Technology & Engineering Group, Beijing 100013, China

80 Intelligent Long Wall Top Coal Caving Mining
Jiachen Wang, Yang Li[1]

[1]China University of Mining and Technology, Beijing, China

81 Early Detection of Pipeline Fractures In Aged Infrastructure in the Water Industry
Matthias Fabian[1], Shailendra Singh[1], Richard Scott[1], Tong Sun[1], Kenneth T V Grattan[1], Heriberto Bustamante[2], Timothy Hill[2], James McCulloch[2]

[1]City St George's, University of London, London, EC1V 0HB, UK
[2]Sydney Water Corporation, Parramatta, NSW 2124, Australia

82 Fiber Optic-Based Thermometry: Evolution and Development Spanning Five Decades
Kenneth T V Grattan[1,2], Tong Sun[1,2], Matthias Fabian[1,2]
[1]Sensors & Instrumentation Centre, City St George's, University of London, London, EC1V 0HB, United Kingdom;
[2]City Optotech Ltd, London, United Kingdom

1: ADLAYER STRUCTURE INNOVATION AND FILM-BASED FLUORESCENT SENSORS

*Yu Fang**

School of Chemistry and Chemical Engineering, Shaanxi Normal University, Xi'an, China,

Plenary Session Two, August 12, 2024, 4:00 PM - 4:45 PM

Abstract – Film-based Fluorescent Sensors (FFSs) represent a crucial option in the realm of developing high-performance sensors for dangerous, toxic, harmful chemicals, biological substances, and radioactive materials. By focusing on aspects such as mass transfer, energy transfer, microenvironment effects, and the utilization rate of sensing units that significantly impact the performance of FFSs, we elaborate on the pivotal role of adlayer structure innovation in the development of FFSs. This encompasses key areas like sensing units design and synthesis, modulation of excited state processes, and optimization of adlayer structures. Furthermore, we delve into innovations in sensor hardware structure and advancements in detection equipment. Drawing from these discussions, we explore the development prospects and major challenges facing FFSs.

***Keywords*:** film-based fluorescent sensors (FFSs); adlayer structures; mass transfer; energy transfer; micro-environment effect

1. OVERVIEW OF FILM-BASED FLUORESCENT SENSORS

Sensors serve as the cornerstone of modern industry and digitalization, playing a crucial role in the Fourth Industrial Revolution driven by artificial intelligence and big data. Sensor technology research has gained significant importance over the years, becoming a key field in which countries worldwide are investing in and competing. However, it is important to recognize that sensor research and development require substantial investments, involve inherent risks, and often have long development cycles.

Unlike traditional gas-sensitive sensors, the key to advancing odor recognition sensors capable of rapidly and highly sensitively detecting hazardous, toxic, harmful chemicals, biological substances, and radioactive materials on-site for critical disease diagnosis lies in the development of sensitive organic thin film materials. This necessitates the rational design and precise preparation methods for creating organic structures on substrate surfaces, along with the implementation of complementary characterization techniques and strategies.

Film-based Fluorescent Sensors (FFSs) represent a cutting-edge advancement in chemical sensing technology, leveraging the sensitivity of excited states of fluorescent substances to detect microenvironment changes. In the realm of sensor innovation, FFSs offer a host of distinctive advantages, including: (1) ample room for innovation and exceptional detection sensitivity; (2) seamless device integration and effortless array formation; (3) no pollution to the testing system, enabling reusability; (4) compact dimensions, low power consumption, no need for radioactive sources, and straightforward structure, enhancing portability and versatility.

As a result of these features, research on FFSs is garnering increasing interest and is positioned as a highly promising next-generation technology for trace detection of harmful substances, following in the footsteps of ion migration spectroscopy.

The fundamental technologies underpinning FFSs primarily revolve around two key areas: (1) advanced techniques for preparing high-performance sensitive materials, and (2) sensor structures, particularly the optical system configurations of the sensors. Original research endeavors are predominantly concentrated on these critical domains. While there is limited scope for hardware structure innovation in FFSs, the primary thrust lies in the innovative fabrication of sensitive thin films.

Presently, the spotlight is on achieving selective and ultra-sensitive detection of organic compounds in the gas phase, with significant implications for public safety, environmental preservation, and human well-being. Unlike previous emphasis on inorganic elements such as NOx and SOx, the detection of such organic substances in the gas phase necessitates specialized organic structures. This poses notable challenges, including: (1) precise control over the preparation of substrate surface organic structures and optimization of sensing performance, (2) mitigation of photochemical degradation of substrate surface organic structures, and (3) autonomous design and optimization of sensor configurations. These focal points represent crucial areas of research in the realm of FFSs.

When it comes to fluorescent-sensitive thin films, their structure typically comprises substrates and sensing elements. The arrangement of sensing elements within the sensitive layer (adlayer) plays a pivotal role in determining the sensing performance and photochemical stability of the thin film. The sensing process typically unfolds through the following steps: (1) target molecules diffuse to the adlayer surface and adsorb, (2) target molecules move within the adlayer, (3) target molecules interact with excited state sensing elements in the adlayer, inducing changes in the film's fluorescence properties, and (4) target molecules desorb from the adlayer. It is evident that the type of sensing elements, substrate chemistry, substrate surface characteristics, and thin film fabrication techniques all influence the overall performance of the film. Therefore, to develop sensitive thin film materials with superior sensitivity, selectivity, and high photochemical stability, a comprehensive approach is essential. This entails focusing on various aspects such as the rational design of sensing elements, thin film preparation methodologies, and the effects of the substrate.

DOI: https://doi.org/10.34961/researchrepository-ul.29266895.v1

2. DEVELOPMENT OF FILM-BASED FLUORESCENT SENSORS

In response to challenges such as the complexity of achieving a balance between high photochemical stability, adaptability, and selectivity in sensitive materials used for detecting explosives and drugs, the monopolization of sensor structures centered around waveguide tubes, and the stringent requirements for system technology integration, stability, and weather resistance, a comprehensive research approach has been undertaken. This approach includes the design and synthesis of sensing units, innovative thin film preparation, sensor structure design, system technology integration, and equipment development.

Through dedicated efforts, an all-encompassing and distinctive thin film fluorescent sensing technology system has been created, which is distinguished by the utilization of small molecule compounds as sensing active materials and layered sensor structures. The advancements include the development of explosive single-mode, drug single-mode, and explosive/drug dual-mode detection technologies, complemented by the appropriate detection equipment.

2.1 Sensing film fabrication

Sensitive films are at the heart of FFS technology, and the innovative preparation and high-performance characteristics of these films play a crucial role in determining the advancement of FFS technology. Over the past two decades, the author's team has addressed the challenging balance between the photochemical stability and sensing performance of conventional sensitive film materials by developing various strategies for creating fluorescent sensitive films. These films are characterized by small molecule fluorescent materials and finely controlled adlayer structures.

Film Formation through Chemical Assembly：One of the key strategies employed is the formation of chemical monolayer assembly films. This involves chemically bonding polycyclic aromatic hydrocarbons to the substrate surface using flexible connecting arms. By leveraging the excited state properties of these materials and the influence of the connecting arm conformation on the microenvironment, the team has successfully developed high-performance fluorescent sensitive films for detecting explosive materials like TNT and nitroaromatic compounds such as picric acid. This approach has unveiled the "connecting arm layer shielding effect/enrichment effect." Additionally, by utilizing conjugated oligomers as sensing units and implementing surface chemical bonding, the team has achieved a synergistic effect combining the "signal amplification effect" of large conjugated units with the benefits of chemical assembly. The introduction of environment-responsive side-chain structures has further expanded the innovative space for creating chemical assembly films with conjugated oligomers as sensing units. This has led to the achievement of sensitivity and response speed records for TNT detection at the 10^{-15} mole level, enabling high-performance detection of various substances in water, including nitromethane, nitrobenzene, black powder, Octogen, and more.

Film Formation through Gel Mediation: By capitalizing on the diverse network structure characteristics of molecular gels, the team has developed highly permeable fluorescent sensitive film materials through the design and synthesis of small molecule fluorescent gelators. This approach has effectively addressed issues such as mass transfer difficulties and low utilization of sensing units commonly encountered in traditional physically coated films. The result is a significant improvement in film response speed, response reversibility, and signal-to-noise ratio, enabling high-sensitivity, high-selectivity, and rapid reversible detection of typical explosives, drug simulants, nerve agent simulants, and other substances.

Combination Design Film Formation: To address the gas-phase detection challenges posed by highly volatile liquid explosives (triacetone triperoxide, TATP, and diacetone diperoxide, DADP) and drugs, the author's team has innovatively designed and synthesized fluorescent sensing units with non-planar structures. By employing different fabrication approaches such as solution assembly, Langmuir-Blodgett (L-B) film assembly, and substrate-induced assembly, the team has successfully developed a diverse range of fluorescent sensing films enriched with "molecular channels" within the adlayer, which is expected to integrate chromatographic effects, capillary condensation, and the microenvironment sensitivity of the excited state of sensing units, enabling high-performance sensing. This strategy has facilitated successful detection of extremely challenging explosives and drugs such as "Mother of Satan" (TATP, DATP), methamphetamine, fentanyl, and more.

Film Formation through Interface-Constrained Dynamic Condensation: In response to the significant challenges posed by non-uniform film structures and the intricate control of adlayer structures due to substrate effects and "coffee ring" phenomena, the team has engineered a series of structurally complete, flexible, self-standing yet durable nanoporous films with adjustable thickness ranging from tens to hundreds of nanometers. Through the innovative approach of interface-constrained dynamic condensation and the design and synthesis of low molecular weight building blocks, these self-standing, self-healing films exhibit exceptional sensitivity and reversibility in detecting a wide range of substances including formic acid, HCl, ammonia, hydrazine hydrate, ozone, ClO_2, and more.

2.2 Hardware structure innovation

Hardware structures are necessaries for sensitive materials to showcase their full potential and become sensors with practical application value. Addressing the challenges of structural looseness, high power consumption, and difficulty in miniaturization faced by front-surface measurement systems in commercial fluorescence instruments, as well as the dominance of patented waveguide-based fluorescence measurement technologies, a novel axial arrangement of layered thin film sensor structures was developed. This innovative design includes components such as light sources, narrow-band filters, sample chambers, sensing units, broad-band filter arrays, and light signal collection units, resulting in patents being granted in both China and the United States.

Compared to commercial instruments and waveguide structures, the layered structure offers superior integration, enhanced stability, and reduced power consumption. The breakthrough in hardware structure holds significant importance for advancing the development of new FFSs and sensor arrays based on FFSs.

2.3 Development of FFSs and related detectors

By optimizing pairing of optical components, developing

low-noise power supply systems, enhancing weak signal collection, and amplification circuits, utilizing layered sensor structures, and incorporating newly developed sensitive thin films, a range of high-performance explosive sensors, drug sensors, explosive/drug array sensors, and corresponding explosive single-mode, drug single-mode, and explosive/drug dual-mode detectors with fully independent intellectual property rights have been successfully engineered (refer to Figure 1). This achievement has led to the establishment of a comprehensive explosive/drug detection technology system and the inception of Shenzhen Lijian Defense Technology Co., Ltd., a specialized company focused on the research, production, and distribution of chemical sensors.

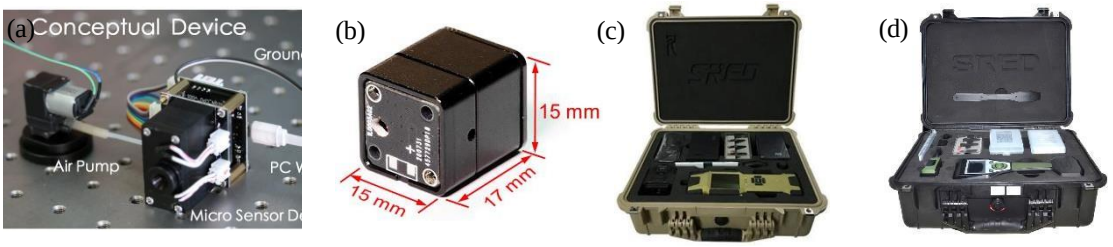

Figure 1. Examples of different types of explosive/drug sensors and various models of detectors.

Note: (a) Conceptual explosive/drug dual-function FFSs; (b) Commercial explosive FFSs; (c) FFSs-based SRED-EPI type explosive detector; (d) FFSs-based SRED-I type drug detector

3. RESEARCH PROSPECTS OF FILM-BASED FLUORESCENT SENSORS

Miniaturization, intelligence, and multi-functionalization stand out as pivotal trends in sensor development. With the emergence of FFSs, focusing on diversifying types, bolstering anti-interference capabilities, and enhancing operational stability are key areas for future advancement. It is imperative to recognize that despite the numerous advantages of FFSs, challenges such as suboptimal photochemical stability in thin-film devices, multiple interferences in sensing processes, and inconsistent sensing performance persist. Therefore, continuous efforts are essential in refining sensor unit structure design, controlling excitation state processes, advancing interface engineering, selecting optimal device fabrication methods, and improving advanced multidimensional signal acquisition and processing techniques.

Moreover, the rapid evolution and integration of artificial intelligence and big data technologies present unprecedented opportunities for sensor research, alongside imposing unparalleled demands. Essentially, research on FFSs should transcend mere detection of hazardous substances and instead actively cater to the pressing need for novel sensors in non-invasive disease diagnosis through volatolomics, as well as in remote health management. The development of FFSs technology capable of analyzing complex samples like exhaled breath, body odor, and bodily volatile compounds for wearable, real-time, in-situ, and online detection is indispensable. Consequently, the advancement of FFSs will encounter heightened challenges, necessitating integrated approaches encompassing enrichment, separation, and detection as pivotal solutions.

In conclusion, FFSs exhibit vast application potential and significant market opportunities, yet they confront substantial hurdles. Leveraging the exceptional design flexibility rooted in organic structures, the high sensitivity of sensing performance, the integrability within hardware structures, and the portability in FFSs utilization, ongoing research in FFSs will play an increasingly pivotal role in addressing major national infrastructure needs and ensuring public health security. Chemical researchers, particularly physical chemists specializing in interfacial concerns, will assume an increasingly crucial role in driving these advancements forward.

ACKNOWLEDGMENTS

I am grateful for the continuous financial support provided by the Ministry of Science and Technology, the National Natural Science Foundation of China, the Ministry of Education, the Science and Technology Department of Shaanxi Province, and Shaanxi Normal University. I would like to extend my special thanks to my collaborators both at home and abroad and all my students and colleagues who have contributed to this project.

FUNDING STATEMENT

This work was supported by the Ministry of Science and Technology of China (2022YFA1205502, and the 111 project B14041), the National Natural Science Foundation of China (22132002, 21820102005) and the Basic Science Center (Chemistry) of Shaanxi Province.

REFERENCES

[1] Y. Shu, Y. Luo, H. Wei, L. Peng, J. Liang, B. Zhai, L. Ding, Y. Fang, **Fabrication of large-area multistimulus responsive thin films via interfacially confined irreversible Katritzky reaction,** Angew. Chem. Int. Ed., 2024, e202402453.
DOI: https://doi.org/10.1002/anie.202402453

[2] K. Liu, J. Zhang, Q. Shi, L. Ding, T. Liu and Y. Fang, **Precise manipulation of excited-state intramolecular proton transfer via incorporating charge transfer toward high-performance film-based fluorescence sensing,** J. Am. Chem. Soc., 2023, 145, 7408-7415.
DOI: https://pubs.acs.org/doi/10.1021/jacs.2c13843

[3] J. Zhang, Z. Shi, K. Liu, Q. Shi, L. Yi, J. Wang, L. Peng, T. Liu, M. Ma and Y. Fang, **Fast and selective luminescent sensing by Langmuir–Schaeffer films based on controlled assembly of perylene bisimide modified with a cyclometalated Au^{III} complex,** Angew. Chem. Int. Ed., 2023, 62, e202314996.

DOI: https://doi.org/10.1002/anie.202314996

[4] R. Huang, C. Wang, D. Tan, K. Wang, B. Zou, Y. Shao, T. Liu, H. Peng, X. Liu and Y. Fang, **Single-fluorophore-based organic crystals with distinct conformers enabling wide-range excitation-dependent emissions,** Angew. Chem. Int. Ed., 2022, 61, e202211106.
DOI: https://doi.org/10.1002/anie.202211106

[5] Z. Wang, X. Gou, Q. Shi, K. Liu, X. Chang, G. Wang, W. Xu, S. Lin, T. Liu and Y. Fang, **Through-space charge transfer: A new way to develop a high-performance fluorescence sensing film towards opto-electronically inert alkanes,** Angew. Chem. Int. Ed., 2022, 61, e202207619.
DOI: https://doi.org/10.1002/anie.202207619

[6] X. Chang, S. Lin, G. Wang, C. Shang, Z. Wang, K. Liu, Y. Fang, P. J. Stang, **Self-assembled perylene bisimide-cored trigonal prism as an electron-deficient host for C_{60} and C_{70} driven by "like dissolve like"**, J. Am. Chem. Soc., 2020, 142, 15950-15960.
DOI: https://pubs.acs.org/doi/10.1021/jacs.0c06623

[7] X. Chang, Z. Zhou, C. Shang, G. Wang, Z. Wang, Y. Qi, Z. Y. Li, H. Wang, L. Cao, X. Li, Y. Fang and P. J. Stang, **Coordination-driven self-assembled metallacycles incorporating pyrene: Fluorescence mutability, tunability, and aromatic amine sensing,** J. Am. Chem. Soc., 2019, 141, 1757-1765.
DOI: https://doi.org/10.1021/jacs.8b12749

[8] K. Liu, C. Shang, Z. Wang, Y. Qi, R. Miao, K. Liu, T. Liu and Y. Fang, **Non-contact identification and differentiation of illicit drugs using fluorescent films,** Nat. Commun., 2018, 9, 1695.
DOI: https://doi.org/10.1038/s41467-018-04119-6

5: CONTRACTION OF FLUORESCENT COMPOUNDS EXHIBITING STRONG LUMINESCENCE AND HIGH PHOTOCHEMICAL STABILITY FOR VOC SENSING

Zhijie Zhou, Rongrong Huang, Yangtao Shang, Haonan Peng *

School of Chemistry and Chemical Engineering, Shaanxi Normal University, Xi'an, Shaanxi 710119 (P. R. China)

Applications Cont., EM009, August 14, 2024, 11:00 AM - 12:10 PM

Abstract – Sensors, as core components of information technology, are crucial for data acquisition and are widely recognized for their technological significance and expansive market potential. Film-based fluorescence sensing stands out among various technologies for its exceptional sensitivity, selectivity, and adaptability, making it an ideal candidate for trace substance detection. This technology, particularly through the use of fluorescent units exhibiting twisted intramolecular charge transfer (TICT) properties, shows remarkable sensitivity to microenvironmental changes. However, TICT can also quench fluorescence, thereby diminishing the units' photostability. To address this, we employed theoretical models to integrate ring strain and steric hindrance, leading to the development of a new series of highly luminescent fluorescent derivatives. These derivatives demonstrate enhanced photostability and are capable of sensitively detecting gaseous substances, including triacetone triperoxide (TATP).

Keywords**:** fluorescence sensing; intramolecular charge transfer; triacetone triperoxide

1. INTRODUCTION

Sensors serve as the origin of data collection and are essential core components of information technology, noted for their high technological content and broad market prospects. Film-based fluorescence sensing, because of its excellent sensitivity, selectivity, and adjustability, is seen as the most promising micro-trace substance detection technology and has evolved into a multidisciplinary frontier hot spot focusing on interfacial phenomena and principles in chemistry, physics, and materials science. The core component of a film-based fluorescence sensor is the fluorescent sensing film, typically composed of a film substrate and a fluorescent active layer consisting of sensing units. Unlike homogeneous systems, film-based fluorescence sensing involves more complex interfacial interactions. During sensing, interactions occur between the sensing units and analyte molecules, altering the energy changes during the luminescence process of the sensing units, resulting in changes in fluorescence intensity, lifetime, and emission wavelength. Traditional fluorescence sensing systems are mainly designed based on the specificity recognition mode similar to that between antibodies and antigens, where the sensing unit and the target analyte have high specificity and selectivity at the interaction sites and energy levels. However, for analytes lacking photoelectric activity, this highly specific sensing recognition faces significant limitations.

The rapid development of fluorescence sensing technology demands sensing units that exhibit higher brightness and photostability. Fluorescent units with TICT properties are extremely sensitive to microenvironment polarity. These molecules display a polarized structure in their ground state; however, upon photoexcitation, the molecular dipole moment increases, accompanied by the rotation of internal groups, transitioning from a locally excited (LE) state to a lower energy ICT state. Research has shown that the TICT process often quenches fluorescence and significantly reduces the photostability of the fluorescent units. Through theoretical calculations, we have discovered that incorporating ring strain and steric hindrance into the structural design of these fluorescent units effectively prevents the formation of the TICT state upon photoexcitation, thereby significantly enhancing their fluorescence intensity and photostability. Based on this strategy, we have designed and synthesized a series of fluorescent derivatives with intramolecular charge transfer properties and high luminescence efficiency, achieving sensitive gaseous detection of liquid explosives like TATP.

1.1. Reversible fluorescence monitoring of TATP in a vapor phase

Naphthalene diimide (NDI), a prototypical electron-deficient compound, exhibits excellent thermal stability, strong electron affinity, antioxidative properties, high charge carrier mobility, low molecular weight, and good solubility, making it extensively utilized in optoelectronics and biomedical fields. Utilizing NDI as the core fluorescent unit, we enhanced the luminescence efficiency and solubility of the compound by modifying it with nitrogen-containing heterocyclic butane. This modification led to the design and synthesis of DNNDI, a fluorescent compound characterized by intramolecular charge transfer properties. The compound was applied as a coating on filter paper to create a fluorescent sensing film with outstanding sensing performance. Our custom-built gaseous sensing platform demonstrated that this film could specifically detect acetone, enabling its use for trace-level sensing of the liquid explosive TATP, with a detection limit as low as 0.5 μg/mL. Remarkably, this sensing process was unaffected by common household products and volatile organic compounds (VOCs), allowing clear differentiation between the target and interfering signals. Additionally, the film facilitated the rapid visual detection of trace amounts of TATP.

DOI: https://doi.org/10.34961/researchrepository-ul.29267114.v1

1.2. Dual-phase emission AIEgen with ICT properties for VOC chromic sensing

Pyrene and its derivatives represent a quintessential class of polycyclic aromatic hydrocarbons characterized by large planar conjugated systems, high fluorescence quantum yields, long fluorescence lifetimes, ease of forming exciplexes, and monomer state emission sensitivity to polarity, rendering them highly promising for constructing high-performance fluorescent sensors. However, pyrene derivatives typically exhibit significant aggregation-induced quenching (AIQ) effects in aggregated and solid states, impeding their practical applications. The AIQ effect describes the scenario where these fluorescent molecules exhibit high fluorescence quantum yields in solution as monodispersed states, but their emission intensities significantly decrease or even disappear in aggregated or solid forms. This quenching occurs as molecules aggregate to form exciplexes, dissipating energy through various non-radiative processes. Additionally, due to photobleaching, pyrenes possess poor photochemical stability in aggregated or solid states. Consequently, designing and synthesizing pyrene-based fluorescent compounds that exhibit strong luminescence and high photochemical stability in both solution and solid states remains a challenge.

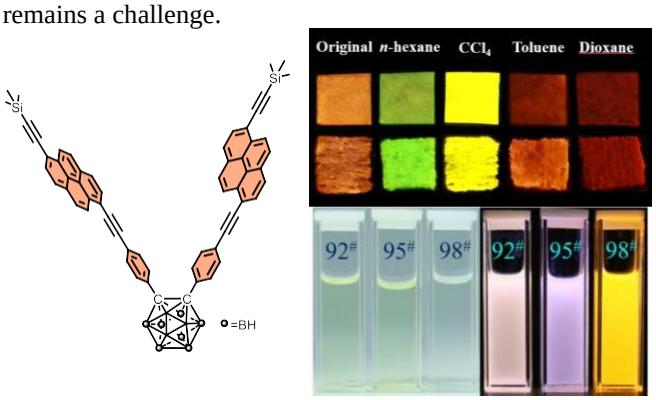

Figure 1. Molecular structure and fluorescence images of AIEgen (CB-PY). The pictures next to the structure are its fluorescence images (up) CB-PY based on test strips with filter paper and cotton cloth as substrates (~0.5 cm ×0.5 cm) before and after dipping in different VOCs, (bottom) Fluorescence emission spectra of the (a) pure gasolines (92#, 95#, 98#) and (b) 92#, 95#, and 98# gasolines under visible light and UV light (365 nm) and (d) 92#, 95#, and 98# gasolines with CB-PY under visible light and UV light (365 nm).

Carboranes, a class of atomic cluster compounds composed of boron and carbon, are readily functionalizable and exhibit excellent thermal and chemical stability. Notably, it has been discovered that introducing aromatic units into the C-C bonds of carboranes can yield derivatives exhibiting aggregation-induced emission (AIE) properties. Furthermore, due to the inherent electron-deficient nature of the boron clusters, carboranes can act as electron acceptors in solvent polarity-sensitive intramolecular charge transfer (ICT) systems. However, in solution, the ICT fluorescence of excited-state carborane derivatives is often quenched due to vibrations in the C-C bonds.

Motivated by this research background, we have developed a novel carborane-pyrene fluorescent molecule (CB-PY), where the carborane segment acts as the electron acceptor and the pyrene unit as the electron donor. The compound CB-PY exhibits excellent photochemical stability and ICT characteristics, emitting strong fluorescence in both solution and solid states. Experimental and theoretical calculations indicate that two large pyrene-derived substituents on the carborane C-C bonds significantly hinder non-radiative energy dissipation in solution, enhancing fluorescence emission. Leveraging the unique photophysical properties of CB-PY, we explored its application in the visual differentiation of various VOCs in both solution and film states.

1.3. Single-fluorophore-based organic crystals with distinct conformers enabling wide-range excitation-dependent emissions

For complex sample analysis, such as disease diagnostics and precision agriculture, constructing film-based fluorescent sensor arrays with interactive response characteristics offers unique advantages and broad application prospects. Such sensor arrays require sensing units that can interact differentially with various components, generating sufficient signal diversity and interactive responsiveness to provide rich fingerprint identification information. However, conventional sensing units typically only offer low-dimensional data such as intensity values, which limits their accuracy in differentiating structurally similar analytes. Therefore, enhancing the multidimensional response recognition signals of sensing units is key to improving their discriminative ability in complex sample analysis. Ideally, a sensor array should comprise a single sensing unit, creating what is termed a virtual sensor array, and utilize this unit to provide ample interactive response recognition information for differentiating multiple target analytes. To this end, we have designed and synthesized a class of fluorescence probes based on excitation wavelength-dependent luminescence. Employing *o*-carborane as an electron-accepting segment with three-dimensional structural features and high rotational flexibility, we constructed a D-π-A molecular system. By modulating two rotational angles (α and β) within the structure, we endowed the molecule with diverse conformations, thus developing a universal design strategy for multicolor luminescent materials with excitation wavelength dependency. By altering the excitation wavelength, different emission spectra are obtained, thereby adding a temporal dimension to the sensing information. Additionally, the sensing signals under various excitation wavelengths can self-calibrate, effectively mitigating noise interference from factors such as instrumentation and temperature.

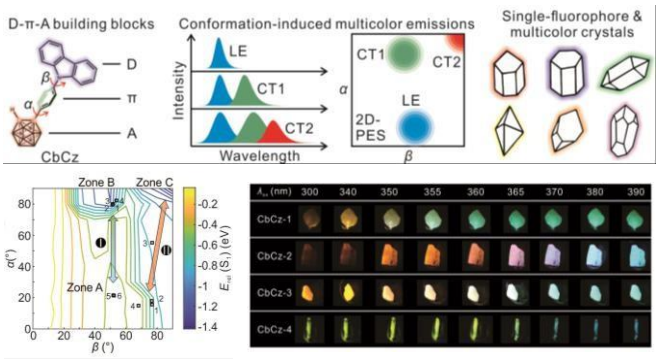

Figure 2. Molecular structure of CbCz. Illustration of the excited-state potential energy surface of CbCz and corresponding multiple emission bands. Illustration of using

the *o*-carborane-based single fluorophore to induce multicolor emissions in crystals. Fluorescence images of crystals CbCz-1, CbCz-2, CbCz-3 and CbCz-4 under illumination of different UV-lights. Illustration of the two pathways, Path I and Path II, on the S1 PES of CbCz in chloroform.

1.4. Unlocking multicolor emissions in the crystalline state through dimerization and configurational transformation of a single fluorophore

Molecular materials with color-tunable emissions have been explored through methods like modifying cocrystal or coassembly compositions, regulating their packing conformations, and adjusting the energy transfer processes between various components. However, the emission durability of multifluorophore materials often fails to meet practical expectations. This shortfall is attributed to potential spectral instability, which arises from the varying photostability of different types of fluorophores, and to potential aggregation-caused quenching resulting from strong intermolecular interactions. Furthermore, energy transfer mechanisms from short-wavelength to long-wavelength fluorophores can induce quenching of short-wavelength emissions. This complicates the process of color tuning, presenting a significant challenge in achieving the desired spectral outcomes. These shortcomings significantly limit their practical applications. Consequently, there is a growing demand for single-fluorophore-based multicolor emissive materials.

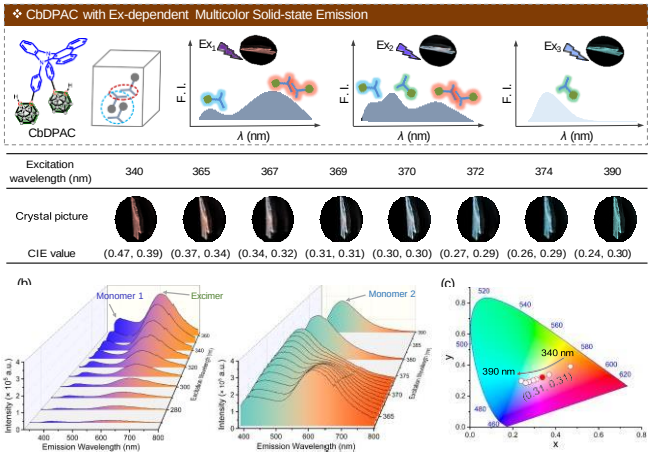

Figure 3. (a) Fluorescence images of the CbDPAC crystal under illumination at various wavelengths and the corresponding Commission International de l'Eclairage (CIE) values. (b, c) Fluorescence spectra of the CbDPAC crystal recorded at various excitation wavelengths. (d) CIE coordinate diagram of crystal CbDPAC under illumination at various wavelengths. The red dot represents the CIE value under the excitation wavelength of 369 nm. Notes: monomer 1 and monomer 2 refer to stable and metastable conformational isomers, respectively.

We have introduced *N,N′*-diphenyl dihydrodibenzo[*a,c*]-phenazines (DPAC), augmented with two *o*-carboranyl units, to create a novel fluorophore CbDPAC, which represents probably the first single-fluorophore system featuring three emission centers in the crystalline phase, formed through the blend of intramolecular conformational changes and intermolecular interactions. TheCbDPAC crystal exhibits excitation wavelength-dependent multicolor emissions characterized by three emission bands peaking at 405, 470, and 620 nm, respectively. We have unveiled the underlying molecular mechanisms responsible for these unique photophysical properties and demonstrated conceptual applications of CbDPAC in advanced encryption and information storage.

2. CONCLUSIONS

While significant progress has been achieved in the construction and application of film-based fluorescence sensor, several challenges and opportunities remain to be addressed and explored in this field. First, there is a need for a deeper understanding of the exact mass transfer mechanisms involved in film sensing. Prevailing diffusion models, such as Knudsen diffusion and molecular diffusion theories, focus mainly on the physical characteristics of analyte molecules, such as the gas constant and molecular weight, while overlooking the chemical properties of the molecules. Second, comprehensive investigations are urgently needed to gain profound insights into the development of superior sensing films. This entails the synthesis of novel sensing molecules and the construction of active layers with well-defined molecular channels. These aspects form the foundation for the preparation and application of FFSs. In-depth studies in these areas will enable the design and fabrication of advanced sensing films with enhanced performance and sensitivity. Lastly, the design and integration of robust environmental sensors pose a major challenge. Real samples containing target analytes in complex mixtures can be prone to interference from other compounds, thereby affecting the accuracy and selectivity of the sensing process. Consequently, the development of grid environmental sensors with high selectivity is an emerging approach that requires dedicated efforts and attention.

ACKNOWLEDGMENTS

We appreciate the financial support from the National Natural Science Foundation of China (No. 22272101), and the Program of Introducing Talents of Discipline to Universities ("111" project, No. B14041). The Scientific Research Plan of Shaanxi Province of China (Nos. 2021TD-18, 2021KJXX-14) and the Fundamental Research Funds for the Central Universities (No. GK202305001) are acknowledged.

REFERENCES

[1] H. Peng, L. Ding, Y. Fang, **Recent Advances in Construction Strategies for Fluorescence Sensing Films**, J. Phys. Chem. Lett., 15, 2024, pp. 849-862.

[2] Y. Shao, R. Huang, G. Jiang, Q. Shi, H. Wei, G. Wang, W. Chi, H. Peng, X. Liu, Y. Fang, **Unlocking Multicolor Emissions in the Crystalline State through Dimerization and Configurational Transformation of a Single Fluorophore**, Chem. Mater., 36, 2024, pp. 3223–3232.

[3] R. Huang, C. Wang, D. Tan, K. Wang, B. Zou, Y. Shao, T. Liu, H. Peng, X. Liu, Y. Fang, **Single-Fluorophore-Based Organic Crystals with Distinct Conformers Enabling Wide-Range Excitation-Dependent Emissions**, Angew. Chem. Int. Ed. 2022, e202211106.

[4] X. Gao, R. Huang, W. Fang, W. Huang, Z. Yin, Y. Liu, X. Huang, L. Ding, H. Peng, Y. Fang, **A Portable Fluorescence**

Sensor with Improved Performance for Aniline Monitoring, Adv. Mater. Interfaces, 2022, 9, 2201275.

[5] W. Fang, K. Liu, G. Wang, Y. Liang, R. Huang, T. Liu, L. Ding, J. Peng, H. Peng, Y. Fang,. **Dual-Phase Emission AIEgen with ICT Properties for VOC Chromic Sensing**, Anal. Chem. 93, 2021, 24, 8501–8507.

[6] R. Huang, M. Li, D. Lin, Y. Shao, C. Shang, Q. Liu, G. Liu, N. Li, R. Miao, H. Peng, Y. Tang, Y. Fang, **A fluorescent film sensor for high-performance detection of Listeria monocytogenes via vapor sampling**, Aggregate, 2022, e203.

6: OPTIMIZATION OF SENSOR PLACEMENT FOR GAS LEAK DETECTION IN COMMERCIAL AREAS

Sui Zhewen [a], *Yuan Xiaobing* [b, *], *Ye Fangqi* [b]

[a] College of Mechanical and Electronic Engineering, China University of Petroleum, Qingdao, China
[b] Shenzhen Urban Public Safety Technology Institute, Shenzhen,China,

Environmental Sensing, EM010, August 13, 2024, 4:20 PM - 6:10 PM

Abstract – This paper investigates the optimization problem of sensor placement based on distance measurements for acoustic underwater target localization. A sensor placement method based on distance measurements is proposed to enhance the accuracy and reliability of underwater target localization.

Keywords**:** Gas leak detection;Sensor placement optimization; Particle swarm algorithm;CFD simulation

1. INTRODUCTION

In commercial enclosed areas, the safety risks associated with natural gas leaks are particularly significant. Natural gas, primarily composed of methane, is highly flammable and explosive. At certain concentrations, when mixed with air, natural gas forms a combustible mixture that can explode upon contact with an ignition source. Moreover, since natural gas is colorless and odorless in its raw state, leaks are often difficult to detect timely. To enhance detection, artificially added sulfur compounds such as hydrogen sulfide can serve as odor indicators, although this method is not always effective in certain situations. Furthermore, natural gas leaks can also lead to a reduction in oxygen levels in enclosed spaces, posing a risk of suffocation. Although natural gas itself is not very toxic, trace harmful substances it carries, such as carbon monoxide, can also pose a health threat with prolonged exposure.

Existing optimizations of sensor placements do not specifically address indoor gas leak detection sensors. Gas leak detection sensors are particularly important due to their high safety requirements. This paper explores a sensor placement optimization method that combines greedy algorithms with Particle Swarm Optimization (PSO). The greedy algorithm provides initial optimization based on given risk values, setting the stage for the PSO, reducing subjective assessments of the number of sensors needed, and helping the PSO avoid local optima. The PSO ultimately addresses the challenges posed by the varying shapes of walls in commercial buildings and the complex paths of gas diffusion in enclosed spaces. Using the Gaussian plume diffusion model to simulate gas diffusion, it designs a layout plan constrained by specified detection times, concentration levels, and maximum placement distances, verifying its accuracy.

A sensor placement method based on discrete particle swarm optimization algorithm is developed by Kong, Cai, Liu, Zhu, Liu + 4 another authors [1], which evaluates fault propagation and sensor response time through a simulation model, thereby achieving fast convergence speed and optimization results. Furthermore, their method shows significant advantages in reducing the number of sensors and data redundancy, especially in a real case application of a subsea blowout preventer control system, demonstrating the practicality and effectiveness of their method.

Some literature reveals various methods and approaches toward optimizing sensor placement for environmental monitoring, highlighting the dynamic nature of this field. A paper by Aydin, Hagedooren, Rutten, Delsman, Essink + two another authors explored the optimization of salinity sensor placement within a polder network, employing a greedy algorithm [2]. The study primarily focused on the estimation of unmeasured salinity levels in main polder channels, using root mean square error (RMSE) as a metric for "goodness of fit". Their method integrated a hydrodynamic and salt transport model with principal component analysis (PCA), which proved effective in reducing model complexity while capturing significant salinity dynamics across the network. The placement of just three optimally positioned sensors, determined by the algorithm, was shown to robustly model and measure errors, approaching a global optimum identified through exhaustive search methods.

In exploring optimal sensor placement for structural health monitoring, significant advances have been made to refine methodologies that balance sensor efficiency and comprehensive coverage. Notably, Liu, Yan, Soraes delved into various sensor placement strategies tailored for modal identification, introducing an innovative minimal root mean square (Min-RMS) algorithm [3]. This method stands out by minimizing the RMS value over the mass-weighted modal assurance criterion (MMAC), which optimally positions sensors to capture critical modal information while mitigating measurement noise and model uncertainty. Their approach employs a thorough analysis involving both cantilever beams and jacket-platform models, providing a robust evaluation of sensor performance across multiple criteria, including modal orthogonality and system independence.

In the domain of sensor placement and maintenance optimization within process networks, the recent study I reviewed introduces a mathematical programming model that strategically identifies the optimal measurement locations and the precise number of redundant and spare sensors required for an effective corrective maintenance program which proposed by Ko and Chen [4]. This model is designed to maximize system availability while adhering to predefined constraints on life-cycle costs and the precision of estimators. To solve this complex optimization problem, the researchers employed genetic algorithms, leveraging their evolutionary capabilities to efficiently navigate the solution space. This

DOI: https://doi.org/10.34961/researchrepository-ul.29269250.v1

method's efficacy was validated through comprehensive case studies, demonstrating its practical applicability and robustness in enhancing maintenance strategies and system reliability.

In the field of mobile sensor networks for target tracking, the study by Martínez and Bullo provides a comprehensive examination of optimal sensor placement and motion coordination strategies [5]. Their work focuses on the determinant of the Fisher Information Matrix to evaluate the optimal configuration of range sensors for both 2D and 3D cases, achieving a global optimum in the 2D scenario. They developed decentralized motion coordination algorithms that effectively direct the mobile sensor network towards an optimal arrangement, which is crucial for enhancing the performance of target tracking systems, particularly when using an extended Kalman filter. This research is pivotal as it bridges the gap between theoretical sensor placement and practical application in dynamic environments, offering valuable insights into decentralized control and the sensitivity maximization of sensor networks.

In the context of my dissertation on sensor placement for 3-D time-of-arrival target localization, the study by Xu, Ou, and Wu presents a comprehensive exploration of optimal sensor deployment strategies using the A-optimality criterion [6]. This criterion minimizes the trace of the inverse Fisher Information Matrix (FIM), facilitating enhanced estimation accuracy in 3D spaces. Their methodological innovation introduces two novel closed-form solutions for determining optimal sensor geometries, addressing both uniform and non-uniform measurement noise scenarios without constraints on sensor number, elevation, or target range.

Moreover, In the field of sensor placement for multistatic narrowband systems, Kreucher's work provides significant insights into optimizing the deployment of a sensor constellation to enhance target localization and tracking efficiency [7]. This study uniquely applies the posterior Cramér-Rao lower bound (PCRLB) to compute and minimize localization errors based on sensor positions within a non-Gaussian and nonlinear pixelated sensor model. Notably, the research incorporates practical elements like antenna beam patterns and target impulse responses to tailor sensor placements, significantly advancing the theory into applicable strategies for real-world scenarios.

In examining advancements in underwater target localization, the study by Moreno-Salinas, Pascoal, and Aranda offers a pivotal contribution through its exploration of optimal sensor placement for acoustic underwater target positioning using range-only measurements [8]. Their approach maximizes the Fisher Information Matrix (FIM) determinant to achieve the best possible estimator precision for 3D target positioning. This method is particularly notable for its use of a theoretical estimation framework to calculate the optimal sensor configurations, with variations considered for specific operational constraints like sensor placement and target depth.

2. METHODS AND PROCEDURES

To optimize the placement of sensors while reducing computational load and increasing computational speed, the blueprint is segmented into different zones based on varying risk values. A combined approach using greedy algorithms and PSO is employed for optimizing sensor positions. The greedy algorithm provides preliminary optimizations that serve as initial conditions for the subsequent PSO. The results are obtained through the PSO, which incorporates the Gaussian plume diffusion model to simulate gas dispersion effectively.

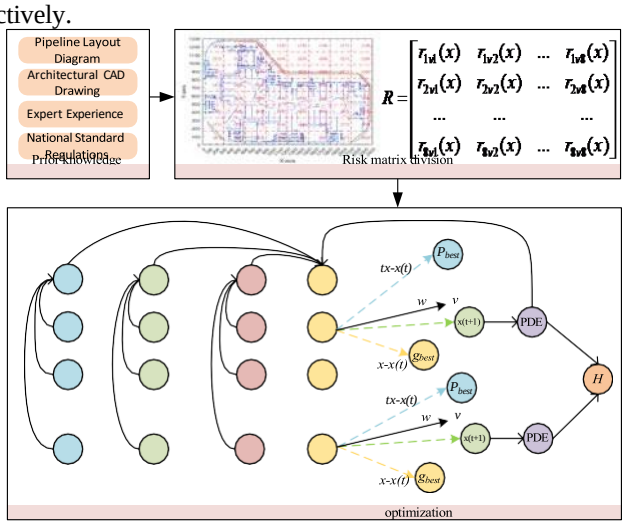

Figure 2-1: Overall Methodology Diagram

2.1. *Drawing Pre-processing*

In this study, image processing techniques are employed to pre-process the floor plans of commercial areas. Using edge detection and image segmentation techniques, key infrastructures such as walls and pipelines are identified, setting spatial constraints for the sensor layout. In the MATLAB environment, the floor plans are divided into an 8x8 grid, allowing detailed risk assessments for each cell. A comprehensive risk matrix is constructed, providing crucial data for the optimization of sensor placement.

$$R = \begin{bmatrix} r_{1v1}(x) & r_{1v2}(x) & \cdots & r_{1v8}(x) \\ r_{2v1}(x) & r_{2v2}(x) & \cdots & r_{2v8}(x) \\ \cdots & \cdots & \cdots & \cdots \\ r_{8v1}(x) & r_{8v2}(x) & \cdots & r_{8v8}(x) \end{bmatrix} \quad (2\text{-}1)$$

2.2. *Risk Classification and Initial Sensor Allocation*

Based on the risk matrix, risk value X is categorized into four levels, and according to these levels, an initial number of sensors is allocated to each area. A multi-level decision-making approach is employed to provide preliminary guidelines for the quantity and layout of the sensors. This method helps to ensure that the sensors are distributed efficiently, prioritizing areas with higher risk to maximize detection capabilities and resource allocation

Table 1. Relationship diagram between risk levels and sensors.

X	Risk Level	Number of sensors
75≤S<100	Low risk	0
50≤S<75	Medium risk	1
25≤S<50	Higher risk	2
0≤S<25	High risk	3

2.3. *Preliminary optimization of greedy algorithm*

In the optimization process of this study, a greedy algorithm is initially used for layout optimization.

Specifically, n points are randomly selected on the map, and one of these points is chosen as the initial position P for a sensor. The algorithm then iterates through these points, calculating their distances from sensor position P, and adds the furthest point to the sensor layout list. This process is repeated until a predetermined coverage rate is achieved. Through this method, a preliminary sensor placement plan can be quickly obtained. Although this plan does not fully consider the effects of wall diffusion, it sufficiently serves as a starting condition for the PSO, reducing the randomness in the generation of initial conditions for the PSO. The rough coverage range of the sensors is as follows:

$$G = S \times T \quad (2\text{-}2)$$

Where S represents the running speed of the gas; T represents the alarm time when the sensor receives the gas.

2.4. *Layout Optimization of PSO*

Based on the greedy algorithm, the PSO algorithm is used for a more refined optimization of sensor layout. The key functions used in this process include the coverage count function and the coverage rate function. The coverage count function calculates the coverage based on the target area's longitudinal and latitudinal coordinates (m and n), while the coverage rate function assesses the overall coverage based on the total number of sensors N and the side lengths of the target area (L1 and L2)..The coverage count function is:

$$C = \begin{cases} 1, D \le R. \\ 0, D > R \end{cases} \quad (2\text{-}3)$$

Where m is the horizontal coordinate of the target area; n is the vertical coordinate of the target area.

The coverage rate function is:

$$Z = \sum_{i=1}^{N} \frac{\sum_{m=1}^{L} \sum_{n=1}^{L} C(m, n)}{L_1 * L_2} \quad (2\text{-}4)$$

Where N represents the total number of sensors; L_1 and L_2 represent the side lengths of the target area.

The core of the optimization lies in adjusting the fitness function, which is the sensor coverage rate function, to achieve multi-objective optimization: maintaining a minimum distance of over 25 meters between each sensor, while minimizing the number of sensors used and maximizing area coverage. The PSO function is:

$$v_i^{(t+1)} = w \cdot v_i^{(t)} + c_1 \cdot r_1 \cdot (p_{best,i} - x_i^{(t)}) + c_2 \cdot r_2 (g_{best} - x_i^{(t)}) \quad (2\text{-}5)$$

Where $v_i^{(t)}$ represents the velocity of particle i at time t, w is the inertia weight, which controls the magnitude of velocity changes. c_1 and c_2 are learning factors. r_1 and r_2 are random numbers within the range [0,1]. $p_{best,i}$ is the best position found so far by particle i. g_{best} is the best position found by the all swarm.

In this study, to fully consider the impact of buildings on gas diffusion in real environments, a plume dispersion model was specifically used to simulate the gas diffusion at leak-prone parts such as bends and flanges in gas pipelines. Using the PDE toolbox in MATLAB, we successfully built a detailed two-dimensional partial differential equation (PDE) model. Various coefficients were set for the PDE equation, and the equation was solved by generating a mesh. The key role of this model is that it can verify whether the selected sensor layout can detect a specific concentration of gas within a set time. If some sensors at certain locations do not meet this requirement, the algorithm will re-optimize until the most suitable sensor layout is found.

Through precise algorithm training and validation, we finally obtained the sensor placement matrix H. Notably, a coverage of 97% was achieved after just 10 iterations, demonstrating the high efficiency of this research method. Particularly, comparison graphs between the Greedy & PSO method (combined Greedy algorithm and PSO) and the sole PSO method showed that not only did the combined method accelerate the speed of coverage improvement, but it also quickly reached a high coverage rate in the early iterations, showing a significant advantage. The Greedy & PSO curve has a steeper slope in the initial iterations, indicating a faster rate of coverage growth. In contrast, the slope of the PSO algorithm's curve is smaller, showing a slower rate of coverage growth. However, as the number of iterations increases, the coverage rates of the two methods tend to converge, illustrating the efficiency advantage of the combined algorithm in the early iterations. In the comparison between Greedy & PSO and the SA algorithm, Greedy & PSO rapidly achieved a 97% coverage rate after about 10 iterations, while the growth of the SA algorithm's coverage rate was relatively slow. This rapid growth in the early iterations highlights the efficiency of the combined algorithm in the early optimization process and its significant advantage in quickly achieving high coverage rates. Additionally, the floor plan demonstrates the practical application of the algorithm in spatial layouts, where sensor positions are evenly distributed at key monitoring points to adapt to the building layout's influence on gas diffusion. This layout optimization not only improves monitoring efficiency but also emphasizes the algorithm's adaptability and effectiveness in handling complex constraints in the real world.

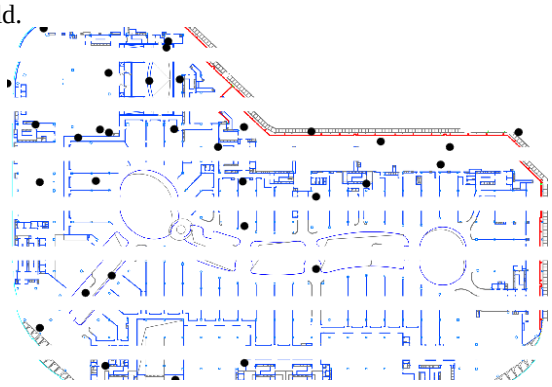

Figure 2-2. Diagram of Sensor Placement Results

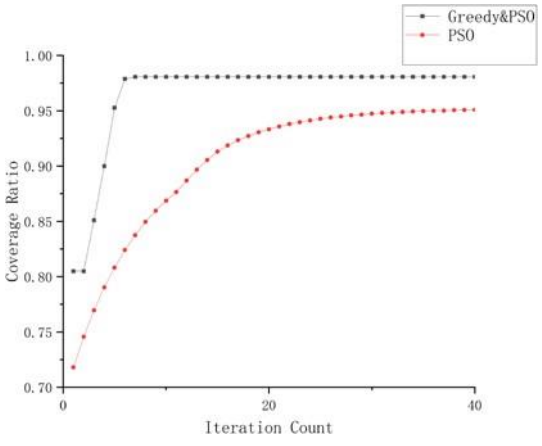

Figure2-3. Algorithm Optimization Comparison Chart

3. RESULTS AND DISCUSSION

In this study, a detailed computational fluid dynamics (CFD) simulation was conducted for one of the 64 segmented small areas to analyse the leakage process within a specific region. This area, due to its complex piping configuration including bends, flanges, and joints, has multiple potential leakage points, making it the focus of the simulation analysis, Ansys simulation is used to verifies the accuracy of the sensor optimization results.

Under the simulation conditions, the pressure of the gas pipeline in the commercial complex is set at 10 MPa, assuming that the leakage occurs at the position of a bend, with a leak area of 1 cm^2.

The CFD simulation setup reflects the actual scenario where the leak point is directed indoors to simulate the process of gas leakage spraying into a building. The Species Transport model used in the simulation accurately analyses the mixture components of methane gas and air. The SIMPLEC solver method, along with the settings for the time step and number of iterations, ensures the precision and stability of the simulation solution.

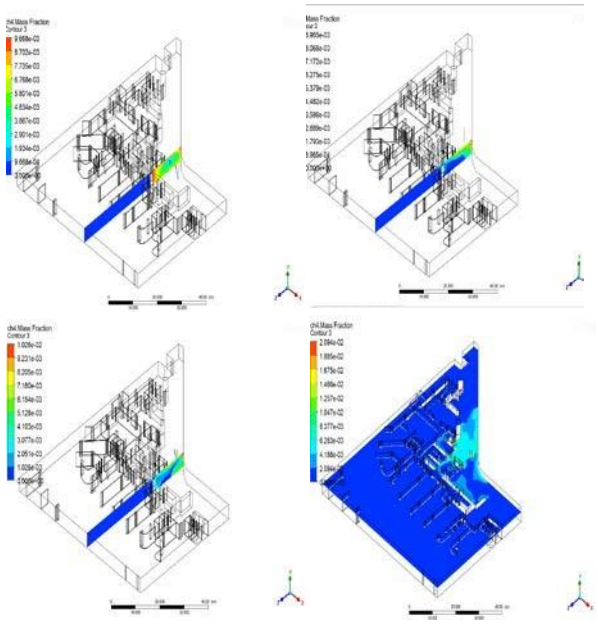

Figure 2-3 Simulation Results Graph

By placing sensors in key areas, we monitored the methane concentration components. When the methane concentration detected by the catalytic combustion sensor reaches 20% LEL (Lower Explosive Limit), the sensor will trigger an alarm. According to the simulation results, the monitoring data under the original sensor arrangement showed that not all leak points could reach this set threshold. With the optimized layout, we observed that the concentration curves at all leak points rose to or exceeded the standard of 0.002 within 100 seconds. This rapid response time provides ample margin for action within the emergency handling window (set at 3 minutes), thereby confirming the effectiveness of the sensor layout optimization. Moreover, the concentration curves showed a stable or declining trend after reaching the threshold, suggesting improvements in data stability with the optimized system.

In summary, the optimization of algorithms has significantly enhanced the monitoring capability of the gas leakage detection system and improved the system's efficiency in issuing warnings at critical moments. This progress not only demonstrates the value of combining computational fluid dynamics with algorithmic optimization in practical applications but also lays a solid foundation for further research in this field.

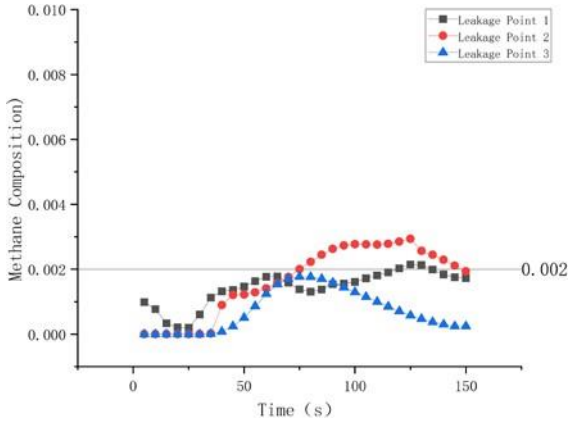

Figure 2-4 Original Methane Composition Graph of Sensor

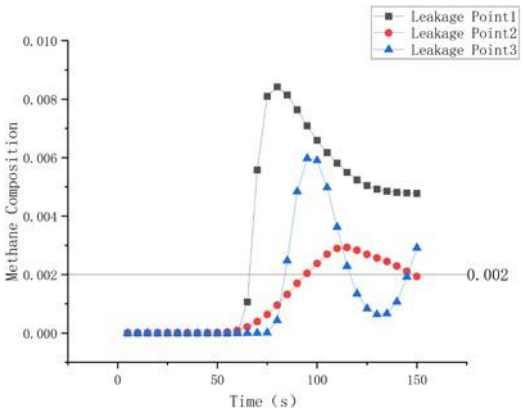

Figure 2-5 New Methane Composition Graph of Sensor

4. CONCLUSIONS

This study integrates greedy algorithms and PSO with CFD simulations to successfully optimize the layout of indoor gas leak detection sensors. The optimization considers the complex spatial structures and gas diffusion paths in commercial areas, as well as the need for rapid detection in emergency situations. Through precise simulation processes, the optimal placement of sensors in key areas was determined to trigger alarms promptly in the event of a leak.

Simulation results show that the optimized sensor layout can detect methane concentrations exceeding 20% LEL (Lower Explosive Limit) at all potential leak points within 100 seconds, significantly outperforming the original layout. This response time meets the set requirement for emergency handling within three minutes and ensures the data collected are highly stable and reliable. Moreover, the optimization of

sensor placement reflects a thorough understanding of the convection-diffusion process and a deep grasp of environmental characteristics and safety requirements.

The application of the combined algorithm and CFD simulation results not only enhances the performance of the gas leak detection system but also provides an effective safety monitoring solution for commercial areas. Future research should expand to different scales and complexities of environments to further verify the applicability and resilience of the algorithm. Additionally, improvements to the algorithm itself, such as introducing more advanced optimization mechanisms, will further enhance the performance of the sensor network, thereby ensuring public safety in a broader range of applications.

FUNDING STATEMENT

This work was supported by the National Key Research and Development Program of China (No. 2022YFC3004801)

REFERENCES

[1] Kong, Xiangdi, et al. "Optimal sensor placement methodology of hydraulic control system for fault diagnosis." Mechanical Systems and Signal Processing 174 (2022): 109069.

[2] Aydin, B.E., Hagedooren, H., Rutten, M.M., Delsman, J., Oude Essink, G.H., van de Giesen, N. and Abraham, E., 2019. A greedy algorithm for optimal sensor placement to estimate salinity in polder networks. Water, 11(5), p.1101.

[3] Liu, K., Yan, R.J. and Soares, C.G., 2018. Optimal sensor placement and assessment for modal identification. Ocean Engineering, 165, pp.209-220.

[4] Lai, C.A., Chang, C.T., Ko, C.L. and Chen, C.L., 2003. Optimal sensor placement and maintenance strategies for mass-flow networks. Industrial & engineering chemistry research, 42(19), pp.4366-4375.

[5] Martínez, S. and Bullo, F., 2006. Optimal sensor placement and motion coordination for target tracking. Automatica, 42(4), pp.661-668.

[6] Xu, S., Ou, Y. and Wu, X., 2019. Optimal sensor placement for 3-D time-of-arrival target localization. IEEE Transactions on Signal Processing, 67(19), pp.5018-5031.

[7] Kreucher, C., 2012. Optimal sensor placement for a constellation of multistatic narrowband pixelated sensors. IEEE Transactions on Systems, Man, and Cybernetics, Part C (Applications and Reviews), 42(6), pp.1374-1383.

[8] Moreno-Salinas, D., Pascoal, A. and Aranda, J., 2016. Optimal sensor placement for acoustic underwater target positioning with range-only measurements. IEEE Journal of Oceanic Engineering, 41(3), pp.620-643.

7: CHARACTERIZATION OF TILTED FIBRE GRATINGS UNDER BENDING

S. C. Zheng [a], *Z. Q. Song* [a], *X. Sun*[b], *J. Y. Wang* [a], *J. S. Ni* [a, *], *W. Zhang* [a, *], *and K. T. V. Grattan* [c]

[a] Laser Research Institute, Qilu University of Technology (Shandong Academy of Sciences), Jinan 250353, China
[b] School of Science, Shandong Jianzhu University, Jinan 250101, China
[c] School of Science & Technology, City, University of London, London EC1V 0HB, United Kingdom

Optical Fibre Sensors 1, EM010, August 12, 2024, 1:30 PM - 3:00 PM

Abstract – The characteristics of low- and high-order cladding modes of tilted gratings (TFBG) under bending has little been investigated despite the popularity of TFBGs in different sensing applications. In this work a theoretical model to investigate the interaction between core and cladding modes in a bent fibre has been established. The influence of bending curvature on the low- and high- order cladding modes has been analyzed, based on the use of both simulation and theoretical calculation. The simulation and calculations carried out show that due to the different mode characteristics, the resonance wavelengths of the different cladding modes will shift in different way, as the bending curvature increases. A 3° tilted grating has been used as a bending sensor, whose operation was based on the mode characteristics of the low-order cladding modes. A linear response between the resonance wavelength of a low-order cladding mode and bending curvature has been obtained, creating a useful result for fibre optic bending mode sensors.

Keywords**:** Tilted Fibre Grating; Bending curvature; Cladding Modes Characteristics; Light Intensity Distribution; Resonance wavelength

1. INTRODUCTION

Fibre Bragg Gratings have attracted much attention since their initial development for a range of sensor applications. In addition to having both the advantages of optical fibre and optical fibre sensors, the features of wavelength modulation, ease of inscription and their multiplexing capability give them a key role in many measurement applications. Fibre Gratings, used as passive optical fibre devices are widely seen in different aspects of fibre optic sensing, optical communication, fibre laser and indeed other fields [1].

The Tilted Fibre Bragg Grating (TFBG) is a special type of short-period fibre grating in which a specific angle between the grating and the direction of the fibre axes is created, due to the non-perpendicular placement of the phase mask with regard to the grating axial direction, during grating fabrication. The tilt grating region thus formed causes the light propagating forward in the fibre core to be coupled backward into the core and cladding, so that both the core mode and a series of cladding modes in the tilted grating transmission pattern can be observed. The core and cladding modes in a tilted grating can be sensitive to changes in the external environment. By analysing the imparity transmission response of the tilted grating, information on changes in external environmental factors such as temperature, refractive index, stress, curvature and so on can be deduced [2].

The research in the work described here on tilted grating characteristics has focused more on the measurement of important parameters such as refractive index, temperature and other useful characteristics [2], and they can have an important role in better Structural Health Monitoring (SHM) of buildings and other structures using them in fibre networks, as such tilted gratings are easy to embed in the structure. Their small size and large multiplexing capability allow them to be adapted to small, confined environments or large structures, as required. Further, sensing of fibre bending (and therefore the bending of structures to which the fibre is attached) remains one important applications of interest for TFBGs [3]. A number of investigations in which tilted grating based bending has been exploited are seen in the literature – where for example it has been suggested that the bent region of tilted grating has a significant impact on the transmission intensity of its low-order cladding modes [4]. An algorithm has been proposed for calculating the contour length of the low-order cladding modes to determine the degree of curvature [4] achieved. It has also been proposed to determine the magnitude of the curvature of the fibre (or the work piece to which it is attached) by determining the curvature cutoff mode of the lower order cladding modes [5].

So far the investigations on the bending characteristics of such tilted gratings have mainly focused on the influence of the bent grating on the transmission intensity of the low-order cladding modes, while the characteristics of the high-order cladding modes and the resonance wavelength shift of cladding modes under bending are little addressed. Given the importance of this in SHM applications, in this work, both a theoretical analysis and an experiment investigation have been carried out to understand better and thus to propose to exploit more widely the characteristics of low-order and high-order cladding modes of tilted gratings, under bending. To further verify the theoretical analysis a 3° tilted grating has been used here as a bending sensor. Results show that a linear relationship between the resonance wavelength of a low-order cladding mode and bending curvature has been obtained and results of the investigation of this are reported.

2. THEORY AND SIMULATION

2.1. Theoretical analysis

The electromagnetic field of the incident light modes in the fibre will interact in transmission, so that modal energy exchange occurs, the phenomenon of mode coupling. The refractive index of the ordinary single-mode optical fibre core and cladding are distributed showing a uniform circular symmetry, and as different modes are orthogonal to each

DOI: https://doi.org/10.34961/researchrepository-ul.29269412.v1

other, there is no energy exchange. The Tilted Fibre Bragg Grating (TFBG), due to its inclined periodic change of core refractive index, destroys the circular symmetry of the fibre and causes an energy exchange between different modes in the fibre. As a result, the forward-propagating incident light entering the grating region is coupled into the forward core mode, the backward core mode and the backward cladding mode.

When the TFBG is subjected to bending, the fibre axis is curved, leading to a varying effective tilt angle of the grating. It is suggested that the series of responses in the tilted grating transmission pattern caused by grating bending is due to the change in the effective tilt angle of the grating area [6]. Since the core/cladding diameter (9/125 μm) is small compared to the radius of curvature (10 mm – 10 m), the small change in the effective tilt angle caused by the bending of the grating area can be considered to have a small effect on the grating transmission pattern. In fact, when the grating area is bent, more light is coupled from core to cladding, which indicates the change in core/cladding effective refractive index. This consequently affects the grating transmission pattern [7].

As shown in Fig. 1, when a fibre is bent it will cause a longitudinal strain parallel to the optical axis. The strain can be expressed as:

$$\varepsilon = Kx \tag{1}$$

where *K* is the curvature of bending, which is the inverse of bending radius *R*. A change in the effective refractive index of the cladding/core then takes place due to the photo-elastic effect. The effective refractive index change, Δn , can be expressed as:

$$\Delta n = -(n^3/2)[(1-\nu)p_{12} - \nu p_{11}]Kx \tag{2}$$

where ν is Poisson's ratio, p_{11}, p_{12} are the photo-elastic constants.

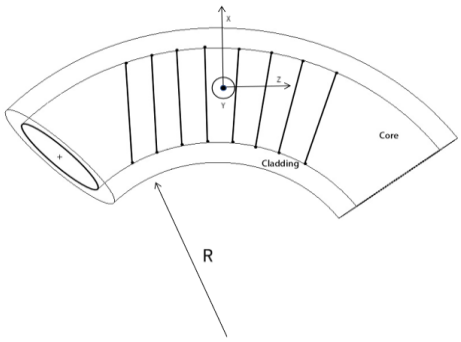

Figure. 1. Conceptual diagram of tilted grating area bending.

The above expression clearly shows the effect of bending on the effective refractive index of fibre grating mode. The optical field transmission inside the fibre, however, is affected by many factors, as discussed below.

Bending changes the symmetry of mode field distribution in the fibre, thus reducing the mode field overlap factor of the core guide mode and cladding mode. Further analysis shows that the change of the mode effective refractive index caused by the fibre bending is not only related to the bending curvature, but also related to the normalized frequency of the fibre and the order of the mode. This means, for different modes in the same waveguide, the change of effective refractive index caused by bending is different, which may increase or decrease the effective refractive index. On the other hand, for the modes of the same order in waveguides with different normalized frequencies, the changes of effective refractive index caused by bending are also different, which may increase or decrease the effective refractive index [8]. The change of the effective refractive index of the mode has an effect on the resonant wavelength excited by the mode. The above analysis is further verified by the simulation below.

2.2. Simulation

The optical simulation discussed here was carried out by using commercially available software (Mode Solutions) to analyse the optical field intensity distribution and calculate the effective refractive index of different cladding modes in the bent fibre. The refractive index of core/cladding was set to 1.4509/1.444 respectively, and the ambient refractive index set to 1. The fibre model was established by assuming a three-layer cylindrical structure. The fundamental mode light intensity was centrally distributed in the core and almost unaffected by bending. The low-order cladding modes, LP_{03} and LP_{07}, and the high-order cladding modes, LP_{018} and LP_{019}, were selected as examples used to analyse the mode field intensity distributions under different curvatures. The results of this analysis are shown in Table 1.

Table 1 indicates that the selected low-order cladding modes, such as LP_{03} and LP_{07}, have a zero curvature when the light intensity is centrally distributed in the core (Black circle in the center of the figure) and its nearby areas. With the curvature increasing, the centre of the intensity distribution constantly moved away from the core. The selected higher-order cladding modes of LP_{01} and LP_{019} exhibit the same tendency in the curvature range of 0 to 20 m^{-1} as the curvature increases. However, in the curvature range of 20 to 40 m^{-1} the optical intensity of the light field of the selected higher-order cladding modes shows a tendency to re-coupling into the core, in a way much different from the low-order cladding modes of LP_{03} and LP_{07}.

This indicates that the variation of light intensity distribution of different modes with curvature change is different, depending on multiple effects of bending curvature, normalized frequency and mode order. From Table 1, it can be seen that the low-order cladding modes are more susceptible to bending as they have a more concentrated light intensity distribution moving away with increasing curvature. From the coupling theory, the mode light intensity distribution is related to the effective refractive index of the mode. In the curvature range of 20 to 40 m^{-1} the light intensity distribution of the selected low and high order cladding modes varies in the opposite way, indicating the effective refractive index change occurs in opposite way. The effective refractive index changes of the LP_{07} and LP_{018} modes in the 0 to 40 m^{-1} range curvature were calculated and the results shown in Figures 2 and 3.

It can be seen that the effective refractive indices of these two modes vary with the curvature change in the same direction until the value of K = 12 m^{-1}, even if the high-order mode shows a smaller sensitivity over the curvature change. After this value of *K*, they vary with the curvature in the opposite direction. This observation verifies the predication of the modal light intensity distribution with different curvature seen in Table 1. The change of the effective refractive index of the cladding mode will affect the corresponding excitation mode resonance wavelength.

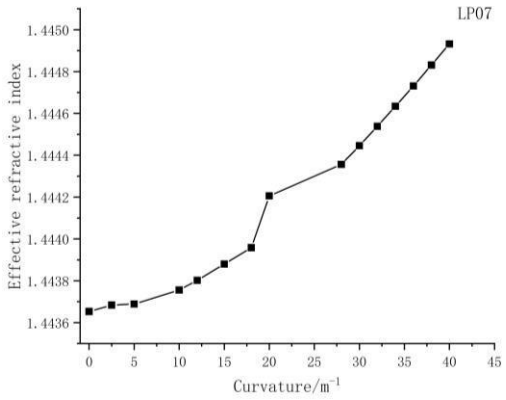

Figure 2. Effective refractive index of LP_{07} mode vs curvature.

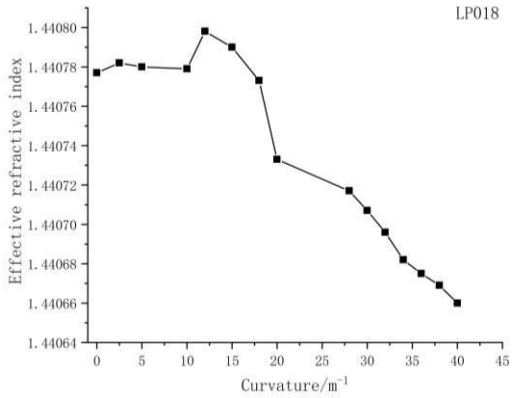

Figure 3. Effective refractive index of LP_{018} mode vs curvature.

This also indicates that due to the effect of curvature, the resonance wavelengths of different mode will shift to a different direction in the grating transmission. As discussed above, the lower-order cladding modes are more sensitive to curvature and more of their lightintensity distributions are seen to move away from the core, as the curvature increases. According to the calculation carried out, the low-order cladding modes in the tilted grating will shift to the long wavelength side, while the resonance wavelengths of higher-order cladding modes will shift in different way, depending on specific mode. Figure 4 simulates the variation of the LP_{07} mode wavelength with the effective refractive index of the cladding mode. This shows that the resonant wavelength of this low-order cladding mode changes linearly with the mode effective refractive index. This important feature makes tilt gratings an ideal basis for fiber bend sensors.

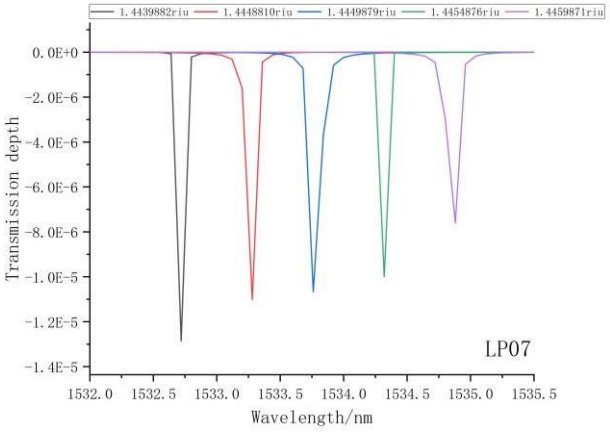

Figure 4. Simulates the variation of the LP_{07} mode wavelength with the effective refractive index of the cladding mode.

Table 1. Simulated mode light intensity distribution with different curvature.

Mode / Curvature	LP_{03}	LP_{07}	LP_{018}	LP_{019}
$K=0m^{-1}$	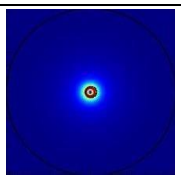	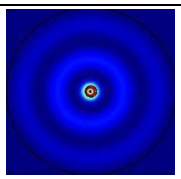	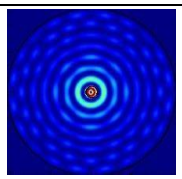	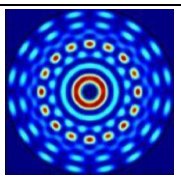
$K=2.5m^{-1}$	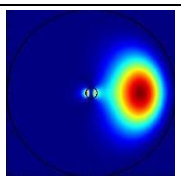	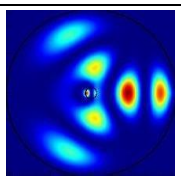	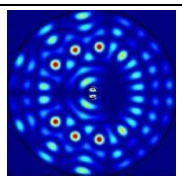	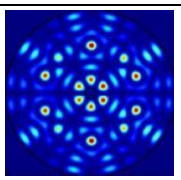
$K=20m^{-1}$	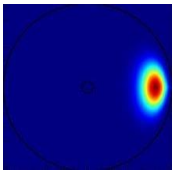	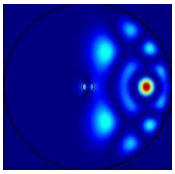	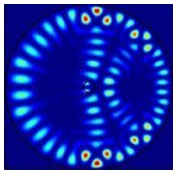	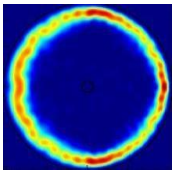
$K=40m^{-1}$	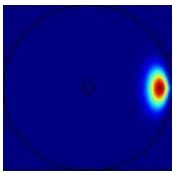	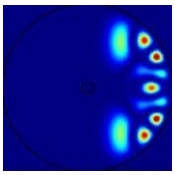	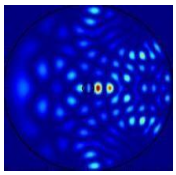	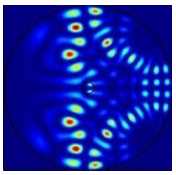

3. EXPERIMENTAL TESTS

A 3° tilted grating is used to experimentally verify the results of the simulation carried out as the basis for the design of a better fibre optic sensor. Fig. 5 shows a schematic diagram of the measurement system. A length of the fibre with the tilted grating is looped into a ring and by changing the diameter of the ring, the radius of curvature, *R*, and the curvature, *K*, of the bent grating can be readily adjusted. The resonance wavelengths of cladding modes of tilted grating under different curvatures can be observed.

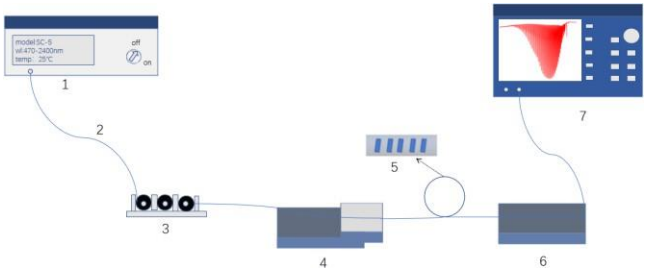

Figure 5. Schematic of experimental arrangement. 1: supercontinuum light source, 2: optical fibre, 3: polarizer controller, 4: linear translation stage, 5: tilted fibre grating, 6: fibre holder, 7: Optical Spectrum Analyser (OSA).

The light from the supercontinuum light source used is fed via the polarization controller to be coupled into the tilted grating under curvature. The radius of the ring was precisely controlled by the linear translation stage, to change the bending curvature of the grating. The transmission spectrum of the tilted grating was measured in real time by using the Optical Spectrum Analyser (OSA).

The transmission spectra of the tilted grating under curvatures of 0, 25.2 and 39.3 m^{-1} are shown in Fig. 6. It can be seen that with the increase of curvature, the intensity of lower and higher order cladding modes has altered to a different extent. The transmission intensity of the low-order cladding modes (1544nm after) is suppressed more significantly. This is because low-order cladding mode is more sensitive to the curvature change, and the light intensity distribution moves away from the fibre core, as the curvature increases.

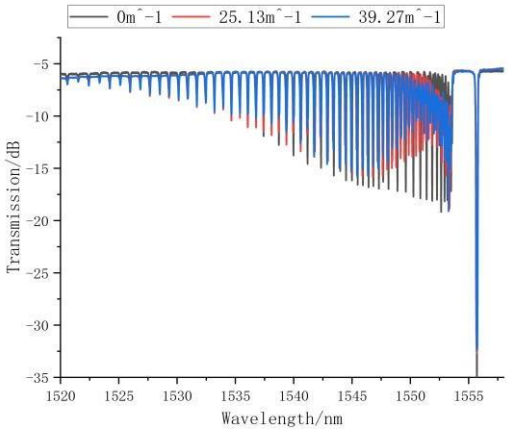

Figure 6. Transmission spectra of tilted grating under different bending curvatures.

The transmission spectra of the tilted grating under 8 different curvatures were then captured. One low-order and one high-order cladding mode situation was selected and analysed, respectively, as shown in Figures 7 and 8. It is obvious that the resonance peak corresponding to the selected two-order cladding mode has the opposite shift trend when the curvature increases. The selected low-order cladding mode whose resonance wavelength is initially at ~1548.45 nm was shifted toward the long-wavelength direction with curvature increasing, while the higher-order cladding mode at ~1540.6 nm was shifted toward the short-wavelength direction with the curvature increasing.

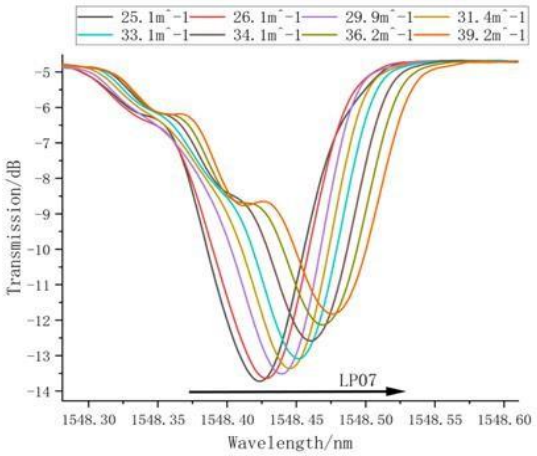

Figure 7. The resonance wavelength of the low-order cladding mode (LP_{07}) varies with curvature change.

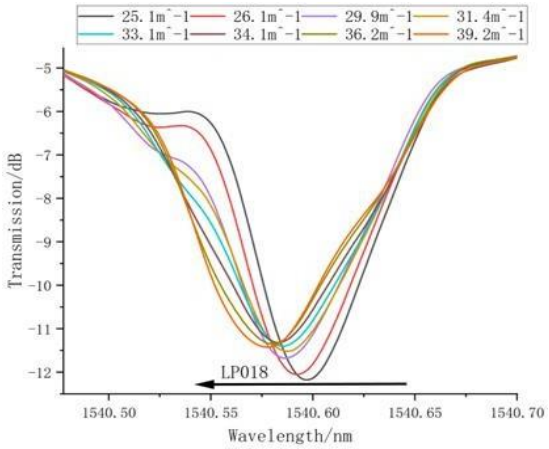

Figure 8. The resonance wavelength of the high-order cladding mode (LP_{018}) varies with curvature change.

It can also be noted that when subject to the bending the low-order cladding mode exhibits larger changes in resonance strength and wavelength than the high-order cladding mode, which indicates that the low-order cladding modes are the more sensitive to curvature sensing, an outcome which is in agreement with the above simulation results.

The above study shows that the low order cladding mode of the tilted grating has a good sensitivity with regard to fibre bending, making it an important feature which can be used for bending sensing. Fig. 9 shows the captured transmission spectra of the 3° tilted grating subject to the curvature from

25 to 40 m^{-1}. When the curvature increases, the lowest order of the cladding modes in the transmission spectrum is observed, whose resonance wavelength and strength vary with the curvature increasing.

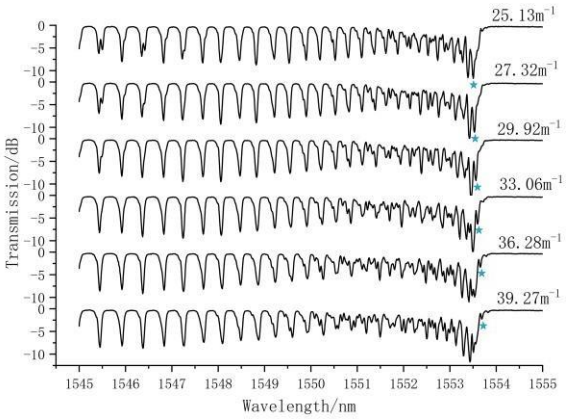

Figure 9. Captured transmission spectra of a 3° tilted grating under different bending curvature.

The resonance wavelength of this cladding mode as a function of curvature has been plotted and shown in Fig. 10. This shows a good linearity, indicating a sensitivity value of 0.01363 nm/m^{-1}. The bending curvature therefore can be determined by this resonance wavelength shift of the cladding mode in a fibre optic sensor using this effect for monitoring the degree of curvature of a structure to which it is attached.

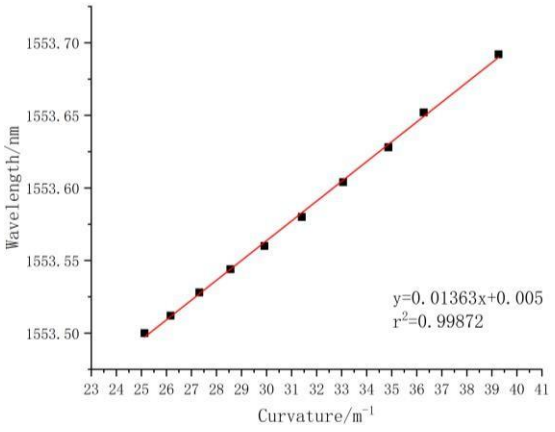

Figure 10. Resonance wavelength vs curvature.

4. CONCLUSIONS

Taking advantage of the fibre mode characteristics, it has been observed that low and high-order cladding modes of tilted grating have different behaviours under fibre bending. The light intensity distribution of the low-order cladding modes moves away from the fibre core, and the resonance wavelength has been shifted to the longer wavelength region, as the curvature increases. On the other hand, the light intensity distribution of the high-order cladding modes moves away from the fibre core, first as the curvature increases, and then shows the tendency to re-coupling into the core. This leads to the resonance wavelength first increasing, and then decreasing, with the increase in curvature. The resonance wavelength of low-order cladding modes shows a larger and a monotonic response to the bending.

Such a feature has been demonstrated for curvature measurement in an optical fibre sensor by locating the wavelength of a lowest-order cladding mode. Compared with the curvature sensing realized by measuring the intensity change of the low-order cladding mode of tilted grating, this type of sensor which uses the change in wavelength (and thus wavelength measurement) is more attractive and more reliable for a range of practical applications taking advantage of the sensitivity of the measurement. This type of sensing mechanism is of real significance for a fibre optic based device which allows accurate measurement of curvature and this has potential use in a variety of applications in engineering today.

FUNDING STATEMENT

This work was partly supported by the Shandong Provincial Key Research and Development Program (2019GSF111011), National Nature Science Foundation of China (Grant No. U2006216), Innovation Team Program of Jinan, China (Grant No. 202228032), and the Taishan Scholars Program (Grant No. tsqn202306254). Grattan acknowledges the support of the Royal Academy of Engineering.

REFERENCES

[1] L. Wang, C. Xiao, W. Ding，J. Wu，C. Shi，**Application Overview of Fiber Bragg Grating Sensors in Structural Health Monitoring**，2022 IEEE 6th Advanced Information Technology, Electronic and Automation Control Conference，Beijing, China，2022，pp. 1946-1950. https://doi.org/10.1109/IAEAC54830.2022.9929863

[2] F. Huang, Y. Moreno, J. Cai, **Refractive Index Sensitivity Characterization of Tilted Fiber Bragg Grating Based Surface Plasmon Resonance Sensor**, Lightwave Technology, vol. 41, no. 17, 2023, pp. 5737-5743. https://doi.org/10.1109/JLT.2023.3262759

[3] Y. -P. Li， W. -G. Zhang， S. Wang ， **Bending Vector Sensor Based on a Pair of Opposite Tilted Long-Period Fiber Gratings**，IEEE Photonics Technology Letters, vol. 29, no. 2, 2017, pp. 224-227. https://doi.org/10.1109/LPT.2016.2636446

[4] D. Harasim, **Temperature-insensitive bending measurement method using optical fiber sensors**，Science Direct, vol. 332, no. 2, 2021. https://doi.org/10.1016/j.sna.2021.113207

[5] S. Ciszczyk, D. Harasim, A. Ormanbekov**, Methods of Projecting Mode Amplitude Changes on the Wavelength Axis in Order to Determine the Bending Radius on the Basis of TFBG Grating Spectra**，Sensors, 2021, pp. 21-22. https://doi.org/10.3390/s21227526

[6] Z. Duan, Y. Zhang, F. Wang, Z. Jing, D. Zhou and W. Peng, **Bending sensor based on tilted fiber Bragg grating**, 2018 Asia Communications and Photonics Conference (ACP), Hangzhou, China, 2018, pp. 1-3. https://doi.org/10.1109/ACP.2018.8595958

[7] L. -Y. Shao, L. Xiong, C. Chen, A. Laronche and J. Albert, **Directional Bend Sensor Based on Re-Grown Tilted Fiber Bragg Grating**, Lightwave Technology, vol. 28, no. 18, 2010, pp. 2681-2687. https://doi.org/10.1109/JLT.2010.2064158

[8] Y. Wang, Y. Rao, X. Zeng, **Bending characteristics analysis of long-period fiber gratings using coupled-mode theory**, Acta Photonica Sinica, vol.31, no.10, 2002, pp. 1205-1208. https://doi.org/10.1016/S0731-7085(02)00079-1

9: DESIGN AND ANALYSIS OF GROUP ATTITUDE DETECTION DEVICE FOR HYDRAULIC SUPPORT

ZENG Qingliang[a], *BAN Xinliang*[b], *MENG Zhaosheng*[c,*]

[a] Shandong University Of Science And Technology, Qingdao, China,
[b] Shandong University Of Science And Technology, Qingdao, China,
[c] Shandong University Of Science And Technology, Qingdao, China,
* Shandong University Of Science And Technology, Qingdao, China,

Abstract – Hydraulic support is the key supporting equipment in coal mining operation, and its good working condition is the prerequisite for improving coal mining efficiency and ensuring environmental safety. The geological conditions of large dip, thick and extra-thick coal seams are more complicated, and the support is more difficult, so the support stability of hydraulic support must be more reliable. In order to clearly perceive the change of the working attitude of the hydraulic support group, the relative structure model of the hydraulic support was studied, and three different structure detection devices were designed, namely, the position and posture detection device of the parallel cable sensor, the direction Angle detection device and the two-dimensional rocker detection device. Finally, after analyzing the detection accuracy, manufacturing difficulty, reliability and solving speed of the three kinds of detection devices, the combination of the two-dimensional rocker detection device and wire sensor is determined as the best detection device.

Keywords**:** hydraulic support posture; support stability; parallel pull wire sensor; direction angle; two dimensional rocker

DOI: https://doi.org/10.34961/researchrepository-ul.29269757.v1

10: A FIBER SPR RESPIRATION MONITORING DEVICE BASED ON SF-LIBR COMPOSITE FILM

*Z*huo *Ren* [a, b], *Yu Zhang* [a, b], *Zhihai Liu* [a, b], *Yifan Qin* [a, b], *Libo Yuan* [c]

[a] Key Laboratory of In-Fiber Integrated Optics, Ministry of Education, Harbin Engineering University, Harbin, 150001, P. R. China

[b] Key Laboratory of Photonic Materials and Device Physics for Oceanic Applications, Ministry of Industry and Information Technology of China, Harbin Engineering University, Harbin, 150001, P. R. China

[c] Photonics Research Center, Guilin University of Electronics Technology, Guilin, China.

Abstract – Parameters such as respiratory rate and respiratory flow play a crucial role in evaluating human health. To ensure respiratory monitoring equipment can be used in various environments, it must be portable, wearable, and biocompatible. This study introduces a wearable surface plasmon resonance (SPR) humidity sensor that utilizes an SF-LiBr composite film to monitor respiration by detecting humidity changes. The refractive index of the SF-LiBr composite film varies with humidity levels, impacting the phase matching conditions of the SPR and enabling humidity detection. Experimental results demonstrate that the SF-22.1 wt % LiBr sensor has a wide sensing range of 35−99% relative humidity (RH) and can monitor different breathing states in real-time. This innovative sensor concept offers valuable insights for the advancement of wearable health monitoring devices.

Keywords**:** surface plasmon resonance, relative humidity, SF-LiBr composite film, wearable respiration monitoring

1. INTRODUCTION

Respiratory monitoring devices assess the health of the human respiratory system[1]. At present, respiratory monitoring equipment generally realizes long-term signal monitoring by integrating various sensor devices. The fiber is soft and can be wound, which has the benefit of real-time online monitoring. Therefore, it can be utilized in the production of wearable devices. Fiber optic sensors commonly used for respiratory monitoring include fiber optic strain sensors and fiber optic humidity sensors. Fiber optic strain sensors can monitor respiratory status by recording contractions and expansions of the chest and abdomen. Therefore, the movement of the human body will be detrimental to the test results. Fiber optic humidity sensors can monitor humidity changes during inhalation and exhalation processes, so that respiratory status can be monitored with more accurate detection results. In summary, fiber optic humidity sensors are of great significance for the development of wearable respiratory monitoring devices.

The realization of a fiber humidity respiration sensor relies on the deposition of a moisture-sensitive coating on the fiber surface. Currently, graphene oxides (GOs), poly(vinyl alcohol) (PVA), and ZnO nanorods have been applied as the moisture-sensitive coating. However, the humidity sensor is used for human health monitoring, and the moisture-sensitive materials used should be biocompatible, biodegradable, and sustainable. Silk fibroin (SF) is a natural protein biopolymer with good biocompatibility. SF can be extracted from silkworm cocoons and processed into regenerated films. SF films have moisture-sensitive properties. The hydrogen bonds in the native SF can interact with the hydrogen bonds in the SF, so the SF can absorb water quickly, resulting in a change in the refractive index of the SF[2]. The addition of Li-Br to SF can further improve the stream water performance of SF membranes[3]. Different respiration states and patterns may change relative humidity (RH) in 30−99%, and the refractive index (RI) of the SF-LiBr composite film will vary with RH accordingly. Thus, humidity sensors using SF-LiBr composite films can respond to respiration signals and enhance the sensitivity of respiration sensors, pushing the detection limit.

Therefore, this paper proposes an optical fiber SPR sensor based on SF-LiBr composite membrane that can be used for wearable respiratory monitoring devices. The sensor can monitor changes in relative humidity. When coated with an SF-22.1 wt % LiBr composite film, the respiration sensor has a broad sensing range of 35−99% RH and a reasonable overall sensitivity of −6.5 nm/% RH. The performances can meet the requirements of various respiration states and patterns. If the sensor is encapsulated in a nasal oxygen cannula, it can be used for breath detection. By using the intensity demodulation method, the signal obtained by the sensor can be read in real time. In this paper, the sensor device was used to monitor different breathing patterns in real time, such as slight, normal, and deep breathing. The sensor is not only biocompatible, portable and wearable, but also can monitor signals in real time, providing an effective idea for the development of Point of Care Testing (POCT).

2. METHODS AND PROCEDURES

Figure 1 shows the structure of the sensor. The light is transmitted in the form of total internal reflection within a plastic-clad fiber with a diameter of 200 μm. The light is transmitted to the exposed core and comes into contact with the gold film to form the evanescent wave. The evanescent wave resonates with the surface plasmon wave on the surface of the metal film, and the energy of the incident light that satisfies the condition is greatly attenuated, and there is an SPR resonance valley at this wavelength in the spectrum. When the refractive index of the metal surface medium changes, it is reflected in the spectrum that the SPR resonance wavelength changes. In addition, since water molecules can

DOI: https://doi.org/10.34961/researchrepository-ul.29269847.v1

interact with the hydrogen bonds of SF-LiBr composite film, their refractive index will change with the change of humidity, so this sensor can detect humidity.

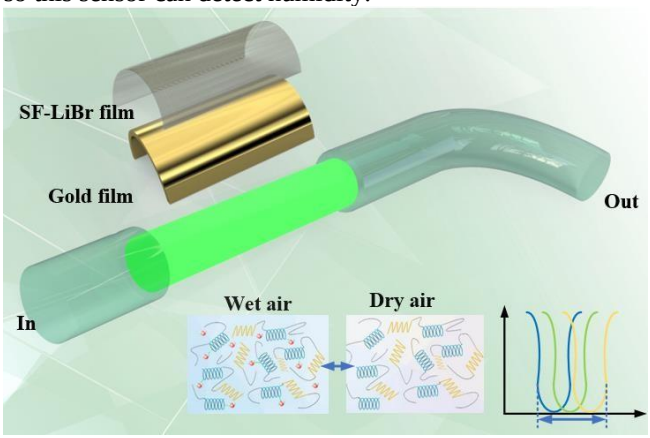

Figure 1. Schematic diagram of the SPR sensor

2.1. Preparation of SF-LiBr Composite Film

There are three steps in the production process of SF-LiBr composite membrane.

The first step is to prepare the SF solution, which is shown in Figure 2.(a) B. mori silkworm cocoons cut into small pieces. (b) Dissolve the pieces in a Na_2CO_3 solution at a concentration of 0.02 M. (c) Boil the solution at 90 °C for 1 hour to achieve the purpose of degumming. (d) Use deionized water to put B. Mori Silkworm Cocoons debris is cleaned and dried in a drying oven at 50°C for 5 hours. (e) Degummed silk fibers were placed in a 9.3 M LiBr solution and allowed to stand at 60 °C for 4 h. (f), (g) Filter and dialyze. (h) We concentrate the solution with 50% poly(ethylene glycol) (PEG 8000) at room temperature for 5 h. The concentration of the pure SF solution is about 16.5 wt %.

The second is to dissolve different masses of LiBr in pure SF solution to obtain SF-LiBr composite solutions with different mass percentages. Finally, the SFLiBr composite solution is dried at 50 °C for 1 h to form the SF-LiBr composite film.

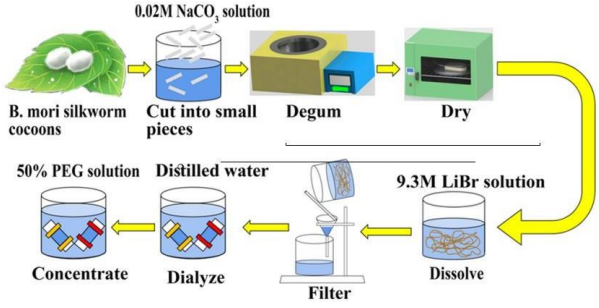

Figure 2. Schematic diagram of the SPR sensor

2.2. Fabrication and Design of the Sensor.

In this paper, a plastic-clad optical fiber (PCOF) with a diameter of 200 μm is used to fabricate the sensor. After stripping off the coating layer of the optical fiber, a gold film is applied to the surface of the sensing area using a DC sputtering instrument (JS-1600, HTCY). The thickness of the gold film was then measured using a 3D morphology analyzer (NewView7200, Zygo), and the results are shown in Figure 3(a) and (b). In order to make the best performance of the SPR sensor, we coated the PCOF with gold films with thicknesses of 40 nm, 45 nm, 50 nm, 55 nm, and 60 nm, respectively. We investigate the resonance dips of the sensors. A halogen lamp (HL-2000, Ocean Optics) with a 360–2000 nm spectral range is connected to the gold-coated sensors. The transmitted light is detected by an optical spectrum analyzer (OSA, AQ6373, Yokogawa), whose wavelength range is 350–1200nm. The sensors are immersed in water. The test results are shown in Figure 3(c). The resonance dip of the sensor with a 50 nm thick gold film has the narrowest full width at half-maximum (FWHM) width with a reasonable depth. It indicates that the 50 nm thick gold film provides high detection accuracy.

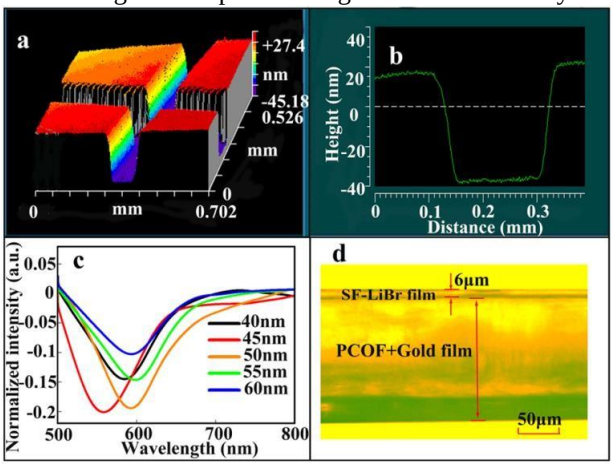

Figure 3. Fabrication of the sensor. (a) Three-dimensional morphology of a grooved gold film. (b) Groove depth of the gold film. (c) Resonance dips of sensors with different gold film thicknesses. (d) Image of a sensor.

3. RESULTS AND DISCUSSION

3.1. Humidity Measurement

In order for the results of the breath test to be more accurate, the humidity sensor should have excellent sensing performance. Therefore, the humidity sensing performance of the sensor should be tested before performing a breath test. The device required for the test is shown in Figure 4. One end of the sensor is connected to a halogen lamp (HL-1000, Ocean Optics) and the other end is connected to an OSA (AQ6373, Yokogawa). Place the sensing area in the humidity chamber and keep the temperature at 20 °C.

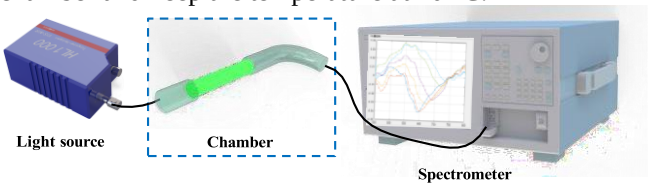

Figure 4. Experimental setup for SPR humidity sensor tests.

This is shown in Figure 5(a) and (b)， with the sensing range of 35-99% RH and a reasonable overall sensitivity of -6.5 nm/% RH, the SF-22.1wt%LiBr sensor is suitable for monitoring a wide range of respiratory states and modes. In addition to detection range and sensitivity, reversibility and repeatability are also important indicators for sensing. We first increased the humidity around the SF-22.1 wt % LiBr sensor and then decreased it, and the resulting two curves roughly coincided, so the sensor is reversible. We have performed three humidity tests on the same sensor, and the experimental results can also be coincident, which proves that

the sensor has good repeatability. The results are shown in Figure 5(c) and (d).

The water absorption capacity of SF-LiBr composite film varies depending on the mass fraction, which can affect the test results. We tested the water absorption capabilities of the six SF-LiBr films with different composition ratios. Figure 5(e) defines the water absorption ratio as the mass ratio of the absorbed water and the film. As the LiBr doping ratio increases, the water absorption capability also improves. However, LiBr can break the hydrogen bonds in the SF film and make β-sheets into irregular rolls, weakening the water absorption capability of the heavily doped film. Therefore, the SF-22.1 wt % LiBr composite film has the best water absorption capability. So the SF-22.1 wt %LiBr sensor is chosen for the following experiments.

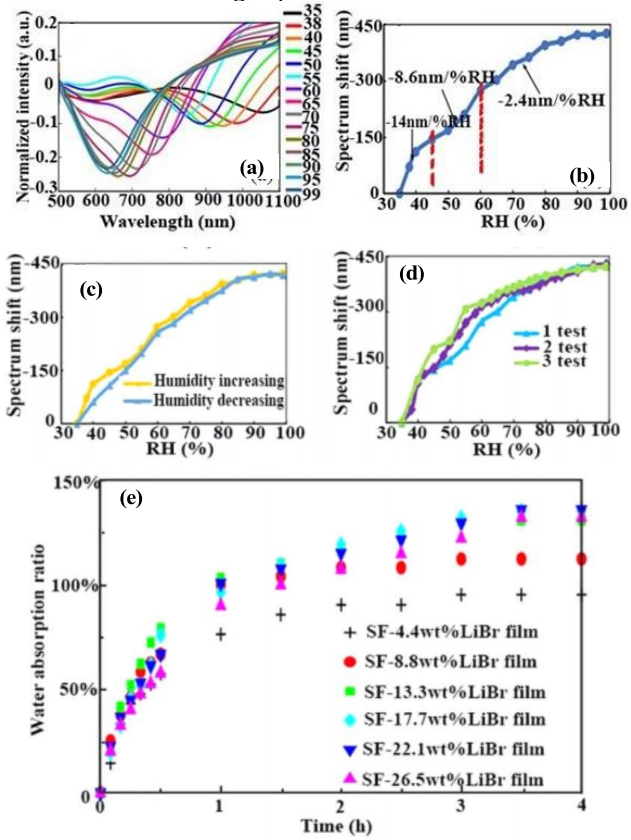

Figure 5. (a) Spectral responses of SPR sensor coated with SF-22.1wt%LiBr film. (b) Show the sensitivity of SPR sensor coated with SF-22.1wt%LiBr film. (c) Show the reversibility of the SF-22.1 wt % LiBr sensor. (d) Show the repeatability of the sensor. (e) Tests of water absorption capabilities of different SF-LiBr composite films (90% RH).

Table 1 compares the performance of the sensor coated with SF-22.1 wt % LiBr film presented in this work and other fiber humidity sensors in previously published papers. Our sensor provides a competitive RH range and a much higher RH sensitivity. In addition, SF is a natural protein biopolymers, which is more suitable for the monitoring of human health conditions such as respiratory monitoring due to its good biocompatibility and safety and non-toxicity compared with the moisture-sensitive materials mentioned in table 1.

Table 1. Comparison of Different Fiber Sensors for RH Measurement

Sensor type	RH range (% RH)	RH sensitivity (nm/% RH)	Reference
Long-period fiber grating coated with GO/Co-MOF-74	30-50	-0.20	[4]
Hollow core fiber filled with GQDs-PVA	13-81	0.12	[5]
Fiber tip coated with SF film	10-90	1.22	[6]
Fiber SPR based on CMC and PDMS	50-80	-1.27	[7]
Fiber Mach−Zehnder interferometer coated with PVA	30-95	-0.26	[8]
Fiber SPR based on SF-LiBr film	35-99	-6.5	This work

3.2. Respiration states monitoring

After the sensor's humidity detection performance has been tested, respiratory monitoring is also required. Therefore, the humidity sensor is encapsulated in a conventional nasal oxygen cannula and placed at a suitable distance in front of the nose of the person to be tested for wearable online respiratory monitoring. The experimental setup is shown in Figure 6(a). The input of the inspection device is connected to a single-wavelength laser (VLSP-C-M-TL, Connet) and the output is connected to an InGaAs photoreceiver (Model 2117-FC, New Focus). The photoreceiver signal is then processed by DAQ (PCI-6221, NI) to obtain a voltage signal on the computer. As shown in Figure 5(a), if the wavelength of the incident light is constant, the valley depth of the SPR resonance valley is different, so different voltage signals are obtained depending on the humidity, and the respiratory state can be monitored in real time. First, the response time of the SF-22.1 wt %LiBr sensor was tested. The results are shown in Figure 6(c) with a response time of 135 ms and a recovery time of 150 ms. Then, without changing the distance between the sensor and the nose, three states of slight breathing, normal breathing, and deep breathing were tested. As shown in Figure 6(c), since the humidity of the three respiratory states is different, it can be seen that the voltage peak is different in different respiratory state.

Respiratory rate is also an important indicator for the assessment of human condition, so the sensor also needs to monitor respiratory rate. Figure 6(d) shows the test results of slow breathing, which has sufficient time for gas exchange, so the humidity in the sensing area does not increase significantly, so the voltage value is relatively stable. As shown in Figure 6(e), the voltage value tends to increase slightly, and it tends to stabilize after 6 seconds. This may be due to persistently high humidity in the sensing area. The results confirm that the SF-22.1 wt %LiBr sensor is suitable for real-time, wearable monitoring of respiration patterns.

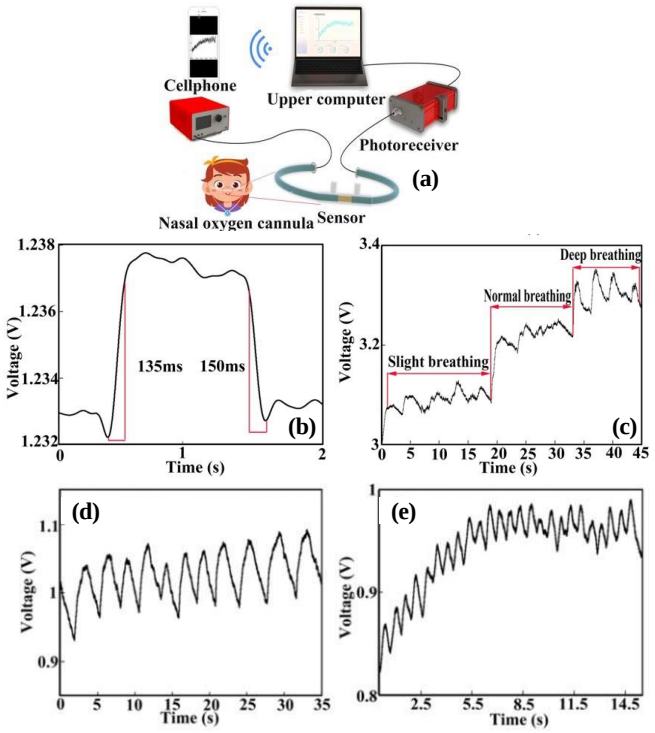

Figure 6. (a) Experimental setup for wearable respiration monitoring. (b) The response and recovery time of the SF-22.1wt%LiBr sensor.(c) Three respiration states recorded by the sensor. (d) Show slow breathing recorded by the wearable respiration sensor. (e) Show fast breathing recorded by the wearable respiration sensor.

4. CONCLUSIONS

In conclusion, we propose a wearable fiber SPR respiration sensor using an SF-LiBr composite film. First, the SF-22.1wt%LiBr sensor is chosen for respiration monitoring. The sensor has a detection range of 35 - 99% RH and a detection sensitivity of -6.5 nm/% RH. Compared with other fiber optic humidity sensors, the sensor has a wider RH detection range and higher detection sensitivity. Second, we confirm that the SF-22.1wt%LiBr sensor can track different respiration states, i.e., slight, normal, and deep breathing. In general, the sensor uses natural protein biopolymers as moisture-sensitive materials, which are safe and non-toxic to the human body and have good humidity detection performance. The sensor can also monitor the signal in real time, and the sensor is small in size and soft and can be wound, which is expected to be used in the development of POCT equipment.

ACKNOWLEDGMENTS

Zhuo Ren: Data curation, Investigation, Writing original draft, Methodology. Yu Zhang: Validation, Supervision, Resources, Funding acquisition. Zhihai Liu: Supervision, Resources, Methodology. Yifan Qin Review and editing. Libo Yuan: Supervision, Resources, Funding acquisition.

FUNDING STATEMENT

This work was supported by The Basic Research Support Program for Excellent Young Teachers of Heilongjiang Province (grant numbers YQJH2023281); Taishan Scholars Program; China Postdoctoral Science Foundation (grant numbers 2022M720940); Qingdao Natural Science Foundation (grant numbers 23-2-1-214-zyyd-jch); Fundamental Research Funds of Harbin Engineering University.

REFERENCES

[1] J. Dai, H. Zhao, X. Lin, S. Liu, Y. Liu, + another 3 authors., **Ultrafast response polyelectrolyte humidity sensor for respiration monitoring**, ACS Appl. Mater. Interfaces, vol. 11, nº. 6, 2019, pp. 6483-6490. DOI: https://doi.org/10.1021/acsami.8b18904

[2] S. Li, Y. Zhang, X. Liang, H. Wang, H. Lu, + another 6 authors., **Humidity-sensitive chemoelectric flexible sensors based on metal-air redox reaction for health management**, Nat. Commun., vol. 13, nº. 1, 2022, pp. 5416. DOI: https://www.nature.com/articles/s41467-022-33133-y

[3] K. I. Lee, X. Wang, X. Guo, K.-F. Yung, and B. Fei, **Highly water-absorbing silk yarn with interpenetrating network via in situ polymerization**, Int. J. Biol. Macromol., vol. 95, 2017, pp. 826-832. DOI: https://doi.org/10.1016/j.ijbiomac.2016.11.090

[4] J. Yan, J. Feng, J. Ge, J. Chen, F. Wang, + another 4 authors., **Highly sensitive humidity sensor based on a Go/Co-MOF-74 coated long period fiber grating**, IEEE Photonic Tech L, vol. 34, nº. 2, 2022, pp. 77-80. DOI: https://doi.org/10.1109/LPT.2021.3139114

[5] Y. Zhao, R. Tong, M. Chen, and F. Xia, **Relative humidity sensor based on hollow core fiber filled with GQDs-PVA**, Sensors Actuators B: Chem., vol. 284, nº., 2019, pp. 96-102. DOI: https://doi.org/10.1016/j.snb.2018.12.130

[6] Z. Opilski, M. Procek, S. Aznar-Cervantes, J. Cenis, and X. Muñoz-Berbel, **Fiber optic humidity sensor based on silk fibroin interference films**, Photonics Letters of Poland, vol. 12, nº., 2020, pp. 49. DOI: https://doi.org/10.4302/plp.v12i2.1018

[7] T. Cheng, B. Li, F. Zhang, J. Chen, Q. Zhang, + another 5 authors., **A surface plasmon resonance optical fiber sensor for simultaneous measurement of relative humidity and temperature**, IEEE Sens. J., vol. 22, nº. 4, 2022, pp. 3246-3253. DOI: https://doi.org/10.1109/JSEN.2022.3141239

[8] Z. Dong, Y. Jin, G. Zhang, J. Zhou, C. Liu, + another 5 authors., **Single core-offset mach-zehnder interferometer coated with PVA for simultaneous measurement of relative humidity and temperature**, Opt. Express, vol. 29, nº15., 2021, pp. 24102-24117. DOI: https://doi.org/10.1364/OE.430367

11:MULTIPLEXED FIBER STRAIN SENSORS FOR FIELD SEISMIC MONITORING

Shanshan Li [a, b], *Wei Jin* [a, b], *Jiaxing Gao* [a ,b], *Zhihai Liu* [a,b], *Yifan Qin* [a ,b], *Yu Zhang* [a ,b *]

[a] Key Laboratory of In-Fiber Integrated Optics, Ministry of Education, Harbin Engineering University, Harbin, 150001, P. R. China

[b] Key Laboratory of Photonic Materials and Device Physics for Oceanic Applications, Ministry of Industry and Information Technology of China, Harbin Engineering University, Harbin, 150001, P. R. China

Industrial Sensing Session 1, EM009, August 12, 2024, 11:30 AM - 12:40 PM

Abstract – Fibre optic sensors have been widely researched in the field of geophysical science due to their high sensitivity, and can work in harsh environments. In this paper, a strainmeter based on fiber Bragg grating-based Fabry-Perot interferometer is proposed and applied in the field of seismic monitoring. The strainmeters series arrays used the Pound-Drever-Hall technique, enabling accurate strain measurements. A 10-channel array was built, and more than 100 earthquakes and the Earth's daily tidal signals were successfully recorded at the Lijiang National Seismic Station. The FBG-FFPIs had a strain resolution of 4.80 pε/√Hz @ 30 Hz. In addition, a 4-channel array was set up at the Heqing seismic station for comparison. The results showed that the FBG-FFPI strainmeters array has great potential for early warning of earthquakes and can provide abundant seismic data.

Keywords**:** field observation; fiber Bragg grating, fiber Fabry-Perot interferometer; strainmeter; Sensor multiplexing

1. INTRODUCTION

Earthquake is a major disaster that causes catastrophic losses to human beings [1]. Mitigating earthquake risk is essential. The establishment of an earthquake early warning system has become an important and pragmatic strategy to minimise the damage caused by major seismic events [2]. The accuracy of such systems depends on the use of advanced geological instruments, including creep [3], tilt and strainmeter [4]. Strainmeter, in particular, play a unique role in the field of seismology due to their ability to effectively capture seismic waves and ground motion.

Earthquake prediction can be achieved by predict surface deformation data collected by strainmeter [5]. Conventional strain gages limit their application due to their large size and high cost. Fiber optic sensors are preferred for geophysical monitoring due to their cost-effectiveness, wide bandwidth and strong immunity to interference. In recent years, fiber-optic based strainmeter technology has developed rapidly, and long-baseline fiber-optic strainmeter have been used for seismic detection [6] and crustal deformation monitoring [7], but they require ultra-long optical fibers, which are difficult to deploy. Therefore, the development of short-baseline fiber-optic strain gages for wider range strain data collection is important to enhance seismic monitoring capability.

Fibre Bragg grating (FBG)-based fibre optic sensors are preferred for short-baseline strainmeter due to their high integration, easy installation and support for multiplexing operation [8]. They include π-FBG sensors, FBG laser sensors and fiber Bragg grating-based Fabry-Perot interferometer (FBG-FFPI) sensors. Especially, the FBG-FFPI sensor possesses high sensitivity due to its comb reflectance spectrum and achieves ultra-wide dynamic range by continuous hopping locking technique. However, applying FBG-FFPI strainmeter to multiplexed in situ observations is still challenging due to the much wider range of the FBG reflectance spectrum than that of the Pound-Drever-Hall (PDH) tracking technique.

To address these challenges, Q. Liu et al. proposed an innovative solution: a time-domain multiplexing technique using optical delay line (ODL) implementation for the simultaneous acquisition of three independent strain signals. At the same time, they also developed an optical frequency comb (OFC)-based Pound-Drever-Hall (PDH) detection method for the measurement of two strain signals. Despite the theoretical advancement of these techniques, the use of ODL may exacerbate the thermal noise problem of optical fibres, and the cost of the OFC technique limits the prospect of its application in large-scale field observations.

In this study, a fibre Bragg grating fibre-optic Fabry-Perot interferometer (FBG-FFPI) strainmeter array with large-scale deployment capability, ultra-high accuracy and real-time multiplexing has been successfully developed. The technology combines optical spatial division multiplexing(SDM) and electrical time-domain division multiplexing(TDM). A 10-channel FBG-FFPI strainmeter array was deployed at the Lijiang National Seismic Monitoring Station for one year of observation. The array not only recorded more than 100 seismic events, but also accurately captured the daily tidal changes of the earth. At the same time, a 4-channel FBG-FFPI strainmeter array was built at Heqing seismic monitoring station. Through the comparative analysis, we found that the multiplexed FBG-FFPI strainmeter array has significant data acquisition advantages in the field of earthquake early warning. These data are of great value for the in-depth understanding of seismic activity patterns and for improving the accuracy of earthquake prediction.

2. METHODS AND PROCEDURES

2.1. Working principle

The improvement of strain resolution requires that the formant of fiber grating on the nanoscale becomes narrower. We chose to use the FFPI interferometer structure, which consists of two identical FBGs, as a high mirror manufactured by PM fiber, with a distance L of 0.25 m between the two FBGS and a fiber grating length l of 0.05 m, for in-core Fabry

DOI: https://doi.org/10.34961/researchrepository-ul.29270090.v1

Perot (F-P) interference (Figure 1a). At the core of PM FFPI, the reflectivity of fbg is 99.5%. There are a series of narrow transmission peaks in the reflection band of fiber grating. The simulation spectrum is shown in Figure 1b.

The PDH technique can lock laser onto the corresponding FBG-FFPI resonance peaks for precise strain measurement. The feedback signal generated by the locking process is then used to extract sensing information. The lasers' track ranges are slightly wider than FBG-FFPIs' free spectral range (FSR) to ensure that at least one resonance peak is obtained.

The FFPI's free spectral range (FSR) and the full-width-at-half-maximum ($\Delta\nu_{FWHM}$) of the resonance peak are expressed as

$$\begin{cases} \mathrm{FSR} = \dfrac{c}{2nL} \\ \Delta\upsilon_{\mathrm{FWHM}} = \dfrac{c}{2nL}\cdot\dfrac{1-R}{\pi\sqrt{R}} \end{cases} \quad (1)$$

where c is the speed of light, n is the PM fiber core's refractive index, L is the distance between two FBGs, and R is the reflectivity of the FBGs, as shown in Fig 1c. When the FFPI experiences a temperature drift ΔT and strain ε, its resonant wavelength λ_v will vary linearly. The wavelength variation can be expressed as

$$\lambda_u = k_T \cdot \Delta T + k_\varepsilon \cdot \varepsilon \quad (2)$$

where k_T is the thermal coefficient, including the thermal expansion and thermo-optic coefficients. k_ε is the fiber's effective elasto-optic constant. Using the PDH technique can convert the Lorentz shape of the FFPI's resonance peak to an error signal with a zero-crossing shape. The laser will track the zero point's variation. The simulated error signal is shown in Fig. 1d.

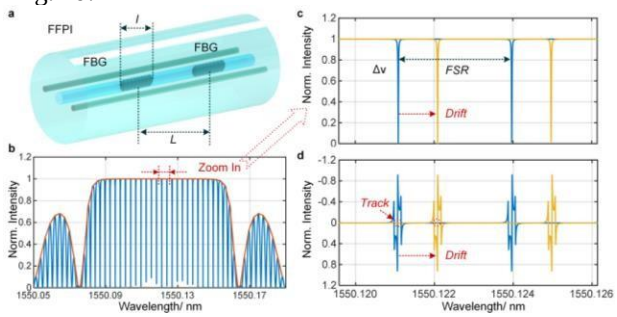

Figure. 1 (a) The 3D structure diagram of FBG-FFPI. (b) In the simulation spectra, the center wavelength of the FBG-FFPI is 1550.12 nm. (c) Zoomed-in spectra. The FSR of the FBG-FFPI is 408 MHz, and the FWHM of the resonance peak is 0.65 MHz. (d) The PDH technique generates the error signal of the resonance peak with fast modulation.

To enhance the measurement accuracy further, the strain-free FBG-FFPI (Ref.FFPI) is used as a temperature reference around the sensing FBG-FFPI (Sen.FFPI). Both are synchronously deflected when the temperature changes and the laser drift is eliminated by locking the main laser to Ref.FFPI.The laser for Sen.FFPI is provided by a single sideband modulator.

2.2. System configuration

The setup of the multiplexed FBG-FFPI strainmeters array is shown in Fig. 2a. A computer (PC) is connected to a wavelength-tunable narrow-linewidth master laser (Koheras BASIK E15, NKT Photonics) and a field programmable gate array (FPGA, PCIe-7856R) to configure settings and store the sensing results. The master laser is modulated by a straight waveguide phase modulator (SPM, SPM-301A, PANWOO), driven by a signal generator (SG). The laser is then split into two beams by a 1:99 PM fiber coupler (CP). The beam with 1% power is directed into the Ref. FFPI through a PM circulator (CIR), while the beam with 99% power is modulated by an SSB modulator (KY-CS-SSB-15, KEYANG).

The SSB modulator is powered by a voltage-controlled oscillator (VCO, CVCO55BE-1100-1600, CRYSTEK).The SSB modulator generates individual sidebands that are split into ten beams. Each beam is then directed to the corresponding Sen. FFPI through a CIR. The reflected light from the FBG-FFPI is collected by multiple photodetectors and converted into an electrical signal. the SPMT switch array queries the output signal of the pd and sequentially demodulates the reflected signal via a dual-channel I/Q demodulator (AD8333, Analog Devices). the SPMT switch array is powered by a VCO (VCO, CVCO55BE-1100-1600, CRYSTEK).

The SG produces a steady 60-MHz sine-wave directed into the demodulator's 4×LO (local oscillator) port, while a 15-MHz sine-wave is used to operate the SPM. The FPGA processes the dual error signals and generates the closed-loop feedback voltage. Additionally, the FPGA can generate a burst pulse to coordinate the VCO and SPMT during a single query time.

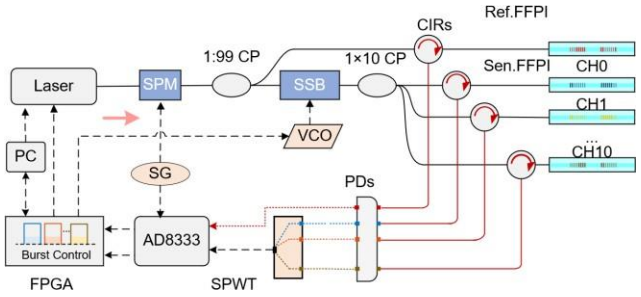

Figure. 2. The multiplexed FBG-FFPI strainmeters array. PC, computer; 1:99 CP, 1:99 PM fiber coupler; SSB, single-sideband modulator; 1×10CP, 1×10 PM coupler; CIRs, PM circulators; Ref. FFPI, strain-free FBG-FFPI; Sen. FFPI, sensing FFPI; PDs, photodetectors; SPMT, single-pole multi-throw switch; AD8333, dual-channel I/Q demodulator; VCO, voltage-controlled oscillator; SG, signal generator; FPGA, field programmable gate array.

Field observation deployment strategies need to consider costs. The FBG-FFPI array and SDM are located in the observation cave. The FBG-FFPI array is installed on the bedrock or connecting platform. The fibers from the FBG-FFPI array are routed to the SDM. Two 240-m long armored PM fiber cables and an armored multicore single-mode (SM) fiber cable connect the SDM and interrogator through the cave entrance.

3. FIELD OBSERVATION AT LIJIANG NATIONAL SEISMIC STATION

Field observation was first conducted at Lijiang National Seismic Station, Yunnan Province, China.

3.1. Deployment strategy

The FBG-FFPI sensor developed in this study has a centre

wavelength of 1549.87 nm, which is pre-tensioned to achieve a match with the wavelength range of the reference FFPI sensor of 1550.24 nm. All sensors were fabricated with uniform parameters, including an FBG bandwidth of 0.32 nm, 99.5% reflectivity, an FFPI FSR of 3.68 pm, an FFPI FWHM of 0.72 MHz, and a cavity length of 0.22 m. The sensors were fabricated with the FFPI FSR of 3.68 pm. The sensor is mounted on an Inva alloy base for seismic monitoring via a fibre optic fixture. The pedestals were spaced 0.3 m apart, slightly larger than the sensor cavity length, and were fixed to a concrete platform with bolts embedded vertically in the concrete.

Fig. 3a illustrates the distribution of the FBG-FFPI strainmeters array in the observation cave. The room's dimensions are approximately 3×9 m^2, containing three concrete platforms. The SDM is positioned at the cave's center, with the Ref. FFPI sensor placed on its top. Please refer to Fig. 3b for a photo of the installation site of the FBG-FFPI strainmeter array.

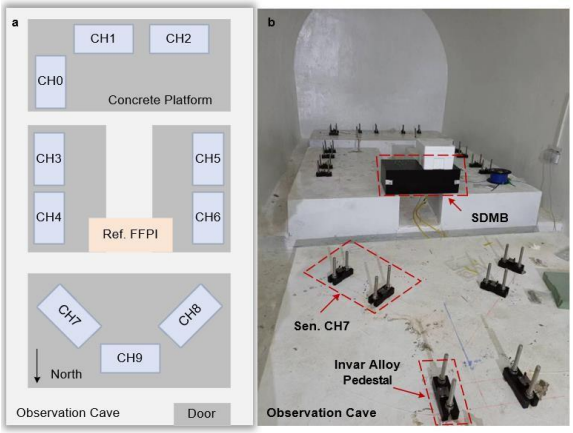

Figure. 3. Deployment strategy at Lijiang National Seismic Station. (a) The distribution of the FBG-FFPI strainmeters array in the observation cave. (b) On-site picture.

3.2. Earthquake monitoring

The FBG-FFPI strainmeters array system in this study can effectively monitor and record natural earthquakes signals. For instance, on 2 January 2022, China Earthquake Networks Center (CENC) recorded a magnitude 5.5 earthquake in Ninglang, Yunnan Province, China, with a depth of 10 km. All strainmeters successfully captured seismic waves including P-waves, S-waves and surface waves, and the signals were detected 18 seconds after the earthquake. The small differences in amplitude between different strainmeters.

The four orientations of different channels provide a complete vector of vibration information about the earthquake. The normalized seismic waves of the north-south orientated strainmeters (CH4, CH5) and west-east orientated strainmeters (CH1, CH9) are displayed in Fig. 4a,b, respectively. The figures show that the waveforms of the same direction have the same phase.

Fig. 4c illustrates the waveforms of two other oblique components, i.e., north-west (CH7) and north-east (CH8). Meanwhile, Fig. 4d compares the waveforms of orthogonal components, including east-west direction (CH2) and north-south direction (CH3).The waveforms of CH2 and CH3 have opposite phases. For CH7 and CH8, while their waveforms are in the same phase in some regions, there are differences in other regions, which are attributed to the fact that the deployments of these two channels are not perfectly orthogonal.The waveforms of CH7 and CH8 can be obtained by synthesising the east-west and north-south components.

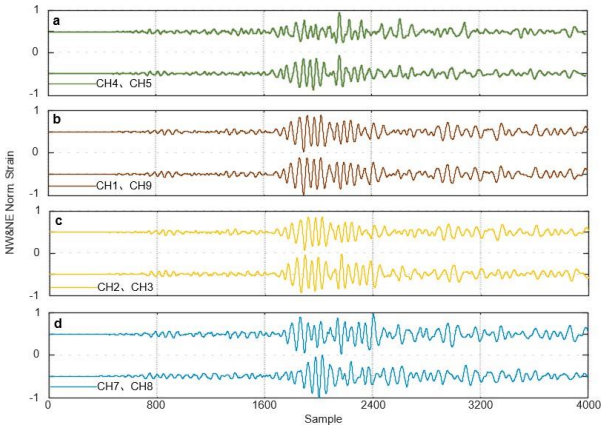

Figure. 4. The normalized seismic waves of the (a) north-south orientated strainmeters (CH4, CH5), (b) west-east orientated strainmeters (CH1, CH9), (c) north-west orientated strainmeter (CH7), and north-east orientated strainmeter (CH8). (d) Comparison of the waveforms in orthogonal directions.

The distance between the epicentre of an earthquake and the monitoring station can be estimated by determining the difference in arrival time between the first-to-arrival (P-wave) and second-to-arrival (S-wave) waves, which have a velocity difference of about 6 to 8 km/sec. Figure 5a shows a seismic signal recorded by CH3, which occurred on 20 October 2021 in Yangbi Yi autonomous county, Yunnan province, China, with a magnitude of 3.4 on the Richter scale, epicentral coordinates of 25.73°N, 100.00°E, and a depth of 8 km. The difference in the arrival times of the P-wave and the S-wave is about 18 s, and the distance between the epicentres is estimated to be 108 to 144 km.

Figure 5b shows another seismic signal recorded by CH3, which occurred in Laos on 20 December 2021, with a magnitude of 6.0 on the Richter scale, epicentre coordinates 19.60°N, 101.40°E, and depth of epicentre of 10 km. The difference in arrival time between the P- and S-waves was about 105 s, and the estimated distance from the epicentre was between 630 and 840 km.The signals of a small aftershock are also clearly recorded in Figure 5b.

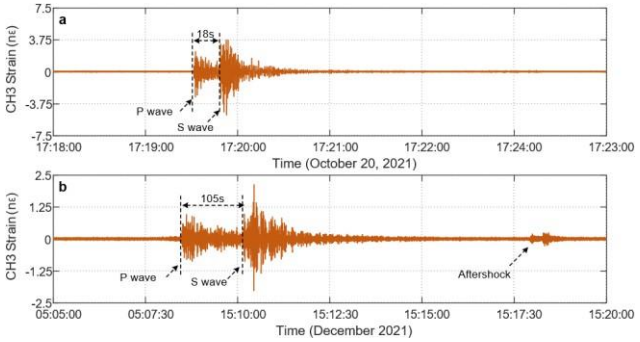

Figure. 5. Earthquake signal recorded by CH3. (a) An earthquake occurred in Yangbi Yi autonomous county, Yunnan province, China. (b) An earthquake occurred in Lao People's Democratic Republic.

The multiplexed FBG-FFPI strain-gauge array system successfully recorded more than 100 earthquakes during a year of continuous monitoring. The performance of the

multiplexed FBG-FFPI strainmeters array system was demonstrated by the fact that the epicentre of the farthest earthquake recorded was located in Peru (4.50°S, 76.70°W), which had a magnitude of 7.3 on the Richter Scale, with an estimated epicentre distance of 17,000 km.

3.3. Ultra-low frequency strain signal detection

In addition to monitoring seismic activity, it is equally important to detect ultra-low frequency strain signals below 1 mHz. For this purpose, we installed a standard 30-metre SS-Y telescope in the east-west direction of the observation hole for comparison. Figure 6 shows the ultra-low frequency strain signals recorded from 1-11 October 2021 by CH3 and SS-Y. The signal from CH3 was downsampled to be consistent with the sampling rate of SS-Y. Both the FBG-FFPI strainmeters array and SS-Y show a signal with a ~24 hour period, which includes semi-diurnal variability features. We believe that the signal is correlated with Earth tides.

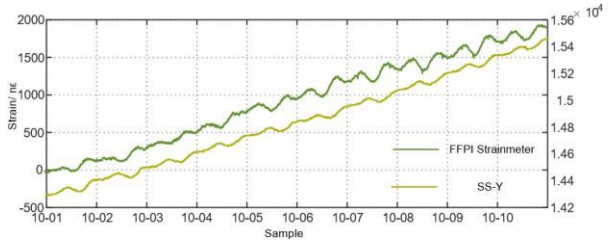

Figure. 6. The ultra-low frequency strain signals of CH3 and SS-Y from October 1 to October 11, 2021.

4. FIELD OBSERVATION AT HEQING SEISMIC STATION

A field observation was conducted at Heqing Seismic Station in Yunnan Province, China. The system operation started on March 14, 2022, and concluded on March 26, 2022.

4.1. Deployment strategy

In order to improve the observation sensitivity of the Heqing seismic monitoring station, we use FBG-FFPI strain gages with higher accuracy. These FBG-FFPI strain gages follow a uniform manufacturing standard and have an FBG bandwidth of 0.4 nm, a reflectivity of 99.5%, an FFPI free spectral range of 0.781 picometres, an FFPI full-width-half-height of 0.25 MHz, and a cavity length of 1.4 metres. In addition, the original single-sideband (SSB) modulator power supply was replaced using a voltage-controlled oscillator (VCO), which has a tuning range of 95 MHz. The strain sensitivity of each FBG-FFPI strain gage was tested using a piezoelectric nano-actuator, and the test result was 34.17 n ε/V. As shown in Fig. 7b, this Inva alloy base consists of a long pillar, an auxiliary platform, a bracket and three fibre optic fixtures.

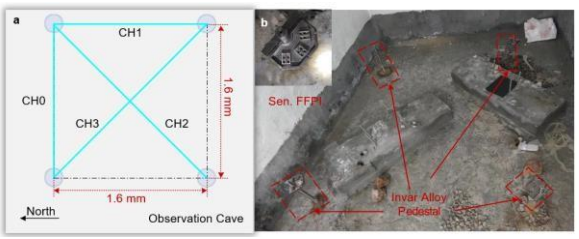

Figure. 7. Deployment strategy at Heqing Seismic Station. (a) The distribution of the FBG-FFPI strainmeters array in the observation cave. (b) On-site picture.

The long struts are vertically embedded in concrete and anchored into bedrock using grouting material. The auxiliary platform is fixed to the long pillar by brackets. Three fibre-optic fixtures are distributed on the auxiliary platform at equal intervals at a 45-degree angle to capture the strain signals in different directions. Figures 7a and 7b show the layout of the FBG-FFPI strainmeters array in the observation hole. Four Invalid bases are arranged in a square with 1.6 m sides, one at each corner, and the FBG-FFPI strain gages are mounted directly on these bases by fibre-optic fixtures, which are specially designed for seismic monitoring.

4.2. Earthquake monitoring

On 16 March 2022, an earthquake measuring 7.4 on the Richter scale occurred in the town of Namie, Fukushima Prefecture, Japan, with an epicentre at 37.65°N latitude and 141.95°E longitude and a depth of 63 km. This major earthquake had been preceded by a foreshock of magnitude 6.0 on the Richter scale at 22:34:22 on the same day. Figure 8 illustrates the seismic waveforms after the infinite impulse response (IIR) filtering process. The figure clearly shows a foreshock signal, followed by a large earthquake immediately after, separated by only 127 s. The response consistency of the FBG-FFPI strainmeters array is better than that recorded at the Lijiang National Seismic Station due to its improved sensitivity.

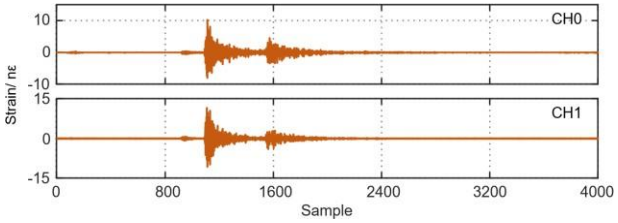

Figure. 8. (a) The seismic waveforms after applying IIR filtering. On March 16, 2022, the ML = 7.4 earthquake struck Namie, Fukushima, Japan, at 22:36:29. The epicenter coordinate is 37.65°N, 141.95°E. The focal depth is 63 km. (b) Zoomed-in waveform.

4.3. Comparison of field observation in two seismic stations

This study compares and analyses the seismic data recorded by two seismic monitoring stations.On 23 March 2022, an earthquake of magnitude 6.6 on the Richter scale occurred in Taitung City, Taiwan Province of China, at a depth of 20 km, with an epicentre geographically coordinated at 23.45°N latitude and 121.55°E longitude. Figure 9 illustrates the seismic waveforms captured by the two stations. The slight difference in the epicentral distance between the Lijiang National Seismic Station and the Heqing Seismic Station resulted in a difference of about 4.85 s in the arrival time of the seismic waves received by the two stations.

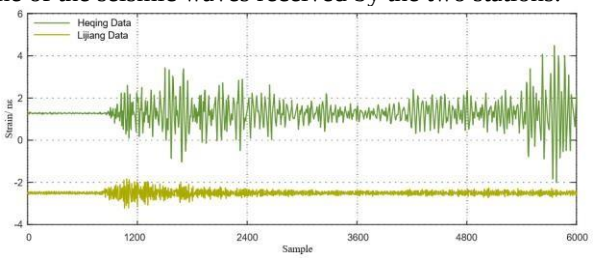

Figure. 9. Seismic waveform recorded by the two stations. The ML = 6.6 earthquake occurred in Taidong, Taiwan province, China. The focal depth is 63 km.

Fig. 10 shows the Power spectral density (PSD) of the two stations.The resolution of the FBG-FFPI strainmeters array at the Heqing seismic station is better than 1 pε/√Hz at frequencies above 10 Hz. Specifically, the resolution of the array at the Heqing station reaches 476 fε/√Hz at 30 Hz, whereas the resolution of the array at the Lijiang national seismic station is 4.80 pε/√Hz at the same frequency.

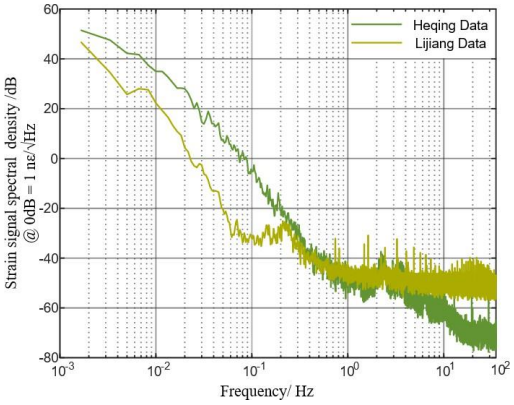

Figure. 10. shows the PSD of the two stations.

5. DISCUSSION AND CONCLUSION

In this study, we successfully developed and deployed large-scale, ultra-high resolution, real-time multiplexed FBG-FFPI strainmeters arrays for field observation, a technological breakthrough that has brought innovations to the field of seismic monitoring. 10-channel strainmeters deployed at Lijiang seismic monitoring station and 4-channel strainmeters deployed at Heqing seismic monitoring station effectively captured a large number of seismic signals. More than 100 seismic signals were acquired during the deployment of the seismic monitoring station. By improving the parameters of the strainmeters, the PSD of the Heqing station was 476 fε/√Hz @ 30Hz, which was significantly higher than that of the Lijiang station.The results of this research lay the foundation for future advances in early warning of earthquakes, and the combination of strainmeters arrays with advanced data analysis and data mining algorithms foreshadows the future direction of earthquake early warning systems.

ACKNOWLEDGMENTS

Shanshan Li: Data curation, Investigation, Data curation, Methods. **Wei Jin**: Writing – original draft, Investigation, Formal analysis, Data curation, Conceptualization. **Jiaxing Gao**: Investigation, Data curation, Conceptualization. **Zhihai Liu**: Supervision, Resources, Funding acquisition. **Yifan Qin**: Supervision, Resources, Methods, Funding acquisition. **Yu Zhang**: Writing – review & editing, Validation, Supervision, Resources, Funding acquisition.

FUNDING STATEMENT

The Basic Research Support Program for Excellent Young Teachers of Heilongjiang Province (YQJH2023281); Taishan Scholars Program; China Postdoctoral Science Foundation (2022M720940); Qingdao Natural Science Foundation (23-2-1-214-zyyd-jch); Fundamental Research Funds of Harbin Engineering University.

REFERENCES

[1] B. Lee, **Review of the present status of optical fiber sensors**. Optical fiber technology, 2003, 9(2), pp.57-79. DOI: https://doi.org/10.1016/S1068-5200(02)00527-8

[2] H. Kanamori, E. Hauksson, and T. Heaton, **Real-time seismology and earthquake hazard mitigation.** Nature, 1997, 390(6659), pp.461-464. DOI: https://doi.org/10.1038/37280

[3] A. M. Thomas, N. M. Beeler, Q. Bletery, R. Burgmann, and D. R. Shelly, **Using low-frequency earthquake families on the San Andreas Fault as deep creepmeters.** Journal of Geophysical Research: Solid Earth, 2018, 123(1), pp.457-475. DOI: https://doi.org/10.1002/2017JB014404

[4] G. Mentes, **Quartz tube extensometer for observation of Earth tides and local tectonic deformations at the Sopronbánfalva Geodynamic Observatory, Hungary.** Review of Scientific Instruments, 2010. 81(7). DOI: https://doi.org/10.1063/1.3470100

[5] B. Rouet-Leduc, C. Hulbert, N. Lubbers, K. Barros, C. J. Humphreys and P. A. Johnson, **Machine learning predicts laboratory earthquakes.** Geophysical Research Letters, 2017, 44(18), pp.9276-9282. DOI: https://doi.org/10.1002/2017GL074677

[6] Z. Zhan, M. Cantono, V. Kamalov, A. Mecozzi, R. Müller, S. Yin and J.C. Castellanos, **Optical polarization–based seismic and water wave sensing on transoceanic cables**, Science, 2021, 371 (6532), 931-936. DOI: https://doi.org/10.1126/science.abe6648

[7] S. DeWolf, F.K. Wyatt, M.A. Zumberge, W. Hatfield, **Improved vertical optical fiber borehole strainmeter design for measuring Earth strain**, Review Of Scientific Instruments , 2015, 86 (11) 114502. DOI: https://doi.org/10.1063/1.4935923

[8] Q.W. Liu, T. Tokunaga and Z.Y. He, **Realization of nano static strain sensing with fiber Bragg gratings interrogated by narrow linewidth tunable lasers**, Optics Express, 2011, 19(21) ,20214-20223. DOI: https://doi.org/10.1364/OE.19.020214

12: A SIGNAL PROCESSING METHOD TO IMPROVE THE DETECTION ACCURACY OF CO GAS CONCENTRATION IN TDLAS DETECTION

Yingshuai Li[a]*,Guangdi Mao*[b]*,Qiaofeng Yi*[b]*,Jie Hu*[b]*,Hongmin Zhang*[b]*,Yanong Ning*[b]*,Tongyu Liu*[a,b,*]

[a] Laser Institute, Qilu University of Technology (Shandong Academy of Sciences), Jinan Shandong, China, 250104:
[b] Shandong Micro-sensor Photonics Co. Ltd, Jinan Shandong, China, 250103:

Spectroscopy, EM010, August 12, 2024, 11:30 AM - 12:40 PM

Abstract – This paper presents a signal processing scheme that can suppressing background noise arising from laser-induced interference within the detection signal in a tunable diode laser absorption spectroscopy (TDLAS). The constraints imposed on high-precision gas detection in the system by interference fringes were discussed, with particular emphasis on investigating the mechanisms underlying interference fringe generation. In this scheme, the detected signal was processed with a number of "steps" in order to remove part of the signal variation caused by the interference in the TDLAS system. A test set up was used to verify the scheme. The experimental results demonstrate that this algorithm enhances the stability of gas detection. The dispersion of carbon monoxide concentration values decreased by 24.3%. Moreover, this algorithm exclusively addresses the inherent interference noise floor from the laser, and it can be integrated with algorithms aimed at suppressing other interference fringes, thereby enhancing its denoising capability.

Keywords**:** gas detection; TDLAS; interference noise; signal processing

1. INTRODUCTION

The concentration of CO gas stands as one of the paramount parameters in preventing and managing spontaneous combustion within coal mine goafs[1]. By monitoring trace variations in carbon monoxide composition within coal mines, it becomes feasible to assess the potential hazards for spontaneous combustion; therefore, continually enhancing the concentration detection accuracy of carbon monoxide sensors is imperative. Currently, conventional methods for measuring gas concentration typically involve utilizing the physical and chemical properties of the gases to be monitored, traditional gas detection methods encompass techniques such as potentiometric electrolysis, catalytic combustion, and gas chromatography, among other non-spectroscopic analytical approaches. While these methods offer advantages such as low cost and simplicity in measurement principles, they require frequent calibration to minimize false alarms. Additionally, sensors of this kind are susceptible to corrosion damage in the harsh underground environment of mines, exhibiting poor real-time capabilities and intelligence. With the continuous advancement of the semiconductor laser industry, Tunable Diode Laser Absorption Spectroscopy (TDLAS) technology, renowned for its high sensitivity, excellent selectivity, and rapid response time, has found wide-ranging applications in gas concentration detection and related fields[2]. It is well-known that the fundamental principle of TDLAS technology relies on the Lambert-Beer Law, utilizing the distinct spectral absorption characteristics of various gases for concentration measurements. In a TDLAS system, the laser beam emitted by the laser diode traverses through the gas medium, the output wavelength of the laser diode is tuned with a saw-tooth wave current, when the tuned wavelength aligns with the absorption peak wavelength of the gas, the energy of the laser beam will be absorbed by the gas absorption peak, resulting in attenuation of energy at that wavelength. With the interaction length between the measured gas and the laser beam being fixed in the sensing chamber, by measuring the relative attenuation of light intensity at that wavelength at a photo detector that receives the laser beam. After the calibration, the relationship between gas concentration and the detected light beam intensity can be established. Subsequently, the concentration of the measured gas can be inferred through inversion formulas. Currently, in TDLAS measurement technology, commonly employed detection methods include direct absorption, wavelength-tuned differential absorption detection, and wavelength modulation harmonic detection. The direct absorption method utilizes the detected changes in light intensity to infer the gas concentration, while the wavelength-tuned differential absorption detection relies on the difference in optical intensities between the absorption spectral signals and non-absorption spectral signal to estimate gas concentration. The wavelength modulation harmonic detection, on the other hand, involves analyzing and calculating gas concentration through the analysis of the second harmonic signal using a lock-in amplifier. As TDLAS technology fundamentally involves the detection and processing of analog signals, it constitutes a linear measurement process. Therefore, various interference noise signals generated by the sensor detection system can significantly impact measurement accuracy. How to suppress the noise floor of the detection signal is one of the crucial means to enhance the measurement precision.

In a typical TDLAS gas sensor, the light beam is often converted into a parallel light with the use of a collimating lens and then focused onto a photo detector with a focusing lens. If the light beams reflected from the surfaces of these optical components enter the laser, an interference noise will be introduced into the signals output when the wavelength of the laser is modulated with a saw-tooth wave current. In order to reduce the interference noise, the anti-reflection coatings are applied onto these optical components[3]. Webster et al. introduced vibrating Brewster windows into optical systems to reduce interference fringes[4]. Persson et al. demonstrated

DOI: https://doi.org/10.34961/researchrepository-ul.29270129.v1

that balanced detection methods can effectively suppress interference fringes as well[5]. Although these techniques can be employed to reduce interference fringes, the potentially increase costs will be increased, and the sensor system becomes more complicated. Recently, the rapid development of machine learning technologies has provided more solutions for improving signal processing. Pang et al. demonstrated that a Back propagation neural network (BPNN) can effectively reduce interference fringe noise in a TDLAS system[6]. However, this method is prone to getting trapped in a local optimum, leading to suboptimal results. Although such approaches avoid adding complexity to sensor systems, the requirements of high demand power for chips also lead to significant challenges in practical applications. In engineering applications, digital signal filtering techniques remain main stream. Wang et al. proposed an improved model based on CEEMDAN-WTD to enhance detection accuracy to 0.65%[7]. While these methods have been proven effective in suppressing interference fringes, in certain cases, especially when gas concentrations are low, gas absorption spectra are often overshadowed by low-frequency, high-intensity interference fringes. The random variation in interference fringe phases complicates gas concentration measurements[8].

To address the issue of significant errors caused by interference noise floor generated by the laser itself, especially the impact of low-frequency, high-intensity interference fringes in harsh environmental engineering conditions, this paper reports a signal processing scheme that is capable of suppressing noise floor in detection signals during gas concentration measurements.

2. THEORY

2.1. TDLAS

It is well-known that the TDLAS technology is based on the infrared characteristic absorption of gas molecules. When a laser beam with a wavelength of λ (nm) passes through a gas, the absorb line of the gas will absorption the optical energy at the same wavelength. The change in optical intensity at a photo detector satisfies the Beer-Lambert Law:

$$I_t(v) = I_0(v)\exp\left[-\alpha(v)CL\right] \quad (1)$$

where, I_t denotes the intensity of the light after absorption, I_0 represents the initial light intensity, C stands for the volume fraction of the gas under measurement, L signifies the effective absorption path length, and $\alpha(v)$ indicates the absorption coefficient at the wavelength(λ). Hence, under conditions of stable pressure, temperature, and other factors, by computing the relative attenuation of light intensity, the amount of absorbed light energy for the gas under measurement at that wavelength can be derived, thus the actual gas concentration can be calculated. Therefore, TDLAS technology essentially constitutes a linear measurement process for detecting and processing analog signals. However, in TDLAS systems, various interference noise signals introduced from reflections on different optical component surfaces can impact measurement accuracy. This interference effect is particularly pronounced when gas concentrations are low, as the gas absorption spectra are often obscured by low-frequency, high-intensity background noise. Additionally, the random variation of interference fringe phases with environmental temperature renders precise measurement of low gas concentrations challenging.

2.2. Mechanism of Interference Fringe Generation

In conventional gas sensing systems based on absorption spectroscopy techniques, various types of lasers such as Distributed Feedback (DFB) lasers, Vertical-Cavity Surface-Emitting Lasers (VCSEL), Quantum Cascade Lasers (QCL), or inter-band Cascade Lasers (ICL) are utilized. These lasers are preferred for their narrow line widths, tenable, and ability to precisely tune the output wavelength to scan individual gas absorption lines. This facilitates high-sensitivity gas concentration detection using TDLAS technology. However, it is precisely due to the narrow line widths of the laser beams, the long coherence lengths of these laser beams will introduce interference if there are light reflected into the laser resonator cavity, especially when the coherence length far exceeds twice the length of the gas absorption cell, that any reflection from the reflective surfaces within the absorption cell back into the laser resonator cavity, under the influence of the laser wavelength scan tuned by the drive current, there will be interference fringes in the output beam of the laser, result in an interference noise at the output signal form the system.

As illustrated in Figure 1, in gas sensors based on TDLAS measurement technology, the laser requires a collimating lens to collimate the divergent laser beam into a parallel beam. This beam then passes through the sensing chamber and is converged onto the photosensitive surface of the detector by a converging lens, where the light energy is gathered. Hence, whenever a light beam reflected from the surface of a lens or the photosensitive surface of the detector enters the laser cavity after reflection and exits the laser outlet, interference occurs within the laser resonator cavity. Due to the different positions of the reflecting surfaces along the optical path, the spatial frequency of the interference fringes, or the size of the fringes, varies accordingly. For interferometer with smaller cavity lengths, larger interference fringes (low-frequency, high-intensity interference fringes) are produced, whereas for interferometers with larger cavity lengths, smaller interference fringes (high-frequency, low-intensity interference fringes) are generated. If the laser wavelength is tuned by the driving current while multiple interferometers coexist in the optical path, various interference fringes will superimpose in the photo detector and the interference noise appears in the detected optical signal. This results in the formation of interference noise in the detection signal, as depicted in Figure 1.

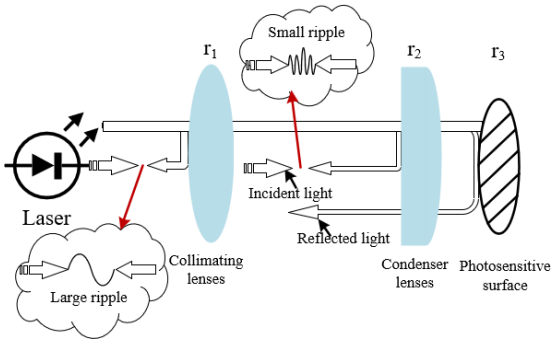

Figure 1. Generation of interference noise floor

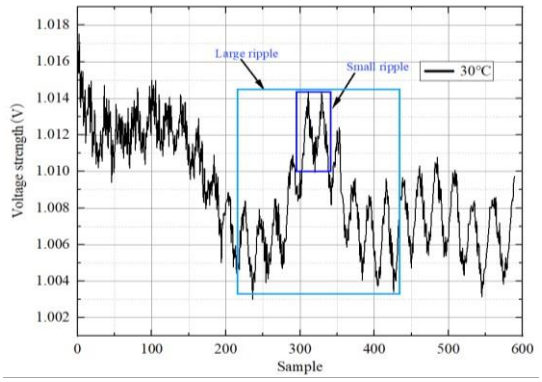

Figure 2. Interference signal at 0°C conditions

As shown depicted in Figure 2, the interference signal contains two types of interference fringe patterns, namely low-frequency, high-intensity interference fringes, or "large ripples" and high-frequency, low-intensity interference fringes or and "small ripples". The different fringe types are generated by the different interferences between the light emitted by the laser and the reflected light at different surfaces of optical lenses in the system. The position where the reflection occurs can be determined using Equation (2):

$$L = \frac{k}{2}\left(\frac{\lambda_1 \times \lambda_2}{\lambda_2 - \lambda_1}\right) \quad (2)$$

Where L represents the cavity length, k is the number of interference fringes within the sampling range, λ_1 is the starting wavelength of the scan, and λ_2 is the ending wavelength of the scan. By calculating the coherence length, two types of interference cavity lengths are identified: "large ripples" and "small ripples". By comparing the cavity lengths within the optical system, the "large ripples" interference primarily occurs between the laser resonator cavity and the inter-surface of the collimating lens, while the "small ripples" are produced between the laser resonator cavity and the surface of the photo detector. The primary factor affecting our detection accuracy is the low-frequency, high-intensity interference fringes generated between the laser resonator cavity and the inter-surface collimating lens, i.e. large ripples.

As depicted in Figure.3, when the laser is driven by a saw-tooth wave current, the large ripples directly superimpose on the absorption spectrum signal, introducing a non-linear enhancement in the signal strength of the zero baseline. This affects the accurate measurement of the baseline reference value, reducing the measurement accuracy when the low concentration methane is measured. Meanwhile, since the phase of interference fringes varies with changes in environmental temperature, the baseline of the signal will change accordingly. By comparing zero baseline signals at different temperatures, it can be seen in Figure 3, that this interference fringe phase changes cause the fluctuations of the signal baseline. Consequently, the irregular variation in signal intensity with temperature during the gas concentration measurements further increases the difficulty of high-precision detection. Hence, this paper proposes an algorithm to reduce the "large ripples" superimposed on the detection signal, thereby enhancing detection accuracy.

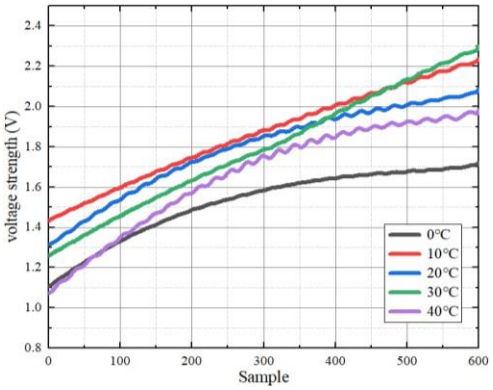

Figure 3. Detection signals at zero concentration for different temperatures

3. NEW SIGNAL PROCESSING METHOD

In order to reduce the measurement errors introduced by the larger ripples, a new signal processing method was used. In this method, the measured base line of the signal is extracted from each scanned signal, which is then compared with the theoretic baseline, resulting in the corresponding larger ripple baseline for each scan signal. Then by subtracting the corresponding larger ripple baseline from the original signal, the signal variations due to the corresponding larger ripple baseline are removed. Because the process of removing larger ripples is taken at the temperature when the measurement is made, as a result, the effect of the temperature induced base line variations is reduced. The steps used to process the signal are as the following:

1. To subtract the DC-bias caused by the photo detector and the detection circuit from the raw data measured in the experiment. The DC-bias of the photo detector at each scanning measurement is present in the detection signal obtained by the detector in each wavelength scanning cycle, and the corresponding DC-bias value is removed to obtain the raw detection signal.
2. To measure the temperature of the laser and the gas chamber respectively. The laser temperature is used to ensure that the center of the laser's wavelength scanning range coincides with the centerline of the Gaussian gas absorption spectrum of the methane gas, while the temperature of the sensor gas chamber is used to compensate for temperature-induced variations in the measured value.
3. In each scan cycle, subtract the starting signal value I_0 of the first sample point from the detector signals of 600 sample points respectively, and then, divide the detector signals of the 600 sampling points by the ending signal value I_{600} of the last sample point to obtain normalized data.
4. Use the detector signals of the first 100 sample points and those of the last 100 sample points from the normalized data, do a quadratic polynomial fit, and then subtract the ideal baseline from the quadratic polynomial fit data to obtain the ripple difference. The ideal baseline can be represented by Equation (3).

$$I_{idea} = \frac{1}{600} X \quad (3)$$

Where X represents the sample point, and I_{idea}

denotes the corresponding theoretic baseline value. The ideal detection baseline is obtained by multiplying the termination signal value I_{600} by the formula 3.

5. Subtract the ripple difference from the normalized data obtained in step 3 to obtain the signal data that are free from ripple interference.
6. Divide the idea baseline, I_{idea}, by the processed detection signal, *I*, which is free from ripple interference to obtain the absorbance ratio I_{idea}/I. Then, perform a *LN* transformation to get the processed measurement data.
7. Find the highest point or peak value and the position of its sampling point in the processed measurement data, which is located around the center of the wavelength scanning range or at the centerline of the Gaussian-shaped gas absorption spectrum. Integrate the processed measurement data over a range of 50 sampling points to the left and right of the peak value to obtain the measured value of the gas concentration. This method is designed to eliminate the uncertainty in the location of the highest point due to small ripples fluctuations, and to achieve the goal of improving the accuracy of the data.
8. The linear relationship between the measured value and the standard gas can be obtained by the calibration with the use of the standard gas. When the sensor is energized with different concentrations of the measured gas at different concentrations, the calibrated linear relationship can be then used to invert the measurement values to the corresponding concentration values.

4. EXPERIMENT

4.1. Experimental Setup

In order to verify if this algorithm can improve gas detection stability, an experiment set up as shown in Figure 4 was used. the temperature of the module is changed when a constant gas concentration is applied to the module, the tested results can be used to assess the measurement dispersion of gas concentration. The testing gas used in this experiment is carbon monoxide.

In can be seen from Figure 4, the outlet of the gas cylinder (Fig 4①) is connected to the inlet of a calibration nozzle (Fig 4②) that is placed onto the inlet of a CO module (Fig 4③), both the calibration nozzle and the module are placed in a temperature test chamber (Fig 4④). In the experiment, the CO module with the new algorithm firmware is placed inside the temperature test chamber. The calibration nozzle is securely fixed onto the outlet of the CO module. Then, the CO module is connected a communication module (Fig 4⑤) to enable online monitoring and debugging with the use of a computer(Fig 4⑥). The experimental setup is illustrated in the Figure 4.

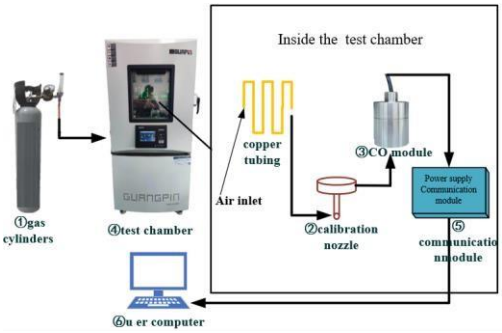

Figure 4. Diagram of the experimental setup

Using a control User interface in the computer, the temperature of the TEC inside the CO module is set to be 30°C for the laser in the module. A saw tooth driving current is applied to the laser to tuning the laser wavelength, so that the scanning range of the laser output wavelength covers the absorption spectrum of carbon monoxide. When the laser is at its set temperature, the center point of its wavelength scanning range aligns with the gas absorption spectrum line.

In order to check the temperature caused variation in the measurement, the experiment is carried out: Apply the gas concentration of 19.7 ppm onto the CO sensor, and allow ventilation for two minutes before the measurement and record data. The temperature of the test chamber is set at 0°C, 10°C, 20°C, 30°C, 40°C respectively. Wait for the temperature inside the test chamber to reach the preset temperature and stabilize. A two-minute socking time is applied between every two different temperature measurements. For every gas concentration, the measurements are repeated ten times.

4.2. Experimental Results

Figure 5 and Figure 6 show the comparison between the measured results before and after the optimization of the test data for the concentration of 19.7ppm at different temperatures.

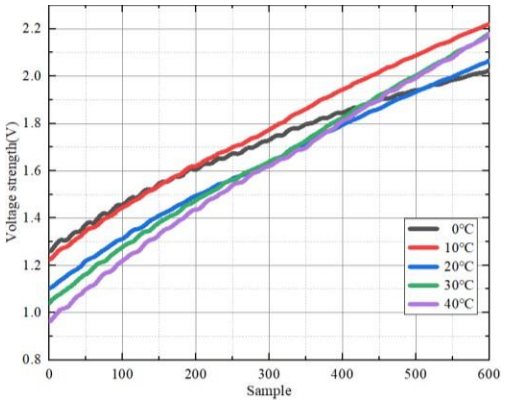

Figure 5. Detection signals at different temperatures

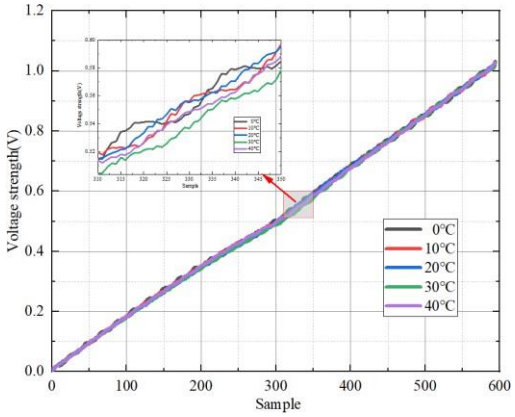

Figure 6. Detection signals at different temperatures after optimization

The noticeable improvement in the linearity of the detection signals at different temperatures after algorithm optimization suggests that the new algorithm effectively suppresses the non-linear enhancement of detection signal intensity caused by the irregular variation of interference fringes with temperature, Hence, this new algorithm enhances the stability of gas concentration detection.

With the use of this new algorithm to the CO module, the improvement of the gas detection stability can be verified. The results are presented in Figure 7.

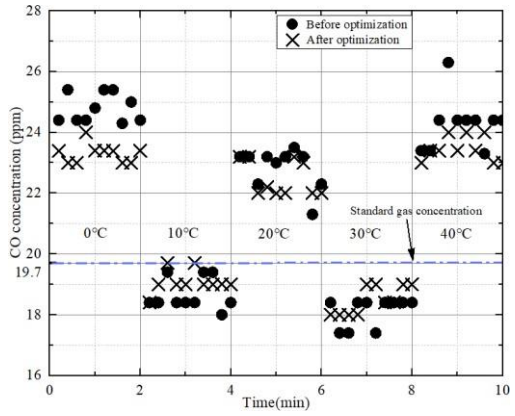

Figure 7. Comparison of Gas Concentrations before and after the Optimization

In Figure 7, the detected concentration values of 19.7 ppm under different ambient temperatures before and after the optimization using the new algorithm are shown. A comparison reveals that the concentration values (shown as “X” in Figure 7) obtained after the optimization are closer to those of the actual concentration. The calculated standard deviation before and after the optimization are 2.88 and 2.18 respectively. By comparing these values, it can be seen that the dispersion of the concentration values decreases by approximately 24.3% after the optimization. Hence, the new algorithm exhibits a mitigating effect on the irregular changes in interference fringes caused by variations in ambient temperature, leading to an improvement in the stability of CO concentration measurement.

5. CONCLUSION

The paper presents a signal processing scheme aimed at suppressing noise floor in the detection signals arising from laser interference variations during the gas concentration measurements, particularly targeting the mitigation of "large ripples" caused by the inference between the laser outlet and the surface of the collimating lens. The new algorithm was experimentally validated with the use of the experimental setup. The experimental results demonstrate that after processing with this new algorithm, the measured CO gas concentrations at different ambient temperatures are closer to the actual concentrations. The dispersion of the concentration values are decreased by 24.3%. This enhancement indicates an improvement in both the stability and accuracy of gas detection. Additionally, this algorithm exclusively targets the interference noise generated by the laser itself, and it can be combined with other algorithms designed to suppress additional interference fringes to enhance the capabilities of the measurement system on noise suppression. Preliminary results indicate that this new algorithm has potential for interference suppression in TDLAS systems and could be applied to methane, carbon dioxide, and other gas detection systems in the future.

ACKNOWLEDGMENTS

This work was supported by Shandong Micro-sensor Photonics Co. Ltd (91370100768729253k) and National Key Research Development Program of China (2022YFB3207602).

FUNDING STATEMENT

This work was supported by Shandong Micro-sensor Photonics Co. Ltd (91370100768729253k) and National Key Research the Development Program of China (2022YFB3207602).

REFERENCES

[1] Li Ma, Li Zou, Li-Feng Ren, Yi-Hong Chung, Peng-Yu Zhang, Chi-Min Shu. Prediction indices and limiting parameters of coal spontaneous combustion in the Huainan mining area in China[J]. Fuel, 2020, 264: 116883.

[2] J. Y. Li, L. H. Li, S. Zhao, P. Ren, S. J. Tian, H. L. Jin, Application research of tunable diode laser absorption spectroscopy in petroleum industry, Laser Optoelectron. P. 59 (13) (2022) 1300006, https://doi.org/10.3788/LOP202259.1300006.

[3] Ahlberg, H., Lundqvist, S., Shumate, M. S., & Persson, U. (1985). Analysis of errors caused by optical interference effects in wavelength-diverse CO 2 laser long-path systems. *Applied optics*, *24*(22), 3917-3923.

[4] C.R. Webster, Brewster-plate spoiler: a novel method for reducing the amplitude of interference fringes that limit tunable-laser absorption sensitivities, J. Opt. Soc. Am. B: Opt. Phys. 2 (9) (1985) 1464–1470.

[5] Persson, L., Andersson, F., Andersson, M., & Svanberg, S. (2007). Approach to optical interference fringes reduction in diode laser absorption spectroscopy. *Applied Physics B*, *87*, 523-530.

[6] Dongdong Pang, Lei Li, Lin Ma, Zhaohan Lin, Peng Liu, Xin Zhou, Interference fringe suppression in tunable diode laser

absorption spectroscopy based on BPNN, Optics Communications, Volume 544,2023,129630, ISSN 0030-4018

[7] Wang, S., Gong, W., Wang, Z., Wei, Y., Li, Y., Zhang, T., ... & Liu, T. (2022). Interference fringe suppression in tunable diode laser absorption spectroscopy based on CEEMDAN-WTD. *Frontiers in Physics*, *10*, 1057519.

[8] Reid, J., Shewchun, J., Garside, B. K., & Ballik, E. A. (1978). High sensitivity pollution detection employing tunable diode lasers. *Applied Optics*, *17*(2), 300-307.

15: ULTRAHIGH-RESOLUTION WHISPERING GALLERY MODE THERMOMETER BASED ON SILICA-MICROSPHERE

*Jiaxing Gao [a, b], Wei Jin [a, b], Shanshan Li [a, b], Yu Zhang [a, b, *], Yifan Qin [a, b], Zhihai Liu [a, b]*

[a] Key Laboratory of In-Fiber Integrated Optics, Ministry of Education, Harbin Engineering University, Harbin, 150001, P. R. China:

[b] Key Laboratory of Photonic Materials and Device Physics for Oceanic Applications, Ministry of Industry and Information Technology of China, Harbin Engineering University, Harbin, 150001, P. R. China:

Optical Fibre Sensors 1, EM010, August 12, 2024, 1:30 PM - 3:00 PM

Abstract – This paper proposes and implements a high-resolution sensing system using an ordinary microsphere whispering gallery mode (WGM) sensor. In exceptional cases, the microsphere resonators can produce satisfactory and dense resonant dips when coupled with tapered fiber, and these resonant dips usually have extremely high-quality factors. This paper explores the advantages of Pound-Drever-Hall (PDH) laser frequency stabilization technology in characterizing the resonance dip variation of high-order WGM in microsphere cavities. PDH technology reduces the difficulty of sensor signal monitoring and improves the detection accuracy and resolution of the WGM sensor. Finally, the system monitors the ambient temperature continuously in real-time and achieves an ultra-high resolution of 2.32×10^{-5} °C.

Keywords**:** whispering gallery mode; silica microsphere; fiber thermometer; Pound-Drever-Hall technology; quality factor

1. INTRODUCTION

Temperature is critical in various physical, chemical, and biological processes. High-resolution temperature measurements can significantly enhance research across multiple fields, e.g., earthquake monitoring[1], energy harvesting[2], and marine exploration[3]. Fiber sensors, celebrated for their high resolution, excellent linearity, and resistance to electromagnetic interference, are broadly applied in temperature sensing. Fiber thermometers based on various schemes have been developed, such as fiber Bragg grating, long-period fiber grating, Fabry-Perot interferometer, Michelson interferometer, and Mach-Zehnder interferometer. However, the demand for high resolution isn't fully addressed using these fiber thermometers.

Whispering gallery mode (WGM) is a circularly symmetric microresonator based on beam confinement. WGM can respond significantly to minor environmental changes. Thus, fiber thermometers based on WGM have become a notable choice for temperature sensing. Several WGM resonator structures have been applied for temperature measurement, including microsphere, microtoroid, microring, microdisk, microbubble, and microbottle. The WGM-based fiber thermometers all show high quality (Q) factors, compact mode volumes, and convenience of integration[4].

Organic materials like polydimethylsiloxane (PDMS) and poly(methyl methacrylate) (PMMA) have been used to fabricate WGM thermometers, achieving high resolution and sensitivity due to the high thermal expansion coefficient. However, it's important to note that the organic WGMs have shown slow response and lack repeatability due to their low thermal conductivity and significant hysteresis nature. Liquid-based WGMs have been proposed for reasons similar to their organic counterparts[5]. However, their storage poses a challenge due to volatility. Furthermore, substantial cavity optical loss can negatively impact the resolution. WGM-based optomechanical thermometers have been developed for enhanced sensitivity without sacrificing resolution. This advancement is primarily due to the enhanced interaction between the optical and mechanical resonant modes. While these thermometers have benefits, their intricate structures can challenge mass production. Besides all the deficiencies above, the highest resolution of existing WGM thermometer schemes can only reach 10^{-4} °C, limited by the probing laser linewidth and the noise of an open-loop detection system, e.g., optical spectral analyzer (OSA).

Pound-Drever-Hall (PDH) technology is commonly used for maintaining and securing laser frequency in stabilization systems. With the application of PDH technology, associated fiber thermometers can attain a much higher resolution because the probing laser can be closed-loop locked to the resonance dips. Recently, a laser stabilized by PDH was used to probe an FFPI sensor, boosting the temperature resolution by two orders of magnitude[6]. Additionally, PDH can realize real-time temperature monitoring, broadening the application scenario of fiber thermometers.

In this paper, we combine the PDH technology with a silica-microsphere WGM resonator for real-time ultrahigh-resolution temperature measurement. The endface of a silica single-mode fiber (SMF) is melted by high-voltage discharge using a fusion splicer. This process results in the formation of a smooth microsphere with ellipticity at the SMF tip, thanks to the natural process of surface tension. Adjusting the discharge time can modify the microsphere's diameter from 20 to 500 μm. The detailed fabrication method of the silica microsphere can be addressed in our previous work[20]. Then, a 1550-nm probing laser is coupled into a 300-μm silica-microsphere through a tapered fiber for the generation of high-order WGM, which is brought by ellipticity-introduced azimuthal degeneracy. The high-order mode displays a significantly greater Q factor (10^7) than the fundamental mode. PDH technology can lock the probing laser to a resonant dip of the high-order WGM, yielding a real-time ultrahigh-resolution (2.32×10^{-5} °C) temperature response. Moreover, the cost-effective silica-based thermometer stands

DOI: https://doi.org/10.34961/researchrepository-ul.29270282.v1

out for its ease of storage, excellent repeatability, and suitability for mass production.

2. METHODS AND PROCEDURES

2.1. Sensor preparation

The tapered fiber was fabricated using a flame-heated drawing technique. Since the taper region of the tapered fiber is only 2 μm in diameter, it is directly fixed on a specially designed slide to prevent breakage during sampling. Tapered fiber is supported to a certain height by the a and b glass plates on the slide to avoid direct contact with the slide. The side of the slide is designed with a supporting glass sheet c, which is used to fix the well-coupled microsphere (Fig 1).

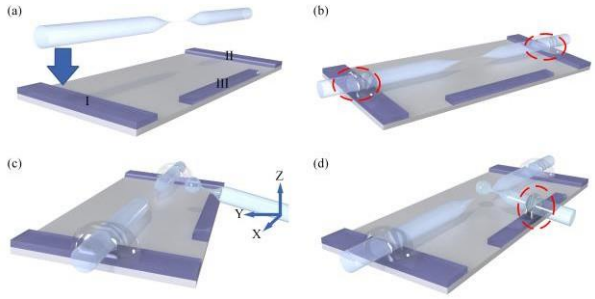

Figure 1. Probe packaging process (a, b) The tapered fiber is placed on the platform in the center along the long side and fixed with ultraviolet curing adhesive. The red dotted line shows the fixed point. (c, d) X-Y-Z three-dimensional micro-displacement platform was used to clamp the microsphere's pigtail and move the microsphere close to the cone region of the tapered fiber. After the coupling position was determined, the pigtail of the microsphere was fixed on the supporting glass sheet c, and the red dotted line was shown as the fixed point.

The microspheres and fibers are positioned under the microscope using a three-dimensional X-Y-Z platform to adjust the coupling position and state more precisely. In the coupling process, the transmission spectrum is obtained by the narrow line-width laser through fine scanning until the resonant dip with a series of high order WGMS with high Q values is obtained. In this case, the microsphere is further placed close to the conical region of the conical fiber to improve the stability of the packaged structure. After that, the microsphere pigtail was fixed on glass sheet c with UV-curable glue. After UV-curable glue is applied, it needs to rest for 15 minutes before curing to reduce the viscosity and gravity of glue induced coupling position changes. The packaged WGM microsphere sensing probe and its picture under the microscope are shown in the Fig. 2.

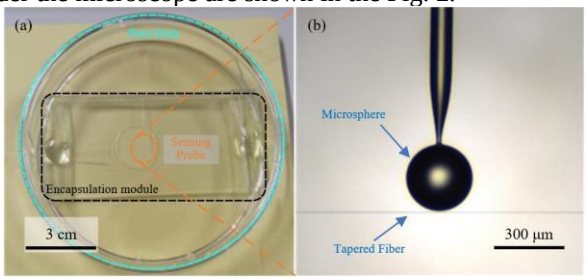

Figure 2. (a) The finished probe made in the laboratory (b)The probe observed under a microscope.

2.2. Spectral Signature

Fig. 3 (a) shows the transmission spectrum of the microsphere resonator after packaging, which offers a relatively dense and fine mode spectrum. The diameter of the microsphere is 300 μm, and the calculated free spectral range (FSR) of its fundamental mode in the band of 1550 nm is about 1.75 nm, more significant than the distance between resonant peaks obtained by the fabricated microsphere resonators. This phenomenon is because the spherical structure formed by the molten optical fiber through discharge has a certain ellipsometry under the influence of gravity, arc disturbance, and other factors. This flaw leads to the depravity of the azimuth modulus m of the resonant cavity, which leads to the resonance peak of the transmission spectrum of the microsphere resonant cavity being quite dense and complex. It is worth noting that the resonant dip produced by these mode resonances has high Q factors, with an average Q factor above 10^7, as shown in Fig. 3 (b)[7]. The differences in the Q factor of different resonant dips are due to the differences in coupling efficiency between modes, of which quite a few are over-coupling.

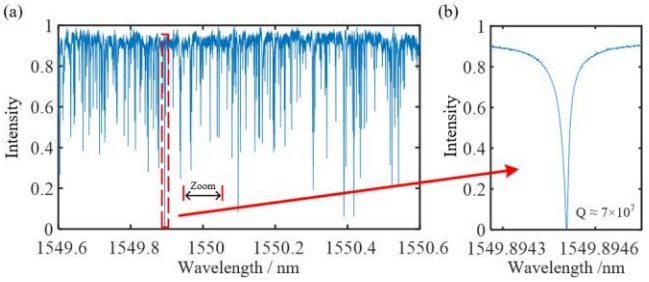

Figure 3. Probe spectrogram (a) transmission spectrum of the microsphere resonator after packaging (b) amplified formant.

Although the WGM sensor with fine resonant dip can improve the system's sensitivity, the dense and irregular mode spectrum raises the requirements on the hardware of the sensor system. It increases the difficulty of spectral analysis, which limits the application of high-order WGM mode sensing.

2.3. PDH frequency locking system

The traditional PDH frequency locking method is used to stabilize the output frequency of the laser. It is well known that electronic devices cannot directly measure the frequency of light, so some indirect characterization and measurement methods have been proposed. A Fabry–Perot interferometer in a stable environment has a fixed resonance spectrum. After the laser passes through it, the intensity and phase of the reflected light change with the frequency of the incident light. In the PDH system, the phase of incident light is modulated, so the optical frequency entering the FP cavity dithers around the output optical frequency of the laser, and two symmetrical sidebands are generated. After the FP cavity reflects the modulated light, a beat pattern will appear at the modulated frequency, and the phase of this beat pattern reflects the phase of the reflected beam.

The difference between the laser frequency and the FP resonance frequency is reflected by measuring the phase of the beat pattern. The laser frequency is dynamically adjusted according to the feedback of the error signal and locked on a resonant frequency of the FP cavity to stabilize the output frequency.

The technology used in sensing is the reverse process of laser frequency stabilization. A light source with stable output is used to track the drift of resonant dip produced by the environmental influence, and the relevant feedback indirectly represents the change degree of the monitored ecological quantity[6]. Fig. 4 shows the specific process of using PDH technology to characterize WGM thermometer.

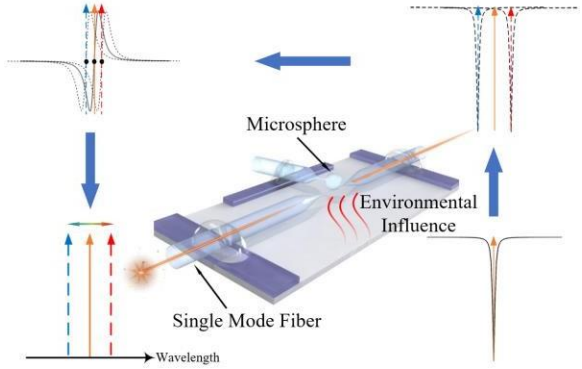

Figure 4. The process of using PDH technology to characterize WGM thermometer

2.4. Experimental System

By using the PDH frequency locking system, we realize the locking of the resonance frequency of the microsphere. The structure of the system is shown in Fig. 5. The continuous laser output from a tunable narrow-width laser (NKT, E15) is first modulated in a phase modulator (PM, PANWOO, SPM-301A), then regulated by a polarization controller (PC) and coupled to the microcavity probe. Signal generators (SG, SIGLENT, SDG1000X) output sine wave signals to drive the phase modulator and the phase-locked amplifier. The modulated light is interfered in a microsphere and then sent to the photodetector (PD, AOSHOW, PDA1008) and converted into an electrical signal. The electrical signal is further converted into an error signal representing the difference between the laser's output frequency and the microcavity's resonant frequency by a lock-in amplifier (LIA, Analog Devices, AD8333). A field-programmable gate array (FPGA, NI, PCIE-7856R) is used to collect error signals and adjust the output frequency of the laser. At the same time, the feedback signals are uploaded to the computer to realize tracking of the resonant frequency of the microcavity and real-time monitoring of frequency changes.

At the modulation frequency of 15Mhz, the output optical frequency of the laser is scanned at a frequency of 3Hz within the range of 600 MHz. The corresponding error signal pattern is shown in Fig. 6. Then the system is set to lock and track the zero crossing position of any complete error signal. The signal transformation controlled by the feedback is linearly related to the wavelength transformation of the microsphere WGM resonance[8].

It can be observed from Figure 6 that the average distance of the resonant dips excited by the microsphere with a diameter of 300 μm is 0.2GHz, which is smaller than the frequency modulation range of the laser, which is 0.6GHz. Multiple resonant peaks can be obtained by a single frequency sweep, which provides a new idea for improving the sensor's detection range. When the detected environment changes significantly, the tracking resonance frequency will exceed the frequency modulation range of the laser, and the laser is faced with lock-out.

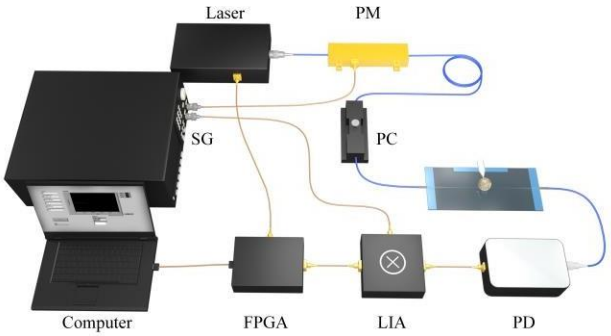

Figure 5. Experimental system

In order to solve this problem, we designed the logic of relocking connection measurement in the locking system. When one resonant dip moves outside the frequency modulation range, other resounding drop in the frequency modulation range are automatically found and tracked. This process is completed in less than 0.2s, and the missing data in the middle can be predicted by fitting the data for a short period before the lock loss. Since each resonant dip changes uniformly under the influence of external environmental factors, the measurement range can be improved by relocking the new resonant peak for continuous measurement.

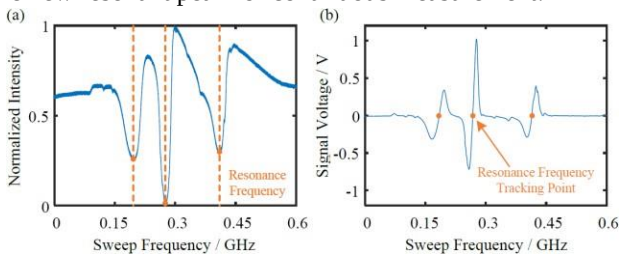

Figure 6. (a) The spectrum in the sweep frequency range of 600M (b) Error signal generated by the system.

2.5. Experimental Process

Because the temperature change will change the size and refractive index of silica microspheres and then cause the drift of resonant frequency, that can be expressed as

$$\Delta\nu = -(\alpha_W + \alpha_T)\nu\Delta T. \quad (1)$$

Where α_W and α_T represent the thermal expansion and thermal-optical coefficients of microspheres, respectively, and ΔT represents the temperature change. As seen from (1), frequency and temperature are linearly correlated.

The probe is placed in the temperature chamber, and the temperature in the temperature chamber is controlled to increase in a particular range. During this period, the feedback signal of the system is recorded in real time, and the change in the output frequency of the actual laser is obtained through calculation. The target temperature set by the temperature chamber increases by 0.5 °C every two hours. The blue dashed line in Fig. 7(a) shows the observed trend data of the quartz thermometer (HUAFAN, CWYS-14) when the temperature increases from 30 °C to 34.5 °C. The solid orange line in Fig. 7(a) shows the detected data the microcavity probe sensing system recorded during this time. Comparing the two data curves in Fig. 7(a), there is a good consistency in the change trend. The difference is because the temperature chamber adopts the heating method of heat conduction, and the temperature of different positions is different simultaneously.

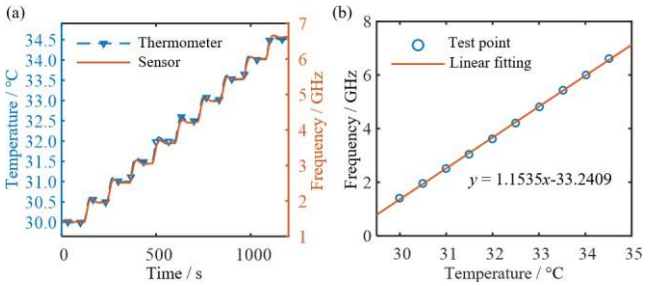

Figure 7. (a) The comparison of Quartz thermometer observation data and Sensor measurement data (b) Frequency curve with temperature.

To eliminate the influence of differences, the average value of temperature and frequency data within half an hour before the set temperature change was selected as the sampling points of temperature and frequency, and a total of ten groups of relevant data were obtained. The Pearson correlation coefficient was 0.9998, indicating a strong linear correlation between temperature and frequency, consistent with the theory. Fig. 7(b) shows the relationship curve between temperature and frequency after linear fitting. The temperature sensitivity of the probe is calculated to be 1.1535 GHz/°C.

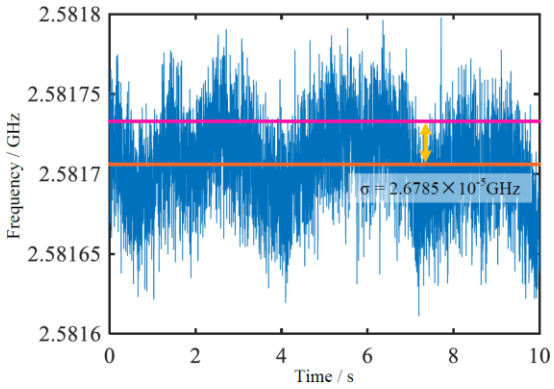

Figure 8. Frequency fluctuations in a stable environment.

When the ambient temperature is stable, the measured data in 10s are selected, and the standard deviation of these data is calculated. The resolution of the probe is estimated to be better than 2.32×10^{-5} °C (Fig. 8), which is much higher than the existing WGM temperature sensing system.

3. RESULTS AND DISCUSSION

In the fabrication and packaging of the micro scout head, the monitoring scheme of locking high-order WGM mode resonant peak is adopted to weaken the precision of microsphere processing and the rigor of coupling package, which means that the system has higher robustness and stability, which is conducive to achieve a broader range of applications. However, it is worth mentioning that the polarization state dramatically affects the higher-order WGM mode, which can be weakened by changing the input and output fiber to polarization-maintaining fiber.

In terms of temperature sensitivity, the microcavity probe still has a lot of room for improvement. It can be coated with heat-sensitive material on the microsphere's surface to improve the temperature sensitivity or coated with heat-stabilized material to suppress the influence of temperature change on other sensing quantity detection. The sensitivity of the sensing quantity also directly affects the resolution of the sensing system. High sensitivity means higher system resolution.

4. CONCLUSIONS

In this paper, using PDH technology, the laser source is locked on the microsphere cavity to generate high order WGM resonant dip, and a WGM high-resolution sensor, which can be observed in real-time, is realized. It achieves a high resolution of 2.32×10^{-5} °C with a sensitivity of 1.1535 GHz/°C in the temperature sensing response, which is much higher than existing conventional WGM sensors. At the same time, due to its high sensitivity in biomolecular detection, WGM is expected to provide faster and more efficient means in virus detection, water quality detection, and other directions requiring high sensitivity and resolution.

FUNDING STATEMENT

The Basic Research Support Program for Excellent Young Teachers of Heilongjiang Province (YQJH2023281); Taishan Scholars Program; China Postdoctoral Science Foundation (2022M720940); Qingdao Natural Science Foundation (23-2-1-214-zyyd-jch); Fundamental Research Funds of Harbin Engineering University.

REFERENCES

[1] S. Hall, **What Turkey's earthquake tells us about the science of seismic forecasting**. Nature, vol. 615 , 7952, 2023, pp. 388-389. DOI: https://doi.org/10.1038/d41586-023-00685-y

[2] L. Lan, C. Jiang, Y. Yao, J. Ping, Y. Ying, **A stretchable and conductive fiber for multifunctional sensing and energy harvesting.** Nano Energy, vol. 84, 2021, pp. 105954. DOI: https://doi.org/10.1016/j.nanoen.2021.105954

[3] R. Min, Z. Liu, L. Pereira, C. Yang, Q. Sui, C. Marques, **Optical fiber sensing for marine environment and marine structural health monitoring: A review.** Opt. Laser Technol. Vol. 140, 2021, 107082. DOI: https://doi.org/10.1016/j.optlastec.2021.107082

[4] D. Yu, M. Humar, K. Meserve, R. C. Bailey, S. N. Chormaic, **Whispering-gallery-mode sensors for biological and physical sensing.** Nat. Rev. Method. Prime. Vol. 1, 1, 2021, pp. 83. DOI: https://doi.org/10.1038/s43586-021-00079-2

[5] Y. Wang, H. Li, L. Zhao, Y. Liu, S. Liu, J. Yang, **Tapered optical fiber waveguide coupling to whispering gallery modes of liquid crystal microdroplet for thermal sensing application.** Opt. Express. vol. 25, 2, 2017, pp. 918-926. DOI: https://doi.org/10.1364/OE.25.000918

[6] S. Zhao, Q. Liu, J. Chen, Z. He, **Resonant fiber-optic strain and temperature sensor achieving thermal-noise-limit resolution.** Opt. Express, vol. 209, 2021, pp. 1870–1878. DOI: https://doi.org/10.1364/OE.415611

[7] G. C. Righini, Y. Dumeige, P. Féron, M. Ferrari, G. Nunzi Conti, D. Ristic, and S. Soria, **Whispering gallery mode microresonators: Fundamentals and applications**. La Rivista Del Nuovo Cimento. Vol. 34, 2011, pp. 435-488. DOI: https://doi.org/10.1393/ncr/i2011-10067-2

[8] Y. Zhang, W. Jin, Y. Zhang, Z. Liu, Y. Yuan, Z. Yu, J. Yang, Y. Wang, and Y. Qin, **High-resolution Optical Fiber Strain Sensor Array Based on Pound-Drever-Hall Technique**

with Fast Phase Regulation Method. J Lightwave Technol. Vol. 41, 6, 2022, 1-7. DOI: 10.1109/JLT.2022.3225815

17: STRAIN MEASUREMENT WITH A HIGH SENSITIVITY BASED ON AN OPTOELECTRONIC OSCILLATOR INCORPORATING CHIRPED FIBER BRAGG GRATINGS

Yunxin Wang [a, b], *Qiming Su* [a], *Jing Zhang* [a, *], *Dayong Wang* [a, b], *Jie Zhao* [a, b], *Yu Zhang* [a]

[a] School of Physics and Optoelectronic Engineering, Beijing University of Technology, Beijing, China
[b] Engineering Research Center of Precision Measurement Technology and Instruments, Beijing, China

Abstract – A scheme for high-sensitivity strain measurement is proposed and experimentally demonstrated based on an optoelectronic oscillator (OEO). In the OEO, two identical chirped fiber Bragg gratings (FBGs) are introduced to form a Michelson interferometer. Due to the dispersion property of chirped FBG, the wavelength shift induced by strain will lead to a variation in the free spectrum range of Michelson interferometer, which will then cause an oscillating frequency shift of OEO with a large scale factor. Therefore, strain measurement with a high sensitivity can be realized by monitoring the frequency shift of the microwave signal generated by OEO. Experimental results show that the strain measurement sensitivity is 1.8 MHz/με within a range from 0 to 1333.33 με.

Keywords**:** optoelectronic oscillator; strain measurement; chirped fiber Bragg grating; Michelson interferometer; chromatic dispersion; microwave photonic filter

1. INTRODUCTION

Fiber optical sensors have attracted much attention in recent years because of their compact structure, high sensitivity, anti-electromagnetic interference, and compatibility with the existing communication systems [1]-[4]. For fiber optical sensing systems, demodulation schemes must be taken to convert the optical sensing signals into electrical signals so that thay can be processed and analysed. Therefore, the demodulation method has a significant influence on the system performance. Microwave photonics, which is an emerging discipline that studies the interaction between microwaves and photonics [5], [6], provides a new way for the demodulation of fiber optical sensors. With microwave photonics technology, the physical information to be measured can be directly mapped into the parameters of electrical signal, while the sensing process is still implemented in the optical domain. Therefore, the microwave-photonics-based sensing system combines the advantages of fiber optical sensor and electrical signal processing technology [7], [8]. Among various sensing methods based on microwave photonics, optoelectronics oscillator (OEO) shows great potential to realize measurements with high sensitivity, high resolution and high sensing speed [9], [10].

The main concept for the OEO-based sensor is to translate the physical information into the oscillating frequency of OEO, thus by monitoring the frequency shift of the microwave signal generated by OEO, the physical information to be measured can be obtained. For OEO-based strain measurements, there are usually two ways to realize the strain-to-frequency mapping. One is to get the loop length of OEO changed with strain, which can be achieved with a uniform fiber Bragg grating (FBG) as the sensing unit. Based on a broadband source and dispersion effect, the applied strain on the FBG is finally mapped into the oscillating frequency shift of OEO [11], [12]. For this method, the measurement range is restricted by the free spectrum range (FSR) of OEO, which is usually in the order of MHz or kHz. Besides, the broadband advantage of the light source is not fully utilized and the measurement sensitivity still needs to be improved. The other way to map strain into the oscillating frequency of OEO is to make the central frequency of filter used in the OEO loop varies with strain. By using a microwave photonic filter incorporating a tunable laser source and a phase-shifted FBG (PS-FBG), an OEO-based strain sensor with a high sensitivity can be realized [13], [14]. Nevertheless, the stability of the laser source has a great impact on the measurement results.

In this paper, an OEO using a broadband light source is proposed to realize a high-sensitivity strain measurement. Two identical chirped FBGs are introduced as the sensing head and they form a Michelson interferometer. Thanks to the wide reflection spectrum of chirped FBG, the broadband property of the light source can be fully utilized and a microwave photonic filter with a single bandpass is obtained. The filter is used for the frequency selection of OEO and its central frequency is related to the time delay difference between the two arms of the Michelson interferometer. When a strain is applied to one of the chirped FBGs, its wavelength shift will produce a variation in signal transmission latency due to the chromatic dispersion of chirped FBG. As a result, the applied strain is finally mapped into the oscillating frequency of OEO with a scale factor proportional to the dispersion coefficient of chirped FBG.

1. SYSTEM PRINCIPLE

The schematic diagram of the proposed system is shown in Figure 1. An amplified spontaneous emission (ASE) light source is used to generate the broadband optical signal. After passing through an optical bandpass filter (OBPF), the signal is polarized with a polarizer (Pol) and then sent to a Michelson interferometer via an optical circulator (OCir). The Michelson interferometer is formed with a 2×2 3-dB optical coupler (OC1), a polarization controller (PC), an optical variable delay line (OVDL), and two identical chirped FBGs (CFBG1 and CFBG2).

DOI: https://doi.org/10.34961/researchrepository-ul.29278217.v1

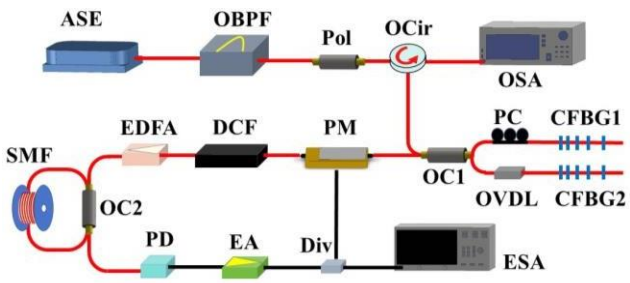

Figure 1. Schematic diagram of the proposed system for high-sensitivity strain measurement.

One part of the output signal from Michelson interferometer is launched into an optical spectrum analyzer (OSA), and the other part is modulated by the oscillating signal of OEO with a phase modulator (PM). Then the modulated optical signal is sent to a section of dispersion compensation fiber (DCF) and converted into electrical signal via a photodetector (PD) subsequently. After amplified by an amplifier (EA), the signal is equally divided into two parts through a power divider (Div). One part is monitored by an electrical signal analyzer (ESA), and the other part is sent back to the phase modulator to close the OEO loop.

The ASE light source, optical bandpass filter, polarizer, Michelson interferometer, phase modulator, dispersion compensation fiber and PD in the system form a microwave photonic filter, and its central frequency can be written by [15]

$$f_0 = \frac{1}{D_1 \lambda_{FSR}}, \tag{1}$$

where D_1 is the dispersion coefficient of the dispersion compensation fiber with a unit of ps/nm, and λ_{FSR} is the free spectrum range of the Michelson interferometer. It can be expressed as

$$\lambda_{FSR} = \frac{\lambda_0^2}{c\Delta\tau}, \tag{2}$$

where λ_0 is the central wavelength of the broadband signal, c is the light velocity in vacuum, and $\Delta\tau$ is the time delay difference between the two arms of Michelson interferometer.

When there is a strain applied to one of the chirped FBGs (CFBG1 for example), a wavelength shift will happen for the reflection spectrum of CFBG1. The relationship between the wavelength shift and applied strain can be written by [16]

$$\Delta\lambda = \lambda_0(1 - p_e)\varepsilon, \tag{3}$$

where p_e is the photo-elastic coefficient of fiber, and ε is the applied strain. As the wavelength of the optical signal keeps constant, the signal transmission delay will change with $\Delta t = D_2\Delta\lambda$ due to the chromatic dispersion of chirped FBG, where D_2 is the dispersion coefficient of CFBG1. It can be derived from (1) and (2) that a variation on the free spectrum range of Michelson interferometer will be introduced, which will then cause a frequency shift of the microwave photonic filter. Note that the microwave photonic filter in the OEO system plays the role of oscillating mode selection, thus the applied strain on CFBG1 is finally mapped into the oscillating frequency shift of OEO. The relationship between them is

$$\Delta f = \frac{cD_2(1 - p_e)\varepsilon}{D_1\lambda_0} = K\varepsilon, \tag{4}$$

where K is constant. From (4), we can see that the oscillating frequency of OEO has a linear relationship with the applied strain, and the scale factor is proportional to the dispersion coefficient of CFBG1. Therefore, a high-sensitivity strain measurement can be realized by monitoring the oscillating frequency of OEO.

To guarantee a single-mode oscillation, an infinite impulse response filter, formed with a 2×2 3-dB optical coupler (OC2) and a length of single mode fiber (SMF), is added in the OEO loop for the fine selection of oscillating frequency.

2. RESULTS AND DISCUSSION

A proof-of-concept experiment is performed based on the setup shown in Figure 1. A broadband optical signal with a power of 18 dBm is tailored by a Gaussian-shaped filter (WaveShaper 4000A), whose central wavelength and 3-dB bandwidth were set to 1552 nm and 5 nm, respectively. The chirped FBGs that make up the Michelson interferometer have a 3-dB bandwidth of 30 nm with a central wavelength of 1550 nm and a dispersion coefficient of 33.3 ps/nm. Since the bandwidth of the chirped FBG is wider than that of the optical signal, it can be considered the wavelength of the broadband optical signal keeps constant when there is a wavelength shift for the chirped FBG. One part of the optical signal reflected by the Michelson interferometer was sent to a 20-GHz phase modulator, and the other part was monitored with an optical spectrum analyzer (Ando AQ 6317C). The dispersion compensation fiber placed after the phase modulator has a dispersion coefficient of about 1600 ps/nm. To compensate the optical loss, an Erbium-doped fiber amplifier (EDFA) is added before the infinite impulse response filter, which is mainly formed with a 200-m SMF and a 2 × 2 3-dB optical coupler. The bandwidth of photodetector used for optical-to-electrical conversion is 10 GHz and the electrical amplifier has a tunable gain from 0 to 66 dB within a frequency range of 2-6 GHz.

When the OEO loop is closed and the gain is tuned to be large enough, an oscillating signal can be generated by carefully adjusting the OVDL to make the central frequency of microwave photonic transversal filter within the operating bandwidth of the electrical amplifier. Figure 2 shows the output spectrum of Michelson interferometer when both chirped FBGs are relaxed at room temperature. It can be seen from the inset that the free spectrum range of the interference signal is 0.16 nm.

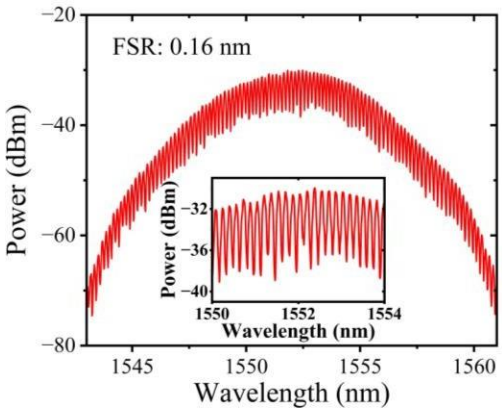

Figure 2. Output spectrum of Michelson interferometer when both chirped FBGs are relaxed at room temperature.

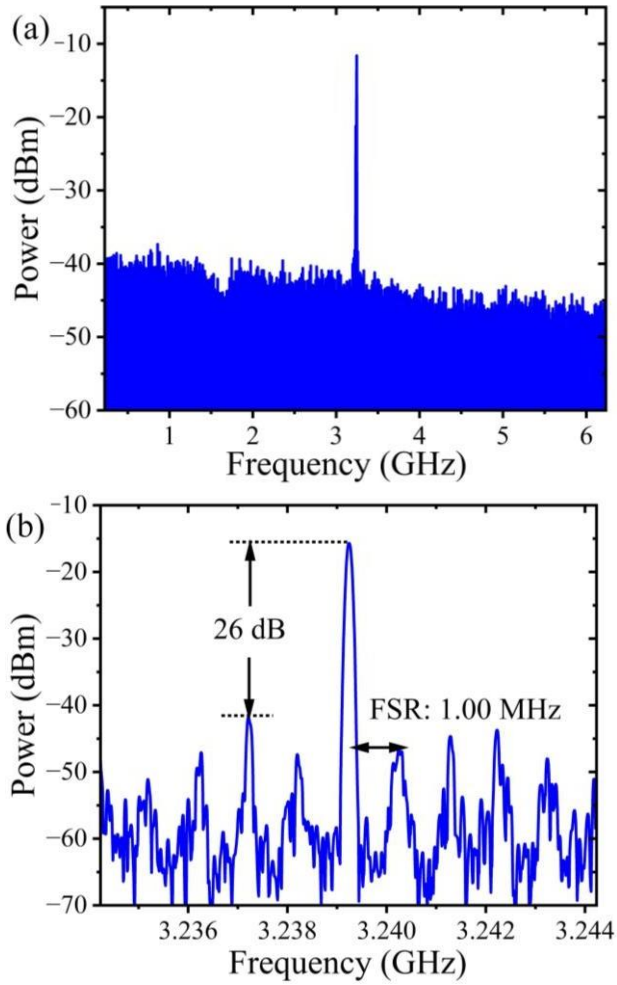

Figure 3. Spectrum of the oscillating signal with a span of (a) 6 GHz and (b) 100 MHz.

Figure 3(a) and 3(b) present the oscillating spectrum of OEO with a frequency span of 6 GHz and 100 MHz, respectively, which are measured by a 26.5-GHz electrical signal analyser (Keysight, N9020A). It can be seen from Figure 3(b) that the oscillating frequency is 3.2392 GHz with a side mode suppression ratio of 26 dB. The free spectrum range of the OEO is about 1 MHz, consistent with the length of SMF constituting of the infinite impulse response filter (200 m).

To verify the system performance for strain measurement, one of the chirped FBGs is fixed with two fiber clamps. By stretching the chirped FBG with different displacements, different strain will be applied on it. During the measurement, the other chirped FBG always keeps relaxed. Figure 4(a) presents the measured spectra of oscillating signals generated by OEO when the strain changes from 0 to 1333.33 με with a step of 83.33 dispersion coefficient. The linear fitting of the experimental data is given in Figure 4(b). It is apparent from the result that the oscillating frequency shift of OEO has a linear relationship with the strain and the sensitivity is 1.88 MHz/με. For the proposed system, the minimum strain that can be measured is determined by the free spectrum range of the OEO and it can be calculated to be 0.53 με. However, limited by the resolution of the translation stage used in our experiment, the minimum identifiable applied strain on the chirped FBG is 83.33 με.

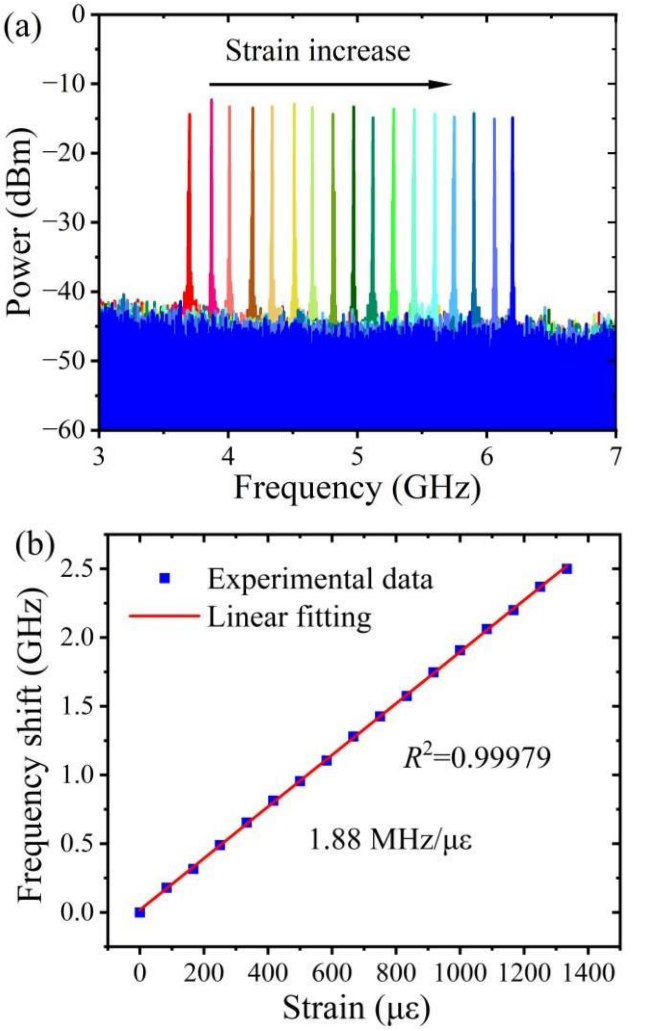

Figure 4. (a) Oscillating spectra of OEO under different strains. (b) The relationship between the oscillating frequency shift of OEO and the applied axial strain.

3. CONCLUSIONS

In this paper, an OEO-based strain measurement is proposed and demonstrated based on a broadband light source and two identical chirped FBGs. The wide reflection spectrum of the chirped FBG, together with the broadband light source, helps to implement a single bandpass microwave photonic filter that can be used for the frequency selection of OEO. With one of the chirped FBGs as the sensing head, the applied strain on it is firstly transformed into the frequency shift of the microwave photonic filter, and then mapped into the oscillating frequency shift of OEO. The measurement sensitivity is proportional to the dispersion coefficient of the chirped FBG and inversely proportional to the dispersion coefficient of the dispersion compensation fiber. Experimental results show that it is 1.88 MHz/με when the chirped FBG has a dispersion coefficient of 33.3 ps/nm and the dispersion compensation fiber has a dispersion coefficient of 1600 ps/nm. If the dispersion coefficients are properly designed, then strain measurement with a higher sensitivity can be realized.

FUNDING STATEMENT

This work was supported by the National Natural Science Foundation of China under Grant 62275008 and Grant 62220106005.

REFERENCES

[1] X. Gui, Z. Y. Li, X. L. Fu, H. Y. Guo, Y. M. Wang, C. J. Wang, J. Q. Wang, D. S. Jiang, **Distributed Optical Fiber Sensing and Applications Based on Large-scale Fiber Bragg Grating Array: Review**, J. Lightwave Technol. vol. 41, no. 13, 2023, pp. 4187-4200.

[2] E. Vavrinsky, N. E. Esfahani, M. Hausner, A. Kuzma 1, V. Rezo, M. Donoval, H. Kosnacova, **The current state of optical sensors in medical wearables**, Biosensors, vol. 12, no. 4, 2022, 217.
DOI: https://doi.org/10.3390/bios12040217

[3] H. Bai, S. Li, J. Barreiros, Y. Tu, C. R. Pollock, R. F. Shepherd, **Stretchable distributed fiber-optic sensors**, Science, vol. 370, no. 6518, 2020, pp. 848-852.

[4] X. Z. Zhang, B. Y. Yang, J. F. Jiang, K. Liu, X. J. Fan, Z. Z. Liu, M. Peng, G. L. Chen, T. G. Liu, **Side-polished SMS based RI sensor employing macro-bending perfluorinated POF**, Opto-Electron. Adv. vol. 4, no. 10, 2021, 200041.

[5] T. Berceli, P. R. Herczfeld, **Microwave Photonics - A historical perspective**, IEEE T. Microw. Theory. Vol. 58, 2010, pp. 2992-3000.

[6] J. Capmany, D. Novak, **Microwave photonics combines two worlds**, Nat. Photonics. vol. 1, no. 6, 2007, pp. 319-330.

[7] J. Hervás, A. L. Ricchiuti, W. Li, N. H. Zhu, C. R. Fernández-Pousa, S. Sales, M. Li, J. Capmany, **Microwave photonics for optical sensors**, IEEE J. Sel. Top. Quant. vol. 23, no. 2, 2017, pp. 327-339.

[8] J. P. Yao, **Microwave photonic sensors**, J. Lightwave. Technol. vol. 39, no.12, 2020, pp. 3626-3637.

[9] X. H. Zou, X. K. Liu, W. Z. Li, P. X. Li, W. Pan, L. S. Yan, L. Y. Shao, **Optoelectronic oscillators (OEOs) to sensing, measurement, and detection**, IEEE J. Quantum. Elect. vol. 52, no. 1, 2015, pp. 1-16.

[10] J. P. Yao, **Optoelectronic oscillators for high speed and high resolution optical sensing**, J. Lightwave. Technol. vol. 35, no. 16, 2017, pp. 3489-3497.

[11] Z. W. Xu, X. W. Shu, H. Y. Fu, **Fiber Bragg grating sensor interrogation system based on an optoelectronic oscillator loop**, Opt. Express. vol. 27, no. 16, 2019, pp. 23274-23281.

[12] L. G. Gao, Y. P. Wang, X. Z. Tian, Y. H. Xiao, Q. Liu, D. Zhu, **High-precision temperature-compensated fiber Bragg grating axial strain sensing system based on a dual-loop optoelectronic oscillator with the enhanced Vernier effect**, Appl. Opt. vol. 62, no. 19, 2023, pp. 5317-5324.

[13] O. Xu, J. J. Zhang, H. Deng, J. P. Yao, **Dual-frequency optoelectronic oscillator for thermal-insensitive interrogation of a FBG strain sensor**, IEEE Photonic. Tech. L. vol. 29, no. 6, 2017, pp. 357-360.

[14] B. Yin, M. G. Wang, S. H. Wu, Y. Tang, S. C. Feng, H. W. Zhang, **High sensitivity axial strain and temperature sensor based on dual-frequency optoelectronic oscillator using PMFBG Fabry-Perot filter**, Opt. Express vol. 25, no. 13, 2017, pp. 14106-14113.

[15] J. Mora, B. Ortega, A. Díez, J. L. Cruz, M. V. Andrés, J. Capmany, D. Pastor, **Photonic microwave tunable single-bandpass filter based on a Mach-Zehnder interferometer**, J. Lightwave. Technol. vol. 24, no. 7, 2006, pp. 2500-2508.

[16] E. Vorathin, Z. M. Hafizi, A. M. Aizzuddin, M. K. A. Zaini, K. S. Lim, **Temperature-independent chirped FBG pressure transducer with high sensitivity**, Opt. Lasers Eng. vol. 117, 2019, pp. 49-56.

18: BESSEL GAUSSIAN BEAM CHIP BASED ON METASURFACE

Bo Wu[a], *Yiyang Xie*[a] *, *Chen Xu*[a], *Baolu Guan*[a], *Weiling Guo*[a]

[a].Key Laboratory of Optoelectronics Technology, Ministry of Education, Beijing University of Technology ,Beijing, 100124, China,

Photonic Sensors, EM010, August 12, 2024, 4:50 PM - 5:30 PM

Abstract-Bessel Gaussian beams, recognized as a type of "lossless beam," hold significant value. In this study, we propose the design of a metasurface-integrated vertical cavity surface emitting laser capable of directly generating high-order Bessel Gaussian beams. Leveraging metasurfaces as a medium, we seamlessly integrate the functionality of Bessel Gaussian beams into a Vertical Cavity Surface Emitting Laser (VCSEL). This innovative approach enhances the practical applicability of VCSELs and opens new possibilities for generating high-order Bessel Gaussian beams directly.

Keywords**:** Bessel Gaussian beam, metasurfaces, vertical cavity surface emitting laser, integrated chip design

1. INTRODUCTION

The vortex beam, a novel type of laser, exhibits promising applications in optical communication, detection, optical processing, quantum information processing, and various other fields, attributed to its distinctive spiral wavefront distribution. Examples of commonly encountered vortex beams that exhibit this characteristic include Bessel beams and Bessel Gaussian beams. The concept of the ideal Bessel beam was first introduced by J. Durnin from the University of Rochester in the United States [1]. The Bessel beam possesses a "lossless characteristic," allowing it to recover naturally when encountering obstacles during propagation, making Bessel beams highly preferred. With the advantages of large depth of field and self-healing, Bessel beam has a wide range of applications in quantum entanglement, underwater 3D imaging, space communication, optical micromanipulation and other fields. However, the term "ideal beam" stems from the mathematical concept that a Bessel beam comprises infinite concentric circles, possesses an infinite radius, and carries infinite energy. In practical applications, achieving a truly ideal Bessel beam is impractical. Consequently, Bessel Gaussian beams replace most scientific research work [2]. Currently, Bessel Gaussian beams can be generated using methods like ring slit lens, cone lens, holography, etc. However, these methods exhibit limited control accuracy and cannot achieve nanoscale beam control. Additionally, the generation process involves a large volume and various optical components, hindering system integration and being incompatible with photon integrated systems. Addressing the key challenge of using micro-nano photonic devices to manipulate the phase information of Bessel Gaussian beams in extremely small optical chips is imperative. This involves achieving flexible generation and control. To be effectively embedded in network systems, components must meet the criteria of being ultra-small, adjustable, ultra-fast, and low-loss. Simultaneously, integrating all optical components onto a single substrate and ensuring compatibility with CMOS technology is necessary. Metastructured surfaces, a novel type of two-dimensional material at the nanoscale, have emerged. Unlike traditional optical components relying on transmission distance for optical information control, metastructured surfaces can achieve strong light-matter interactions at the sub-wavelength scale, controlling beam phase, amplitude, and other properties [3-4]. In 2020, Professor Yiyang Xie proposed an integrated metasurface laser, demonstrating its potential by directly preparing metasurfaces on the back of VCSEL. In 2021, a team from the University of Melbourne designed a laser with an integrated metasurface on the front exit surface of VCSEL, capable of not only controlling laser beams but also detecting and identifying the polarization type of external incident lasers [5-6]. Consequently, research on metasurfaces and micro-optical devices has become a hot topic [7-9].

In this study, our primary objective is to extract the phase distribution of Bessel Gaussian beams and simulate their generation in theory. Subsequently, we integrate these functions into the lower emitting end of the laser chip by employing a metasurface as a medium. Concurrently, we design a metasurface to facilitate the emission of Bessel Gaussian beams, thereby

DOI: https://doi.org/10.34961/researchrepository-ul.29278295.v1

successfully fabricating a laser chip capable of directly emitting unique beams.

2. DESIGN AND PREPARATION

Considering the high transmission characteristics of the GaAs substrate in VCSEL chips, we employ the circular GaAs nanopillar structure directly as the basic crystal cell of the metasurface, as shown in Figure 1b, with a lattice period (p) of 250nm. The height is set at 650nm, and Figure 1a provides a summary of simulated transmission and phase delay for GaAs nanorods with diameters ranging from 60nm to 230nm under fixed height and period conditions (incident wavelength of 978nm). In this diameter range, the phase control of the nanorods can span a full 2 π periods, with a transmittance exceeding 70%. Taking into account the interaction between the metasurface and the incident laser and aiming to avoid physical boundary diffraction, the overall size of the integrated metasurface is set to D=100um. This design consideration ensures effective interaction while minimizing diffraction effects at physical boundaries.

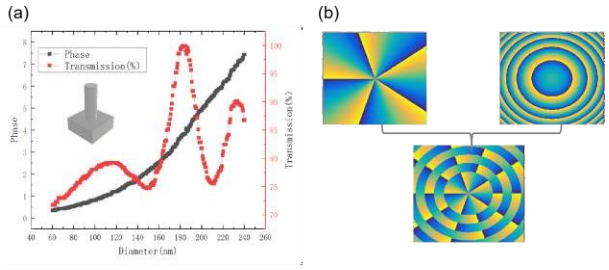

Figure 1 (a) Phase change and transmittance under different nanopillar diameters. （b）. The phase profile of the designed metasurface which superimposes two-phase profiles of a spiral and an axicon

Following the principle of optical diffraction, converting a Gaussian beam emitted by the laser into a high-order Bessel Gaussian beam can be achieved by cascading a spiral phase plate and an axial prism. This process initially generates an l-order single-ring vortex beam through the spiral phase plate, which is then transformed into an l-order Bessel Gaussian beam through the axial prism. In this design, the metasurface is configured as a phase distribution structure encompassing both spiral and axial prism phases, facilitating the direct conversion of Gaussian beams into higher-order Bessel Gaussian beams, as illustrated in Figure 1b. Adopting this method helps circumvent optical losses resulting from the transmission of multiple optical components. The phase distribution in the design is described by the following expression：

.

$$\varphi_{pov} = l \cdot arctan\frac{y}{x} + 2\pi\frac{r}{d} \quad (1)$$

r represents $\sqrt{x^2 + y^2}$ ， d is the period of the prism, and represents the distance of phase change 2π in the radial direction. Figures 2a and 2b show the phase distribution and intensity distribution corresponding to simulated Bessel Gaussian beams with different topological charges, respectively.

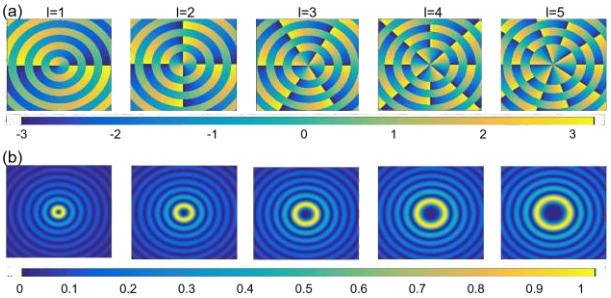

Figure 2 Simulation results of phase distribution and intensity distribution corresponding to Bessel Gaussian beams with different topological charges

During the actual device preparation, an additional collimation phase was introduced to enhance beam quality by applying a hyperbolic phase delay distribution to the incident end of the beam. This improvement was aimed at refining the spatial characteristics and structure of the beams.Considering processing conditions and nanopillar coupling issues, Bessel Gaussian beams with topological charges of l=3, 4, and 5 were selected for processing, and the mentioned phase was discretized into the 6th order. This selection was made to address specific requirements and optimize the beam characteristics. To integrate metasurfaces with VCSEL chips, a sequence of processes was implemented. Initially, electron beam lithography (EBL) patterned 180nm thick hydrogen silsesquioxane (HSQ). Subsequently, inductively coupled plasma reactive ion etching (ICP-RIE) was employed to create a metasurface at the bottom of a small oxide aperture without compromising the fundamental structure of the VCSEL. This approach is distinct from conventional methods, as it modulates the beam solely on the surface, preserving the core characteristics of the VCSEL chip. Through this method, the metasurface was seamlessly integrated onto the back-emitting VCSEL chip. The final scanning electron microscope (SEM) results, displayed in Figures 3a and 3b, reveal a clear nano-column pattern post-ICP etching, with a smooth outer wall and

excellent steepness. This indicates successful integration without compromising the structural integrity of the VCSEL.

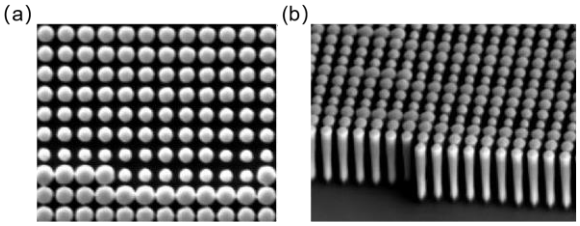

Figure 3 Characterization of the microstructure surface morphology of the bottom emitting end of the prepared device.(a) top view of the details of the metasurface unit. (b) observation view of the metasurface unit at a 52°oblique angle.

3. RESULTS AND DISCUSSION

To meet the testing requirements, diverse testing methods and high-precision device testing platforms, including far-field observation systems and beam profile scanning systems, were employed. A comprehensive analysis was conducted on the laser output, focusing on beam quality and photoelectric characteristics. The near-field observation system primarily comprises a 40x microscope objective with a large numerical aperture (NA=0.6), amplifying and collimating the collected laser beam. Additionally, it includes a beam analyzer with an infrared silicon-based CCD detector array. The far-field testing system characterizes far-field beam characteristics, encompassing the device spot divergence angle, far-field spot morphology, and other parameters. The laser output beam propagates through free space at a distance of L and is projected onto a light screen with transparent diffuse reflection, creating an XY direction spot distribution. Image acquisition is carried out using a laser beam quality analyzer. In our test, as shown in Figures 4, the near-field test light field intensities for different orders of Bessel Gaussian beams at a current of 3mA are displayed. Figures. 4(a)(b)(c) shows the optical field distribution of third-order, fourth-order and fifth-order Bessel light respectively. As the order increases, the diameter of the central ring increases. This presentation provides insights into the expected performance of the laser under specific conditions.

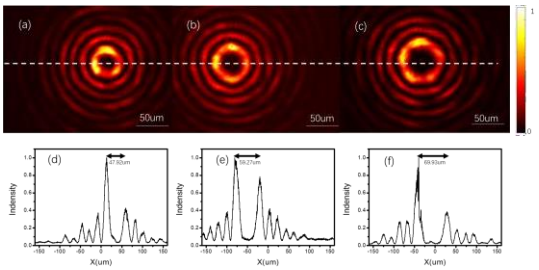

Figure 4 shows the far-field and near-field test optical field intensities of different orders of Bessel Gaussian beams with an injection current of 3mA.

In summary, the measured mode was very similar to the simulated result; The slight error may be due to the error in the process, such as the etching depth of the nano-column does not reach the target height.

4. CONCLUSION

We designed a comprehensive system of VCSEL chips integrated with metastructured surfaces, showcasing the phase transition characteristics of GaAs nanorods of various sizes. Additionally, we constructed a complete nanodatabase for phase transitions. In the practical integration applications, we conducted an analysis of the differences between Bessel Gauss beams and theoretical predictions. Moreover, we successfully developed a VCSEL chip capable of directly emitting Bessel Gaussian beams. This achievement addresses existing challenges in the complexity of Bessel Gaussian beam preparation processes, the requirement for independent feeding sources, and the demand for high-quality incident beams. These challenges are often beyond the capability of traditional optical designs. The outcome of our work is anticipated to open up new prospects for Bessel Gauss beams in the realm of miniaturization applications.

ACKNOWLEDGMENTS

We acknowledge financial support from the National Natural Science Foundation of China and Beijing Nova Program. The authors acknowledge the Nanofabrication Laboratory at National Centre for Nanoscience and Technology for sample fabrication.

FUNDING STATEMENT

National Natural Science Foundation of China(62074011, 62134008).

Beijing Nova Program (No. Z201100006820096).

REFERENCES

[1] Durnin J, Exact Solutions for Nondiffracting Beams. I. The Scalar Theory, Journal of the Optical Society of America A, 1987, 4(4): 651~654.

[2] Gori, F. , G. Guattari , and C. Padovani . "Bessel-Gauss beams." Optics Communications 64.6(1987):491-495.

[3] Tianye Huang,Huang Tianye,Zhao Xiang,Zeng Shuwen,Crunteanu Aurelian,Shum Perry Ping,Yu Nanfang. Planar nonlinear metasurface optics and their applications[J]. Reports on Progress in Physics,2020,83(12).

[4] Gohar Varamini, Asghar Keshtkar, Mohammad Naser-Moghadasi. Miniaturization of microstrip loop antenna for wireless applicatios based on metamaterial metasurface[J]. AEUE - International Journal of Electronics and Communications,2018,83.

[5] Xie, Y.-Y., P.-N. Ni, Q.-H. Wang, Q. Kan, G. Briere, P.-P. Chen, Z.-Z. Zhao, A. Delga, H.-R. Ren, H.-D. Chen, C. Xu, and P. Genevet, Metasurface-integrated vertical cavity surface-emitting lasers for programmable directional lasing emissions. Nature Nanotechnology, 2020, 15(2),125-130.

[6] Wen, D., J. Meng, J. J. Cadusch, and K. B. Crozier, VCSELs with On-Facet Metasurfaces for Polarization State Generation and Detection. Advanced Optical Materials, 2021, 9(9),2001780.

[7] Fu, Pan ; Ni, Pei-Nan ; Wang, Qiu-Hua ; Liu, Yu-Fei ; Wu, Bo ; Chen, Pei-Pei ; Kan, Qiang ; Wang, Shuang-Peng ; Chen, Hong-Da ; Xu, Chen ; Xie, Yi-Yang. "Multichannel Generations of Orbital Angular Momentum Modes with On- Demand Characteristics on a Chip." Advanced optical materials, 2021, Vol.9 (24).

[8] Kang K, Im S, Lee C, et al. Nanoslot metasurface design and characterization for enhanced organic light-emitting diodes[J]. Scientific Reports, 2021, 11(1): 9232.

[9] Wang, Q.-H., Ni, P.-N., Xie, Y.-Y., et al. On-chip generation of structured light based on metasurface optoelectronic integration[J]. Laser & Photonics Reviews, 2021, 15: 2000385

19: ULTRASENSITIVE VISUALIZED ARTIFICIAL OLFACTORY SYSTEM

*Xincun Dou**

Center of Materials Science and Optoelectronics Engineering, University of Chinese Academy of Sciences, Beijing, China,

Biomedical Sensors Session 3, EM009, August 13, 2024, 11:30 AM - 1:10 PM

Abstract The exploration of efficient artificial olfactory systems has always been a hot topic in the field of high-performance chemical sensors. However, it is extremely challenging to promote the capabilities regarding the sensing signal perception, transfer and recognition. We tried to build a brand new visual artificial olfactory system that combines vision and smell together. Firstly, to realize the highly sensitive and specific recognition of different types of analytes by the reaction-based olfactory receptor, multi-mode response probes were proposed. Secondly, to simulate the olfactory mucosa, a series of hydrogels with different structures were explored to improve the fidelity of the visualized signal. Furthermore, to realize the function of the olfactory center, a super-recognition method of the image signal based on deep learning was established. Finally, an ultrasensitive visualized artificial olfactory system with capabilities of intelligent and super-recognition of analytes was constructed and utilized for various analytes identification.

Keywords**:** artificial olfactory system; trace sensing; deep learning; specific recognition;

1. INTRODUCTION

As a cutting-edge research hotspot, artificial olfactory system has aroused intense attention in trace analysis from delving into the recognition mechanism to exploiting advanced materials [1]. Most researches focused on the substance in a form of gas or liquid due to their inherently high reactivity, on the contrary, while the relatively few technical means could chemically interact with solid substance, limiting the research wideness and depth [2]. In this paper, a fire-new artificial olfactory sensing system for trace solid microparticulates is introduced. It should be particularly highlighted that this sensing system has made breakthroughs in terms of integrity, surpassing the existing bionic strategies, achieving the detection of solidus particulate. More significantly, the bionic outcome further exceeds the functionality of biological olfactory, especially at strengthening recognition from non-specific to specific, reducing receptor numbers from numerous to numerable, transforming signal form from invisible bioelectricity to visible optics.

2. RESULTS AND DISCUSSION

A remarkable research paradigm of artificial olfactory-driven sensing for airborne particulates with the visualized output signal has been unprecedentedly proposed (Figure 1). To be specific, it consists of a series of studies in which the olfactory system is imitated from different angles, i) specific optical probe representing olfactory receptor, ii) functionalized hydrogel sensing substrate standing for olfactory mucosa and bulb, iii) signal processing module denoting the olfactory neural center.

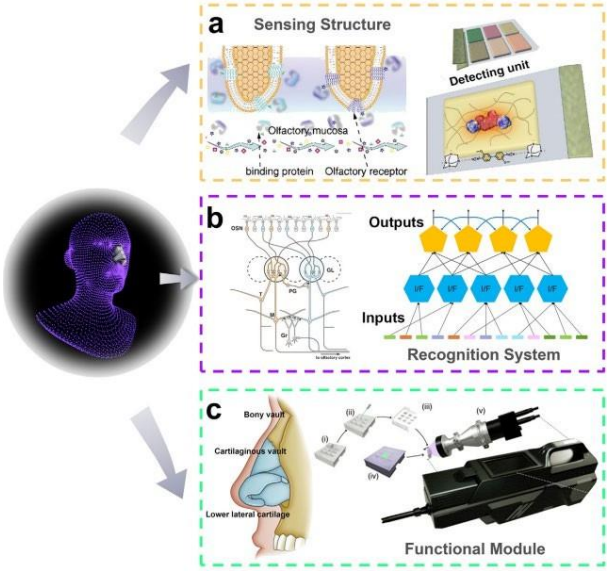

Figure 1. Schematic of an ultrasensitive visualized artificial olfactory system from the sensing structure construction, recognition system building to the functional module realization.

2.1 OPTICAL SENSING PROBE AS SPECIFIC OLFACTORY RECEPTOR

Figure 2. Schematic of optical probes designed with different interaction principles.

Benefiting from the adjustable structure, the regulation strategies focusing on the covalent/non-covalent interaction between optical probe and target chemical substances were developed [3, 4], which promotes the recognition specificity, notably differing from the natural olfactory applying numerous receptors to sense one substance (Figure 2).

DOI: https://doi.org/10.34961/researchrepository-ul.29278355.v1

2.2. STRUCTURALLY MODULATED HYDROGEL AS OLFACTORY MUCOSA AND BULB

Isolated application of sensing probe normally is limited due to the operability, portability, stability and extensibility, etc., thus, massive efforts have been devoted to developing substrate material to mimic the role of olfactory mucosa and bulb for addressing the above issues by loading the probe, providing reaction medium and transporting signal. Furthermore, the sensing substrate is also expected to promote the sensing performances, for which, an appealing research thought is to enhance sensing sensitivity by preventing the diffusion of the detection product with hydrophilic-hydrophobic hydrogels to receive the intensified colorimetric or fluorescent signal (Figure 3) [5].

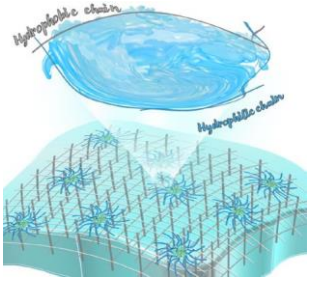

Figure 3. Schematic of a superior water anchoring hydrogel composed of the interpenetration skeleton of Pluronic F127 hydrophilic micelles and bisphenol A glycerolate dimethacrylate hydrophobic rigid chains.

2.3 INTEGRATED ARTIFICIAL OLFACTORY SYSTEM-FROM PROTOTYPE DEVICE TO APPLICABLE DETECTOR

On the basis of the above-mentioned simulation towards olfactory receptor, mucosa and bulb, further integrating various statistical or logical strategies as olfactory center, a fire-new artificial olfactory sensing system has been constructed, in which the entire process of the natural olfactory precepting unknown substances was reproduced. Specifically, the colorimetric reagents were separately anchored in the hydrogels as the main sensing substrates which were further individually immobilized in the mutually independent units of a poly(dimethylsiloxane) (PDMS) mould to constitute a sensing array (Figure 4).

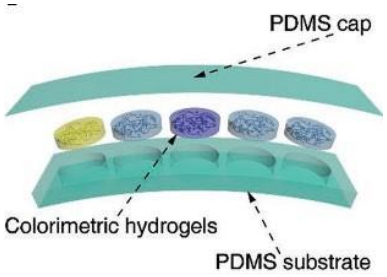

Figure 4. Schematic of a colorimetric artificial olfactory system built by hydrogel array.

Furthermore, based on the intelligent image processing through deep learning techniques, it is proposed to establish the intelligent and super-recognition method of the image signal [6]. Upon the systematically technological study, a handheld device was developed with prominent features non-contact sampling, one-step analysis, and simultaneously precise identification of multi-analyte, etc.

3. CONCLUSIONS

In summary, after adequately analysing the working process of olfactory system and inspired by the operating principle of olfactory mucosa and neuroepithelium, here we propose and constructed an ultrasensitive visualized artificial olfactory system based on hydrogel array for detecting airborne microparticulates instead of vapours for the first time. We believe the present concept would show potentials in public security, environmental monitoring, etc., and we hope it would greatly revolutionize the optical sensing and trace sensing fields.

FUNDING STATEMENT

This work was supported by the National Key Research and Development Program of China (2022YFA1205500), National Natural Science Foundation of China (52172168), Key Research Program of Frontier Sciences (CAS Grant No. ZDBS-LY-JSC029).

REFERENCES

[1] T. S. Zhang , W. F. Ren , F. F. Xiao , J. G. Li , B. Y. Zu , X. C. Dou, **Engineered olfactory system for in vitro artificial nose**, Engineered Regeneration 3, 2022, 427-439
DOI: https://doi.org/10.1016/j.engreg.2022.09.003
[2] T. S. Zhang , X. Y. Hu , B. Y. Zu , X. C. Dou, **A March to Shape Optical Artificial Olfactory System toward Ultrasensitive Detection of Improvised Explosives**, Advanced Photonics Research 3, 2022, 2200006
DOI: https://doi.org/10.1002/adpr.202200006
[3] Z. W. Ma , J. G. Li , X. Y. Hu , Z. Z. Cai , X. C. Dou, **Ultrasensitive, Specific, and Rapid Fluorescence Turn-On Nitrite Sensor Enabled by Precisely Modulated Fluorophore Binding**, Advanced Science 7, 2020, 2002991
DOI: https://doi.org/10.1002/advs.202002991
[4] F. F. Xiao , Y. S. Li , J. G. Li , D. Lei , G. F. Wang , T. S. Zhang , X. Y. Hu , X. C. Dou, **A family of oligo(p-phenylenevinylene) derivative aggregation-induced emission probes: Ultrasensitive, rapid, and anti-interfering fluorescent sensing of perchlorate via precise alkyl chain length modulation**, Aggregate 4, 2023, e260
DOI: https://doi.org/10.1002/agt2.260
[5] X. Y. Hu , Z. W. Ma , J. G. Li , Z. Z. Cai , Y. S. Li , B. Y. Zu , X. C. Dou, **Superior water anchoring hydrogel validated by colorimetric sensing**, Materials Horizons, 7, 2020, 3250-3257
DOI: https://doi.org/10.1039/D0MH01383H
[6] Y. Q. Wu , D. Lei , J. W. Li , Y. Luo , Y. W. Du , S. Zhang , B. Y. Zu , Y. H. Su , X. C. Dou, **Controlled Synthesis of Preferential Facet-Exposed Fe-MOFs for Ultrasensitive Detection of Peroxides**, Small 20, 2024, 2401024
DOI: https://doi.org/10.1002/smll.202401024

20: SOLID ROCKET MOTOR INTEGRITY HEALTH MONITORING BASED ON HIGH PERFORMANCE FEMTOSECOND GRATING ARRAY

Yunshan Zhang[a], *Dayong Wang*[a,b,*], *Jie Zhao*[a,b], *Yunxin Wang*[a,b], *Jing Zhang*[a], *Yu Zhang*[a]

[a] School of Physics and Optoelectronic Engineering, Beijing University of Technology, Beijing, China
[b] Engineering Research Center of Precision Measurement Technology and Instruments, Beijing, China

Industrial Sensing:2 , EM009, August 12, 2024, 1:30 PM-3:00PM

Abstract – In order to meet the requirements of damage detection and interface debonding detection of solid rocket motor (SRM) composite case, a novel embedded femtosecond grating array was proposed to measure the strain parameters of SRM in real time and online, and the strain parameters were used to reflect the damage and debonding state of SRM structure. The mechanical analysis and simulation of the SRM are established, and the multi-layer strain transfer model between the sensor and the SRM is proposed. A high-performance femtosecond grating array is inscribed and effectively coated and packaged. And overcome that technical problem of shell and interface implantation. The debonding simulation experiment was carried out. For the first time in the world, the production, storage and ignition stages of the SRM were effectively monitored. The strain distribution state in the whole life cycle of the SRM is given. It provides data support for the evaluation of SRM structural integrity.

Keywords**:** Solid rocket motor; Integrity health monitoring; femtosecond grating array

1. INTRODUCTION

Solid rocket motor is an important device of strategic missile weapon, which plays an important role in the development of space technology in the world[1]-[3]. The structure of solid rocket motor is composed of shell, insulation layer, liner and grain. During the production, transportation and storage stages of the SRM, the composite shell damage, interface debonding and other failures will occur, which will damage the structural integrity of the SRM[4]-[5]. Therefore, it is of great military significance to master the structural integrity and health status of the SRM.

The traditional state judgment is mainly based on non-destructive testing, but the non-destructive testing equipment is large and the cost is high, so it is difficult to achieve online monitoring[6]-[7]. Another method is the sensor contact measurement, which is used to evaluate the health status of the grain by measuring the strain. Such as button sensors and piezoelectric excitation sensors [8], but such sensors are large in size, mostly rigid materials, and difficult to be compatible with the grain[9]. Summarizing the above analysis, it is found that the existing technology can not meet the monitoring requirements. Optical fiber sensor has the advantages of small size, intrinsic safety and multiplexing, which provides a new method for SRM on-line monitoring[10]-[12]. In 2021, Zhirnov *et al*. Designed an interferometric sensor to monitor SRM conditions during ignition [13]. In 2022, an interferometer sensor based on oxide-doped optical fiber was designed to monitor the filling status of the liquid level of the large solid rocket motor [14]. In 2023, Zhao *et al.* proposed to monitor the curing of propellant with FBG [15].The above studies and reports are mainly simulation experiments, and have not been applied to practice.

Therefore, considering the complex application conditions of the actual SRM, we propose to implant the femtosecond grating array into the SRM to realize the integrity and health monitoring of the structure. Grating arrays are written on oxide-doped fibers using femtosecond lasers. Through the establishment of viscoelastic mechanical model and multi-layer strain transfer model, the compatibility problem caused by material heterogeneity is solved, and the analysis method of strain transfer efficiency is mastered. The grating sensor is effectively packaged to solve the problem of implanting the sensor in the SRM, and the internal strain and temperature of the SRM can be effectively distinguished and measured. The layout strategy of sensor array in the SRM was studied, and the mechanical state of the SRM in the whole life cycle was monitored, which provided a new technical method for the structural integrity assessment of the grain.

2. THEORETICAL ANALYSIS AND MODELING

2.1. Mechanical analysis of SRM during storage

The mechanical analysis of SRM in the stage of vertical storage was carried out by finite element method. During the vertical storage of the SRM, the gravity load acts on the whole SRM in the form of an axial acceleration of 1 G. It is considered that the elastic modulus of the propellant, the insulation and the shell are significantly different, and the propellant itself is viscoelastic. Under the action of gravity, stress and strain will inevitably occur in the interior of the grain and the bonding surfaces, which will affect the safety of the bonding interface. The strain and deformation of the grain and the bonding interface under the long-term action of gravity acceleration are calculated by simulation. Figure 1 illustrates the effect of storage time on the propellant. Figures 1 (a), 1 (b), and 1 (c) show the stress, strain, and displacement distributions of the SRM after one year of storage, respectively.

With the long-term action of gravity, the stress of the convex ring before and after the artificial removal of the explosive column increases slowly with the extension of the standing storage time. The stress and strain of the front and rear artificial decharging convex ring of the grain increase significantly due to the gravity load. Gravitational load leads to grain creep, which decreases from both ends to the middle of the grain. The creep effect of the grain in long-term vertical

DOI: https://doi.org/10.34961/researchrepository-ul.29278457.v1

storage is obvious.

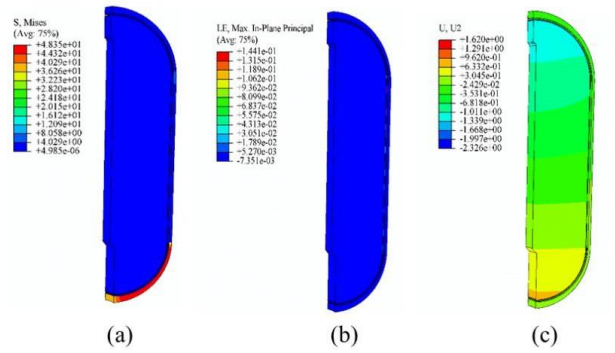

Figure1. Mechanical Simulation of SRM Vertical Storage. (a) Stress distribution; (b) strain distribution; (c) displacement distribution.

2.2. Establishment of strain coupling model

A multi-layer strain transfer coupling analysis model is established for the internal frame of the fiber optic sensor implanted actuator, as shown in Fig. 2. The sensors in the composite shell of the implanted actuator is fixed to the shell through the resin in the composite wrapping process. The sensors at the interface between the heat dissipation layer and the lining layer is implanted and arranged in the process of the lining layer being brushed.

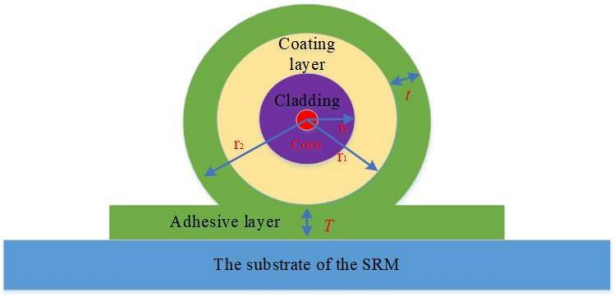

Figure 2. Coupling Model of Fiber Optic Sensor and SRM Matrix

The cladding radius of the fiber in the figure is r_f. And that radiu of the coating lay and the adhesive layer of the optical fiber are r_1 and r_2, respectively. The length of the grating region of a single femtosecond grating is L. The bottom thickness of the adhesive layer is T, and the top thickness is t.

The shear stress at any point in the sensor can be represented as

$$\tau(z,r)=\frac{r_f\tau_f(z)}{r} \tag{1}$$

where Z is the longitudinal coordinate of the fiber. And R is the radial distance from the center of the fiber. The displacement u_f of the optical fiber relative to the SRM matrix is further obtained as follows

$$u_f-u_c=\int_{r_f}^{a}\gamma(z,r)dr=k\tau_f(z) \tag{2}$$

where u_c is the matrix displacement. G_1, G_2, and G_a are the shear moduli of the fiber optic cladding, coating, and adhesive, respectively.

$$k=r_f\left(\frac{1}{G_1}\ln\frac{r_1}{r_f}+\frac{1}{G_2}\ln\frac{r_2}{r_1}+\frac{1}{G_a}\ln\frac{r_a}{r_2}\right) \tag{3}$$

The control equation for core strain can be expressed as

$$\frac{d^2\varepsilon_f}{dz^2}-\lambda^2\varepsilon_f=-\lambda^2\varepsilon_c \tag{4}$$

Due to the non bonded part of the optical fiber having a strain of 0, the boundary condition of the fiber core is

$$\varepsilon_f(0)=\varepsilon_f(L)=0 \tag{5}$$

By incorporating the boundary conditions into the formula, the strain in the gate region can be obtained as

$$\varepsilon_f(z)=\varepsilon_c\left(1+\tanh\left(\frac{\lambda L}{2}\right)\sinh(\lambda z)-\cosh(\lambda z)\right) \tag{6}$$

The strain efficiency of fiber optic grating sensors is defined as the ratio of the integral of the fiber core over the grating length to the strain of the substrate. When the matrix uniformly elongates, the strain transfer efficiency is

$$\eta(\lambda,L)=\frac{2\int_0^{L/2}\varepsilon_f(z)dz}{\varepsilon_m L}=1-\frac{2}{\lambda L}\tanh\left(\frac{\lambda L}{2}\right) \tag{7}$$

The strain transfer efficiency of the optical fiber is affected by the bonding length, the geometric characteristics and the mechanical properties of the interlayer. When the optical fiber measures the strain of different SRM matrix materials, its transmission efficiency is different. As the bonding length increases, the strain transfer efficiency increases. It shows that the greater the stiffness difference is, the less the shear stress loss is. When selecting the adhesive, the smaller the elastic modulus should be selected as far as possible.

2.3. Grating Sensor Design and Packaging

A new type of optical fiber doped with oxides is designed. The doped materials are Y_2O_3, Al_2O_3 and P_2O_5. The doped oxide is helpful to improve the mechanical strength of the optical fiber and has higher temperature resistance. The fiber grating array is engraved on the core of the oxide-doped fiber by a femtosecond laser. The length of a single grating is 2 mm. The use of a short grating can prevent the spectral chirp caused by the uneven force of the grating in the SRM.

Fig. 3(a) shows the design of a single channel extraction joint containing multiple femtosecond gratings. The coating layer is a polyimide layer, and the withstand temperature is 350 ℃. The length of the grating itself can be optimized. A high performance polyetheretherketone sleeve is designed for the primary encapsulation of the optical fiber from the insertion and extraction position of the housing. A carbon fiber woven mesh is designed outside the PEEK sleeve for secondary encapsulation, and high temperature resistant sealant is filled between the two. The diameter of the optical fiber lead-out head is less than 1mm after being packaged. The lead-out end adopts a high temperature resistant lead-out joint, which is an FC/APC lead-out joint.

In order to measure the strain and temperature in the SRM, it is necessary to isolate the strain of the grating. And encapsulate that last grating in the grate array by adopting a capillary steel tube. One end of the grating is sealed by strong glue, and the other section is freely extended in the steel pipe and is also sealed. The grating is not subjected to axial force in the steel tube, and the diameter of the steel tube is 0.6mm. Unpackaged gratings are subject to both temperature and stress. The temperature sensor can be used for independent temperature extraction and measurement, so that the whole grating system can realize the differential measurement of temperature and strain.

Fig. 3 (b) is the reflection spectrum of the femtosecond

grating array. A single optical fiber is cascaded with 10 femtosecond gratings. The reflection spectrum of the grating has extremely high spectral quality. The reflectivity of the grating array is 96%. The extinction ratio of the grating is greater than 28 dB.

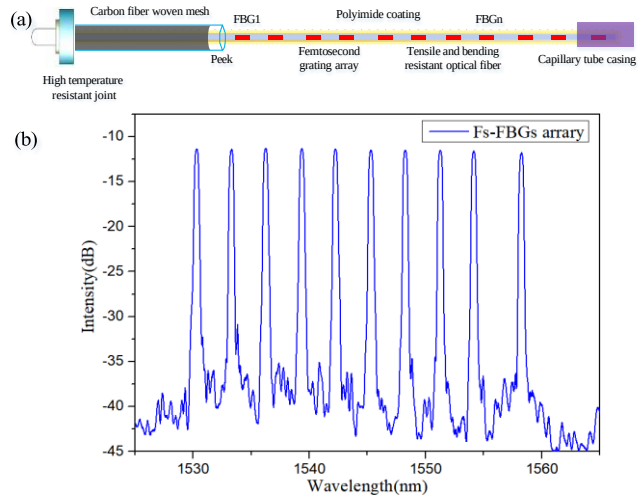

Figure 3. Sensor design and packaging. (a) Encapsulated sensors after strain isolation; (b) Femtosecond grating array reflection spectrum.

3. EXPERIMENTAL RESEARCH AND RESULT ANALYSIS

3.1. Experimental study on interface debonding tooling

In order to realize the interface debonding detection test, a set of interface debonding test device was designed and manufactured. The whole experimental device consists of an interface simulation system, a force application lever system, a load loading system, a bracket and an accessory system. Arrange five optical fiber arrays on the tooling plane, and bond them firmly through the liner used in the SRM. In the experiment, the interface strain increases from the gradual application of force to the final interface cracking, as shown in Fig. 4 (a). The change data of the sensor during the experiment were collected. The data of each grating in the bonding interface show obvious changes, and the interface strain changes dramatically when the final interface cracks. This corresponds to the moment of cracking. A typical change in that grate data is shown in Fig. 4 (b). According to the above test results, it can be preliminarily known that it is feasible to use the optical fiber sensor to detect the interface debonding, and the strain generated by the complete interface debonding is greater than 9000 με.

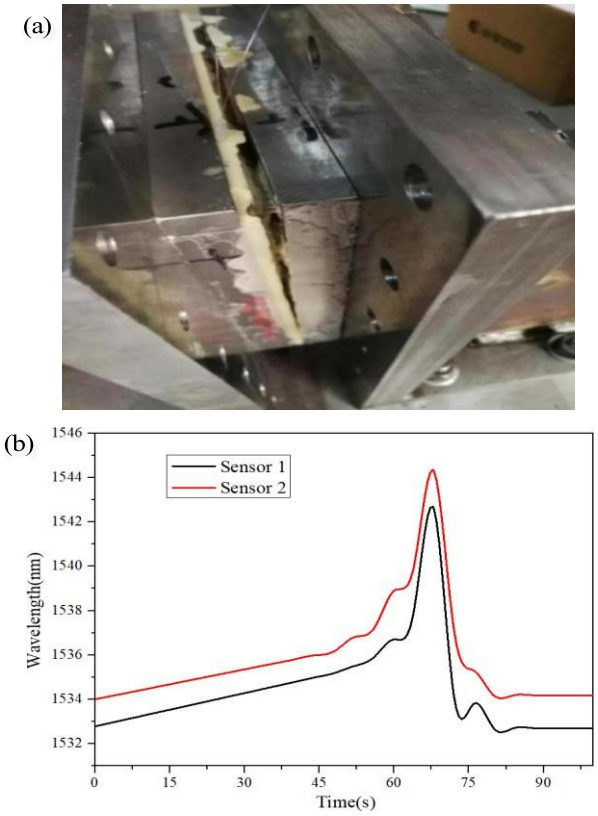

Figure 4. SRM debonding simulation experiment. (a) Interface debonding experiment; (b) Spectral changes of sensors during interface debonding process.

3.2. Implantation and extraction of grating arrays in SRM

For the composite shell, the FBGs sensor is woven in during the material molding process. The shell winding process adopts the alternate mode of spiral winding and circumferential winding. Due to the centrosymmetric structure of the composite wound shell, it is proposed to route the light in the typical positions of the shell, i.e. quadrants I, II, III and IV of the shell. Four FBGs arrays are laid, and each array is equipped with five strain sensors, all of which are located in the column section. The first point is 300 mm from the end face of the skirt, and the spacing between the sensors is 240 mm, as shown in Fig. 5 (a). Fig. 5 (b) shows the actual placement of the sensor in the SRM housing. In the process of pasting, a certain prestress is applied to the FBG sensor, so that the sensor can monitor the negative strain.

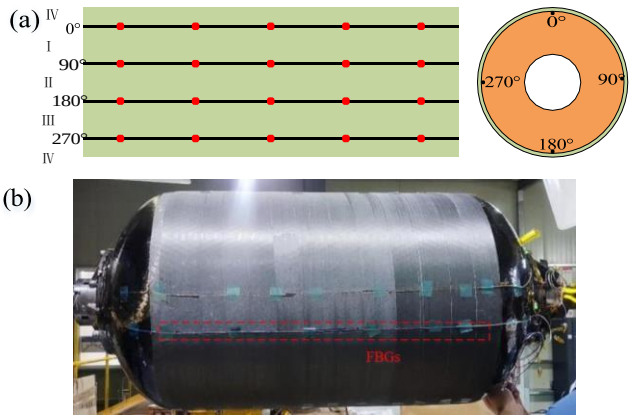

Figure 5. SRM Composite Housing Sensor Placement. (a) Distribution of sensors in the composite shell; (b) Actual implant drawing of the SRM case sensor.

For interfacial debonding, the sensor is implanted

between the shell and the insulation, between the insulation and the liner, and between the liner and the charge. A total of 9 optical fibers were laid in the debonding, including 5 axial optical fibers and 4 annular optical fibers. There are 10 measuring points on each optical fiber on the axial optical fiber, 3 measuring points on the front and rear heads respectively, and 4 measuring points are evenly distributed on the column section, as shown in Fig. 6 (a). There are two specifications of the ring optical fiber, both of which contain 10 measuring points. The two optical fibers are staggered, and 20 measuring points are distributed between the two quadrants. For the first specification, there are 4 measuring points on the front head, 4 measuring points on the column section, and 2 measuring points on the rear head. For the second specification, there are 2 measuring points on the front head, 4 measuring points on the column section, and 4 measuring points on the rear head. Fig. 6 (b) shows the actual implantation and extraction of the sensor in the SRM.

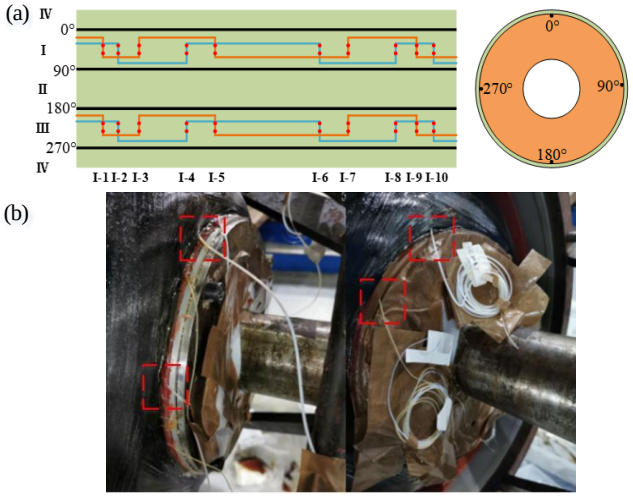

Figure 6. Laying and leading-out of sensor bonding surface. (a) Circumferential distribution of sensor at charge interface; (b) Implantation and extraction of sensors from the SRM.

3.3. Analysis and discussion of monitoring results

Fig. 7 shows the strain distribution inside the SRM monitored by the sensor under different working conditions during the production process of the SRM. The initial strain was calibrated to 0 με, and the strain of the composite shell changed slightly before curing. After the composite shell is cured, the strain monitored by the sensor is obviously larger, and the strain generated at this time is mainly positive strain. When the composite shell is demoulded, the strain distribution produced by the sensors at different positions is different, including positive strain and negative strain. After the shell is made, it is stored for a period of time, and then the lining is coated. The strain was measured prior to coating and found to have a decreasing tendency for negative strain. The strain increases during application of the liner and loading of the propellant. Finally, the SRM was further demoulded and the strain tended to be stable.

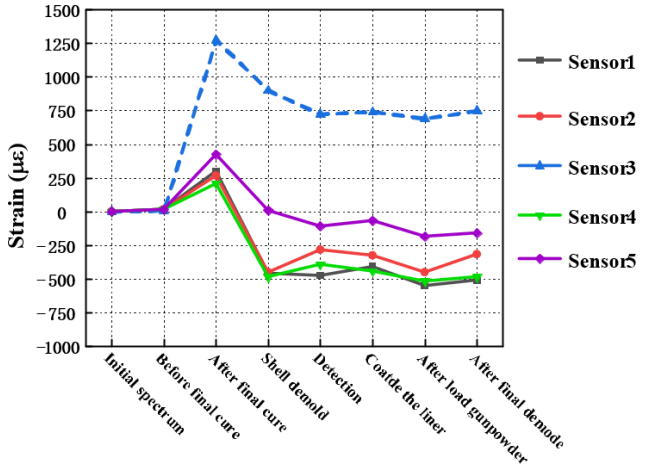

Figure 7. Strain change during SRM production.

For the fiber placed at the interface between the insulation and the liner, the measured strain mainly comes from the charging stage and is slightly released during the demoulding stage. The maximum strain value measured by the sensor implanted in the adhesive surface is -5775με, and the sensor is located in the third quadrant of the SRM. Similarly, the strain value measured by the sensor located in the third quadrant is also very large, reaching -4367με. Figure 8 shows the strain monitored by a typical sensor on the SRM bonding surface. In the whole process, the main generation stage of strain is in the charging process, and there is a tendency to release in the subsequent process. The measured strain is mainly negative strain, which comes from the shrinkage and gravity during the solidification process of the grain.

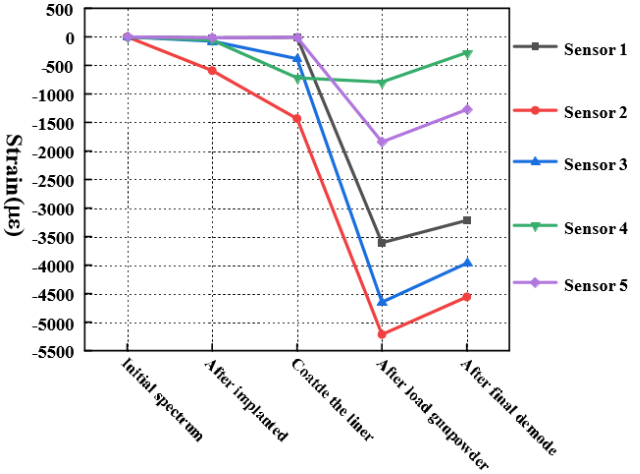

Figure 8. Strain distribution of SRM bonding surface at different state.

The solid rocket motor has been stored for a long time before use, and the internal strain of the motor has been monitored for a long period of time during the long-term storage period of three months. Fig. 9 shows the strain change of a typical sensor during long-term monitoring. It can be seen from the figure that there is a large strain change in the bonding surface of the composite case and the propellant during the storage stage of the motor. The strain increases sharply in the pre-storage stage. With the increase of storage time, the strain change decreases and tends to be stable. The maximum shell strain is 2422με, and the maximum interface strain is 4050με.

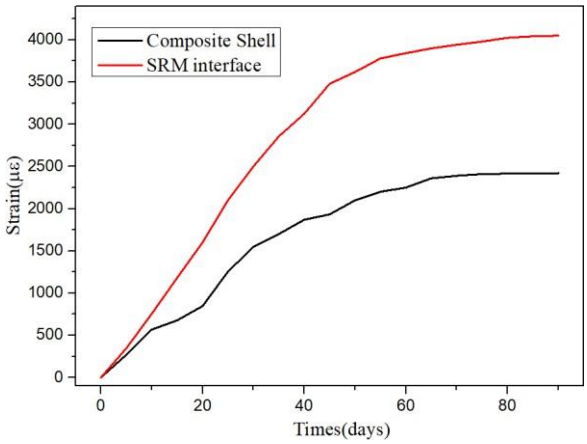

Figure 9. Changes in strain during long-term storage of the SRM.

The SRM in which the optical fiber sensor was implanted was ignited and tested, and the strain of the sensor was monitored during the test, as shown in Fig. 10 (a). The signal of the sensor is relatively stable before the SRM is set. At the beginning of the ignition, the strain felt by the sensor increases sharply. The maximum variation can reach 2300με. It shows that the pressure generated inside the shell increases sharply during the SRM test run, resulting in a sharp change in the stress and strain monitored by the optical fiber sensor inside the shell, as shown in Fig. 10(b).

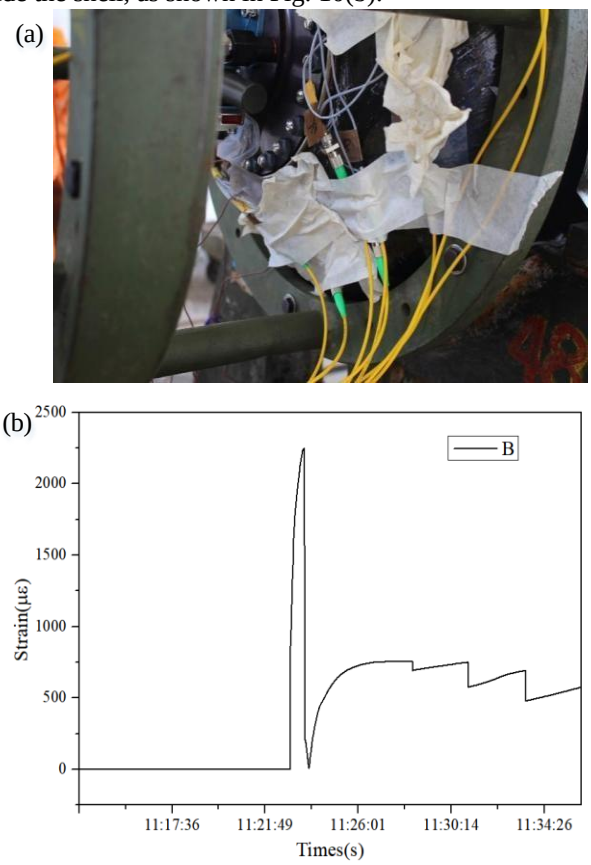

Figure 10. Ignition monitoring experiment. (a) Ignition test signal monitoring of SRM; (b) Change of shell strain signal during ignition test run.

4. CONCLUSIONS

Aiming at the interface debonding, shell damage and defects which may damage the structural integrity of solid rocket motor during the whole life cycle of production, storage and installation, a new type of implanted femtosecond grating array sensor was used to monitor the occurrence and development of damage. The strain distribution of the SRM during storage is simulated. The strain transfer efficiency is obtained. A new type of high performance sensor has been developed. To solve the problem of implanting and extracting the new optical fiber sensor in the SRM, the whole life cycle monitoring experiment was carried out. It provides key technical support for the structural integrity state monitoring of solid rocket motor in the whole life cycle.

FUNDING STATEMENT

This work was supported by the National Natural Science Foundation of China under Grant 62275008 and Grant 62220106005.

REFERENCES

[1] H. Rocha, C. Semprimoschnig, J.P. Nunes, **Sensors for process and structural health monitoring of aerospace composites: A review**, Engineering Structures, vol. 237, June 2021, p. 112231.

[2] M. Wubuliaisan, Y. Wu, X. Hou, F. Huang, **A viscoelastic constitutive model considering deformation and environmental-induced damages for solid propellants**, Aerospace Science and Technology, vol. 132, Jan. 2023, p. 108055.

[3] A. Mahjub, N.M. Mazlan, M.Z. Abdullah, Q. Azam, **Design Optimization of Solid Rocket Propulsion: A Survey of Recent Advancements**, Journal of Spacecraft and Rockets, vol. 57, no. 1, 2020, pp. 3–11.

[4] M. Lei, S. Ren, E. Chen, Z. Zhang, J. Xiao, L. Wen, X. Hou, **Correlation between solid propellant failure and interface debonding in solid rocket motors**, Polymer Testing, vol. 115, Nov. 2022, p. 107755.

[5] F. Wang, J. Liu, P. Song, J. Gong, W. Peng, G. Liu, M. Chen, Y. Wang, **Multimodal optical excitation pulsed thermography: Enhanced recognize debonding defects of the solid propellant rocket motor cladding layer**, Mechanical Systems and Signal Processing, vol. 163, Jan. 2022, p. 108164.

[6] F. Wang, J. Liu, B. Dong, J. Gong, W. Peng, Y. Wang, M. Chen, G. Liu, **Blind image separation for the debonding defects recognition of the solid propellant rocket motor cladding layer using pulse thermography**, Measurement, vol. 174, Apr. 2021, p. 108997.

[7] L. Li, J. Ren, P. Wang, Z. Lü, X. Li, M. Sun, **An adaptive false-color enhancement algorithm for super-8-bit high grayscale X-ray defect image of solid rocket engine shell**, Mechanical Systems and Signal Processing, vol. 179, Nov. 2022, p. 109398.

[8] B. Liu, S. Wang, M. Zhan, H. Wang, G. Zhang, Q. Jian, **Optical nondestructive evaluation for minor debonding defects and interfacial adhesive strength of solid propellant**, Measurement , vol. 194, May 2022, p. 111066.

[9] L. Srivastava, L. Krishnanand, N. Kishore Nath, C.K. Hirwani, M.R.M. Babu, **Online structural integrity monitoring of high-performance composite rocket motor casing**, Materials Today: Proceedings, vol. 56, Jan. 2022, pp. 1001–1009.

[10] C. Fu, P. Li, Z. Bai, Y. Wang, **Helical Long Period Fiber Grating Inscribed in Elliptical Core Polarization-Maintaining Fiber**, IEEE Access, vol. 9, 2021, pp. 59378–59382.

[11] S. Liu, M. Zhou, Z. Zhang, Z. Sun, Z. Bai, Y. Wang, **Ultrasensitive refractometer based on helical long-period fiber grating near the dispersion turning point**, Opt. Lett.,

vol. 47, no. 10, May 2022, pp. 2602–2605.
[12] Z. Liu, Y. Liu, C. Mou, F. Zou, T. Wang, **CO_2 laser- written long-period fiber grating with a high diffractive order cladding mode near the turning point**, Appl. Optics, vol. 57, no. 17, June 2018, pp. 4756–4760.
[13]A.A. Zhirnov, K.V. Stepanov, S.G. Sazonkin, T.V. Choban, K.I. Koshelev, A.O. Chernutsky, A.B. Pnev, A.O. Novikov, D.A. Yagodnikov, **Study of Intra-Chamber Processes in Solid Rocket Motors by Fiber Optic Sensors**, Sensors (Basel), vol. 21, no. 23, Nov. 2021, p.7836.
[14] Y. Zhang, L. Fan, Y. Zhang, D. Wang, Y. Wang, **Solid Rocket Motor Filling Glue Level Sensor Based on Annular Oxide-Doped Fiber Mach–Zehnder Interferometer**, IEEE Sensors, vol. 23, no. 3, Feb. 2023, pp. 2255–2263.
[15] Y. Guo, B. Jiang, L. Liu, Y. Ma, J. Li, W. Ao, Q. Sun, Z. Wang, P. Liu, J. Zhao, **In Situ Monitoring of Curing Reaction in Solid Composite Propellant with Fiber-Optic Sensors**, ACS Sens, vol. 8, no. 7, July 2023, pp. 2664–2672.

21: MICROWAVE PHOTONIC CHAOTIC RADAR WITH FREQUENCY UP/DOWN CONVERSION CAPABILITY

Yu Zhang [a, b], *Jie Zhao* [a, b, *], *Yunxin Wang* [a, b], *Jing Zhang* [a], *Dayong Wang* [a, b]

[a] School of Physics and Optoelectronic Engineering, Beijing University of Technology, Beijing, China
[b] Engineering Research Center of Precision Measurement Technology and Instruments, Beijing, China

Microwave and Photonic Sensors, EM010, August 13, 2024, 2:50 PM - 4:00 PM

Abstract – A microwave photonic chaotic radar with frequency up/down conversion capability is proposed and demonstrated to implement high-resolution ranging. In the proposed radar, the broadband chaotic signal is generated by a chaotic optoelectronic oscillator (OEO) rather than a direct digital synthesizer. Based on photonic-assisted frequency up/down conversion, the radar operating frequency can be adjusted to the K-band without increasing the workload of digital correlation reception. The precise clock synchronization is avoided due to the optical fiber connection between the remote station (RS) and the central station (CS). The experimental results show that chaotic radar with a bandwidth of 6 GHz is established for high-resolution ranging. Detection of two targets is demonstrated with a range resolution of 2.55 cm, and maximum error is less than 0.35 cm.

***Keywords*:** Microwave photonics; chaotic radar; optoelectronic oscillator (OEO); photonic-assisted frequency conversion.

1. INTRODUCTION

Microwave radars hold an irreplaceable position in applications such as autonomous driving, land remote sensing, and aircraft monitoring[1],[2]. To achieve the high-precision target localization, the high-frequency broadband signals are essential. Microwave photonic technology has unique advantages for the generation [4], processing [4], and transmission [5] of high-frequency broadband radio frequency (RF) signals. Microwave photonics has been gradually introduced into radars to enhance system performance [6],[7].

In the past years, many researches on photonic-assisted chaotic radar have been conducted. A remote imaging radar with chaotic signals was proposed [8]. Radio over fiber transmission allows the data process system to be deployed far away from the transceiver antenna. However, the narrow bandwidth of the chaotic signal generated by Colpitts circuit limits the range resolution. In order to increase the bandwidth of the chaotic signal, Reference [9] proposed an OEO based chaotic radar without an electrical bandpass filter. The bandwidth of the chaotic signal depends on the gain passband in the OEO loop, which is up to 15GHz. Despite its range resolution is high, the system places high demands on signal reception and processing, which limits its development into a practical radar. Although photonics and chaotic signals have brought advantages to radar, the scheme of monostatic radar still limits radar performance.

In this paper, we proposed a microwave photonic chaotic radar with frequency up/down conversion for target ranging. By integrating the generation of chaotic signal and photonic-assisted frequency conversion functions within a DP-QPSKM, the radar system has been simplified. A polarization division multiplexing (PDM) device is used to transmit two signals over a single optical carrier, which can achieve digital correlation reception at the central station (CS). The proposed scheme makes full use of the broadband and flat characteristics of chaotic signals generated by OEO, thus realizing a high-resolution ranging.

2. METHODS AND PRINCIPLE

The schematic of the proposed microwave photonic chaotic radar is shown in Figure 1. The RS is composed of a chaotic OEO, a photonic-assisted frequency conversion unit, and a RF transmission unit. Chaotic signals in the OEO loop exist in optical and electrical forms. The chaotic optical signals, as a reference signal, are transmitted to the CS. Meanwhile, the echo signals reflected from the target are modulated onto optical carriers, and transmitted to the CS to achieve down-conversion of the echo signal. One set of PDM device and fibers are used to connect the CS. These optical signals enter the PD to obtain the reference chaotic (RC) and down-converted echo signals at RS. Then they are sampled and calculated the cross-correlation function (CCF) by the ADC and digital signal processor (DSP), respectively. The time delay difference between two signals can be obtained through the CCF.

At the RS, the optical carrier from a laser diode (LD) is sent to a DP-QPSK modulator, which is composed of two parallel dual-parallel Mach-Zehnder Modulators (X-DPMZM and Y-DPMZM) with a 90°polarization rotator (PR) after the Y-DPMZM. A polarization controller (PC) and the polarization beam splitter (PBS) are combined to demultiplex two orthogonal polarization states. The X-DPMZM output signal is divided into two branches by an optical coupler (OC1) after amplified by an optical amplifier (OA1). One branch is sent to a long SMF to form a chaotic OEO.

2.1. Generation of chaotic signal

In this loop, MZMx1 as a nonlinear frequency converter, OA1, electrical amplifier (EA1), and variable optical attenuator (VOA) jointly control the gain, while EBPF1 determines the passband. The normalized dynamics of the bandpass OEO cavity can be described by an integrodifferential delay equation (iDDE) as

$$\left(1+\frac{f_L}{f_H}\right)v(t)+\frac{1}{2\pi f_H}\cdot\frac{dv(t)}{dt}+2\pi f_L\cdot\int_{t_0}^{t}v(t)dt = \beta\cos^2\left[v(t-T_D)+\theta_{DC}\right] \quad (1)$$

DOI: https://doi.org/10.34961/researchrepository-ul.29278829.v1

where $v(t)$ is the signal voltage before MZMx1, and $\theta_i = \pi V_{DCxi}/V_\pi$ (i=1,2,⋯,6) is the phase difference introduced by the DC bias voltage, in which the V_π is the half-wave voltages; f_H and f_L are the high and low cutoff frequencies of the EBPF1; β is the feedback gain in the loop and $\theta_{DC} = \theta_1 - \theta_2$ is the phase shift of the $v(t)$; T_D is loop delay.

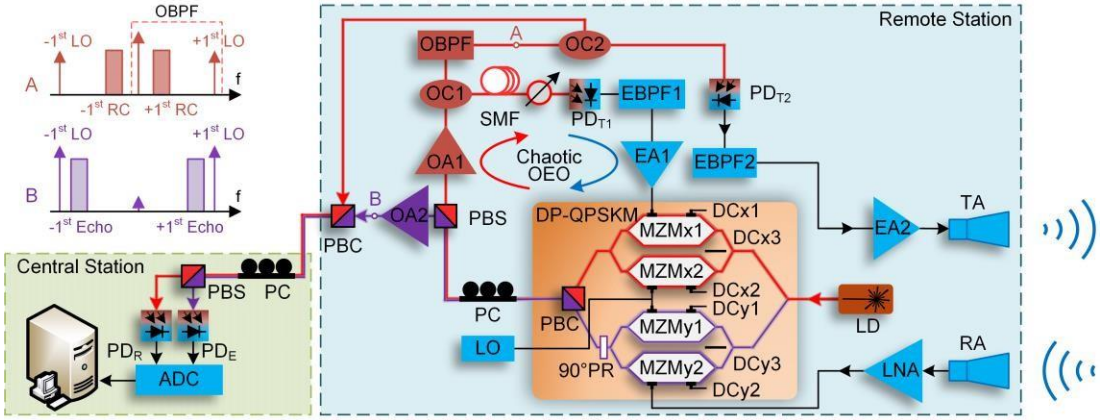

Figure 1. Schematic of the microwave photonic chaotic radar.

As the feedback gain β increases, the OEO will fall into chaotic oscillation, and produce a chaotic signal. The MZMx1 works at the null transmission point ($\theta_1 = \pi$) to improve the OEO nonlinearity and suppress the time-delay signature (TDS) of the chaotic signal. The LO signal is injected to the MZMx2, which works at the linear point ($\theta_2 = \pi/2$) to maintain the optical carrier. After the Jacobi-Anger expansion and small signal approximation, the output optical field of the X-DPMZM can be expressed as

$$E_{\text{X-DPMZM}} \propto E_c e^{j\omega_c t}\left\{\begin{array}{l} 2J_1(m_{\text{RC}})\cos(\omega_{\text{RC}}t) \\ +\left[J_0(m_{\text{LO}}) - 2J_1(m_{\text{LO}})\cos(\omega_{\text{LO}}t)\right]e^{j\theta_3} \end{array}\right\} \quad (2)$$

where E_c and ω_c are the amplitude and angular frequency of the optical carrier, respectively; m_{RC} and m_{LO} are the modulation depths of the RC and LO signals; To facilitate description, the angular frequency of the wideband RC signal denoted by ω_{RC}; ω_{LO} is the angular frequency of LO signal; $J_n(\cdot)$ is the n_{th}-order Bessel function of the first kind.

2.2. *Photonic-assisted frequency conversion*

Both of the ±1st-order sidebands of the RC and LO are sent to PD, which can generate the interested up-conversion frequency signal and chaotic reference signal. However, DSB modulation suffers from high-order harmonics and overlaps in the frequency domain with the up-conversion signal. Dispersion-induced RF power fading is also detrimental to long-distance transmission. Therefore, an optical bandpass filter (OBPF) is applied to filter out the -1^{st}-order sidebands of the RC and LO signals. The output of the OBPF can be written as

$$E_{\text{OBPF}}(t) \propto E_c e^{j\omega_c t}\left\{\begin{array}{l} J_1(m_{\text{RC}})e^{j\omega_{\text{RC}}t} \\ +\left[J_0(m_{\text{LO}}) - J_1(m_{\text{LO}})e^{j\omega_{\text{LO}}t}\right]\cdot e^{j\theta_3} \end{array}\right\} \quad (3)$$

Then it is separated into two identical parts by OC2. One part is sent to the PD_{R2} for optical-to-electrical conversion, and the output photocurrent is

$$i_{\text{RF}}(t) \propto \Re P_c\left\{\begin{array}{l} J_0^2(m_{\text{LO}}) + J_0(m_{\text{LO}})J_1(m_{\text{RC}})\cos(\omega_{\text{RC}}t) \\ -J_0(m_{\text{LO}})J_1(m_{\text{LO}})\cos(\omega_{\text{LO}}t) \\ -J_1(m_{\text{RC}})J_1(m_{\text{LO}})\cos\left[(\omega_{\text{LO}} - \omega_{\text{RC}})t + \theta_3\right] \end{array}\right\} \quad (4)$$

where $\Re$ is the responsivity of the PD; P_c is the power of the optical carrier. After the EBPF2 and EA2, the up-converted chaotic signal $s_{\text{T}}(t)$ at $\omega_{\text{LO}} - \omega_{\text{RC}}$ can be obtained, which is amplified by EA2 and launched through a transmit antenna (TA). The other part of the output signal from OC2 is sent to the PD_{R} of CS, to obtain the RC signal $s_{\text{RC}}(t) \propto \cos(\omega_{\text{RC}}t)$. Because the frequency of the up-conversion signal is higher than the reference chaotic signal, a PD with a bandwidth of f_H can act as a low-pass filter (LPF).

Photonic-assisted down-conversion of the echo signal is achieved in the Y-DPMZM. After passing through a low-noise amplifier (LNA), the echo signal reflected from the target is fed on MZMy2, while the LO signal is modulated via the MZMy1. When $\theta_4 = \theta_5 = \pi$, both of the two sub-MZMs are biased at the null transmission points to achieve the CS-DSB modulation. Here the use of CS-DSB modulation for the down-converted signal has a higher energy utilization efficiency compared with CS-SSB modulation. The output optical signal of the Y-DPMZM can be expressed as

$$E_{\text{Y-DPMZM}}(t) \propto E_c e^{j\omega_c t}\left\{\begin{array}{l} J_1(m_{\text{LO}})\left[e^{j\omega_{\text{LO}}t} + e^{-j\omega_{\text{LO}}t}\right] \\ +J_1(m_{\text{Echo}})\left[e^{j\omega_{\text{Echo}}t} + e^{-j\omega_{\text{Echo}}t}\right]\cdot e^{j\theta_6} \end{array}\right\} \quad (5)$$

where, ω_{Echo} and ω_{LO} are the angular frequency of echo and LO signal. After being transmitted to the CS, the output optical signal of Y-DPMZM is then converted into an electrical signal with a PD. Similarly, a reasonable selection of the response bandwidth for PD_{E} can result in the output electrical signal containing only the intermediate frequency (IF) signal at $\omega_{\text{LO}} - \omega_{\text{Echo}}$. Then the CCF is given as

$$R(\tau) = \frac{1}{T}\int_0^T s_{\text{IF}}(t)s^*_{\text{RC}}(t+\tau)dt \quad (6)$$

where, T is the CCF integration time; $s_{IF}(t)$ and $s_{RC}^{*}(t)$ are the down-converted echo signal and the complex conjugate of RC signal, respectively; τ represents the relative time delay. After correcting the delay time within the system, the propagation distance of radar transmission signal in space can be denoted as $L = c\tau$, where c is the speed of electromagnetic wave.

3. RESULTS AND DISCUSSION

In a proof-of-concept experiment, microwave photonic chaotic radar was constructed according to Figure 1. At the RS, the continuous-wave (CW) light from LD operates at frequency of 193.3 THz, and is injected into a DP-QPSK modulator (Fujitsu FTM7977HQA). The optical signal from OC1 passes through a 2-km SMF and a VOA before sending to the PD_{T1} (3-dB bandwidth 10 GHz). The electrical signal is then sent back to the MZMx1 after passing through an EBPF1 (Passband: 2~8 GHz) and an EA1.

To verify the performance of the chaotic signal generated by OEO is analysed. A four-channel 20 GHz real-time oscilloscope (OSC, Tektronix DSA72004B: 20 GHz, 50 GSa/s) was used to monitor the waveform at the output from the EBPF1. Figure 2 presents the bifurcation behaviour of the amplitude, which is obtained by adjusting the input optical power of PD_{T1}. It can be seen that the amplitude grows and bifurcates as the input optical power increases. Further increase of the gain leads to multi-periodic oscillations, and later to fully developed chaos state.

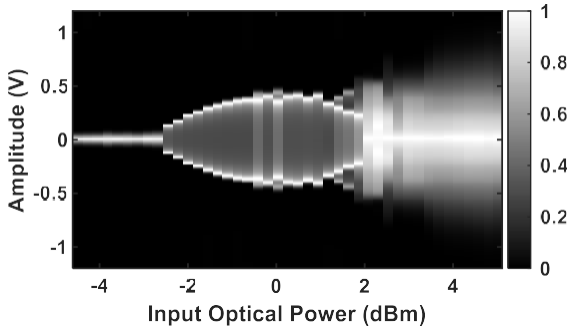

Figure 2 Bifurcation diagrams of the output chaotic signal

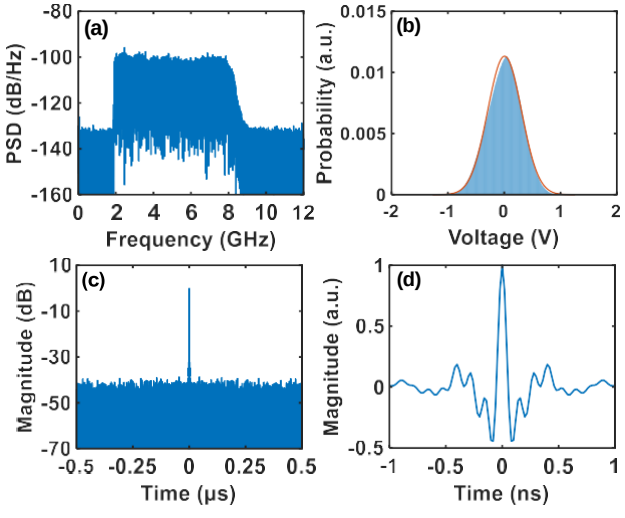

Figure 3 (a) Power spectral density, (b) amplitude histogram, (c) normalized ACF trace of the chaotic signal generated by OEO. And (d) zoom-in view of the normalized ACF around the peak.

As shown in Figure 3(a), power spectral density (PSD) based on the 10 μs time sequence is quite flat across the range of 2 GHz to 8 GHz, which aligns with the passband of the EBPF1. Figure 3(b) shows its amplitude histogram and fitted curve. It can be observed that the amplitude histogram is of Gaussian-like statics, indicating that the amplitude of chaotic signal conforms to a random distribution. Figure 3(c) illustrates the ACF has a narrow and sharp peak without any apparent sidelobe. The full width at half maximum (FWHM) of that the ACF is 65.35 ps, indicating a high Rayleigh time resolution. Figure 3(d) presents the zoom-in view of the normalized ACF trace around the peak.

To demonstrate the photonic-assisted up-conversion function, the optical spectrum before and after OBPF and the electrical spectrum of the EBPF2 output signal were measured. The 20 GHz LO signal is generated by an electrical signal generator (ESG, Rohde & Schwarz SMA100). The central frequency and 3-dB bandwidth of the OBPF are 193.31 THz and 22 GHz, respectively. The output signal from PD_{T2} (3-dB bandwidth: 20 GHz) are filtered and amplified by EBPF2 (Passband: 12~18 GHz) and EA2. Figure 4(a) show the optical spectra of the signal before and after the OBPF, which are measured by an optical spectrum analyzer (OSA, Yokogawa AQ6370D). As can be seen, the output signal of OBPF only retain the optical carrier, the +1st-order sideband of the RC and LO optical signals. After frequency beating at the PD, an up-converted signal is generated.

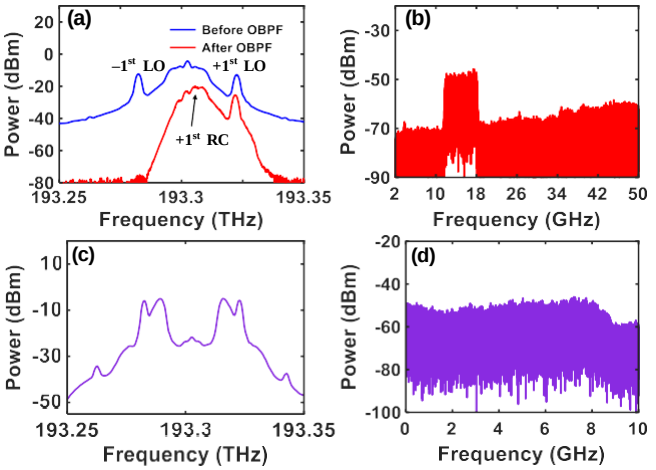

Figure 4 (a) The spectra before and after OBPF outputs, and (b) the spectrum after EBPF2. (c) The optical spectrum after the OA2 and (d) the electrical spectrum of PD_E output.

In order to analyse the output electrical signal over a wide frequency range, we used an electrical spectrum analyzer (ESA, Keysight 9020B) to capture the output signal of the EBPF2. It can be seen that the output signals significantly exceed the noise floor within the range of 12 to 18 GHz. The results demonstrate that the X-DPMZM simultaneously achieves the generation and photonic-assisted up-conversion of chaotic signals. Concurrently, the downconversion functionality was evaluated. Figure 4(c) shows the optical spectrum after OA2, and it can be observed the optical carrier is suppressed. From the PSD in Figure 4(d), the down-converted echo signal in the frequency range of 2 to 8GHz can be clearly seen. After demonstrating three functions, it can be indicated that this configuration can form a chaotic radar within the designed frequency band. The CCF is

calculated by the RC signal and the down-converted echo signal, and the 1-D range profiles of transmission path can be obtained.

Figure 5 illustrates the experimental setup and presents the results of chaotic radar ranging. Two corner reflectors with the same size (3 cm ×3 cm × 3 cm) is taken as targets, and the distances from the reflectors to two antennas are 42 cm and 54 cm, respectively. As shown in the inset, the envelope magnitude at the target position significantly exceeds the background value. Meanwhile, the range errors are both 0.30 cm.

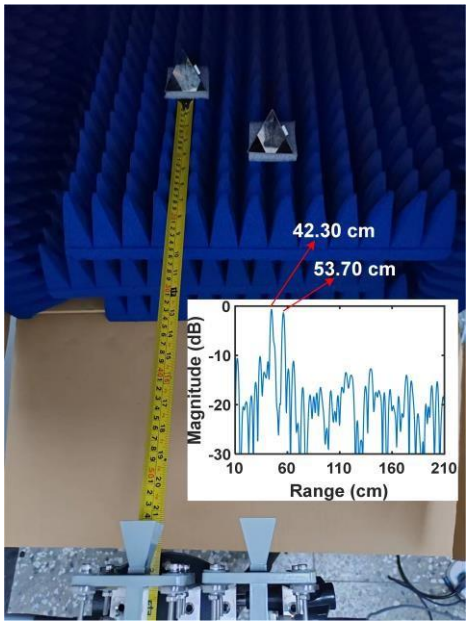

Figure 5 Radar diagram for detection of two targets.

To investigate the range resolution of chaotic radar, detection of two closely placed targets is ranged. Two corner reflectors are 50 cm and 54 cm away from the antenna pair. As shown in Figure 6(a), two peaks were observed at 49.65 cm and 53.85 cm, respectively, with errors of 0.35 cm and 0.15 cm from the actual positions. Based on the envelope of CCF trace in Figure 6(b), the range resolution of the chaotic radar is analysed. The 3-dB widths of the two envelope peaks are 2.55 cm and 2.52 cm, respectively. The result is very close the radar theoretical range resolution $L_R = c/(2B) = 2.50$ cm, where B is the bandwidth of the chaotic signal.

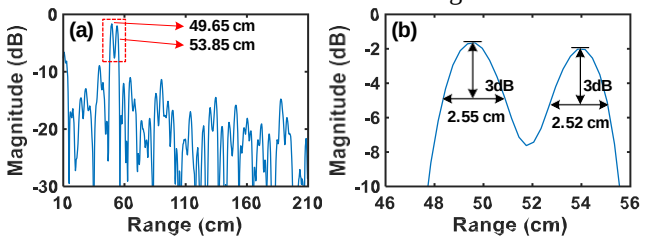

Figure 6 (a) The range profile and (b) zoom-in views of the CCF envelope around the peak.

4. CONCLUSIONS

In conclusion, we have proposed and demonstrated a microwave photonic chaotic radar with frequency conversion capability. The chaotic signal is generated by using a chaotic OEO, and the photonic-assisted up/down frequency conversion are applied for the transmitting and receiving of the chaotic signal. The experimental results verify the capability of high-resolution ranging. The operation frequency can be flexibly adjusted; meanwhile, the workload of the digital correlation receiver is relatively reduced. The proposed scheme would provide a practical scheme for chaotic radar based on microwave photonic technology.

FUNDING STATEMENT

This work was supported by the National Natural Science Foundation of China under Grant 62275008 and Grant 62220106005.

REFERENCES

[1] S Pan, Y Zhang, **Microwave photonic radars**, J. Lightwave Technol., vol. 38, n. 19, 2020, pp. 5450-5484.

[2] J Yao, **Microwave photonic systems**, J. Lightwave Technol., vol. 40, n. 20, 2022, pp. 6595-6607.

[3] L Wang, Y Guo, Li P, T Zhao, Y Wang, A Wang, **White-chaos radar with enhanced range resolution and anti-jamming capability**, IEEE Photonics Technol. Lett., vol. 29, n. 20, 2017, pp. 1723-1726.

[4] C Ma, Y Yang, C Liu, **Microwave photonic imaging radar with a sub-centimeter-level resolution**, J. Lightwave Technol., vol. 38, n. 18, 2020, pp. 4948-4954.

[5] Li S S, Li X Z, Chan S C, **Chaotic time-delay signature suppression with bandwidth broadening by fiber propagation**, Optics letters, vol. 43, n. 19, 2018, pp. 4751-4754.

[6] F Zhang, Q Guo, S Pan, **Photonics-based real-time ultra-high-range-resolution radar with broadband signal generation and processing**, Sci. Rep., vol. 7, n. 1, 2017, pp. 13848.

[7] D S Garmatyuk, R M Narayanan, **ECCM capabilities of an ultrawideband bandlimited random noise imaging radar**, IEEE Aerosp. Electron. Syst. Mag., vol. 38, n. 4: 2002, pp. 1243-1255.

[8] L Liu, R Ma, J Li, **Anti-jamming property of Colpitts-based direct chaotic through-wall imaging radar**, J. Electromagn. Waves Appl., vol. 30, n. 17, 2016, pp. 2268-2279.

[9] Z Xu, H Tian, L Zhang, **High-resolution radar ranging based on the ultra-wideband chaotic optoelectronic oscillator**, Opt. Express, vol. 31, n. 14, 2023, pp. 22594-22602

23: Effect of film forming quality on the performance of PbSe detector

Yanyan Zheng[*], *Xiaoshui Zhang*[*], *Ruiqin Gu*[*], *Zhibo Yang*

Hanwei Electronics Group Corporation, Zhengzhou Winsen Electronics Technology Co., Ltd. Zhengzhou City, China,

Environmental Sensing, EM010, August 13, 2024, 4:20 PM - 6:10 PM

Abstract –The response band of lead selenide is 1 to 5 um. There are high response rates and sensitivity for lead selenide at room temperature. Chemical bath deposition is a common method for the synthesis of thin films. Due to the complexity of thin films prepared by chemical bath deposition, the consistency of thin films prepared at present is poor, it is difficult to prepare large area arrays. The stability constant K of the complex is crucial for film formation. K is mainly related to the concentration of hydroxide. By optimizing the molar amount of each initial solute, the relationship between the molar amount and the film forming mass was studied. The controllability of particle size and the uniformity of the film are further realized by controlling the molar, temperature and PH. It plays an important role in the preparation of infrared photoconductive units and array detectors.

Keywords**:** lead selenide; Chemical bath deposition; stability constant K; the molar, film formation

1. INTRODUCTION

Lead salt semiconductor materials include lead selenide (PbSe), lead sulfide (PbS), and lead telluride (PbTe). This kind of multi-product thin film materials mainly use the internal photoelectric effect of semiconductor materials to make characteristic photoconductive devices. [1]Widely used in temperature measurement, detection, guidance, early warning, astronomical observation and other fields. The common PbSe detector has a response band of 1~ 5μm, which can be made into infrared optical films with high refractive index, and is widely used in infrared detection, fiber laser and solar energy technology fields. [2]

Chemical bath deposition is a common method for preparing PbSe. However, the uniformity and consistency of the prepared films are poor, and it is difficult to large-scale production and application. The main problems are as follows:

There is a temperature field in the solution. As the heating time increases, the maximum flow rate in the reaction vessel decreases, and the maximum flow rate occurs in the center of the vessel. Therefore, when selecting the substrate placement position, in order to reduce the influence of flow field on substrate erosion, the substrate is placed near the cup wall. [3] As soon as the entire liquid system reaches thermodynamic conditions, the crystal immediately begins to nucleate, and in a very short time the crystal nucleates. The monomer concentration quickly reaches a high value, resulting in supersaturation. There is a critical concentration that separates nucleation from crystal growth, when the concentration of each reactant is higher than this concentration value, the system will continue to nucleate, always in the nucleation stage; When the concentration of each reactant is lower than this concentration, the crystal continues to grow and the system enters the growth stage. [4] The reaction speed mainly depends on the concentration of ions in the solution, and too high concentration of ions will cause the reaction to be too fast and poor control. The ion concentration in solution in turn depends on the stability constant K of the complex. The role of the complexing agent is to complex with Pb^{2+} in the lead source to control the concentration of Pb^{2+} in the solution. The stability constant of the complex agent is very sensitive to pH, and usually increases first and then decreases with the increase of PH.

In this work, we did the experiments about the substrate, temperature, PH and the molar. The quality of the deposited film depends on the uniformity, concentration and stability of the deposited liquid at the optimum deposition temperature and particle size. For the identified substrate and sedimentary species, corresponding to the optimal deposition film: the optimal deposition temperature is only related to the definition of the optimal deposition film; The optimal reactant concentration is only relevant to the corresponding optimal deposition film definition.

2. METHODS AND PROCEDURES

This work mainly adopts chemical bath deposition method. The molar ratio of sodium hydroxide, lead source, potassium iodide and selenium source are 8:1:1.3:1.4. The effects of substrate, temperature, PH value and molar amount on the quality of deposited films were studied. We obtained thin films of PbSe with high quality.

3. RESULTS AND DISCUSSION

3.1 The stability constant K

The preparation of PbSe films is very complex, and it is important to understand the principles of film formation and deposition. The following three chemical equations show how PbSe is formed. From the first chemical equation, it can be seen that three times the hydroxide and lead ions combine to form a complex $Pb(OH)_3^-$.

$$Pb^{2+} + 3OH^- \leftrightharpoons Pb(OH)_3^- \quad (1)$$

$$SeSO_3^{2-} + 2OH^- = SO_4^{2-} + Se^{2-} + H_2O \quad (2)$$

$$Pb^{2+} + Se^{2-} = PbSe \downarrow \quad (3)$$

The function of the complexing agent is to complex with lead ions in the lead source to control the concentration of lead ions in the solution. The relationship between complex stability constant K and hydroxide concentration is shown in Figure 1. The stability constant of the complex agent is very sensitive to PH, and usually increases first and then decreases with the increase of PH.

The complex stability constant is the constant of equilibrium between the complexation and the dissociation reversible reaction. The lower the stability constant, the more metal ions the complex dissociates, the higher the stability constant, the fewer metal ions the complex dissociates, or even does not dissociate, and the complex does not change valence in the REDOX reaction. The complexation capacity

DOI: https://doi.org/10.34961/researchrepository-ul.29278871.v1

(complexation capacity) refers to the amount of metal ions that can be complexed per gram of complexation agent, and the higher the complexation capacity, the stronger the complexation capacity. The stability of the complexing agent at different pH values, that is, the change of the stability constant at different pH values, is another important property of the complexing agent. The complexing ability of some complexing agents varies greatly at different pH values, and some even lose the complexing force by hydrolysis, decomposition or reaction.

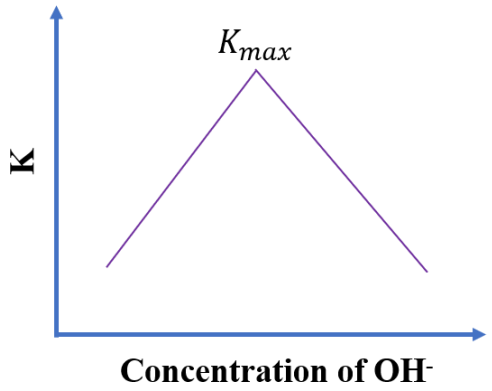

Figure 1 The relationship between the stability constant K of complex and the concentration of OH.

3.2 The difference between different substrate

Figure 2 shows SEM images of PbSe thin-films using substrate of sapphire and silicon dioxide. Figure 2(a) shows the surface of PbSe using substrate of sapphire. There are a lot of holes with the range size of 200-1000 nm in this surface. The size of particle is about 1000 nm. Figure 2(b) shows the cross-section of PbSe using substrate of sapphire. The grain boundaries are clearly shown from this figure. The thickness of this film is about 1 um. The roughness is very large using this way.

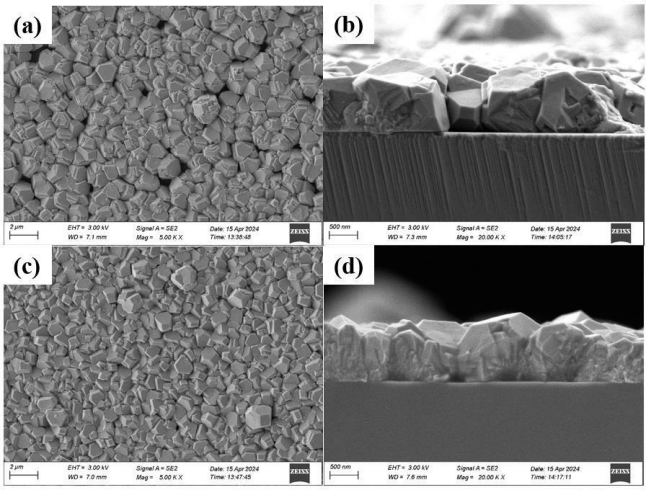

Figure 2 SEM images of PbSe thin films. (a) The surface of PbSe using substrate of sapphire. (b) The cross-section of PbSe using substrate of sapphire. (c) The surface of PbSe using substrate of silicon dioxide. (d) The cross-section of PbSe using substrate of silicon dioxide.

Figure 2(c) shows the surface of PbSe using substrate of silicon dioxide. There are almost no holes in this surface. The size of particle is less than 1000 nm. Figure 2(d) shows the cross-section of PbSe using substrate of silicon dioxide. The grains are very dense shown from this figure. The thickness of this film is about 1 um. The roughness is very small.

3.3 The effect of PH

PH is very important for the forming of PbSe thin film. The thin film of PbSe is prepared using different volume of NaOH. Figure 3 shows images of PbSe thin film using different volume of NaOH of (a) 11 ml, (b) 12 ml, (c) 13 ml, (d) 14 ml and (e) 16 ml. There are different colors for different volume. This indicates that the size of grain particles are different using different volume of NaOH.

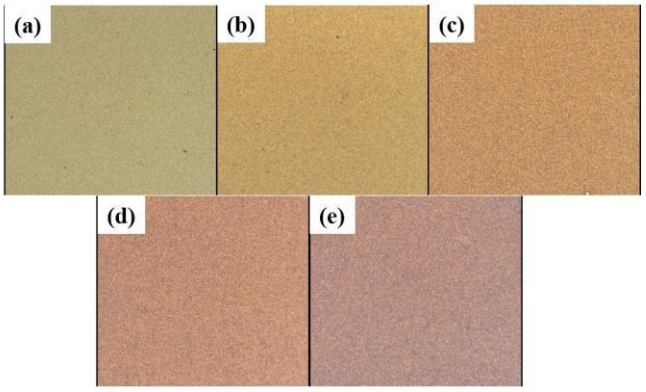

Figure 3 Images of PbSe thin film using different volume of NaOH of (a) 11 ml, (b) 12 ml, (c) 13 ml, (d) 14 ml and (e) 16 ml.

PbSe thin film is first prepared using high concentration of sodium hydroxide, lead source, potassium iodide and selenium source. The temperature is very low in this way. Figure 4 shows the results of thickness of thin film by using different volume of OH. The trend of thickness of thin film increases from the volume of 11 ml NaOH to 13 ml NaOH. The thickness is about 1 um when the volume of NaOH is 13 ml. The thickness of thin film decreases after the volume of 3 ml NaOH. There is a maximum value by using the different volume of NaOH. It indicated that there is a maximum value of complex stability constant.

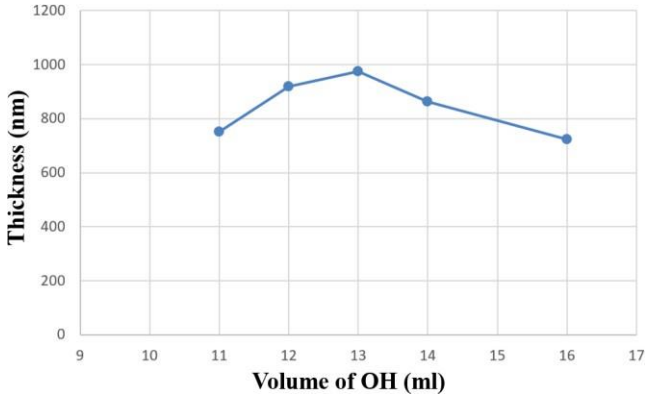

Figure 4 The relationship between the thickness and the volume of OH.

3.4 The effect of temperature

Then, PbSe thin film is prepared using low concentration of sodium hydroxide, lead source, potassium iodide and selenium source. The temperature is 70 ℃, 75 ℃ and 80 ℃, respectively. Figure 5 shows the relationship between the roughness and the volume of NaOH. Figures 5(a-c) show results using the temperature of 70 ℃, 75 ℃ and 80 ℃, respectively. The roughness is increased from 1 h to 2 h except the result using the temperature of 80 ℃ . The roughness is increased from the volume 2.23 ml NaOH to 6.7 ml NaOH except the result using the temperature of 80 ℃. It indicates that the rate of reaction in solution is very high when the temperature is 80 ℃.

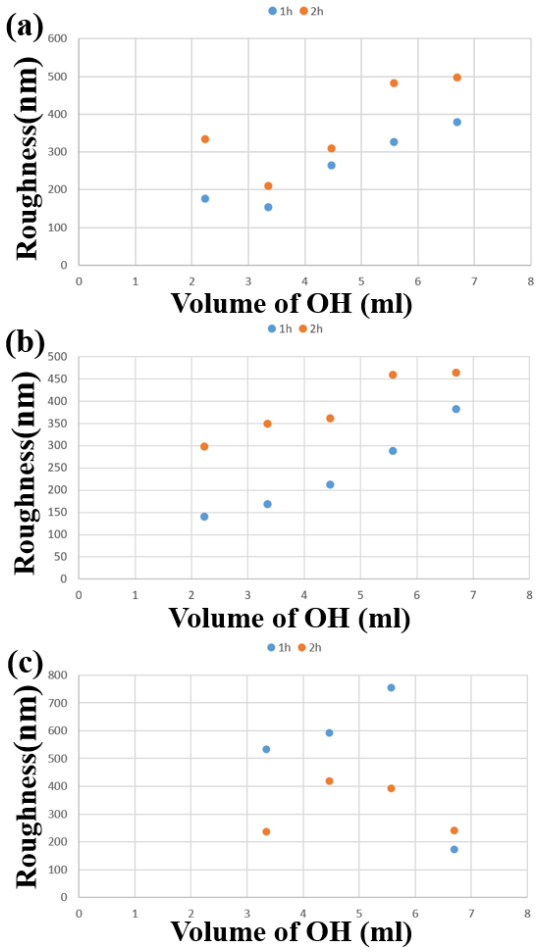

Figure 5 The relationship between the roughness and the volume of NaOH. (a-c) The temperature is 70 ℃, 75 ℃ and 80 ℃, respectively.

Figure 6 shows the relationship between the thickness and the volume of NaOH. Figures 6(a-c) show results using the temperature of 70 ℃, 75 ℃ and 80 ℃, respectively. The thickness is increased from the volume 2.23 ml NaOH to 6.7 ml NaOH except the result using the temperature of 80 ℃. Results is clearly shown in three figures. The thickness is about 600 nm for 2h when the volume of NaOH is 4.47 ml and the temperature is 75 ℃ and it is 2 folds for the thickness of 1 h. It indicates that the growth rate of the film is uniform from 1 h to 2 h. Maybe the thickness is be controlled by using the volume of temperature of 70 ℃ and the volume of 4.47 ml NaOH.

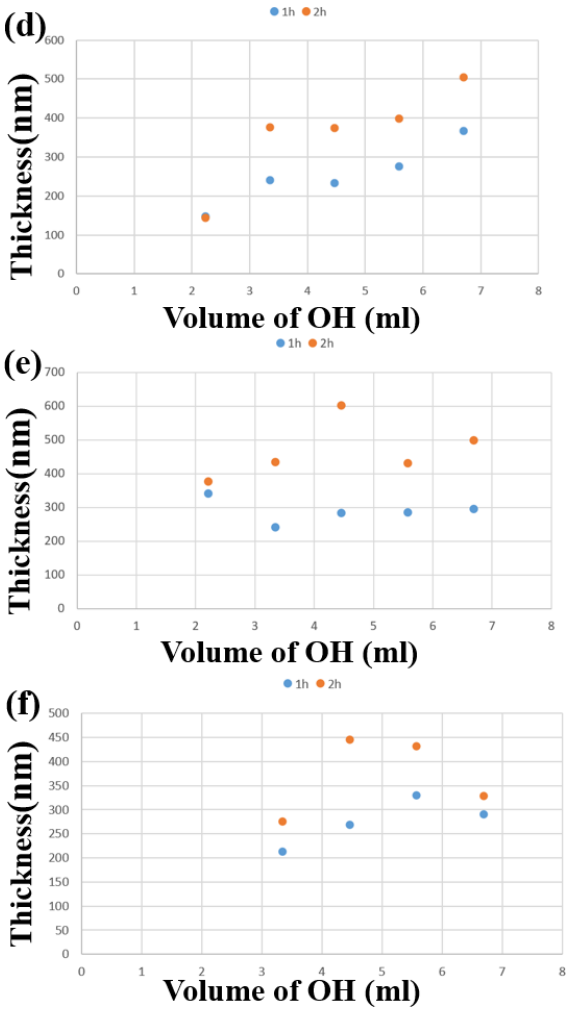

Figure 6 The relationship between the thickness and the volume of NaOH. (a-c) The temperature is 70 ℃, 75 ℃ and 80 ℃, respectively.

In order to the detail of thin film by using the temperature of 75 ℃ and the volume of 4.47 ml NaOH. Figure 7 shows SEM images using this way. Figure 7(a) shows the surface of thin film. The range size of particle is about 200 nm to 500 nm. The grain is dense and there are almost no holes in this surface. Figure 7(b) shows the cross-section of this film. The thickness of this film is about 600 nm. There are at least three layers in the substrate using this way. The particle size is small at the bottom. The particle size is large on the top of layer. It is due to the reaction speed is high at the beginning. The concentration is low after sometime and the particle size increases with time.

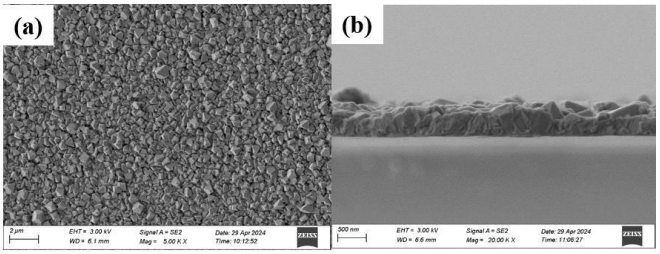

Figure 7 SEM images of PbSe thin films by using the temperature of 75 ℃ and the volume of 4.47 ml NaOH. (a) The surface of PbSe. (b) The cross-section of PbSe.

3.5 The effect of molar

The appropriate temperature of 75 ℃ is determined based on previous experiments. Then, the effect of different molar of each solute was studied for the quality of the forming of the thin film. Experiments were done by using the volume of NaOH of 3.35 ml, 3.91 ml, 4.47 ml, 4.84 ml, 5.21 ml, 5.58 ml and the 4.84 ml with the Pb^{2+} molarity of 0.012 mol/L. The results are shown in Figure 8. The roughness for almost all data increases with time. It indicates there are different ways for the growth of particles on the substrate. The roughness is low for the volume of about 4.84 ml NaOH. It indicates that the maximum of K is along 4.84.

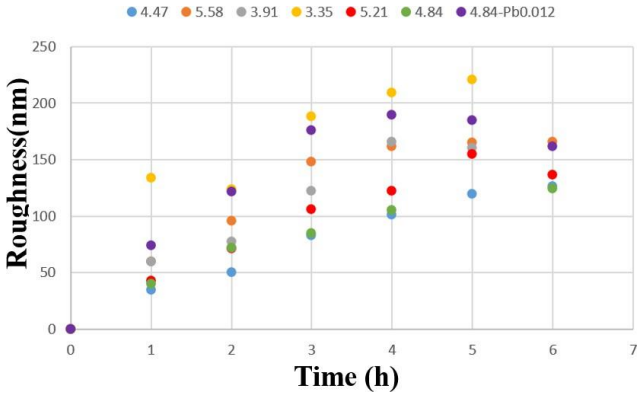

Figure 8 the relationship between the roughness and time from 1 h to 6 h. The volume of NaOH is 3.35 ml, 3.91 ml, 4. 47 ml, 4.84 ml, 5.21 ml, 5.58 ml and the 4.84 ml with the Pb^{2+} molarity of 0.012 mol/L.

Figure 9 shows the relationship between the thickness and time from 1 h to 6 h using the different the volume of NaOH of 3.35 ml, 3.91 ml, 4.47 ml, 4.84 ml, 5.21 ml, 5.58 ml and the 4.84 ml with the Pb^{2+} molarity of 0.012 mol/L. The thickness increases almost for each data from 0 h to 6 h. The thickness decreases for some data after 4 h. It is due to the dissolution of $Pb(OH)_2$. It is linear relation for the volume of 4.84 ml NaOH from 0 h to 2 h. It indicates that the growth speed is uniform in this way. The K is at the maximum value when the reaction is at the beginning. The trend is not changed by decreasing the Pb^{2+} molarity. It indicates that the content of the complex is not the dominant factor in determining the maximum value of K.

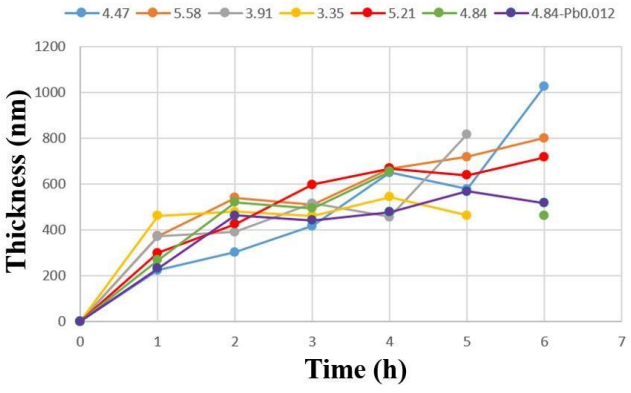

Figure 9 the relationship between the thickness and time from 1 h to 6 h. The volume of NaOH is 3.35 ml, 3.91 ml, 4.47 ml, 4.84 ml, 5.21 ml, 5.58 ml and the 4.84 ml with the Pb^{2+} molarity of 0.012 mol/L.

4. CONCLUSIONS

The preparation of PbSe films is very complex, and it is important to understand the principles of film formation and deposition. The reaction speed mainly depends on the concentration of ions in the solution, and too high concentration of ions will cause the reaction to be too fast and poor control. The deposition rate depends on the reaction rate, and it is necessary to control the deposition rate by controlling the reaction rate. The stability of deposition rate depends on the stability of reaction rate.

The stability coefficient of the lead complex should be the maximum value before the reaction, that is, the stability coefficient decreases with the reaction. There is a threshold interval for the initial molar amount of Pb ion and Se ion, in which the deposition rate is uniform and the reaction is uniform, and the deposition rate is proportional to the reaction rate, which can be expressed as a primary function.

ACKNOWLEDGMENTS

First of all, I would like to give my heartfelt thanks to all the people who have ever helped me in this paper. Thanks to Zhang for his guidance and theoretical analysis. Thanks for the experimental platform and support provided by Gu. Thanks to Yang for his help in the experiment every day.

FUNDING STATEMENT

This research did not receive any specific grant from funding agencies in the public, commercial, or not-for-profit sectors.

REFERENCES

[1] Y. Kim, K. R. Choudhury, J. W. Lee, D. W. Song, G. Sarasqueta, **PbSe nanocrystal-based infrared-to-visible up-conversion device**, Nano lett. 11, 2011, pp. 2109-2113.

[2] Y. Zhu, X. Zhang, G. Liu, G. Qiao and J. Liu, **P-type PbSe nanocrystalline films fabricated using high concentration of ammonia as complexing agent**, Mater. Letter. 281, 2020, pp. 128621.

[3] T. Templeman, M. Biton, T. Safrani, M. Shandalov, E. Yahel and Y. Golan, **Chemically Deposited PbSe Thin Films: Factors Deterring**, CrystEngComm, 16, 2014, pp. 10553-10559.

[4] S. Gorer, A. A. Yaron and C. Hodes, **Chemical solution deposition of lead selenide films: a mechanistic and structural study**, Chem. Mater, 7, 1995, pp. 1243-1256.

24: MICROWAVE PHOTONIC FILTERING FOR FIBRE OPTIC INTERFEROMETER SENSORS

*W. J. Li [a], Z. Q. Yu [a], X. S. Tang [a], Z. W. Wang [a], J. S. Ni [a], W. Zhang [a,] *, and K. T. V. Grattan [b]*
[a] Laser Research Institute, Qilu University of Technology (Shandong Academy of Sciences), Jinan 250353, China
[b] School of Science & Technology, City, University of London, London EC1V 0HB, United Kingdom
Microwave and Photonic Sensors, EM010, August 13, 2024, 2:50 PM - 4:00 PM

Abstract – Microwave photonic filtering has been used to explore new potential directions in sensing technology. In this work a microwave photonic filter (MPF) has been proposed to transfer the optical response of a fibre optic interferometer into the microwave frequency domain and thus to overcome some of the potential limitations imposed by optical measurement. The MPF used consists of a fibre optic Fabry-Perot interferometer (FPI) as the sensing element as well as a spectrum slicer, and a dispersive fibre link as a frequency down-conversion factor. The shift of the central frequency of the MPF passband was modulated by the change of the effective cavity length which can be monitored to demodulate the sensing parameters. FPIs with different cavity lengths were used with different lengths of the fibre link to test the performance and the feasibility of the sensing system. By using the MPF, measurements of temperature and refractive index were successfully demonstrated with adjustable sensitivity and operational frequency.

***Keywords*:** Microwave photonic filtering; Optical delay line; Fibre optic interferometer; Sliced broadband source; Dispersive fibre link; Frequency down conversion.

1. INTRODUCTION

Research into microwave photonics has blossomed in recent years with studies looking at many issues including the basic optical-microwave interaction, photonics devices operating at microwave frequencies, photonic control of microwave devices, high frequency transmission links and the use of photonics to implement various functions in microwave systems [1]. From pioneering experiments in late 1970's, the field has expanded to produce a number of applications with considerable potential commercial importance. Continued progress in photonic components and technology reflects great interest in this field and an expanding acceptance of the use of photonics in microwave systems. Over the past decade, different microwave-photonics technologies have been investigated to allow better optical fibre sensing. By introducing microwave modulation into the optical system, the optical detection can be synchronized with the microwave modulation frequency. As a result, the system created can have a high SNR and thus an improved detection limit. Fiber-optic sensor systems employing microwave photonic technology have been proposed and demonstrated – thus to explore achieving better performance, allowing the sensor parameters to be resolved in the microwave domain. Due to huge gap between optical and microwave frequencies, tiny variations seen in the optical domain will cause significant changes in the microwave domain, which then will enable the microwave photonic-based optical sensors created to show high sensitivity and improved resolution capability. Furthermore, with the development of photonic and mobile network technologies, the realization of microwave photonic signal processing has in practice become more and more convenient and thus more cost effective.

Fiber optic interferometric sensors has been widely used for measuring various physical and chemical parameters and as a powerful tool in fundamental research, thanks to their high measurement sensitivity. Microwave photonic filtering (MWP) technology can be used to interrogate such interferometric sensor, where the sensor information can be deduced directly from the central frequency of the MPF passband. Such Microwave Photonic Interferometers have been used for the measurement of important parameters such as temperature [2], strain [3], humidity [4], and refractive index [5], and in distributed sensing [6], for example. In these cases, the interrogation is usually realized by tracing the resonance frequency of the MPF response.

Microwave photonic sensors generally are based on optical delay line structures. The optical fibre Michelson interferometer was first used as a dual delay line notch filter, where the displacement induced from one of the arms of the interferometer was identified by detecting the frequency of the peak or valley of the microwave response of that interferometer. Multiple delay lines can be used, by adopting certain optical structures such as an array of delay lines, or a recirculating line to, for example, enhance the performance of the microwave photonics sensing system. Since the central frequency of the MPF response is defined by the optical path difference of the delay lines, this leads to a strict application condition: the optical path difference (OPD) of the interferometer should be of the same order of the microwave wavelength. This potentially restricts its application in the field of precision measurement where OPDs around micro/nanometres are addressed. However, the recent developments in advanced manufacturing have driven the need for more precise manufacturing processes and, as a consequence, sensing technologies have evolved. In this work, microwave photonic filtering has been used to transfer the optical response of a fibre optic interferometer into the microwave frequency domain. Using this approach, a Fibre Optic Fabry-Perot interferometer (FPI) and a dispersive fibre link were used to construct a novel optical delay line filter. As a result, the microwave photonic responses of the filters proposed were measured and their use in optical fibre sensor applications considered and evaluated.

DOI: https://doi.org/10.34961/researchrepository-ul.29278913.v1

1. PRINCIPLE OF OPERATION

In an intensity-modulated system using direct modulation or an external optical modulator, optical delay line filtering can be realized by incoherently summing N optical signals with an optical path increment. For a filter with N optical fibre delay lines, the transfer function can be expressed with the z-transform as [7],

$$H(z) = \sum_{n=1}^{N} w_n z^{-(n-1)} \quad (1)$$

where w_n is the weight and z^{-1} represent a unit delay associated with the length increment L_0 between adjacent delay lines. A bandpass response can be achieved using N optical fibre delay lines when the microwave signals constructively add at those frequencies,

$$f_i = \frac{i}{\tau_s} = \frac{i}{nL_0} \quad i = 0, 1, 2, \ldots \quad (2)$$

where τ_s is the unit time delay, n the refractive index of the fibre core, and c the light velocity in vacuum. Any change in the unit time delay leads to a change in the bandpass frequencies f_i.

The optical reflection spectrum of a Fabry-Perot interferometer (FPI) is as shown in Fig. 1. The signal demodulation algorithms for FPIs fall into either *intensity demodulation* or *peak wavelength* tracking. While intensity demodulation allows fast response, the wavelength tracking scheme has the advantage of ultrahigh resolution and notably high accuracy. The peak wavelength in an FPI spectral response is proportional to the effective cavity length, where any change can be measured by tracking the change of a specific peak wavelength. However, the ambiguity in the peak wavelength tracking always occurs, being equivalent to a 2π ambiguity of phase measurement in a coherent interferometer, when subjected to a large, abrupt change. The measurement is usually realized by measuring the change of the Free Spectral Range (FSR), which can simply be expressed in the frequency domain as

$$\Delta\omega = \frac{1}{\tau_0} = \frac{c}{2nL_0} \quad (3)$$

where τ_0 is the unit time delay related to the cavity length L_0, and n the refractive index of the medium. It should be pointed out that either wavelength tracking or FSR monitoring of the relationship between peak wavelength or FSR and effective cavity length of FPI is nonlinear, which implies a varying measurement sensitivity over the measurement range.

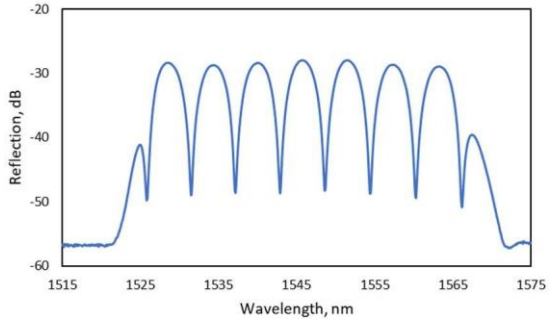

Figure. 1 Typical reflection spectrum of an FPI illuminated by a C-band broadband source.

Considering the optical reflection from an FP interferometer as coming from a sliced broadband source, there are multiple components in such a sliced source, as shown in Fig. 1. After being launched into a fibre link, each component will experience a phase shift, which is wavelength dependent, where its phase can be expressed as,

$$\theta = \omega(t + T) \quad (4)$$

where x is the optical frequency of the corresponding component, and,

$$T = L[\frac{n}{c} + D(\lambda - \lambda_0)] \quad (5)$$

is the time delay corresponding to the fiber link length, showing a different value for a different wavelength, with L, the length of the fibre link, n, the fibre core index, c, the light velocity in vacuum, and D, the fibre group velocity dispersion parameter in ps/nm·km, around the wavelength of λ_o. At the photodetection, a microwave photonic bandpass filtering will be formed. The unit time delay in such a filter using multiple optical delay lines can be expressed by

$$r_s = \Delta T = DL \cdot \Delta\lambda \quad (6)$$

where $\Delta\lambda$ is the FSR of the sliced source. The central frequency of the MPF passband can be expressed as

$$f = \frac{1}{\tau_s} = \frac{1}{DL\Delta\lambda} = \frac{2nL_0}{DL^2} \quad (7)$$

When the FSR of the interference spectrum changes, the central frequency of the MPF passband will change accordingly. Also, by tracking the central frequency shift of the MPF passband, the change in the effective cavity length of the FPI can be monitored. In the microwave photonic configuration discussed, the unit time delay, τ_0, defined by the FPI cavity length, is replaced by a much larger parameter, τ_s, defined by the dispersion of the fibre link. The optical response of such a FP interferometer is then transferred into the microwave photonic response with a frequency down-conversion factor, which is defined by the dispersion of the fibre link. This also indicates that the measurement sensitivity can be adjusted, by increasing the cavity length of the sensing FPI, or reducing the length of the fibre link. Since the central frequency of the passband is linearly proportional to the effective cavity length, a constant measurement sensitivity over the whole measurement range can be expected and this represents an important benefit of this approach.

2. EXPERIMENT APPROACH AND RESULTS

The microwave photonic sensing system discussed in this work is illustrated in Fig. 2. Here the output from a broadband light source was sent to a fibre-optic open cavity Fabry-Perot interferometer (FPI), through an optical circulator (OC). The FPI sensing head used in this work was as shown in Fig. 3. Here a single-mode fibre and a gold-plated reflector were placed in a 5 cm U-shaped quartz glass tube. The fibre and the reflector were both bonded to the glass tube to form a robust and open FPI cavity. The incident light entered the cavity through a single-mode fibre and was reflected by the gold-plated reflector.

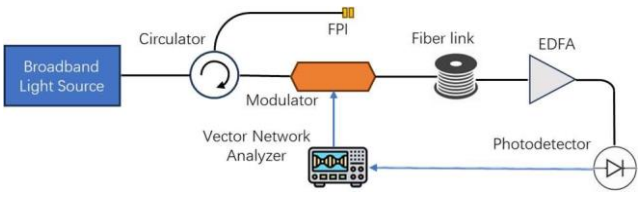

Figure 2 Experimental arrangement used in this work.

The broadband spectrum used was spectrally shaped by the FP interference from the reflection at the fibre end face and the gold-plated reflector, and the reflected spectrum from the sensor was sliced into multiple components, as shown in Fig. 1. The spectrum sliced broadband source was then coupled into an electro-optic modulator (EOM), by which a microwave signal generated from the vector network analyzer (VNA) was used to modulate the optical beam. The optical microwave signal was then sent to a length of single mode fibre, and amplified by an erbium-doped fibre amplifier (EDFA) and was then received by a photodetector. Finally, the frequency response of the proposed single bandpass microwave filter was observed by the VNA used.

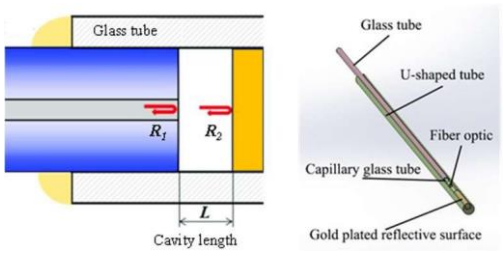

Figure 3 Configuration of fibre optic FPI used.

Four FPIs with cavity lengths of 84 µm, 160 µm, 214 µm, and 326 µm respectively were used in the experiments described. The reflection spectra of these 4 FPIs were measured and are shown in Fig.4. A fibre link with a length of 4 km was used in the experiment, while the microwave frequency responses of the filter discussed, using 4 different FPIs were recorded, while the FPIs were open to the air at room temperature. The results of the measurement made are as shown in Fig. 5.

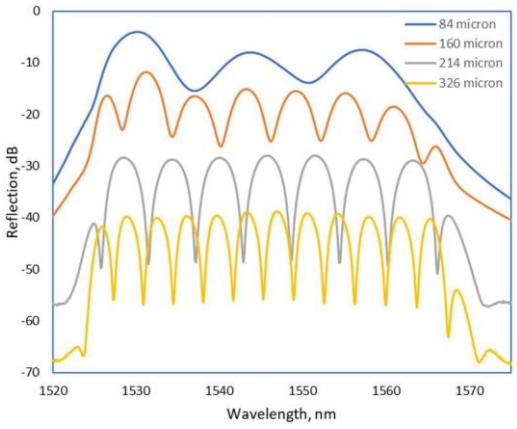

Figure 4 Reflection spectra of FPIs used in the experiment.

From the measured responses, it can be seen that a bandpass filter was formed, where the central frequency of the passband varied the cavity length of the FPI used. The relationship between the central frequency and cavity length is plotted in Fig. 5b, the result of which shows a good level of linearity, in close agreement with (7).

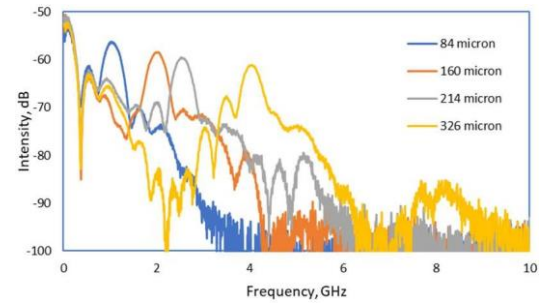

(a)

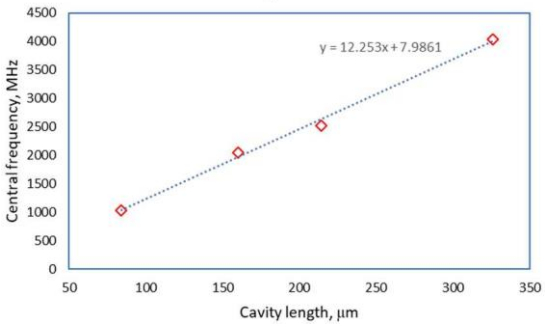

(b)

Figure 5 (a) Microwave responses of the filter described with a 4 km fibre link and different FPI cavity lengths, (b) The central frequency of the passband vs FPI cavity length.

A fibre link, with a length of 30 km, was also used and the microwave frequency responses of the filter discussed, while the FPIs were open to the air (at room temperature) were recorded. The results of such a measurement are as shown in Fig. 6, where it can be seen that the relationship between the central frequency and cavity length shows a good level of linearity. With the larger fibre dispersion used, the central frequency of the passband now fell below 1 GHz.

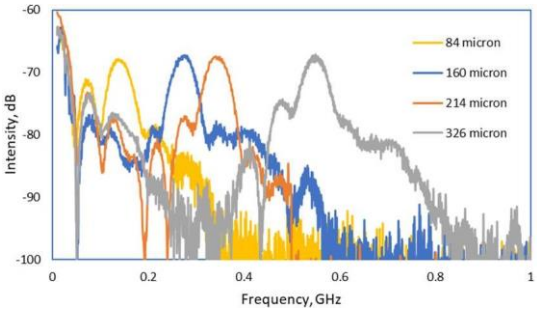

(a)

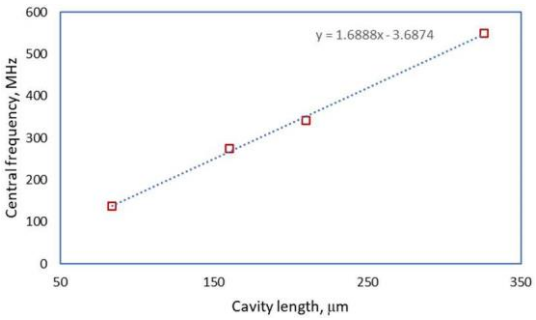

(b)

Figure 6 (a) Microwave responses of the proposed filter with a 30 km fibre link and different FPI cavity lengths, (b) The central frequency of the passband vs FPI cavity length.

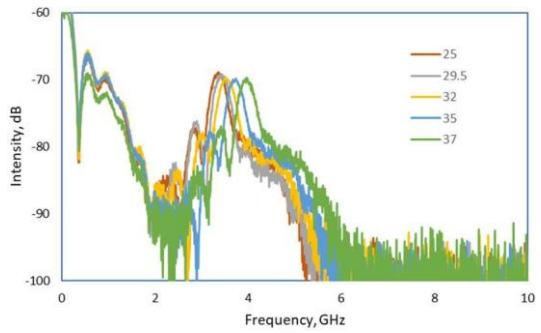

(a)

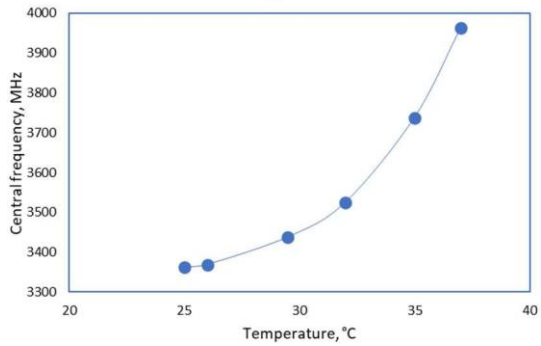

(b)

Figure 7 Temperature measurement (a) Microwave responses at different temperature, (b) The central frequency of the passband vs temperature.

The FPI, with the cavity length of 214 μm, was used in the filter discussed, with a 4 km fibre link employed. Here, the FPI sensing head was inserted in a water bath and the microwave frequency response of the filter was recorded, as a function of the variations of the temperature of the water bath. In this FPI, the gold-plated reflector was glue-bonded, where the glue will expand as the temperature increases, leading to an increased effective cavity length. The measured microwave responses of the filter and central frequency of the passband obtained against temperature are shown in Fig. 7. The relationship between the central frequency of the passband and the temperature can be seen to be nonlinear, which is attributed to the performance of the glue thermal expansion (which is nonlinear). Further, the temperature dependence of the water refractive index makes a contribution to this (although it is small compared with the glue thermal expansion). The relationship between the central frequency and the effective cavity length still is linear, as described by (7).

An experiment to demonstrate refractive index measurement was carried out by using the filter with the FPI of 326 μm cavity length and a 30 km fibre link. In the FPI, the gold-plated reflector was fixed securely to the glass tube, so that the thermal effect on the cavity length was minimized. The FPI sensing head was then inserted into the aqueous glycerol solutions, which exhibit different refractive index values at different concentration. The microwave frequency responses were then measured at these different RI values. The measured microwave responses of the filter and the central frequency of the passband as a function of temperature are shown in Fig. 8 (which has been demonstrated for four different RI values). The graph shows that a clear linear response between the central frequency of the passband and the RI value has been demonstrated. Since a 30 km fibre link was used, the central frequencies all were below 1 GHz. According to (7), the long length of the fibre link may reduce the measurement sensitivity. However, the resulted low central frequency can ease the requirement for the specification of the microwave photonic system when used in different practical applications.

It should be pointed out that in all the measured microwave frequency responses demonstrated here, only the first passband of the proposed MPF was illustrated and used here to monitor the change in the sensing FPIs. However, in practice, there are many passbands in optical delay line filters, as defined by (1). The central frequency of the *N*th passband represents a measurement sensitivity which is *N* times that defined by (7). The microwave frequency response of the filter discussed here in this work, however, shows a lowpass response due to the sliced optical components and dispersion fibre link used [8]. Therefore, the responses from the higher-order passbands are suppressed. The lowpass cut-off frequency is defined by the bandwidth of the sliced single component and the dispersion of the fibre link. However, this lowpass effect can be removed if a single sideband modulator is used.

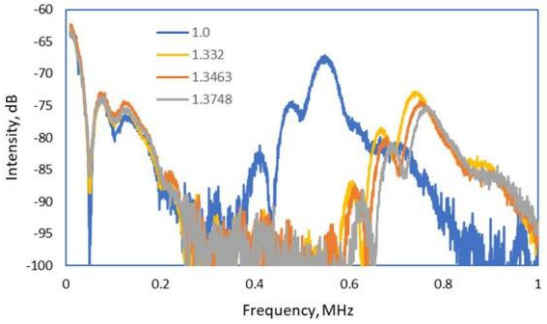

(a)

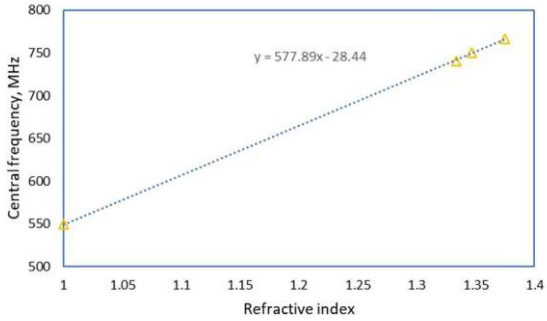

(b)

Figure 8 Refractive index measurement (a) Microwave responses, (b) The central frequency of the passband as a function of the RI.

3. CONCLUSIONS AND FURTHER WORK

A microwave photonic sensing system capable of transferring the optical response of fibre optic interferometer into microwave frequency domain has been proposed and its performance discussed. The microwave photonic filter evaluated consists of a fibre optic FPI as a sensing element as well as a spectrum slicer, and a dispersive fibre link as a transferring factor. The shift of the central frequency of the MPF passband caused by the change of the effective cavity length in the FPI could be monitored to demodulate the variation of sensing parameters. Several experiments with the

FPI sensors using different FP cavity lengths have been carried out for measuring both temperature and RI change. The experimental results show that the central frequency of the passband observed was linearly proportional to the change of the effective cavity length of the sensing FPI. The measurement sensitivity is constant over the measurement, and could be tailored by adjusting the length of the FP cavity, and the length of the fibre link. Doing so can avoid the limitations on the measurement range from the periodic characteristics of the FP interference spectrum, and allow maintaining the sensing performance over the measurement range. The sensing system discussed can be applied to any type of interferometric sensor where the sensitivity can be further increased if the higher order passbands are chosen to demodulate the sensing parameter. The flexibility to choose sensitivity and operating frequency makes it very attractive in the applications where the traditional approach to optical measurement is difficult to handle. The investigation into the characteristics of the MPF is continuing to exploit these for future applications, which will be discussed in future papers.

ACKNOWLEDGMENTS

This work was partly supported by the Innovation Team Program of Jinan, China (Grant No. 202228032). Grattan acknowledges the support of the Royal Academy of Engineering.

REFERENCES

[1] D. Marpaung, J. Yao, J. Capmany, **Integrated microwave photonics**, Nature Photon, vol. 13, 2019, pp. 80–90. https://doi.org/10.1038/s41566-018-0310-5.

[2] C. Zhu, J. Huang, **Sensitivity-enhanced microwave-photonic optical fiber interferometry based on the Vernier effect**, Opt. Express, vol. 29, no. 11, 2021, 16820-16832. https://doi.org/10.1364/OE.426966.

[3] H. Fu, W. Zhang, C. Mou, X. Shu, L. Zhang, S. He, and I. Bennion, **High-Frequency Fiber Bragg Grating Sensing Interrogation System Using Sagnac-Loop-Based Microwave Photonic Filtering**, IEEE Photonics Technol. Lett. vol. 21, no. 8, 2009, pp. 519–521. DOI: 10.1109/LPT.2009.2014077.

[4] P. Pan, X. Cai, S. Chen, T. Xie, H. Wang, W. Dai, and H. Fu, **Highly Sensitive Fiber-Optic Humidity-Sensing System by Using GO-FPI-Based Microwave Photonic Filter**, IEEE Sens. J., vol. 23, no. 3, 2023, pp. 2236-2240. DOI: 10.1109/JSEN.2022.3231597.

[5] C. Zhu, J. Huang, **Multiplexed optical fiber tip refractive index sensor interrogated by microwave photonics**, Opt. Lasers Eng., vol. 163, 2023, 107477. https://doi.org/10.1016/j.optlaseng.2023.107477.

[6] X. Zhu, L. Hua, J. Lei, et al, **Microwave–photonic low-coherence interferometry for dark zone free distributed optical fiber sensing**, Opt. Lett. vol. 46, no. 5, 2021, pp. 1173-1176. https://doi.org/10.1364/OL.414699.

[7] G. Yu, W. Zhang, J. A. R. Williams, **High-Performance Microwave Transversal Filter Using Fiber Bragg Grating Arrays**, IEEE Photon. Technol. Lett., vol. 12, no. 9, 2000, pp. 1183-1185. DOI: 10.1109/68.874229.

[8] W. Zhang, J. A. R. Williams, I. Bennion, **Chromatic dispersion effect in a microwave photonic filter using superstructured fibre Bragg grating and dispersive fibre**, vol. 13, no. 17, Opt. Express, pp. 6429-6437. https://doi.org/10.1364/OPEX.13.006429.

25: DESIGN AND SIMUATION OF A SAW GAS SENSOR FOR DETECTION OF METHANE AND NITRIC OXIDES

Eric Wickens [a], *Dr. Svetlana Slepneva* [b], *Dr. Veda Sandeep Nagaraja* [c, *]

[a] Undergraduate, University College Cork/Munster Technological University, Cork, Ireland,
[b] Department of Physical Sciences, Munster Technological University;
[c] Programme Manager, Senior Researcher, Tyndall National Institute; :

Environmental Sensing, EM010, August 13, 2024, 4:20 PM - 6:10 PM

Abstract – The paper aims to design and simulate a MEMS based surface acoustic waves (SAW) gas sensor for nitric oxides and methane detection. The main advantage of SAW sensors is they have good power management and so could be used in Internet of Things applications. Four different designs for a SAW sensor were simulated using Quanscient Allsolve Multiphysics software. Three of these designs yielded results that were satisfactory, which will lead to their fabrication. The gas sensor was designed for wide frequency range of 50 MHz to 250 MHz. Each gas a particular frequency for detection. Here the authors have tried to understand the method to design and simulate for different types of ITDs for different gases by changing the IDT dimensions and types. It has been found that the focused IDTs are not suitable for sensing as compared to conventional, Dummy electrode and Apodized type of IDT.

Keywords**:** Surface Acoustic Wave, MEMS, Gas sensor, IDT

1. INTRODUCTION

Gas sensing has taken on a greater importance in the last few decades as climate change has become one of the defining challenges of our time. Reliable ways to monitor greenhouse gases and gather data are vital so that these issues can be understood and, hopefully, resolved.

One of the first approaches for gas to be used was monitoring the change in behaviour of Canaries, a type of bird, in the presence of malicious gases in mines and tunnels. The bird would stop singing and die after a period time if exposed to certain toxic gases.

The first modern gas sensor was developed in 1927. Dr.Oliver Johnson invented the catalytic combustion sensor which was able to detect combustible gas mixtures in the air to prevent unplanned explosions. The combustible gases react with a sensing layer inside the sensor which heats up an electrode, increasing its resistance, allowing a relationship to form between resistance and concentration of the gas. However, this required a manual push of a button every time someone wanted to monitor the gas and the detector weighed over 5 kilograms. A lot of progress has been made since, including the miniaturisation and automation of the gas sensors. Nowadays, gas sensing technologies are hitting the micrometre scale and are becoming highly sensitive to a multitude of gases.

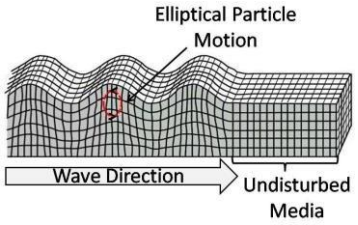

Figure 1. Surface Acoustic Wave moving through a material [1].

Surface Acoustic Waves (SAWs) are waves that travel along the surface of a material. First theorised in 1885 by Lord Rayleigh, these waves cause the particles at the surface a material to move in an elliptical motion (Figure. 1). This creates a sinusoidal wave that propagates along the surface. The amplitude of these waves' decays exponentially into the materials, which causes these waves to only reach around one wavelength in depth. These waves cause strain within the material as they travel. If these waves travel through a piezoelectric material, they can be used to create an electric charge.

SAW gas sensors use mechanical waves to detect the change in mass of a sensing layer that is sensitive to the target gas. An Interdigitated Transducer (IDT) generates the SAW which travels through a piezoelectric substrate, underneath a sensing film, and this is read using another IDT at the other end of the sensor. The change in mass due to target gas deposition causes a shift in SAW frequency which is how the concentration of the target gas can be measured. This is expressed in the equation below [2].

$$\Delta f = -\frac{k\Delta m {f_0}^2}{A},$$

where Δf is the change in frequency, k is the spring constant of the sensing layer, Δm is the change in mass, f_0 is the resonant frequency, and A is the area of the active surface of the sensing layer.

These sensors have high selectivity, they can also be easily integrated into WSNs (Wireless Sensor Networks), as "smart sensors" which can collect and process data before sending out to the wider network. SAW sensors are also able to detect biological cells, such as cancer cells or enzymes, depending on the sensing layer.

The aim of this work is to design and simulate a MEMS based gas sensor using Surface Acoustic Waves (SAW) that can accurately measure a target gas. Four different IDTs configurations have been designed and simulated. The two

DOI: https://doi.org/10.34961/researchrepository-ul.29279027.v1

target gases that the sensor was configured for are nitric oxides and methane.

2. METHODS AND PROCEDURES

2.1. Design

The IDT designs of this sensor were based off previous research as seen in literature [3]. The frequency of the generated SAWs should be at the resonant frequency, so to obtain the highest amplitude of the SAW, and thus the highest admittance which increases sensitivity. The specific resonant frequency is chosen based on the sensing layer. As the sensing layer is not being developed within this paper a range of 50 MHz to 250 MHz was targeted for the resonant frequency. This range of frequency was targeted based on previous work and literature survey [4][5]

The dimensions of the IDT were calculated based upon the desired wavelength of the generated SAWs. The calculation uses the speed of sound within the substrate and the target resonant frequency. The material chosen for the IDTs of the sensor was as aluminium as it has the best phase velocity for SAW as it is a less dense metal. Lithium Niobate was chosen as the piezoelectric substrate due to its high piezoelectric coefficient, which improves the sensitivity and selectivity of the sensor.

The four IDT designs covered in this work are seen below:

Conventional

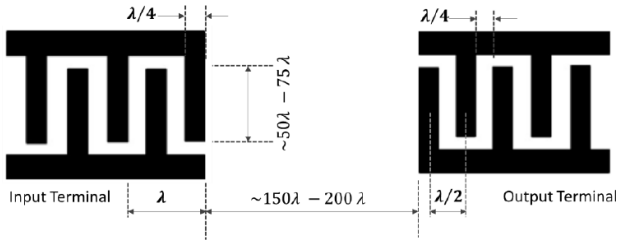

Figure 2. Dimensions of conventional IDT configuration [2].

This IDT design consists of two interlocking sets of electrodes. One set is positively charged with an AC signal, the other is ground. The width of the IDT fingers and the gap between is the same, set at λ/4, where λ is the wave length of SAW. This is optimal for the creation of the desired resonant frequency. As can be seen in Figure. 2, the length of the IDT fingers is designed to be in range of 50λ - 75λ. The distance between the two IDTs should be set within 150λ - 200λ.

Dummy Electrode

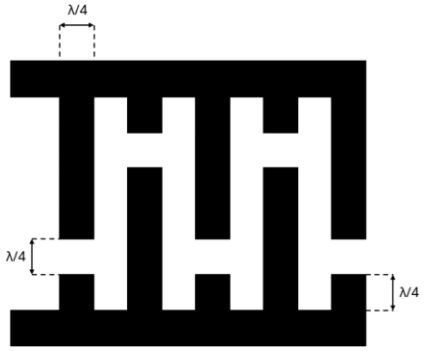

Figure 3. Dummy Electrode IDT configuration.

The dimensions of the dummy electrode IDT are very similar to the conventional configuration. The difference with these two designs is that a small IDT finger is placed opposite to another IDT finger with an opposite charge. The length of this smaller finger is λ/4. This design has been seen to reduce noise and spurious modes within previously fabricated SAW devices (Figure. 3).

Apodized

Figure 4. Apodized IDT configuration.

This design also has similar dimensions to the conventional configuration, but length of the IDT fingers changes throughout the design. Each finger gets 2λ longer the closer it is to the centre of the IDT. This design is pictured in Figure. 4. This design has also been seen to reduce spurious modes within the system, in turn, increasing the sensitivity of the sensor [6].

Focused Electrodes Configuration

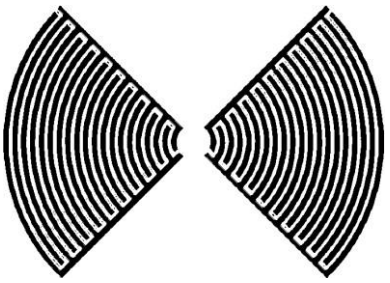

Figure 5. Focused IDT configuration.

The focused electrode configuration was the last design explored in this work. This design has IDT fingers in concentric circles on the substrate to create an extremely focused SAW in the centre of the design, as seen in Figure. 5. This design is mainly used for microfluidic manipulation, projecting individual droplets of a certain fluid [3].

2.2. Simulation

To simulate these designs, Quanscient Allsolve Multiphysics software was used. It is a FEA multiphysics software which utilizes cloud computing to perform its simulations. These four designs were created in the software, with the different material properties and physics conditions applied to them.

A Multiharmonic simulation was then conducted which calculated the resonant frequency and analysed the harmonics of the generated SAW. This was then used to calculate the desired outputs of the simulation, i.e. impedance, admittance, maximum displacement.

A range of frequencies was tested on each design to locate the resonant frequency of each design. Ideally, each design

will observe a resonant frequency at the frequency that the dimensions of the IDTs designed for, but the geometry and material properties will affect the SAW and shift the resonant frequency. Observing a resonant frequency within the range 50 MHz to 250 MHz is desired.

At first, broad frequency ranges are tested on the designs to understand which frequencies are showing increased activity. Then, a finer frequency range is tested on the designs to pinpoint the exact resonant frequency of the sensor. Due to the limitations of the software, the bandwidth of the resonance frequency is idealistic as the software does not take damping or loss into account currently.

3. RESULTS AND DISCUSSION

The output from these simulations comes in the form of an admittance plot, with the Y-axis displaying admittance in dB and the X-axis displaying frequency. A tall, sharp peak is the signifier for the resonance frequency of the sensor. The anti-resonance frequency should also be observed after the resonance frequency. This is important to observe as it allows for an evaluation of the performance of the sensor.

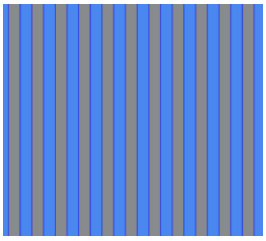

(a)

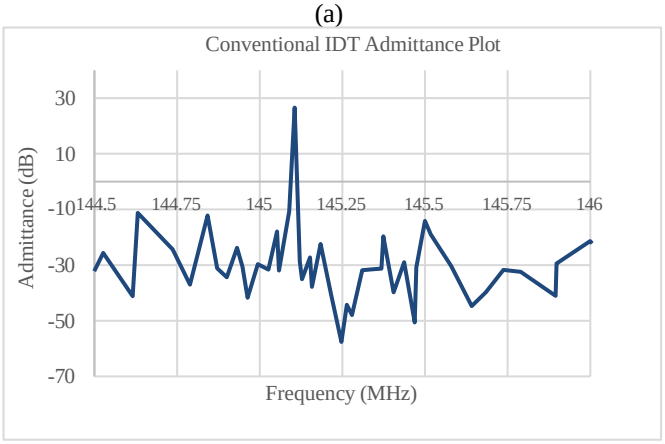

(b)

Figure 6. Conventional IDT (a) geometry and (b) admittance plot.

The conventional IDT gave a resonance frequency of 145.1 MHz as can be seen in Figure. 6 (b). As the plot has a logarithmic scale, this resonance peak is very pronounced. This resonant frequency falls within the desired range. An anti-resonance frequency can also be seen at 145.25 MHz.

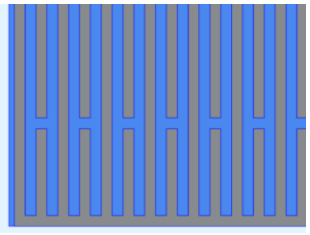

(a)

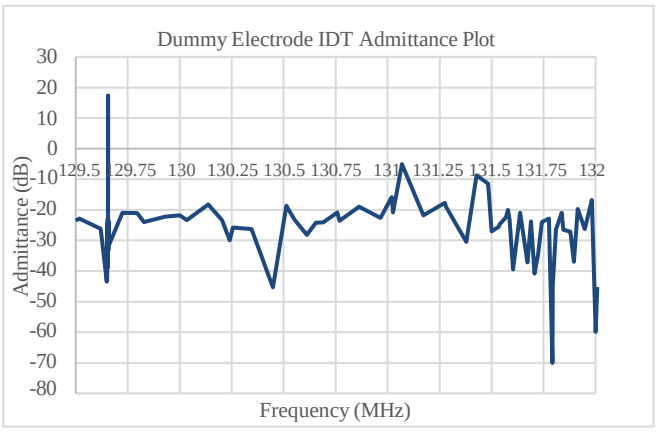

(b)

Figure 7. Dummy Electrode IDT (a) geometry and (b) admittance plot.

This design gave clear peaks at both the resonance and antiresonance frequency. The resonance frequency can be seen at 129.6 MHz, and the antiresonance at 131.8 MHz (Figure. 7 (b)). This is within the desired range and is giving quite strong admittance at the resonant frequency.

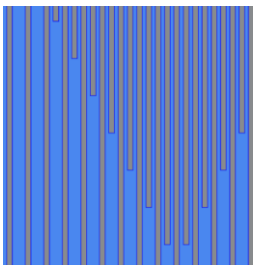

(a)

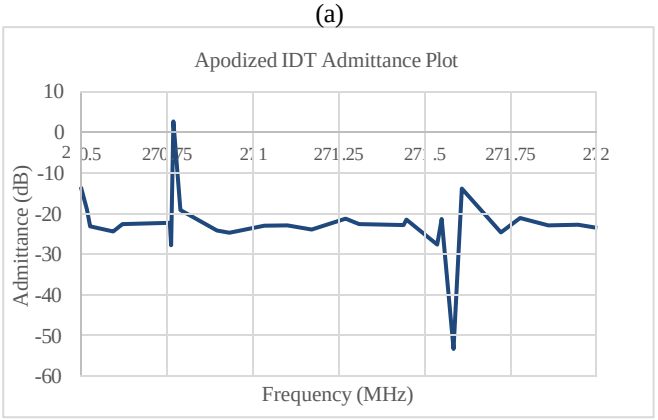

(b)

Figure 8. Apodized IDT (a) geometry and (b) admittance plot.

A clear resonance frequency can be seen at 270.75 MHz, and an antiresonance frequency at 271.6 MHz (Figure. 8 (b)). This is outside the frequency range that is desired, but the dimensions of the IDT can easily be changed to generate the resonance frequency within the desired range. This design is still considered a success as the resonance frequency was successfully found.

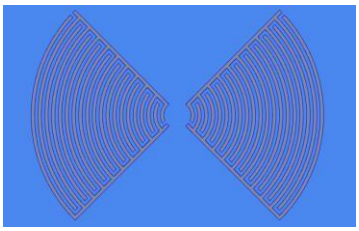

(a)

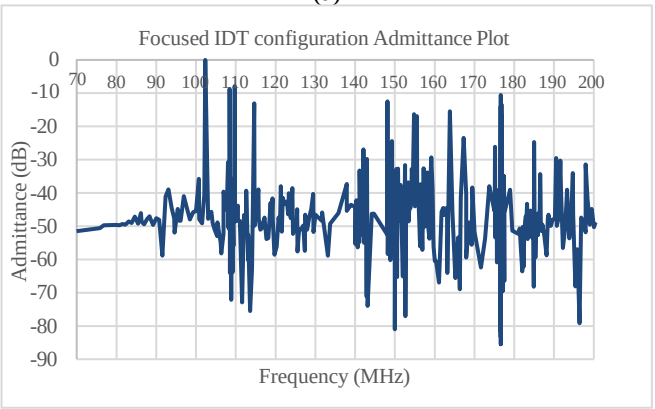

(b)

Figure 9. Focused IDT configuration (a) geometry and (b) admittance plot.

The results from this design were not as desired as the resonance frequency and antiresonance frequency could not be resolved due to the noise and interference (Figure. 9 (b)). These types of IDTs are not found useful for sensing but could be used for SAW streaming applications.

4. CONCLUSIONS

Each of the designs were simulated successfully, with three of the design showing clear resonance frequencies. Though the apodized IDT showed a resonance frequency outside the desired range, its results are still positive.

The three successful designs will be fabricated as future work. They will then be tested so that further complexity and accuracy can be added to the simulations.

Several improvements can be made, these would be to modify the design dimensions to improve the performance of the sensor to detect the gas by resonating at the required frequency. The designs in this work will be further optimised to improve selectivity. The number of IDT fingers has an effect on the performance, as does the distance between the IDTs and the length of the fingers. A parameter sweep can be simulated in the software easily by adding in a sweep function into the simulation, which would test each dimension in a given range and step size. Another improvement to the simulation would be to include environmental conditions to the simulations, such as the addition of a representative element for the sensing layer on the substrate, or a variation in temperature in the model to understand its effect on the performance.

As this was carried out as a final year undergraduate project, time constraints limited the scope of the project. However, three designs were successfully designed and simulated so to be able to sense nitric oxides or methane with an appropriate sensing layer.

ACKNOWLEDGMENTS

The authors would like to acknowledge the help from Quanscient Allsolve Multiphysics software team comprising of Bassou Khouya on the technical side and Nikola Strah and Juha Riippi on the marketing side. The authors would also like to thank the support extended by the Nanotechnology / SAFE Cluster team lead by Prof.Alan O'Riordan from Tyndall National Institute for enabling the work on MEMS gas sensors.

FUNDING STATEMENT

This work was carried out under the SFI CONNECT funding and the authors would like to thanks the funding agency for the support. The future work will be carried out by the Nanotechnology / SAFE Cluster under the SFI CONNECT funding.

REFERENCES

[1] S. Jones, **Ground vibration from underground railways: how simplifying assumptions limit prediction accuracy**, Rose Hulman Institute of Technology, 2010.

[2] He, X. L.; Li, D. J.; Zhou, J. **High sensitivity humidity sensors using flexible surface acoustic wave devices made on nanocrystalline ZnO/polyimide substrates**. J Mater Chem C 2013, 1, 6210

[3] D. Mandal and S. Banerjee, **Surface Acoustic Wave (SAW) Sensors: Physics, Materials, and Applications**, Sensors, vol. 22, no. 3, 2022.

[4] M. I. A. Asri et al, **MEMS Gas Sensors: A Review**, IEEE Sensors, 2021.

[5] S. Hashwan and e. al, **A review of piezoelectric MEMS sensors and actuators for gas**, Discover Nano, 2023.

[6] O. Jl Liang, **Transverse Mode Spurious Resonance Suppression in Lamb Wave MEMS**, IEEE Transactions on Electron Devices, 2015.

28:ULTRASENSITIVE LONG-PERIOD FIBER GRATING REFRACTIVE SENSOR WITH MICROCAVITIES

Shan Gao, Yan Liu, Jing Yang, Jinhui Shi, Chunying Guan**
[a] College of Physics and Optoelectronic Engineering, Harbin Engineering University, Harbin 150001, China
Industrial Sensing: 2, EM009, August 12, 2024, 1:30 PM - 3:00 PM

Abstract – We experimentally demonstrate an ultrasensitive refractive index (RI) sensor based on a single-mode fiber (SMF) and long-period fiber grating (LPFG) with periodic microcavities fabricated using a femtosecond laser. The presence of liquid within the microcavities induces a significant modulation in the refractive index, thereby exciting high-order cladding modes. The proposed sensor has obvious merits of easy fabrication and excellent reproducibility and exhibits an ultra-high RI sensitivity of - 11810 nm/RIU with high linearity within the range of 1.334-1.341 RIU. Additionally, it can function as a temperature sensor, presenting broad application prospects in the field of biochemistry.

Keywords**:** – Femtosecond laser ablation; long-period fiber grating (LPFG); refractive index (RI) sensor; temperature sensor

1. INTRODUCTION

Optical fiber sensors have numerous benefits, including compact dimensions, immunity to electromagnetic interference, and resistance to corrosion. The refractive index (RI) is a fundamental optical parameter which is holds significant significance in various fields such as biology, chemistry, medicine, and industry [1]. LPFGs effectively couple light from the forward propagating core mode to the forward propagating cladding modes, thereby producing loss bands in the transmission spectrum [2]. Various conventional techniques have been employed to fabricate LPFGs, including arc discharge, CO2 laser heating, melting taper, and UV-laser exposure [3-5]. The LPFGs fabricated based on the above methods accomplish RI sensing by monitoring the resonant dip which is modulated by evanescent wave at the interface between the cladding and the measured media, therefore, the sensing media should be close to the fiber RI, a high sensitivity can be obtained. In this work, we present a novel approach to fabricating an ultrasensitive RI sensor on a SMF using femtosecond laser. By ablating the core and a portion of the cladding of the SMF in the form of square microcavities with a specific periodicity, we successfully create a LPFG. The sensor demonstrates excellent repeatability in its measurements. When the liquid enters the microcavities, the periodic structure thereby exciting the higher-order cladding mode and resulting in loss bands within the transmission spectrum. The loss band of the sensor undergoes drift when there is a change in the RI due to alterations in the phase-matching condition. The sensor has a sensitivity of -11810 nm/RIU and demonstrates excellent linearity in its response. The proposed sensor has obvious merits of easy fabrication and excellent reproducibility.

2. METHODS AND PROCEDURES

The fabrication process of the LPFG involved the utilization of a Yb:KGW femtosecond laser (Light Conversion, PH2-20W) with specific parameters. The laser had a wavelength of 515 nm (obtained through second harmonic generators), a pulse width of 290 fs, and a repetition rate of 1000 kHz. To focus the laser, a 20X Olympus objective with a numerical aperture (N.A.) of 0.25 was employed. For precise translation of the SMF, a three-axis stage (Aerotech, ABL1000WB, ABL1000, and ANT130V-5) was assembled and utilized.

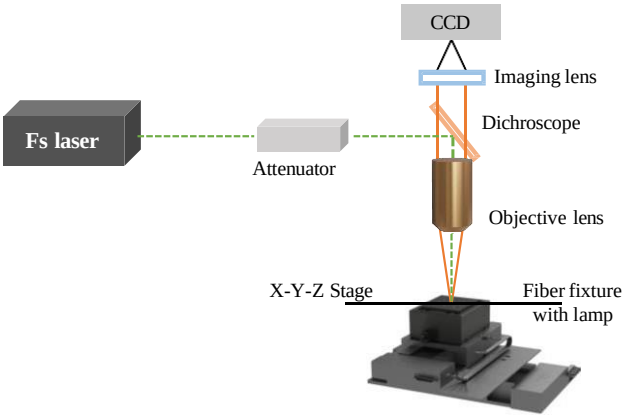

Fig. 1. The schematic diagram of fabricating microcavities in SMF by femtosecond laser.

Following the creation of microcavities on the SMF through ablation using a femtosecond laser. Due to surface tension, the liquid rapidly enters the microcavity. Then, the microcavity and the liquid form a periodic and strong refractive index modulation together, as shown in Figure 2 and the grating includes periodic microcavities, where Λ, L and W are the period, length and width of the microcavity, respectively. This modulation enabled the coupling of light propagating in the LP_{01} mode within the core with higher-order cladding modes at a specific wavelength.

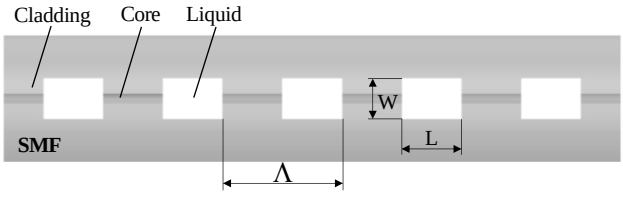

Fig. 2. Schematic diagram of LPFG (Λ=650 μm, L=60 μm, W=40 μm).

DOI: https://doi.org/10.34961/researchrepository-ul.29279072.v1

The LPFG resonant wavelength can expressed by [6, 7]:

$$\lambda_{res} = \Lambda \cdot [(n_{eff}^{co} - n_{eff}^{cl}) + \delta n\gamma] \quad (1)$$

$$\frac{d\lambda_D}{d\Lambda} = \gamma \cdot (n_{eff}^{co} - n_{eff}^{cl}) \quad (2)$$

In the aforementioned equations, λ_{res} represents the resonant wavelength, while n_{eff}^{co} and n_{eff}^{cl} represent the effective refractive indices of the core and cladding modes, respectively. δn denotes the average effective RI change over the grating length, and γ denotes the waveguide dispersion factor, which is positive for the lower order mode and negative for the higher order mode. λ_D is the designed resonant wavelength of the LPFG, representing the wavelength at which the δn approaches 0, resulting in resonance. When the RI of the liquid changes, δn will change. Correspondingly, the resonant wavelength changes and the RI measurement can be realized.

3. RESULTS AND DISCUSSION

During the experimental procedure, a supercontinuum laser (SuperK Compact, NKT Photonics) served as the light source, while a spectrum analyzer (OSA, AQ6370D, Yokogawa) was utilized to monitor the transmission spectra. The transmission spectrum of the LPFG in air is shown in Fig. 3. The transmission spectrum has high insertion loss and multiple resonant dips because of the excessive RI modulation.

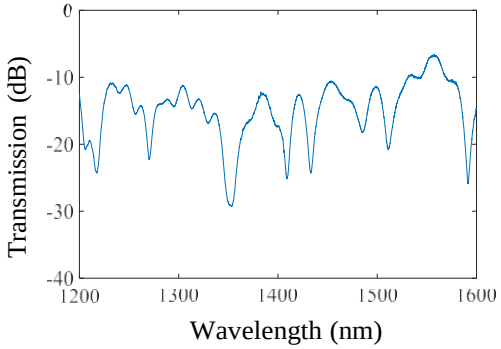

Fig. 3. The transmission spectrum of the LPFG in air (Λ=650 μm, N=7, L=60 μm, W=40 μm).

Figure 4 presents the measured transmission spectra of the gratings at periods Λ and numbers of microcavities N when the RI of the liquid was set to 1.335. According to the experimental results, the dips can be engineered to locate at different wavelengths by adjusting the grating period.

Through analysis of the aforementioned experimental results, the parameters for the gratings have been determined. The chosen values are as follows: the Λ is set to 650 μm, the N is selected as 7, the L is defined as 60 μm, and the W is established at 40 μm.

To demonstrate the excellent reproducibility of proposed method, five samples were prepared by using identical parameters. Each sample was filled with a glycerol aqueous solution with a RI of 1.335, and their corresponding transmission spectra are shown in Figure 5. It is noteworthy that the spectra remained largely unchanged, with the wavelength drift of the dip not exceeding 4 nm. This slight drift can be attributed to a small variation in the grating period caused by the stretching of the fiber during fixation. These results indicate that the fabrication process for the gratings have high level of reproducibility.

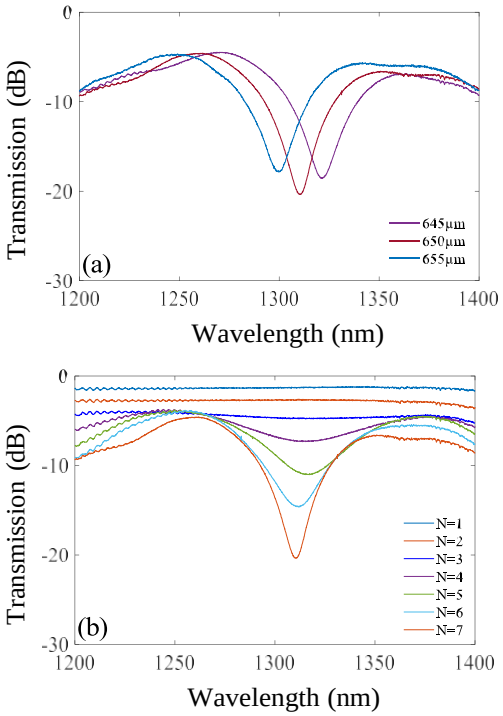

Fig. 4. Measured transmission spectrum for different grating parameters ((RI =1.335): (a) period Λ (N=7, L=60 μm, W=40 μm); (b) the number of microcavities N (Λ=650 μm, L=60 μm, W=40 μm).

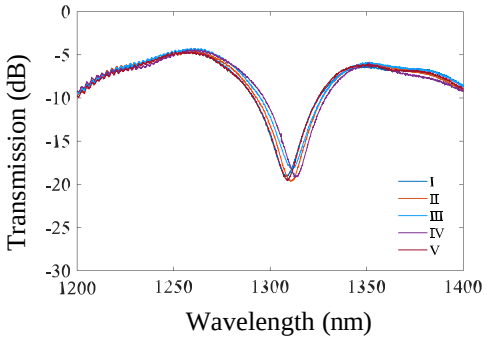

Fig. 5. The transmission spectra of 5 samples fabricated with the same parameters (Λ=650 μm, N=7, L=60 μm, W=40 μm, RI =1.335).

During the RI response testing, the LPFG was immersed in glycerol aqueous solutions with varying RIs, and the reflection spectra were recorded. After each measurement, the sensor was rinsed with alcohol and subsequent tests were conducted once the alcohol had evaporated. Figure 6 shows the evolution of the reflection spectra of the sensor at dip.

As the RI of the liquid increased within the range of 1.334 to 1.342, slight changes in the dip's amplitude were observed, accompanied by a drift in the dip's wavelength from 1323 nm to 1241 nm. Notably, the RI sensitivity attained a value of -11810 nm/RIU, with a high linear fit coefficient of 0.9988. These findings indicate a robust linear relationship between the resonance wavelength and the liquid's RI.

Moreover, the thermal-optical properties of liquids can be harnessed to render sensors responsive to temperature

changes. In this study, water is utilized as the temperature-sensitive medium. The encapsulated temperature sensor is depicted in Figure 7.

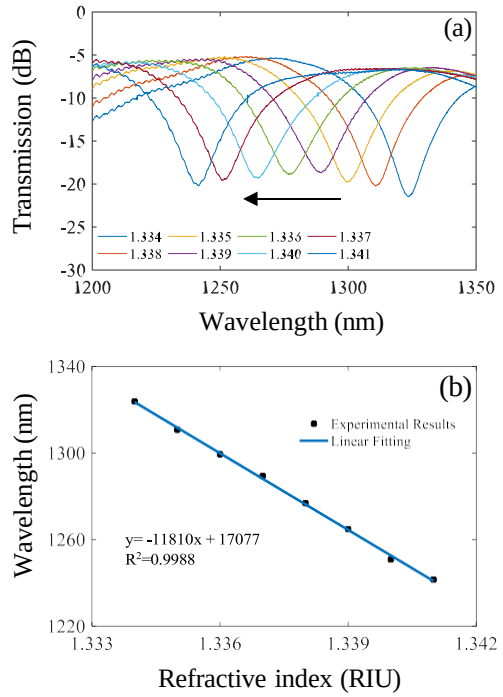

Fig. 6. (a) The reflection spectra of the LPFG. (b) The resonant wavelength shifts of the LPFG as a function of the liquid RI.

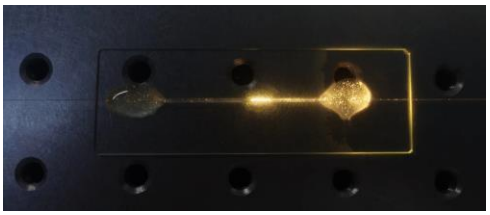

Fig. 6. The encapsulated temperature sensor.

In 1996, Richerzhagen and colleagues [10] constructed a Michelson interferometer. They placed a mirror within a thermally insulated water tank and employed external water circulation to induce heating, resulting in a temperature increase that generated a phase difference between the reference and measurement arms. Subsequently, they employed a detector to quantify alterations in interference fringes, enabling determination of the liquid's refractive index across varying temperatures. The measurement results indicate that the thermal-optical coefficient of water is nonlinear. Within the measurement range of 20 to 60 °C, the thermal-optical coefficient of water increases with rising temperature.

The temperature test results are illustrated in Figure 7 and 8. As the temperature increases, a redshift phenomenon is observed in the resonance peak. This is attributed to the decrease in refractive index of the water solution filled under the thermal-optical effect with increasing temperature, leading to an increase in the phase-matching wavelength. Conversely, when the temperature decreases, a blueshift phenomenon is observed in the resonance peak. This is because the refractive index of the water solution increases with decreasing temperature, resulting in a decrease in the resonance wavelength, manifested as a shift of the resonance peak towards shorter wavelengths in the spectrum. The nonlinear relationship between the resonance wavelength and temperature confirms the findings of [8], which indicate that the refractive index of water decreases and the thermal-optical coefficient increases with increasing temperature. The sensor exhibits its maximum temperature sensitivity at 45 ℃, reaching 1.76 nm/℃.

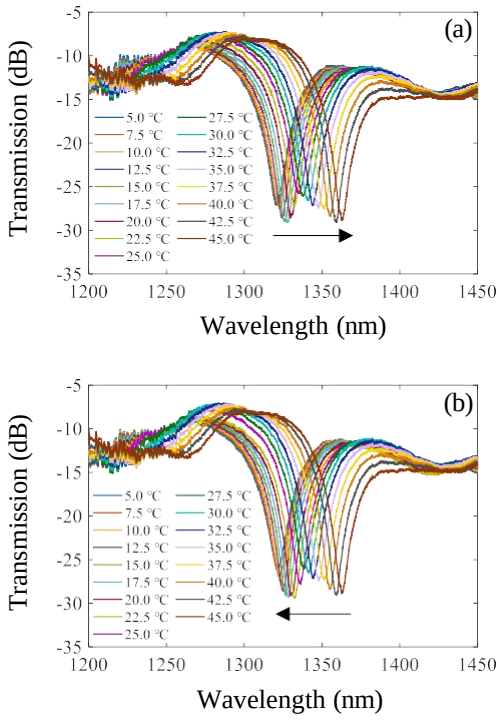

Fig. 7 The transmission spectra of the LPFG. (a) Heating test result. (b) Cooling test result.

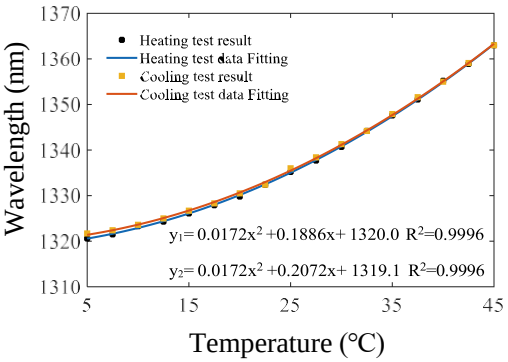

Fig. 8 The resonant wavelength shifts of the LPFG as a function of the temperature.

4. CONCLUSIONS

In conclusion, we have introduced a strong RI-modulated LPFG comprising seven microcavities, which was fabricated using femtosecond laser micromachining. By analyzing the wavelengths of the resonance dip, we are able to accurately determine the refractive index of the surrounding liquid. The achieved sensitivity for RI measurement within the range of 1.334 to 1.342 is an impressive -11810 nm/RIU. The sensor has giant potentials to be used for biochemical or biomedical industries.

FUNDING STATEMENT

This work was supported by the National Natural Science Foundation of China (62105077, 62175049, 62275061); Natural Science Foundation of Heilongjiang Province in China (YQ2021F002). Fundamental Research Funds for the Central Universities (3072022TS2501, 3072022CF2505).

REFERENCES

[1] J. N. Dash, R. Jha and R. Das, **Enlarge-tapered, micro-air channeled cavity for refractive index sensing in SMF**, J. Lightw. Technol., vol 37, 2019, pp. 5422-5427.

[2] T. Xi, D. H. Wang, C. Ma, and L. B. Yuan, **Sensing characteristics of collapsed long period fiber gratings in tri-hole fiber**, J. Lightw. Technol., vol 39, 2021, pp. 6008-6012.

[3] H. C. Deng, R. Wang, X. W. Jiang, C. X. Teng, R. H. Xu, Y. Cheng, W. T. Zhang, and L. B. Yuan, **A long period grating sensor based on helical capillary optical fiber**, J. Lightw. Technol., vol 39, 2021, pp. 4884-4891.

[4] Q. Zhou, W. G. Zhang, L. Chen, Z. Y. Bai, L. Y. Zhang, L. Wang, B. Wang, and T. Y. Yan, **Bending vector sensor based on a sector-shaped long-period grating**, IEEE Photon. Technol. Lett., vol 27, 2015, pp. 713-716.

[5] B. Li, X. Zhan, M. Tang, L. Gan, L. Shen, L. Huo, S. N. Fu, W. J. Tong and D. M. Liu, **Long-period fiber gratings inscribed in few-mode fibers for discriminative determination**, Opt. Express, vol 27, 2019, pp. 26307-26316.

[6] T. W. MacDougall, S. Pilevar, C. W. Haggans, and M. A. Jackson, **Generalized expression for the growth of long period gratings**, IEEE Photon. Technol. Lett., vol 10, 1998, pp. 1449-1451.

[7] Z. Y. Bai, W. G. Zhang, S. C. Gao, P. C. Geng, H. Zhang, Compact long period fiber grating based on periodic micro-core-offset, IEEE Photon. Technol. Lett. vol 25, 2013, pp. 2111-2114.

[8] B. Richerzhagen. **Interferometer for measuring the absolute refractive index of liquid water as a function of temperature at 1.064 μm**, Applied Optics, vol 35, 1996, pp. 1650-1653.

29: DUAL PARAMETRIC SENSORS BASED ON MULTI-CORE FIBER

Liu Yu, Chan Yang, Jing Yang, Jinhui Shi, Chunying Guan**

College of Physics and Optoelectronic Engineering, Harbin Engineering University, Harbin 150001, China

Optical Fibre Sensors 1, EM010, August 12, 2024, 1:30 PM - 3:00 PM

Abstract – Two optical fiber sensors based on a hole-assisted dual-core fiber (HADCF) and a hole-assisted three-core fiber (HATCF) have been proposed and experimentally demonstrated for dual-parameter measurements respectively. For the sensor based on HADCF, the dual-mode interferometer created uses the LP_{01} mode and LP_{11} mode in the suspended core, combined with a directional coupler formed by using the suspended core and the center core in a 16 mm long HADCF. For the sensor based on HATCF, two directional couplers are formed by using the suspended cores and the center core in an 8 mm long HATCF. The dual parameter measurement can be achieved through monitoring the interference dips and resonance dips. The proposed sensors have outstanding advantages such as simple structure, high integration and dual parameter measurement, making them potentially applications in the field of biological detection.

Keywords**:** dual parameter measurement; multi-core fiber; directional coupler

1. INTRODUCTION

Refractive index (RI) is a fundamental parameter reflecting the properties of liquids and can play an important role in the fields of biomedicine, environmental protection, and food safety [1], etc. The optical fiber RI sensors based on different structures and principles have been proposed, such as photonic crystal fibers (PCFs) [2], surface plasmon resonance (SPR) [3], interferometers [4], gratings [5-6] and couplers [7]. In 2016, a RI sensor based on Mach-Zehnder interferometer (MZI) was proposed [4]. Two tapers cascaded in a single mode fiber (SMF) generate the interference between core mode and cladding mode, and the RI sensitivity reaches 158.4 nm/RIU. This sensor is easy to fabricate, but the sensitivity is low and the tapering process will affect the mechanical strength of the sensor. An MZI RI sensor with the sensitivity of 260.8 nm/RIU based on PCF was proposed [2]. However, the high cost of PCF limits the application of such sensors. In 2017, an in-fiber RI sensor based on single eccentric hole-assisted dual-core fiber was proposed [7]. By filling different RI liquid into the air hole, the RI sensitivity of the resonance wavelength between the suspended core and the center core reaches 627.5 nm/RIU. This RI sensor has advantages of good mechanical strength and high sensitivity, however, the RI of the liquid is inevitably affected by temperature, which will lead to the temperature crosstalk.

To suppress temperature crosstalk, many dual-parameter sensors for RI and temperature measurement were proposed. Liu et al. demonstrated a miniature all-fiber sensor based on composite structure of Fabry-Perot interferometer (FPI) and fiber Bragg grating (FBG), the temperature and RI sensitivities of the FPI are -0.189 nm/°C and 1210.490 nm/RIU, respectively [5]. FBG is not sensitive to RI and its temperature sensitivity is 0.011 nm/°C. Chen et al. proposed an all-fiber sensor based on a microprobe with an ultra-short phase-shifted FBG and a common FBG to achieve dual-parameter measurement [6], but the two sensing elements based on different principles will complicate the preparation process and increase the size of the sensor.

In this work, we experimentally demonstrated two all-fiber sensors based on a hole-assisted dual-core fiber (HADCF) and a hole-assisted three-core fiber (HATCF) respectively for simultaneous measurement of RI and temperature. An MZI and a directional coupler fit together well in a single HADCF by splicing a segment of HADCF between two single mode fibers (SMFs) with an offset. Two directional couplers fit together in an 8 mm long HATCF. An air hole is opened by femtosecond laser to expose the suspended core to external environment. The proposed sensor has compact structure, high integration and high sensitivity, making it potentially applications for the field of biological detection.

1. METHODS AND PROCEDURES

The cross-section photographs of HADCF and HATCF are shown in Fig. 1. The HADCF comprises a silica cladding, a center core, a suspended core and a large air hole, where their diameters are 125 μm, 10 μm, 12 μm, and 35 μm, respectively. The air hole is located at the side of the center core. The suspended core used is suspended on the inner wall of the air hole, which is the closest location to the center core. The distance between the centers of the suspended core and the center core was 15 μm and the RI difference between the core and the cladding was 0.005. The HATCF is composed of a center core, two identical suspended cores, two air holes and a cladding. Two suspended cores are attached to the inner side of the air holes closest to the center core. The angle between the center core-suspended core 1 connecting line and the center core-suspended core 2 connecting line is about 110°. The diameters of the center core, suspended cores, air holes and cladding are 8.5, 11.2, 36.9, 125 μm, respectively. The distance between the edges of the suspended core and the center core is 4.8 μm. The RI difference between the center core and cladding is 0.005.

Due to the small distance between the center core and the suspended cores, the fiber can be used as a directional coupler at the phase-matching wavelength. According to the coupling-mode theory, the amplitudes of the optical field in the cores satisfy the following equation:

$$\frac{dA_m(z)}{dz} = -j\sum_{m\neq n} K_{mn} A_n(z) e^{i(\beta_m-\beta_n)z} \quad (1)$$

DOI: https://doi.org/10.34961/researchrepository-ul.29279153.v1

where A_m, A_n, β_m, β_n are the amplitudes and the propagation constants of the modes in each core respectively. The propagation constant β can be written as kn_{eff}. K_{mn} and K_{nm} are the coupling coefficients between the modes in two different cores.

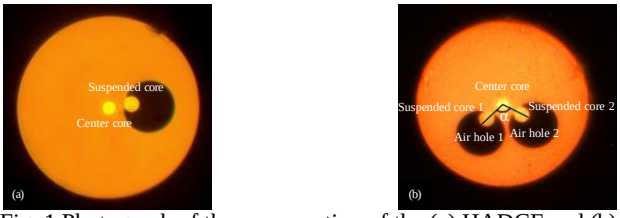

Fig. 1 Photograph of the cross section of the (a) HADCF and (b) HATCF.

According to the Eq. (1), resonance coupling can occur when the propagation constants of guide modes in two cores are equal or extremely close. To determine the resonance wavelength, the effective RIs of the low-order modes in the cores against the wavelength were calculated by using finite element method and are shown in Fig. 2. For the HADCF, as the wavelength increases, the effective RIs of the guide modes decrease. The effective RIs of suspended cores decrease faster due to the different dispersion characteristics between silica and air. The dispersion curves of the fundamental modes of the center core and the suspended core intersect at a wavelength of 1350 nm. The LP_{11} mode in the suspended core cuts off at ~1410 nm. For the HATCF, at 1550 nm, the effective RIs of fundamental modes in two cores are equal, which means resonance coupling can occur here. The LP_{11} mode in the suspended core cuts off at ~1410 nm.

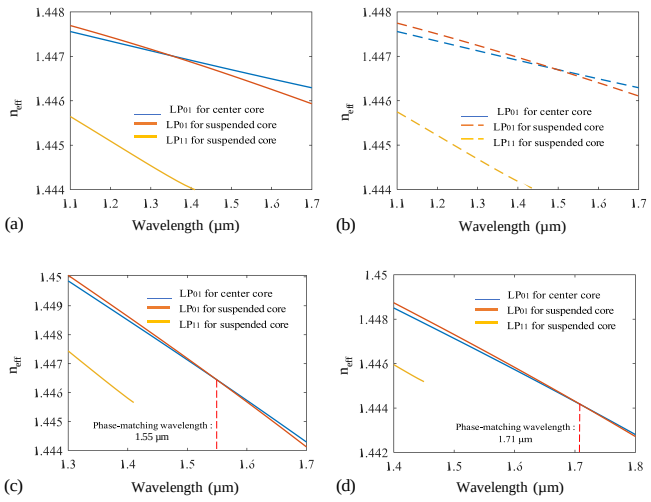

Fig. 2 (a) and (b) The calculated dispersion curves for the low-order modes of the (a) air-filled and (b) water-filled HADCF. (c) and (d) The calculated dispersion curves for the low-order modes of the (c) air-filled and (d) water-filled HATCF.

The structure of the proposed HADCF-based sensor is shown in Fig. 3. The sensor is composed of a section of the HADCF and two SMFs. Both ends of the suspended core are fused to the SMFs with an appropriate offset, as shown in Fig. 3(b). Two micropores near the offset fusing points were fabricated by using femtosecond laser micromachining, to build a microfluidic channel, as shown in Fig. 3(c). The beam from the input SMF passes into the HADCF through the first offset fusing point, allowing the LP_{01} and LP_{11} modes in the suspended core to be excited simultaneously. At the second offset fusing point, the two modes were combined and coupled into the output SMF to form an MZI. The intensity of the interference in the MZI can be expressed as:

$$I = I_1 + I_2 + 2\sqrt{I_1 I_2}\cos(\Delta\varphi) \quad (2)$$

where I_1 and I_2 are the intensities of the light in the LP_{01} and LP_{11} modes in the suspended core. The phase difference between the LP_{01} and LP_{11} modes can be represented by:

$$\varphi = (2\pi\Delta n_{eff} L)/\lambda \quad (3)$$

The free spectra range (FSR) can be expressed as shown below:

$$FSR = \lambda^2/(\Delta n_{eff} \cdot L) \quad (4)$$

where L is the length of the HADCF, and Δn_{eff} is the RI difference between the LP_{01} and LP_{11} modes.

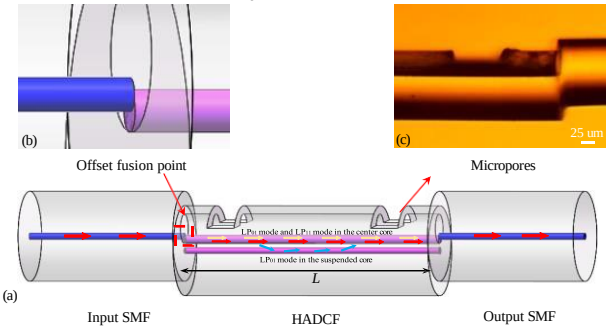

Fig. 3 (a) Schematic configuration of the sensor based on HADCF(b) Enlarged lateral view near the offset point. (c) Micrograph of a micropore fabricated by using a femtosecond laser.

To achieve better interference visibility, the LP_{01} and LP_{11} modes in the suspended core need to be excited equally. With the different offsets, the excitation efficiencies of the LP_{01} and LP_{11} modes in the suspended core are different. At 1210 nm, when the offset was 4.72 μm, the excitation coefficients of the LP_{01} and LP_{11} modes were equal which can obtain the maximum extinction ratio in the interference spectrum.

Meanwhile, due to the small distance between the center core and the suspended core, the HADCF can be regarded as a directional coupler. When the air hole is filled with liquid, the effective RI of the fundamental mode of the suspended core increases as the RI around the core becomes large. Meanwhile, the center core is not affected, so that the phase matching wavelength changes it redshifts. Figure 1(b) shows the calculated effective RIs for different low-order modes in the center and suspended cores of a water-filled HADCF.

The structure of the proposed HATCF-based sensor is shown in Fig. 4. The sensor is constructed by sandwiching a section of the HATCF between two SMFs. Both ends of the center core of the HATCF are spliced to the SMFs without the offset. The beam from input SMF is transmitted directly into the center core of the HATCF. An air hole (marked as hole 1) is opened by femtosecond laser micromachining as a liquid channel. Because of the small distance between the center core and the suspended cores, the HATCF can be seen as two directional couplers. Due to the same RIs and geometric parameters of the two suspended cores, the phase-matching wavelengths between center core and two suspended cores are the same. According to previous analysis, the effective RIs of center core and two suspended cores are equal at 1550 nm. Therefore, strong resonance coupling can

occur here. When the length of the HATCF is an odd multiple of the coupling length, the deepest resonance dip will be obtained.

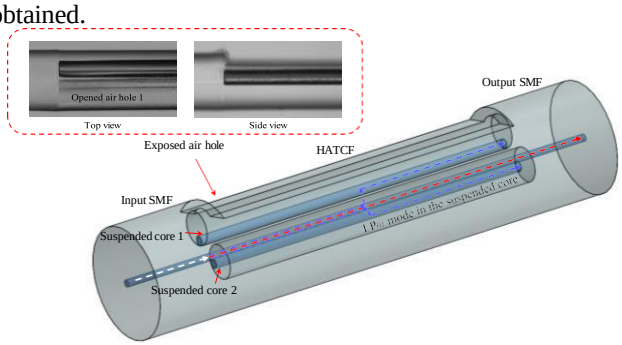

Fig. 4 Schematic configuration of the sensor based on HATCF

Figure 1(d) shows the calculated mode effective RIs of the center and suspended cores in water-filled HATCF. When liquid is filled into the open air hole 1, the RI around the suspended core 1 becomes large, which leads to the increase of mode effective RI in suspended core 1 in the open air hole 1. But the effective RI of the mode in center core is not obviously affected, so that the phase-matching wavelength between center core and the suspended core 1 redshifts to 1710 nm. Meanwhile, the suspended core 2 in the whole air hole 2 is not affected, so that the phase-matching wavelength between the suspended core 2 and the center core is still at 1550 nm. Therefore, the resonance coupling will occur between the center core and the two suspended cores at different wavelength. Hence, two dips will be generated in the transmission spectrum. The resonance dip generated by center core and suspended core 1 in the open hole 1 is sensitive to liquid RI and temperature, while the resonance dip generated by center core and suspended core 2 in the whole hole 2 is only sensitive to temperature. Hence, the simultaneous measurement of temperature and liquid RI can be realized by monitoring the wavelength shifts of the two dips. The demodulation of temperature and RI can be achieved by the coefficient matrix.

2. RESULTS AND DISCUSSION

The sensor based on HADCF was used to detect the characteristics of the salinity and the temperature.

Figures 5(a) and 5(b) show the transmission spectra of the sensor before and after filling with liquid. Their spatial frequency spectra were shown in Figs. 5(c) and 5(d), respectively. Before filling with liquid, the multiple interference dips caused by LP_{01} and LP_{11} modes in the suspended core were observed in the wavelength range of 1100 -1300 nm. In the wavelength range of 1300 - 1400 nm, an obvious resonance coupling dip is seen, overlapping with

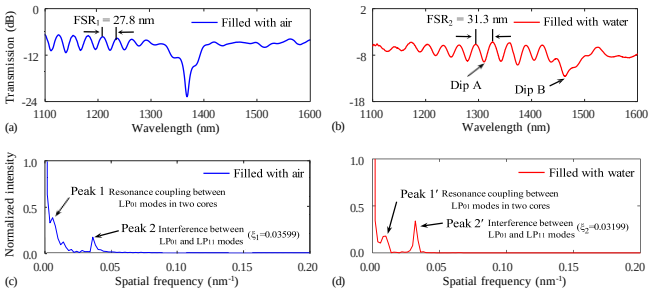

Fig. 5 Transmission spectra and spatial frequency spectra of sample. (a), (c) without liquid and (b), (d) filled with liquid.

the interference spectrum. Interference dips disappear when the LP_{11} mode in the suspended core cuts off beyond a wavelength of ~1410 nm. The Peak 1 in Fig. 5(c) can be attributed to the resonance coupling between LP_{01} modes in the center and suspended core. While the Peak 2 can be attributed to the interference between LP_{01} and LP_{11} modes in the suspended core, as the reciprocal of the spatial frequency (ξ_1) of the Peak 2 is equal to the FSR of the transmission spectrum shown in Fig. 5(a).

An interference dip (denoted as Dip A) and the resonance coupling dip (denoted as Dip B) were selected to measure the performance of the sensor. The responses of the sensor to salinity at the temperature of 25 ℃ are shown in Fig. 6, where the salinity range is from 0 to 80 ‰ with a step of 10 ‰. The wavelength of the interference dip was seen to be linearly red-shifted, with the increase of the salinity, while the coupling resonance dip wavelength also shifts to the long wavelength region. The coupling resonance will weaken, since the coupling efficiency between the center core and the suspended core decreases with the increase of the external RI. The sensitivities to salinity of Dip A and Dip B were 135.7 pm/‰ and 190.7 pm/‰, respectively. In addition, the temperature responses were also measured for different salinities, and the result are shown in Fig. 7. The sensor was placed in a temperature and humidity chamber, and the temperature was increased from 0 to 35 ℃ with a step of 5 ℃. When the salinity of the NaCl solution is 80 ‰, the temperature sensitivities of Dip A and Dip B were -74.8 pm/℃ and -188.2 pm/℃, respectively. The measured results verify the temperature sensitivities are almost identical for different salinities.

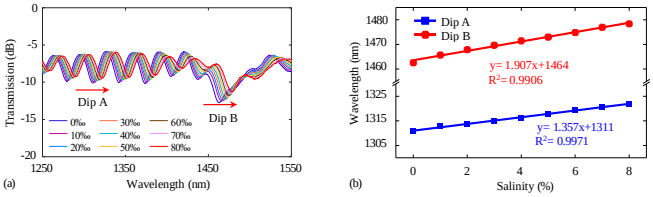

Fig. 6 (a) Transmission spectra of the sensor for different values of salinity. (b) The wavelengths of Dip A and the Dip B as a function of salinity.

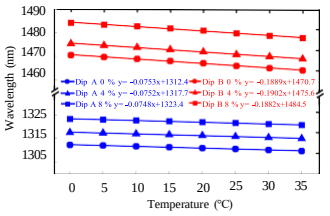

Fig. 7 (a) The wavelengths of Dip A and Dip B as a function of temperature for different salinities.

Based on the above measurement, a sensitivity matrix could be established as follows:

$$\begin{pmatrix} \Delta\lambda_A \\ \Delta\lambda_B \end{pmatrix} = \begin{pmatrix} 135.7\ \text{pm/‰} & -74.8\ \text{pm/℃} \\ 190.7\ \text{pm/‰} & -188.2\ \text{pm/℃} \end{pmatrix} \times \begin{pmatrix} \Delta S \\ \Delta T \end{pmatrix} \quad (5)$$

The sensor based on HATCF was used to detect the characteristics of the RI and the temperature. Before the sensor was submerged into deionized water, there is only one resonance dip at the wavelength of ~1540 nm because the phase-matching wavelengths between center core and two suspended cores are the same. After the sensor was submerged into the deionized water, the initial resonance dip

splits into two resonance dips due to the red-shift of the phase-matching wavelength between the center core and the suspended core 1. The two resonance dips are denoted as dip 1 and dip 2, respectively. Dip 2 is generated by the coupling between center core and suspended core 2 with closed air hole 2, and dip 1 is generated by the coupling between center core and suspended core 1, as shown in Fig. 8 (a).

In the temperature of 25 °C, 35 °C, 45 °C, the RI response of the sensor was measured in glycerinum solutions with the RI range from 1.333 to 1.388 with a step of 0.005. During the measuring process, the sample slot was placed in a temperature chamber to ensure a constant temperature. The transmission spectra for different RIs are shown in Fig. 8 (b). As the RI increases, the resonance dip 1 has a redshift. There is a good linear relationship between the wavelength of dip 1 and the RI. The sensitivity reaches 1369 nm/RIU in the RI range of 1.333-1.388 in 25 °C, as shown in Fig. 8 (c). With the increase of RI around suspended core 1, the effective RI of the fundamental mode in suspended core 1 increases, while that in center core is not changed. Therefore, the phase-matching wavelength between center core and suspended core 1 shows a red-shift. In contrast, the suspended core 2 is isolated from the external environment. The wavelength of resonance dip 2 hardly changes and just fluctuates in the range of 0.05 nm, as shown in Fig. 8 (d), which can be attributed to the temperature fluctuations in the temperature chamber.

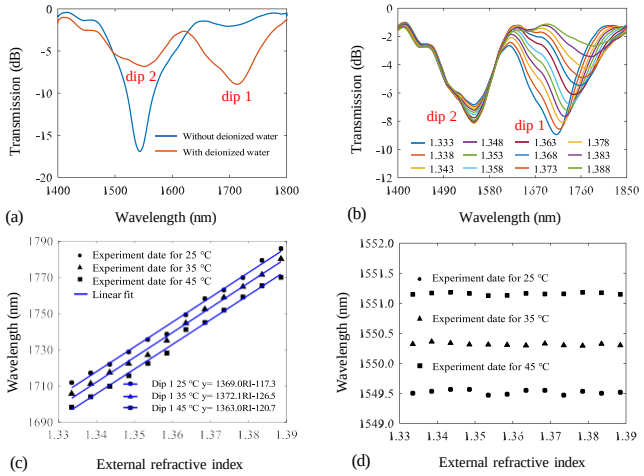

Fig. 8 (a) The transmission spectra of the sensor before and after being submerged into deionized water. (b) The transmission spectrum evolution for different RIs. The RI sensitivities of (c) dip 1 and (d) dip 2 in different temperature.

The temperature characteristics of the sensor were also measured. The sensor was placed in a water bath with deionized water, and the deionized water was heated from 25 to 70 °C and then cooled to 25 °C with a step of 5 °C. With the increase of temperature, the resonance dip 1 has a redshift and the sensitivity is 83.48 pm/°C, while the resonance dip 2 shows a blueshifts with a sensitivity of -500.7 pm/°C.

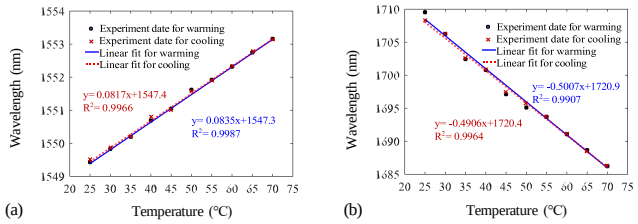

Fig. 9 The temperature responses of (b) dip 1 and (c) dip 2.

Based on the above measurement, a sensitivity matrix could be established as follows:

$$\begin{bmatrix} \Delta\lambda_1 \\ \Delta\lambda_2 \end{bmatrix} = \begin{bmatrix} 1369\text{nm/RIU} & -500.7\text{pm}/^{\circ}\text{C} \\ 0 & 83.48\text{pm}/^{\circ}\text{C} \end{bmatrix} \begin{bmatrix} \Delta n \\ \Delta T \end{bmatrix} \quad (7)$$

3. CONCLUSIONS

In conclusion, we have introduced two dual-parameter optical fiber sensors based on HADCF and HATCF respectively. The measured salinity and temperature sensitivities are 190.7 pm/‰ and -188.2 pm/°C for the sensor based on HADCF. The measured RI and temperature sensitivities are 1369 nm/RIU in the range of 1.333-1.388 and 83.48 pm/°C in the range of 25-70 °C for the sensor based on HATCF. Because of good performance, simple structure and high level of integration, the proposed sensors have great application potential in the field of biological detection.

FUNDING STATEMENT

This work was supported by the National Natural Science Foundation of China (62105077, 62175049, 62275061); Natural Science Foundation of Heilongjiang Province in China (YQ2021F002). Fundamental Research Funds for the Central Universities (3072022TS2501, 3072022CF2505).

REFERENCES

[1] P. R. Cooper, **Refractive-index measurements of liquids used in conjunction with optical fibers**, Appl. Opt. vol 22, 1983, pp. 3070-3074.

[2] Q. Wang, L. Kong, Y. Dang, F. Xia, Y. Zhang, Y. Zhao, H. Hu, and J. Li, **High sensitivity refractive index sensor based on splicing points tapered SMF-PCF-SMF structure Mach-Zehnder mode interferometer**, Sens. Actuators B: Chem. vol 225, 2016, pp. 213-220.

[3] C. Teng, P. Shao, R. Min, H. Deng, M. Chen, S. Deng, X. Hu, C. Marques, and L. Yuan, **Simultaneous measurement of refractive index and temperature based on a side-polish and V-groove plastic optical fiber SPR sensor**, Opt. Lett. vol 48, 2023, pp. 235-238.

[4] Q. Wang, W. Wei, M. Guo, and Y. Zhao, **Optimization of cascaded fiber tapered Mach-Zehnder interferometer and refractive index sensing technology**, Sens. Actuators B: Chem. vol 222, 2016, pp. 159-165.

[5] Y. G. Liu, X. Liu, T. Zhang, and W. Zhang, **Integrated FPI-FBG composite all-fiber sensor for simultaneous measurement of liquid refractive index and temperature**, Opt. Laser Technol. vol 111, 2018, pp. 167-171.

[6] M. Q. Chen, T. Y. He, Y. Zhao, and G. Yang, **Ultra-short phase-shifted fiber Bragg grating in a microprobe for refractive index sensor with temperature compensation**, Opt. Laser Technol. vol 157, 2023, pp. 108672-108678.

[7] J. Yang, C. Guan, P. Tian, T. Yuan, Z. Zhu, P. Li, J. Shi, J. Yang, and L. Yuan, **In-fiber refractive index sensor based on single eccentric hole-assisted dual-core fiber**, Opt. Lett. vol 42, 2017, pp. 4470-4473.

30: COVALENT/NON-COVALENT RECOGNITION STRATEGIES FOR VISUALIZED SENSING OF TRACE ORGANIC AMINES

Yuan Liu[*]

Xinjiang Technical Institute of Physics and Chemistry, Chinese Academy of Sciences, Urumqi, China,
Spectroscopy, EM010, August 12, 2024, 11:30 AM - 12:40 PM

Abstract Precise, timely and visualized recognition of trace organic amines is of great significance for safeguarding human health, ecological environment, public security, etc., especially crucial for adopting appropriate disposition measures. For this purpose, great efforts have been made to finely design the optical probe structure which is the core of the specific recognition. Here, we proposed the recognition strategies based on either covalent nor non-covalent interactions to achieve the detection towards the targets with primary amine, tryptamine and ethylenediamine [1-2]. These sensing strategies exhibited ppb/nM level sensitivity, specific recognition without disturbance to the potential interferents, as well as rapid optical response within 1 s. Furthermore, by integrating the optical probe with the portable sensing chip, the sensing performances were verified to be capable for detecting the trace analytes in the complicated practical scenarios, providing a valuable reference for designing optical probe and driving the development of the visualized sensing field.

***Keywords*:** covalent reaction; hydrogen bonding interaction; optical sensing; organic amines; trace detection

REFERENCES

[1] H. Zhao, Y. Liu*, G. S. Li, D. Lei, Y. W. Du, Y. D. Li, H. Tang*, X. C. Dou*, **Electrophilicity Modulation for Sub-ppm Visualization and Discrimination of EDA**, Adv. Sci., 11, 2024, 2400361.

[2] L. Pang[#], T. S. Zhang[#], Y. Liu*, D. Z. Li, J. G. Li, M. Guan*, X. C. Dou*, **Dual Noncovalent Interaction Facilitated Highly Sensitive and Specific Colorimetric–fluorescent Sensing for Tryptamines**, Sens. Actuat. B, 391, 2023, 134061.

DOI: https://doi.org/10.34961/researchrepository-ul.29279561.v1

31: VERTICAL CAVITY SURFACE EMITTING LASERS WITH SIO_2/ZNS DIELECTRIC DISTRIBUTED BRAGG REFLECTOR

Xiaodong Yan[a],Bo Wu[a], Baolu Guan[a], Weiling Guo[a],Yiyang Xie[a]**

[a].Key Laboratory of Optoelectronics Technology, Ministry of Education, Beijing University of Technology ,Beijing, 100124, China,

Photonic Sensors, EM010, August 12, 2024, 4:50 PM - 5:30 PM

Abstract--- Vertical-cavity surface-emitting lasers are wi dely used in optical communication, 3D sensing and ot her fields because of their good beam quality and easy coupling. Distributed Bragg mirror is an important com ponent of laser. We use SiO_2/ZnS alternating growth to prepare DBR with a reflection bandwidth of 250nm. The threshold current of the VCSEL is 0.5mA, and the maximum optical power is 0.88mW at 4.7mA.

Keyword： VCSEL; DBR; SiO2/ZnS；

1. INTRODUCTION

Distributed Bragg Reflectors (DBRs) have proven over the years to be an integral part of major optoelectronic devices, such as vertical-cavity surface emitting lasers (VCSEL's) [1], resonant-cavity light emitting diodes, and eventually polaritonic devices. DBR is essentially a multilayered stack of high and low refractive index materials, with each layer having a quarter-wavelength（$\lambda/4n$）thickness, where λ is the wavelength of maximum reflectivity and n is the layer's refractive index. The active region of the optoelectronic device is placed in a Fabry-Perot optical resonator composed of DBR at both ends to achieve wavelength selection [1]. The dielectric distributed Bragg (DDBR) reflector has the advantages of wide high reflectance region, high reflectance in less layers, narrow spontaneous emission spectrum, simple fabrication and low cost, so it is suitable for the fabrication of top mirrors of optical resonators [2]. Unlike the widely used direct DBR deposition by MOCVD or PECVD, Magnetron sputtering can be direct preparation of DDBR at lower temperatures. Magnetron sputtering can fabricate dielectric Distributed Bragg Reflector on the device, like vertical cavity surface emitting lasers, resonant cavity light-emitting diodes and others.

Vertical-Cavity Surface-Emitting Lasers (VCSEL) is a high-performance semiconductor laser. VCSEL has been used in many fields such as: optical communication, 3D sensing and laser pump because of its low threshold, single longitudinal mode work, high beam quality [3-9].

In this paper, we report a new method for the direct growth of SiO_2/ZnS DBR on quartz plate by magnetron sputtering. This method can direct growth dielectric DBR with a low temperature (25℃）. On this basis, the reflectivity of the as-grown dielectric DBR is 99% with the reflection bandwidth is 250nm. Then, we used the as-grown dielectric DBR instead of top DBR to fabricate VCSEL. The maximum output optical power of the VCSEL can reach 0.884mW, the side mode rejection ratio can reach 25dB, and the maximum far-field divergence Angle of the laser is 25deg.

2. EXPERIMENT AND RESULTS

A . fabrication of SiO2/ZnS DBR

The production of cavity. The SiO_2 and ZnS films were grown using magnetron sputtering, and then the refractive index of refraction of SiO_2 and ZnS is 1.45 and 2.229 by measured using an ellipsometry. According to equation (1), to calculate the thickness of the SiO_2 and Si3N4.

$$\cdot = /4 \quad (1)$$

d is the thickness of the DBR's layer, n is the refractive index of material, is the center wavelength.

The reflectivity of 4, 6, 8 pairs to dielectric film is tested with spectrophotometer. As Fig1 shown, The reflectance of SiO_2/ZnS DBR grown on quartz substrate is 96.9%, 99.7%, 99.9%. Fig1 show the reflectivity of the central wavelength is 850nm. At 8 pairs, the reflectivity is 99.9% and the reflection bandwidth is 250nm.

DOI: https://doi.org/10.34961/researchrepository-ul.29279612.v1

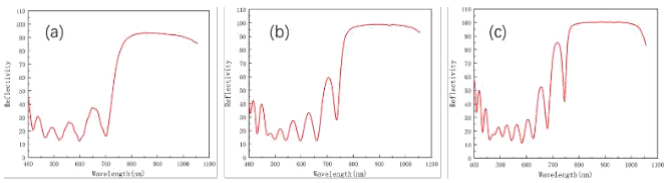

Figure1. The reflectivity of 4,6,8 pairs SiO_2/ZnS DBR on quartz substrate

Then, the SiO_2/ZnS DBR is deposited on the GaAs substrate by magnetron sputtering at the temperature of 25℃. As the Fig2 shown, the reflectivity of 8 pairs-DBR is 99.9% at the center wavelength is 850nm. The reflection bandwidth of it is 230nm.

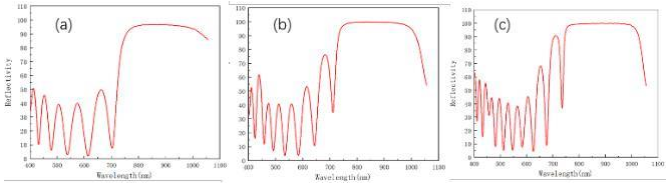

Figure2. The reflectivity of 4,6,8 pairs SiO_2/ZnS DBR on GaAs substrate

B. The preparation of VCSEL

As shown in Figure 3, the DDBR-VCSEL fabricated in this experiment are roughly the same as the traditional oxidized VCSEL.

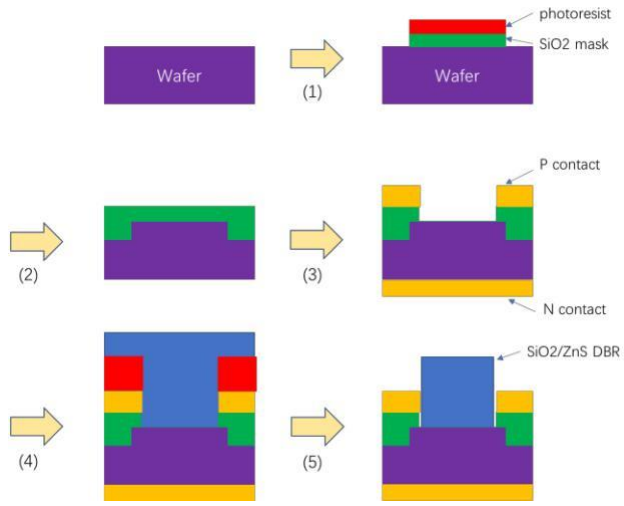

Figure3. Fabricated process of VCSEL with SiO_2/ZnS DBR.

The oxide layer is etcher by inductively plasma etching (ICP) with SiO_2 as mask until exposed. Then the oxide layer is selectively oxidized by wet oxidation in the oxidation furnace. Using PECVD to deposit silicon oxide as a passivation layer to prevent current leakage. Use hydrofluoric acid to etch silicon oxide to form an electrode window. And metal electrode is sputtered. The SiO_2/ZnS dielectric film was growth by magnetron sputtering after lithography at 25℃. Because of the dielectric is growing at low temperatures, the photoresist does not deteriorate. The excess was stripped by ultrasound.

C. Experimental results and discussions

In this experiment, a VCSEL with SiO_2/ZnS DBR was fabricated, tested and characterized. The figure4 shows the oxidation aperture under a microscope. The diameter of the oxidation limitation hole is 6 microns and 7 microns.

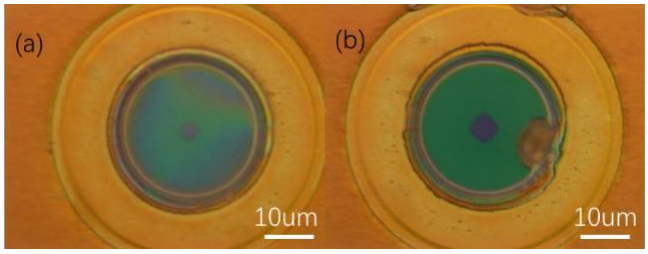

Figure4. The top view of the VCSEL with different oxidation aperture. (a)6um (b)7um

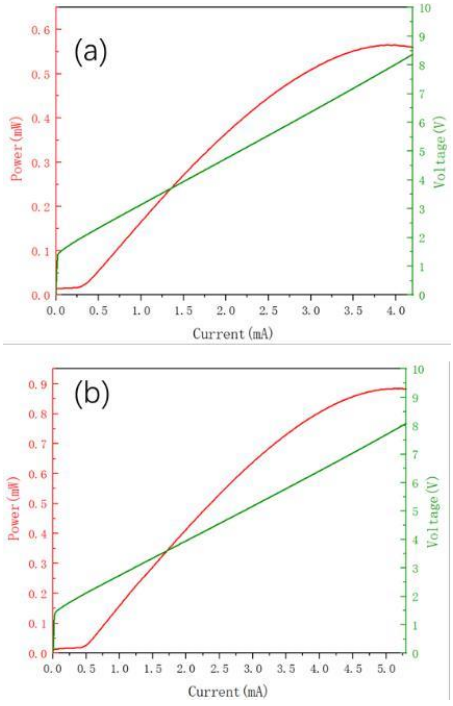

Figure 5. The P-I-V characteristic curve of VCSEL with different oxidation aperture. (a)6um (b)7um

As shown in figure5, the light power(P)-current(C)-voltage(V) curve showed the maximum optical power was

0.55mW when the current was 3.8mA. And the threshold current was 0.3mA. When the oxidation aperture is 7um the maximum optical power is 0.88mW at 4.7 mA injection current, and the threshold current is 0.5mA.

Figure6 shows the measured spectral curve. It was tested at room temperature with continuous power supply injection. Under a 1mA current, the center wavelength is 846nm and mode suppression ratio is more than 25dB. With the current changes to 2mA, the center wavelength is redshifted to 846nm.

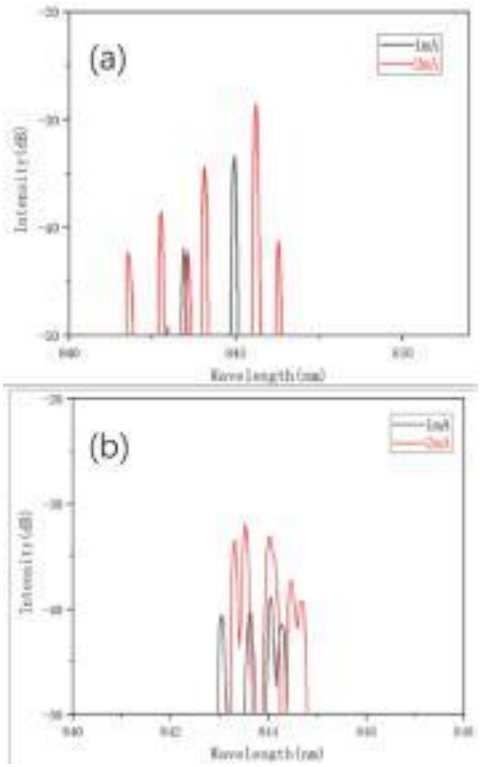

Figure 6.the spectral curve of VCSEL with different oxidation aperture. (a)6um (b)7um

As shown in Figure 7, the plane far-field beam pattern at different currents is measured by a CCD camera and a monitor. The distance between the sensor head and the device being tested is around 2.2cm. By measuring the divergence angle of the far field will increase with the increase of the current. As shown in Figure7(a)-(b), as the current increases from 1mA to 3mA, the divergence Angle of the spot increases from 19.3 deg to 23.8 deg. As shown in Figure7(c)-(d), as the current increases from 1mA to 4mA, the divergence Angle of the spot increases from 17.2 deg to 24.5 deg.

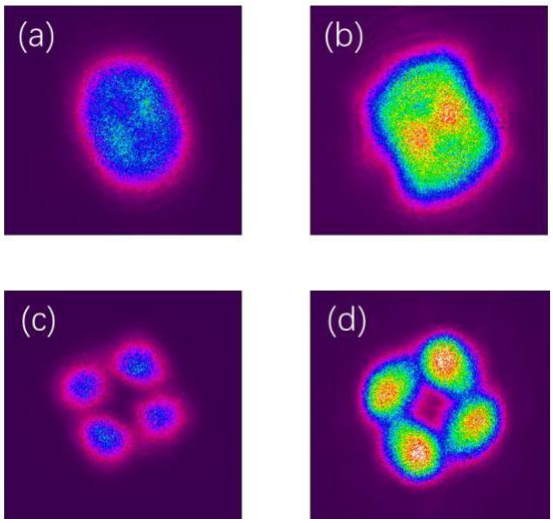

Figure7. The far-field spot of VCSEL under different currents. (a)-(b)6um oxidation aperture. (c)-(d)7um oxidation aperture.

As can be seen, a shallow depression appears in the peak of the far-field pattern. A doughnut-like pattern when the bias current is over 1.5mA, as illustrated in Fig. 7.

3. CONCLUSIONS

In summary, the DBR was fabricated using SiO_2 and ZnS, and the reflectivity reached 99.9% at 8 pairs, which met the requirements of VCSEL for DBR. The VCSEL was fabricated using the dielectric film as the top DBR. The maximum output optical power of the VCSEL can reach 0.88mW, the side mode rejection ratio can reach 25dB, and the maximum far-field divergence Angle of the laser is 25deg. While the properties of the single-mode emission of the fabricated device are not ideal, the structure has great potential to find the optimal parameters through later software simulations.

ACKNOWLEDGMENTS

We acknowledge financial support from the National Natural Science Foundation of China and Beijing Nova Program. The authors acknowledge the Nanofabrication Laboratory at National Centre for Nanoscience and Technology for sample fabrication.

FUNDING STATEMENT

National Natural Science Foundation of China(62074011, 62134008).

Beijing Nova Program (No. Z201100006820096).

REFERENCES

[1] Zhang J, Zhang X, Zhu H, et al. High-temperature operat ing 8946nmVCSELs with extremely low threshold for Cs -based chip scale atomic clocks[J]. Optics Express, 2015, 23(11):14763.

[2] Lee, YH, [Lee. Vertical-Cavity Surface-Emitting Lasers [J]. Proceedings of SPIE - The International Society for Optical Engineering, 1997,101(10):2229-2233.

[3] Huang, Yetian; Chen, Haoshuo; Fontaine, Nicolas K. Opti cal Broadcasting Employing Incoherent and Low-Coheren ce Spatial Modes for Bi-Directional Optical Wireless Co mmunications. JOURNAL OF LIGHTWAVE TECHNOL OGY, 2021,39:833-838.

[4] Mena P V, Morikuni J J, Kang S M, et al. A Comprehe nsive CircuitLevel Model of Vertical-Cavity Surface-Emitt ing Lasers [J]. Journal of Lightwave Technology, 2000,1 7(12):2612-2632.

[5] Zhu, Paikun; Yoshida, Yuki; Kanno, Atsushi. High-fidelity indoor MIMO radio access for 5G and beyond based o n legacy multimode fiber and real-time analog-to-digital-c ompression. OPTICS EXPRESS, 2021,29:1945-1955.

[6] Zhi, Ting; Tao, Tao; Liu, Bin.(2021) High Performance Wide Angle DBR Design for Optoelectronic Devices. IE EE PHOTONICS JOURNAL. 2021,13,

[7] Serkland D K, Geib K M . VCSELs for atomic clocks [C], 2006 Vertical-cavity Surface-emitting Lasers X. Inter national Society for Optics and Photonics.

[8] J.-L. Yen, K.-L. Chi, J.-W. Jiang, Y.-J. Yang, and J.-W. Shi, “Single-mode vertical-cavity surface-emitting lasers a rray with Zn-diffusion aperture for high-power, single-spo t, and narrow divergence angle performance,” IEEE J. Q uantum Electron. 2014,50, 787–794.

[9] J.-W. Shi, J.-I. Guo, M. Kagami, P. Suni, and O. Zieman n, “Photonic technologies for autonomous cars: feature in troduction,” Opt. Express,2019,27:7627–7628.

33: HIGH-PERFORMANCE VISUALIZED SENSING MATERIALS: FROM SINGLE MODE TO TRIPE MODE

*Baiyi Zu**

Center of Materials Science and Optoelectronics Engineering, University of Chinese Academy of Sciences, Beijing, China,

Biomedical Sensors 4, EM009, August 13, 2024, 2:50 PM - 4:00 PM

Abstract − The design and development of visualized sensing materials with the highly sensitive, anti-interferent and on-site detection capabilities is of great significance to chemical sensing in complex practical scenarios. We have recently proposed serial novel strategies for the construction of visualized sensing materials from single mode to triple mode: 1) A highly sensitive (nanogram level), rapid (in seconds) and facile colorimetric probe was designed by the effective electrostatic interaction. 2) A colorimetric and fluorescent dual mode organic small-molecule probe was designed by finely modulating the electron-donating capability of thiol to obtain the excellent sensing performances; A chromone-based ligands grafted QDs system was designed and showed complete EET from QDs to the ligands drived specifically by trace analyte with fluorescent and colorimetric dual-mode responses. 3) An ultra-accurate tri-mode visualization platform through colorimetric, fluorescent and UCL visualization analysis was constructed based on an elaborated designed organic small-molecule probe coupled with picked UCNPs through inner filter effect (IFE).

Keywords**:** visualized sensing materials; colorimetric sensing; colorimetric-fluorescent sensing; colorimetric, fluorescent and UCL sensing

1. INTRODUCTION

Visualization detection technique, which has been employed as a preferable strategy for environmental pollutant or illegal narcotics detection due to the advantages of high sensitivity, fast response, strong specificity, and visualization of the detection signal [1]. To date, various visualization materials have been explored for high-performance sensing, such as organic small-molecule probes [2], metal-organic frameworks (MOFs) [3], and quantum dots (QDs) [4]. Practically, the visualized detection signal is inevitably disturbed by the structural analogues, colorful substances, fluorescent interferents and the low signal-to-background. In this paper, to solve this problem, a series of strategies was designed to construct a selectively colorimetric probe, a dual-mode visualized sensing materials with the independent colorimetric and fluorescent signals, and an ultra-accurate tri-mode visualization platform through colorimetric, fluorescent and upconversion luminescence (UCL) visualization analysis, respectively.

2. RESULTS AND DISCUSSION

2.1. Colorimetric single mode sensing material

From the aspect of the molecular structural design of organic small-molecule probe, based on the electrostatic interaction between the lone pair electrons of N of urotropin and the diazonium compound, a serial of diazonium salts were designed and examined due to their electrophilic character (Figure 1), showing that fast blue B with strong electropositivity stood out from other diazonium salts to interact with urotropin and showed a distinct colorimetric change. This probe exhibits high sensitivity towards urotropin solution (9 μM) as well as great anti-interference capability towards potential co-existing substances under a mild condition [5].

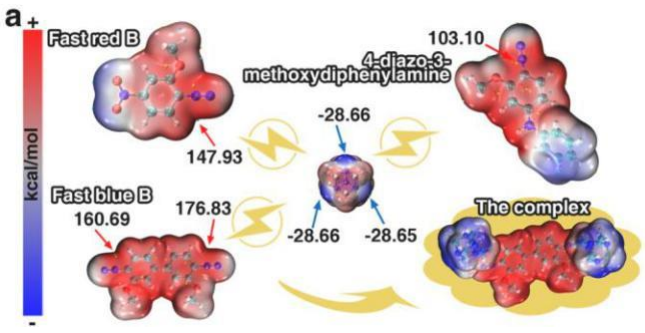

Figure 1. The design strategy for colorimetric single mode probe by the electrostatic interaction.

2.2. Colorimetric and Fluorescent dual mode sensing materials

From the aspect of the fluorescence generation mechanism, we targeted a fundamental descriptor—electron transferring capability to investigate how electron tuning acts on the entire molecule behavior to achieve an improved fluorescence emission in responding to ethylenediamine (EDA), a molecule model was constructed comprising a thiol-substituted heteroaromatic compound (Figure 2) [6]. By thoroughly analyzing the individual influence as well as the interplay between multi-descriptor, the finely modulated electron-donating capability of thiol was proven as the prominent descriptor corelating to the fluorescence intensity. Consequently, -SH in mercaptosuccinic acid (MSA) with remarkable electron-donating capability was verified to give rise to an intense fluorescence. Experimental demonstration empowered a quantitative detection of EDA, accompanied by a dual-response composed of a color change and a turn-on green fluorescence. The excellent sensing performances including ultrahigh sensitivity, outstanding selectivity and

DOI: https://doi.org/10.34961/researchrepository-ul.29279714.v1

anti-interference capability facilitated a desirable analysis of EDA in industrial wastewater.

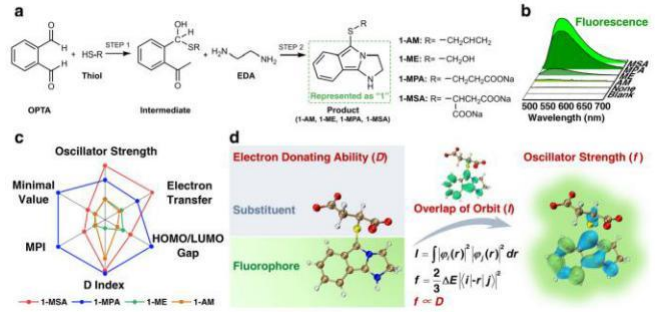

Figure 2. a) The proposed reaction mechanism of OPTA/thiol recognizing EDA and the structures for a set of thiols used in this work. b) The fluorescence spectra for the product from the reaction between OPTA and EDA in the presence of different thiols. c) The radar map for the main physical quantities of model molecules with different substituents. d) Schematic correlation between electron-donating capability, overlap of orbit and oscillator strength.

With superior optical features and unrivaled photostability luminescence, functionalized QDs have been widely utilized for sensing applications based on Förster resonance energy transfer (FRET), photoinduced electron transfer (PET), inner filter effect (IFE), or a combination with each other. In this work, the chromone-based ligand grafted QDs (QDs-Chromone) were initiated to realize the electronic energy transfer (EET) driven specifically by EDA in the absence of spectral overlap (Figure 3)[7]. The fluorescent and colorimetric dual-mode responses (from red to blue and from colorless to yellow, respectively) resulting from the expanded conjugated ligands reinforced the analytical selectivity, endowing an ultrasensitive (0.11 and 2.94 μM in fluorescent and colorimetric mode) and specific response to EDA compared with the structural analogues and other common interferents. In addition, a QDs-Chromone-based sensing chip was constructed to achieve the ultrasensitive recognition of EDA vapor with a naked-eye observed response at a concentration as low as 10 ppm, as well as a robust anti-interfering ability in complicated scenarios monitoring.

Figure 3. Schematic illustration of design strategy for colorimetric and fluorescent dual mode sensing materials by EET mechanism.

2.3. Colorimetric, fluorescent and UCL triple mode sensing materials

In order to avoid the interference of the colorful and fluorescent substances on the detection performance in real environment, a self-accelerating naphthalimide-based probe with fast response and high sensitivity toward hydrogen peroxide is designed. By coupling with the specially selected upconversion nanoparticles (UCNPs), an ultra-accurate colorimetric-fluorescent-upconversion luminescence (UCL) tri-mode platform is constructed (Figure 4) [8]. Owing to the promoted reaction process, this platform demonstrates rapid response (< 1 s), an ultra-low detection limit (4.34 nM), and superb anti-interferent ability even in presence of > 21 types of oxidants, explosives, metallic salts, daily compounds, colorful or fluorescent substances. In addition, the effectiveness of this design is further verified by a sponge-based sensing chip loaded with the UCNPs/probe in recognizing trace hydrogen peroxide vapor from interferents with the three characteristic colors existing simultaneously.

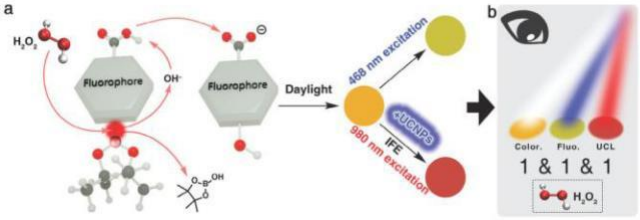

Figure 4. Schematic illustration of design strategy for the B-R-COOH probe to detect H_2O_2 through colorimetric and fluorescent channels, as well as the UCL channel with the aid of UCNPs.

3. CONCLUSIONS

In summary, we have demonstrated the precise design and modulation of the visualized sensing materials is of great significance to boost their detection performance with desirable colorimetric/fluorescent/UCL signals. We expect that the proposed design strategies of the visualized sensing materials with single/dual/triple mode would open up a brand-new methodology for ultra-accurate sensing.

FUNDING STATEMENT

This work was supported by the National Natural Science Foundation of China (22374161), and the Youth Innovation Promotion Association, CAS (Y2022106).

REFERENCES

[1] T. S. Zhang，X. Y. Hu，B. Y. Zu，X. C. Dou, **A March to Shape Optical Artificial Olfactory System toward Ultrasensitive Detection of Improvised Explosives**, Advanced Photonics Research 3, 2022, 2200006
DOI: https://doi.org/10.1002/adpr.202200006

[2] F. F. Xiao#, D. Lei#, C. G. Liu, Y. S. Li*, W. F. Ren, J. G. Li, D. Z. Li, B. Y. Zu*, X. C. Dou*, **Coherent Modulation of the Aggregation Behavior and Intramolecular Charge Transfer in Small Molecule Probes for Sensitive and Long-term Nerve Agent Monitoring**, Angewandte Chemie International Edition 136, 2024, e202400453.
DOI: https://doi.org/10.1002/ange.202400453

[3] Y. Luo, D. Lei*, M. H. Li, Y. S. Ge, J. G. Li, B. Y. Zu, J. Yao*, X. C. Dou*, **Fluorophore Branching Boosted Photo-induced Energy Transfer in UiO-66 for Ultrasensitive and Instant Hydrazine Sensing**, Journal of Materials Chemistry A 12, 2024, 12088.
DOI: https://doi.org/10.1039/D4TA01549E

[4] H. Y. Cao, Z. Z. Cai, Y. S. Li*, G. F. Wang, X. C. Dou*, **Colorimetric-fluorescent Dual-mode Sensing of Peroxide Explosives Based on Inner Filter Effect with Boosted**

Sensitivity and Selectivity, Chinese Journal of Analytical Chemistry 50, 2021, 4.
DOI: https://doi.org/10.1016/j.cjac.2021.10.002

[5] W.F. Ren[#], Y. Liu[#], B. Y. Zu*, J. G. Li, D. Lei, T. S. Zhang, X. C. Dou*, **Ultrasensitive and Rapid Colorimetric Detection of Urotropin Boosted by Effective Electrostatic Probing and Non-covalent Sampling**, Journal of Hazardous Materials 436, 2022, 129263.
DOI: https://doi.org/10.1016/j.jhazmat.2022.129263

[6] Y. L. Ke[#], Y. Liu[#], B. Y. Zu[*], D. Lei, G. F. Wang, J. G. Li, W. F. Ren, X. C. Dou[*], **Electronic Tuning in Reaction-based Fluorescent Sensing for Instantaneous and Ultrasensitive Visualization of Ethylenediamine**, Angewandte Chemie International Edition 61, 2022, 202203358.
DOI: https://doi.org/10.1002/anie.202203358

[7] W. F. Ren[#], J. G. Li[#], B. Y. Zu[*], D. Lei, X. C. Dou[*], **Design of Highly Efficient Electronic Energy Transfer in Functionalized Quantum Dots Drived Specifically by Ethylenediamine**, JACS Au 4, 2024, 545.
DOI: https://doi.org/10.1021/jacsau.3c00667

[8] Y. N. Feng[#], D. Lei[#], B. Y. Zu[*], J. G. Li, Y. J. Li[*], X. C. Dou[*], **A Self-Accelerating Naphthalimide-Based Probe Coupled with Upconversion Nanoparticles for Ultra-accurate Tri-mode Visualization of Hydrogen Peroxide**, Advanced Science 11, 2024, 2309182.
DOI: https://doi.org/10.1002/advs.202309182

34: PEAK WAVELENGTH TRACKING FOR ENHANCED MEASUREMENT SENSITIVITY AND RANGE IN AN FIBRE OPTIC INTERFEROMETRIC SENSOR

Z. Q. Yu [a], W. J. Li [a], D. Chen [a], J. S. Ni [a], W. Zhang [a, *], and K. T. V. Grattan [b]

[a] **Laser Research Institute, Qilu University of Technology (Shandong Academy of Sciences), Jinan 250353, China** [b] **School of Science & Technology, City, University of London, London EC1V 0HB, United Kingdom**

Emerging Sensing Strategies and Applications, EM010, August 14, 2024, 9:30 AM - 10:30 AM

Abstract Spectral peak wavelengths observed in an Fabry-Perot interferometer (FPI) are proportional to the effective cavity length (ECL). Ambiguity in the tracking of the peak wavelength always occurs, an effect which limits the measurement range to half of the operation wavelength. In this work we propose a new demodulation method that can unambiguously recognize the spectral peak wavelengths. The evaluation of the ECL was realized by using the farthest-separated peak pairs, leading to a negligible integer rounding error in determining the peak order value. A new set of peak wavelengths could then be calculated based on the obtained ECL and peak order value. The difference between the measured and calculated peak wavelengths then was used as error correction factor to further improve the accuracy of the ECL and the peak order. Using this method, an accurate value of the peak order can be quickly obtained to achieve high measurement sensitivity and large dynamic range.

Keywords: Fabry-Perot interferometer; Peak wavelength tracking; Phase ambiguity; Integer rounding error; Refractive index measurement.

1. INTRODUCTION

Fibre optic interferometers have been used in many scientific and industrial applications. Integrated with optical fibre technology, such fibre-optic Fabry-Perot interferometers (FPIs) enable great flexibility in the design of the sensitive Fabry–Perot cavity combined with state-of-the-art micromachining and conventional mechanical fabrication. FPIs have emerged as unique candidates for high sensitivity sensing of different quantities with excellent performance in measurement accuracy, resolution, and stability [1]. The extrinsic Fabry–Perot interferometer (FPI) has a cavity which is open to the environment. It can be used to measure the parameters such as refractive index (RI), density, temperature, and concentration etc and finds a wide range of applications in the field such as oceanography. For these applications, the wavelength demodulation approach is preferred due to the demanding requirement on measurement resolution. All these parameters are evaluated by measuring the effective cavity length through FPI spectral response. Direct tracking of the peak wavelengths of the FPI spectral response normally produces the highest measurement sensitivity. However, most such techniques are limited by an issue that is widely known and termed '2 phase ambiguity' (or 'integer ambiguity') [2]. This is an effect which prevents the sensor from being used to measure over a large dynamic range. When the spectrum drifts over half the Free Spectral Range (FSR), the drift direction of the interference peaks becomes ambiguous due to the periodicity of the Fabry–Perot interference spectrum. Therefore, the dynamic range of any FPI sensor based on the wavelength tracking method will be limited to less than half FSR, resulting in the limitation of the measurement range. Many demodulation algorithms have been reported to identify the sensing peak of FPI sensors, such as the method that calculates the optical path difference (OPD) between two adjacent peak wavelengths in the spectrum [3], the wavelength tracking method of finding the interference peak order number by using the adjacent pair of the tracked peaks [4], or the accurate model of the characteristics of a fibre-optic sensor to match the FPI spectrum and thus retrieve the cavity length [5]. These methods have either limited dynamic range or offer deficient resolution. The Fourier transform was applied on the interference spectrum to avoid the fringe direction ambiguity [6]; nevertheless, its basic frequency is insensitive to OPD changes. The reported wavelength tracking methods suffer from large integer rounding errors. A method has been proposed to reduce the integer rounding error using a series of peak pairs and the average of the calculated peak orders [7] – however, the algorithm needed is highly complicated. Another peak identification method has recently been developed in which the intensity of interference maximum is taken as the characteristic to distinguish interference peaks [8], which may fail in field operation as the optical intensity is susceptible to the environmental perturbation.

In this work, a new demodulation method that can unambiguously recognize the spectral peaks of a fibre optic FPI sensor is proposed. The farthest-separated pair of peak wavelengths is used to evaluate the ECL and calculate the peak order with much reduced integer rounding error. An error correction was then designed to keep improving the accuracy of the ECL and the peak order. The unambiguous peak orders and the true peak wavelengths can thus be obtained based on the proposed demodulation to achieve high measurement sensitivity and large dynamic range.

1. THEORETICAL BACKGROUND

The interferometric sensor used in this work was an extrinsic fibre optic Fabry-Perot interferometer with an air cavity, formed by the fibre end face and an external reflective surface which act as two mirrors, as shown in Fig. 1. The open cavity structure allows the liquid to enter the sensor more efficiently and shortens the response time of the sensor.

By setting the reflectance of both mirrors as R, the interference intensity of the reflected is given by:

DOI: https://doi.org/10.34961/researchrepository-ul.29279978.v1

$$= \frac{(\quad)}{} \tag{1}$$

where I_0 is the incident light intensity, the phase difference obtained from the optical path difference. Given the wavelength of the incident light source of λ, the phase difference can be expressed as:

$$= \frac{nL}{} \tag{2}$$

where L is the cavity length. Note that for an open FPI shown in Fig. 1 a phase shift arising from the reflection at R_2 of light incident from an optical sparse medium to an optical

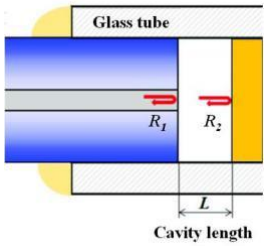

Figure 1. Schematic of fiber optic FPI sensor

dense medium should be added to , though this will not affect the subsequent theoretical derivation.

The wavelength corresponding to the peaks in the reflection spectrum of an FPI can be defined as,

$$= \ , (= 1,2, \ ) \tag{3}$$

The effective cavity length of the FPI can be calculated using the reflection spectra of multi-beam interference,

$$= \cdot \ - \frac{+k}{m} \tag{4}$$

where λ_m and λ_{m+k} are the wavelengths corresponding to the mth and (m+k)th peaks of the interference intensity. The free spectral range (FSR) can be defined as the wavelength difference between two adjacent peaks,

$$= - = \frac{}{} \tag{5}$$

The most straightforward way to extract the ECL from the interference is to use two adjacent peaks of the fringes, as described by (5). In this case the relative change of two peaks is measured to evaluate the ECL and the dynamic range of the sensor – however this is limited to /2 [2].

Building on this method, an improved technique is proposed [4] to find the exact fringe peak order number m. A rough estimate of the ECL can be derived by using (5) to estimate the interference peak order number m. If m is precisely determined and the peak wavelength known, the value of ECL can be extracted by using (3) without any ambiguity. However, due to the error in determining the peak wavelength and other system imperfection m always is not an integer and needs to be round to the closest integer. The larger integer rounding error means a larger error is obtained in the value of ECL.

As can be seen from the analysis above, the error in determining the peak wavelength and other system imperfections play a critical role in determining the peak order number m. From (3) and (4), the value of m can be expressed as,

$$= \frac{}{(\ m \ )} = \frac{m+k}{} \tag{6}$$

where FSR_k is considered as a nominal FSR averaged over k fringes. The error in determining m can then be estimated as,

$$\Delta \approx - \frac{}{} \frac{\Delta}{} \tag{7}$$

which represents the integer rounding error. Clearly the integer rounding error depends on the accuracy of the measured peak wavelength , and decreases with the increase of k. Therefore, the farthest-separated peak pairs should be used to calculate the peak order number m, as described in (6).

Similarly, the error in obtaining ECL can be estimated as,

$$\Delta \approx - \frac{m\,m+k}{\sqrt{\ }} \Delta \tag{8}$$

2. METHODS AND RESULTS

The experimental system designed in this work is shown in Fig. 2. A high-resolution FBG interrogator (CASSTK FT-16) was used both as a swept laser and as a spectrometer. The laser beam (wavelength range used: 1525 nm – 1565 nm) launches light into Port 1 of the optical fibre circulator and reaches the FPI cavity sensing probe through Port 2, which is placed in the solution with different refractive index. The solutions were prepared as test samples and with the RIs of the solutions were calibrated by using an Abbe refractometer (2WAJ, Shanghai Precision Instrument Co., Ltd).

The reflection from the sensing probe carrying the solution information was detected at Port 3. The wavelength response caused by the change of the external quantity acting on the FPI cavity can be obtained by the data acquisition. LabVIEW programming was used to demodulate the FPI cavity spectral response and obtain the RI information of the solution. The programming particularly involves functions such as data acquisition, peak finding algorithm, cavity optical length demodulation algorithm, experimental data analysis and anomaly warning. This eventually produces a real-time monitoring of the RI change.

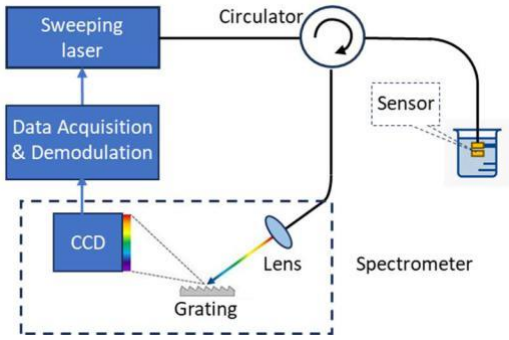

Figure 2. Experimental arrangement used in this work.

The first measurement was carried out by immersing the fibre optic FPI cavity sensor in solutions of different values of RI. The sensor remained in each solution for 5 minutes to obtain the sensing response. The effective cavity length, nL, was measured based on the recorded peak wavelengths. The results of measured effective cavity length are summarized in Fig. 3 where a sensor with an open cavity length of ~346 m was submerged, sequentially, in the solutions having 6 different values of RI which had been prepared. The ECL of the FPI was determined by measuring either two adjacent peak wavelengths or two separated peak wavelengths, based

on (4). From Fig. 3 it can be seen that the results measured from the 2 adjacent peaks (k=1) and the 2 separated peaks (k=9) both show a good linearity against the refractive index. The trendline from the peak pair of k=9 with an R-squared value of 0.9989 exhibits a more accurate measurement than that from the adjacent peak pair with an R-squared value of 0.9875, indicating a smaller deviation from the linearity. The slopes of the two trendlines represent the cavity length in air. The trendline from the peak pair of k=9 gives an estimated L of 345.82 m, very close to the designed L of 346 m.

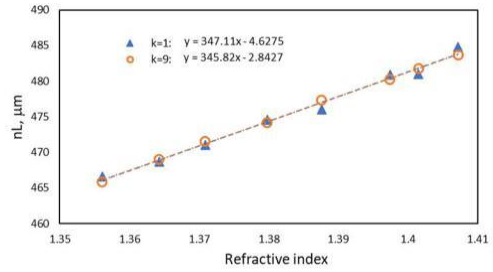

Figure 3. Measured effective cavity lengths vs refractive index.

According to Equations (7) and (8), both the integer rounding error and the error in evaluating ECL depend mainly on the accuracy of the measured peak wavelength . The smaller value of leads to smaller errors in determining the peak wavelength order and ECL. The results show that the measurement from two far-separated peaks gives more accurate estimation of the cavity length. This will also give a smaller integer rounding error in tracking the peak wavelength of the FPI response.

Based on the above analysis, a peak wavelength tracking scheme has been proposed here. The block flow diagram of this demodulation process is shown in Fig. 4.

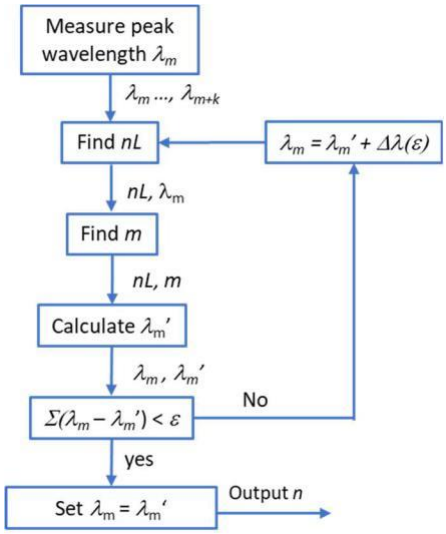

Figure 4. Block flow diagram of the demodulation process.

1) The FPI spectrum is captured from which the peak wavelengths ($_m$ to $_{m+k}$) in the range of 1525 nm – 1565 nm are obtained by using the peak finding algorithm;
2) Based on the obtained $_m$ to calculate the ECL by using (4);
3) Based on the calculated ECL and the obtained $_m$ to calculate m by using (3); round the calculation result to an integer;
4) Based on the calculated ECL and the integer of m to find a $_m$' by using (3);
5) $_m$ is the difference between $_m$ and $_m$'. If $_m$ is larger than an expected error, the calculated m is considered as false. $_m$ will be replaced by $_m$' plus a wavelength correction factor;
6) Repeat 2) – 5) until $_m$ is less than an expected error;
7) The obtained m now is considered as true and the obtained peak wavelengths $_m$' can be considered as true peak wavelengths;
8) The information on the ECL can be retrieved from the true peak wavelengths.

Fig. 5 shows the captured FPI spectral responses at 6 different RIs. One can see the variations of the spectra with changing RI. The ECL can be estimated by using a pair of peak wavelengths as did in the first measurement. This produces a low measurement sensitivity. Moreover, the relationship between the measurement sensitivity and the ECL is nonlinear, implying an inconsistent performance over the measurement range. The peak wavelength change offers much higher sensitivity. For the responses shown in the Fig. 5 all the peak wavelengths change over several FSRs when RI changes from 1.356048 to 1.364253. However, it is difficult to directly obtain the change of a specific peak from the FPI spectral response.

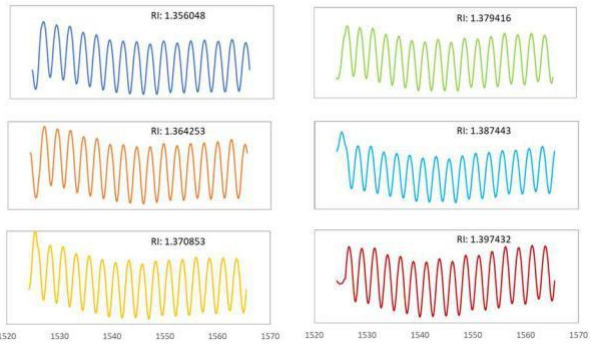

Figure 5. FPI spectral responses at 6 different RIs.

The demodulation system proposed has then been used to process the captured FPI spectral responses. Table 1 shows the processed data of the FPI spectral response at the RI of 1.356048 for phase-1 (step 1 to step 5 in the flow diagram), where $_m$ is the measured peak wavelength, $_m$' the calculated wavelength, $_m$ the difference between $_m$ and $_m$', $m_{calculated}$ the peak order calculation based on $_m$ and nL, 2^{nd}-$_m$ the sum of $_m$' and a wavelength correction factor.

Table 1 The phase-1 processed data for the FPI spectral responses

k	$_m$, nm	nL, nm	$m_{calculated}$	$_m$', nm	$_m$	2^{nd}-$_m$, nm
	1526.3106		611.25885	1526.9572	-0.6466	1526.6283
1	1528.8069	467393.0193	610.26079	1529.4604	-0.6536	1529.1315
2	1531.3234	466266.9849	609.25791	1531.9719	-0.6485	1531.6430
3	1533.8399	466403.8051	608.25832	1534.4916	-0.6517	1534.1627
4	1536.3564	466854.4255	607.26201	1537.0196	-0.6632	1536.6907
5	1538.8932	466682.4965	606.26096	1539.5559	-0.6627	1539.2270
6	1541.4300	466824.3542	605.26320	1542.1006	-0.6706	1541.7717
7	1544.0074	466085.5653	604.25284	1544.6538	-0.6463	1544.3249
8	1546.5645	466189.1966	603.25376	1547.2154	-0.6508	1546.8865
9	1549.1419	466032.1840	602.25009	1549.7855	-0.6436	1549.4566
10	1551.7193	466061.8509	601.24976	1552.3642	-0.6449	1552.0353
11	1554.2764	466558.8560	600.26058	1554.9515	-0.6750	1554.6226
12	1556.8741	466492.3078	599.25902	1557.5474	-0.6732	1557.2185
13	1559.4921	466276.4641	598.25302	1560.1520	-0.6598	1559.8231
14	1562.1101	466203.8036	597.25039	1562.7653	-0.6552	1562.4364
15	1564.7078	466485.4371	596.25885	1565.3874	-0.6796	1565.0585

In Table 1, nL can be calculated by using peak pair of $_m$ and $_{m+k}$ where values of k ranging from 1 to 15 are used. The variation of nL with different values of k can be seen. Only the farthest-separated pair of $_m$ and $_{m+k}$ are selected and used to calculate m. For the first peak wavelength, the value of $m_{calculated}$ is not an integer, and the closest integer is 611. Clearly, the integer rounding error is something to be noted. This means that the values of both $_m$ and nL used for calculating m may not be accurate enough for what is required, as the accuracy of the measured peak wavelength greatly affects the accuracy of m and nL, according to (7) and (8). Actually, it can be seen that the difference between $_m$ and $_m$' is significant. To improve the accuracy in the result, a wavelength correction is added to $_m$', generating the 2nd $_m$ for further processing.

The processed data from the subsequent phases are listed in Tables 2 and 3. In Table 2 the value of $_m$ has been replaced by that of 2nd $_m$ from Table 1. Still the farthest-separated pair of $_m$ and $_{m+k}$ has been selected and used to calculate m. It can be seen that both the difference between $_m$ and $_m$', and the error in calculated peak order are much reduced, but still larger than the expected error. Another wavelength correction is thus added to $_m$', generating the 3rd $_m$, aiming to improve the result obtained.

Table 2 The phase-2 processed data for the FPI spectral responses

k	2nd-$_m$	nL	$m_{calculated}$	$_m$'	$_m$	3rd-$_m$
	1526.6283		610.87162	1526.3076	0.0030	1526.3076
1	1529.1315	466284.6653	609.87162	1528.8097	-0.0029	1528.8097
2	1531.6430	466284.8297	608.87162	1531.3201	0.0033	1531.3201
3	1534.1627	466284.9941	607.87161	1533.8387	0.0012	1533.8387
4	1536.6907	466285.1585	606.87161	1536.3656	-0.0092	1536.3656
5	1539.2270	466285.3229	605.87161	1538.9009	-0.0077	1538.9009
6	1541.7717	466285.4873	604.87161	1541.4445	-0.0145	1541.4445
7	1544.3249	466285.6517	603.87160	1543.9966	0.0108	1543.9966
8	1546.8865	466285.8162	602.87160	1546.5571	0.0074	1546.5571
9	1549.4566	466285.9806	601.87161	1549.1261	0.0158	1549.1261
10	1552.0353	466286.1450	600.87161	1551.7037	0.0156	1551.7037
11	1554.6226	466286.3094	599.87161	1554.2899	-0.0135	1554.2899
12	1557.2185	466286.4738	598.87161	1556.8847	-0.0106	1556.8847
13	1559.8231	466286.6382	597.87162	1559.4882	0.0039	1559.4882
14	1562.4364	466286.8026	596.87162	1562.1004	0.0097	1562.1004
15	1565.0585	466286.9671	595.87162	1564.7214	-0.0136	1564.7213

Table 3 The phase-3 processed data for the FPI spectral responses

k	3rd-$_m$	nL	$m_{calculated}$	$_m$'	$_m$	final-$_m$
	1526.3076		610.99999	1526.3075	0.0031	1526.3075
1	1528.8097	466286.9482	609.99999	1528.8097	-0.0028	1528.8097
2	1531.3201	466286.9482	608.99999	1531.3200	0.0033	1531.3200
3	1533.8387	466286.9482	607.99999	1533.8386	0.0012	1533.8386
4	1536.3656	466286.9482	606.99999	1536.3656	-0.0092	1536.3656
5	1538.9009	466286.9482	605.99999	1538.9008	-0.0076	1538.9008
6	1541.4445	466286.9483	604.99999	1541.4445	-0.0144	1541.4445
7	1543.9966	466286.9483	603.99999	1543.9965	0.0109	1543.9965
8	1546.5571	466286.9483	602.99999	1546.5570	0.0075	1546.5570
9	1549.1261	466286.9483	601.99999	1549.1261	0.0159	1549.1261
10	1551.7037	466286.9483	600.99999	1551.7037	0.0157	1551.7037
11	1554.2899	466286.9483	599.99999	1554.2898	-0.0134	1554.2898
12	1556.8847	466286.9483	598.99999	1556.8846	-0.0105	1556.8846
13	1559.4882	466286.9484	597.99999	1559.4881	0.0040	1559.4881
14	1562.1004	466286.9484	596.99999	1562.1003	0.0098	1562.1003
15	1564.7213	466286.9484	595.99999	1564.7213	-0.0135	1564.7213

In Table 3 it can be seen that the difference between $_m$ and $_m$' has not changed much. However, the calculated value of m is almost perfect, i.e., the integer rounding error m is near zero. Since m is proportional to the accuracy of the measured peak wavelength , the conclusion can be reached that the value of $_m$' used to calculate m in this stage is almost the true peak wavelength. It should be pointed out that $_m$ will never be zero, as when the peak wavelength $_m$ is measured, there always is some error. In this work, the FPI spectrum was sampled at a wavelength interval of 0.022 nm. This means there exists a sampling error of ±0.011 nm in measuring the peak wavelengths. The value of $_m$ shown in Table 3, shows an error in this range. Therefore, at this stage, the final values of m and $_m$ are obtained. The FPI spectral responses for the other values of the RIs considered can be processed in the same way. Generally, the final peak orders and the peak wavelengths can be obtained at the phase-3. This makes the demodulation process both simple and quick to use, so that it is clear that a real-time measurement can be realised.

Some demodulated peak orders and the corresponding peak wavelengths at these values of the RIs considered are summarised in Table 4. Although 16 peaks can be observed in the spectral response of each RI, as shown in Fig. 5, many peak orders move out of the swept wavelength range quickly, as the RI varies. Clearly the peak wavelength tracking offers a very high measurement sensitivity. There is no a single order of the peak wavelength that can cover the whole measurement range in this work. The demodulated data are shown in Fig. 6 to demonstrate the measurement range and sensitivity of each peak order. It can be seen that more than one peak order would be needed to be measured for the full RI measurement range considered in this work. Also, the measurement sensitivities for the different orders of the peak wavelengths are different. The lower order of the peak wavelength exhibits a higher measurement sensitivity.

Table 4 The demodulated peak orders and the corresponding peak wavelength at different RIs

RI	1.356048	1.364253	1.370854	1.379416	1.387443	1.397432
611	1526.3075	1536.8904	1545.7067	1556.2040		
612		1534.3792	1543.1810	1553.6612	1563.1211	
613		1531.8761	1540.6636	1551.1267	1560.5711	
614		1529.3812	1538.1543	1548.6004	1558.0295	
615			1535.6533	1546.0823	1555.4961	
616			1533.1603	1543.5725	1552.9709	1563.6990
617			1530.6755	1541.0707	1550.4964	1561.1647

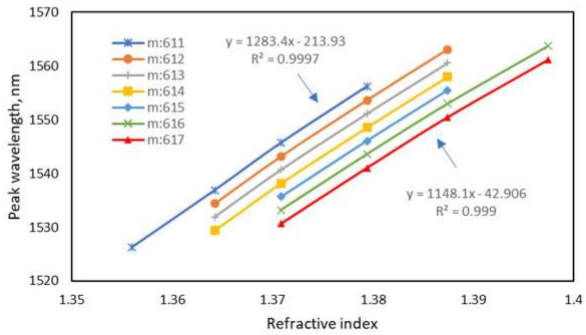

Figure 6 Peak wavelengths vs. RIs

3. CONCLUSIONS

In summary, an effective demodulation process to unambiguously track the interference fringe peaks of the reflection spectrum of a fibre optic FPI has been demonstrated. In this approach, a high measurement sensitivity, over a large dynamic range, has been realized. The demodulation scheme proposed has involved the evaluation of the effective cavity length and the calculation of the peak order value from the measured peak wavelengths. Since the accuracy of the evaluated ECL and the calculated peak order value greatly depend on the accuracy of the measured peak wavelengths, a wavelength error correction has been introduced to find the true peak wavelengths and keep improving the accuracy of the ECL and the peak order value. The demodulation scheme has been applied to measure the

refractive index of the solution sample and here a fibre optic FPI with a cavity length of 346 m was used in this work. All the peak wavelengths were measured in one measurement, by using the wavelength swept laser and the spectrometer. By using the demodulation scheme developed in this work, the wavelength peak order values have been found – and importantly with almost zero integer round error. Further, the true peak wavelengths containing the RI information have successfully been obtained. Thus, this approach has shown that a real-time measurement scheme, using a fibre optic FPI with high sensitivity and large dynamic range, can readily be realised and applied in the measurement of a range of Ris of different solutions. Such measurements have a range of important industrial applications.

ACKNOWLEDGMENTS

This work was partly supported by the Innovation Team Program of Jinan, China (Grant No. 202228032), the Shandong Provincial Key Research and Development Program(2019GSF111011), National Nature Science Foundation of China (Grant No. U2006216), and the Taishan Scholars Program (Grant No. tsqn202306254). Grattan acknowledges the support of the Royal Academy of Engineering.

REFERENCES

[1] Y. J. Rao, D. A. Jackson, Principles of Fiber-Optic Interferometry, in K. T. V. Grattan and B. T. Meggitt (Eds.), Optical Fiber Sensor Technology, Kluwer Academic Publishers, 2000, pp. 167-191.

[2] V. Bhatia, M.B. Sen, K.A. Murphy and R.O. Claus, Wavelength-tracked white light interferometry for highly sensitive strain and temperature measurements, Electron. Lett., vol. 32, no. 3, 1996, 247-249. DOI:10.1049/EL:19960174.

[3] T. Liu, M. Wu, Y. Rao, D. A. Jackson, G. F. Fernando, A multiplexed optical fibre-based extrinsic Fabry-Perot sensor system for in-situ strain monitoring in composites, Smart Mater. Struct., vol. 7, no. 4, 1998, 550. DOI 10.1088/0964-1726/7/4/016.

[4] B. Qi, G. R. Pickrell, J. C. Xu, P. Zhang, Y. H. Duan, '(+ another 5 authors), Novel data processing techniques for dispersive white light interferometer. Opt. Eng., vol. 42, no. 11, 2003, pp. 1736–1738. https://doi.org/10.1117/1.1613958.

[5] M. Han, Y. Zhang, F. Shen, G. R. Pickrell, A. Wang, Signal-processing algorithm for white-light optical fibre extrinsic Fabry–Perot interferometric sensors, Opt. Lett., vol. 29, no. 15, 2004, 107477. https://doi.org/10.1364/OL.29.001736.

[6] T. Liu, G. F. Fernando, A frequency division multiplexed low-finesse fiber optic Fabry–Perot sensor system for strain and displacement measurements, Rev. Sci. Instrum., 2000, vol.v71, no. 3, pp. 1275–1278. https://doi.org/10.1063/1.1150453.

[7] G. Liu, W. Hou, M. Han, Unambiguous Peak Recognition for a Silicon Fabry–Perot Interferometric Temperature Sensor, J. Light. Technol., vol. 36, no. 10, 2018, pp. 1970-1978. DOI: 10.1109/JLT.2018.2797202.

[8] B. Yang, B. Yang , J. Zhang, Y. Yin, Y. Niu, M. Ding, A Sensing Peak Identification Method for Fibre Extrinsic Fabry–Perot Interferometric Refractive Index Sensing, Sensors, vol. 19, no. 1, 2019, 96. https://doi.org/10.3390/s19010096.

35: PEDIATRIC CONSULTATIONS: A MULTI-SENSORY MONITOR FOR OPTIMAL ENGAGEMENT AND DIAGNOSIS

Ifunanya Barbara Onyekwelu [a], *Marit Skårsmoen* [b], *Andreas Andersen Kjernlie* [a], *Morten Ødegård* [a], *Peyman Mirtaheri* [a], *Olga Korostynska* [a, *]

[a] Department of Mechanical, Electrical and Chemical Engineering, Oslo Metropolitan University, Oslo, Norway [b] Department of Computer Science, Oslo Metropolitan University, Oslo, Norway

Biomedical Sensors Session 2, EM009, August 13, 2024, 10:05 AM - 11:15 AM

Abstract − There is an increasing recognition that children, especially those on the autism spectrum, experience challenges in emergency rooms and outpatient clinics due to sensory overload: these environments are often brightly lit, loud, and filled with unfamiliar people and equipment. This study aims to design a child-friendly device that will resolve these challenges. Teddy-Beat is a teddy-bear, housing a pulse monitoring sensor coupled with visual, tactile, and auditory actuators to display the sensor results in various artistic ways. The device was tested on five volunteers. The actuators responded in sync with every pulse output from the sensor, allowing users to see, feel, and hear their heartbeat in real-time. The pulse rate from the device is synchronized with recordings from a BPM monitor. The only child tested, showed positive emotions and relaxation.

Keywords**:** multi-sensory monitoring, pulse monitoring, pediatric care, artistic display

1. INTRODUCTION

Over the years, considerable technology has been developed to address the problem of pacifying children undergoing medical treatment. Experience and studies have shown that having a calm child during medical consultations can lead to a less stressful experience for both caregivers and the child [1] . Research also shows that children, especially those on the autism spectrum are often impatient in clinical settings. The reason for these behaviours is that clinical environments such as the emergency room (ER) can be counter-therapeutic to children due to its often noisy and highly stimulating nature.

Furthermore, while some young patients seek care in specialized pediatric emergency departments, most children receive care in general ERs not explicitly designed for children which may increase their anxiety and stress levels. Additionally, children expect their attending doctors to build a safe relationship with them by engaging with them, verbally or non-verbally, during consultations rather than speaking over their heads to their caregivers [2]. Every child should be involved in the communication, based on their age and level of maturity. This statement is supported by the 1989 United Nations Convention on the Rights of the Child, which states that children have a right to participate in their medical consultations. Research shows that millions of children seek care in emergency departments every year. Parents may take their child to an ER for a myriad of reasons, including perceived urgency, difficulties with getting an appointment with a general practitioner, lack of nearby primary care facilities.

Pediatric consultations can be a daunting experience for children, especially when it involves monitoring vital signs. Convincing a child to cooperate during a health care visit can be difficult and is often a trial-and-error process. Traditional methods of displaying vital signs, typically through numerical readouts or graphical trends, though adequate for medical professionals, can be intimidating or meaningless to pediatric patients. Studies also show that humour and play are useful tools in reducing anxiety and stress levels in children undergoing medical treatment and in improving communication and interaction between caregivers and children [3]. Art is one way of implementing humour and children are easily captivated by visual art and sound. The use of art in healthcare has been shown to positively impact patients' physical and emotional well-being [4].

Recognizing the need for a more child-centric approach, this paper introduces a novel and cost-effective Teddy-Beat device designed to make medical consultations more engaging and less intimidating for pediatric patients. Utilizing a standard pulse sensor, this device diverges from conventional display methods. Instead, it translates pulse readings into a multi- sensory experience: visually through a multi-colour LED strip, auditorily via a speaker, and tactilely through a vibration motor. These actuators synchronize with each pulse detected, creating an interactive and artistic representation of the patient's heartbeat. The sensor and actuators for the device were housed in a nice textured teddy bear to provide aesthetic comfort to its users.

1.1. Related Works

There are few published studies on approaches and tools developed to enhance children's experience at the ER and outpatient clinics. In a recent study, Litwin et al. [5] used insights from stakeholders to design and implement a low-cost sensory kit that could improve the ER experience for children on the autism spectrum and their families. The kit included various items such as squishy balls, fidget toys, vibrating pillows, spinning toy, noise-cancelling headphones, etc. In a similar study [6], a coping kit with simple communication cards, a social script book, and distraction items (toys), was developed to enhance communication and distract children with developmental disabilities (including autism spectrum disorder) undergoing procedures in the hospital. Findings from the evaluation of the study, showed that Nurses perceived the coping kits to be effective for distraction before or during a procedure, but not as helpful for communication to prepare for a procedure. James Bennett and

DOI: https://doi.org/10.34961/researchrepository-ul.29280077.v1

M.J. Lee [7, 8] in their patents, designed sensory toys in the form of teddy bears aimed at pacifying children in their distress.

It is evident that these existing solutions, while beneficial, have certain limitations in terms of interactive engagement and comprehensive sensory stimulation. The novel device presented in this paper transcends these traditional approaches by offering a dynamic, multi-sensory experience that is more actively engaging for pediatric patients. The device integrates real-time physiological data (the child's pulse) with an interactive display, creating a direct and meaningful connection between the child and their physiological state.

The objective of the Teddy-Beat device is to utilize a teddy bear's familiar and comforting form to mitigate the clinical ambiance that can overwhelm young patients. By doing so, a friendly and engaging environment is created for pediatric patients during medical consultations. This approach not only eases the stress and anxiety in young patients, but also enhances their cooperation, thereby enabling healthcare providers to conduct examinations and procedures with greater ease and accuracy. Also, the rights of children participating in their medical consultations will be protected.

2. METHODS AND PROCEDURES

The materials used in this project include:

- A pulse sensor.
- An 8Ω speaker.
- A vibration motor.
- A 60 LED digital RGB LED flexi-strip.
- A 16 x 2 LCD monitor
- An Arduino UNO microcontroller.
- A 2,5W class D audio amplifier.
- A 3D-printed finger clamp.
- A teddy-bear.
- A 10KΩ potentiometer.
- Resistors and capacitors.

2.1. The Sensor

The pulse sensor used in this project is a photoelectric sensor that uses a light emitting diode and photodetector to convert physical changes in a system (to be measured) into an optical signal, and further into an electric signal using the photoelectric effect. This effect refers to how metals or other compounds emit electrons when exposed to irradiation of a certain wavelength and intensity. In other words, the electrons absorb the energy from the photons, producing corresponding electrical effect/signal. This electrical signal can then be processed to create meaningful output, like a pulse wave or SpO2 measurement. For example, SpO2 can be determined by implementing Beer-Lamberts-law to analyze the optical signal.

The pulse sensor consists of a green LED with specific wavelength, a photodetector (ambient light) sensor and a noise-cancellation circuitry. The circuitry eliminates the noise to enhance the reading of the pulse rate.

Vital signs help in detecting or monitoring medical problems, exercises, or emotions, and the four main vital signs are body temperature, breathing rate, blood pressure and pulse rate. The pulse sensor detects and monitors the pulse rate by measuring the volumetric changes of blood flow, or the movement of the blood through the arteries. The pulse rate is measured in heartbeats per minute (BPM). The resting heart rate for children decreases as they get older. Typical normal resting heart rate ranges are: (1) babies (birth to 3 months of age): 100–150 BPM; (2) kids 1–3 years old: 70–110 BPM; (3) kids by age 12: 55–85 BPM.

2.2. The Actuators

A 9000rpm mini vibration motor was used for the tactile output of the pulse sensor. Whenever there was a pulse from the user i.e. when the input is HIGH, the motor would vibrate just like a cell phone in silent mode.

The digital RGB LED full coloured flexi-strip which consists of 60 full-colour lamps and an integrated driver chip, was used for the visual output of the sensor. The control circuit and RGB chip are integrated into a package of 5050 components. The LED strip has low driving voltage and power consumption.

An 8Ω speaker was used for the auditory output of the sensor. The audio output was amplified using a class D audio amplifier. The audio output mimicked a heart rhythmic sound instead of the traditional beeping sound from the regular vital signs monitors used in hospitals. The mimic heartbeat sound offered a more natural and intuitive auditory experience compared to the traditional beeping sound of regular hospital vital signs monitors. A volume control was utilized to vary the volume of the soothing sound.

A 16 x 2 LCD monitor was added to display the output of the pulse sensor more professionally. A 10KΩ potentiometer was added to control the brightness of the LCD monitor.

2.3. The Microcontroller

The Arduino UNO R3 board microcontroller, based on ATmega328P is used in this project. The Arduino board has 14 digital input and output pins, 6 analog inputs, a 16 MHz ceramic resonator, a USB connection, a power jack, an ICSP header and a reset button. The libraries used for execution include: (1) the Pulsesensor Playground for the pulse sensor; (2) Adafruit NeoPIXEL for the digital RGB LED; (3) LiquidCrystal for the lcd display; (4) PCM.h library and the Audacity application for playing back the heartbeat sound. The 'wav' file for the selected heartbeat sound was converted from a 32-bit float, 48000Hz sample-rate, to a 16-bit PCM, 8000Hz sample-rate .mp3 file after which it was converted into an array of data that the Arduino can play back using the speaker.

2.4. The Finger Clamp

The pulse sensor is designed to be used on the fingers or clipped to the earlobes of the user. However, for stability and to mitigate ambient light interference, the finger clamp was designed using Tinkercad and some basic templates from Thingiverse, and then 3D printed (s e e *Figure 1*) . Thingiverse is a website dedicated to the sharing of user-created digital design files. The modified dimensions for the

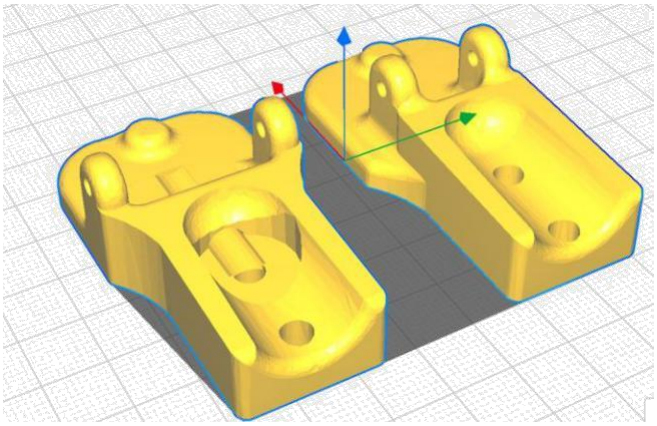

Figure 1. 3D model of finger clamp.

printed clamp include making a 16mm by 17mm and 4mm by 5mm extrusions for the optical sensor and its cables respectively.

2.5. The Teddy Bear

For aesthetic appeal and comfort, a soft, huggable and nice textured teddy bear was used to house all electronic components. The vibration motor was placed in the foot of the teddy bear, while the digital LED strip was shaped like a heart and glued to a lacy material. This material was then sewn onto a cut-out space on the teddy bear as shown in Figure 2.

2.6. Tests

The device was tested on volunteers comprising four adults and one child. The adults were also hooked to a BPM monitor while testing the Teddy-Beat device.

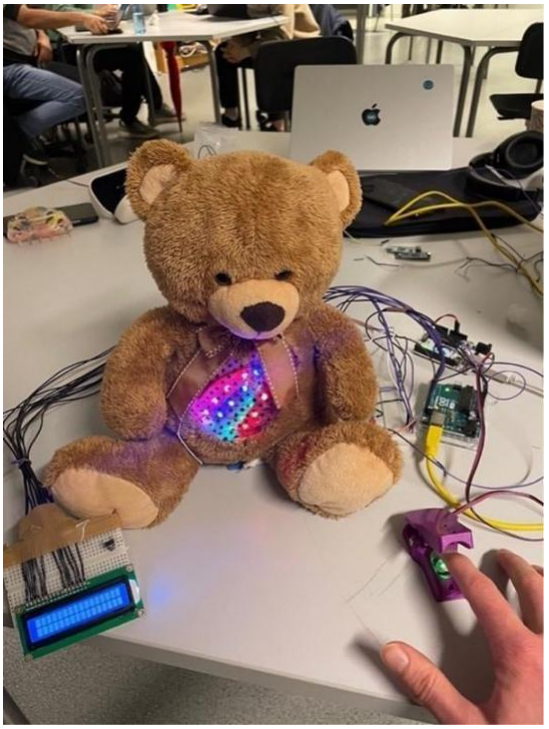

Figure 2. The Teddy-Beat device.

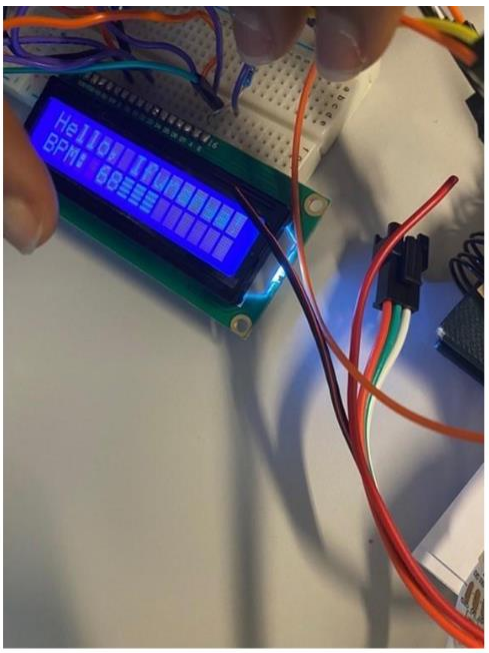

Figure 3. BPM reading from the Teddy-Beat.

Figure 4. BPM reading from the BPM monitor.

3. RESULTS AND DISCUSSION

It was observed that both the Teddy.Beat device and BPM monitor showed pulse rate readings that varied at a maximum of ±3 at the initial but later synchronised after 5 to 10 seconds. For instance, both devices showed a pulse rate of 68 BPM after about 6 seconds in one volunteer (see Figure 3 and Figure 4).

Additionally, a positive response was observed in the child who appeared elated at the artistic display of the pulse readings. For every pulse sensed, the motor vibrated, the LED strip blinked, and the mimic heartbeat sound played.

This is a preliminary report aimed at introducing Teddy-Beat to the medical world for the examination of children in emergency rooms and outpatient clinics. This paper presents a case study, and a potential extension could involve testing the Teddy-Beat within a larger sample size. This would enable a more comprehensive examination of the statistical significance related to its effects in the future.

The results from the BPM monitor validate those of the Teddy-Beat device and therefore, gives credence to the accuracy of the device. Furthermore, the device can be used to measure the pulse rates of young patients. The visual and auditory thrills induced by the device in young patients will facilitate a relaxing and friendly environment for medical examination.

The preliminary findings, underscore the potential of the Teddy-Beat device not only in creating a more child-friendly healthcare environment, but also in paving the way for future innovations in pediatric care that can prioritize the emotional well-being of young patients.

Hypersensitivity to the environment is the most described difficulty in the emergency room for children, especially those on the autism spectrum. Hence, in a busy and highly stimulating ER environment, a familiar stuffed animal can be a lifeline, a cuddly friend turning into a comfort hero for both the child and the parents. With sensors tucked discreetly inside, a child's favourite toy can monitor their pulse rate, obviating the use of cables directly on the child. This makes the experience less scary, and the vital sign gathered by their furry friend can help doctors provide the best possible care.

During the project, feedback was received from the medical personnel working in a hospital, and all confirmed that such a device has the potential to transform paediatric consultations. Further exploration into the long-term effects of such multi-sensory experiences on patient anxiety, cooperation during medical procedures, and overall satisfaction could provide valuable insights.

4. CONCLUSIONS AND FUTURE WORKS

The development and validation of the Teddy-Beat device marks a significant advancement in pediatric healthcare technology. As demonstrated in this study, the readings from the device were synchronised with the BPM monitor after 5 to 10 seconds, thereby confirming its reliability for clinical use.

The positive response from the child who tested the Teddy- Beat device underscores the device's potential to transform pediatric consultations, making them more engaging and less intimidating for young patients. This highlights the importance of incorporating patient-centered design principles in medical device development.

Future work will focus on extending this technology beyond the clinical environment. The Teddy-Beat device can be refined further by integrating more vital sign biosensors and IoT technology to enable real-time remote monitoring of users. This will be useful for young patients with long-term conditions after discharge, as the cuddly companion can continue monitoring vitals at home, thereby reducing the frequency of their hospital visits.

It is recommended that future studies also focus on testing the device on a larger sample size.

ACKNOWLEDGMENTS

This student research project was conducted as part of the ACIT Masters' course "Medical Sensors and Actuators" (ACIT4720) at Oslo Metropolitan University (OsloMet), in Oslo, Norway. The authors acknowledge the cooperation with Strategic OsloMet funding "Intelligent Health".

REFERENCES

[1] M. Gripko, A. Joseph, and S. MohammadiGorji, "Effects of the physical environment on children and families in hospital-based emergency departments: A systematic literature review," (in eng), *J Environ Psychol*, vol. 86, Mar 2023, doi: https://doi.org/10.1016/j.jenvp.2023.101970.

[2] C. Dedding, R. Reis, B. Wolf, and A. Hardon, "Revealing the hidden agency of children in a clinical setting," *Health Expectations*, vol. 18, no. 6, pp. 2121-2128, 2015, doi: https://doi.org/10.1111/hex.12180.

[3] M. Bertini, E. Isola, G. Paolone, and G. Curcio, "Clowns benefit children hospitalized for respiratory pathologies," (in eng), *Evid Based Complement Alternat Med*, vol. 2011, p. 879125, 2011, doi: https://doi.org/10.1093/ecam/neq064.

[4] S. L. Nielsen, L. B. Fich, K. K. Roessler, and M. F. Mullins, "How do patients actually experience and use art in hospitals? The significance of interaction: a user-oriented experimental case study," *Int J Qual Stud Health Well-being*, vol. 12, no. 1, p. 1267343, Dec 2017, doi: https://doi.org/10.1080/17482631.2016.1267343.

[5] S. Litwin and K. Sellen, "Designing a Sensory Kit to Improve the Environment for Children with Autism Spectrum Disorder in the Pediatric Emergency Department," *J Autism Dev Disord*, vol. 53, no. 9, pp. 3369-3379, Sep 2023, doi: https://doi.org/10.1007/s10803-022-05651-7.

[6] J. Drake, N. L. Johnson, A. V. Stoneck, D. M. Martinez, and M. Massey, "Evaluation of a Coping Kit of Items to Support Children with Developmental Disorders in the Hospital Setting" *College of Nursing Faculty Research and Publications. 155*, 2012, url: https://epublications.marquette.edu/nursing_fac/155.

[7] J. Bennett, "Sound and Heartbeat Playback System," US Patent Appl. 10/679,094, 2009. [Online]. Available: https://patentimages.storage.googleapis.com/fe/83/0e/77190e9192f38d/US7510521.pdf.

[8] M. J. Lee, "Child calming toy with rythmic stimulation," US Patent US20070037474A1 Patent Appl. 11/203,570 2007. [Online]. Available: https://patents.google.com/patent/US20070037474A1/en#patentCitations.

36: SPECIFIC AND SENSITIVE DETECTION WITH NUCLEIC ACID SENSORS

*Luyan Yang**

Center of Materials Science and Optoelectronics Engineering, University of Chinese Academy of Sciences, Beijing, China,

Biomedical Sensors Session 1, EM009, August 12, 2024, 4:50 PM - 5:30 PM

Abstract − The adaptability and modifiability of nucleic acid structures endow them with distinct advantages in biosensor applications. Nonetheless, improving the accuracy and precision of detection remains a major challenge. Our goal is to create a biosensor system that is highly specific and sensitive by harnessing the customizable and targetable properties of nucleic acids. Initially, Capture-SELEX technique was utilized to isolate DNA aptamers of specifically recognizing small chemical molecules, resulting in versatile probes with fluorescence activation and nuclease activities. Additionally, we engineered a miniaturized six-helix DNA nanopore to enhance the detection sensitivity of trace miRNA. Despite encountering the limited insertion efficiency and conductance overlap, we integrated DNA origami technology to improve the binding efficiency and significantly enhance the detection sensitivity. Ultimately, we believe that the proposed sensing strategy would provide a valuable research paradigm for other nucleic acid-relevant target analysis.

Keywords**:** aptamer; DNA nanopore; DNA origami; trace sensing; specific recognition

1. INTRODUCTION

The nucleic acid probe's precise targeting capabilities have resulted in its extensive utilization in various fields, such as cell biology, molecular biology, and chemical biology, among others. In comparison to traditional diagnostic methods such as real-time quantitative PCR, electrochemical immunoluminescence analysis, and histopathological examination, nucleic acid probe technology offers significant advantages in terms of speed, accuracy, and sensitivity, making it an ideal tool for early disease detection and monitoring. This paper discusses how nucleic acid probes can be rationally designed as fluorescent probes based on hybridization and fluorescence resonance energy transfer, which emit fluorescence signals proportional to the amount of target molecules in the sample. Furthermore, by utilizing the programmability of nucleic acids, DNA nanopores with specific functions can be engineered through sequence design. These nanopores can selectively bind target nucleic acid sequences, inducing conformational changes that enable highly sensitive and specific detection of targets. The advancements outlined herein highlight nucleic acid probes as efficient transducers, capable of converting imperceptible molecular interactions into measurable optical, electrical, or magnetic signals, thereby expanding the scope of nucleic acid probe applications in bioanalysis.

2. RESULTS AND DISCUSSION

In order to further explore the essential properties of nucleic acids and maximize their highly specific binding ability, this study focuses on developing sensing technologies based on the intrinsic characteristics of nucleic acids. Specifically, we employ refined theoretical calculations and computer-assisted techniques to predicts the multi-level structures of nucleic acids (Figure 1). Moreover, we are exploring the potential applications of nucleic acid structures in various conformations, from multiple research directions such as DNA aptamers, DNA nanopores, and DNA origami. By integrating various experimental techniques and principles, we aim to advance innovation in the fields of biosensing and molecular diagnostics.

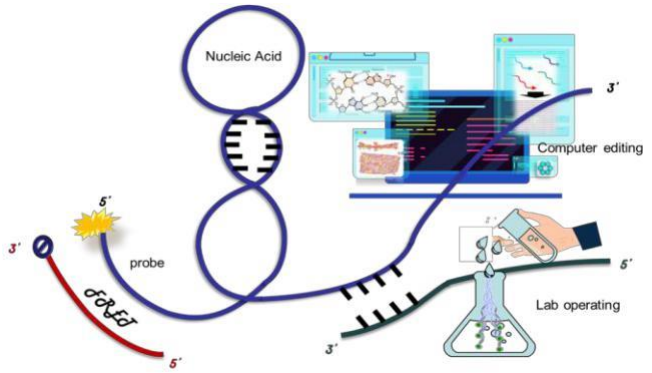

Figure 1. Schematic diagram of the design of nucleic acid probe systems that combine computer editing with laboratory operations.

2.1. DNA Aptamer Sensor

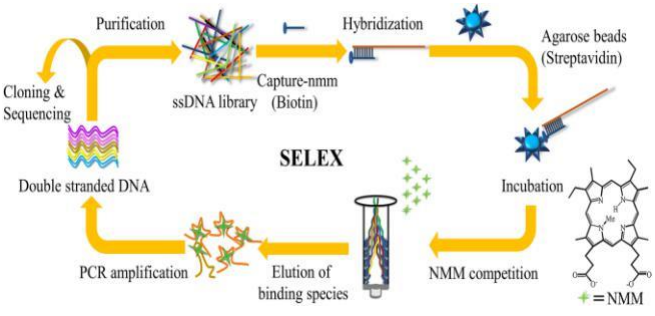

Figure 2. Diagram of capture-SELEX procedure. Initially, biotin-modified capture-nmm strand immobilized on streptavidin-coated agarose beads and incubated with a denatured ssDNA library. Then, the beads incubated with N-methyl mesoporphyrin IX (NMM), and unbound DNA are removed, followed by the collection of binding complexes through competitive elution. Next, collected sequences are amplified to generate ssDNA sublibrary, which is repeated until obtained an enriched library. Finally, the library is proceeded with cloning and sequencing to identify the binding sequences.

DOI: https://doi.org/10.34961/researchrepository-ul.29281430.v1

Through the integration of in vitro screening and PCR amplification, a strategy has been developed focused on the modulation of non-covalent interactions between aptamers and target chemical molecules. The approach utilizes the inherent flexibility and conformational diversity of nucleic acids to select aptamers with high specificity for targets from large libraries of random oligonucleotides (Figure 2) [1]. This method has proven to be highly effective in designing probes for molecular targeting.

2.2. DNA Nanopore Sensor

Given the characteristics of miRNA sequences — short length (18–24 nt), low concentration (0.1–100 nM), and high sequence similarity, their detection presents significant challenges. Therefore, we have employed "stochastic detection" principle that relies on the correlation between the presence of analytes and current that passes through a single channel [2]. By designing a hexagonal DNA nanopore, we were able to specifically monitor miR-21, that circulating miR-21 might be a good diagnostic marker for identifying colorectal cancer [3]. The conductance of the nanopore can be modulated accordingly when specific oligonucleotides are present (Figure 3). To capture these conformational changes, we measured the electrical conductance alterations upon the nanochannel insertion into a lipid bilayer, where two nanopore conformations yield quite different levels of conductance [4]. For 14 nm-long nanopores, our research strategy involves monitoring the opening and closing conformations, counting the number of nanopores inserted, to precisely measure the signal concentrations at the single-molecule level, thus enhancing the sensitivity of detection.

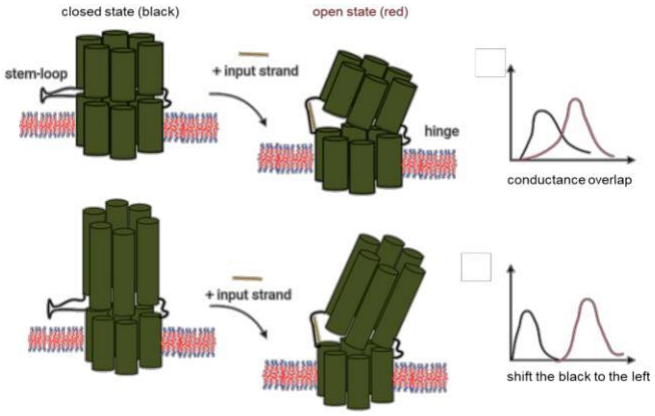

Figure 3. Schematic diagram of shorter and asymmetric nanopores. DNA nanopore structure consists of two interconnected barrels. In the closed state, the stem-loop maintains a minimal distance between the two barrels. Upon the addition of input signal (DNA analogue of miR-21), the stem-loop unravels, producing a combination of single-and double-stranded linkers that divide the nanopore into two halves. This additional steric hindrance triggers the nanopore opening. Each green cylinder represents to a double helix.

2.3. DNA Origami Sensor

By incorporating DNA origami technology, we have refined the defects of the previous small hexameric hexagonal nanopores. The optimization was carried out primarily from three aspects: (i) the poor insertion capability of DNA hexameric nanopores, resulting in insufficient electrical conductance changes in detection; (ii) the inadequate difference in conductance between the “closed” and “open” states of the nanopores, indicating that some of insertion events cannot be clearly distinguished; (iii) the strong tendency of nanopores to leave the lipid bilayer and the existence of positive and negative jumps, with no clear correlation between jump frequency and the number of detected nanopores at opening states. In the design of the rectangular DNA tile, we also employed multi-crossover DNA staples inspired by Rothemund’s work [5]. Ultimately, we successfully constructed a novel nanopore-based molecular switch, consisting of a long, asymmetric hexagonal nanopore immobilized on a two-dimensional DNA surface containing multiple hydrophobic sites, achieving sensitive detection of target oligonucleotides at the nanomolar level (Figure 4).

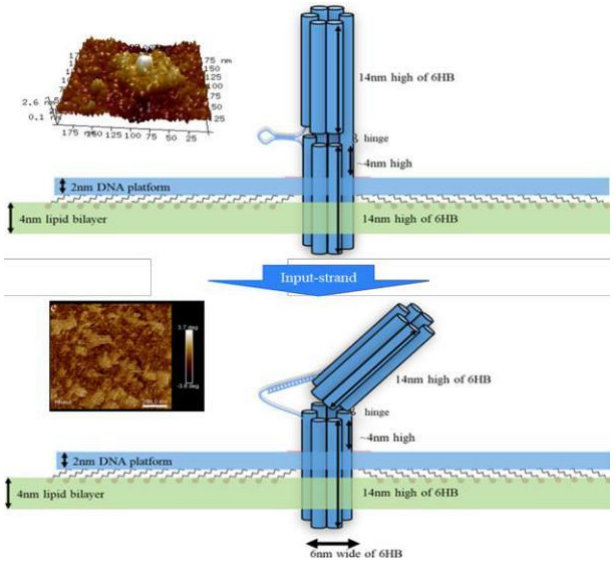

Figure 4. Schematic diagram of a protocol for inserting T-shaped nanopores into lipid bilayers by multiple hydrophobic sites anchoring for oligonucleotide detection.

3. CONCLUSIONS

Having thoroughly comprehended the operational mechanisms of nucleic acid probes, we have developed simple yet reliable sensors based on theoretical modelling and experimental validation. These optimized probes have overcome previous design challenges, offering a crucial tool for early disease detection and intervention. We anticipate the application of enhanced probes in sensing, such as the selection of aptamers within hydrogels, the integration of aptamer technology with nanopore technology [6], etc. This research presents an effective methodology for analysing nucleic acid probe conformations and designing functional probes, which is of significant importance for the synthesis and development of powerful nucleic acid sensors.

FUNDING STATEMENT

This work was supported by the Natural Science Foundation of China (21575154, 21775160, 81801837, 31800685), the Science Foundation of Jiangsu Province (BE2018665, BK20180250, BK20180258, BK20180261), the CAS/SAFEA International Innovation Teams program, the China Postdoctoral Science Foundation (2017M620228, 2018T110550), University of Bordeaux (department STS), Ligue contre le Cancer (Aquitaine), INSERM (PCSI call) and China Scholarship Council for funding.

REFERENCES

[1] L. Y. Yang, P. Ding, Y. Luo, J. N. Wang, H. Y. Lv, W. J. Li, Y. W. Cao and R. J. Pei, **Exploration of Catalytic Nucleic Acids on Porphyrin Metalation and Peroxidase Activity by in Vitro Selection of Aptamers for N-Methyl Mesoporphyrin IX**, ACS Comb. Sci., 21, 2019, 83
DOI: https://doi.org/10.1021/acscombsci.8b00129

[2] H. Bayley and P. S. Cremer, **Stochastic Sensors Inspired by Biology**, Nature, 413, 2001, 226
DOI: https://doi.org/10.1038/35093038

[3] M. Dillhoff, J. Liu, W. Frankel, C. Croce and M. Bloomston, **MicroRNA-21 is Overexpressed in Pancreatic Cancer and a Potential Predictor of Survival**, J. Gastrointest. Surg., 12, 2008, 2171
DOI: https://doi.org/10.1007/s11605-008-0584-x

[4] L. Yang, C. Cullin and J. Elezgaray, **Detection of Short DNA Sequences with DNA Nanopores**, Chemphyschem, 23, 2022, e202200021
DOI: https://doi.org/10.1002/cphc.202200021

[5] S. Woo and P. W. K. Rothemund, **Programmable Molecular Recognition Based on the Geometry of DNA Nanostructures**, Nat. Chem., 3, 2011, 620
DOI: https://doi.org/10.1038/nchem.1070

[6] W. Q. Zhang, Y. D. Tu, H. Liu, R. Liu, X. J. Zhang, L. Jiang, Y. Huang and F. Xia, **A Single Set of Well-Designed Aptamer Probes for Reliable on-site Qualitative and Ultra-Sensitive Quantitative Detection**, Angew. Chem. Int. Ed. Engl., 63, 2024, e202316434 DOI: https://doi.org/10.1002/anie.202316434

37: Sensing the Cyber-Physical: Extended Reality in Smart Manufacturing

Adam Dooley[a], Denis Moore[a], William O'Brien[a], Mihai Penica[a], Dr. Sean McGrath[a], Prof. Eoin O'Connell[a]

[a] *Dept. of Electronic and Computer Engineering*, University of Limerick, Limerick, Ireland

Industrial Sensing, EM009, August 13, 2024, 4:20 PM - 6:10 PM

***Abstract*— Extended Reality (XR) for Manufacturing is a new reality of development now possible for the factory floor thanks to the introduction of 5G and similar high-speed connectivity. The benefits of using a high-speed infrastructure make the virtual space an ideal development environment for factories to benefit from in areas such as financial, training, design, troubleshooting and maintenance. The adoption of enabling technologies such as XR and 5G by manufacturing is allowing the physical world to be designed and simulated virtually through digitalized processes before a physical product is even created.**

Keywords— XR, AR, VR, 5G, Smart Manufacturing

I. Introduction

The factory floor has historically served as the epicentre of industrial revolutions, and Industry 4.0 has undeniably left its mark. However, as we transition into the era of Industry 5.0, characterized by increased collaboration between humans and machines, the landscape of manufacturing is poised for another profound transformation.

The evolution of eXtended Reality (XR) technologies, including Virtual Reality (VR), Augmented Reality (AR), and Mixed Reality (MR), is set to catalyse this transformation, revolutionizing both consumer markets and industrial applications. With plummeting costs and burgeoning content availability, the imminent years will witness an explosion of advancements in XR technology, reshaping the fabric of manufacturing processes.

Traditionally, barriers such as limited access speed to information, cable tethering, storage constraints, and communication reliability have impeded progress on the factory floor. However, the advent of 5G connectivity and the proliferation of Internet of Things (IoT) devices are set to overcome these hurdles. With near-instantaneous access to real-time data from factory floor machines and seamless wireless connectivity, humans and robots can coexist in the same workspace. The convergence of XR and IoT enables the creation of digitally assisted workspaces, enhancing operational efficiency and productivity.

By leveraging cloud computing and historical data analytics, predictive maintenance, bottleneck identification, task automation, staff monitoring, and training programs can be optimized to maximize productivity and profitability. Industry 5.0 aims to achieve complete transparency across all manufacturing processes and assets, providing unparalleled insights into the manufacturing world.

In this paradigm, XR technology emerges as a cornerstone, harnessing the synergies between artificial intelligence (AI), real-time IoT data streams, and AR-enhanced work instructions. When integrated into factory settings, this immersive technology unlocks the potential for "EXTRA(M)" capabilities, driving efficiency and innovation across industries. The engineering and manufacturing sectors are set to experience significant advancements through the seamless integration of XR technology within the framework of Industry 5.0.

II. Potential for XR in manufacturing

There is a fundamental gap between the vast amount of digital data available and its application in the physical world. XR can very quickly become a key tool for driving efficiency, technology adoption, the proofing of concepts, standards development and eventually process validation. A recent example of XR's impact is Xerox, which used XR to connect field engineers with remote experts via camera linked smart glasses. It eliminated the need to provide service manuals and reduced telephone support. First-time fix rates increased by 67% and the engineers' efficiency increased by 20%. The average time to resolve problems dropped by more than 2 hours. In short, upskilling and intellectual renewal need to become commonplace for any company that expects to thrive. [1]

XR does more than present digital characters, images, or other information for manufacturing operators and technicians. It imports expertise into the workplace.

In the paper "Importance & Applications of Virtual Reality in Engineering sector" by Gandhi et al. the authors defined XR as an emerging technology that can realise capability in working environments. Furthermore, the paper also explores the importance and the appliance of virtual reality in engineering sectors e.g. design, manufacturing, inspection, tooling, prototyping etc. [2]

III. Existing XR Equipment

The existing Extended Reality equipment presents a broad spectrum of immersive solutions suited to diverse industry requirements. Ranging from standalone VR headsets to augmented reality smart glasses, XR technology undergoes constant evolution, expanding the horizons of virtual and augmented experiences. These devices, featuring advanced sensors, displays, and computing power, enable users to engage with digital content in innovative manners. This section delves into essential XR equipment offerings, examining their characteristics, functionalities, and potential utilizations across engineering and other sectors. This section highlights the range of various VR and AR devices on display, with the two flagship devices in each section highlighted, the Oculus Quest 3 and the Apple Vison Pro.

DOI: https://doi.org/10.34961/researchrepository-ul.29290088.v1

Table 1 - Comparison of existing XR Devices

Make	Processor	Memory	Storage	View	Resolution	Battery
Oculus Quest 2	Qualcomm® Snapdragon™ XR2	6GB LPDDR4	128GB/256GB eMMC Flash	100 degrees	1832x1920 per eye	2-3 Hrs
Oculus Quest 3	Qualcomm® Snapdragon™ XR2 Gen 2	8GB DDR5	128GB/512GB eMMC Flash	110 degrees	2064x2208 per eye	2-3 Hrs
Apple Vision Pro	Apple M2 and R1 Chips	16GB Unified Memory	256GB/512GB/1TB	110 degrees	3660x3200 per eye	2Hrs
Google Glass Edition 2	Qualcomm Snapdragon XR1	3GB LPDDR4	32GB eMMC Flash	83 degrees	720px per eye	8Hrs
VUZIX M400	Qualcomm XR1	6GB LPDDR4 RAM	64GB internal flash memory	16.8 degrees	640x360px per eye	2Hrs
Oppo Air Glass	Qualcomm Snapdragon Wear 4100	n/a	n/a	28 degrees	640x480px per-eye	3Hrs
Toshiba dynaEdge	Intel® Pentium® 4406Y	Up to 16GB LPDDR3	128GB - 512GB M.2 SSD	n/a	1280 x 720px per eye	4Hrs
Shadow Creator Action One	Qualcomm Snapdragon 835	8GB	64 GB	45 degrees	1280x720 Per eye	2Hrs
Kopin Solos	n/a	n/a	4GB flash storage	10 degrees	400×240px per eye	5Hrs
Magic Leap One	Nvidia Tegra X2	8 GB	128 GB	50 degrees	1300 px per-eye	3Hrs

Augmented Reality devices, typified by Microsoft HoloLens and Apple Vision Pro, represent another frontier in engineering ingenuity. By leveraging advanced spatial mapping algorithms and depth-sensing capabilities, AR devices overlay digital content onto the physical world with unparalleled precision, revolutionizing fields from industrial design to remote maintenance. Apple launched their first headset in the form of the Vision Pro. This headset is apples first attempt in the XR market, with the AR headset providing user with a new way to consume Apple technology.

Mixed Reality headsets, such as the Magic Leap One and Meta Quest, epitomize the fusion of virtual and real-world elements through sophisticated optical architectures and spatial computing algorithms. These devices offer engineers unprecedented opportunities for prototyping and visualization, enabling seamless interaction with virtual objects in real-world environments. In October of 2023, Oculus released the third generation of their Quest line up, the Quest 3. The Oculus Quest 3 improved on the Quest 2 in all aspects; more RAM, more storage, a better processor, a wider field of view and a better screen all while maintaining the same battery life. The Quest 3 uses the latest Qualcomm® Snapdragon™ XR2 Gen 2 processor. This processor acts as the upgrade to the XR2 featured in the Quest 2, providing the Quest 3 with an all-round smoother experience over the Quest 2. The real improvement of the Quest 3 is the integrated AR capabilities of the headset, allowing it to be a true mixed reality headset.

Furthermore, the rapid pace of technological innovation continues to drive the diversification and refinement of XR hardware. From advancements in display technologies to the miniaturization of sensors, engineering breakthroughs underpin the proliferation of lightweight, high-performance XR devices. As engineers navigate this dynamic landscape, a nuanced understanding of the underlying technologies and design principles is indispensable for harnessing the full potential of XR in engineering applications.

IV. Industry 5.0 and XR

The integration of Extended Reality technologies within the framework of Industry 5.0 heralds a new era of transformation in engineering practices. This subsection explores the symbiotic relationship between XR and Industry 5.0, elucidating how XR innovations redefine engineering processes and foster innovation across disciplines.

XR technologies, including Virtual Reality and Augmented Reality, revolutionize how engineers visualize and collaborate on complex projects. By immersing users in virtual environments, XR facilitates enhanced visualization of intricate designs and simulations. Moreover, XR fosters seamless collaboration among multidisciplinary teams, enabling real-time interaction with digital models and data. This enhanced visualization and collaboration accelerate decision-making, streamline communication, and drive innovation throughout the engineering lifecycle.

In Industry 5.0, XR emerges as a powerful tool for training and skills development in engineering. XR-based training programs offer immersive simulations of real-world scenarios, providing firsthand experience without physical prototypes. Engineers can practice operating machinery, troubleshooting problems, and executing complex procedures in a risk-free virtual environment. This immersive training enhances skill development, improves retention rates, and prepares engineers for diverse challenges in their field.

XR technologies empower engineers to optimize maintenance operations and provide remote assistance in Industry 5.0 environments. AR-enabled devices equipped with real-time data overlays and digital work instructions streamline maintenance tasks, reducing downtime and enhancing equipment reliability. Additionally, XR-based remote assistance enables experts to remotely guide on-site technicians through complex procedures, facilitating rapid problem-solving and knowledge transfer across distributed teams.

Engineers leverage XR technologies to push the boundaries of design and innovation in Industry 5.0. Virtual prototyping allows engineers to iteratively evaluate and refine designs in immersive environments, accelerating the product development process. XR also facilitates the exploration of novel design concepts and the visualization of alternative solutions, fostering creativity and innovation in engineering endeavours.

The integration of XR within the context of Industry 5.0 revolutionizes engineering practices by enhancing visualization, collaboration, training, maintenance, and design innovation. By embracing XR technologies, engineers can unlock new possibilities, drive efficiency, and usher in a new era of transformative innovation in the engineering domain.

V. XR Deployments in Manufacturing

Given that one of the most pressing issues facing manufacturers is the loss of skilled workers as manufacturing transitions towards digitisation. XR provides a way to minimise the loss of the expertise of experienced workers by placing them in the role of remote experts guiding newer technicians and engineers. Here are three examples of how Extended Reality is currently being deployed to enhance manufacturing processes or products.

- Boeing is using AR to improve traditional training practices and has reduced the time required to train an employee in aircraft door assembly by four times. [3]
- Xerox connected field technicians with remote experts and saw a 67% increase in first-time fix rates and a 20% improvement in efficiency, in addition to saving time resolving problems. When used directly by customers, AR produced a 76% increase in customers being able to solve problems themselves, without a technician. [4]
- Another use case is the Volkswagen Group, a manufacturer of automobiles, which began testing AR in their factory in 2016. Their internal AR initiative — one of the first of its kind — uses highly sophisticated lasers to scan finished parts, including full vehicles, and compare them against specifications stored in the cloud. [5]

Equipment maintenance is crucial to the smooth running of most factories. The unexpected breakdown of equipment can cost companies substantial amounts depending on how long the process is halted. Engineers can use the historical data to counteract this, but this alone will still lead to excessive downtime. The use of AR glasses will allow access to the constantly generated equipment data will allow deeper analysis to highlight problem equipment well before it fails to allow them to choose when to maintain the equipment to minimize the fiscal impact. Repair manuals can be accessed in real-time and a walkthrough of how to get access to or removal and refitting of parts can be displayed on an AR headset. This will lead to more efficient repairs and significantly less mentoring for training staff. With production and flow values displayed in near real-time Identifying bottlenecks is easier. The cause of the slowdown can be identified and recommended action scenarios can be analysed to make an informed change to alleviate the problem. The data can also help identify repeated actions and by eliminating repetitive tasks the process can be streamlined maximizing output.

Figure 1 - XR support for a manufacturing environment.

VI. 5G and Extended Reality

XR content requires an enhanced wireless connection. High bandwidth connectivity to share and consume the XR content. The technology predominantly shaping the future of communications and computing currently is 5G. Technologies and user acceptance are aligning for 5G Mobile technologies widespread deployments; this is accelerating XR adoption. [6]

5G connectivity has the potential to unleash a tidal wave of innovative XR experiences that require low latency and ultra-fast data speeds. What makes 5G revolutionary is the reduced latency. The stability and low latency that 5G networks will bring and the utilising of short-range frequencies, as well as advancements within both hardware and software, is making the industry excited about the future use cases and applications of XR.

It is envisaged that 5G will be the next substantial change in cellular technology spurring a new era of intelligent, connected devices and enabling new opportunities in the ever-growing volume of connected cars, remote delivery of health care services, and the IoT - including smart cities, smart homes, and wearables.

All aspects of AR, VR, and MR are data-heavy, so the faster connections drastically reduced latency, an increased number of connected devices with 5G allow for a more seamless and richer XR user experience.

Figure 2 - VR Headsets

VII. XR Potential with 5G and Next-Gen Networks

Traditional model VR headsets, as shown in figure 4 are still at the top of the value for money/usability indexes. The Oculus Rift, HTC, and Rift S work in tandem with a PC to deliver virtual reality experiences. They connect to your PC via a USB 3.0 port and a DisplayPort connection, using a lengthy cable that comfortably accommodates the room-scale experiences that the Rift S can provide. It's more limiting in terms of free movement than the superb wireless Oculus Quest, but the trade-off is that, by being powered by a PC, it's capable of powering more detailed and dynamic experiences.

Next-Gen Wi-Fi and 5G networks offer manufacturers the chance to build smart factories and truly take advantage of technologies such as automation, artificial intelligence, and extended reality for troubleshooting whilst leveraging the growth in the deployment of Internet of Things (IoT) devices. The continued automation of robots and warehouse transportation and cutting cables to become truly flexible continues to become more of reality daily. 5G and IoT will be key to enhancing and enabling these advances in manufacturing.

Figure 3 – Limitless uses of AR – virtual details layered over real world location.

Qualcomm has released the XR2 Snapdragon platform for extended reality. The XR2 platform is the world's first 5G-supported extended reality (XR) platform. The Oculus quest 2 was developed upon the first generation of Qualcomm's XR2 platform, and the newer Quest 3 was then built upon the enhanced second generation of the XR2 to provide an improved experience on the newer Oculus flagship model.
It will not demand that users are at home connected to Wi-Fi, they can now be outside away from their owners' Wi-Fi network and still able to stream high-quality video into the headset. The Snapdragon XR2 Platform comes with other improvements also, compared to the current widely adopted premium-tier XR platforms it improves on the previous model by not only having twice the CPU and GPU performance, four times more video bandwidth, six times higher resolution but also with 11x AI improvement. The Snapdragon XR2 Platform supports seven (7) concurrent cameras and a dedicated computer vision processor. [7]

Another example of the type of headsets available capable of supporting Next-Gen networks is the VUZIX M400 SMART LENS, which runs on Android and offers USB-C connectivity. As the necessary technologies have become more ubiquitous and evolved to be ergonomically less obtrusive, new markets and use cases have emerged. These types of smart glasses allow forward-thinking manufacturers to capitalise on features such as built-in GPS, a multi-finger support pad, noise-cancelling earphones, wireless connectivity, 4K cameras, native voice processing, motion tracking, and head tracking. [8]
To meet the demands of a truly immersive XR environment, the Vuzix platform has customized visuals, interactivity, and audio technologies, all of which utilize the foundational technologies of AI and with an option of 5G connectivity. The opportunities provided by these 5G-enabled smart glasses mean that XR can now extend beyond the confines of buildings, utilizing the expanding 5G networks to enable a wide range of future use cases.

VIII. XR Deployment Challenges

Extended Reality technologies have emerged as powerful tools for creating immersive virtual environments, but their implementation poses significant challenges. Firstly, XR technologies collect and process vast amounts of detailed data, necessitating robust data protection measures. Moreover, the creation of virtual environments demands powerful computer systems to manage the computational load. Consequently, organizations must navigate the dual challenge of managing voluminous data and complying with legislative data security requirements. A comprehensive data management policy is essential before XR deployment to address these concerns effectively.

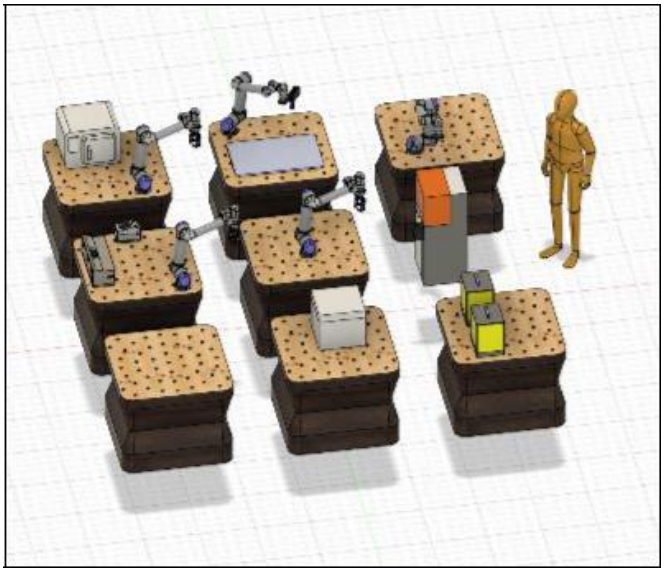

Figure 4 – Virtual Environment for use with headset for virtual control.

The seamless operation of virtual environments relies on streaming relevant data to users in real-time with minimal latency. This is crucial due to the high bandwidth needed for adaptive graphics, with streaming requirements ranging from 1.5Mbps for standard definition to 25Mbps for ultra-high-definition applications. The proprietary nature of XR software limits the use of network proxies or caching services, as XR systems demand reliable quality of service, which could be compromised by proxies or caching.

Cost is another significant consideration hindering the adoption of XR technologies, particularly for enterprises. Immersive setups such as the immersive cave system may be financially prohibitive for many organizations. However, alternatives such as smart glasses offer a more affordable option for certain use cases, mitigating the financial burden associated with XR deployment.

Despite the rapid development of XR technologies, there remains a significant lack of awareness among potential users regarding their advantages, disadvantages, and applications. Therefore, concerted efforts are needed to raise awareness and educate stakeholders about XR technologies and their potential implications.

IX. Conclusions

Manufacturing is one of the markets most heavily impacted by IoT today. It is estimated that the number of sensors globally will grow to over twenty-six billion by 2050 (Gartner, 2018) Manufacturers are realizing that by engineering IoT technology into products and equipment already in the design process, engineers and managers will be able to monitor not only the equipment's performance to predict when it needs repair, but also how and when it is being used — -providing game-changing competitive advantages. Currently, the manufacturing industry is using/delivering extended reality experiences over the 4G network, these experiences require a lot of data to be processed which can strain the network. Immersive XR collaboration tools have the potential to improve processes and support remote workers in many industries. 5G's bandwidth and latency capabilities give the ability to have a collaborative session with multiple connected devices anywhere in the world, enabling users to share data and interact in near real-time. It is an area that requires further research; to identify use cases that provide end to end capabilities and explore the limitations they impose on network infrastructures as XR deployments grow in usage and deployments.

X. References

[1] Å. F.-B. L. G. D. Li, "Testing and validating Extended Reality (xR) technologies in manufacturing," *Procedia Manufacturing*, vol. 25, 2018, doi: 10.1016/j.promfg.2018.06.054.

[2] R. D. Gandhi and D. S. Patel, "Virtual reality–opportunities and challenges," *Virtual Reality*, vol. 5, no. 01, 2018.

[3] M. Campbell, S. Kelly, R. Jung, and J. Lang, "The State of Industrial Augmented Reality 2017," ed: PTC, White Paper, 2017.

[4] M. E. Porter and J. E. Heppelmann, "Why every organization needs an augmented reality strategy," *HBR'S 10 MUST,* p. 85, 2017.

[5] A. Doshi, R. T. Smith, B. H. Thomas, and C. Bouras, "Use of projector based augmented reality to improve manual spot-welding precision and accuracy for automotive manufacturing," *The International Journal of Advanced Manufacturing Technology*, vol. 89, no. 5-8, pp. 1279-1293, 2017.

[6] H. Nagata, D. Mikami, H. Miyashita, K. Wakayama, and H. Takada, "Virtual reality technologies in telecommunication services," *Journal of Information Processing*, vol. 25, pp. 142-152, 2017.

[7] H.-J. Zepernick, "Toward immersive mobile multimedia: From mobile video to mobile extended reality," in *2018 Third International Conference on Informatics and Computing (ICIC)*, 2018: IEEE, pp. 1-6.

[8] P. J. Travers and M. McCrackan, "Interactive wearable and portable smart devices," ed: Google Patents, 2019.

38: A DISTURBANCE LOCALIZATION METHOD BASED ON REGION SEGMENTATION AND FNLM ALGORITHM FOR Φ-OTDR

Wei Shen [a], *Chengyong Hu* [a], *Ziyi Wei* [a], *Yi Huang* [a], *Chuanlu Deng* [a], *Qi Zhang* [a], *Sujuan Huang* [a], *Xiaobei Zhang* [a], *Tingyun Wang* [a, *]

[a] Key Laboratory of Specialty Fiber Optics and Optical Access Networks, Joint International Research Laboratory of Specialty Fiber Optics and Advanced Communication, Shanghai Institute for Advanced Communication and Data Science, Shanghai University, Shanghai, China.

* Corresponding author: tywang@shu.edu.cn

Abstract – Aiming at the problem of the low real-time performance of phase-sensitive optical time-domain reflectometer (Φ-OTDR) technique in disturbance localization, a localization method based on the combination of region segmentation and fast non-local means (FNLM) algorithm is proposed. By dividing the whole link of the fiber optic into regions, the disturbance region is quickly located. The FNLM algorithm is introduced to process the signals of the perturbed target region, which is intended to further achieve the precise positioning of the perturbation location. Experiments are conducted using a Φ-OTDR system to test the localization of disturbances at three frequencies. The results show that the region segmentation approach can reduce the computation to a large extent, resulting in an order-of-magnitude reduction in processing time. The introduction of the FNLM algorithm enables the system to maintain a low positioning error of 2.47 m while positioning quickly.

Keywords: Phase-sensitive optical time-domain reflectometer; Disturbance localization; Fast non-local means; Noise reduction; Fast positioning

1. INTRODUCTION

As a distributed optical fiber sensing technology, phase-sensitive optical time domain reflectometer (Φ-OTDR) has been widely used in the field of perturbation positioning due to its advantages such as its fast response speed, large dynamic range, and wide measurement range [1]. However, in practical applications, the positioning effect of the system can be unsatisfactory due to the long link for laying optical fibers, the complexity of the surrounding terrain and the susceptibility to environmental noise. Although the positioning effect can be improved by upgrading the performance of the system hardware, the overall cost will increase subsequently. Therefore, in recent years, fast and efficient positioning algorithms have become one of the key research directions in this field.

Reference [3] proposed a fusion noise reduction method based on empirical mode decomposition and time-frequency peak filtering (EMD-TFPF) algorithm. The EMD algorithm is used to reduce the initial noise level, and the random noise is further suppressed by the TFPF algorithm, which make it possible to extract the position information of low-frequency disturbances in strong background noise. Reference [3] proposed a variable step size normalized least mean square (VSS-NLMS) denoising method, which can adaptively filter the input signal and adjust the parameters. The signal-to-noise ratio (SNR) is improved by 13.17 dB. Reference [4] proposed a Rayleigh backscattering (RBS) signal denoising method based on sparse representation. In this method, the effective signals can be sparsely represented by the linear combination of dictionary atoms, while the noise signals are discarded as the residual. This method makes the noise separated and improves the SNR of the system by 3.44 dB. Although the introduction of some advanced signal processing strategies can improve the positioning performance of Φ-OTDR systems, the data computation time will subsequently increase, which is unsatisfactory for the real-time demand in practical applications.

In this work, a method that combines region segmentation with the fast non-local means (FNLM) algorithm is proposed. The full fiber-optic link is spatially divided into subregions at equal distances, and the disturbance region is initially identified by processing the phase difference signals in each region. Afterwards, the amplitude signals of the corresponding region are differenced and converted into two-dimensional (2D) grey-scale images. On this basis, the FNLM algorithm is introduced to reduce the noise and smooth the image to achieve the final disturbance localization. The experimental results show that the proposed method enables the fast determination of the perturbation location while maintaining a low localization error.

2. METHODS AND PROCEDURES

The flowchart of the proposed method is shown in Figure 1. The phase and amplitude signals are obtained by demodulating the raw RBS signals acquired by the Φ-OTDR system, both of which are divided into the same number of subregions in the spatial dimension. The length of each subregion is a fixed number of spatial sampling points. The phase signal $\varphi_l(t)$ at the lth region splitting point is first obtained by demodulation. Subsequently, the phase signals of the two endpoints of each subregion are differentiated, and the phase difference signal is used to indicate the perturbation of each subregion. On this basis, disturbance determinations are made for each region to initially identify the region where the disturbance is located. The corresponding perturbed region is selected from the matrix of amplitude signals that have been regionalized in the same way. Then the 2D matrix of this region is differenced in the time dimension to highlight the perturbation traces, whose noise will be reduced by using the FNLM algorithm. Finally, the location of the perturbation is framed.

DOI: https://doi.org/10.34961/researchrepository-ul.29290178.v1

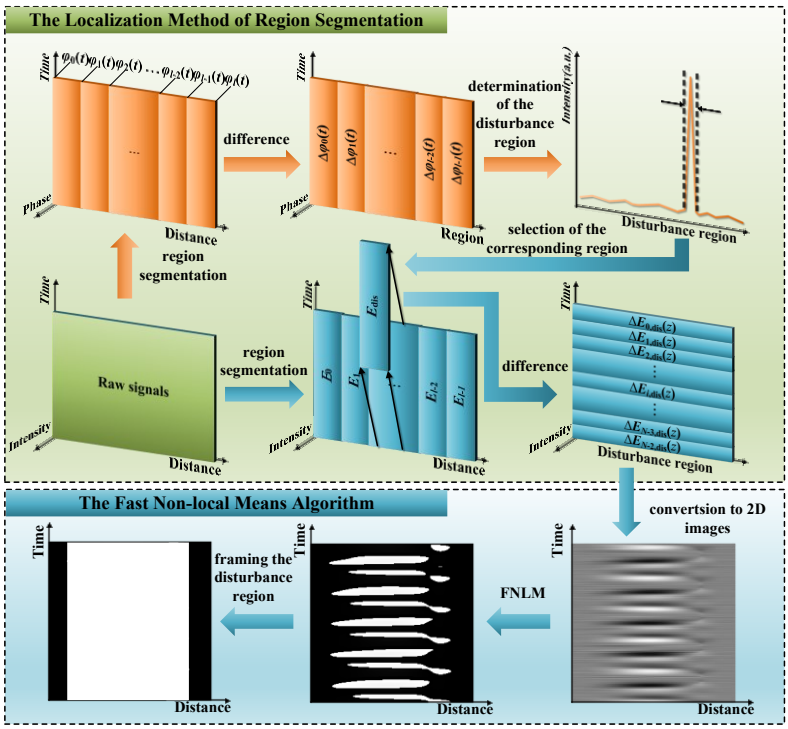

Figure 1. Flow diagram of the localization method.

2.1 The localization method of region segmentation

The coherent detection Φ-OTDR system emits light pulses with a high degree of coherence due to the use of the narrow linewidth laser (NLL) as the light source. The RBS light generated within the range of optical pulses in the sensing fiber optic is coherently superimposed, enabling the detection of weakly disturbed signals. When the fiber optic is externally perturbed, the phase of the RBS light at the point of perturbation changes, ultimately leading to a change in the amplitude of the RBS light [5]. With the help of certain algorithms, the combination of phase and amplitude signals can effectively realize the localization of disturbance on the fiber optic link.

The signals acquired by the Φ-OTDR system each time can be expressed as a matrix of size $N \times M$, which represents N RBS signals with spatial sampling points of M. The proposed localization method selects observation points at intervals of k sampling points among M spatial sampling points to achieve an equally spaced division of the entire fiber optic, as shown in Figure 2. Here a piezoelectric ceramic transducer (PZT) is used and a signal is applied to it as a source of disturbance on the optical fiber.

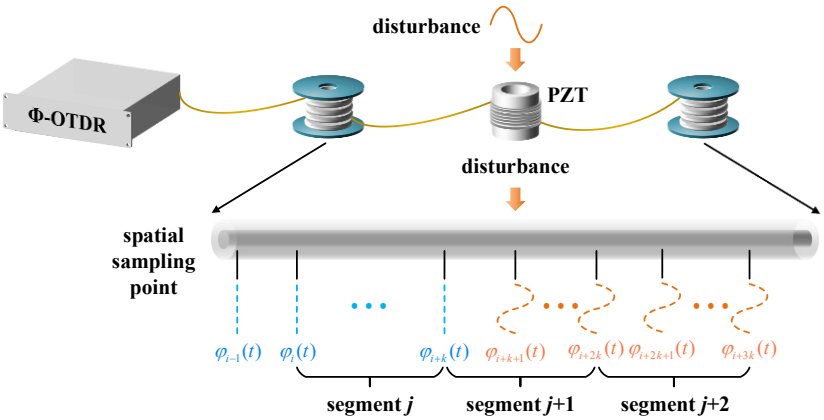

Figure 2. Schematic diagram of region segmentation.

For phase signals, only the phase signals at the ends of each subregion are retained to form the phase matrix, which can be expressed as

$$\boldsymbol{\Phi} = [\varphi_0(t), \varphi_k(t), \cdots, \varphi_{nk}(t)], \quad (1)$$

where $\varphi_i(t)$ is the phase time-domain signal at the position of the ith spatial sample point, and $n = \lceil M / k \rceil$, which is the total number of subregions divided at intervals of k spatial sampling points. Aiming to characterize the overall disturbed condition of the subregion segment, the phase signals at the ends of each subregion are differenced to obtain a phase difference time domain signal for each subregion, which can simultaneously eliminate the effects of the initial randomness of the laser phase and the phase noise accumulated at the front

end of the fiber optic [5]. The phase difference time-domain signal can be expressed as

$$\Delta\varphi_j(t) = \varphi_{kj}(t) - \varphi_{k(j-1)}(t)\ ,\ 1 \le j \le n\ , \tag{2}$$

where $\Delta\varphi_j(t)$ denotes the phase difference time-domain signal corresponding to the jth subregion. External disturbances on the sensing fiber will cause large fluctuations in the phase difference signal within the corresponding region, the variance of the signal can be consequently calculated to reflect the degree of fluctuation to achieve the determination of the disturbed region, which can be written as

$$V(j) = \frac{1}{N}\sum_{i=1}^{N}\left[\Delta\varphi_j(i) - \overline{\Delta\varphi}_j\right]^2\ ,\ 1 \le j \le n\ , \tag{3}$$

where N denotes the total number of samples of the phase difference signal in the time domain, $\Delta\varphi_j(i)$ is the phase value of the phase difference signal within the jth subregion at the ith time sampling point, and $\overline{\Delta\varphi}_j$ is the average value of the phase at all time points on the jth subregion.

Once the disturbed region has been initially identified, the amplitude signal can be used for the next step in the processing. When an external perturbation causes a change in the RBS light in an optical fiber, the amplitude signal reflects more directly the change in the intensity of the optical signal, helping to locate the source of the perturbation more accurately. During processing, the amplitude signal matrix $\boldsymbol{E}$ is divided into regions in the same way, which can be expressed as

$$\boldsymbol{E} = [\boldsymbol{E}_0, \boldsymbol{E}_1, \cdots, \boldsymbol{E}_{j-1}, \boldsymbol{E}_j]\ , \tag{4}$$

where $\boldsymbol{E}_j$ is the amplitude signal matrix of the jth subregion. Based on the initial localization result of the phase signal, the corresponding region $\boldsymbol{E}_{\text{dis}}$ in the amplitude signal where the disturbance occurs is selected. The region $\boldsymbol{E}_{\text{dis}}$ can be represented as

$$\boldsymbol{E}_{\text{dis}} = \left\{E_{0,\text{dis}}(z), E_{1,\text{dis}}(z), \cdots, E_{i,\text{dis}}(z), \cdots, E_{N-1,\text{dis}}(z)\right\}\ , \tag{5}$$

where $E_{i,\text{dis}}(z)$ represents the amplitude signal corresponding to the ith RBS signal in this region, and z is the sampling point in the spatial dimension. The amplitude signals within region $\boldsymbol{E}_{\text{dis}}$ are differenced in the time dimension, which can effectively improve the comparability of time series signals. The differential amplitude signal can be calculated as

$$\Delta E_{i,\text{dis}}(z) = E_{i+1,\text{dis}}(z) - E_{i,\text{dis}}(z)\ , \tag{6}$$

where $\Delta E_{i,\text{dis}}(z)$ represents the result of differencing a sequence of amplitude signals. The overall differential amplitude signal can be written as

$$\Delta\boldsymbol{E}_{\text{dis}} = \left\{\Delta E_{0,\text{dis}}(z), \Delta E_{1,\text{dis}}(z), \cdots, \Delta E_{i,\text{dis}}(z), \cdots, \Delta E_{N-2,\text{dis}}(z)\right\}\ . \tag{7}$$

The processed amplitude signal will be converted into a 2D image, which combined with the subsequent image noise reduction algorithm can be used for further disturbance determination.

2.2 The fast non-local means algorithm

The non-local means (NLM) algorithm performs noise reduction filtering by selecting the pixel points to be processed. When filtering noise, the pixel points with similar features within the window are weighted and averaged by setting a search window to minimize the loss of the image itself [7]. Therefore, NLM algorithm is widely used in 2D image denoising. Since the 2D signals acquired by the Φ-OTDR system have similar characteristics, the NLM algorithm is also suitable for Φ-OTDR vibration signal processing to achieve the effect of reducing the localization signal noise. The amplitude signal $E_{\text{NLM}}(i)$ processed by the algorithm can be expressed as

$$E_{\text{NLM}}(i) = \frac{1}{N(i)}\sum_{j\in D}\omega(i,j)x(i)\ , \tag{8}$$

where $\omega(i, j)$ represents the weight, and it can be interpreted as the similarity between two search windows centered on i and j. D denotes the search window and $x(i)$ is the pixel intensity in the search window. $N(i)$ is a normalization parameter that represents the sum of the similarity of all search windows, and it can be expressed as

$$N(i) = \sum_{j\in D}\omega(i,j)\ . \tag{9}$$

During the search for pixel points, if the similarity between two samples is higher, the weight $\omega(i, j)$ will be higher and vice versa. The weight $\omega(i, j)$ can be expressed as

$$\omega(i,j) = \exp\left(\frac{-\left\|I(D(i)) - I(D(j))\right\|_{2,G_k}^2}{h^2}\right)\ , \tag{10}$$

where $I(D(i))$ and $I(D(j))$ respectively denote the intensity of the pixel blocks centered at points i and j in the search window D. h denotes the smoothing parameter, which is used to control the degree of decay and denoising strength of the exponential function, and G_k is the Gaussian kernel function.

In the NLM algorithm, each time the distance between neighbours is calculated, it is necessary to traverse each pair of pixel points in the two neighbourhoods to find the difference, which results in the need for significant computational time. If the image has T pixel points, the search window size is $D \times D$ and the neighbourhood window size is $d \times d$, the time to compute the similarity between two rectangular neighbourhoods is $O(d^2)$. For each pixel point, the similarity between it and D^2 pixels in the search window needs to be calculated, so the algorithm complexity is $O(TD^2d^2)$.

In order to reduce the complexity and increase the computational efficiency, the integral image method is introduced to optimize the algorithm. The original image is converted to an integral image by summing all the pixel values within the rectangular area in the upper left corner of each point in the original image. An integral image can be constructed as

$$S_t(x_1,x_2) = \sum_{z_1\le x_1, z_2\le x_2} I(z_1,z_2)\ , \tag{11}$$

where $I(z_1, z_2)$ represents the pixel value at the position (x_1, x_2) of the image. The integral image can be computed in an incremental manner [7]. The calculation of the distance between two neighbourhoods can be done in constant time and the complexity of the algorithm will be reduced to $O(TD^2)$.

3 EXPERIMENTAL RESULTS AND DISCUSSION

3.1 Experimental setup

A coherent detection type Φ-OTDR system was built in the experiment, and the system structure is shown in Figure 3. The continuous light from a NLL with a central wavelength of 1550 nm is divided into detection light and local oscillation light in a ratio of 90:10 after passing through an optical coupler (OC1). An acousto-optic modulator (AOM) modulates continuous detection light into pulse light and provides a frequency shift of 200 MHz. The detection pulse light is amplified by an erbium-doped fiber amplifier (EDFA) and fed into port 1 of the circulator and through port 2 into the fiber under test (FUT), where the pulsed light is repetitive at a frequency of 1 kHz with a pulse width of 100 ns. The RBS light generated during transmission returns to the circulator and is output through port 3 of the circulator, where it interferes with the local oscillation light at the 50:50 fiber optic coupler (OC2) to generate the beat signal. Finally, the beat signal is photoelectrically converted by a balanced photodetector (BPD). The converted electrical signals are collected by a data acquisition card (DAQ) with a sampling rate of 500 MS/s and sent to a personal computer (PC) for data processing and analysis.

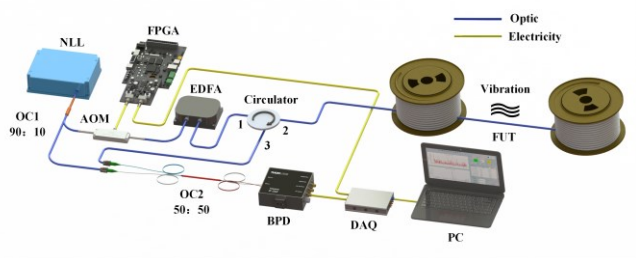

Figure 3. Schematic diagram of the Φ-OTDR system.

A single-mode fiber with a total length of 3 km is connected to the Φ-OTDR system as the FUT. The fiber is wound around a PZT at the disturbed target location and the PZT is driven to vibrate to simulate external disturbances. In the experiments of this paper, the PZT is placed at 2050 m of the FUT and a sinusoidal signal of 10 Hz is applied to it as a perturbation. 256 RBS signals generated after the emission of pulsed light are collected in one detection cycle, and the size of the acquired raw signal matrix is 256×15674.

3.2 Experimental results and analysis

For the region segmentation localization method, the length of each subregion needs to cover the disturbed area to ensure that the disturbance will not span an entire region and thus affect the subsequent noise reduction process. Therefore, the length of the region division in this experiment is 256 spatial sampling points to cover the vibration range of most of the perturbation events. The fiber optic length corresponding to the 256 sampling points is approximately 54 m. The size of the differential phase matrix obtained after region segmentation and phase differencing is 256×62. Preliminary disturbance localization results are obtained by doing a variance operation on each column of the matrix, as shown in Figure 4. The position indicated by the localization peak is the 40th region, which corresponds exactly to where the actual disturbance is located.

Based on the initial localization of the perturbation, the corresponding region of the amplitude matrix is differentiated to highlight the change in the perturbation, and the converted 2D image is shown in Figure 5. Different from the neighbouring domains, periodically varying stripes are visible in the intermediate region.

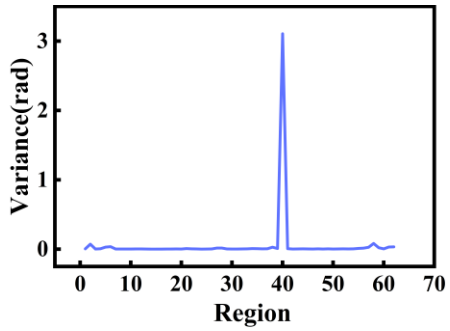

Figure 4. Disturbance localization curves after region segmentation.

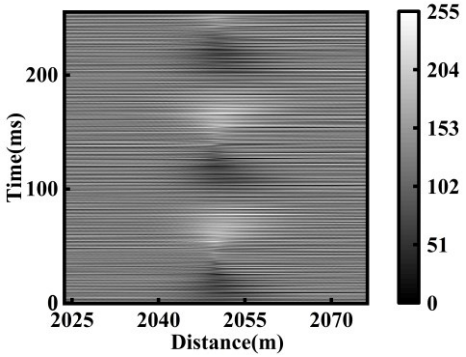

Figure 5. Differential 2D amplitude signal.

The FNLM algorithm is subsequently used for noise reduction and smoothing of the image. To further validate the effectiveness of the proposed method, 10 Hz, 20 Hz and 50 Hz signals are respectively applied to the PZT to perform multiple localization tests. The multiple 2D images processed by the FNLM algorithm are shown in Figure 6. Due to the weighted average processing of the FNLM algorithm, the image becomes smoother and the noise is suppressed. Meanwhile, for different frequencies of disturbances, the stripes in the middle region all show corresponding changes.

In order to further determine the location of the perturbation, the output signal after noise reduction processing is subjected to a disturbance framing process, where the grey-scale image is binarized, and the perturbation region is framed using the adaptive thresholding method. The results are shown in Figure 7 and Figure 8. The perturbation traces of each frequency are more evident after binarization. The center point of the framed area is chosen as the final disturbance determination point, from which the actual positioning point after processing can be obtained. For the three perturbed positioning test results, the final maximum positioning error is only 2.47 m.

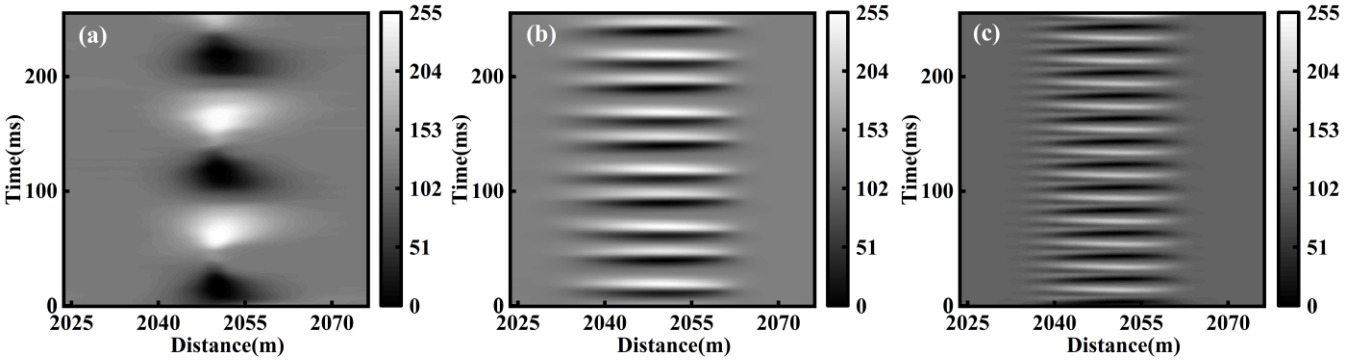

Figure 6. Images of disturbed regions after processing by the FNLM algorithm. (a) 10 Hz, (b) 20 Hz, (c) 50 Hz.

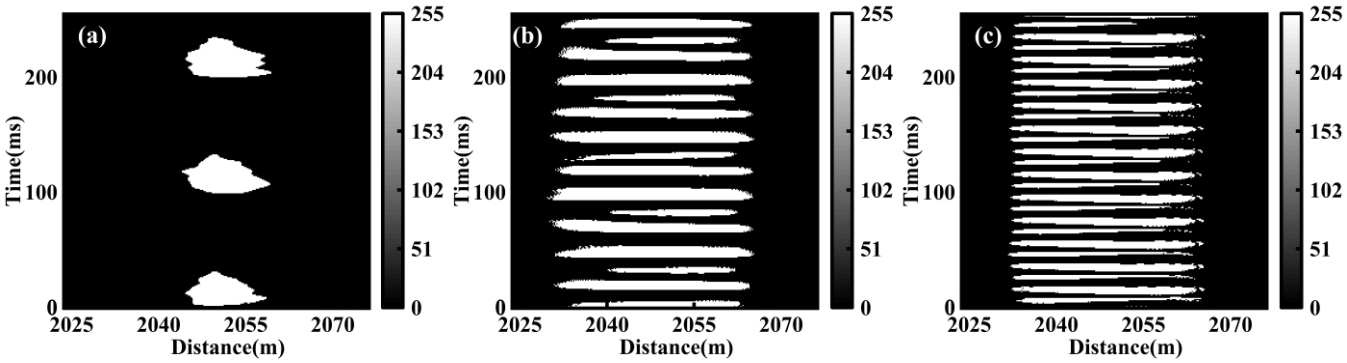

Figure 7. Images of disturbed regions after binarization. (a) 10 Hz, (b) 20 Hz, (c) 50 Hz.

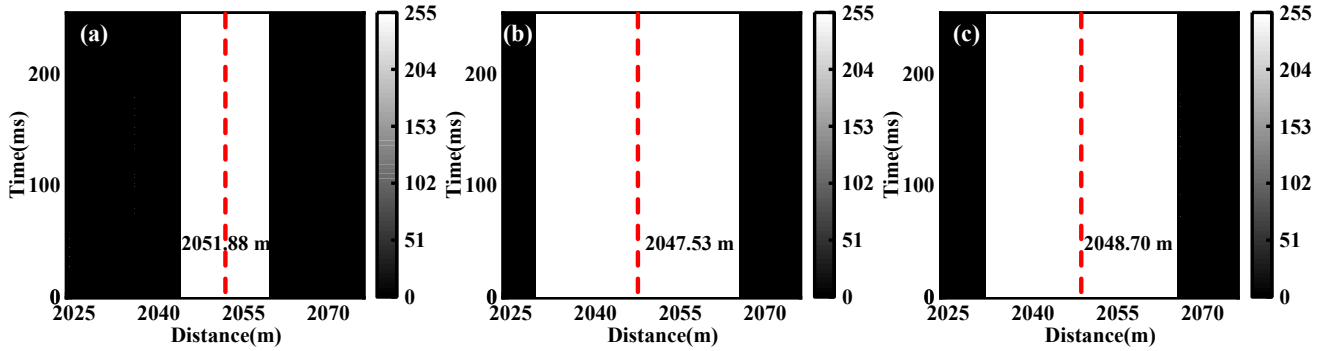

Figure 8. Images of framing disturbance. (a) 10 Hz, (b) 20 Hz, (c) 50 Hz.

In order to highlight the effectiveness of the combination of region segmentation combined with the FNLM algorithm, the computational time used by this method is compared with that used by the FNLM algorithm alone, and the results are shown in Table 1. Due to the fact that the region segmentation reduces the overall computational effort and the combined FNLM algorithm has low computational complexity, the processing time of the disturbance localization used in the proposed method are all lower than the normal FNLM algorithm. The average processing time is reduced by 3.287 s.

Table 1. Comparison of calculation times used by different methods.

Type of disturbance	The proposed method /s	FNLM /s
10 Hz	0.172	3.185
20 Hz	0.192	3.145
50 Hz	0.196	4.092

4 CONCLUSIONS

In order to improve the real-time and accuracy of the Φ-OTDR system in the practical application of disturbance localization, this paper proposes a localization method that combines the area division and the FNLM algorithm. Firstly, the phase and amplitude signals are divided into equal subregions along the spatial direction in the same way, and the region where the disturbance is located is quickly captured by calculating the variance of the phase difference signal in each subregion. Then, the amplitude signal of the disturbance region is extracted and differenced to convert it into a 2D image containing the perturbation, and accurate localization is achieved by introducing the FNLM algorithm. Finally, the Φ-OTDR system is used to test the localization of disturbances at different frequencies. The experimental results show that the proposed method can reduce the time of

positioning computation by an order of magnitude while maintaining a low positioning error of 2.47 m. This provides a promising solution for real-time positioning of disturbances based on Φ-OTDR.

ACKNOWLEDGMENTS

This work was supported by the Key Laboratory of Specialty Fiber Optics and Optical Access Networks at Shanghai University.

FUNDING STATEMENT

This work was supported by National Natural Science Foundation of China (62022053, 62027818); Science and Technology Commission of Shanghai Municipality (22ZR142300, 22010500100, 22ZR1424800); 111 Project (D20031); Advanced Optical Waveguide Intelligent Manufacturing and Testing Professional Technical Service Platform of Shanghai (19DZ2294000).

REFERENCES

[1] Y. J. Rao, Z. N. Wang, H. J. Wu, Z. L. Zeng. B. Han, **Recent advances in phase-sensitive optical time domain reflectometry (Φ-OTDR)**, Photonic Sens., vol. 11, no. 1, 2021, pp. 1-30.
DOI: https://doi.org/10.1007/s13320-021-0619-4

[2] Y. X. Bai, T. T. Lin, Z. C. Zhong, **Noise reduction method of Φ-OTDR system based on EMD-TFPF algorithm**, IEEE Sens. J., vol. 21, no. 21, 2021, pp. 24084-24089.
DOI: https://doi.org/10.1109/JSEN.2021.3107039

[3] Q. L. Ma, X. Gao, Y. Gao, **A study on noise reduction of Φ-OTDR system based on VSS-NLMS algorithm**, IEEE Sens. J., vol. 21, no. 6, 2021, pp. 7648-7656.
DOI: https://doi.org/10.1109/JSEN.2021.3049390

[4] J. C. Li, Y. Wang, X. Liu, Q. Bai, B. Q. Jin. **SNR improvement for Φ-OTDR with sparse representation denoising method**, Opt. Fiber Technol., 76, 2023, 103231.
DOI: https://doi.org/10.1016/j.yofte.2023.103231

[5] Z. Y. Wang, B. Liu, Q. Ye, H. W. Cai, **Recent progress in distributed fiber acoustic sensing with Φ-OTDR**, Sensors, vol. 20, no. 22, 2020, 6594.
DOI: https://doi.org/10.3390/s20226594

[6] Z. Zhong, F. Wang, M. Zong, Y. X. Zhang, X. P. Zhang, **Dynamic measurement based on the linear characteristic of phase change in Φ-OTDR**, IEEE Photonics Technol. Lett.,vol. 163, no. 6, 2021, pp. 1191-1194.
DOI: https://doi.org/10.1109/LPT.2019.2921608

[7] M. F. Wu, Y. F. Chen. P. B. Zhu, W. Chen, **NLM parameter optimization for φ-OTDR signal**, J. Lightwave Technol., vol. 40, no. 17, 2022, pp. 6045-6051.
DOI: https://doi.org/10.1109/JLT.2022.3186830

[8] S. H. Kang, J. Y. Kim, **Application of fast non-local means algorithm for noise reduction using separable color channels in light microscopy images**, Int. J. Environ. Res. Public Health, vol. 18, no. 6, 2021, 2903.
DOI: https://doi.org/10.3390/ijerph18062903

39: CYBER RANGES – REAL WORLD SKILLS DEVELOPMENT FOR OT & IT CYBERSECURITY EDUCATION

Dr George D. O'Mahony [a]*, *Paudie Walsh* [b], *Killian Sanceo* [c], *Dean Brennan* [a], *Dr Muzaffar Rao* [b], *Prof. Thomas Newe* [b] *& Prof. Donna O'Shea* [a]

[a] Dept. Computer Science, Munster Technological University, Cork, Ireland,

[b] Dept. Electronic & Computer Engineering, University of Limerick, Limerick, Ireland,

c Airbus Defence and Space Cyber,

Emerging Sensing Strategies and Applications, EM010, August 14, 2024, 9:30 AM - 10:30 AM

Abstract − Cybersecurity has emerged as a primary concern for governments, organizations, and citizens. However, a significant deficit persists in the number of available cybersecurity professionals and the skill sets of those already in the field. This characteristic results in insufficient numbers of skilled professionals and doubts among companies regarding graduates' readiness for the workforce due to perceived inadequacies in essential skills. Additionally, cyberattacks are prevalent but the consequences mean professionals aim to prevent as many breaches as possible and reduce the impact, contain and eradicate any attack that exploit a system. The problem that arises is that cyber security professionals require realistic breach scenarios and cyberattacks to train and become sufficiently skilled but cyber professionals are consistently working hard to prevent such attacks in the real-world. The research question that this paper explores is how do we train cyber security professionals to deal with the challenging ever-changing cyber environment and ensure new technologies will not negatively impact security? This paper investigates the use of Cyber Range technology, particularly a mobile cyber range, as the identified solution in education.

Figure 1: Airbus Mobile Cyber Range

A cyber range is a secure sandbox environment designed to provide hands-on training and research and development in cybersecurity. This virtual environment is designed to mimic real-world enterprise infrastructures including Information and communications technology (ICT), operational technology (OT), mobile, software and physical systems, applications, networking systems, traffic, and threats, allowing users to interact with and respond to dynamic and challenging cybersecurity scenarios. The mobile cyber range enables the simulation/emulation of cyber-attacks, users and their activities. For this paper, an Airbus Mobile Cyber Range, Figure 1, will be utilized in the context of understanding the importance of cyber range technology for education and skill development. The mobile Cyber Range provides additional capabilities for cybersecurity skill development as it includes a physical switch that can be connected to lab environments, specific hardware and Internet of Things (IoT) networks deployed on physical assets such as monitoring and control systems. Additionally, the cyber range environment can load software applications for security skills assessment or for the gamification of cybersecurity education.

In cybersecurity education, this paper explores several critical benefits that the mobile cyber range offers for skill development across IT, OT and IoT domains, including:

- Realistic Simulation: The cyber range provide a safe, controlled environment where students can encounter the types of cyber threats they will face in real-world scenarios. This practical experience is invaluable for understanding the complexities and dynamics of enterprise security.
- Hands-on Learning: By engaging directly with the systems and tools used in cybersecurity, learners can develop practical skills that are difficult to acquire through traditional lecture-based education.
- Skill Assessment and Enhancement: Cyber ranges allow both instructors and learners to assess skills in a tangible way, through, for example, capture the flag, gamified learning scenarios where users can receive immediate feedback on their actions and decisions, helping them to improve and refine their capabilities over time.
- Projects: These environments are ideal for developing university level cybersecurity projects for additional hands-on research and skill development without the risk of affecting real networks. This encourages innovation and experimentation, leading to advancements in security practices and tools.

DOI: https://doi.org/10.34961/researchrepository-ul.29290265.v1

- Teamwork and Collaboration: Cybersecurity often requires coordinated efforts among various team members. The cyber range can simulate multi-threat scenarios that necessitate teamwork, thus helping learners to develop communication and collaboration skills crucial for effective incident response.
- Compliance and Best Practices: With cyber range technology, educators can ensure that their students are well-versed in compliance requirements and industry best practices. This is essential for maintaining security standards and protecting against legal or financial repercussions.

Overall, this paper analyses how the mobile cyber range is a requirement for modern cybersecurity education, equipping individual students with the necessary skills to protect digital assets and respond effectively to incidents. Their role in developing a skilled cybersecurity workforce with real-world applicable skills is vital as threats continue to evolve and increase in sophistication. The work will also emphasise the importance of tailoring the education learning environment using a cyber range to create a positive student experience and combat the current skills deficit in this crucial area.

40: OPTICAL FIBER-BASED SENSOR USING THE LOCALIZED SURFACE PLASMON RESONANCE EFFECT

V.R. Anand[a], *Abhijnan Bhat*[b], *Baljit Singh*[b,c], *Zhe Wang*[a], *Zhuochen Wang*[a], *Anuradha Rout*[a], *Rayhan Habib Jibon*[a], *Furong Tian*[b,d], *Yuliya Semenova*[a*]

[a] Photonics Research Centre, School of Electrical and Electronic Engineering, Technological University Dublin, Grangegorman, Dublin 7, Ireland

[b] School of Food Science & Environmental Health, Technological University Dublin (TU Dublin), Grangegorman, Dublin, D07 ADY7, Ireland

[c] MiCRA Biodiagnostics Technology Gateway, Technological University Dublin (TU Dublin), Dublin, D24 FKT9, Ireland

[d] Nanolab Research Centre, FOCAS Research Institute, Technological University Dublin (TU Dublin), Camden Row, D08 CKP1 Dublin, Ireland

* Corresponding author and e-mail address: yuliya.semenova@tudublin.ie

Abstract – This paper reports and experimentally demonstrates a localized surface plasmonic resonance (LSPR) refractive index sensor based on gold nanoparticles (AuNPs) coated multimode optical fiber. The optical properties of the AuNPs were modelled using the finite element method (FEM) simulation model. AuNPs were synthesised chemically and immobilized on the surface of a multimode fibre (MMF) to realise the LSPR fiber optic sensor. Our results show that the proposed LSPR sensor demonstrates a refractive index (RI) sensitivity of 3.7 AU/RIU in the intensity domain.

Keywords: LSPR, Fiber optic sensors, gold nanoparticles

1. INTRODUCTION

Fiber optic sensors have been extensively investigated due to their inherent advantages, including immunity to electromagnetic interference, lightweight, ease of fabrication, high sensitivity, fast response time, remote sensing capability and multiplexing capability, etc. [1]. Fiber optic plasmonic sensors are based on the LSPR or surface plasmonic resonance (SPR) [2]. The LSPR is termed as the collective oscillation in conductive nanoparticles driven by incident light waves [3]. The nanoparticles' size, shape, composition, interparticle spacing, and dielectric characteristics significantly influence the resonant frequency at which light is reflected, causing the conduction electrons to oscillate collectively [3]. The LSPR resonant wavelength can be tuned by varying nanoparticles' size, shape and composition. The LSPR sensors have high potential in clinical diagnosis, biomolecular interaction research, medication supply monitoring, and in situ biofilm detection due to their excellent biocompatibility, sensitivity and stability [4,5]. The stable physical properties and ease of fabrication make AuNPs a good candidate for LSPR sensors [6]. However, the poor molecular affinity of AuNPs in comparison with silver nanoparticles, limits their applications in biosensing [7]. On the other hand, the physical properties of silver nanoparticles are susceptible to the influence of the external environment resulting in poor stability of the silver nanoparticle based LSPR sensors. To improve the sensitivity of the fibre optic LSPR sensor, different sensitivity enhancement techniques such as fibre tapers [8], U-bent [9], D-shaped fibre [3], etc. have been proposed. Fiber optic LSPR sensors with gold-silver alloy nanoparticles [10] and triangular nanoparticles [11] were also studied.

Here, we report and investigate an LSPR-RI sensor based on AuNPs-coated MMF. The optical properties of the AuNPs were modelled using the FEM simulation model. AuNPs were synthesised chemically and immobilised on the MMF surface to realise the LSPR fibre optic sensor. An RI sensitivity of 3.7 AU/RIU at 585 nm was obtained in the intensity domain.

2. FEM SIMULATION

The optical properties of the spherical AuNPs were modelled using the COMSOL Multiphysics simulation tool. This FEM for the rigorous solution of Maxwell's equations is based on the Kretschmann configuration considering various optical parameters. Fig. 1 depicts the simulated absorbance spectra for AuNPs with different diameters ranging from 4 to 12 nm. As observed from the simulated spectra, an increase in the NPs size leads to a red shift of the absorbance spectrum, suggesting the possibility of controlled spectral tuning of the plasmonic band.

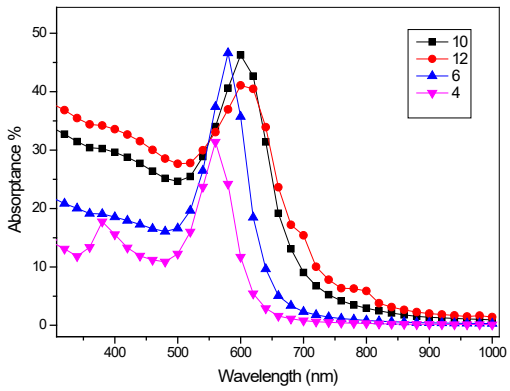

Figure 1. Simulated absorbance dependencies for the AuNPs with different diameters of 4, 6, 10 and 12 nm.

DOI: https://doi.org/10.34961/researchrepository-ul.29290307.v1

3. SENSOR FABRICATION

3.1. Nanoparticles synthesis

A 50 mL solution of 0.25 mM tetra chloroauric acid ($HAuCl_4 \cdot H_2O$) was prepared in an Erlenmeyer flask. Separately, a 34.0 mM (1.0 wt.%) trisodium citrate ($Na_3C_6H_5O_7$) solution was prepared. The precursor solution flask was heated on a hotplate with vigorous and constant stirring. To prevent contamination and evaporation of the solvent during the synthesis, a disposable petri dish was used to cover the flask. Once the $HAuCl_4$ solution reached its boiling point under ambient pressure, 0.5 mL of the citrate solution was quickly injected into the boiling $HAuCl_4$ solution. Within approximately 5 minutes, the solution changed from yellow (the precursor salt colour) to wine red (indicating the formation of gold nanoparticles). The solution was then kept boiling and stirred vigorously for an additional 10 minutes to ensure complete reduction of the gold ions. In this process, trisodium citrate served as both a reducing agent, converting gold ions (Au^{3+}) to metallic gold (Au^0), and a capping agent, preventing excessive aggregation of the nanoparticles. Finally, the solution was removed from heat and allowed to cool to room temperature.

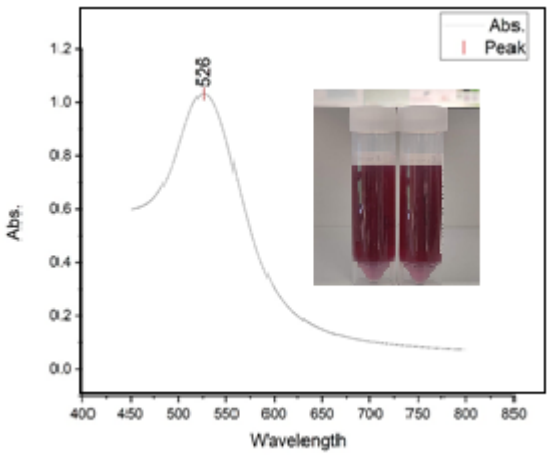

Figure 2. Absorption spectrum of AuNP. Inset shows the photograph of the fabricated colloidal nanoparticles.

Figure 2 shows the absorption spectra of the synthesised AuNP measured using a UV-Vis spectrophotometer, LSPR peak at a wavelength of 526 nm.

3.2. AuNPs immobilization on optical fiber

The standard hard cladding multimode fiber (BFL37-200, Thorlabs) with a core diameter of 200 µm was used for the sensor fabrication. A multimode fibre (MMF) section of 40 cm in length was taken for the present studies. The polymer coating at the ends of the MMF was removed (0.5 cm) and then cleaved properly to avoid coupling loss. Polymer coating from the centre part of the MMF (3 cm) was also removed and the surface was cleaned using ethanol. This portion of the MMF will be acting as the sensing region.

The schematic of the AuNP immobilization is depicted in Figure 3. The sensing region of MMF is treated with Piranha solution composed of sulfuric acid (H2SO4, 95%) and hydrogen peroxide (H2O2, 34.5%) with a volume ratio of 3:1 for 40 min. This process will activate OH functional groups in the sensing region. Next, the sensing region was rinsed with DI water and dried. The next step is silanization, whereby the sensing region of MMF was treated with 3-mercatoptopropyltrimethoxysilane (MPTMS) with mercapto group (-SH)

The MPTMS (1 vol%) in ethanol was introduced in the sensing region of MMF for 12 hours. The thiol functionalized MMF surface was cleaned with ethanol to remove unbound monomer and dried. After that, the sensing region of MMF was coated with the prepared AuNPs by dip coating method for 48 hours. Upon completion of the coating process, the Au-coated sensing region of MMF was rinsed with ethanol and dried.

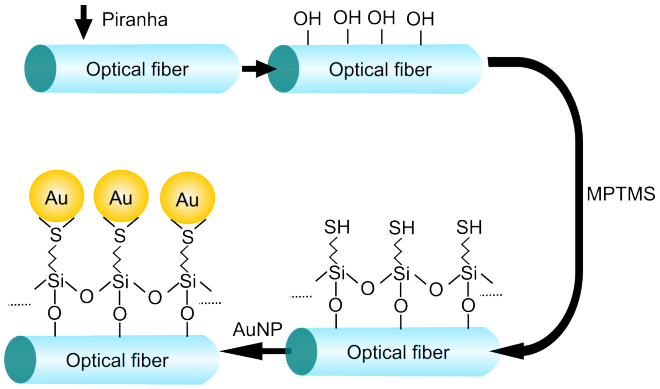

Figure 3. Schematic of AuNPs immobilization on optical fiber surface by using the chemical modification of MPTMS.

4. RESULTS AND DISCUSSION

4.1. LSPR from Au/PVA nanocomposite

Initially, AuNPs were dissolved in poly vinyl alcohol (PVA), and after ultrasound sonication, the hybrid was coated on the glass slide and absorption spectra was recorded using a spectrometer with a detection range of 350 nm – 700 nm and a fiber-coupled light source (SLS201/M).

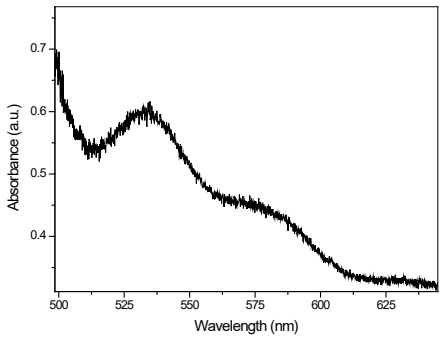

Figure 4. The absorption spectrum recorded from Au/PVA nanocomposite coated glass.

The recorded absorption spectrum of the Au/PVA nanocomposite-coated glass is shown in Figure 4. The LSPR peak can be clearly seen at a wavelength of 533 nm.

4.2. LSPR from Au NP coated on MMF

A fiber-optic-based measurement system was constructed for the AuNPs-coated MMF-based LSPR sensor. The schematic diagram of the optical measurement system is shown in Figure 5. The optical system comprises the broadband light source, Au NP-MMF and a spectrometer. The Broadband light source delivers light to the MMF, and the LSPR absorption spectra can be recorded with the spectrometer.

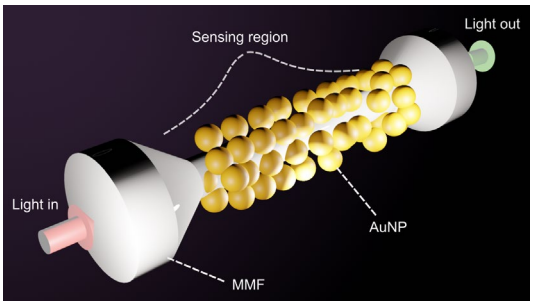

Figure 5. Schematic of the sensing region.

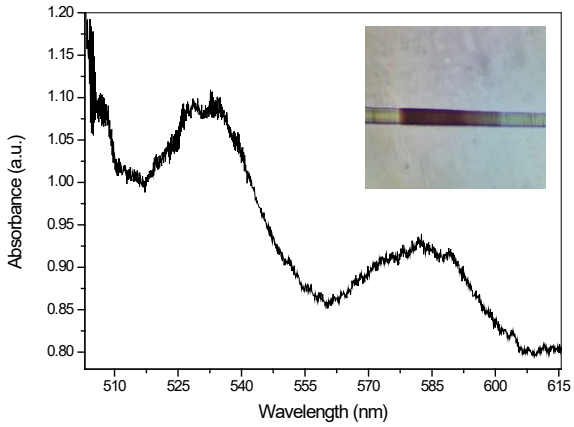

Figure 6. LSPR spectrum of the AuNPs- coated MMF. Inset shows the microscope image of the AuNP coated MMF.

As shown in Figure 6, the LSPR peak of the AuNPs-coated MMF is at 533 nm. The coated MMF and Au/PVA nanocomposite-coated glass show similar LSPR spectral characteristics.

4.3. Bulk refractive index sensing

The sensing region of the MMF is fixed on a glass substrate to investigate the refractive index sensitivity. Then, calibrated RI liquid (Cargille) samples were drop-casted onto the MMF sensing region. The liquid samples with RIs of 1.47, 1.49 and 1.51 were drop cast, and corresponding LSPR spectra were recorded. The LSPR spectra corresponding to the different RIs are shown in Figure 7.

The increasing RI causes a general increase in the LSPR absorbance. An RI sensitivity of 3.7 AU/RIU at 585 nm was obtained in the intensity domain. The LSPR spectral peak is also showing a redshift with increasing of the surrounding RI.

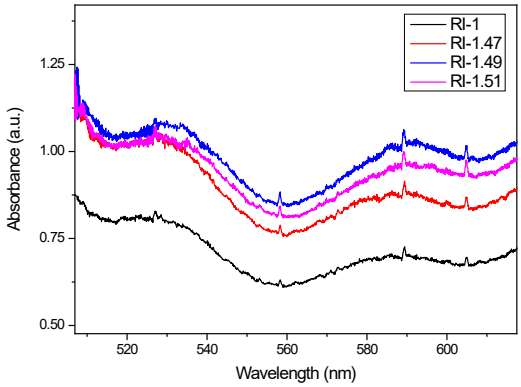

Figure 7. Absorption spectra for the sensor immersed in different RI liquids.

5. CONCLUSIONS

In conclusion, an LSPR refractive index sensor was realized using an MMF coated with an AuNPs layer. An FEM simulation model was realized for predicting the optical properties of the AuNPs coating. AuNPs were synthesized chemically and immobilized on the MMF surface to realize the LSPR fiber optic sensor. A RI sensitivity of 3.7 AU/RIU at 585 nm was obtained in the intensity domain. Several sensitivity enhancement techniques can be incorporated into the proposed sensor, and it can be potentially used in bio-sensing applications.

FUNDING STATEMENT

This publication has emanated from research supported in part by a grant from Science Foundation Ireland under Grant numbers 13/RC/2077_P2 and 18/CRT/6222, Fiosraigh Scholarship Award 2019 (TU Dublin), and Royal Society International Exchanges 2022 (IES\R3\223005).

REFERENCES

[1] Chauhan, M., & Singh, V. K. (2021). Review on recent experimental SPR/LSPR based fiber optic analyte sensors. Optical Fiber Technology, 64, 102580.

[2] Dos Santos, P. S., Mendes, J. P., Dias, B., Pérez-Juste, J., De Almeida, J. M., Pastoriza-Santos, I., & Coelho, L. C. (2023). Spectral analysis methods for improved resolution and sensitivity: enhancing SPR and LSPR optical fiber sensing. Sensors, 23(3), 1666.

[3] Feng, J., Gao, J., Yang, W., Liu, R., Shafi, M., Zha, Z., ... & Jiang, S. (2022). LSPR optical fiber sensor based on 3D gold nanoparticles with monolayer graphene as a spacer. Optics Express, 30(6), 10187-10198.

[4] Chauhan, M., & Singh, V. K. (2021). Review on recent experimental SPR/LSPR based fiber optic analyte sensors. Optical Fiber Technology, 64, 102580.

[5] Zhang, H., Zhou, X., Li, X., Gong, P., Zhang, Y., & Zhao, Y. (2023). Recent advancements of LSPR fiber-optic biosensing: combination methods, structure, and prospects. Biosensors, 13(3), 405.

[6] García, J. A., Monzón-Hernández, D., Manríquez, J., & Bustos, E. (2016). One step method to attach gold

nanoparticles onto the surface of an optical fiber used for refractive index sensing. Optical Materials, 51, 208-212.
[7] Chen, J., Shi, S., Su, R., Qi, W., Huang, R., Wang, M., ... & He, Z. (2015). Optimization and application of reflective LSPR optical fiber biosensors based on silver nanoparticles. Sensors, 15(6), 12205-12217.
[8] Wang, Z., Singh, R., Marques, C., Jha, R., Zhang, B., & Kumar, S. (2021). Taper-in-taper fiber structure-based LSPR sensor for alanine aminotransferase detection. Optics Express, 29(26), 43793-43810.
[9] Jiang, S., Li, Z., Zhang, C., Gao, S., Li, Z., Qiu, H., ... & Liu, Y. (2017). A novel U-bent plastic optical fibre local surface plasmon resonance sensor based on a graphene and silver nanoparticle hybrid structure. Journal of Physics D: Applied Physics, 50(16), 165105.
[10] Tu, H., Sun, T., & Grattan, K. T. (2013). SPR-based optical fiber sensors using gold–silver alloy particles as the active sensing material. IEEE Sensors Journal, 13(6), 2192-2199.
[11] Song, H., Zhang, H., Sun, Z., Ren, Z., Yang, X., & Wang, Q. (2019). Triangular silver nanoparticle U-bent fiber sensor based on localized surface plasmon resonance. AIP Advances, 9(8).

41: A REVIEW OF UNCOOLED THERMAL IMAGER SPECIFICATIONS AND THEIR INFLUENCE ON IMAGER PERFORMANCE

Juan-Wian Coetzer [a,*], *Joseph Walsh* [a]

[a] IMaR Research Centre, Munster Technological University, Tralee, Ireland

Applications Cont., EM009, August 14, 2024, 11:00 AM - 12:10 PM

Abstract − Thermal imaging is becoming a more accessible field due to the reduced cost of uncooled imagers as technology advances. When a person unfamiliar with the field reviews their options, the wall of specifications offered by manufacturers can often be confusing. This article is aimed at taking some of the important specifications found in uncooled thermal imagers and reviewing them in an easy-to-grasp way that the reader can understand without having to be an expert in thermography.

Keywords**:** microbolometer; thermal imaging; thermal sensitivity; pixel resolution; uncooled thermal imager;

1. INTRODUCTION

Thermal imagers are imaging devices used to visualise and measure the heat emitted from objects. Similarly to how digital cameras translate light into an image viewable on a screen, thermal imagers detect and transpose thermal radiation into electrical signals that can be used to display a digital heat map [1]. Thermal imagers are very widely used throughout a range of industries for tasks such as building inspection, production line inspection, fire detection, military applications and even medical analysis [2,3].

At the heart of the imager system is a thermal sensor. This sensor works as a transducer that converts emitted thermal radiation into a useable electrical signal. Thermal sensors can be divided into two groups namely cooled and uncooled sensors [4]. The differences of how these two types of sensors operate will briefly be reviewed to provide a basic operational understanding. Due to technological advancements, uncooled sensors are getting better and are becoming a viable alternative to some cooled sensors [5]. This article has the focus of reviewing important specifications of uncooled thermal imaging systems and will provide the reader with an understanding of what these specifications mean and what they need to consider when choosing a thermal imager. The following specifications will be explored:

- Pixel Resolution
- Thermal Sensitivity
- Sensor Time constant
- Image Frequency

2. COOLED AND UNCOOLED SENSORS

Thermal imaging sensors all have a working principle based on the law of Planck's distribution. This law states that the wavelength of radiating energy is distributed according to temperature [2]. With the emitted radiation being a function of the material's temperature. The higher the temperature of the object, the shorter the wavelength [6]. This can be seen in action when observing the glow of hot objects, the wavelength of the emitted energy enters the visible light spectrum. Infrared detectors respond to absorbed photons from the emitted infrared energy. The difference between cooled and uncooled sensors are the mechanisms used. The differing mechanisms between the two types causes variation such as differing response time and sensitivity [7].

2.1. Cooled Sensors

Cooled sensors, otherwise known as Photon detectors, are not the focus of this paper but will be briefly reviewed so the reader can understand the operational fundamentals. Photon detectors absorb photons transmitted by infrared radiation. The absorption leads to a change in the mobility or concentration of free charge carriers within the detector element. These sensors are classified as single step transducers since absorbed photons cause a direct and measurable change in the resistance or current [4].

When compared to uncooled sensors, Photon detectors have a faster response time and are more sensitive. Because they are more expensive, they are mostly used in applications where performance is the main concern such as certain medical and astronomical observation instruments [8].

2.2. Uncooled Sensors

Uncooled sensors mostly make use of microbolometer focal plane arrays (FPA). These arrays consist of thousands of microbolometer 'pixels' typically arranged in a square array[9]. Figures from an article by Jimenez R et al. contains images taken on a scanning electron microscope (SEM)[10]. Part of the focal plane array can be seen in Figure 1a and an individual microbolometer is shown in Figure 1b.

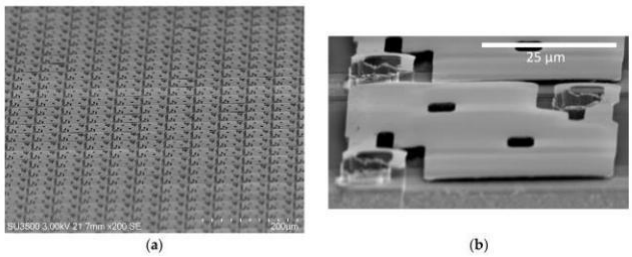

Figure 1. (a) SEM image of microbolometer array (b) SEM image of a single microbolometer[10].

Microbolometers are two step transducers that consist of an absorptive layer and a thermometer layer. Infrared radiation that is absorbed by the absorptive layer results in an increase in temperature of that layer which is then measured by the thermometer[8].

This thin bolometer film is supported on a microbridge structure with supporting legs that offer both thermal

DOI: https://doi.org/10.34961/researchrepository-ul.29290697.v1

insulation and an electrical connection between the resistant bolometer and readout circuit[11,12]. The operating principle of a microbolometer has been illustrated in Figure 2.

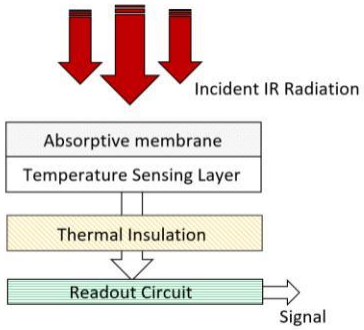

Figure 2. Block diagram of microbolometer thermal detector

Because of a microbolometer's working principle, it can be expected that the response time and sensitivity would be less than cooled sensors due to the absorptive layer taking time to heat up or cool down when experiencing changes in incident IR radiation. This will be further discussed in section 3.3.

3. PARAMETERS AND THEIR INFLUENCE ON IMAGER PERFORMANCE

When selecting a thermal imager there are certain parameters that needs to be taken into consideration in order to choose the best imager for the required task. This section offers a review of four important parameters and what effect they have on the final thermal image. It is good to understand these parameters to know what to expect from the selected imager.

3.1. Pixel resolution

In thermal imagers, the pixel resolution of a sensor refers to the mount of microbolometer 'pixels' on the given sensor array. This directly effect the image quality displayed on the screen. Pixel or Thermal resolution needs to be taken into consideration based on imager application and the required image quality. For example, a thermal imager with a resolution of 640 x 480 has a pixel count of 306,200 pixels. This means that the FPA contained in the imager uses 306,200 points of measurement in order to construct a thermal image[1].

When the image quality itself is the determining factor in imager selection then pixel resolution should be the most significant consideration. In a paper by Rivadeneira et al. discussing thermal imager super-resolution there is mosaic to show a comparison between low, medium and high resolution thermal imagers that can be observed in Figure 3[13].

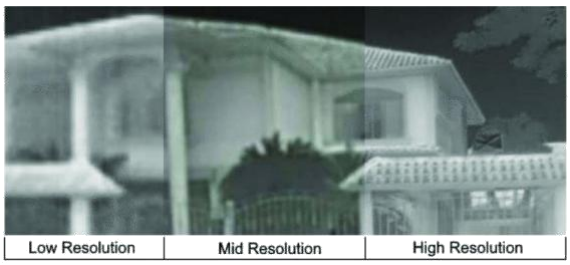

Figure 3. Mosaic image constructed from low, medium and high-resolution thermal imagers with resolutions of 160x120, 320x240 and 640x512 respectively [13].

3.2. Thermal Sensitivity

In simple terms Noise Equivalency Temperature Difference (NETD) is a figure of merit used my manufacturers in order to convey thermal sensitivity of an Imager, but there is still no standard definition for the terms [14]. This is a complicated area when examined in detail and although it is widely used, NETD is applied to different imaging systems under different conditions with different meanings [15].

When looking at the NETD specification from a consumer point of view, briefly understanding what it is and how it affects the imager results would suffice. Thermal imagers all have a certain level of noise associated with the detector system. The NETD value is a method of measuring the minimum temperature required to overcome system noise and produce a response from the sensor which means a lower value is preferred[1,16]. In very simple terms this can be explained by the minimum temperature difference a sensor can distinguish from the background. The value is given by manufacturers in the form of mK at a given temperature for example 50mK @ 30°C meaning the minimum temperature that the sensor can differentiate at 30°C would be 50mK. It should be noted that with an increase in background temperature, the sensitivity of a sensor increases and the NETD value decreases[1].

Although NETD values offer a good way to evaluate sensor sensitivity, it should be understood that the electronics, display and the observer are not taken into account in the measurement [17]. This suggests that NETD offers limited value as a specification metric [18].

In a performance assessment conducted by Villa et al. on the use of low-cost thermal imagers in medical applications, the practical influence of NETD values can be seen. Figure 4 displays three images taken by cameras with differing specifications. Figure 1a was taken on a camera with a thermal sensitivity of 110mK, and subsequently figure 1b and 1c were taken on cameras with a sensitivity of 63mK[19]. When observing the images, the difference in the color palette and temperature details can be observed. Although Figure 1b and 1c have similar NETD values there is still a clear difference in color palette due to factors such as pixel resolution.

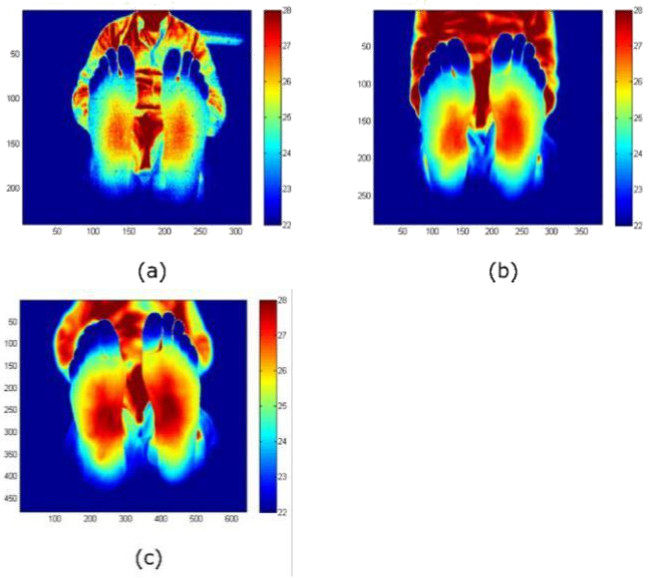

Figure 4. Feet images taken with cameras containing having a thermal sensitivity of (a) 110 mK (b) 63.3 mK (c) 63.4 mK. The x- and y- axis representing sensor pixels[19].

3.3. Sensor Time Constant

The sensor time constant of microbolometer thermal imagers are seen as a measure of response time and can be responsible for blur when imaging dynamic targets [20]. The response time is influenced by the thermal conductance of the material used in the microbolometer. Having low thermal conductance means low heat capacitance and a faster response time for the sensor [4]. When incident radiation changes, the microbolometer takes time to fully heat up or cool down in order to give the final temperature reading. Figure 5 was constructed in order to demonstrate the basics of this principle. The square wave represents a snap change in incident temperature, and the green line represents the microbolometer temperature.

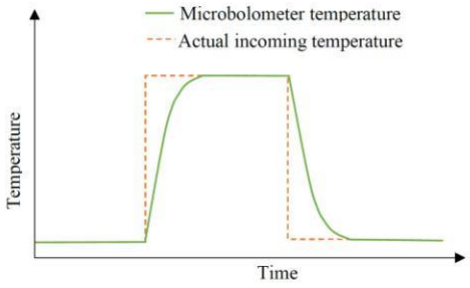

Figure 5. Thermal detector response time when compared to incoming square-wave temperature pulse.

This exponential rise and decay in sensor temperature are a significant factor to consider if the thermal imager application involves the measurement of moving objects or static objects with a quick changing dynamic temperature. In a thesis by Najib Denial investigating the use of a shutter system in order to reduce blur caused by sensor time constant, the effects can be clearly seen[21]. Figure 6 shows the motion blur of a cooled steel ball dropped in front of a hot background when imaged with a FLIR A35 imager that has a time constant of 12ms. When choosing a thermal imager, a lower time constant is generally favourable.

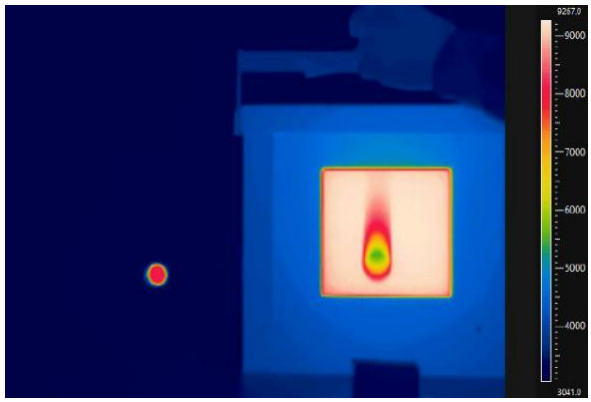

Figure 6. Motion blur observed when imaging a colder steel ball dropped in front of a warmer background with an imager time constant of 12ms[21].

4. CONCLUSIONS

With the increased availability of cheaper uncooled thermal imagers, it is often easier to order online instead of consulting with a thermography specialist before deciding on an imager. With the highlighted parameters of this paper the reader would have a better un-derstanding of certain specifications given by manufacturers and can make a more educated choice when obtaining an imager for their application.

FUNDING STATEMENT

This work was supported with the financial support of the Science Foundation Ireland grant 13/RC/2094_P2 and co-funded under the European Regional Development Fund through the Southern & Eastern Regional Operational Programme to Lero - the Science Foundation Ireland Research Centre for Software (www.lero.ie)

REFERENCES

[1] Havens, K.J.; Sharp, E.J. **Thermal Imaging Techniques to Survey and Monitor Animals in the Wild: A Methodology**; Elsevier/Academic Press: Amsterdam ; Boston, 2016; ISBN 978-0-12-803384-5.

[2] Yongqing, W.; Zongqing, G.; Shuonan, W.; Ping, H. **The Temperature Measurement Technology of Infrared Thermal Imaging and Its Applications Review**. In Proceedings of the 2017 13th IEEE International Conference on Electronic Measurement & Instruments (ICEMI); IEEE: Yangzhou, October 2017; pp. 401–406.

[3] Gade, R.; Moeslund, T.B. **Thermal Cameras and Applications: A Survey.** Mach. Vis. Appl. 2014, 25, 245–262, doi:10.1007/s00138-013-0570-5.

[4] Vollmer, M.; Möllmann, K.-P. **Infrared Thermal Imaging: Fundamentals, Research and Applications;** Second edition.; Wiley-VCH Verlag GmbH & Co. KGaA: Weinheim, Germany, 2018; ISBN 978-3-527-69332-0.

[5] Tissot, J.L. IR **Detection with Uncooled Sensors**. Infrared Phys. Technol. 2004, 46, 147–153, doi:10.1016/j.infrared.2004.03.018.

[6] Usamentiaga, R.; Venegas, P.; Guerediaga, J.; Vega, L.; Molleda, J.; Bulnes, F. **Infrared Thermography for**

Temperature Measurement and Non-Destructive Testing. Sensors 2014, 14, 12305–12348, doi:10.3390/s140712305.

[7] Daniels, **A. Field Guide to Infrared Systems, Detectors, and FPAs;** SPIE field guide; Third edition.; SPIE Press: Bellingham, Washington, USA, 2018; ISBN 978-1-5106-1864-0.

[8] Bhan, R.; Saxena, R.; Jalwani, C.; Lomash, S. **Uncooled Infrared Microbolometer Arrays and Their Characterisation Techniques.** Def. Sci. J. 2009, 59, 580–589, doi:10.14429/dsj.59.1562.

[9] Soloman, S. **Sensors Handbook;** 2010; ISBN 9780071605717.

[10] Jimenez, R.; Moreno, M.; Torres, A.; Morales, A.; Ponce, A.; Ferrusca, D.; Rangel-Magdaleno, J.; Castro-Ramos, J.; Hernandez-Perez, J.; Cano, E. **Fabrication of Microbolometer Arrays Based on Polymorphous Silicon–Germanium. Sensors** 2020, 20, 2716, doi:10.3390/s20092716.

[11] Kimata, M. **Uncooled Infrared Focal Plane Arrays**: UNCOOLED INFRARED FOCAL PLANE ARRAYS. IEEJ Trans. Electr. Electron. Eng. 2018, 13, 4–12, doi:10.1002/tee.22563.

[12] Bieszczad, G.; Kastek, M. **Measurement of Thermal Behavior of Detector Array Surface with the Use of Microscopic Thermal Camera.** Metrol. Meas. Syst. 2011, 18, 679–690, doi:10.2478/v10178-011-0064-6.

[13] Rivadeneira, R.E.; Sappa, A.D.; Vintimilla, B.X.; Guo, L.; Hou, J.; Mehri, A.; Ardakani, P.B.; Patel, H.; Chudasama, V.; Prajapati, K.; et al. **Thermal Image Super-Resolution Challenge** - PBVS 2020. In Proceedings of the 2020 IEEE/CVF Conference on Computer Vision and Pattern Recognition Workshops (CVPRW); IEEE: Seattle, WA, USA, June 2020; pp. 432–439.

[14] North Atlantic Treaty Organization; **Research and Technology Organization Experimental Assessment Parameters and Procedures for Characterisation of Advanced Thermal Imagers** = Paramètres et Procédures d'évaluation Expérimentale Pour La Caractérisation d'imageurs Thermiques Avancés.; North Atlantic Treaty Organization, Research and Technology Organization: Neuilly-sur-Seine Cedex, France, 2003; ISBN 978-92-837-1095-0.

[15] Rogalski, A. **Infrared Detectors;** 2nd ed.; Taylor & Francis: Boca Raton, 2011; ISBN 978-1-4200-7671-4.

[16] Kinch, M.A. **State-of-the-Art Infrared Detector Technology;** SPIE Press: Bellingham, Washington, USA, 2014; ISBN 978-1-62841-289-5.

[17] Redjimi, A.; Knežević, D.; Savić, K.; Jovanović, N.; Simović, M.; Vasiljević, D. **Noise Equivalent Temperature Difference Model for Thermal Imagers, Calculation and Analysis.** Sci. Tech. Rev. 2014, 64, 42–49.

[18] Rajic, N.; Street, N. **A Performance Comparison between Cooled and Uncooled Infrared Detectors for Thermoelastic Stress Analysis.** Quant. InfraRed Thermography. J. 2014, 11, 207–221, doi:10.1080/17686733.2014.962835.

[19] Villa, E.; Arteaga-Marrero, N.; Ruiz-Alzola, J. **Performance Assessment of Low-Cost Thermal Cameras for Medical Applications.** Sensors 2020, 20, 1321, doi:10.3390/s20051321.

[20] Waldron, D.L.; Lohrmann, D.J. **Per-Pixel Time Constant Measurement of Bolometer Cameras.** IEEE Trans. Instrum. Meas. 2020, 69, 7725–7739, doi:10.1109/TIM.2020.2985138.

[21] Nadjib Danial, A. **Using High Speed Shutter to Reduce Motion Blur in a Microbolometer.** Bachelor, Luleå University of Technology: Department of Computer science, Electrical and Space engineering, 2013.

42: LEVERAGING DEEP LEARNING FOR RECONSTRUCTION OF CANCER CELLS FROM 3D IR THERMOGRAPHY FOR FASTER CANCER DIAGNOSIS

Suzad Mohammad [a,b], *Charlie O'Mahony*[a*], *Sadia Sharmin*[b], *Fahmida Gulshan*[c], *Syed A. M. Tofail*[a]

[a] Department of Physics, University of Limerick, Limerick, Ireland
[b] Department of Computer Science and Engineering, Bangladesh University of Engineering and Technology, Dhaka, Bangladesh
[c] Department of Materials and Metallurgical Engineering, Bangladesh University of Engineering and Technology, Dhaka, Bangladesh

Biomedical Sensors Session 1, EM009, August 12, 2024, 4:50 PM - 5:30 PM

Abstract – Cancer remains a leading cause of death worldwide, underscoring the critical need for early detection methods. This research addresses this challenge by leveraging deep neural networks to reconstruct cancer cells using 3D Infrared (IR) thermography. Our novel approach captures angular radiation by projecting infrared rays from multiple angles, obtaining more comprehensive information compared to traditional 0-degree measurements. We trained neural networks to predict excitation angles, defect sizes, and defect lengths, which are integrated to create 2D defect images. The Filtered Back Projection (FBP) algorithm enhances these images by constructing hidden angular views, resulting in a detailed 3D reconstruction of affected cells. Real test data is captured using micro-imager sensor cameras with micro lenses, while simulated data from COMSOL is used for training and validation. Achieving a detailed tissue reconstruction, this method marks a significant advancement in early cancer detection, potentially improving patient outcomes.

Keywords**:** cancer diagnosis; 3D IR thermography; micro-imager sensors; deep convolutional neural network; COMSOL;

1. INTRODUCTION

Early and accurate cancer diagnosis plays a pivotal role in successful treatment outcomes. Survival rates plummet from 93% in the initial stage to a mere 13% in the final stage, emphasizing the critical importance of timely intervention. Traditional cancer detection methods, such as biopsies, can be invasive and time-consuming. Infrared (IR) thermography offers a non-invasive alternative for cancer detection, but its ability to diagnose cancer in its early stages can be limited. This limitation arises from the analysis of IR thermographic images captured from a single angle, which may not provide sufficient detail about the size, shape, and depth of cancerous tissue.

This research proposes a novel approach for leveraging deep learning and 3D IR thermography for faster and more accurate cancer diagnosis. Our method utilizes four deep neural networks trained to extract critical information from IR thermographic images captured from multiple angles. Unlike conventional single-angle IR thermography, our approach, utilizes the concept of 3D-IR thermography (3D-IRT) to obtain a comprehensive view.

The proposed deep learning architecture analyzes the multi-angular IR thermographic images to detect the angle of excitation of the IR radiation and defect length within the tissue. This comprehensive analysis allows the network to identify patterns and features indicative of cancerous cells. Subsequently, image processing techniques are employed to reconstruct a 2D image from each analyzed angle. By combining these multiple 2D images, we utilize the Filtered Back Projection (FBP) algorithm to construct a 3D representation of the cancerous cells.

This research has the potential to revolutionize cancer diagnosis by offering a faster, less invasive, and more informative approach compared to traditional methods. The reconstruction of cancerous cells using deep learning and 3D-IR thermography holds significant promise for improving early cancer detection rates and ultimately enhancing patient outcomes.

2. LITERATURE REVIEW

2.1. Problems in traditional cancer diagnostic approaches

Traditional cancer diagnostic methods frequently encounter limitations that impede early detection and effective treatment. While techniques such as biopsies are highly accurate, they involve invasive procedures that require puncturing or extracting tissue samples, causing discomfort and posing risks of infection or bleeding [1]. Additionally, imaging methods like X-rays and CT scans expose patients to ionizing radiation, which can pose health risks, particularly with repeated use [2]. Moreover, these procedures can be costly and time-consuming, with the duration often dependent on the patient's physical condition.

2.2. Current Landscape of IR Thermography in Cancer Diagnosis

Several studies have explored the potential of IR thermography for cancer detection in various body areas. Research suggests IR thermography may identify abnormal thermal patterns in the breast, potentially indicative of breast cancer [3]. These patterns can sometimes appear before mammograms detect abnormalities. Studies have shown the use of IR thermography for detecting skin cancers, particularly melanoma [4]. The technology can help identify suspicious lesions for further investigation. Emerging research explores the use of IR thermography for detecting

DOI: https://doi.org/10.34961/researchrepository-ul.29290745.v1

oral cancer [5], with some studies indicating its ability to identify potential lesions.

Despite its potential, IR thermography faces limitations that hinder its widespread adoption for definitive cancer diagnosis. Traditional IR thermography captures data from a single angle, potentially missing crucial details about the size, shape, and depth of the underlying tissue abnormality. This limitation can hinder accurate diagnosis, particularly in early stages.

2.3. 3D IR Thermography

Traditional IR thermography, while offering a non-invasive approach, is limited by its reliance on single-angle data acquisition. Unlike its single-angle counterpart, 3D IR thermography captures thermal data from multiple angles around the target. This multi-angular approach provides a more comprehensive view of the underlying structures, allowing for a more detailed analysis of potential abnormalities. It offers a better understanding of the depth of underlying defects compared to single-angle approaches [6]. The additional information obtained from multiple angles can potentially lead to a more accurate assessment as well.

2.4. Deep Learning for Medical Image Analysis

The field of medical imaging has witnessed a significant revolution with the emergence of deep learning techniques. Deep learning, a subfield of artificial intelligence, utilizes artificial neural networks with complex architectures to learn intricate patterns from vast amounts of data.

Deep learning algorithms excel at automatically extracting critical features from medical images, such as textures, shapes, and subtle variations in contrast. This ability to identify these features without the need for extensive manual programming is a significant advantage [7].

The integration of deep learning with medical imaging presents a powerful approach for enhancing cancer diagnosis [8]. By leveraging the ability of deep learning to extract complex features and patterns, we can achieve improved accuracy, objectivity, and early detection of cancers.

3. METHODOLOGY

This section describes the research methods employed to achieve the objectives outlined in the introduction. It details five broad phases of the methodology as depicted in figure 1.

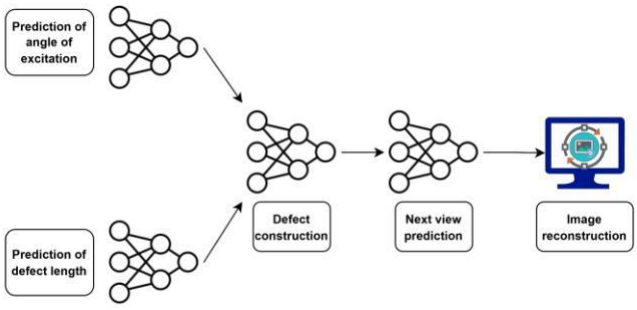

Figure 1. Overview of methodology.

3.1. Dataset preparation and augmentation

Image data simulation

Preparing the dataset for this study was one of the most significant challenges we faced. Given the critical need to obtain sufficient real tissue images, we opted to accumulate images from a simulated system using COMSOL programming. This approach allowed us to generate a robust dataset for training and validating our neural network, while the limited real data available were reserved for testing purposes to verify the authenticity of our study.

Cropping region of interest

Our data preparation process incorporates an automated Python script to ensure consistency and efficiency. This script performs targeted cropping of the IR thermographic images, isolating the region of interest (ROI) for further analysis. The cropping removes irrelevant background information, allowing the deep learning model to focus on the relevant thermal data associated with the suspected cancerous tissue.

The script employs pre-defined values for cropping based on the known resolution of the output images generated by the COMSOL simulation. This predetermined approach ensures consistency in the size and focus of the ROI across all images within the dataset. Specifically, the script removes 67 pixels from the top, 35 pixels from the bottom, and 130 pixels from both the left and right sides of each image.

Image augmentation

To enrich the dataset and improve the model's ability to handle variations in real-world scenarios, we employ a data augmentation strategy. This technique involves applying controlled modifications to the cropped images. In this case, we introduce Gaussian noise and blur effects with varying intensities. The range of the noise and blur effect spans from 5 to 50, and these effects are applied in 100 different combinations to create a diverse set of augmented images. The detailed distribution of augmented image dataset is presented in Table 1.

Table 1. Image dataset distribution for training and validation of neural network.

Category	No. of images	Augmented images
Excitation angle (0° - 50°)	50	5,000
Defect Length (0mm, 1mm, 3mm, 5mm)	200	20,000

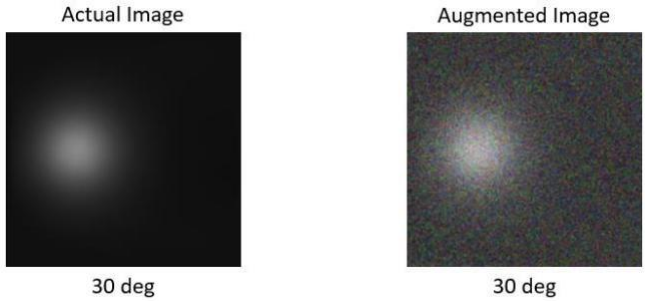

Figure 2. Actual thermogram image and its associated augmented thermogram image used in this study.

The simulated IR thermographic images served as a robust foundation for training and validating our deep learning model. To further strengthen the model's performance, we employed data augmentation techniques.

This strategy involved applying a range of blur effects (intensities from 5 to 50) and Gaussian noise to the images in 100 different combinations. Figure 2 depicts a randomly selected image data used in this study. This process effectively expanded and diversified the dataset, allowing the model to learn from a wider range of scenarios.

Accumulating real image data for testing neural network

While our primary dataset consisted of simulated IR thermographic images, a limited set of real tissue images captured using a microimager sensor with a micro lens played a critical role in validating the model's performance in a practical setting. Evaluating the model's accuracy with real-world data strengthens the study's overall validity and ensures that the findings are applicable to real-world cancer diagnosis scenarios. By combining the advantages of a comprehensive simulated dataset with the crucial validation provided by real data, we adopted a balanced approach to developing and validating our deep learning model for tissue image analysis.

3.2. Neural Network Architecture

For our training purposes, we utilize the *EfficientNetB0* neural network, leveraging pre-trained weights from the *ImageNet* dataset. While EfficientNetB7 is acclaimed for its superior accuracy and its ability to outperform other neural networks, it is not suitable for our study due to our relatively small dataset. The intricate structure of EfficientNetB7, which comprises 66 million parameters and 813 layers, makes it prone to overfitting with such a limited dataset. Therefore, we choose EfficientNetB0 to mitigate this risk.

To adapt the network to our specific image set, we modify the architecture by removing the final prediction layer and incorporating three dense layers with 256, 128, and 50 nodes, respectively. We use the *Adam* optimizer, a widely accepted choice, with a learning rate of *0.001*. Each layer is followed by a *ReLU* activation function, except for the top layer, which uses the *softmax* activation function, known for its effectiveness in multiclass classification tasks.

To further prevent overfitting, we employ the *categorical crossentropy* loss function at each layer. The output of each layer is flattened and used as input for the subsequent layer. The entire network is trained for 30 epochs, ensuring that it learns the necessary parameters from our image set effectively.

3.3. Prediction of angle of excitation

Our research investigates the application of a deep neural network for the detection of infrared (IR) radiation excitation angles. We leverage a comprehensive dataset of thermographic images encompassing a range of angles from 0° to 50°. To train and validate the neural network's ability to accurately predict the excitation angle based solely on the image data, we employ a data augmentation strategy. This technique involves creating additional variations of the original thermograms, effectively expanding the dataset and improving the network's generalizability.

We meticulously split the augmented dataset into two distinct subsets: a training set and a validation set. The training set, comprising 4,000 images, is used to train the neural network. During the training process, the network iteratively learns to identify patterns and relationships within the image data that correspond to specific excitation angles. The validation set, containing 1,000 images, serves a critical purpose. It allows us to assess the network's performance on unseen data and helps prevent overfitting, a phenomenon where the network memorizes the training data rather than learning generalized patterns.

The proposed neural network architecture incorporates 50 parameters within its output layer. These parameters are crucial elements that the network adjusts during training to optimize its ability to map image features to the corresponding 50 different excitation angles. To achieve a balance between accuracy and efficiency, we train the network for 30 epochs. Epochs represent complete cycles of the training process where the network is exposed to the entire training set. By carefully selecting the number of epochs, we can ensure that the network learns sufficiently from the data.

3.4. Prediction of defect length

In addition to detecting the excitation angle, we utilized a third independent deep learning model, employing the architecture described in section 3.2. This model specifically focused on predicting the length of potential defects within the tissue.

We leveraged a comprehensive dataset containing 20,000 images. We strategically split this dataset for robust training and validation. 16,000 images were designated for training the network, while the remaining 4,000 images formed the validation set used to assess the model's performance. To achieve a high degree of accuracy in defect length prediction, the training process continued for 30 epochs.

3.5. Construction of defect from specific angle

To extract the desired information from the processed images, we employed a two-pronged approach. First, we combined the outputs from the two independent neural networks, each dedicated to detecting the excitation angle and defect length. These networks, described in section 3.2, provided crucial insights into the characteristics of potential abnormalities within the tissue.

Secondly, to further enhance the information gleaned from the images, we implemented image filtering techniques. One such technique, homomorphic filtering, is particularly adept at improving image quality and revealing hidden details that might not be readily apparent in the raw data. By applying this filtering process, we aimed to extract the most comprehensive information possible from the images.

3.6. Extending next angular views from limited angular images

We employed a deep convolutional neural network (DCNN) to achieve a more comprehensive angular view for the reconstruction process. While the original captured images spanned angles from 0° to 50°, the DCNN facilitated the extension of this view to encompass a wider range, ideally up to 120°. This enhancement is crucial for generating a more accurate 3D representation of the tissue structure.

3.7. 3D image reconstruction

The FBP algorithm plays a pivotal role in reconstructing the 3D structure of the tissue. This iterative process leverages the series of 2D images, potentially including those generated by the DCNN to achieve a wider angular view. The extended set of 2D images, encompassing various angles, is used to generate a mathematical representation called a sinogram. An initial prediction of the 3D image is made. This prediction is then mathematically transformed back into a sinogram using a process called backpropagation. The obtained sinogram

from the predicted 3D image is compared to the original sinogram. The difference between these two sinograms is quantified using a metric like the Mean Squared Error (MSE). This MSE serves as an indicator of the discrepancy between the predicted and actual data. It iterates through these steps multiple times. In each iteration, the predicted 3D image is refined based on the MSE from the previous iteration. This iterative process continues until the MSE falls below a predefined threshold, signifying a satisfactory level of convergence between the predicted and actual sinograms.

4. RESULTS AND DISCUSSION

Our findings indicate significant potential for utilizing 3D IR Thermography in cancer diagnosis. The system achieved an impressive 92.96% validation accuracy in identifying the excitation angle, demonstrating its effectiveness in real-world scenarios. While the training accuracy was slightly higher at 94.40%, the validation accuracy is a more crucial metric, as it reflects the model's performance on unseen data. Notably, these accuracy levels surpass those reported in existing conventional cancer diagnostic studies.

Figure 3 depicts a line chart showcasing the training and validation accuracy over the course of 30 training epochs. This visualization would be helpful in understanding how the model's performance improved with each training iteration.

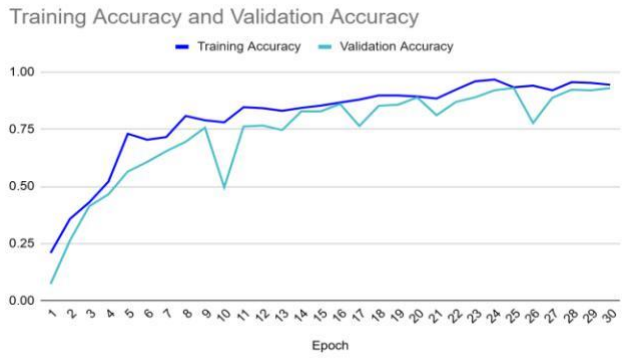

Figure 3. Accuracy line chart of angle of excitation prediction across 30 epochs.

While the initial focus of our study centered on predicting specific features of the defect itself, the investigation yielded valuable insights across various aspects. Analyzing the influence of angles on defect characterization through 3D IR thermography provided a strong foundation for further exploration in this area. Similarly, the experiments on predicting defect length advanced our understanding of the relationship between these parameters and their detectability within the reconstructions. Additionally, the exploration of predicting subsequent views of the defect yielded promising initial results, suggesting the potential for a more comprehensive approach to defect information gathering. Overall, the findings from these phases contribute significantly to our knowledge base regarding the application of 3D IR thermography for defect characterization. These observations lay the groundwork for further development and refinement of this technique for various applications.

5. CONCLUSIONS

The key contribution of this research lies in the development of a novel deep learning architecture trained to extract crucial information from multi-angle IR images, such as excitation angles and defect lengths. This approach enables a more thorough analysis of potential cancerous tissues than traditional single-angle methods. Using image processing techniques like FBP, we demonstrate the ability to reconstruct detailed 3D models of cancerous cells.

While this research represents a significant step forward, further investigation is warranted to refine the proposed approach. Future work will focus on optimizing the deep learning architecture for improved accuracy and generalizability. Additionally, clinical validation on a larger dataset will be crucial to assess the real-world effectiveness of this method in diagnosing cancer.

Overall, this research opens new possibilities for using 3D IR thermography and deep learning in cancer diagnosis. Its non-invasive nature and detailed 3D reconstructions show great promise for early detection, potentially improving patient outcomes and disease management.

REFERENCES

[1] Iacovino, Marialucia, et al. "Use of liquid biopsy in monitoring therapeutic resistance in EGFR oncogene addicted NSCLC." Exploration of Targeted Anti-tumor Therapy 1.6 (2020): 391. DOI: https://doi.org/10.37349/etat.2020.00024

[2] Dey, Subhrajit, et al. "Screening of breast cancer from thermogram images by edge detection aided deep transfer learning model." Multimedia Tools and Applications 81.7 (2022): 9331-9349. DOI: https://doi.org/10.1007/s11042-021-11477-9

[3] Mahoro, Ella, and Moulay A. Akhloufi. "Breast cancer classification on thermograms using deep CNN and transformers." Quantitative InfraRed Thermography Journal 21.1 (2024): 30-49. DOI: https://doi.org/10.1080/17686733.2022.2129135

[4] Verstockt, Jan, et al. "Skin cancer detection using infrared thermography: Measurement setup, procedure and equipment." Sensors 22.9 (2022): 3327. DOI: https://doi.org/10.3390/s22093327

[5] Thukral, Ruchika, et al. "Artificial intelligence-based prediction of oral mucositis in patients with head-and-neck cancer: A prospective observational study utilizing a thermographic approach." Cancer Research, Statistics, and Treatment 6.2 (2023): 181-190. DOI: https://doi.org/10.4103/crst.crst_332_22

[6] O'Mahony, Charlie, et al. "Investigation of reconstructed three-dimensional active infrared thermography of buried defects: multiphysics finite elements modelling investigation with initial experimental validation." Journal of Thermal Analysis and Calorimetry 142.1 (2020): 473-481. DOI: https://doi.org/10.1007/s10973-020-09678-9

[7] Zhang, Hao, BinBing Liu, and Peng Fei. "Self-supervised next view prediction for limited-angle optical projection tomography." Biomedical Optics Express 13.11 (2022): 5952-5961. DOI: https://doi.org/10.1364/BOE.472762

[8] Najafiaghdam, Hossein, et al. "3D Reconstruction of cellular images from microfabricated imagers using fully-adaptive deep neural networks." Scientific Reports 12.1 (2022): 7229. DOI: https://doi.org/10.1038/s41598-022-10886-6

43: USE OF DEEP LEARNING TECHNIQUES TO CLASSIFY ACOUSTIC EMISSION DATA FROM KNEE JOINTS

I. Vatolik [a], *G. Hunter*[a], *N. Swann*[b], *M. Everington*[a], *O. Lanets*[a,c], *S. Liaskovka*[a,c] , *C. Mbachu*[a] *and A.T. Augousti*[a,*]

[a] Faculty of Engineering, Computing and the Environment, Kingston University London, London SW15 3DW, UK
[b] School of Biosciences & Medicine, Faculty of Health and Medical Sciences, University of Surrey, UK
[c] Department of Technical Mechanics and Dynamics of Machines, Lviv Polytechnic National University, Lviv, S. Bandery Street 12 Ukraine

Biomedical Sensors 4, EM009, August 13, 2024, 2:50 PM - 4:00 PM

Abstract − We report here on the application of deep learning techniques to distinguish acoustic emission signals from human knees, recorded on 30 volunteers divided into three age groups 18-34, 35-49 and 50+. The deep learning model developed and applied to this data was able to correctly identify samples from each category with success rates of up to 89.5% in some cases, an outcome that is much higher than would be expected from random selection.

Keywords**:** acoustic knee emissions; deep learning

1. INTRODUCTION

We report here on a study to monitor acoustically the emissions from the knee joints of a range of human subjects. Although first investigated over a decade ago [1] this has been a topic of growing importance in recent years [2], in particular its applicability in joint health assessment, with the application of deep learning techniques [3]. The technique has proved itself to be promising in detecting of knee damage such as osteoarthritis [4]. We give in the following sections a brief description of the multi-modal detection arrangement used in this work, and the application of deep learning methods in classification of the resulting acoustic emission signals, including a description of a novel method of data augmentation which is appropriate to the data under investigation here.

2. METHODS AND PROCEDURES

We have reported elsewhere [5] on the details of the arrangement used to record acoustic knee emissions from subjects, and the sit-stand-sit protocol employed. In this instance we used 15 male and 15 female volunteers, divided into three age categories, 18-34 years, 35-49 years and 50+ years. Subjects had 28 reflective markers placed on specific body landmarks [4]. Reflections from these markers were captured using nine Qualisys Oqus 700+ cameras, and a typical sit-stand-sit procedure captured by the Qualisys system. Simultaneously force measurements were recorded on a Kistler Force platform (although these are not presented here), and the acoustic signal from the knee joint was recorded using a Laryngograph DSP Unit and a sensitive condenser microphone.

3. RESULTS AND DISCUSSION

3.1. Classical signal processing

The recorded data was subjected to some signal processing, for example to synchronise the visual signal recorded by the Qualisys system with the acoustic signal recorded by the Laryngograph system, and from the former of these kinematic variables such as knee angle, knee angular velocity and knee angular acceleration were calculated (Figure 2).

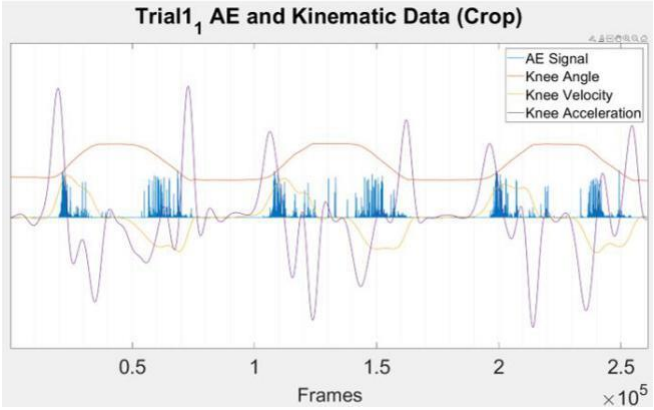

Figure 2. A scaled graph showing the calculated knee angle, knee angular velocity and knee angular acceleration versus the acoustic signal as a function of time (units not displayed, scaled to fit the same graph) for a typical sample.

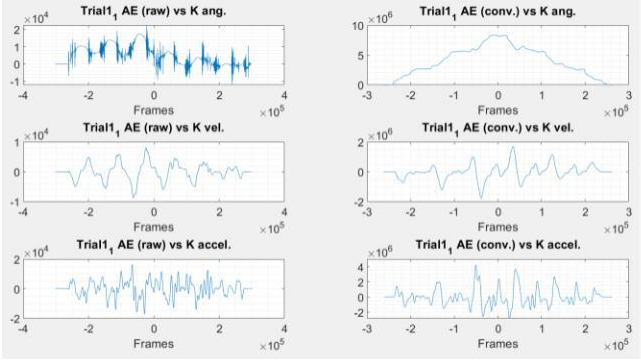

Figure 3. Cross correlation between the acoustic emission signal and each of the kinematic signals.

Some classical signal processing was also carried out, as shown in Figure 3, in order to establish potential correlations between the acoustic signal (AE) and these

DOI: https://doi.org/10.34961/researchrepository-ul.29290907.v1

kinematic variables. These appear to indicate a degree of correlation of the AE signal with all of the kinematic variables.

3.2. Correlation with knee angle

In order to analyse the correlation between acoustic emission events and the relative phase of the knee angle movement, the position of those events that exceed a specific threshold are indicated in Figure 4, with the plot showing the occurrence as a function of frame number. Figure 5 shows a scatter plot of the location of the AE events plotted as a function of knee angle. This plot is also colour coded to indicate the location of the events when the knee joint is either extending or flexing. These graphs demonstrate a few points of interest. Firstly, there appears to be good repeatability of the AE events at specific angles across all participants during the respective trials. Secondly, the events are not confined either to flexing or extending specifically, although they appear to be well correlated for individual knees. This repeatability for individuals, but distinctiveness between them, implies that there may be good potential for automated identification and classification of specific recordings by use of deep learning techniques, and this was explored further.

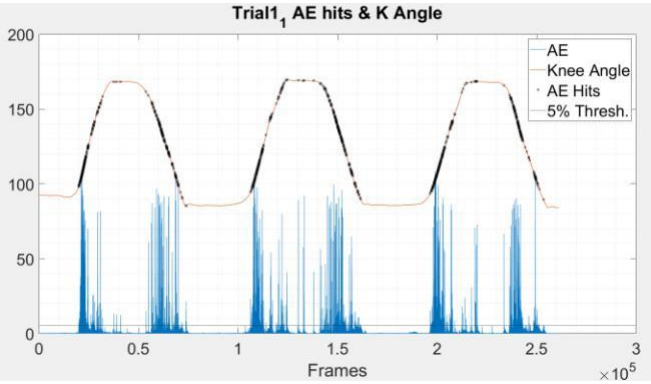

Figure 4. The plot displays AE hits over a 5% threshold plotted on a curve representing the knee angle synchronised with the AE signal.

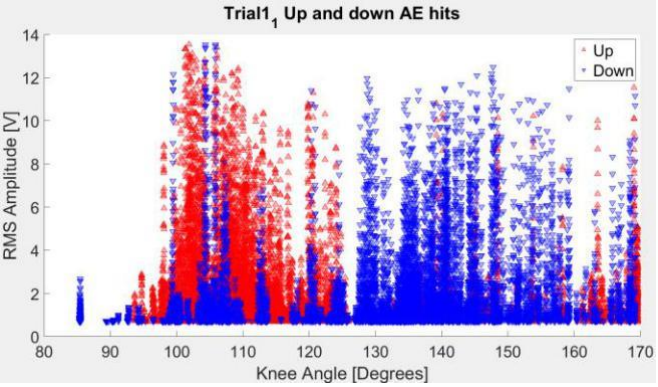

Figure 5. Shows a scatter graph of AE hits plotted over a knee angle with red triangles = knee extension, and blue triangles = knee flexion

3.3. Application of deep learning methods

Several approaches have been used to formulate the recorded information in a way in which it can be presented to a deep learning algorithm to work on. Initial attempts involved producing spectrograms of the AE signals, both 'raw' and denoised (Figure 6) and employing both a long-short-term memory recurrent neural network (RNN LSTM) and trained on the data. In the case the data used was an earlier version of this study employing 440 samples altogether, with a ratio of training:validation:testing of 80%:10%:10%.

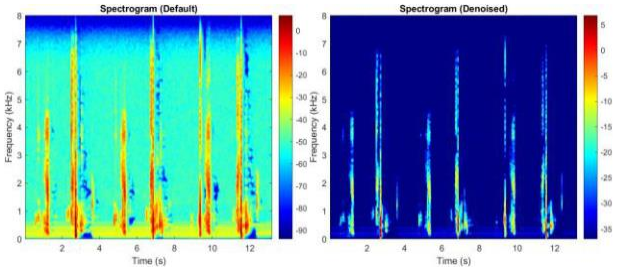

Figure 6. 'Raw' and denoised spectrograms of acoustic signals.

The results of this training are shown in Table 1 and Figures 9 and 10.

Table 1. Validation and testing accuracies of RNN and CNN

Network	Samples	Valid. Accuracy	Test. Accuracy
RNN-LSTM	440	78.3%	68.2%
CNN Train. Iter. 1	440	93.5%	77.3%
CNN Train. Iter. 2	440	86.9%	81.8%

a

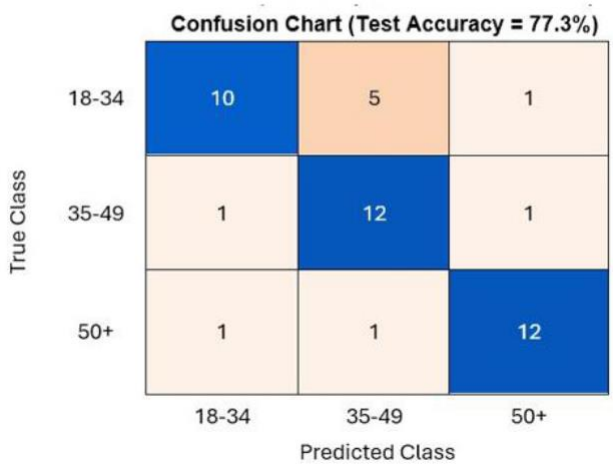

b

Figure 9. Confusion Matrix of CNN 1

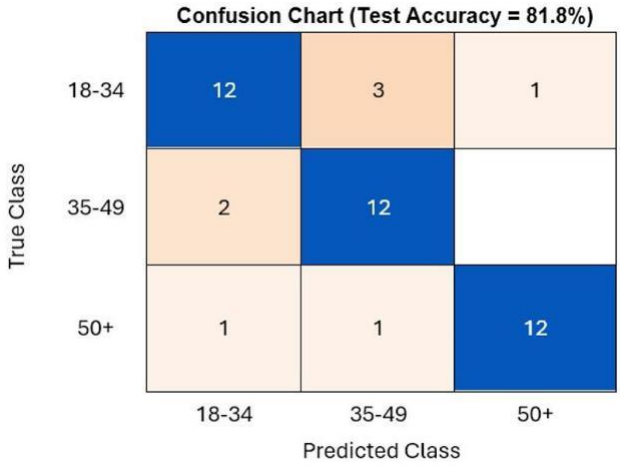

Figure 10. Confusion Matrix of CNN 2

Such initial results provided promising results based on the presentation of spectrograms and relatively limited datasets.

3.4. Alternative data representations and novel data augmentation technique

Following further development and use of the dataset described for in section 1, a set of '2D' images and a range of '3D' images were generated and used for training a reduced-layer CNN network (see Figure 11). The datasets were augmented in a way that is more appropriate for the 3D nature of the graphs presented, and it is clear that useful discriminatory power is consequently achieved.

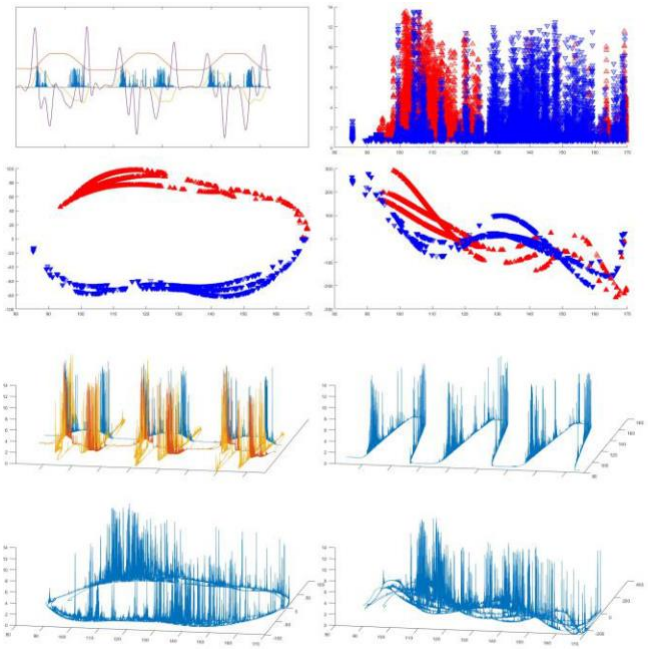

Figure 11. Presents 'collages' of a) 2D images of AE hits plotted on the kinematic variables b) 3D plots of AE hits plotted on the kinematic variables generated from the 2D images used for training of the CNNs

The comparison of the highest testing accuracy results between the 2D and 3D datasets can be seen in Table 2.

Table 2. Validation and testing accuracies of 3 types of datasets

Dataset	Samples	Valid. Accuracy	Test. Accuracy
2D	856	58.5%	61.5%
3D (3 rotations)	2568	84.2%	86.7%
3D (6 rotations)	5136	89.9%	89.5%

The confusion matrix supports the hypothesis that there is a trend in the noisiness of the signals with increasing age category, and furthermore indicated nearly 90% testing accuracy in category classification which is much higher than would be expected by chance (see Figures 12 and 13). Further work will be undertaken to customise and enhance the performance of the CNN in future.

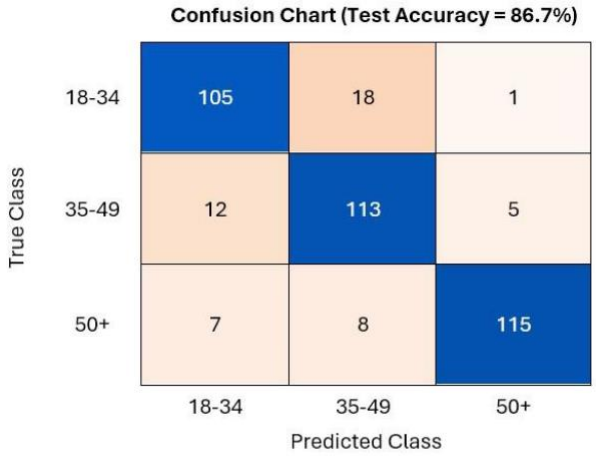

Figure 12. Confusion Matrix for customised CNN for testing accuracy using augmented 3D dataset with 3 rotations.

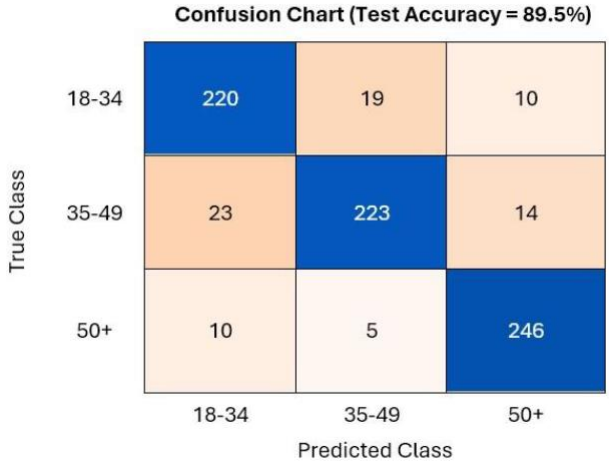

Figure 13. Confusion Matrix for customised CNN for testing accuracy using augmented 3D dataset with 6 rotations.

4. CONCLUSIONS

We have recorded a variety of acoustic knee joint emissions from 30 test subjects divided into three age categories and analysed these using both classical signal processing techniques as well as modern deep learning methods, developing also a novel method of data augmentation that is appropriate for the data investigated. The results support the hypothesis that there is an increasing trend in the signal with increasing age category, as well as demonstrating a true positive identification rate from the deep learning system developed that is much higher than would be expected by chance alone.

ACKNOWLEDGMENTS

We acknowledge the support of the Royal Academy's Researchers at Risk programme that has supported two of the authors (OL and SL) to be involved in this research.

REFERENCES

[1] L. Shark, H. Chen and J. Goodacre, (2010). **Discovering Differences in Acoustic Emission Between Healthy and Osteoarthritic Knees Using a Four-Phase Model of Sit-Stand-Sit**, *Open Med Inform J*, 4, pp116-125

[2] K. Kalo, D. Niederer, F. Stief, L. Wurzberger, S. van Drongelen, A. Meurer and L. Vogt, (2020). **Validity of and recommendations for knee joint acoustic assessments during different movement conditions,** *J Biomech*, Aug 26;109:109939. doi: 10.1016/j.jbiomech.2020.109939. Epub 2020 Jul 8. PMID: 32807320.

[3] R. Karpinski, P. Krakowski, J. Jonak, A. Machrowska, M. Maciejewski and A. Nogalski, (2022). **Diagnostics of Articular Cartilage Damage Based on Generated Acoustic Signals Using ANN—Part I: Femoral-Tibial Joint**, *Sensors*, (Basel). 2022 Mar 10;22(6):2176. doi: 10.3390/s22062176. PMID: 35336346; PMCID: PMC8950358.

[4] J. Kiselev, B. Ziegler, H. Schwalbe, R. Franke and U. Wolf, (2019) **Detection of osteoarthritis using acoustic emission analysis**, *Med. Eng. Phys*, 65:57-60. doi: 10.1016/j.medengphy.2019.01.002. Epub 2019 Jan 23. PMID: 30685113.

[5] I. Vatolik, M. Everington, G. Hunter, N. Swann and A. Augousti, (2022). **Development of a multi-modal sensor network to detect and monitor knee joint condition**, *Measurement: Sensors*, 24
DOI: https://doi.org/10.1016/j.measen.2022.100483

44: UTILISING INSTRUMENTATION TO MONITOR THE CONSTRUCTION OF A LARGE UNDERGROUND SHAFT IN IRELAND

Laura Willis [a*], *Ronan Royston* [b], *Declan Phillips* [c]

[a*] Ward and Burke Construction Ltd., Galway, Ireland & Faculty of Science and Engineering, University of Limerick, Ireland,

[b] Ward and Burke Construction Ltd., Galway, Ireland & Faculty of Science and Engineering, University of Limerick, Ireland,

[c] Faculty of Science and Engineering, University of Limerick, Ireland,

Abstract - This paper presents a case study of the construction of a 28 m diameter caisson as part of the €114 million Athlone Main Drainage Scheme in County Westmeath, Ireland. The caisson was built at ground level and sunk 15 m through soft clay, sands and gravel, and rock to formation. Three instrumentation systems were utilised to guide the installation and to record the performance of the shaft during and after construction: 1) a levelling system for guiding the sinking phase, 2) a novel automated lubrication system and 3) strain gauges to monitor hoop strain in the wall of the structure (utilising Fiber Bragg Grating, and vibrating wire, strain gauges). These three systems were successfully installed, operated, and monitored throughout the construction process. The data collected were processed and made available to onsite personnel via an online platform in real time, allowing engineers to make informed decisions in response to varying ground conditions. This case study provides insight into the instrumentation systems deployed and offers guidance for future projects with similar construction methodologies.

***Keywords*:** Construction; Instrumentation; Monitoring.

1. INTRODUCTION

This paper discusses the use of instrumentation systems to guide and inform the construction of a large-diameter caisson in Ireland. Three different instrumentation systems were installed in the shaft for this purpose: the liquid level system (LLS), the lubrication monitoring system (LMS) and the strain measurement system utilising both fiber-optics (FO) and vibrating wire (VW) strain gauges. These systems employed pressure transducers (PTs), fiber Bragg grating (FBG) FO armoured cables, and embedment VW strain gauges. The shaft was sunk through very soft clay before reaching formation on bedrock. It was anticipated that the shaft would move in several phases due to the varying ground conditions. Conveying this information to site personnel, particularly the excavator operator, through an online platform reduced the health and safety risks associated with the works and increased efficiency onsite.

1.1. Project Overview

The Athlone Main Drainage Scheme upgrades the existing wastewater collection infrastructure for the town. The River Shannon, a designated environmentally sensitive area, is frequently polluted due to the insufficient capacity of the sewer network. This is not compliant with the European Union's Urban Wastewater Directive [1]. As part of this upgrade a new pump station, located in Golden Island Athlone adjacent to the River Shannon, is being built to increase the wastewater management capacity by 4,500 m^3 (see Figure 1 (a)). This pump station was constructed as a 28 m internal diameter shaft, with a wall thickness of 1.6 m and a depth of 15.4 m.

1.2. Open Caisson Construction

A caisson is a large retaining structure, see Figure 1 (b) for an example of an open caisson during construction. The sinking of an open dug caisson shaft is a top-down construction method used to safely construct deep excavations. The self-weight of the structure provides the downwards kentledge, while simultaneously excavating the soil within the caisson causes the caisson to sink to the required formation level. A generic construction sequence of an open caisson is shown in Figure 1 (c).

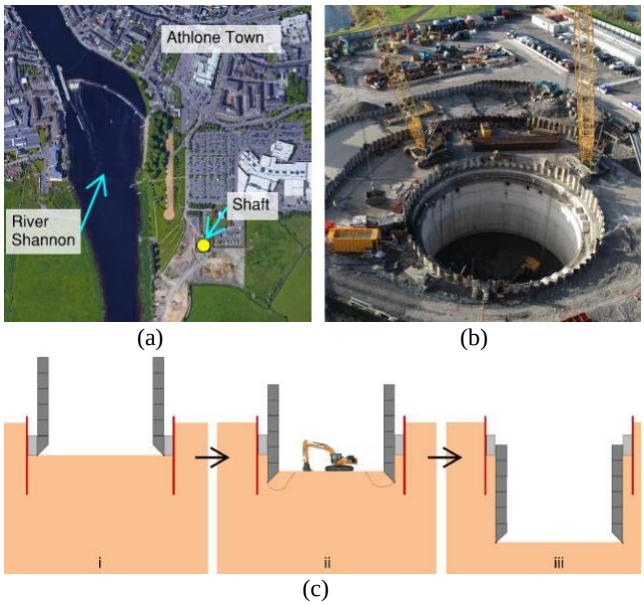

Figure 1: (a) Shaft location indicated on a map of Athlone; (b) 28 m internal diameter shaft during construction in Athlone; and (c) Section through shaft for different phases of construction : (i) Build wall creating downward kentledge, (ii) Dig internally to help fail the ground beneath the wall in bearing, and (iii) Caisson at formation level.

Some challenges associated with large diameter caisson construction include maintaining verticality while sinking, ensuring controlled movements into the ground and minimising friction at the soil-structure interface.

DOI: https://doi.org/10.34961/researchrepository-ul.29290949.v1

A typical cross-section of the base of a shaft is shown in Figure 2 (a) and consists of a tapered concrete edge with a leading steel edge. This leading edge creates an annulus on the external face of the shaft equal to its width [2]. Lubricating the annulus is achieved by fitting a lubrication line into the cutting edge as shown in Figure 2 (a) and pumping it with a lubricating fluid [3]. This fluid, typically bentonite, aims to minimise the frictional forces at the soil-shaft interface. Annulus failure can occur if positive pressures are not maintained and soil falls into the space, as shown in Figure 2 (b) [4].

Maintaining positive fluid pressure can be challenging. Failure of a lubrication annulus in coarse-grained soils during the construction of an instrumented caisson has been documented based on fluid pressure measured along the external face of the caisson [5]. It has been suggested that the effectiveness of a lubrication annulus should be estimated conservatively for coarse-grained soils and can result in a thicker walled structure [6]. This is not economical or environmentally friendly.

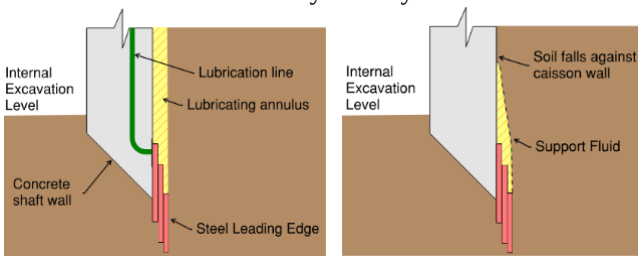

(a) (b)

Figure 2: (a) Schematic of the lubrication line fitted to the leading edge; and (b) The failure of an annulus in coarse-grained soils.

2. INSTRUMENTATION SYSTEMS

This section describes the instrumentation equipment installed in the shaft. The wall was constructed in seven consecutive vertical pours before being sunk as indicated in Figure 1 (c). A summary of instruments and their location is summarised in Table 1 and shown on a plan view and rolled out elevation of the structure in Figure 4 and Figure 5.

Table 1: Summary of instrumentation cast into the structure wall.

Pour No.	Instrument	Quantity	System
1	VW strain gauge	5	VW
1	FBG FO line	2	FO
2	PT	4	LLS
3	PT	8	LMS
3	VW strain gauge	5	VW

All instruments were wired back to a customised control container designed and built by Ward and Burke. The control container had four screens for monitoring instruments during the project, an electrical panel with computers, data loggers, power supply etc., and storage of components, see Figure 3.

(a) (b)

Figure 3: (a) Control container on site; and (b) Internal layout of the control container.

2.1. Liquid Level System (LLS)

The purpose of the level system is to inform the excavator driver of shaft movements vertically and any corresponding tilts of the structure in real time while sinking. This information then guides the digging process so that excavation can be sequenced such that the shaft remains vertical while sinking. Traditionally this would require a minimum of two site personnel working to relay the information. One person acting as a banksman standing on top of the wall and radioing the information to the driver, while the second person circles the shaft with a spirit level and measuring tape informing the banksman of any tilts and movements in the shaft.

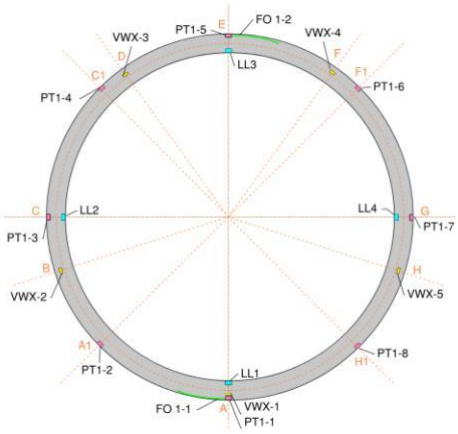

Figure 4: Plan view of instrumentation layout for all systems.

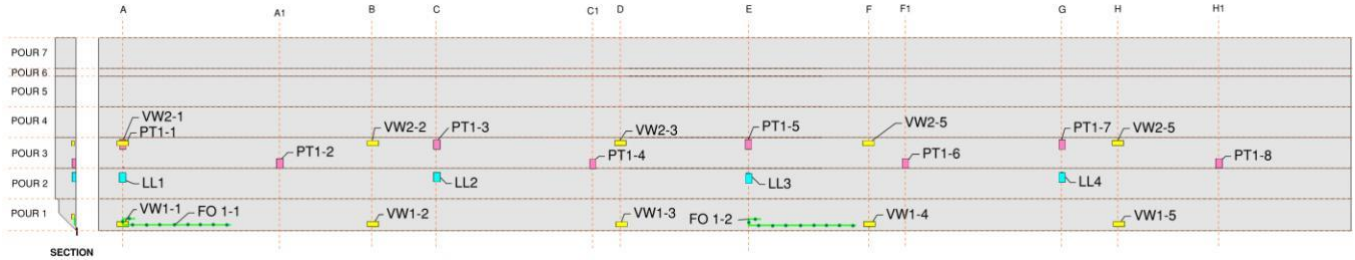

Figure 5:Rolled out elevation view of all the instrumentation cast into the wall.

LLS Theory

The level system comprises five pressure transducers (PTs), four cast into the wall at quarter points and the fifth one fixed to a stationary point at ground level, see Figure 6 (a) and (b). The five sensors are in an open loop system with a header tank located above all five PTs, using a fluid of known density, with a typical mix of water, drain dye and anti-freeze. Each PT reads pressure at a given location relative to the header tank, these are converted to elevations using Equation (1).

$$=\ \_\_\_ \quad (1)$$

Where P = Pressure reading (kPa), H = Head (m), = density of fluid (kgm^{-3}) and g = standard acceleration of gravity (ms^{-2}).

As the reference PT is at a known fixed elevation the difference in readings between the reference and the individual sensors gives the elevation of the shaft at quarter points. The difference in these elevations is used to determine the tilt of the shaft.

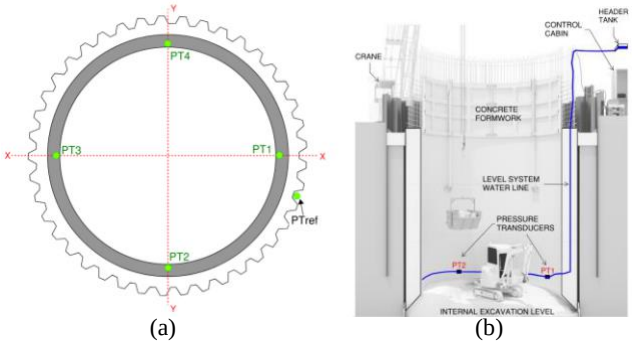

(a) (b)

Figure 6: (a) Plan view of level system with the PTs set out 90° apart; (b) Section through onsite set up of the level detection system.

Installation

The pressure transducers were configured inside IP68 boxes, tied to the structural rebar and pushed up against the shutter of the internal face of the wall, see Figure 7 (a) and (b). The PTs were accessible upon project completion and can be utilised on future projects, see Figure 7 (c). The hosing and cabling are run through glands on the box, brought around to a single point in the shaft and brought up through the concrete, see Figure 7 (d). The cable is run up to a data logger within the control cabin located adjacent to the shaft, (see Figure 3), while the hosing runs to the header tank, located over the control cabin.

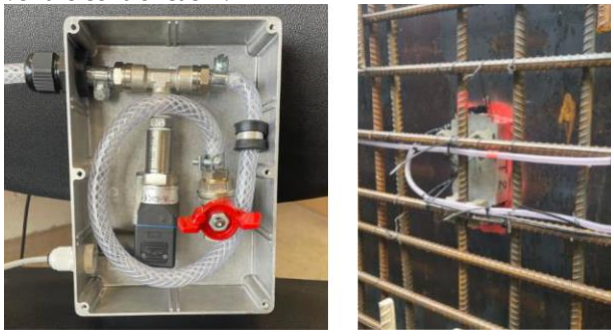

(a) (b)

(c) (d)

Figure 7: (a) Pressure transducer configuration within IP68 container; (b) IP68 box tied to rebar and flush up against shutter; (c) Box accessible from the inside of the shaft; and (d) Cables coming out though the concrete at the top of the pour.

Application

This data is processed in real time and relayed to the operatives on site through a python script and in-house web platform. This guides the excavation process to ensure that the shaft maintains verticality while sinking. A relatively simple 'stop go' system is utilised to inform the driver where to dig and is indicated with red and green icons on the screen of a tablet within the cab of the excavator, see Figure 8.

(a) (b)

Figure 8: (a) Level detection system inside the cab of a vehicle on site; and (b) Web platform display of level detection system data.

Results

The data from this system was processed post construction to investigate the relationship between site activities, ground conditions and corresponding shaft movements. A sample data set is shown in Figure 9 with the elevation on the primary y-axis, tilt on the secondary y-axis and time on the x-axis. The shaft movements over time are indicated by the black line, with the corresponding tilts along perpendicular axes indicated by the green and blue lines. The soil conditions at the base of the shaft over time are also noted on the graph.

The first notable movement in the shaft was a significant vertical drop of 2.9 m over 5 minutes on the 4th of January 2024, resulting in a maximum tilt across the shaft of 0.5°. The next notable movement was when the shaft sunk 1.5 m over 3 minutes on the 15th of January 2024, increasing the maximum tilt to 0.6°. Both movements occurred in soft clay, where larger quicker movements were expected.

The shaft progressed steadily from 24.93 mOD to 20.75 mOD while in silty ground conditions, however the tilt got progressively higher along the axis of PTs 2 and 4. Finally the shaft encountered boulders and bedrock for the remainder of the sinking process, however, this was not uniform across the footing of the shaft. While excavating through this ground the tilt of the shaft reduced to 0.2° before the final stage of sinking from 17.26 mOD to formation at 16.47 mOD with a final tilt of 0.7°.

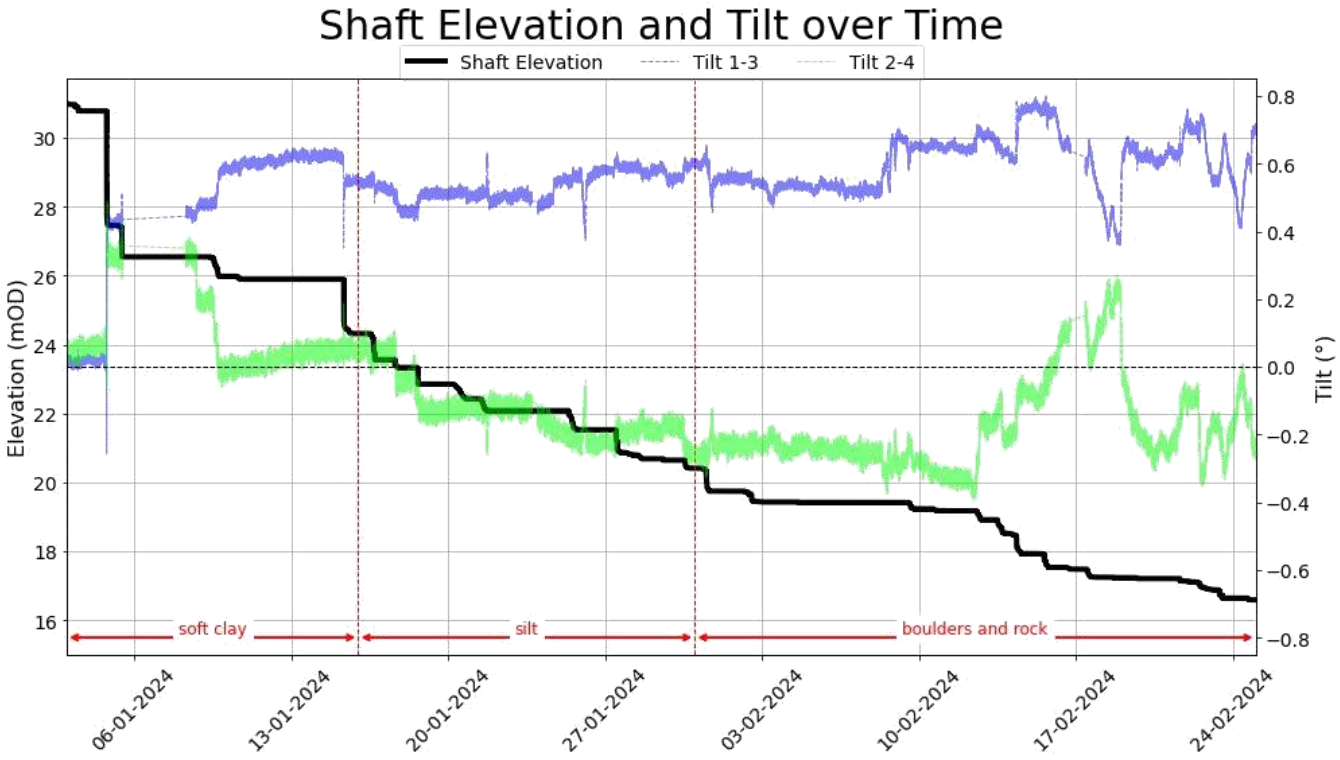

Figure 9: LLS results plotted; Shaft elevation over time on the primary axis and tilts for perpendicular axes plotted on the secondary axis.

2.2. Lubrication Monitoring System (LMS)

A bespoke lubrication system was developed for large diameter shaft projects. The purpose of the LMS is to both automate the operation of valves for the pumping of lubricating fluid as well as informing the lubrication process to ensure targeted and controlled lubrication.

LMS Theory

Based on the Ward and Burke caisson footing design, a 75 mm overcut was created by the steel cutting shoe on the external face of the shaft, see Figure 2 (a). The theory is that if this annulus can remain charged with a lubricating fluid the friction generated at the soil-structure interface can be minimised. However, maintaining a charged annulus can be difficult to achieve due to the non-homogeneity of the soil in the ground. Therefore, adapting the lubrication process in response to the varying ground to ensure effective lubrication is essential. To inform this process eight PTs were cast to the external face of the shaft wall to measure fluid pressure in the annulus.

To apply the information from these PTs, the lubrication process needed to control and target lubrication around the shaft. Therefore, two rings containing 12 lubrication sections were cast into the wall. These ports were plumbed back to a 24-valve manifold with solenoid valves within the control container, see Figure 10 (a). These valves were wired to relay switches which were controlled using a LabVIEW script. These valves could be manually selected or put on an automated sequence, see Figure 10 (b), which could be altered as sinking progressed.

Installation

Twelve lubricating sections (Figure 11 (a)) were tied to the steel and cast into the wall. At 8 points circumferentially pressure transducers were cast to the external face of the wall so that fluid pressure in the annulus could be monitored in real time, see Figure 11 (b). Again, these instruments were wired back to the control container for monitoring.

(a)

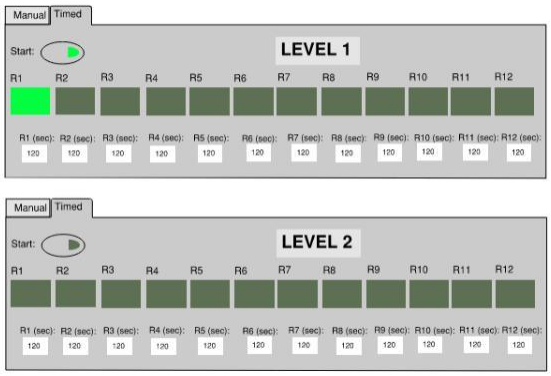

(b)

Figure 10: (a) The manifold with 24 valves before being plumbed in the LMS; (b) The user interface of the control system for the valves, this script allows the user to allocate the length of time each valve opens for on a cycle.

(a) (b)

Figure 11: (a) Lubrication ports before being tied into the shaft wall; and (b) The pressure transducer tied to the external face of steel in the wall and the lubrication port tied into the wall.

Application

On site the data from the PTs was available on the same platform as the LLS. This data was conveyed on a radar plot as shown in Figure 12. This data allowed the site team to adapt to the observed pressure readings by adjusting the length of time lubricating fluid was pumped to each section with the goal of ensuring uniform pressure in the annulus. For example, the response to the scenario depicted in Figure 12 would be to increase the length of time lubrication was being pumped to lubrication sections adjacent to PT5 and PT6.

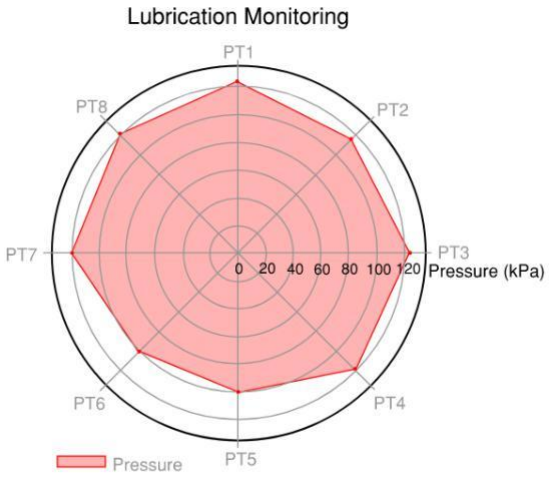

Figure 12: Radar plot of real-time pressure readings from LMS.

2.3. FO and VW Strain Measurement Systems

FO and VW Strain Sensing Theory

Instruments such as vibrating-wire strain gauges or metal foil gauges have typically been used to measure strain in reinforced concrete elements [7] [8]. The construction industry has seen an uptake in fiber optic strain sensing technologies in recent times. The use of FO strain sensing can replace hundreds of individual strain gauges by using a single fiber cable. This can significantly reduce the onsite time required to fit strain sensors and minimises the number of cables. It can also capture a more exhaustive strain profile with an increased number of gauges rather than discrete readings at a single point. FO strain sensors eliminate the risk of electrical magnetic interference or the effects of water damage, which are often observed in vibrating wire strain sensors, thus providing more robust strain sensing systems.

Fiber Bragg sensors, (short interference gratings), can be used to determine mechanical strain and temperature changes at discrete points along the fiber by measuring the shift in the reflected Bragg wavelength at each grating. Therefore, isolating of a single Fiber Bragg grating from mechanical strains by measuring only thermal effects using a casing with a known coefficient of thermal expansion can be achieved, for example aluminium casing. This methodology can be used to distinguish thermal and mechanical effects in a fiber optic line. This technology has already been successfully adopted to monitor strains in piles [9], and in diaphragm wall segments [10].

The purpose of the FO and VW strain measurement systems is to measure hoop strain on the external face of the shaft wall to provide guidance for future design methodologies for similar projects. The rationale for installing both systems is to validate the FO gauges with the VW gauges and to gather more data circumferentially due to the limited number of channels on the FO logger.

Installation

The installation of both FO and VW strain gauges was relatively straightforward as both systems were tied directly to rebar and required minor preparation beforehand. One FO FBG gauge in a ‘string’ was isolated for temperature compensation in a precisely milled aluminium casing, wrapped in insulation, and located adjacent to a VW strain gauge to validate the temperature compensation. The rest of the string was rolled out circumferentially to measure hoop strain as shown in Figure 13 (a). Each strain sensing gauge was held in place by cable-tying the FO cable on either side of the FBG, along with intermittent supports, see Figure 13 (b).

(a) (b)

Figure 13: (a) The isolated temperature sensing FBG located adjacent to the VW strain gauge; and (b) The ‘string’ of FBGs rolled out circumferentially.

The isolated grating will read thermal strain only. The data from this grating is then used to calculate the change in temperature measured at the location of this FBG. This change in temperature is calculated using Equation 2 and the data gathered from the temperature strain gauge. The value of S_1 for the aluminium casing used to isolate the temperature gauge was found experimentally in the lab.

$$\Delta = \frac{\ln \frac{\lambda}{\lambda_0}}{(\alpha_{alu} - \alpha_f) + s_1} \quad (2)$$

Where ΔT is the change in temperature °C, λ is the measured wavelength, λ_0 is the reference wavelength (zero strain), k is the sensor gauge factor, α_{alu} and α_f are the coefficients of thermal expansion for the aluminium casing and fibers respectively, and s_1 is the linear sensitivity factor.

This temperature change is then used to calculate the mechanical strain ($\epsilon_{mech,s}$) induced at the location of each fiber grating on the lines using Equation 3 [11]. Depending on the orientation of the grating when tied in place on site this strain can be either hoop strain (horizontal grating) or vertical strain (vertical grating) for a circular shaft.

$$= \frac{1}{\quad} \cdot [\ln(\quad\quad\quad\quad) - \Delta] - (\quad -) \cdot \Delta \qquad (3)$$

Application

Post-construction processing of all strain sensing elements will be conducted after all construction is complete (internal walls are still under construction). This data set will be used to validate the methodology outlined and interrogated to be compared with design hoop strains.

3. CONCLUSIONS

Three instrumentation systems were successfully installed in the caisson shaft and remained operational in a harsh construction environment. The instruments relayed critical information to site personnel in real time, allowing construction efficiencies to be achieved. The following are the main conclusions from this case study.

- A dense array of instrumentation systems were installed without any negative implications to the construction program.
- The LLS provided essential data in real time to guide the verticality of the shaft sinking process to within 1° throughout construction.
- The FO system's robustness has been demonstrated by the continuous operation and consistent data readings of all 20 FBGs. In contrast, water damage has compromised some thermistors in the VW strain gauges, causing them to fail. Therefore, based on this study, FO strain sensing has proven to be a more reliable and repeatable system.
- The correlation of site activities, and the ground profile with the instrumentation output revealed anomalies in shaft movements.
- The LMS allowed the onsite team to make pump adjustments to optimise annulus performance with lubrication fluid throughout the sinking process. The automated valve operation allowed for targeted and controlled lubrication.
- The instrumentation minimised health and safety risks by reducing the need for site personnel to measure shaft movements and tilt during the sinking process.

ACKNOWLEDGMENTS

The authors gratefully acknowledge the technical guidance and financial support provided by Ward & Burke Construction Ltd for this research, as well as the efforts of the site team at Golden Island pump station, Athlone. The authors also thank Shane Cosgrove of Ward and Burke's Information Technology team for developing the in-house online platform.

FUNDING STATEMENT

This work was financially supported by Ward and Burke Construction Ltd.

REFERENCES

[1] Department of Housing, Local Government and Heritage, **Approval for €113.6 million Athlone Main Drainage Network Upgrade Project**, Dublin, Ireland, 2022.

[2] E. Nonveiller, **Open Caissons for Deep Foundations**, Journal of Geotechnical Engineering, vol. 113, 1987, pp. 424-439.

[3] R. Royston, **Investigation of Soil-Structure Interaction for Large Diameter Caissons**, Doctoral thesis, University of Oxford, 2018.

[4] K. Terzaghi, R. B. Peck & G. Mesri, **Soil Mechanics in Engineering Practice**, New York: John Wiley & Sons, 1996.

[5] R. Royston, B. B. Sheil & B. W. Byrne, **Monitoring the construction of a large-diameter caisson in sand**, Proceeding of the Insititute of Civil Engineers – Geotechnical Engineering, 2020.

[6] D. Allenby, G. Waley & D. Kilburn, **Examples of open caissons sinking in Scotland**, Proceeding of the Institute of Civil Engineers – Geotechnical Engineering, 2009, pp 59-70.

[7] S. A. Austin, P.J. Robins and J.W. Bishop, **Techniques for the early-life in-situ monitoring of concrete industrial ground floor slabs**, In Specialist techniques and materials for concrete construction, Proceedings of International Conference, Dundee, 1999, pp 319-329.

[8] D. R. Coutts & J. Wang, **Monitoring of reinforced concrete piles under horizontal and vertical loads due to tunnelling**, In Tunnels and underground structures, Routledge, 2018, pp 541-546.

[9] A. Bell, K. Soga, Y. Ouyang, J. Yan and F. Wang, **The role of fiber optic instrumentation in the re-use of deep foundations**, In Proceedings of the 18th International Conference on Soil Mechanics and Geotechnical Engineering, Parix, 2013, pp 1863-1866.

[10] T. Schwamb, K. Soga, R.J. Mair, M.Z. Elshafie, R. Sutherden, C. Bouquet and J. Greenwood, **Fibre optic monitoring of a deep circular excavation**, Proceedings of the Institution of Civil Engineers – Geotechnical Engineering, vol. 167, 2014, pp. 144-154.

[11] FBGS International N.V., **Instruction Manual Strain Gage Kit**, 3rd Edition.

45: Laser Structure Based on a Fiber Ring and Peanut-Shaped Whisper Gallery Mode Microresonator

Anuradha Rout[a], Zhe Wang[a], Zhouchen Wang[a], Rayhan Habib Jibon[a], Anand V.R[a], Yiming Shen[a], and Yuliya Semenova[a]*

[a] Photonics Research Centre, School of Electrical and Electronic Engineering, Technological University Dublin, Grangegorman, Dublin 7, Ireland

Optical Fibre Sensors 1, EM010, August 12, 2024, 1:30 PM - 3:00 PM

Abstract – This study introduces a novel optical fiber laser system integrating a peanut-shaped whispering gallery mode microresonator (PSM) and an Erbium-doped fiber ring laser. We investigate the influence of the position of the light coupling fibre taper on the performance of the proposed laser to achieve lasing wavelength tunability, mode-switching, and multi-wavelength operation. Our findings demonstrate that varying the geometric dimensions of the PSM and the coupling taper position directly influences lasing performance, allowing precise control over emission wavelengths and mode characteristics. The unique peanut shape of the microresonator enables distinct mode solutions, which enhances the stability and tunability of the laser output. This research underscores the potential of geometrically tailored PSMs to advance the development of photonic devices, offering significant implications for next-generation optical systems in telecommunications and beyond. The results highlight the importance of microresonator geometry in optimizing the performance of fiber lasers.

Keywords: Whispering Gallery Modes (WGMs); fiber ring laser; peanut-shaped microresonator; mode switching; multi-wavelength laser.

1. INTRODUCTION

Optical Whispering Gallery Mode (WGM) resonators have attracted considerable attention due to their high quality factors (Q) and compact sizes, leading to exceptionally small mode volumes (V). This synergy significantly lowers the threshold for observing nonlinear optical phenomena ($\sim V/Q^2$), enabling the development of microcavity lasers with ultra-low power thresholds of less than a microwatt [1], [2], [3], [4], [5], as well as Kerr frequency comb sources with minimal power requirements [6], [7], [8], [9], [10]. Microresonators with a peanut shape have been previously explored by several researchers [11,12], however in most of the studies the focus was on minimizing the “valley effect” rather than exploiting it. Such resonators exhibited nearly identical modes to single-bottle resonators. Noted that previous studies primarily focused on minimizing the "valley effect" in these PSMs, which refers to a characteristic of the resonator where the energy of certain modes is concentrated in the centre of the peanut shape. However, unlike micro bottle resonators which lack a significant valley, in peanut shaped microresonators (PSMs), the valley depth is comparably smaller (150 μm). This structural distinction leads to unique modal solutions. However, in contrast to PSMs, the authors claimed to excite whispering gallery modes (WGMs) of a central resonator between the microspheres rather than of the joint structure [11].

This paper utilises a fiber WGM microresonator with a distinctive peanut shape, consisting of two closely adjoined spheres creating a valley between them, also known as peanut-shape microresonator (PSM). In this study, we introduce a novel laser structure utilizing an Erbium-doped fiber ring (EDFR) combined with a peanut-shaped microresonator (PSM) featuring spherical lobes with diameters of 210 μm and 190 μm, and a central or valley region with a diameter of 150 μm. The PSM serves as the wavelength-selective component. The tunability of the laser was explored by adjusting the coupling point of light along the PSM's long axis. Building upon this research, we have expanded our investigation to analyze the impact of PSM geometry on lasing performance and explore capabilities such as laser tuning, mode switching, and multi-wavelength operation. This study represents the first exploration of peanut-shaped microresonators with its unique variable diameters, combining experimental analyses to unveil their unique properties and showcase their promising characteristics. These resonators exhibit unique WGM properties and Q factors circa 10^4, making them suitable for mechanical tuning similar to that of microbottle resonators [13]. This work, the first to report on peanut-shaped resonators' response to mechanical tuning, within the fiber ring on the system’s output spectrum, highlighting the role of PSMs in the future of optical technologies.

2. METHODS AND PROCEDURES

A manual mode commercial optical fusion splicer (Sumitomo Electric Industries, Type-36) was utilized to fabricate the PSM sample by joining two cleaved ends of standard single mode fibers (SMFs). The process is depicted in Figure 1. Initially, as shown in Figure 1(a), two SMF ends with stripped coatings were cleaned and cleaved, then aligned within the splicer. In the subsequent step (Figure 1(b)), each fiber end was heated and partially melted using a single electric arc discharge to form two distinctive microspheres. Next, the two partially melted microspheres were brought close together, but not in direct contact, by controlling the fusion splicer motors. This process aimed to create a "peanut" shape rather than a solid connection. Subsequently, a single arc discharge lasting 5 seconds was applied at the vicinity of their contact, resulting in the formation of a PSM as depicted in Figure 1(c), characterized by its widest diameter at the upper lobe region of approximately 210 μm, lower lobe diameter 190 μm . The

DOI: https://doi.org/10.34961/researchrepository-ul.29291018.v1

middle section diameter of PSM is approximately 150 µm. This shape is crucial for the resonator's optical properties, as it influences factors like light confinement, mode distribution, and the quality factor of the resonator. After the splicing, the surface of the resonator is meticulously polished using ethanol to minimize scattering losses, ensuring efficient light transmission.

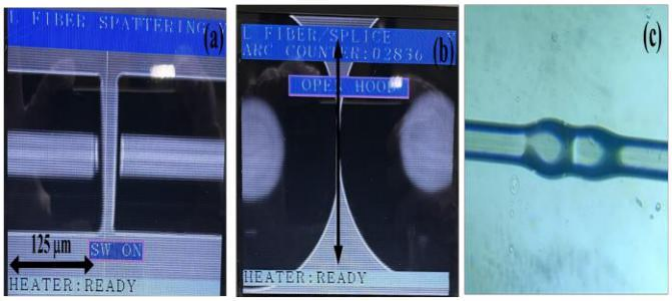

Fig. 1. Fabrication of a PSM using fusion splicer: (a) alignment of the fiber ends; (b) partially melted fiber ends after application of one arc; (c) fabricated PSM.

The proposed fiber ring laser configuration, as depicted in Figure 2, and incorporates a laser diode (LD) operating at 980 nm as the pump source, controlled by a current driver for power modulation. A wavelength division multiplexer (WDM) directs the pump laser signal into the fiber ring laser cavity. Within the setup, a 13 m segment of Erbium-doped fiber (EDFL) absorbs the pump light, generating amplified spontaneous emissions (ASEs) spanning from 1500 to 1600 nm. These emissions are then channelled through one port of a three-port optical fiber circulator (OFC), establishing a fiber ring loop. The second port of the OFC connects to a fiber taper (FT) with a uniform waist diameter of approximately 1 µm through a PSM, positioned perpendicular to and in direct contact with the resonator. This connection was achieved through precise alignment using a microscope and translation stage to adjust the position of the taper with respect to the different points along the microresonator axis. The ASE spectrum injected into the FT excites whispering gallery modes (WGMs) within the PSM. The signal reflected from the PSM is reintroduced into the ring cavity via the third port of the OFC. In this setup, the PSM with its unique variable diameters functions as a wavelength-selective filter, providing external feedback into the fiber laser ring. The WGM spectrum induced in the PSM through coupling in and out of the resonator generates weak reflections, which are fed back into the ring cavity, resulting in single- or multi-mode lasing emissions at wavelengths corresponding to specific WGM spectra and polarization states. Additionally, a polarization controller is introduced into the ring cavity to investigate the impact of light polarization on system performance and enhance stability. The output laser spectrum is monitored using an optical spectrum analyzer (OSA) with a spectral resolution of 0.01 nm.

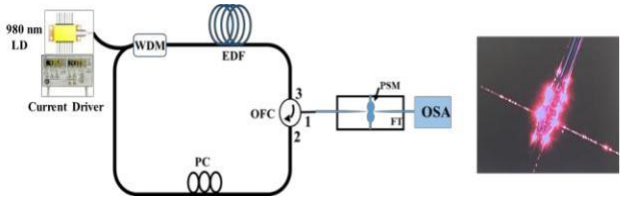

Fig.2 Schematic diagram of the proposed fiber laser: LD - laser diode; WDM - wavelength- selective coupler; EDF - Erbium-doped fiber; OFC - optical fiber circulator; FT - fiber taper; PC - polarization controller; PSM - peanut-shaped-micro bottle resonator; OSA- optical spectrum analyser.

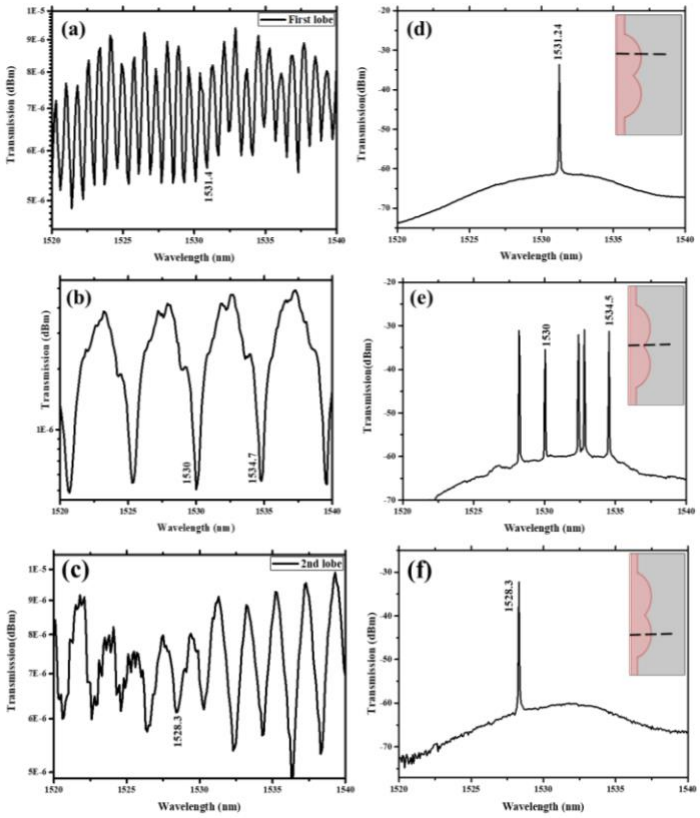

Fig.3 WGM spectra of the PSM sample (transmission spectra of the light coupling FT) (a) when the FT is coupled to the first lobe; (b) when the FT is coupled to the center of the "valley" and (c) when the FT is coupled to the second lobe; (d) output lasing spectrum corresponding to the FT position (a), (e) output lasing spectrum corresponding to the FT position (b) and (f) output lasing spectrum corresponding to the FT position (c). The coupling points are illustrated schematically in the insets of the graphs.

As can be seen from the above results, it is possible to tune the spectral positions of the lasing modes by moving the FT along the PSM axis. It should be noted, however, that the tuning laws for both lobes differ, and the spectral shifts appear to be non-monotonic. This can be explained by the differences in modal density of the transmission spectra of the microbottle resonator (MBR) when the FT is moved along the axis of the MBR, as reported by Murugan et al. in [14]. The study showed that as the tapered fiber is moved from the bottle centre to the neck of the microbottle, significant changes in the WGM modal density in the transmission spectrum of the coupling FT occur due to differences in modal excitation and selectivity. This, in turn, changes the filtering properties of the PSM spectrum in the proposed setup giving rise to various lasing modes in the fiber ring cavity. This is also illustrated in Fig. 3 above, where graphs (a), (b) and (c) show the transmission WGM spectra of the PSM sample when the TF is coupled to its first lobe (a), central point (b) and second lobe (c). Figures 3 (d), (e) and (f)

illustrate the corresponding lasing spectra after the coupled PSM was connected to the fiber ring. It can be seen that the different coupling positions of the taper lead to different modal densities of the WGM spectra [(a) (b) and (c)].

By gradually adjusting the position of the FT with respect to the lobes of the PSM, researchers were able to observe specific experimental outcomes. This lobe, being one of the widest region of the PSM, was expected to exhibit unique optical properties due to its curvature and size. This region of PSM was found to be 210 µm. The transmission spectra were carefully recorded. . A laser peak was observed at wavelength of 1531.24 nm as shown in figure 3 (a). This concludes the resonance condition created by the PSM's geometry that supports unique whispering gallery modes (WGMs) by the wider lobe, optical feedback within the cavity, and the precise alignment ensuring optimal coupling efficiency.

The central axis, representing the narrow connecting bridge between the two lobes of the PSM has a diameter of 150 µm. Multiple wavelengths were observed at 1528.2 nm, 1530.05 nm, 1532.4 nm, 1532.8 nm, and 1534.55 nm in figure 3 (b). The graph illustrates that multiple WGM modes are reflected back into the fiber ring cavity when the FT is coupled at the narrowest region of the PSM, providing valuable insights into the PSMs optical behavior. The bridging "valley" region induces strong coupling between high-order WGMs of the two spheres, resulting in a unified structure rather than two distinct spherical resonators.

A single dominant laser wavelength at 1528.3 nm is excited when the FT is in contact with the second lobe (190 µm) as shown in figure 3 (f).

The observation of single lasing wavelengths at the lobes and multiple wavelengths at the waist of a peanut-shaped optical resonator is a fascinating phenomenon that arises from the resonator's unique geometry and the dynamics of the WGMs within it. At the lobes, the smoother curvature and larger volume allow for well-defined modes that resonate at specific wavelengths, determined by the material's refractive index. These modes are relatively stable, leading to the observation of single, distinct wavelengths. In contrast, the waist, the narrowest part of the resonator, acts as a bridge that facilitates stronger coupling between the lobes. This region can support hybrid modes resulting from the interaction between the modes of each lobe, leading to mode splitting [15]. The tight confinement at the waist and allowing multiple wavelengths to coexist due to the enhanced field overlap. This complex interplay between the resonator's structure and the light within exemplifies how geometry can influence optical properties, enabling the coexistence of multiple wavelengths at the waist while maintaining singular wavelength resonances in the lobes.

Polarization Stability:

In subsequent experiments, we examined the effects of polarization by employing a three-paddle polarization controller (FPC030, Thorlabs). To alter the polarization state within the fiber ring, the central half-wave plate paddle's vertical starting position was adjusted across a range of angles: from 0^0 to 45^0, 90^0, -45^0, and -90^0. Meanwhile, the quarter-wave plates remained in their initial vertical orientations. The rotation of the paddle by a given angle resulted in the fiber's twisted sections inducing a corresponding rotation in the polarization angle:

$$\theta=\alpha\tau \quad (1)$$

where $\alpha=-n^2\ p_{44}$ [16], P_{44} is the fiber's elasto-optic coefficient, and n is the core's refractive index. The elasto-

the numerical values of P_{11} and P_{12} are 0.121 and 0.270, respectively [17]. Equation (1) allows us to calculate the rotation of polarization from the original position as 14.44^0.

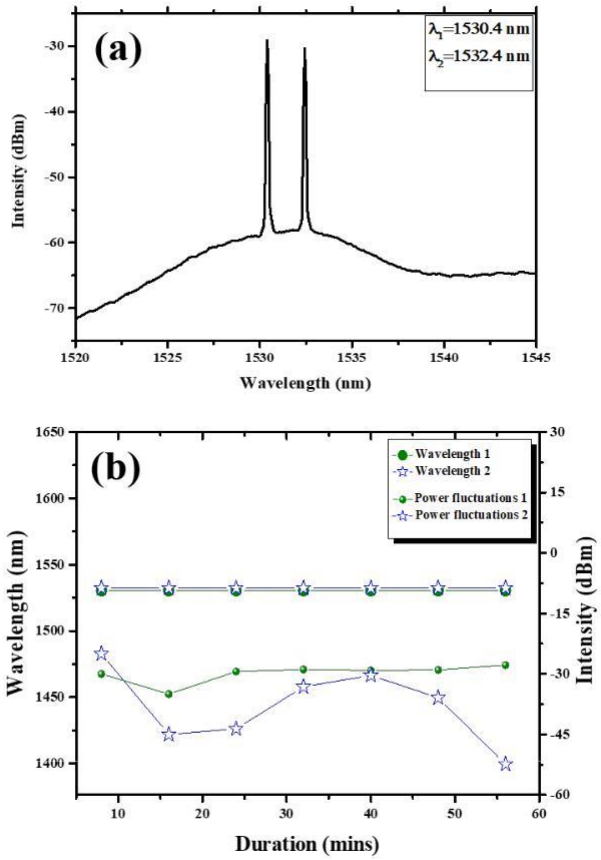

Fig.4 (a) Output spectrum of the PSM-based system at 14.44^0 polarization state and laser pump power of 150 mW; (b) wavelength drift and power fluctuations during the 60 min experiment for the single laser peak.

3. CONCLUSIONS

This investigation into the use of peanut-shaped WGM microresonators within a fiber ring laser framework has highlighted significant advancements in the control and manipulation of laser characteristics. The unique geometrical configuration of PSMs enables distinct mode solutions, enhancing laser tuning and stability. Our experiments confirmed that varying the PSM geometry directly influences the lasing performance, allowing for controlled manipulation of emission wavelengths and mode characteristics. Moving forward, further exploration of different materials and shapes will continue to expand our understanding and application of WGM microresonators in optical technologies.

ACKNOWLEDGMENTS

This work has emanated from research conducted with the financial support of the Science Foundation of Ireland.

FUNDING STATEMENT

This work was supported by Science Foundation Ireland grants 18/CRT/6222 and 13/RC/2077_P2.

REFERENCES

1. T. J. Kippenberg, K. J. Vahala, and S. M. Spillane, “Ultralow-threshold Raman laser using a spherical dielectric microcavity,” *Nature*, vol. 415, no. 6872, pp. 621–623, 2002.
2. V. Sandoghdar, F. Treussart, J. Hare, V. Lefèvre-Seguin, J. Raimond, and S. Haroche, “Very low threshold whispering-gallery-mode microsphere laser,” *Phys. Rev. A*, vol. 54, no. 3, pp. R1777–R1780, 1996.
3. S. Zhu, B. Xiao, B. Jiang, L. Shi, and X. Zhang, “Tunable Brillouin and Raman microlasers using hybrid microbottle resonators,” *Nanophotonics*, vol. 8, no. 5, pp. 931–940, 2019.
4. B. Jiang, S. Zhu, L. Ren, L. Shi, and X. Zhang, “Simultaneous ultraviolet, visible and near-infrared continuous-wave lasing in a rare-earth-doped microcavity,” *Proc. SPIE*, vol. 4, 2022, Art. no. 046003.
5. B. Jiang et al., “Room-temperature continuous-wave upconversion white microlaser using a rare-earth doped microcavity,” *ACS Photon.*, vol. 9, no. 9, pp. 2956–2962, 2022.
6. I. H. Agha, Y. Okawachi, M. A. Foster, J. E. Sharping, and A. L. Gaeta, “Four-wave-mixing parametric oscillations in dispersion compensated high-Q silica microspheres,” *Phys. Rev. A*, vol. 76, no. 4, pp. 0438371–0438374, 2007.
7. I. H. Agha, H. Imad, O. Yoshitomo, and L. G. Gaeta, “Theoretical and experimental investigation of broadband cascaded four-wave mixing in high-Q microspheres,” *Opt. Exp.*, vol. 17, no. 18, pp. 16209–16215, 2009.
8. Z. Chen, X. Tu, M. Dai, Q. Li, and H. Y. Fu, “Kerr frequency comb generation in microsphere resonators with normal dispersion,” *J. Light.Technol.*, vol. 40, no. 4, pp. 1092–1097, 2022.
9. P. Del’Haye, A. Schliesser, O. Arcizet, T. Wilken, R. Holzwarth, and T. J. Kippenberg, “Optical frequency comb generation from a monolithic microresonator,” *Nature*, vol. 450, no. 7173, pp. 1214–1217, 2007.
10. B. P. Scott et al., “Microresonator frequency comb optical clock,” *Optica*, vol. 1, no. 1, pp. 10–14, 2014.
11. H. Qin, Y. Yiheng, and D. Ming, "Strain-induced tunable dual-bottle-shaped optical microresonator." Opt. Lett., vol. 44, no. 24, pp. 6017-6020 (2019).
12. E. Yacoby and Y. London, "Saddle-Shape Whispering Gallery Mode Microresonators," in *Journal of Lightwave Technology*, vol. 41, no. 10, pp. 3139-3144, 15 May15, 2023, doi: 10.1109/JLT.2023.3237696.
13. Anuradha Rout, Zhe Wang, Zhuochen Wang, and Yuliya Semenova, "Laser structure based on an erbium-doped fiber ring and a whispering gallery mode microbottle resonator," Appl. Opt. 62, E103-E108 (2023)
14. G. S. Murugan, J. S. Wilkinson, and M. N. Zervas, “Selective excitation of whispering gallery modes in a novel bottle microresonator,” Opt. Express 17, 11916–11925 (2009).
15. Lei Shang, Liying Liu, Lei Xu; Highly collimated laser emission from a peanut-shaped microcavity. *Appl. Phys. Lett.* 18 February 2008; 92 (7): 071111. https://doi.org/10.1063/1.2839383
16. R. Ulrich and A. Simon, “Polarization optics of twisted single-mode fibers,” Appl. Opt. 18, 2241–2251 (1979).
17. D. C. Brown and H. J. Hoffman, “Thermal, stress, and thermo-optic effects in high average power double-clad silica fiber laser,” IEEE J. Quantum Electron. 37, 207–217 (2001).

46: Development of an optical fibre-based plasmonic sensor for specific detection of target biomolecules

Payel Ghosh[1],NVS Praneeth[2], Gayatri Joshi[2], Arup Lal Chakraborty[1], Sharmistha Dutta Choudhury[3], VV Raghavendra Sai[4], Saumyakanti Khatua[2,*]

[1] *Department of Electrical Engineering, Indian Institute of Technology Gandhinagar, Gujarat, India*
[2] *Department of Chemistry, Indian Institute of Technology Gandhinagar, Gujarat, India*
[3] *Radiation & Photochemistry Division, Bhabha Atomic Research Centre, Mumbai, India*
[4] *Biomedical Engineering Group, Department of Applied Mechanics, Indian Institute of Technology Madras, Chennai, India*

Biomedical Sensors Session 3, EM009, August 13, 2024, 11:30 AM - 1:10 PM

We report on the development of an optical fibre-based plasmonic sensing platform for specific detection of target biomolecules. The sensing platform uses a U-bent optical fibre covered with a monolayer of chemically synthesized triangular nanoprisms-shaped gold nanoparticles. The sensor relies on the refractive index dependent shift of the surface plasmon resonance (SPR) wavelength of the nanoparticles upon binding with the target molecules. The chemical fabrication process was optimized to tune the SPR wavelength of the nanoparticles to NIR wavelengths for optimized refractive index sensitivity. The nanoprisms were deposited on the fibre via directly dip-coating in nanoparticle solution. A portable CCD-spectrometer was used to measure the SPR wavelength shift.

We tested the sensing platform for the detection of miRNA (25 base pairs) of specific sequences. For this, nanoparticles were first functionalized with the complementary cDNA sequence (DNA-A). The probes are exposed to two different miRNA sequences: (a) miRNA-A: complementary to cDNA-A and (ii) miRNA-C: mismatch pair of the cDNA-A. We observed up to 20 nm red shift in nanoparticle SPR wavelength for miRNA-A. On the other hand, no spectral shift was observed in case of miRNA-C sequence, demonstrating the specificity of our detection scheme.

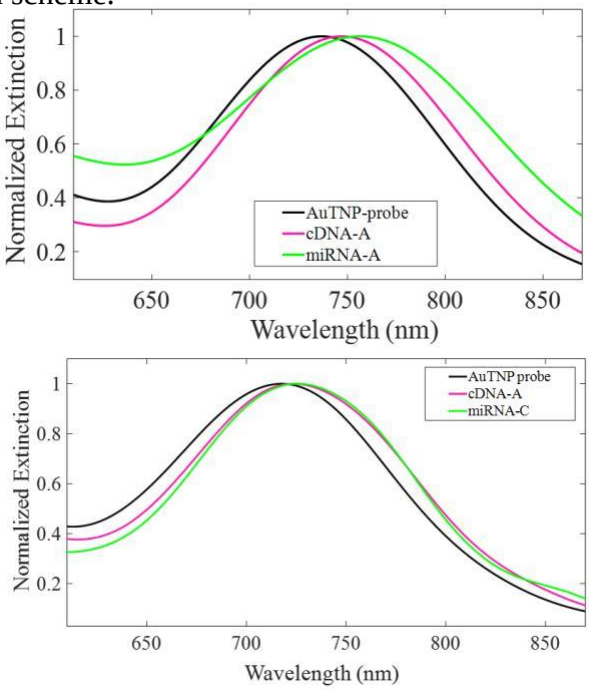

Figure 1: (upper panel) SPR shift of 19 nm was seen due to binding of cDNA-A with complementary sequence miRNA-A. (lower panel) No shift was observed for mismatched miRNA-C.

DOI: https://doi.org/10.34961/researchrepository-ul.29291108.v1

47: RADIO FREQUENCY DIRECTION SENSING ENABLED BY BROADSIDE COUPLED SPLIT RING RESONANTORS

Xiaoguang Zhao [a, *], *Zhenci Sun* [a], *Rui You* [b], *and Jiahao Zhao* [a]

[a] Department of Precision Instrument, Tsinghua University, Beijing 100084, China,
[b] School of Instrument Science and Opto-Electronic Engineering, Beijing Information Science and Technology University, Beijing 100016, China,

Emerging Sensing Strategies and Applications Cont., EM010, August 14, 2024, 11:00 AM - 12:10 PM

Abstract – Directional radio frequency (RF) sensing plays an essential role in various applications that concern localizing RF sources. However, current directional RF sensing technologies are hampered by their large antenna sizes and complex RF signal processing circuits, hindering the development of miniaturized subwavelength direction sensors. This paper presented a non-Hermitian broadside coupled split ring resonators (BC-SRRs), which can identify the direction of an incident RF signal with angles ranging from 0° to 180°. The non-Hermitian Hamiltonian of the system can be interpreted by the temporal coupled mode theory (TCMT). We further employed a one-stage Dickson voltage multiplier to rectify the RF signals and demonstrated directional RF sensing ability. Our results showcase the potential of the proposed technique using non-Hermitian BC-SRRs as a pathway towards subwavelength antenna-based RF direction finding.

Keywords**:** Non-Hermitian; broadside coupled split ring resonators; directional RF sensing

1. INTRODUCTION

Radio direction finding (RDF) is a crucial radio frequency (RF) sensing technique in various applications, such as radar systems, navigation, and electronic warfare, among others [1]. Conventional RDF techniques enable the detection of signal angles utlizing an array of large receiving antenna [2]. Moreover, it is also impractical to achieve the complicated signal processing, such as obtaining phase differences between output signals, in the low-power miniaturized systems, or microsystems [3].

Seeking inspirations from nature, we found that the auditory system of small animals, including geckos and flies, provides insights into directional sensing. The small animals with short ear-to-ear separations relative to the sound wavelength cannot directly perceive the intensity differences of sound waves between their ears. They can exhibit directional hearing through a coherent coupling of acoustic waves between the two closely spaced ears [4]. Thus, this natural phenomenon offers a design paradigm to achieve compact directional sensors with a deep subwavelength spacing. Biologically inspired directional sensors, consisting of two coupled components, have been reported in the fields of acoustics [5] and optics [6]. These miniaturized directional sensors greatly reduce the volume and system complexity, promoting their application in microsystems.

In this article, we proposed a subwavelength RF directional sensor comprising broadside coupled split ring resonators (BC-SRRs) capable of detecting the incident angle of electromagnetic (EM) waves. Using the temporal coupled mode theory (TCMT), we theoretically demonstrated the non-Hermitian coupling of scattered waves from the sub-wavelength BC-SRRs (< 0.1 λ_0). The giant difference of transmission coefficients at resonance originated from this non-Hermitian coupling, which was benefit for improving the angle sensing ability. Experimental validation confirms that the BC-SRRs in conjunction with the voltage multiplier can directly sense the incident angle of RF signal without the need of complicated signal processing circuit. This work provides an insightful understanding of non-Hermitian coupled resonance from the BC-SRRs, and presents an effective solution for directional RF sensing solution using the coupled subwavelength resonators.

2. RESULTS AND DISCUSSIONS

2.1. Design and simulation

The proposed non-Hermitian coupled system is described in Figure 1a, in which the transmitter antenna is considered as a resonator a_1, and the detector comprises of resonators a_2 and a_3, respectively. Using TCMT, the response of this system can be modelled by [7]

$$\frac{d}{dt}\begin{matrix}a_1\\ a_3\end{matrix} = jH_0\begin{matrix}a_1\\ a_3\end{matrix} + jH_i\begin{matrix}a_1\\ a_3\end{matrix} + \mathrm{K}\begin{matrix}s_{1+}\\ s_{3+}\end{matrix} \quad (1)$$

in which a_i is the oscillation strength of each resonator (i = 1, 2, or 3), H_0 is the usual Hamiltonian for the independent resonators, H_i represents the coupling between resonators, and K is the coupling matrix between the ports. The Hamiltonians and coupling may be expressed by

$$H_0 = \begin{matrix}\omega_{01} + j(\gamma_{n1} + \gamma_{r1}) & 0 & 0\\ 0 & \omega_{02} + j(\gamma_{n2} + \gamma_{r2}) & 0\\ 0 & 0 & \omega_{03} + j(\gamma_{n3} + \gamma_{r3})\end{matrix} \quad (2)$$

$$H_i = \begin{matrix}0 & k_{12} & k_{13}\\ k_{21} & 0 & k_{23}\\ k_{31} & k_{32} & 0\end{matrix} \quad (3)$$

$$\mathrm{K} = \begin{matrix}k_{11} & 0 & 0\\ 0 & k_{22} & 0\\ 0 & 0 & k_{33}\end{matrix} \quad (4)$$

DOI: https://doi.org/10.34961/researchrepository-ul.29291177.v1

in which, ω_{0i}, γ_{ni}, and γ_{ri} represent the resonance frequency, intrinsic loss, and radiative loss of each resonator, respectively. k_{im} (i, m = 1, 2, 3, and i ≠ m) is the coupling strength between resonators, and k_{ii} is the coupling strength between the port in the corresponding resonator. The excitation is only fed through Port 1, i.e. $s_{1+} \neq 0$, while s_{2+}, s_{3+} = 0. Owing to the reciprocity of the RF antenna system, the couplings between the ports inside the same finite region are equal, and thus k_{im} is equal to k_{mi}. The resonator a_1 emanates RF energy and excites resonance in resonators a_2 and a_3 through k_{21} and k_{31}.

In the non-Hermitian coupled system, each BC-SRR consists of two SRRs, separated by a dielectric substrate, as shown in Figure 1a. The two identical SRRs are placed in parallel, and their slits are rotated 180° with respect to each other. When the magnetic field component of the incident EM wave crosses through the SRR, the surface currents will be excited in the rings.

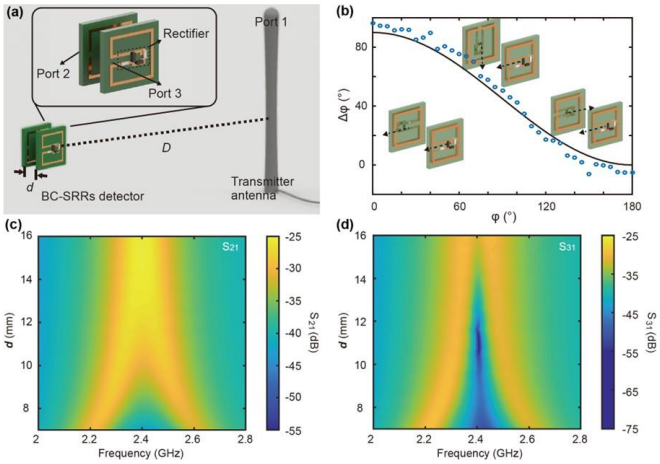

Figure 1. Simulation of the broadside coupled split ring resonators (BC-SRRs) detector.

The relative position of the BC-SRRs can be described by the relative rotation angle (φ) and the separation (d). The coupling effects within BC-SRRs arise from capacitive and inductive coupling, resulting in the mutual coupling factor (μ) and the mode splitting. The phase difference between the BC-SRRs is related to the relative rotation angle, as shown in Figure 1b.

Numerical simulations were conducted to investigate the effects of separation (d) on the transmission coefficients in BC-SRRs. The phase difference (Δφ) of two BC-SRRs is set to be 90° in the φ = 0° configuration. The simulation results of varied d are shown in the colormaps in Figure 1c (S21) and Figure 1d (S31), respectively. As the separation (d) increases from 7 to 16 mm, the coupling factor (μ) decreases. When d is less than 11 mm, the two BC-SRRs are strongly coupled, and the electromechanically induced transparency (EIT) phenomenon appears in both S21 and S31, resulting in frequency splitting [8].

When the separation is 11 mm, the BC-SRRs detectors are critical coupled. The S31 response reaches a minimum of approximately -75 dB at the resonant frequency, while the S21 is about -25 dB. When d is larger than 11 mm, the two BC-SRRs are weakly coupled, frequency splitting vanishes in both S21 and S31. Additionally, a critical separation can be chosen to achieve the maximum difference in transmission coefficients (|ΔT| = |S21-S31|) at resonance.

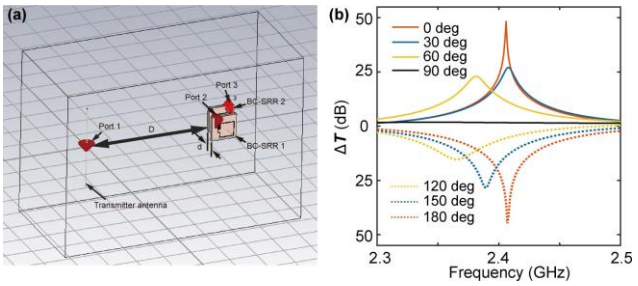

Figure 2. Simulation of the incident angle sensitive response.

Besides, we also studied the EM responses of the BC-SRRs for different incident angles of RF signal (θ) by numerical simulations. In the simulation model, the transmitter antenna is modelled as a single thin perfect electric conducting (PEC) cylinder as a dipole antenna, as shown in Figure 2a. A gap is formed in the PEC cylinder as Port 1 for feeding the excitation. The Port 2 and Port 3 are placed at the slits of two SRRs for RF energy reception. The material of SRRs and dielectric layer are set as copper and FR4, respectively. The ΔT was calculated to quantify the difference between simulated S21 and S31, as shown in Figure 2b for θ = 0°, 30°, 60°, 90°, 120°, 150°, and 180°. As θ increases from 0° to 180°, ΔT decreases from the largest positive value to the smallest negative value at the operating frequency. When θ is 90°, ΔT remains below 2 dB in the range of 2.3 ~ 2.5 GHz. Thus, the difference of the two transmission coefficients shows a strong angular dependence, which holds promise for directional RF sensing applications.

2.2. Experimental demonstration

To measure the transmission coefficient difference (ΔT), we connected a commercial RF antenna (transmitter) to the output port of a vector network analyzer (VNA, Agilent E8361A) by a co-axial cable. The operating frequency and power of the transmitting RF signals can be tuned by the VNA. The BC-SRRs was fabricated by using the standard printed circuit board (PCB) process, and the SMA connectors were welded at the output ports. The BC-SRRs were placed at a 10 cm from the transmitter antenna.

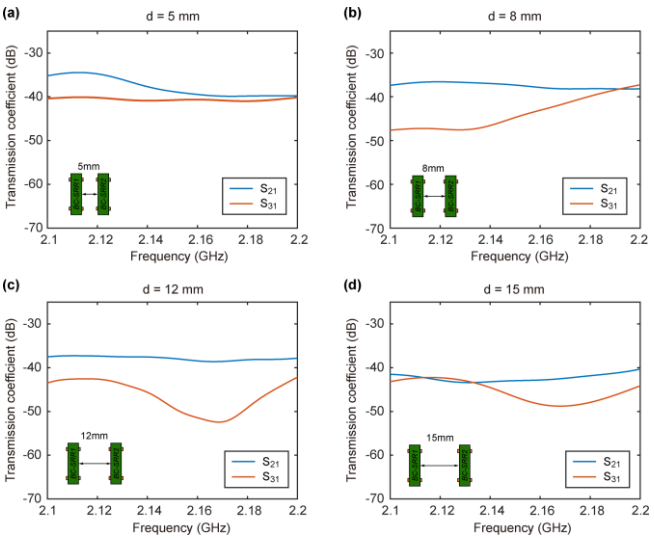

Figure 3. Measured S21 and S31 of the BC-SRRs with different d.

The separation (d) of the two BC-SRRs was determined by the different lengths of nylon hexagonal columns. The

measured S21 and S31 curves for four different separation distances are shown in Figure 3 (d = 5, 8, 12, and 15 mm). Therefore, we can then determine the critical separation of two BC-SRRs.

When d is 10 mm, the transmission coefficient difference |ΔT| reaches 26.25 dB at the resonant frequency of 2.16 GHz, as shown in Figure 4a. Figure 4b demonstrates the relationship between ΔT and d. When the separation is small (e.g. 5 mm) or large (e.g. 20 mm), ΔT is below 3 dB at resonance, resulting in the poor angle sensitivity. Thus, an optimal separation (d = 10 mm) had better be chosen to achieve a large ΔT.

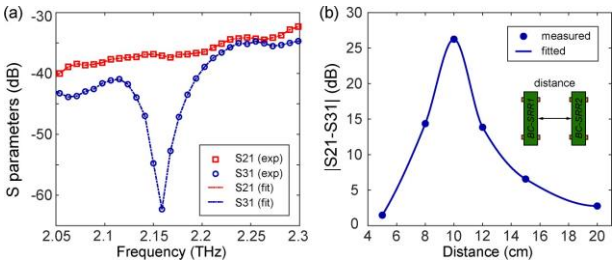

Figure 4. Determination of the critical separation.

Then, we measured the transmission coefficients (S21 and S31) for different incident angles of RF signal. The BC-SRRs with a separation of 10 mm were mounted on the centre of a rotation stage, and the distance between the transmitter antenna and BC-SRRs detector was fixed as 10 cm. The incident angle (θ) of the RF signal can be controlled using the rotation stage. As the incident angle increases from 0° to 180°, the S21 decreases from -40.2 dB to -64.3 dB, while the S31 increases from -66.8 dB to -37.4dB at the resonant frequency, as shown in Figures 5a-5e. When θ is 90°, the ΔT is approximately 0 dB within the frequency band of interest (gray area). Figure 5f illustrates the transmission coefficient difference (ΔT) as a function of the incident angle θ. The measured ΔT at resonace decreases from 27.7 dB to -26.1 dB with the increase of θ. Therefore, the incident angle (θ) of RF signal can be obtained by calculating ΔT.

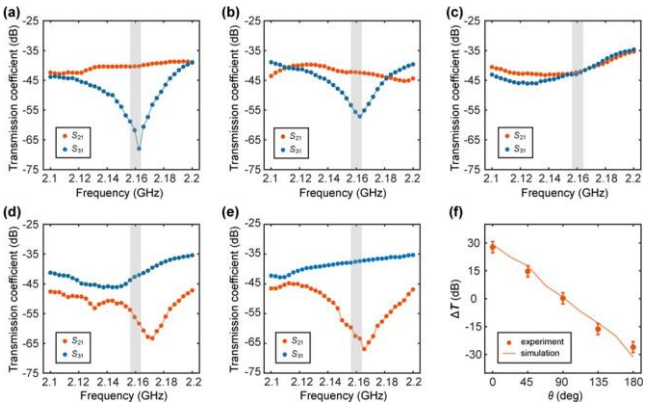

Figure 5. Experimental spectrum of S21 and S31 for different incident angles.

To enable the extraction of DC voltage from the RF signal, we introduced a single-stage Dickson voltage multiplier to the output port of the BC-SRRs, as shown in Figure 6a. For the efficient rectification, we utilized Schottky diodes (SMS7630-061) due to their low threshold voltage (0.34 V). The capacitances of C_1 and C_2 are 100 nF and 1 nF, respectively. The rectified DC voltages from the two BC-SRRs were then measured using a digital oscilloscope (Tektronix TBS2000B).

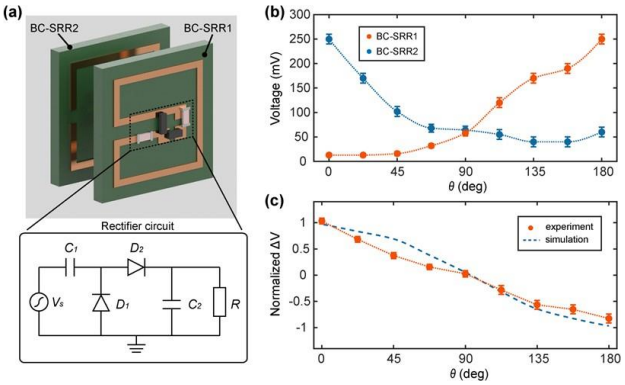

Figure 6. Demonstration of direction sensing using the rectified voltage.

The incident RF signal power was set to 8 dBm at 2.16 GHz. As θ increases, the rectified voltage of BC-SRR1 (V_1) decreases while that of BC-SRR2 (V_2) increases, as shown in Figure 6b. The maximum output voltage of each BC-SRR is up to be about 250 mV. When θ is 90°, the DC outputs of both BC-SRRs were similar as ~ 60 mV. Then, the rectified voltages from two BC-SRRs of different incident angles were normalized to the peak value (V_{max}). Figure 6c shows the calculated difference between the two normalized voltages, i.e., $\Delta V = (V_1-V_2)/V_{max}$. Note that the normalized voltage difference drops as the incident angle θ increases. The angle sensing sensitivity can be further improved by increasing the rectified voltages and reducing machining and assembly errors.

3. CONCLUSIONS

In summary, we presented a direction sensing scheme of RF sources by employing the BC-SRRs. Our design provides a promising platform for realizing compact RF directional sensor, which has a deep subwavelength side length (< 0.1 λ_0). We observed distinct spectral responses of the two critical coupled resonators by analyzing the EM responses of this non-Hermitian coupled system based on the TCMT theory. The measured transmission coefficient difference |ΔT| reaches the maximum as 26.25 dB at the resonant frequency. In addition, the ΔT decreased from 27.7 dB to -26.1 dB with the increase of the incident angle, implying that the proposed coupled system can effectively sense the angle of an incident RF signal within a range of 0° to 180°. Each BC-SRR can directly convert the RF signal into DC voltage through the integration of rectifying circuits. Our experimental demonstration has showcased the multifunctionality of the BC-SRRs-based microsystems, encompassing directional sensing and RF energy harvesting capabilities. In future design, we envision to enhance the output voltage of BC-SRRs by increasing the maximum power of transmitting antenna and incorporating additional stages in the rectifier circuits, thereby expanding its potential for various applications such as micro-robotics.

ACKNOWLEDGMENTS

Xiaoguang Zhao acknowledges the startup funding from Tsinghua University.

FUNDING STATEMENT

This work is supported by the National Key R&D Program of China (Grant no. 2021YFB2011800), the National Nature Science Foundation of China (Grant No. U21A6003), and the Beijing Natural Science Foundation (Grant No. 4222068).

REFERENCES

[1] T. S. Rappaport, J. H. Reed, B. D. Woerner, **Position location using wireless communications on highways of the future**, IEEE Communications Magazine, 34, 1996, pp. 33-41.

[2] C. Qin, J. A. Zhang, X. Huang, Y. J. Guo, **Virtual-subarray-based angle-of-arrival estimation in analog antenna arrays**, IEEE Wireless Communications Letters, 9, 2020, pp. 194-197.

[3] L. Zhao, L. K. Yeung, K. L. Wu, **A coupled resonator decoupling network for two-element compact antenna arrays in mobile terminals**, IEEE Transactions on Antennas and Propagation, 62, 2014, pp. 2767-2776.

[4] M. R. Nikkhah, K. Ghaemi, N. Behdad, **An electronically tunable biomimetic antenna array**, IEEE Transactions on Antennas and Propagation, 66, 2018, pp. 1248-1257.

[5] T. Lee, T. Nomura, X. Su, H. Iizuka, **Fano-like acoustic resonance for subwavelength directional sensing: 0-360 degree measurement**. Advanced Science, 7, 2020, 1903101.

[6] S. Y. Yi, M. Zhou, Z. F. Yu, P. Y. Fan, N. Behdad, D. M. Lin, K. X. Z. Wang, S. H. Fan, M. Brongersma, **Subwavelength angle-sensing photodetectors inspired by directional hearing in small animals**, Nature Nanotechnology, 13, 2018, pp. 1143-1147.

[7] K. Ding, C. Fang, G. Ma, **Non-Hermitian topology and exceptional-point geometries**, Nature Reviews Physics, 4, 2022, pp. 745-760.

[8] J. D. Teufel, D. L. Li, M. S. Allman, K. Cicak, A. J. Sirois, J. D. Whittaker, R. W. Simmonds, **Circuit cavity electromechanics in the strong-coupling regime**, Nature, 471, 2011, pp. 204-208.

48: MONITORING OF COMPOSITE PRESSURE VESSELS USING SURFACE-APPLIED DISTRIBUTED FIBRE OPTIC SENSORS

Christos Karapanagiotis [*], *Marcus Schukar, Mathias Breithaupt, Katerina Krebber*

Bundesanstalt für Materialforschung und-prüfung, Berlin, Germany
* christos.karapanagiotis@bam.de

Abstract **-** In this paper, we report on surface-applied distributed fibre optic sensors for monitoring composite pressure vessels designed for hydrogen storage. Previous reports have revealed that integrating optical fibres within vessel composite structures effectively enables the monitoring of structural behavior throughout their lifetime. However, integrating optical fibres during the manufacturing process is complex and time-consuming. Therefore, we aim to simplify this process by attaching the optical fibres to the vessel's surface. This method is significantly more time-efficient than the integration process and can be applied to any vessel. Our results demonstrate that surface-applied fibre optic sensors can detect and precisely localise damage. Additionally, signs of damage can be recognised even before the damage occurs. Predictive maintenance using fibre optic sensors could reduce premature maintenance costs and periodic inspections while increasing safety and extending the vessel's useful service life. The role of machine learning in predictive maintenance is also discussed.

Keywords**:** fibre optic sensors; hydrogen; structural health monitoring; predictive maintenance; composite pressure vessels; machine learning

1. INTRODUCTION

Hydrogen is typically stored in type IV composite overwrapped pressure vessels under high pressures of approximately 700 bar. Therefore, their structural integrity is of high importance for the hydrogen industry. These vessels are designed with safety margins to minimise any potential risks. Additionally, to ensure safety, they undergo regular inspections throughout their specified operational lifetime. Structural health monitoring (SHM), however, could contribute to reducing these periodic inspections and minimizing the associated costs while enhancing safety.

Distributed fibre optic sensors (DFOS) belong to the well-known SHM methods that have seen a lot of applications over the last few years [1]. DFOS have been extensively utilised to monitor infrastructures such as bridges and tunnels. In geotechnical engineering, DFOS have been used to enhance the safety and efficiency of structures by monitoring stress distribution and deformation. They have been also applied in the transportation sector for monitoring railways and roads. Furthermore, DFOS have been successfully applied in the oil and gas industry for condition monitoring of long pipelines. In the renewable and green energy sectors, DFOS have been employed to assess the structural integrity of wind turbines, subsea cables, and composite pressure vessels for hydrogen storage.

Due to their small size, optical fibres can be integrated into the composite structure of the pressure vessels. Integrated optical fibres have already been used to identify structural deformations of type IV composite pressure vessels before burst events [2,3]. Although the integrated optical fibres in the composite structure are sensitive to structural deformations, the manufacturing process is complex and time-consuming.

In this paper, we report on a simple approach that involves solely optical fibres applied on the vessel's surface. Our results demonstrate that the surface-applied optical fibres are also sensitive to structural deformations and have the potential to be used for SHM and predictive maintenance.

2. METHODS AND PROCEDURES

The DFOS technique that was employed is based on the well-known optical frequency domain reflectometry (OFDR) working principle. Specifically, we made use of the commercial device LUNA OBR 4600 produced by LUNA Innovations Inc. (Roanoke, VA, USA). This system is capable of measuring changes in temperature or strain with high spatial resolution on the millimetre range along optical fibres with a length of up to 70 m. Details about the OFDR working principle and signal processing can be found in [4]. Here, we want only to note that the signal processing involves the estimation of the so-called frequency shift which depends linearly on temperature and strain changes. The temperature and strain linear sensitivity coefficients are characteristic of the optical fibre variant.

The optical fibre that was used is a 60-m single-mode fibre coated with polyimide and manufactured by Fibercore Inc. (Southampton, UK). Specifically, the fibre type SM1500(6.4/125)P was used for the tests. This fibre was chosen because preliminary studies have shown that it is better suited for strain sensing purposes than the standard acrylate-coated fibres due to the higher numerical aperture and backscatter amplitude [5]. This fibre variant was also used in our previous paper for monitoring type IV pressure vessels with integrated optical fibres [2].

The process of attaching the optical fibres onto the vessel's surface was relatively simple. The fibres were wrapped around the vessel's cylindrical part and dome areas, as shown in Figure 1. Circumferential winding is generally expected to provide higher pressure sensitivity compared to axial directions; hence, this winding direction was chosen. As can be seen, one end of the fibre was connected to the measurement system while the other was connected to an appropriate terminator to minimise back reflection and obtain a high SNR signal. The optical fibres were glued with a layer

DOI: https://doi.org/10.34961/researchrepository-ul.29291219.v1

of flexible epoxy resin. The ingress and egress points were additionally covered by an elastic adhesive.

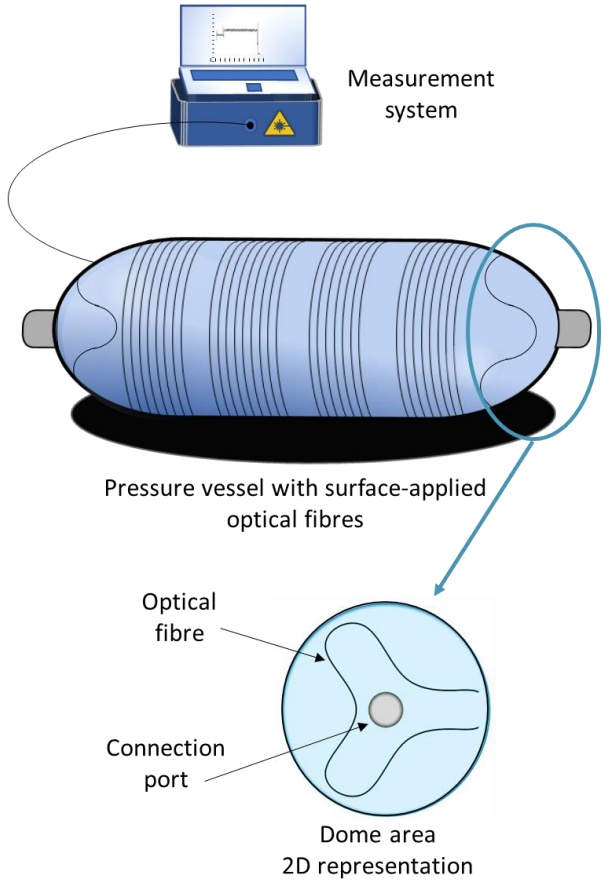

Figure 1. Illustration of the experimental setup consisting of a fibre optic measurement system and the pressure vessel with the surface-applied optical fibres.

Figure 2 presents a photograph of the real pressure vessel with the surface-applied optical fibres. We observe that the fibres were wrapped around the vessel's cylindrical part with an almost constant pitch angle. Furthermore, the fact that the optical fibres are visible is a great advantage over the integrated optical fibres because the measured strain profile, as we see later, can be easily mapped to specific positions on the vessel's surface.

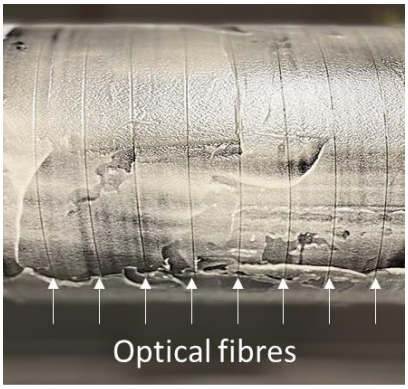

Figure 2. Photograph of the pressure vessel with the surface-applied optical fibres.

Once the optical fibres were installed, the vessel was placed in a hydraulic pressure machine for load cycling. The maximum pressure level of the load cycles was set to 800 bar, with the rate of load cycles set to 5 per minute. The hydraulic load tests were initially performed at a temperature of 50 °C but after 22000 load cycles, the temperature was increased to 65 °C to facilitate the degradation of the material. Because LUNA OBR is designed for static measurements, pressure ramps consisting of fixed pressure steps every 50 bar were introduced at periodic time intervals during the load cycling.

3. RESULTS AND DISCUSSION

The results show that the surface-applied optical fibres are very sensitive to pressure changes. Figure 3 shows the strain profile of the entire optical fibre under different pressure levels. The segments that correspond to the two dome sections are located at the start (blind dome section) and at the end of the optical fibre (dome section with the connection port). The optical fibre wrapped around the cylindrical part is divided into four segments which can also be seen in Figure 1. The positions with almost zero strain correspond to the fibre segments that were left unattached to the vessel so that they are free of strain and thus able to measure temperature.

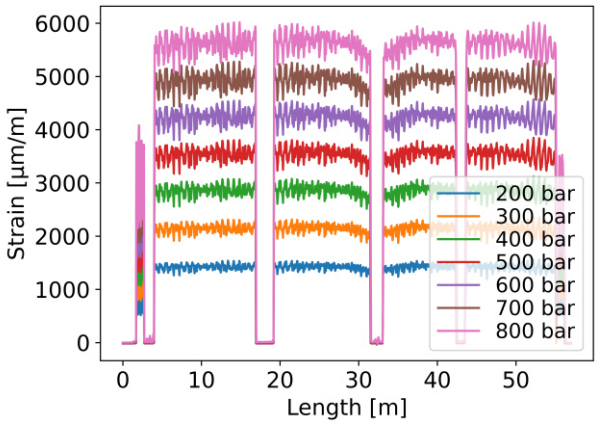

Figure 3. Strain profile of the entire optical fibre under different pressure levels.

We observe that the strain increases with pressure. The analysis of these results reveals that the relation between strain and pressure is linear with the pressure sensitivity (linear coefficient) varying depending on the position along the optical fibre. The changes in pressure sensitivity along the optical fibre can be attributed to to variations in material thickness and the optical fibre wrapping angle with respect to the wrapping angle of the composite fibres. Specifically, in the dome areas, the average pressure sensitivity of the optical fibre is 3.7 με/bar, while at the cylindrical part, it is 6.9 με/bar. This indicates that the average pressure sensitivity in the dome sections is approximately 46% lower than that in the cylindrical part.

The hydraulic pressure machine stopped after approximately 60000 load cycles due to the detection of a leakage. The pressure vessel did not burst with the outer part seemed in good condition. However, a photograph of the inner side revealed that the liner in the blind dome section was destroyed. This is visible in Figure 4a.

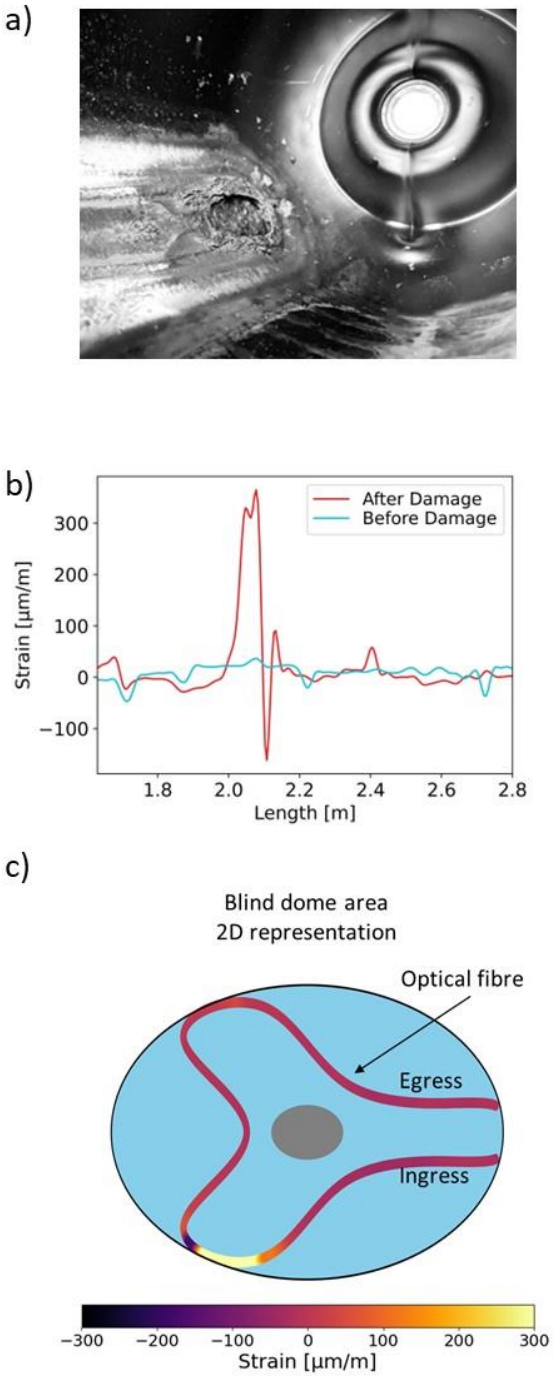

Figure 4. Damage detection and localisation using surface-applied distributed fibre optic sensors a) Internal view of the damage. b) Strain profile before and after the damage under pressureless conditions. c) 2D representation of the strain change profile.

After the failure, a final measurement was conducted under pressureless conditions and compared with previous measurements also taken under approximately pressureless conditions. The results, shown in Figure 4b, indicate that the optical fibres wrapped close to the damage experienced a significant strain change. For visualisation reasons and to help the reader to map the strain changes to specific positions on the vessel, a 2D representation of the blind dome area with the applied optical fibre is presented in Figure 4c. The colours represent the measured strain change.

While these results are very significant and demonstrate the high sensitivity of the surface-applied optical fibres in detecting and localising relatively small-scale damage that occurred at the vessel's liner and innermost composite layers, it is even more crucial to detect damage precursors. Therefore, we examined the strain change close to the damaged area during the last load cycles.

Figure 5 presents the strain difference between fixed pressures of 700 bar and 800 bar during different cycles until failure. The strain differences were calculated using the same reference measured at 700 bar 24900 cycles before the failure. This approach ensures that the comparisons are made relative to the same baseline and provides a clear depiction of how strain evolves over time. The reason that we chose to compare high-pressure levels is because structural deformations tend to become more visible as the pressure increases.

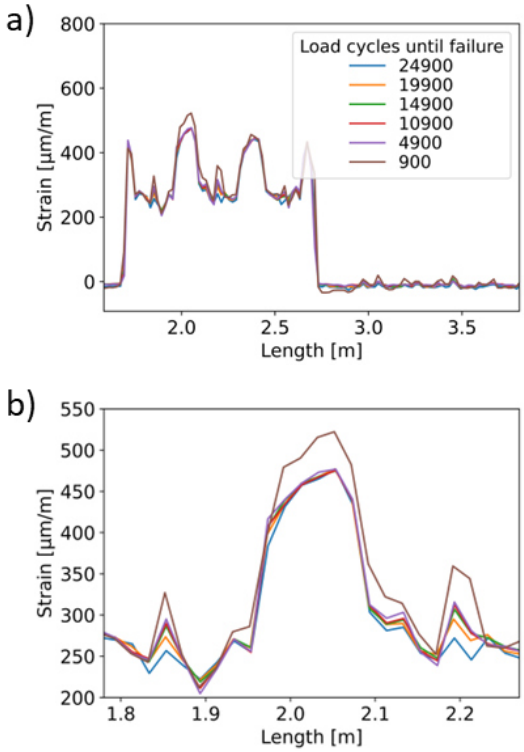

Figure 5: a) Measured strain evolution until vessel failure in the blind dome area. b) Zoomed-in view of critical positions.

Figure 5a illustrates the evolution of strain from 24,900 to 900 load cycles at the blind dome area before failure. The measurement at 900 cycles before failure is the last one that was recorded. We observe that the final measurement shows increased strain values compared to previous measurements, around the position where the damage eventually occurred. Figure 5b provides a closer look at the positions of the observed strain changes. Here we see that while the significant strain change occurred 900 cycles before the damage, signs of structural deformation had already started to appear 19,900 cycles before. While in the area around 2.05 m only the final measurement shows higher strain values, at the positions around 1.85 m and 2.2 m, the strain progressively increases as failure approaches. These observations indicate material degradation and can serve as warnings for potential damage.

To facilitate predictive maintenance with surface-applied optical fibres, detecting early signs of damage is crucial. Machine learning-assisted data analysis could significantly contribute to this goal. Recently, machine learning has been

widely applied in the field of SHM to identify damage indicators. In DFOS applications, in particular, the use of machine learning is very promising as it can enable automatic analysis of a large amount of data very efficiently, recognising patterns that are difficult to detect with conventional analysis. Apart from these small strain differences shown in Figure 5, previous studies have shown that other damage indicators can be used as well [5]. One of these is the error of the pressure sensitivity. The error tends to increase when structural deformations start to appear because the strain and pressure relation cease to be perfectly linear.

Furthermore, real-time measurements will generate more data, which could enable the extraction of useful statistical pamamters over time and help a machine learning model to detect anomalies. However, for real-time measurements a different DFOS system will be required.

It is important to note that due to the temperature and strain cross-sensitivity issues, it was necessary to distinguish between the temperature and the strain effects. In this case, howeve, because the temperature inside the hydraulic pressure machine and the temperature sensitivity coefficient of the optical fibre were known, the temperature and strain influences could be decoupled. For the sake of completeness we mention that the fibre's temperature sensitivity coefficient was -1.6 GHz/°C. The vessel's thermal expansion coefficient was also taken into account when compensating the temperature effects. As we have already reported in [6], machine learning could also be used to enhance the DFOS signal processing in terms of strain accuracy and provide solutions for temperature and strain discrimination as well.

We believe that the presented approach of the surface-applied optical fibres could be beneficial for monitoring composite pressure vessels considering the advantages over the integration process which are the simpler and faster implementation and the possibility to monitor every vessel even after its manufacturing. However, we need to note surface-applied optical fibres can not be used to assist and optimise the manufacturing process of the pressure vessels as has been done with integrated fibre Bragg grating sensors [7].

4. CONCLUSIONS

We demonstrated the capability of distributed fibre optic sensors to monitor composite pressure vessels using surface-applied optical fibres. The results showed that the surface-applied optical fibres are sensitive to structural deformations and can detect and localise even small-scale damages occurring at the inner side of the vessel. We also demonstrated that this approach is very promising for detecting damage precursors. In the future, more pressure vessels will be tested using this approach in order to collect more data and train a machine learning model for predictive maintenance. This will significantly reduce the number of periodic inspections, minimise maintenance costs, and increase safety. We believe that the use of fibre optic sensors for monitoring hydrogen composite pressure vessels can boost confidence in hydrogen technology and supporting the ongoing energy transition.

ACKNOWLEDGMENTS

The authors would like to thank their partners and colleagues from the research project QI-DIGITAL for the great collaboration. Special thanks to our colleague Eric Duffner from the Division 3.5 "Safety of Gas Storage Systems" for the technical support. We also thank our colleague Wolfgang Horn from the Division 4.5 "Analysis of Artefacts and Cultural Assets" for providing the facilities to conduct the temperature measurements.

FUNDING STATEMENT

This work has received funding from the German Ministry of Economic Affairs and Climate Action within the QI-Digital initiative.

REFERENCES

[1] M. F. Bado and J. R. Casas, **A Review of Recent Distributed Optical Fiber Sensors Applications for Civil Engineering Structural Health Monitoring**, Sensors, vol. 21, no. 5, 2021, p. 1818.

[2] D. Munzke, E. Duffner, R. Eisermann, M. Schukar, A. Schoppa, M. Szczepaniak, J. Strohhaecker, G. Mair, **Monitoring of type IV composite pressure vessels with multilayer fully integrated optical fiber based distributed strain sensing**, Materials Today: Proceedings, vol. 34, no. 1, 2021, pp. 217–223.

[3] G. Souza and J. R. Tarpani, **Using OBR for pressure monitoring and BVID detection in type IV composite overwrapped pressure vessels**, Journal of Composite Materials, vol. 55, no. 3, 2020, pp. 423-436.

[4] M. Froggatt and J. Moore, **High-spatial-resolution distributed strain measurement in optical fiber with Rayleigh scatter**, Appl Optics, vol. 37, no. 10, 1998, pp. 1735-1740.

[5] C. Karapanagiotis, M. Schukar, and K. Krebber, **Distributed fiber optic sensors for structural health monitoring of composite pressure vessels**, Technisches Messen, vol. 91, no. 3-4, 2024, pp. 168-179.

[6] C. Karapanagiotis, K. Hicke, and K. Krebber, **Machine learning assisted BOFDA for simultaneous temperature and strain sensing in a standard optical fiber**, Opt. Express, vol. 31, no. 3, 2023, pp. 5027-5041.

[7] P. Gąsior, R. Rybczyński, J. Kaleta, S. Villalonga, F. Nony, C. Magnier, **High pressure composite vessel with integrated optical fiber sensors: Monitoring of manufacturing process and operation**, *Proceedings of the ASME 2018 Pressure Vessels and Piping Conference*, *Prague, Czech Republic,* 15–20 July 2018, pp. 1-10.

49: PIEZOELECTRIC ENERGY HARVESTING AND SELF-POWERED PRESSURE SENSING WITH HEN EGG WHITE LYSOZYME

Krittish Roy [a*], *Charlie O'Mahony*[a], *Dinesh Barnana*[a], *Sarah makham* [a], *Ehtsham Ul Haque*[a], *Syed A. M. Tofail* [a*]

[a] Department of Physics and Bernal Institute, University of Limerick, Limerick V94 T9PX, Ireland
Industrial Sensing: 2, EM009, August 12, 2024, 1:30 PM - 3:00 PM

Abstract – Lysozyme is a well-recognized antimicrobial, and antifungal globular protein generally found in different mammalian secretions such as tears and saliva. It is commercially extracted from avian sources such as hen egg white and can be crystallized in different forms. In its crystalline state, it was found to be piezo, pyro and ferroelectric. Here, we have designed a piezoelectric energy harvesting device using engineered tetragonal aggregate film of lysozyme. Prepared films exhibited a longitudinal piezoelectricity of approximately ~3 pC/N. Subsequent output voltage/current of the device have been recorded. Thus, its promising mechanical energy harvesting performance and considering the non-toxicity and biocompatibility make it suitable over inorganic/synthetic piezoelectric materials as self-powered pressure sensor, implantable power source in body, and motion sensing applications.

Keywords**:** lysozyme, piezoelectricity, energy harvesting, self-powered sensing.

1. INTRODUCTION

Leveraging green energy practices to harvest energy from living environment is slowly becoming a requirement due to low availability of fossil fuels and to meet the increasing demand of energy. Mechanical energy is one of the abundant energy forms among the different types of ambient energy sources (solar, light, thermal, chemical energy) in the environment. Therefore, many approaches have been adapted to successfully harvest the mechanical energy, one of a kind is self-powered piezoelectric devices. Till date, several works have been reported to build piezoelectric nanogenerators (PNGs) using various semiconducting materials, e.g., ZnO, GaN, InN and lead based $Pb(Zr,Ti)O_3$, (PZT) with superior energy conversion efficiency.[1-2] However, the content of lead in PZT has an adverse effect on human beings and the ecosystems, which could inhibit their practical applications. In addition, their brittleness, heavy weight, cost intensive synthetic procedures are other important parameters to think of.

In this scenario, biomaterials could provide a better alternative of piezoelectric platforms because of its excellent biocompatibility and biodegradability. Biological entities are naturally piezoelectric due to their inherent non-centrosymmetry[3] and till date numerous biomaterials have been processed to fabricate self-powered PNGs[4-5].

Among the protein crystals, lysozyme is a globular protein abundantly found in hen egg white (HEW) and other mammalian secretions. Piezoelectricity of lysozyme is previously established in its pristine polycrystalline tetragonal and monoclinic forms[6-7]. In this work, we developed a flexible film of piezoelectric lysozyme and later used it for preparing PNG. This lysozyme-based PNG (L-PNG) shows moderate piezoelectric performance under repeated external pressure. In addition, the mechanoelectrical conversion of L-PNG fundamentally contributes to establish a self-powered pressure sensor for human joint-motion monitoring.

2. MATERIALS AND METHODS

Lysozyme powder (HR7-110) and polyvinyl alcohol (Mw ~ 13000-23000, Sigma Aldrich) were mixed thoroughly in deionized water (volumetric ratio of 1:1) to prepare a homogeneous composite solution. Afterwards, the resulting solution was casted on petridish followed by a temperature aided evaporation for 5 hrs for complete removal of solvent. Finally, the free-standing films were peeled off from the petridish and further characterizations and experiments were carried out.

3. RESULTS AND DISCUSSION

The prepared free-standing film exhibits outstanding flexibility, as shown from Figure 1a. The surface morphology study using FE-SEM (Figure 1b) shows a quite rough upper surface due to the presence of micro-sized lumps of lysozyme crystals and single layered structure of the film (Figure 1c). XRD pattern (inset of Figure 1b) confirms that prepared film consists of tetragonal crystals of lysozyme with a $P4_32_12$ space group reported by Wang et al.[8] Additionally, a quasi-static piezoelectricity measurement reveals the average longitudinal piezoelectricity of the film is approximately ~ 3 pm/V.

Afterwards, a lysozyme-based PNG (L-PNG) was fabricated by sandwiching the film between two electrodes to check its applicability as an energy harvester. It could harvest mechanical energy and generated a maximum open-circuit output voltage of 350 mV (peak to peak) under repetitive finger imparting motion under ~ 6 kPa pressure (as shown in Figure 1d). The ordered zwitterionic structure of different amino acids in lysozyme get deformed along with α-helices and other helical structures during repetitive press-release

DOI: https://doi.org/10.34961/researchrepository-ul.29291273.v1

condition, which creates a potential difference between electrodes and resulting in electrical outputs. The self-powered pressure sensing was further revealed by combing output voltage patterns and a wide pressure region.

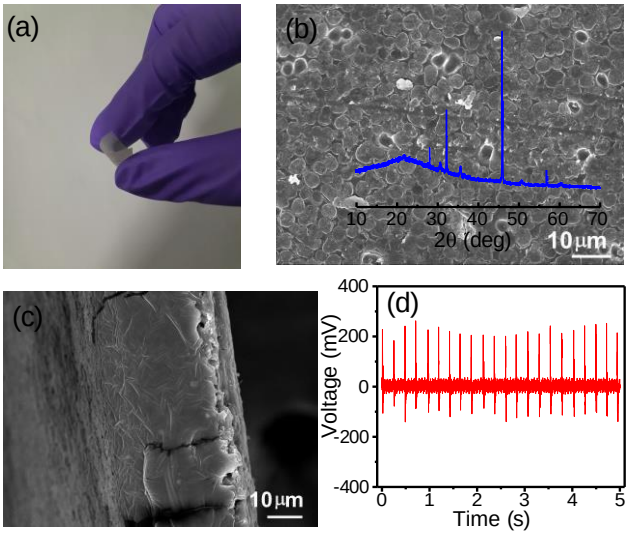

Figure 1. (a) Digital photograph showing flexibility of the film. (b) FE-SEM image of the upper surface with XRD pattern inside. (c) Cross sectional FE-SEM image of the composite film. (d) Open-circuit output voltage of the L-PNG device.

4. CONCLUSIONS

In summary, a PVA-lysozyme composite film was prepared through a simple scalable route where aggregated tetragonal crystals of lysozyme played a pivotal role in generating the piezoelectricity with a longitudinal piezoelectric coefficient of ~ 3 pm/V. In addition, a PNG was designed using the as-prepared film, which in turn generates an open circuit voltage of 350 mV. Therefore, the outcomes demonstrated its prospective towards small scale energy scavenging for self-powered pressure sensing systems.

5. REFERENCES

[1] B. Saravanakumar, R. Mohan, K. Thiyagarajan and S. J. Kim, **Fabrication of a ZnO nanogenerator for ecofriendly bio-mechanical energy harvesting**, RSC Adv. 3, 2013, pp. 16646–16656.

[2] K. I. Park, C. K. Jeong, J. Ryu, G. T. Hwang and K. J. Lee, **Flexible and large-area nanocomposite generators based on lead zirconate titanate particles and carbon nanotubes**, Adv. Energy Mater. **3**, 2013, pp. 1539–1544.

[3] S. Guerin, S. A. M. Tofail, D. Thompson, **Organic piezoelectric materials: milestones and potential**, NPG Asia Mater 11, 2019, pp. 10.

[4] Q. Xu, X. Gao, S. Zhao, Y-N. Liu, D. Zhang, K. Zhao, H. Khanbareh, W. Chen, Y. Zhang, C. Bowen, **Construction of biopiezoelectric platforms: from structures and synthesis to applications**, Adv. Mater., 33, 2021 pp. 2008452.

[5] R. Wang, J. Sui, X. Wang, **Natural piezoelectric biomaterials: a biocompatible and sustainable building block for biomedical devices**, ACS Nano, 16, 2022, pp. 17708-17728.

[6] A. Stapleton et al., **The direct piezoelectric effect in the globular protein lysozyme**, Appl. Phys. Lett. 111, 2017, pp. 142902.

[7] A. Stapleton et al. **Converse piezoelectricity and ferroelectricity in crystals of lysozyme protein revealed by piezoresponse force microscopy**, *Ferroelectrics* 525, 2018, 135.

[8] Z. Wang, T. Liu, C. Lu, L. Dang, CrystEnggComm, **Manipulating crystallization in lysozyme and supramolecular self-arrangment in solution using ionic liquids**, 20, 2018, pp. 2284.

6. ACKNOWLEDGEMENTS

The research was supported by CURAM- Science Foundation Ireland (SFI) centre for medical devices (Grant Number 13/RC/2073_P2). S.M. acknowledges Irish Research Council Postdoctoral Fellowship (GOIPD/2021/928): Disposable, biodegradable, endoscopic ultrasonic imaging probe (DISPOSON). SFI Opportunistic Fund (no. 12/RI/2345/SOF) is acknowledged for the NTEGRA Hybrid Nanoscope used in Piezoresponse Force Microscopy.

50: Challenges in Adapting Fiber Optic Sensors for Biomedical Applications

*Sahar Karimian[1,2 *], Muhammad Mahmood Ali [1,2, *], Dineshbabu Duraibabu[1,2], Waqas Saleem[3], Marion McAfee[1,2], Elfed Lewis[4]*

[1]Centre for Mathematical Modelling and Intelligent Systems for Health and Environment (MISHE), Atlantic Technological University, Sligo, Ireland
[2]Department of Mechatronic Engineering, Faculty of Engineering and Design, Atlantic Technological University, Sligo, Ireland
[3]Technological University Dublin, Dublin, Ireland
[4]Optical Fibre Sensors Research Centre, University of Limerick, Limerick, Ireland

Optical Fibre Sensors Session Three, EM010, August 13, 2024, 11:30 AM - 1:10 PM

Abstract – Fiber optic sensors (FOSs) have developed as a transformative technology in healthcare, offering unparalleled precision and sensitivity in monitoring various physiological and biochemical parameters. Their applications range from monitoring vital signs to guiding minimally invasive surgeries, promising to revolutionize medical diagnostics and treatment. However, the integration of FOSs into biomedical applications faces numerous challenges. This article delves into the specific hurdles encountered in adopting FOSs for biomedical purposes, exploring technical and practical obstacles, and examining innovative solutions. From ensuring biocompatibility and miniaturization to addressing signal processing complexities and regulatory standards, the article provides an overview of the challenges and some of potential solutions. By explaining these challenges, a better understanding of FOSs technology in biomedical settings and the way for their implementation, would be possible and will lead to enhancing patient care and medical outcomes and wider usage of them.

Keywords**:** Fiber Optic Sensors (FOSs), Biomedical applications, Challenges, Healthcare Technology, Medical Standards

1. INTRODUCTION

In the evolving landscape of sensor technology, Fiber Optic Sensors (FOSs) stand out due to their exceptional precision, sensitivity, and immunity to electromagnetic interference. These characteristics make them particularly attractive for biomedical applications, where accurate and reliable measurements are crucial. From monitoring physiological parameters to aiding in minimally invasive surgeries, fiber optic sensors hold the potential to revolutionize medical diagnostics and treatment[1], [2].

Despite their promise, the adoption of fiber optic sensors in the biomedical field requires numerous obstacles to overcome. The integration of these sensors into medical devices requires overcoming challenges related to biocompatibility, miniaturization, and effective an efficient signal processing. Additionally, ensuring the robustness, real time responsivity and reliability of FOSs in the dynamic and often harsh environments of the human body presents another layer of complexity. Also, their use requires meeting International Standards which can also be very challenging on the path to commercialisation[3]–[5].

This article investigates the specific challenges encountered in the adoption of fiber optic sensors for biomedical applications. It explores the technical and medical practice obstacles, examines innovative solutions, and highlights the ongoing research aimed at bridging the gap between potential and practical implementation. Through this analysis, we aim to provide a comprehensive understanding of the current state of FOS technology in biomedicine and the future directions that could unlock their full potential.

1.1. Background

FOS operate by transmitting light through optical fibers and includes modulation of one or more of light properties (such as intensity, phase, or wavelength) indicating the condition of specific physiological parameters. In the biomedical field, FOSs can be utilized for real-time monitoring of vital signs including pressure and temperature etc., detecting biochemical changes, and guiding minimally invasive surgical procedures. Despite their potential, the adoption of FOSs in healthcare is hampered by several challenges. These include but are not limited to ensuring biocompatibility, scaling up manufacturing processes to meet healthcare industry standards, and creating efficient real-time signal processing algorithms. These are crucial steps to fully harness the capabilities of FOS technology in medical diagnostics and treatment. Addressing these challenges is essential for the integration of fiber optic sensors into everyday medical practice, where they could provide unprecedented accuracy and reliability in patient care[6], [7].

1.2. Working Principles of FOSs

FOSs vary widely and their operating principles are correspondingly diverse, each utilizing distinct principles to measure different parameters. The primary FOS classification splits into intrinsic and extrinsic sensors. Intrinsic FOS relies on the light-matter interaction occurring wholly within the fiber itself, where changes in light properties (intensity, phase, polarization, or wavelength) occur due to external influences such as temperature, pressure, or strain. Extrinsic fiber optic sensors, on the other hand, use the optical fiber merely to transmit light to and from an external sensing

DOI: https://doi.org/10.34961/researchrepository-ul.29291645.v1

element. Fiber Bragg Gratings (FBGs)[8], [9], represented a revolution in sensing using optical fibres. They operate via reflecting specific wavelengths of light that shift in response to strain or temperature changes. Interferometric sensors (of which the FBG is an example), generally measure phase changes in light caused by external perturbations[3], [10], [11]. FBGs interaction with light as it passes through the grating planes depends on the Bragg condition and the first-order Bragg condition can be stated as below:

$$\lambda_B = 2n_{eff}\mathbf{\Lambda} \quad (1)$$

where n_{eff} denotes the effective refractive index of the wave-guide node, while $\mathbf{\Lambda}$ represents the periodicity of the grating, and λ_B stands for the Bragg wavelength.

There exist several different types of FOS based on different working principles which cannot be included in this article owing to page length restrictions. e.g. fluorescence-based sensors[12], [13] detect variations in fluorescence emitted by certain materials subject to external light excitation, and are often used for biochemical measurements. Other diverse types of FOSs include interferometric-based devices such as Fabry-Perot[10], [14], Surface Plasmon Resonance (SPR)[15], [16], Optical Coherence Tomography (OCT)[17], [18] utilized in imaging applications and often incorporate specialist fiber e.g. Photonic Crystal Fiber (PCF)[12], [19]. They all leverage the interaction between light and the external environment to provide sensitive and accurate measurements, in a wide range applications[11], [20]–[22].

1.3. Physical measurands in healthcare

FOSs are well suited for providing measurements of various physical measurands are increasingly accepted tools for patient monitoring and diagnostics. These measurands include temperature, pressure, strain, flow, liquid level, displacement, vibration, rotation, radiation, and biochemical markers. Temperature measurements are vital for tracking body temperature fluctuations during surgeries, post-operative care, and critical care settings, ensuring patient stability and the early detection of infections [23], [24]. Pressure sensors are extensively used to monitor blood pressure, Intracranial Pressure (ICP)[25], [26], and Intraocular Pressure (IOP)[27], [28], which are critical for managing conditions like hypertension, Traumatic Brain Injuries (TBI)[29], and glaucoma[28]. Strain sensors are employed to monitor respiratory patterns by measuring chest wall movements, offering valuable data for respiratory therapy[3], sleep studies, and managing conditions like asthma or chronic obstructive pulmonary disease (COPD)[4], [30]. By providing real-time data, fiber optic sensors can enhance clinical decision-making, improve patient outcomes, and contribute to the advancement of personalized medicine[31], [32].

1.4.1. Biomechanical measurands in healthcare

Biomechanical measurands encompass the physical parameters of the human body where the focus is on structure and movement, and accurate measurement is crucial for various medical applications. FOSs can measure strain and deformation in tissues and organs, providing critical data for orthopaedic and rehabilitation applications [1], [2]. For instance, it is possible to monitor the stress and strain on bones and joints during physical activities, aiding in the assessment and treatment of musculoskeletal disorders. Additionally, for posture monitoring and ulcer formation detection in patients who are required to use a wheelchair [33]. Furthermore, these sensors are employed in the development of prosthetics and wearable devices, providing real-time feedback on the mechanical performance and interaction with the body. By measuring these biomechanical parameters, FOSs support the diagnosis, treatment, and rehabilitation of various conditions and advancing the field of biomechanics in healthcare[4], [5], [34]–[37].

1.5. Biochemical measurands in healthcare

All biochemical measurands could be considered vital parameters in healthcare, providing essential information about the whole physiological and metabolic states of patients. FOSs are increasingly used to measure these biochemical markers with high sensitivity and specificity. Glucose monitoring is one of the most critical applications, especially for managing diabetes; fiber optic sensors can continuously measure glucose levels in blood or interstitial fluid, offering real-time data that help in maintaining optimal glycemic control[38], [39]. pH monitoring is another crucial application, particularly in assessing metabolic conditions and the body's acid-base balance, which is vital in critical care and surgical settings[40], [41]. Additionally, fiber optic sensors are used for blood detection[42], to detect specific proteins, enzymes, and hormones, aiding in the diagnosis and monitoring of various diseases, such as cancer, cardiac conditions, and hormonal imbalances[43]. These sensors can be functionalized to detect biomarkers at the molecular level, enabling early disease detection and the tracking of treatment efficacy. By measuring these biochemical parameters, fiber optic sensors provide data that enhance diagnostic precision and treatment monitoring which could be directly related to biochemical measurands[44]–[46].

FOSs are adept at detecting various substances in both gas and liquid phases. In the gas phase, FOSs can detect trace gases such as oxygen, carbon dioxide, and volatile organic compounds with high sensitivity. In respiratory monitoring, proper ventilation is vital in medical settings, and detecting harmful gases in environmental health studies. In the liquid phase, FOSs are widely used for measuring biochemical substances, such as glucose, electrolytes, and pH levels in bodily fluids like blood, urine, and saliva[47], [48]. This capability is essential for continuous glucose monitoring in diabetic patients, assessing kidney function through electrolyte levels, and monitoring the body's acid-base balance. By providing accurate, real-time measurements in both phases, these sensors provide vast range of usage in different biomedical fields[12], [40], [49].

2. CHALLENGES FOR FOSs IN BIOMEDICAL APPLICATIONS

For implementing FOSs in healthcare applications there are some challenges which still needs to be overcome such as biocompatibility, cost, manufacturing, standards, and regulatory approval. Some of these challenges are listed as

below so that these sensors can be used in a more useful and practical ways and secure a clear path to commercialisation.

2.1. Biocompatibility

Ensuring non-toxicity for the material to be used in fabricating sensors is one of the primary challenges to achieving biocompatibility. The selection of materials needs to ensure that the FOSs are mechanically safe, non-toxic and do not provoke an immune response when implanted in or used on the human body. This requires extensive testing to ensure that the materials do not cause inflammation, allergic reactions, or any other adverse effects[5], [50]. This is generally conducted by regulating bodies such as the Food and Drug Administration (FDA) in the USA (section 2.5 of this article).

FOSs often require coatings to enhance biocompatibility. These coatings must be able to withstand the harsh biological environment without degrading. Ensuring long-term stability and functionality of these coatings is crucial for the reliable performance and regulatory approval of the sensors. Furthermore, sensors often need to endure various sterilization methods such as autoclaving, gamma irradiation, or chemical sterilization. The challenge is to design sensors that maintain their performance characteristics post-sterilization, as these processes can sometimes compromise sensor integrity and functionality[8], [51].

2.2. Miniaturization, Durability and Longevity

Reducing the size of fiber optic sensors without sacrificing sensitivity or accuracy is a significant challenge. Miniaturized sensors must still be capable of delivering precise and reliable measurements. Also, small-sized sensors need to be seamlessly integrated into medical devices and systems, often requiring custom design solutions. This integration must ensure that the sensors do not interfere with the overall device performance and that they are easy to incorporate into existing medical infrastructure[38], [45].

Producing miniaturized sensors at scale while maintaining high quality and consistency presents additional manufacturing challenges. Advanced fabrication techniques and stringent quality control measures are necessary to address these issues. FOSs often need to maintain their functionality over extended periods, particularly in chronic disease management and long-term monitoring applications. This requires materials and designs that are resistant to degradation over time[6], [52], [53].

Sensors must be able to withstand the dynamic and often harsh conditions encountered within the human body, such as movement, pressure changes, and exposure to various bodily fluids. Ensuring mechanical robustness while maintaining sensor sensitivity is a critical challenge[54], [55].

Ideally, fiber optic sensors used in medical applications should require minimal maintenance. Developing sensors that can operate reliably over long periods without the need for frequent recalibration or replacement is essential for their practical use[56], [57]. Also, it is highly advantageous if the sensor can be delivered inside a standard medical catheter as this often overcomes the problem of mechanical robustness.

2.3. Signal Processing, Data Integration, and Interoperability

Biological environments are often inherently noisy e.g. external electromagnetic interference from scanning equipment (MRI and CT), which can interfere with the signals detected by fiber optic sensors. If it is not possible to make the sensor immune to these sources of interference, developing advanced algorithms and signal processing techniques to filter out this noise becomes crucial for accurate measurements. The signals from FOSs often require sophisticated interpretation, especially when monitoring dynamic biological processes. This necessitates the development of advanced computational models and machine learning algorithms to accurately analyse and interpret the data[58]–[60].

Many types of medical applications require real-time data processing and feedback. Ensuring that the sensor systems can handle the computational load and providing timely, accurate information is a significant and ongoing technical challenge. FOSs must be compatible with existing healthcare IT systems and electronic health records (EHRs). Ensuring seamless integration and data interoperability is therefore essential for effective use in clinical settings[61], [62].

Developing standardized data protocols to ensure that data from fiber optic sensors can be easily shared and interpreted across different platforms and systems is crucial. This includes ensuring sound data security and maintaining patient privacy. Finally, at this stage providing user-friendly interfaces that allow healthcare professionals to easily interact with and interpret data from fiber optic sensors is important for their adoption. This involves developing intuitive software and visualization tools[45], [52], [63].

2.4. Cost and Manufacturing

High production costs can be a barrier to the widespread adoption of fiber optic sensors in healthcare. Developing cost-effective manufacturing processes without compromising quality and performance is crucial for making the sensors affordable[46], [64]. Scaling up production while maintaining consistency and reliability is another challenge. This requires advanced manufacturing techniques and stringent quality control measures to ensure that each sensor meets the required standards. Finally, achieving economies of scale to lower costs involves not only improving manufacturing processes but also increasing market demand and production volumes. This can be challenging in the early stages of technology adoption[65], [66].

2.5. Medical Standards and Regulatory Approval

FOSs must meet stringent regulatory standards set by organizations such as the FDA (Food and Drug Administration) and EMA (European Medicines Agency) for use in medical applications[67]–[72]. This involves extensive testing to demonstrate safety, efficacy, and reliability.

Ensuring compliance with international standards for medical devices is critical. This includes adhering to ANSI (American National Standards Institute) /AAMI (Association for the Advancement of Medical Instrumentation) or ISO standards such as AAMI/ISO 10993, ISO 13485, AAMI TIR42: Evaluation of Biocompatibility of Medical Devices and other relevant guidelines that govern the design, manufacturing, and testing of medical devices[67], [73]–[75].

Also, the EU Medical Devices Regulation (MDR) and the In Vitro Diagnostic Regulation (IVDR) are regulatory frameworks governing medical devices within the European Union (EU)[70], [71], [73]. The process of obtaining regulatory approval can be lengthy and complex, requiring significant time and resources. This can delay the introduction of new fiber optic sensor technologies to the market and wider usage of them.

3. CONCLUSIONS

FOSs have been transformative in healthcare, offering high precision and versatility in monitoring physiological and biochemical parameters including temperature, pressure, strain, and biochemical markers, enhancing diagnostics and patient outcomes. However, their integration into healthcare faces challenges. Biocompatibility requires non-toxic, durable materials suitable for biological environments. Miniaturization is necessary for seamless integration into medical devices without sacrificing performance. Signal processing needs advanced algorithms for accurate, real-time data interpretation in noisy biological environments. Data integration and interoperability demand compatibility with healthcare IT systems and standardized protocols for seamless data exchange. Ensuring durability and longevity of sensors is crucial.

Addressing high costs and manufacturing challenges is essential for widespread adoption of FOSs. Navigating and achieving standards and regulatory approval, as well as ensuring user training and acceptance, are also critical for the effective clinical integration and widespread use of FOSs in biomedical applications.

ACKNOWLEDGMENTS

Authors expand sincere gratitude to colleagues and collaborators who provided valuable insights and support throughout this research. This research is supported by a postgraduate research bursary from the Atlantic Technological University.

REFERENCES

[1] L. A. Ngiejungbwen, H. Hamdaoui, and M. Y. Chen, "Polymer optical fiber and fiber Bragg grating sensors for biomedical engineering Applications: A comprehensive review," *Opt Laser Technol*, vol. 170, no. October 2023, p. 110187, 2024, doi: 10.1016/j.optlastec.2023.110187.

[2] M. A. Abdhul Rahuman *et al.*, "Recent Technological Progress of Fiber-Optical Sensors for Bio-Mechatronics Applications," *Technologies*, vol. 11, no. 6, 2023, doi: 10.3390/technologies11060157.

[3] K. Bartnik, M. Koba, and M. Śmietana, "Advancements in optical fiber sensors for in vivo applications – A review of sensors tested on living organisms," *Measurement*, vol. 224, no. November 2023, p. 113818, 2024, doi: 10.1016/j.measurement.2023.113818.

[4] B. Padha, I. Yadav, S. Dutta, and S. Arya, "Recent Developments in Wearable NEMS/MEMS-Based Smart Infrared Sensors for Healthcare Applications," *ACS Appl Electron Mater*, vol. 5, pp. 5386–5411, 2023, doi: 10.1021/acsaelm.3c00860.

[5] X. Zhang, C. Wang, T. Zheng, H. Wu, Q. Wu, and Y. Wang, "Wearable Optical Fiber Sensors in Medical Monitoring Applications: A Review," *Sensors*, vol. 23, no. 15, 2023, doi: 10.3390/s23156671.

[6] L. Yu, B. J. Kim, and E. Meng, "Chronically implanted pressure sensors: Challenges and state of the field," *Sensors (Switzerland)*, vol. 14, no. 11, pp. 20620–20644, 2014, doi: 10.3390/s141120620.

[7] D. L. O. Presti *et al.*, "Fiber Bragg Gratings for Medical Applications and Future Challenges : A Review," *IEEE Access*, vol. 8, pp. 156863–156888, 2020.

[8] Z. Zhang, C. Zhang, and S. Zuo, "A Novel Bioinspired Whisker Sensor for Gastrointestinal Endoscopy," *IEEE/ASME Trans Mechatronics*, vol. PP, pp. 1–11, 2023, doi: 10.1109/TMECH.2023.3289955.

[9] A. Theodosiou, "Recent Advances in Fiber Bragg Grating Sensing," *Sensors (Basel)*, vol. 24, no. 2, 2024, doi: 10.3390/s24020532.

[10] C. Zhu *et al.*, "Advances in Fiber-Optic Extrinsic Fabry-Perot Interferometric Physical and Mechanical Sensors: A Review," *IEEE Sens J*, vol. 23, no. 7, 2023, doi: 10.1109/JSEN.2023.3244820.

[11] M. Elsherif *et al.*, "Optical Fiber Sensors: Working Principle, Applications, and Limitations," *Adv Photonics Res*, vol. 3, no. 11, 2022, doi: 10.1002/adpr.202100371.

[12] B. Moeglen Paget *et al.*, "A review on photonic crystal fiber based fluorescence sensing for chemical and biomedical applications," *Sensors Actuators B Chem*, vol. 400, no. PB, p. 134828, 2024, doi: 10.1016/j.snb.2023.134828.

[13] A. N. Azmi *et al.*, "Review of Open Cavity Random Lasers as Laser-Based Sensors," *ACS Sensors*, vol. 7, no. 4, pp. 914–928, 2022, doi: 10.1021/acssensors.1c02749.

[14] M. Fatima Domingues *et al.*, "Optical Fibre FPI End-Tip based Sensor for Protein Aggregation Detection," *2022 IEEE Int Conf E-Health Networking, Appl Serv Heal 2022*, pp. 129–134, 2022, doi: 10.1109/HealthCom54947.2022.9982774.

[15] F. Wang *et al.*, "3D fiber-probe surface plasmon resonance microsensor towards small volume sensing," *Sensors Actuators B Chem*, vol. 384, no. December 2022, p. 133647, 2023, doi: 10.1016/j.snb.2023.133647.

[16] H. Mi, Y. Wang, P. Jin, and L. Lei, "Design of a ultrahigh-sensitivity SPR-based optical fiber pressure sensor," *Optik (Stuttg)*, vol. 124, no. 21, pp. 5248–5250, 2013, doi: 10.1016/j.ijleo.2013.03.097.

[17] K. Samimi *et al.*, "Optical coherence tomography of human fetal membrane sub-layers during loading," *Biomed Opt Express*, vol. 14, no. 6, p. 2969, 2023, doi: 10.1364/boe.489691.

[18] P. C. Hui *et al.*, "Implantable self-aligning fiber-optic optomechanical devices for in vivo intraocular pressure-sensing in artificial cornea," *J Biophotonics*, vol. 13, no. 7, pp. 1–13, 2020, doi: 10.1002/jbio.202000031.

[19] A. N. Nithish *et al.*, "Terahertz Women Reproductive Hormones Sensor Using Photonic Crystal Fiber With Behavior Prediction Using Machine Learning," *IEEE Access*, vol. 11, no. May, pp. 75424–75433, 2023, doi: 10.1109/ACCESS.2023.3277955.

[20] B. D. Gupta, A. Pathak, and A. M. Shrivastav, "Optical Biomedical Diagnostics Using Lab-on-Fiber Technology: A Review," *Photonics*, vol. 9, no. 2, 2022, doi: 10.3390/photonics9020086.

[21] A. Uniyal, G. Srivastava, A. Pal, S. Taya, and A. Muduli, "Recent Advances in Optical Biosensors for Sensing Applications: a Review," *Plasmonics*, vol. 18, no. 2, pp. 735–750, 2023, doi: 10.1007/s11468-023-01803-2.

[22] Z. Katrenova, S. Alisherov, T. Abdol, and C. Molardi,

"Status and future development of distributed optical fiber sensors for biomedical applications," *Sens Bio-Sensing Res*, vol. 43, no. September 2023, p. 100616, 2024, doi: 10.1016/j.sbsr.2023.100616.

[23] C. Shang *et al.*, "Soft Biomimetic Fiber-Optic Tactile Sensors Capable of Discriminating Temperature and Pressure," *ACS Appl Mater Interfaces*, vol. 15, no. 46, pp. 53264–53272, 2023, doi: 10.1021/acsami.3c12712.

[24] H. Zhang, B. Cong, F. Zhang, Y. Qi, and T. Hu, "Simultaneous measurement of refractive index and temperature by Mach–Zehnder cascaded with FBG sensor based on multi-core microfiber," *Opt Commun*, vol. 493, no. December 2020, p. 126985, 2021, doi: 10.1016/j.optcom.2021.126985.

[25] V. Narayan, N. Mohammed, A. R. Savardekar, D. P. Patra, C. Notarianni, and A. Nanda, "Noninvasive Intracranial Pressure Monitoring for Severe Traumatic Brain Injury in Children: A Concise Update on Current Methods," *World Neurosurg*, vol. 114, pp. 293–300, 2018, doi: 10.1016/j.wneu.2018.02.159.

[26] C. He, C. Teng, Z. Xiong, X. Lin, H. Li, and X. Li, "Intracranial pressure monitoring in neurosurgery: the present situation and prospects," *Chinese Neurosurg J*, vol. 9, no. 1, pp. 1–12, 2023, doi: 10.1186/s41016-023-00327-2.

[27] M. Mimura, T. Akagi, R. Kohmoto, Y. Fujita, Y. Sato, and T. Ikeda, "Measurement of vitreous humor pressure in vivo using an optic fiber pressure sensor," *Sci Rep*, vol. 13, no. 1, pp. 1–6, 2023, doi: 10.1038/s41598-023-45616-z.

[28] R. Raveendran *et al.*, "Current Innovations in Intraocular Pressure Monitoring Biosensors for Diagnosis and Treatment of Glaucoma—Novel Strategies and Future Perspectives," *Biosensors*, vol. 13, no. 6, 2023, doi: 10.3390/bios13060663.

[29] C. Ordookhanian, M. Nagappan, D. Elias, and P. E. Kaloostian, "Management of Intracranial Pressure in Traumatic Brain Injury," *Trauma Brain Inj - Pathobiol Adv Diagnostics Acute Manag*, 2018, doi: 10.5772/intechopen.72829.

[30] C. Zhao *et al.*, "Recent advances in fiber optic sensors for respiratory monitoring," *Opt Fiber Technol*, vol. 72, no. April, p. 103000, 2022, doi: 10.1016/j.yofte.2022.103000.

[31] D. Tosi, S. Poeggel, I. Iordachita, and E. Schena, *Fiber Optic Sensors for Biomedical Applications*. Elsevier Inc., 2018. doi: 10.1016/B978-0-12-803131-5.00011-8.

[32] S. Poeggel *et al.*, "Recent improvement of medical optical fibre pressure and temperature sensors," *Biosensors*, vol. 5, no. 3, pp. 432–449, 2015, doi: 10.3390/bios5030432.

[33] A. X. González-Cely, C. A. R. Diaz, M. Callejas-Cuervo, and T. Bastos-Filho, "Optical fiber sensors for posture monitoring, ulcer detection and control in a wheelchair: a state-of-the-art," *Disabil Rehabil Assist Technol*, vol. 0, no. 0, pp. 1–18, 2023, doi: 10.1080/17483107.2023.2234411.

[34] A. Najafzadeh *et al.*, "Application of fibre bragg grating sensors in strain monitoring and fracture recovery of human femur bone," *Bioengineering*, vol. 7, no. 3, pp. 1–14, 2020, doi: 10.3390/bioengineering7030098.

[35] F. De Tommasi, C. Romano, D. Lo Presti, C. Massaroni, M. Carassiti, and E. Schena, "FBG-Based Soft System for Assisted Epidural Anesthesia: Design Optimization and Clinical Assessment," *Biosensors*, vol. 12, no. 8, 2022, doi: 10.3390/bios12080645.

[36] X. Wang *et al.*, "Highly Sensitive Strain Sensor Based on Microfiber Coupler for Wearable Photonics Healthcare," *Adv Intell Syst*, vol. 5, no. 5, 2023, doi: 10.1002/aisy.202200344.

[37] J. Zhao *et al.*, "Wearable Optical Sensing in the Medical Internet of Things (MIoT) for Pervasive Medicine: Opportunities and Challenges," *ACS Photonics*, vol. 9, no. 8, pp. 2579–2599, 2022, doi: 10.1021/acsphotonics.2c00898.

[38] A. A. Tarar, U. Mohammad, and S. K. Srivastava, "Wearable skin sensors and their challenges: A review of transdermal, optical, and mechanical sensors," *Biosensors*, vol. 10, no. 6, 2020, doi: 10.3390/BIOS10060056.

[39] X. Zhang, Y. Guan, and Y. Zhang, "Ultrathin hydrogel films for rapid optical biosensing," *Biomacromolecules*, vol. 13, no. 1, pp. 92–97, 2012, doi: 10.1021/bm2012696.

[40] B. Zhou, K. Fan, T. Li, G. Luan, and L. Kong, "A biocompatible hydrogel-coated fiber-optic probe for monitoring pH dynamics in mammalian brains in vivo," *Sensors Actuators B Chem*, vol. 380, no. January, p. 133334, 2023, doi: 10.1016/j.snb.2023.133334.

[41] S. E. Pischke, C. Tronstad, L. Holhjem, P. S. Halvorsen, and T. I. Tønnessen, "Perioperative detection of myocardial ischaemia/reperfusion with a novel tissue CO2 monitoring technology," *Eur J Cardio-thoracic Surg*, vol. 42, no. 1, pp. 157–163, 2012, doi: 10.1093/ejcts/ezr278.

[42] W. Qu *et al.*, "Application of Optical Fiber Sensing Technology and Coating Technology in Blood Component Detection and Monitoring," *Coatings*, vol. 14, no. 2, 2024, doi: 10.3390/coatings14020173.

[43] A. Jamal *et al.*, "Insights into Infusion-Based Targeted Drug Delivery in the Brain: Perspectives, Challenges and Opportunities," *Int J Mol Sci*, vol. 23, no. 6, 2022, doi: 10.3390/ijms23063139.

[44] S. Roy Chowdhury, R. Tiwari, N. Ghosh, D. Haldar, and A. Banerjee, "Fabry–Perot Cavity by a Bio-Inspired Hollow Tetragonal Waveguide: Toward Femtomolar Detection," *ACS Appl Opt Mater*, vol. 1, no. 2, pp. 598–606, 2023, doi: 10.1021/acsaom.2c00156.

[45] V. Naresh and N. Lee, "A review on biosensors and recent development of nanostructured materials-enabled biosensors," *Sensors (Switzerland)*, vol. 21, no. 4, pp. 1–35, 2021, doi: 10.3390/s21041109.

[46] C. Leitão *et al.*, "Cost-Effective Fiber Optic Solutions for Biosensing," *Biosensors*, vol. 12, no. 8, 2022, doi: 10.3390/bios12080575.

[47] F. Liu *et al.*, "Development of Taper-in-Taper-Based Optical Fiber Sensors for Chemical and Biological Sensing," *Photonics*, vol. 10, no. 5, 2023, doi: 10.3390/photonics10050567.

[48] A. Maity, S. Maithani, and M. Pradhan, "Cavity Ring-Down Spectroscopy: Recent Technological Advancements, Techniques, and Applications," *Anal Chem*, vol. 93, no. 1, pp. 388–416, 2021, doi: 10.1021/acs.analchem.0c04329.

[49] Y. Zhang *et al.*, "Multiplexed optical fiber sensors for dynamic brain monitoring," *Matter*, vol. 5, no. 11, pp. 3947–3976, 2022, doi: 10.1016/j.matt.2022.07.024.

[50] P. Zhang, J. W. Kim, P. Gehlbach, I. Iordachita, and M. Kobilarov, "Autonomous Needle Navigation in Retinal Microsurgery: Evaluation in ex vivo Porcine Eyes," *Proc - IEEE Int Conf Robot Autom*, vol. 2023-May, pp. 4661–4667, 2023, doi: 10.1109/ICRA48891.2023.10161151.

[51] Y. Liu *et al.*, "Miniature fiber-optic tip pressure sensor assembled by hydroxide catalysis bonding technology," *Opt Express*, vol. 28, no. 2, p. 948, 2020, doi: 10.1364/oe.380589.

[52] L. Li, Y. Li, L. Yang, F. Fang, Z. Yan, and Q. Sun, "Continuous and Accurate Blood Pressure Monitoring Based on Wearable Optical Fiber Wristband," *IEEE Sens J*, vol. 21, no. 3, pp. 3049–3057, 2021, doi: 10.1109/JSEN.2020.3027919.

[53] B. Vogt, "Catheter-Free Urodynamics Testing: Current Insights and Clinical Potential," *Res Reports Urol*, vol. 16, no. January, pp. 1–17, 2024, doi: 10.2147/RRU.S387757.

[54] A. O. Soge, O. F. Dairo, M. E. Sanyaolu, and S. O.

Kareem, “Recent developments in polymer optical fiber strain sensors: A short review,” *J Opt*, vol. 50, no. 2, pp. 299–313, 2021, doi: 10.1007/s12596-021-00699-7.

[55] H. C. Ates *et al.*, “End-to-end design of wearable sensors,” *Nat Rev Mater*, vol. 7, no. 11, pp. 887–907, 2022, doi: 10.1038/s41578-022-00460-x.

[56] M. A. Zawawi, S. O’Keffe, and E. Lewis, “Intensity-modulated fiber optic sensor for health monitoring applications: A comparative review,” *Sens Rev*, vol. 33, no. 1, pp. 57–67, 2013, doi: 10.1108/02602281311294351.

[57] B. Raju, R. Kumar, S. Dhanalakshmi, G. Dooly, and D. B. Duraibabu, “Review of fiber optical sensors and its importance in sewer corrosion factor analysis,” *Chemosensors*, vol. 9, no. 6, pp. 1–29, 2021, doi: 10.3390/chemosensors9060118.

[58] I. Sadek, J. Biswas, and B. Abdulrazak, “Ballistocardiogram signal processing: a review,” *Heal Inf Sci Syst*, vol. 7, no. 1, pp. 1–23, 2019, doi: 10.1007/s13755-019-0071-7.

[59] E. Cibula, S. Pevec, B. Lenardic, E. Pinet, and D. Donlagic, “Miniature all-glass robust pressure sensor,” *Opt Express*, vol. 17, no. 7, p. 5098, 2009, doi: 10.1364/oe.17.005098.

[60] Z. Zhao, J. Chen, J. Yang, and Q. Jiang, “Photonic sensor with radio frequency power detection for body pressure monitoring,” *Optoelectron Lett*, vol. 19, no. 12, pp. 752–755, 2023, doi: 10.1007/s11801-023-3110-1.

[61] L. Yi, B. Hou, and X. Liu, “Optical Integration in Wearable, Implantable and Swallowable Healthcare Devices,” *ACS Nano*, vol. 17, no. 20, pp. 19491–19501, 2023, doi: 10.1021/acsnano.3c04284.

[62] C. Fisher *et al.*, “Perspective on the integration of optical sensing into orthopedic surgical devices,” *J Biomed Opt*, vol. 27, no. 01, pp. 1–15, 2022, doi: 10.1117/1.jbo.27.1.010601.

[63] M. Ochoa, J. F. Algorri, P. Roldan-Varona, L. Rodriguez-Cobo, and J. M. Lopez-Higuera, “Recent advances in biomedical photonic sensors: A focus on optical-fibre-based sensing,” *Sensors*, vol. 21, no. 19, 2021, doi: 10.3390/s21196469.

[64] D. Jauregui-Vazquez *et al.*, “Low-pressure and liquid level fiber-optic sensor based on polymeric Fabry–Perot cavity,” *Opt Quantum Electron*, vol. 53, no. 5, pp. 1–12, 2021, doi: 10.1007/s11082-021-02871-6.

[65] M. S. Xavier *et al.*, “Soft Pneumatic Actuators: A Review of Design, Fabrication, Modeling, Sensing, Control and Applications,” *IEEE Access*, vol. 10, pp. 59442–59485, 2022, doi: 10.1109/ACCESS.2022.3179589.

[66] F. Shen, M. Ai, Z. Li, X. Lu, Y. Pang, and Z. Liu, *Pressure measurement methods in microchannels: advances and applications*, vol. 25, no. 5. Springer Berlin Heidelberg, 2021. doi: 10.1007/s10404-021-02435-w.

[67] E. Bills, “Risk management for IEC 60601-1 third edition.,” *Biomed Instrum Technol*, vol. 40, no. 5, pp. 390–2, 2006, [Online]. Available: http://www.ncbi.nlm.nih.gov/pubmed/17078374

[68] F. Tettey, S. K. Parupelli, and S. Desai, “A Review of Biomedical Devices: Classification, Regulatory Guidelines, Human Factors, Software as a Medical Device, and Cybersecurity,” *Biomed Mater Devices*, vol. 2, no. 1, pp. 316–341, 2024, doi: 10.1007/s44174-023-00113-9.

[69] M. Wirges, A. Funke, P. Serno, K. Knop, and P. Kleinebudde, “Development and in-line validation of a Process Analytical Technology to facilitate the scale up of coating processes,” *J Pharm Biomed Anal*, vol. 78–79, pp. 57–64, 2013, doi: 10.1016/j.jpba.2013.01.037.

[70] The European Parliament and the Council of the European Union, “Regulation (EU) 2017/746 of the European parliament and of the council on in vitro diagnostic medical devices,” *Off J Eur Union*, vol. 5, no. 5, pp. 117–176, 2017.

[71] S. Cruz Rivera *et al.*, “Advancing UK Regulatory Science Strategy in the Context of Global Regulation: a Stakeholder Survey,” *Ther Innov Regul Sci*, vol. 55, no. 4, pp. 646–655, 2021, doi: 10.1007/s43441-021-00263-2.

[72] D. J. Wilson, “Polio,” *Polio*, vol. 2013, no. June 1990, pp. 1–184, 2009, doi: 10.1177/2165079915576935.

[73] S. H. Becker, *Approved American National Standards*, vol. 100, no. 10. 2012. doi: 10.5594/j02445.

[74] “Iso 13485:,” no. January, p. 13485, 2010.

[75] A. E. Alden, “Approved American National Standards,” *SMPTE J*, vol. 90, no. 5, pp. 415–464, 2012, doi: 10.5594/j01468.

51: SENSORS AND ACTUATORS FROM BIODIELECTRICS

Dinesh Barnana [a] *, Charlie O'Mahony* [a], *Krittish Roy* [a], *Ehtsham ul Haq* [a], *Syed A.M. Tofail* [a,]

[a] Department of Physics, and Bernal Institute, University of Limerick, Castletroy Limerick, Ireland, V94 T9PX.

Emerging Sensing Strategies and Applications Cont., EM010, August 14, 2024, 11:00 AM - 12:10 PM

Abstract – Biodielectrics are dielectrics originating or derived from, or inspired by living systems. In this time when we face the challenge of sustainability of materials and their sources, biodielectrics can play a crucial role as alternative materials for sensor and actuator applications, especially in the fields of soft robotics, wearable computing, flexible electronics, and biologically inspired devices. In this work, we present an overview of this class of materials which has recently gained huge attraction from many sensors and actuation applications.

***Keywords*:** Biodielectrics; Biopiezoelectrics; Bioferroelectrics; Low k dielectrics; Sensors; Actuators

1. INTRODUCTION

Biodielectrics are dielectric materials that originate in, derived from, or inspired by living systems. Examples include gutta-percha, wood, amino acids, tissues and bone, or bioinspired self-assembled peptides. They may or may not have been modified and does not have to be bio or environmentally degradable. They will, however, be classified as dielectrics which are different from those originating from petrochemical origins.

In this era of modern life style, sensors and actuators have utmost significance in the fields of science and technology, with diversified applications, such as ultrasonic sensors [1], actuators, oscillator dielectric resonator, frequency generators, transducers, energy harvesting, sonar devices and 3D printing technologies. Materials used as dielectrics in sensors, actuators and transducers can vary from ceramics (e.g. barium titanate) to polymers (PVDF), to composites. Piezoelectricity in electrically poled polycrystalline barium titanate ($BaTiO_3$) is one example of material used in piezoelectrics. Lead zirconate titanate (PZT), despite its high content of toxic lead, has become a material of choice in many sensors and actuator applications due to its superior figures of merits (FOMs). The use of lead is worrisome and, since 2011, on constant grace periods in the European Union due to regulatory restrictions legislation Sustainability, environmental impact, and health impact remains burning issues. Ceramics also suffer from brittleness, low recoverable strain and low malleability.

Polymers are easy to process and manufacture, relatively low in cost, lightweight. They generally possess relatively low permittivity, low loss, and high dielectric breakdown strength. They can be easily drawn into thin wires, complex structures, and coatings, what make them ideal for industrial applications despite their relatively lower piezoelectric FoMs. Commercially successful piezoelectric polymers are fluorine based causing serious health and environmental issues made the researchers to look for sustainable dielectric materials for usage in sensor applications.

Recent discovery of high piezoelectric FoM in biological materials, have gained a lot of attention to use them in both sensing, actuation and transduction applications as technical applications may now be possible to replace fluorine based polymer piezoelectrics. Added benefits will be biodegradability, compatibility and non-toxic nature. Another benefit is the abundance of potential choice for such materials. Several naturally occurring materials such as amines, peptides, proteins, tissues, cells, cellulose, hair, and wood have showed piezoelectric properties. They need to be mapped with respect to their FoMs and suitable applications. Due to these inherent dielectric properties and environmental sustainability, biodielectrics have huge upside potential to replace conventional dielectrics in many applications which includes sonars, sensors, accelerometers, resonators, medical devices, wearable electronics, smart devices, and other energy harvesting applications. These biodielectric materials have brought a huge transformation in the advanced applications of medical science, such as localized drug delivery in cancer therapeutics, health monitoring, bone repair, tissue engineering and usage in other nanoelectromechanical systems (NEMs) [2]. A related phenomenon to piezoelectrics is pyroelectricity. Commercial applications of conventional dielectrics as pyroelectric sensors have been limited to infrared and thermal sensing Ceramics are generally used in commercially successful devices. Relatively lower permittivity in biopyroelectrics may allow large area detection, for example. Due to their inherent low permittivity, these biopolymers can also be used as the active materials in low K dielectrics. Here we present an overview of the developments of these three types of materials with a view to aid materials selection as well future engineering of these materials to improve FoMs for real life applications.

The search for new materials for integrated circuits (ICs) has resulted from the unrelenting quest for microprocessors that are quicker and more efficient. The interconnects within integrated circuits (ICs) became a bottleneck for performance enhancement at the 0.25 μm technology node. In high frequency communication devices, ensuring faster signal transmission with minimal signal loss requires materials with lower relative permittivity and low dielectric losses. These Low k dielectric materials have advantages like lower dielectric loss, faster signal transmission compared to traditional dielectric materials made them to use in high frequency microelectronics such as printed circuit boards (PCBs) and antennas, as well as microwave communication

DOI: https://doi.org/10.34961/researchrepository-ul.29291750.v1

components used in for example, Internet of Things (IoT), Fifth Generation (5G), inter-satellite gesture sensing, communications, and automotive radar applications. thus, interconnection point of view, usage of low k dielectric materials are necessary to limit electronic crosstalk, charge build-up, and signal propagation delay. Low k dielectrics are considered as materials with dielectric constant lower than silicon dioxide dielectric constant (k ~ 3.9). Researchers developed novel materials to lower capacitance and connection resistance in order to overcome this. One such turning point was the switch from aluminum (Al) to copper (Cu). Silicon dioxide which is used for such applications whose relative permittivity ~ 4 which is less when compared with existing inorganic dielectric materials, but still, it is high results in high dielectric losses.

There are two ways to reduce the k value, one is the creating pores and the other is the development of dielectric materials with having molecules of less polarity such as C-H by reducing the high polar groups. Going to the fundamental aspects of polarizability, the materials containing polar components (e.g. Si-O) has higher dielectric constant compared with the materials containing less polar components (e.g. C-C, Si-F, Si-C, C-H). The dipole formation is a result of electronic polarization (displacement of electrons), distortion polarization (displacement of ions), or orientation polarization (displacement of molecules) in an alternating electric field. these phenomena have characteristic dependencies on the frequency of the alternating electric field, giving rise to a change in the real and imaginary part of the dielectric constant between the microwave, ultraviolet, and optical frequency. This led researchers to investigate materials that inherently possess relatively low dielectric constants based on less polar polymeric materials such as polyimides, polyphenylene oxides, and fluoropolymers. These materials offer lower dielectric constants than that of silicon dioxide (typically between 2.5 and 4) but often suffers from low thermal stability, poor mechanical properties, and higher moisture absorption. Polymer based or other inorganic low K dielectrics cannot withstand the high processing temperature (High and Low Dielectric Constant Materials). Here are two ways to answer this, one is the development of low k high temperature resistant dielectric materials, and the other is the development of methods to reduce the processing temperature to use currently available low k dielectric materials (High and Low Dielectric Constant Materials). Also, sustainability of these materials are often overlooked despite they originated from petrochemical precursors, creates environmental burden and are often toxic.

The other way to reduce the dielectric constant is using porous dielectric materials or inducing porosity. SiO2 has been using since long ago for internal insulation of semiconductor chips due to its properties such as compatibility, good thermal and mechanical properties. These dielectric constants can further bring down further by creating a porosity using different techniques such as sol-gel method, precursor route, template method etc. He et al. prepared nanoporous SiOF where they injected fluorine molecules into the system to create Si-F bonds which are less polar helps in reducing the dielectric constant [3]. Ultralow-k porous pSiCOH materials were created to preserve low capacitance as devices scaled further. Nevertheless, there were issues with mechanical strength and compatibility because of these porous materials.

The organic bioelectric whose dielectric properties fall under the desirable range even without inducing any pores have huge potential to replace conventional inorganic and polymer based low k dielectric materials. One more problem with low k dielectrics is the low thermal conductivity. This will reduce the heat dissipation especially in high powder density chips. Recently, thermally conductive ultra-low k dielectric layers based on two dimensional covalent organic frameworks developed by the helps in heat dissipation.

Usually, silica based low k dielectric materials have a dielectric constant of three or four, better thermal stability and high thermal conductivities. On the other hand, organic dielectric materials have desirable low k dielectric properties even without inducing pores, but less resistant heat, mechanical stability and lower thermal conductivities. Thus, organo-metallic dielectric materials provide a solution for long lasting problems in semiconducting industries such as thermal resistance, lower permittivity (porosity and less polar molecules). Though several works already reported organosilicon, organo metallic dielectrics such as (Luminescent metal-organic frameworks for chemical sensing and explosive detection, Metal-organic framework materials as catalysts, Selective gas adsorption and separation in metal-organic frameworks, Understanding and controlling the dielectric response of metal-organic frameworks), yet the progress is not very significant. To develop advanced metal-organic dielectric materials, strong fundamental understanding on the dielectric properties of metals and organic matter is required. Though the dielectric properties of metallic materials are well studied and understood by mankind today but understanding of dielectric phenomena in bio dielectrics even today in minimum. Thus, the following sections of this review articles provide deep and in depth understanding of bio dielectrics.

piezo and Pyro-electrics The breakthrough in the field of dielectrics happened in the year 1880 when French physicists, brothers Jacques and Pierre Curie, discovered piezoelectricity while compressing a certain type of naturally occurring crystals, such as quartz, topaz, Rochelle salt, cane sugar and tourmaline. A year later (1881), Lippaman predicted the converse piezoelectric effect, i.e., expansion or contraction of a non-centrosymmetric materials in response to the applied electric field. Piezo electrics were only of laboratory interest until they were used in sonar applications during World War I by P. Langevin and French co-workers. This led to an increase in research and development of new piezoelectric materials and their applications.

The effect of pyroelectricity is known for 24 centuries, since the Greek philosopher Theophrastus wrote, on stones, c. 315 B.C “It [Lyncurium: Tourmaline, found in urine extracts of Lynx] has the power of attraction, just as amber has, and some say that it not only attracts straws and bits of woods, but also copper and iron, if the pieces are thin…”. Its property of attraction was attributed to electric phenomenon in 1747 by French Physician and Chemist Linné, who called it lapis electricus. Amber is fossilised tree resin, $C_{12}H_{20}O$ having no crystal structure. “It is asserted, too, that these stones [flame coloured stone known as lychnis], when heated by the sun or rubbed between the fingers, will attract chaff and filaments of paper.” Pliny the Elder, Natural History, c. 1st Century, A.D. Lychnis is a kind of ruby (corundum, Al2O3 trigonal, -3m, with some Cr,) ‘lampstone’. In the year

1824, David Brewster, recognized for his work in optics, was the first author to use the term "pyroelectricity" and to observe pyroelectricity phenomenon in various crystals, one among which was Rochelle salt. Joseph Valasek discovered the first ferroelectric material in 1920 potassium sodium tartrate tetrahydrate.

The piezoelectric effect was later identified and measured in crystals of potassium dihydrogen phosphate (KDP) and ammonium dihydrogen phosphate (ADP) in the early 1940s. The ADP crystals were then utilized in highpower acoustic transducers. During the time of World War II, some synthetic piezo-crystals, such as barium titanate (BaTiO3 K >1100) or lead zirconate titanate (PZT) were developed and showed relatively high piezoelectric coefficients. The breakthrough in piezoelectric polymers happened in the year 1969 with the discovery of piezoelectricity in poled polymers, such as nylon and polyvinylidene fluoride (PVDF) Nowadays, PVDF and its copolymers are the most commercially available piezoelectric polymers finding applications in nanogenerators, sensors, energy harvesting, and biomedical fields.

Not long after the discovery of biopiezoelectricity, pyroelectricity was also found in phalanges and hoof tendons of a cow by Lang in 1966 [4]. Since then, pyroelectricity has been observed in various biological entities which includes amino acids, plant leaves, thorax of live insects, hydroxyapatite, lysozyme etc. It was previously concluded that the pyroelectric effect of bone originated from collagen but not from hydroxyapatite based on the formerly established centrosymmetric crystallographic space group for hydroxyapatite, which precluded piezoelectricity. Later on, the crystal group assignment was corrected, which allows both piezo- and pyroelectricity. The measured pyroelectric co-efficient for unpoled hydroxyapatite ceramics is 12 mC/m2K, whereas that of poled hydroxyapatite is ranging from 0.1-40 nC/cm^2 K at 300-500 ◦C [5].

In addition, Martin first observed pyroelectric and piezoelectric phenomena in bundles of wool and hair [6]. AHENSTADT investigated pyroelectricity in wheat. the temperature dependence of the pyroelectric constant for the epidermis of wheat grains [7]. It is interesting to note that winter wheat and spring wheat show quite different results, reflecting the different temperature variation of residual polarization in the grains. It is assumed that the polarization in winter wheat decreases more sharply than that in spring wheat with increasing temperature.

Fukada et al. found that thin films of aromatic polyurea shows pyroelectricity. pyroelectric activity is generated in these films by a poling treatment. The orientation of urea bonds (NH- CO-NH) with a dipole moment of 4.9 D is responsible for a large residual polarization in these films.

The pyroelectric coefficient reported for g glycine (13×10^{-6} C/m^2K 1) is more than three times higher than that of tourmaline, illustrating that strong pyroelectricity is present even in the smallest biological building blocks. Pyroelectric properties of some glycine-based materials are even higher.

In 2018, Stapleton et al. investigated the pyroelectricity in polycrystalline aggregate films of globular protein lysozyme prepared on IDE electrode and the measured pyroelectric coefficient is 1441 ± 536 mC/m^2K [8]. The coefficient is the till date highest obtained among all biological materials and comparable to PZT grown on $SrTiO_3$ substrate. In addition, Kholkin et al. discovered pyroelectric effect and polarization instability after a certain temperature change in self-assembled diphenyl alanine microtubes. The obtained pyroelectric co-efficient for the micro tube bundle is 2 mC/m^2K. Interestingly, a paper by Tofail et al. listed and compared the pyroelectric coefficients of different biological materials.

Recently, Kim et al. demonstrated heat induced electrical polarization in virus. Precisely, they investigated the pyroelectric properties of vertically aligned M13 bacteriophage film and obtained a pyroelectric coefficient of 0.13 mC/m^2 ◦C. It may pave the way for new bio-inspired pyroelectric devices.

CONCLUSIONS

In conclusion, biodielectrics offer a promising alternative to conventional dielectric materials. With their potential for biodegradability, non-toxic nature, and high piezoelectric figures of merit (FoMs), these materials show great promise in a wide range of applications. Their use in fields such as localized drug delivery and health monitoring demonstrates their transformative impact on advanced medical science and technology. Biodielectrics are poised to play a pivotal role in shaping the future of dielectric materials. The potential for improving their figures of merit for real-life applications makes biodielectrics a compelling area for future engineering and materials selection

FUNDING STATEMENT

Authors acknowledge CURAM- Science Foundation Ireland (SFI) centre for medical devices (Grant Number 13/RC/2073_P2).

REFERENCES

[1] L. Pardo, ‘Piezoelectric ceramic materials for power ultrasonic transducers’, in *Power ultrasonics*, Elsevier, 2023, pp. 65–81.

[2] A. Zaszczyńska, A. Gradys, and P. Sajkiewicz, ‘Progress in the applications of smart piezoelectric materials for medical devices’, *Polymers (Basel)*, vol. 12, no. 11, p. 2754, 2020.

[3] Shamiryan, Denis, Thomas Abell, Francesca Iacopi, and Karen Maex. "Low-k dielectric materials." Materials today 7, no. 1 (2004): 34-39.

[4] Lang, Sidney B. "Pyroelectric effect in bone and tendon." Nature 212, no. 5063 (1966): 704-705.

[5] Tofail, S. A. M., C. Baldisserri, D. Haverty, J. B. McMonagle, and J. Erhart. "Pyroelectric surface charge in hydroxyapatite ceramics." Journal of Applied Physics 106, no. 10 (2009).

[6] Martin, A. J. P. "Tribo-electricity in wool and hair." Proceedings of the Physical Society 53, no. 2 (1941): 186.

[7] Athenstaedt, H. "Pyroelectric properties of wheat." Ferroelectrics 14, no. 1 (1976): 753-759.

[8] Stapleton, A., M. R. Noor, E. U. Haq, C. Silien, T. Soulimane, and S. A. M. Tofail. "Pyroelectricity in globular protein lysozyme films." Journal of Applied Physics 123, no. 12 (2018)

52: GAMIFIED ORTHOSIS FOR MUSCLE REHABILITATION: ESCAPE SPLINT

Azadeh Hajian[a], Faten Aboalkhair[a], Firdowsa Cige[a], Olga Korostynska[a,], Morten Ødegård[a], Anne-Marthe Sanders[b]*

[a] Department of Mechanical, Electrical, and Chemical Engineering, Oslo Metropolitan University, Oslo, Norway
[b] Department of Occupational Therapy, Sunnaas Rehabilitation Hospital, Nesodden, Norway
Biomedical Sensors Session 2, EM009, August 13, 2024, 10:05 AM - 11:15 AM

Abstract—**Hand rehabilitation is typically indicated for regaining lost function or reducing pain after injuries, surgeries, or conditions affecting the hand and wrist. This study presents a novel approach to hand rehabilitation using 3D scanning and printing for a customized, inexpensive, and engaging training device. The device aims to motivate patients and improve compliance with rehabilitation exercises. Due to individual 3D-scanning and manufacturing via 3D printing, each personalized hand training device provides a comfortable fit for a specific patient, enhancing efficiency of physical hand rehabilitation program. This hand training device can be beneficial in addressing hand muscle stiffness that occurs following certain hand injuries, such as fractures. In these situations, therapies and exercises are crucial for resolving muscle stiffness, and this orthosis can be a helpful aid. Furthermore, the design incorporates gamified elements on both the dorsal and finger aspects of the hand. The dorsal surface features a labyrinth game specifically designed to promote wrist joint and muscle mobility in hand rehabilitation. These game elements offer the potential for progressive difficulty levels, allowing for tailored rehabilitation programs as patients improve. Moreover, the fingers integrate a musical game that motivates patients to engage in finger flexion and extension movements, generating various sounds. Additionally, a flex sensor embedded within the wrist section continuously monitors the degree of wrist flexion, enabling assessment of patient progress and objective data collection for treatment optimization. A Feedback from occupational therapists suggests that using games in hand rehabilitation is a promising approach, motivating patients, especially children, to adhere to therapy and potentially achieve better outcomes. The output from the flex sensor can be a valuable tool for monitoring hand movements, allowing therapists to assess progress and determine if any adjustments in planned rehabilitation activities are necessary.**

Keywords: wrist orthosis; labyrinth; flex sensor; muscle stiffness; rehabilitation

1. INTRODUCTION

Escape splint suggests that the patient must escape from the labyrinth, and it also implies that the splint will help them escape from their injury. Muscle rehabilitation plays a key role in restoring functionality and mobility for individuals recovering from injuries, surgeries, or conditions such as stroke or arthritis [1]. The primary goal of muscle rehabilitation is to improve strength, flexibility, endurance, and coordination in affected muscles and joints. This process often involves a combination of therapeutic exercise, manual techniques, and assistive devices to facilitate movement and enhance recovery.

Orthoses, or orthotic devices, are commonly used in muscle rehabilitation to support, align, protect, or improve the function of muscles and joints. These devices come in various forms, ranging from simple braces to more complex orthosis with advanced technologies. In the context of wrist rehabilitation, orthoses are often prescribed to stabilize the wrist joint, provide support, and facilitate controlled movement during exercises.

Innovative approaches within orthotics have emerged recently, leveraging technology to create more interactive and engaging rehabilitation experiences. For instance, a pilot randomized controlled trial by Nijenhuis et al. Demonstrated that training with passive hand orthosis combined with game-based exercises at home significantly improved hand function in chronic stroke patients [2].

A Study has shown that muscle stiffness in children often resolves within two weeks, indicating a faster healing process compared to adults. Therefore, immediate hand therapy may not always be necessary in these cases. With consistent practice of the prescribed exercises, most children can regain full range of motion [3].

For simple fractures in fingers and palm bones, a cast is typically used to immobilize the hand and wrist for 3-4 weeks. After cast removal and bone healing, patients may experience stiffness. In most cases, a pediatrician will provide an exercise sheet for children with stiffness to perform at home. However, children with specific needs are referred to one-on-one hand therapy with a physiotherapist [3]. To improve traditional methods and motivate patients to adhere to their treatment, a gamified orthosis was designed, which can be personalized for different ages and levels.

2. LITERATURE REVIEW

Recent advancements in sensor technology have paved the way for significant improvements in the monitoring and rehabilitation processes associated with orthotic devices. This review synthesizes current literature on the subject, highlighting key findings and technological innovations that hold promise for future applications.

Objective methods for monitoring orthotic device usage on extremities were systematically reviewed in [3], where it was revealed that temperature sensors, pressure sensors, accelerometers, and step counters are instrumental in

DOI: https://doi.org/10.34961/researchrepository-ul.29291795.v1

measuring compliance, a critical factor for effective treatment outcomes. The quantitative data derived from these sensors offer invaluable insights for both clinical and research settings [4].

A paper by Megalingam et al. [5] presented an innovative approach to hand rehabilitation utilizing a wearable orthotic device. This device is designed to offer multi-mode control capabilities along with real-time feedback, thereby enhancing the efficacy of hand therapy interventions. The integration of these features addresses a significant gap in existing literature, as previous studies have underscored the importance of wearable devices in hand rehabilitation but lacked comprehensive multi-mode control and real-time feedback functionalities. The integration of these features aligns with the growing trend in rehabilitation technology towards personalized, interactive, and effective interventions.

In another paper, Jackson, and Abdullah [1] introduce a pneumatic hand training device for post-stroke rehabilitation, developed in consultation with physiotherapists. The device, incorporating pneumatic airbag actuators and sensors, was tested on 30 healthy individuals, demonstrating safety, comfort, and repeatability in motion. User feedback emphasized comfort and suitability across demographics. This lightweight and adjustable device shows promise for effective rehabilitation, warranting further validation to confirm its efficacy and long-term benefits for stroke patients.

The integration of sensor technology in orthotic devices represents a transformative approach to rehabilitation. The ability to monitor patient compliance and progress in real-time offers a more personalized and effective treatment pathway, enhancing the quality of life for individuals with motor disabilities.

The wrist orthosis design proposed in this paper, integrating flex sensors, with a game aspect to it, represents a significant advancement in rehabilitation technology. This orthosis not only offers feedback on patient's progress but also provides engaging aspects for the patient undergoing the rehabilitation.

3. DESIGN OF THE ORTHOSIS

3D scanning and printing offer several advantages in the field of orthosis design. Custom-fit orthoses can be created based on precise 3D scans of the patient anatomy. This ensures a better fit and improved patient comfort. Design flexibility is another advantage, 3D printing allows for complex geometries and custom designs. Orthoses can be tailored to specific patient needs. Figure 1 illustrates a three-dimensional scan of the hand, which served as the foundational model for the orthotic design. This precise digital representation captures the intricate contours and dimensions necessary for customizing the orthosis to the patient's unique anatomical structure. Moreover, 3D printing streamlines the production, resulting in faster delivery of custom orthoses [6].

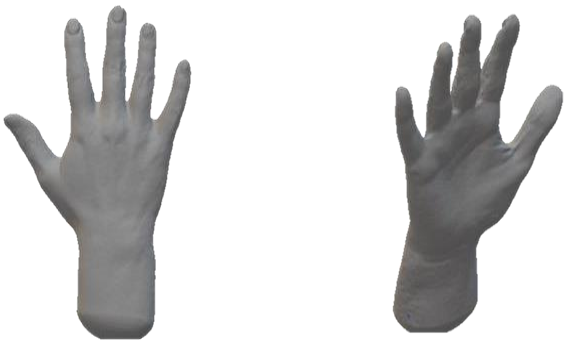

Figure 1. 3D scan of a hand.

Additionally, 3D printing allows for various materials, including biodegradable options, ensuring different patient needs. Various materials are used for 3D-printed orthotics. Polylactic acid (PLA), for example, is biodegradable and commercially available, commonly used for prototypes and custom orthoses. Thermoplastic polyurethane (TPU) is another common material used. Is provides flexibility and shock absorption properties, making it suitable for insoles and orthotics [6]. These advancements in materials and production techniques contribute to the continued evolution of orthosis design and fabrication, offering improved solutions for patients' needs.

3.1. 3D modelling

The orthosis designed for wrist and finger rehabilitation represents a significant advancement in personalized medical devices. Utilizing a 3D scan of a patient's hand, the orthosis was modelled in SolidWorks, ensuring a custom fit tailored to the individual's anatomy. The design prioritizes weight reduction, ventilation, and ease of application. With a wall thickness of 3mm and strategically placed holes, it maintains structural integrity while allowing for breathability and lightweight construction.

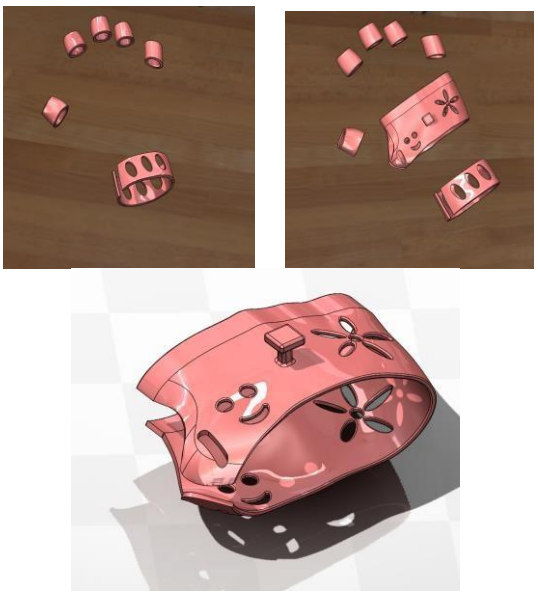

Figure 2. 3D model of the orthosis comprising three interconnected components—finger tops, hand, and wrist sections.

Comprising three interconnected components—finger tops, hand, and wrist sections—the orthosis employs a flexible rubber matrix with perforations. This practical approach not only ensures a snug fit but also introduces adjustable resistance, facilitating muscle exercise and rehabilitation progression. Figure 2 presents the three-dimensional rendering of the orthotic components, encompassing the wrist, hand, and fingers top. This model ensures a precise fit and targeted support. The splint has been realized through 3D printing technology, offering rapid prototyping and the ability to iterate designs efficiently. The orthosis is augmented with a maze attachment, which adds an element of enjoyment to therapy but also serves as a quantitative indicator of the patient's rehabilitation milestones. To successfully complete the maze, patients must execute specific hand rotations as per orthopaedic guidance, necessitating the elbow to be anchored to a table to isolate wrist and hand movements [7]. The movements are shown in the Figure 3.

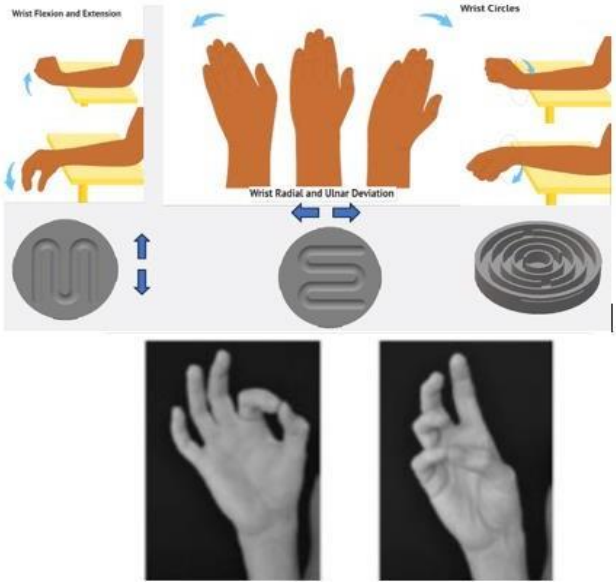

Figure 3. Recommended exercises by physical therapy which can be achieved with Escape Splint.

Enhancing its functionality, the orthosis is equipped with a flex sensor that records the patient's range of motion, providing valuable data for tracking rehabilitation progress. This feature will be elaborated upon in the following sections of the report. Figures 4 and 5 show the various levels of the maze, each more complex than the last. These images display the detailed paths and obstacles that make each level unique and challenging. While Figure 6 displays the orthotic splint with the maze feature attached, illustrating the functional integration of the therapeutic exercise into the splint's design.

Additionally, the orthosis incorporates a musical top fingers component, where a contact between two fingers triggers a distinct musical note for each digit, transforming physical therapy into an interactive and auditory experience. This multisensory approach not only motivates engagement but also improves the therapeutic process.

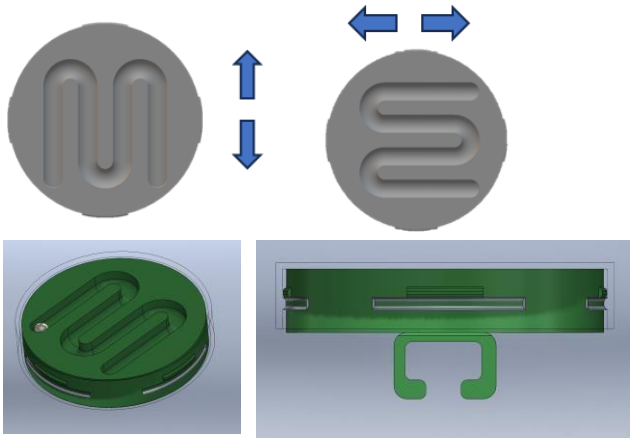

Figure 4.3D model of the maze (level 1)

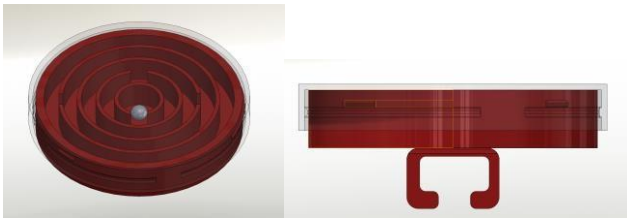

Figure 5. 3D model of the maze (level 2)

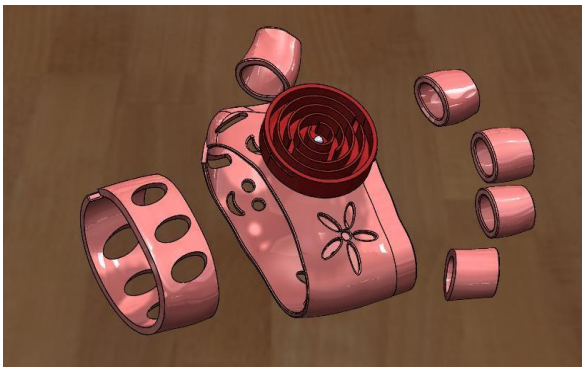

Figure 6. The maze attached to the orthosis.

The maze feature is designed with two levels of difficulty to adapt to the patient's evolving dexterity. Level one is dual-configurable, allowing attachment in two orientations: one facilitates horizontal rotations (right and left), while the other permits vertical movements (up and down). This modularity not only adds variety to the rehabilitation exercises but also tailors the difficulty to the patient's current capability.

Level two presents a more challenging scenario, demanding omnidirectional rotations that engage a broader range of wrist and hand muscles. This level is particularly effective for advanced stages of rehabilitation, where increased complexity aids in the development of finer motor skills and hand-eye coordination. The ease of replacing the maze levels ensures a seamless transition between exercises, including a progressive and engaging recovery process. Figure 7. shows the manufactured orthosis prototype.

Figure 7. Orthosis prototype.

3.2. Material selection

Material selection was a critical decision in this process, with the final contenders being TPU (Thermoplastic Polyurethane) and PLA (Polylactic Acid). TPU, known for its elasticity and durability, offers a more flexible orthosis, although at a higher cost. In contrast, PLA provides a more rigid structure, potentially beneficial for certain stages of rehabilitation [8]. This thoughtful consideration of materials underscores the design's balance between functionality, comfort, and cost-effectiveness, marking it as a noteworthy development in rehabilitative orthotic solutions.

In the Escape Splint's prototype, PLA (Polylactic Acid) was selected for its structural integrity and dimensional stability, and low cost. In contrast, TPU (Thermoplastic Polyurethane) was employed for the hand component to exploit its elastomeric properties, providing the necessary compliance and resilience. The combining between PLA for its stiffness and low cost, and TPU offering the flexibility for dynamic movement, ensures that the orthotic device adequately conforms to the biomechanical demands of the wearer, facilitating ergonomic adaptability during rehabilitation exercises.

3.3. Safety consideration and user guidelines

In the development of the orthosis with an integrated maze for wrist and finger rehabilitation, safety considerations have been addressed. All small components should be properly secured and sealed to ensure safety requirements are met. The orthosis must be used under adult supervision, particularly by parents or guardians, to ensure safe and proper use.

The maze's small ball is securely enclosed to prevent accidental ingestion, and the electrical parts are insulated and designed to operate at low voltages to eliminate the risk of electric shock. Comfort and fit are also paramount; the orthosis is adjustable to prevent pressure points and skin irritation.

Clear instructions have been created to educate users and caregivers on the proper assembly, use, and maintenance of the device. Additionally, the importance of communicating any safety concerns to a healthcare provider has been emphasized.

4. FLEX SENSOR INTEGRATION

Numerous factors contribute to a patient's non-adherence to orthotic treatment. For example, patients may stop using hand orthosis as recommended due to discomfort and challenges in performing daily tasks. Discomfort may arise from physical issues like an improperly fitting orthosis, skin irritation or disturbances in sleep patterns [4].

Additionally, physiological factors such as feeling isolated or stigmatized when wearing an orthosis, can discourage patients from consistence use. Moreover, psychological elements like low self-esteem have been found to influence adherence to treatment. The duration of treatments also plays a role, with longer durations often correlating with lower compliance rates. Patients' attitudes toward the treatment and their trust in healthcare providers are crucial determinants of compliance [4]. Keeping track of how well patients adhere to using orthoses often involves relying on their self-reported information through questionnaires or interviews. But these methods have limitations. Patients tend to overestimate their adherence levels, influenced by a desire to appear compliant. Also, there is a risk of forgetting or misreporting wear rime, especially when assessing compliance after some time has passed. Therefore, there is a need for an objective way to monitor patient compliance with orthoses, one that does not rely on patient input [4].

In this project, integration of 3D scanning and printing techniques addresses the discomforts commonly associated with orthosis. By using 3D scanning technology. Custom fitted orthosis can be tailored precisely to a patient's hand anatomy. This personalized approach shows optimal fit and comfort, rendering concerns about discomfort. Various design elements such as ventilation holes, can be added into the 3D model of the orthosis. These holes enhance airflow reducing issues like sweating and discomfort during prolonged wear.

Another key feature of the orthosis is the integration of a flex sensor which is placed at the wrist area. This sensor detects various response degrees as the patient engages with the labyrinth at the back of the orthoses. By monitoring these bending angles, health care professionals gain valuable insights into the patients' rehabilitation progress. While we utilize the "Cool Terms" software to read and store the data on a laptop, we acknowledge the potential for using more advanced software for future work.

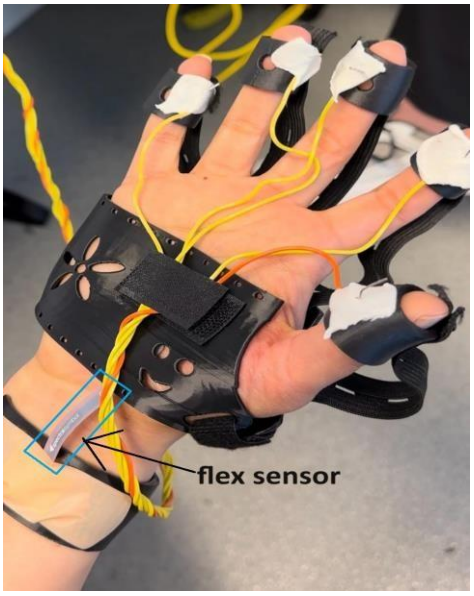

Figure 8. The orthosis with the flex sensor and the musical top fingers.

Notably, the orthosis incorporates an interactive gaming aspects aimed at enhancing patient engagement. A stretchy material is placed to the back of the fingers, prompting the patient to reach and touch their thumb. Each successful touch triggers a musical sound. With each finger corresponding to a different sound. We implemented a code on Arduino to manage these sounds outputs, activating different tones based on which finger touches the thumb. While flex sensors were not integrated into the fingers in this prototype. This could be a promising aspect for the future development to monitor fingers progress comprehensively.

This project represents an innovative approach to orthotic design using 3D scanning, personalized fabrication, flex sensor technology and interactive gaming elements to enhance patient comfort, engagement, and rehabilitation progress monitoring.

5. SENSOR MEASUREMENT

The flex sensor is placed inside the wrist, under the orthosis. You can find a picture of the placements in Figure 8. The sensor measures the bending and straightening of the wrist movement during gameplay with the labyrinth game. The output data can be saved to an Excel file, allowing you to view the results numerically or graphically (charts). This data comparison across different situations helps therapists evaluate patients' conditions and assists them in adjusting the game's difficulty level based on the patient's needs.

Figure 9 illustrates a chart from sensor readings taken during testing. The peaks in the positive direction indicate upward movement, while the dips into the negative represent downward motion. The chart plots the angle of bending in degree against time measured in seconds. The chart has been drowned in Excel based on the readings taken from the sensor.

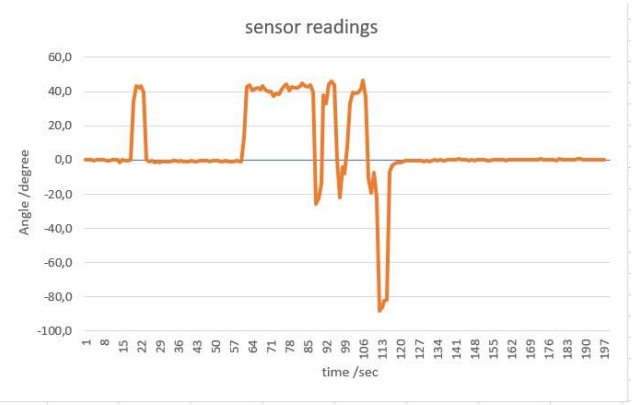

Figure 9. The sensory readings: the y-axis shows the angle of bending while the x-axis shows the time in seconds (negative angles refer to the down bending)

6. CONCLUSION AND FUTURE SCOPE

This study investigated the concept of gamified orthotics as a potential tool to improve rehabilitation outcomes for children and adults experiencing hand stiffness after injury or cast immobilization. This technology utilizes 3D printing to create orthoses for individual patients. Patients can choose the colour and design to suit their preferences, potentially increasing engagement, and compliance during therapy. The design incorporates empty spaces, making the orthosis lightweight and breathable. This can enhance patient comfort, especially during extended wear for rehabilitation purposes.

The prototype demonstrated promising results in two key aspects. Improved Motivation: The labyrinth game, with its progressively increasing difficulty levels, encouraged wrist movement in various directions. Similarly, the musical finger games, triggered by touching different fingers to the thumb, added a motivating element for patients to engage in the exercises and activate their fingers.

The flex sensor output can be represented by a quantitative value that reflects the maximum range of motion achieved. The orthosis can make rehabilitation exercises more engaging and enjoyable for children, potentially leading to better adherence to therapy protocols.

Building on these initial observations, future research should explore the following aspects:

To store the data permanently we can benefit from integrating the Arduino with an SD card as onboard storage. This eliminates dependence on a laptop and allows for data collection even without an immediate connection. The design can also be adaptable to incorporate additional flex sensors for individual finger movements in the future. Additionally, when storing sensitive health data, basic security measures on the Arduino or SD card become important. By addressing these challenges, the system can evolve into a more mobile and data-rich tool for monitoring wrist and potentially finger movement during hand rehabilitation.

The current prototype uses a single wired flex sensor on the wrist to monitor movement data on a laptop. To enhance user experience and data collection, future developments can adopt Bluetooth for transmitting data. This approach also

makes it possible to synchronise the data transmission with mobile devices.

Another approach can be using Wi-Fi and sending the data over the internet. Although sending data securely over the internet has its own challenges, the data can be accessed via trappiest or clinical personal. This data can be monitored to see the patient's activities and the rehabilitation process.

The current design allows for swapping labyrinth layouts, offering some variation in gameplay difficulty. To further enhance rehabilitation engagement, we envision the ability to switch between entirely different games in the future. 3D printing technology provides a unique advantage in this regard. It enables the creation of diverse and personalized games tailored to individual patient needs and preferences. This project opens a door to a world of creative possibilities, potentially revolutionizing hand rehabilitation with a fun and interactive approach.

ACKNOWLEDGMENT

This student research project was conducted as part of the ACIT 4730 Biomedical Engineering Masters' course at Oslo Metropolitan University (OsloMet), in Oslo, Norway. The authors acknowledge the cooperation with Sunnaas Rehabilitation Cluster (SRC) and Strategic OsloMet funding "Intelligent Health".

REFERENCES

[1] G. Jackson and H. A. Abdullah, "Development and Testing of a Soft Exoskeleton Robotic Hand Training Device," Sensors, vol. 23, no. 20, pp. 8395, Oct. 2023.

[2] S. M. Nijenhuis, G. B. Prange-Lasonder, A. H. Stienen, J. S. Rietman, and J. H. Buurke, "Effects of training with a passive hand orthosis and games at home in chronic stroke: a pilot randomised controlled trial," *Clin. Rehabil.*, vol. 31, no. 2, pp. 207-216, Feb. 2017, doi: 10.1177/0269215516629722.

[3] C. Tan, J. Depiazzi, N. Bear, L. Blennerhassett, R. Page, and N. Gibson, "Exercise handout and one-on-one hand therapy for management of stiffness after plaster cast immobilization of simple phalangeal and metacarpal fractures in children: A randomized, noninferiority trial," Journal of Hand Therapy, vol. 34, no. 3, pp. 423-432.e7, 2021. https://doi.org/10.1016/j.jht.2020.03.017.

[4] D. B. Devanand and A. E. Kedgley, "Objective Methods of Monitoring Usage of Orthotic Devices for the Extremities: A Systematic Review," Sensors*, vol. 23, no. 17, p. 7420, 2023. doi: 10.3390/s23177420.

[5] R. K. Megalingam, S. K. M. Sakthiprasad, M. M. Sreekanth, P. K. R. Chennareddy, V. Egumadiri, P. N. V. K. Naveen, and C. Dega, "Wearable Hand Orthotic Device for Rehabilitation: Hand Therapy with Multi-Mode Control and Real-Time Feedback," Applied Sciences, vol. 13, no. 6, p. 3976, 2023. https://doi.org/10.3390/app13063976

[6] R. Kumar and S.K. Sarangi, "3D-Printed Orthosis: A Review on Design Process and Material Selection for Fused Deposition Modeling Process," in Advances in Materials Processing and Manufacturing Applications, A. Patnaik, E. Kozeschnik, and V. Kukshal (eds.), iCADMA 2020, Lecture Notes in Mechanical Engineering, Springer, Singapore, 2021, pp. 55. https://doi.org/10.1007/978-981-16-0909-1_55.

[7] K. DeMatas, "10 Simple Broken Wrist Rehab Exercises for a Quick Recovery," Sporty Doctor, Aug. 17, 2022. [Online]. Available: https://www.sportydoctor.com/broken-wrist-rehab-exercises

[8] F. Wang, Y. Ji, C. Chen, et al., "Tensile properties of 3D printed structures of polylactide with thermoplastic polyurethane," *Journal of Polymer Research*, vol. 29, no. 320, 2022, doi: 10.1007/s10965-022-03172-6.

53: ROBUST ON-HAND ROBOT-3D CAMERA CALIBRATION USING GRADIENT DESCENT IN NOISY SENSOR ENVIRONMENTS

Evgenii Dushkin[a, *], *Niall O' Mahony* [a, *], *Juan Wian Coetzer*[a], *Anshul Awasthi*[a], *Joseph Walsh*[a]

[a] IMaR Research Centre, Munster Technological University, Tralee, Ireland
* Corresponding authors, these authors contributed equally,
Industrial Sensing, EM009, August 13, 2024, 4:20 PM - 6:10 PM

Abstract – This paper presents preliminary results on a novel gradient descent-based method for on-hand robot-camera calibration, addressing the challenges posed by sensor noise. The proposed method, grounded in the AX=XB paradigm, effectively resolves the transformation matrix between the 3D camera frame of reference and the robot's flange frame of reference, achieving a calibration accuracy of 15 mm on test data. The experimental setup includes a KUKA KR16 robot base and an IFM O3D313 time-of-flight camera, with a 200x200 mm AprilTag code positioned within the robot's workspace. The method requires the location of the tag in the robot's workspace and the camera's position in respect to Robot's flange to remain fixed while the tag's position in the camera's frame of reference is established through a detection algorithm.

***Keywords*: On-Hand Robot-3D Camera Calibration, Machine Learning,**

INTRODUCTION

Accurate robot-camera calibration is crucial for applications requiring precise manipulation and interaction within a 3D environment. Traditional calibration methods often struggle with sensor noise, leading to inaccuracies. Recent studies have explored various techniques for improving calibration accuracy in the presence of noise. For example, Li et al. introduced a method combining iterative closest point (ICP) with a robust estimation technique to enhance calibration robustness [1]. Similarly, Fassi et al. proposed a calibration approach using a laser tracker and stereo vision system, demonstrating improved precision despite environmental noise [2]. Zhang et al. explored an adaptive algorithm for on-line calibration, showcasing the potential for real-time applications [3].

This paper introduces a gradient descent method designed to enhance calibration accuracy by effectively mitigating sensor noise impacts. Our method leverages the AX=XB paradigm, focusing on optimizing the transformation matrix through iterative error minimization. By addressing the limitations of existing methods, our approach aims to achieve high calibration accuracy even in challenging environments.

Traditional least squares optimization methods, such as those used in Tsai and Lenz's approach [4] and Lu and Chou's method [5], often suffer from decreased accuracy in the presence of sensor noise. Least squares techniques typically minimize the sum of squared errors, which can be significantly affected by outliers and noise. In contrast, our gradient descent method offers a more robust solution by iteratively adjusting the transformation matrix to minimize a custom-defined loss function that can better handle noisy data.

For instance, Strobl et al. [6] applied a least squares method for robot-camera calibration and reported challenges in achieving consistent accuracy due to sensor noise and environmental variations. Our approach mitigates these issues by leveraging the flexibility of gradient descent to dynamically adjust the optimization process based on the observed error patterns. As a result, we achieved a calibration accuracy of 15mm, which is an improvement over the typical performance of least squares methods under similar conditions.

1. METHODS AND PROCEDURES

The calibration process follows the AX=XB paradigm, where 'A' and 'B' represent known transformations, and 'X' is the unknown transformation matrix to be resolved. Our method employs a gradient descent algorithm to iteratively minimize the difference between vectors AX and XB. Once the difference is minimized, X transformation is considered as optimized.

1.1. Experimental Setup

The calibration procedure included the following components:

Robot and Camera: A KUKA KR16 R2010 robot base and an IFM O3D313 time-of-flight camera are used. The camera is attached to the robot's end effector (tool). The camera has a pixel resolution of 176 x 132 and depth estimation error of approximately 1 mm per metre away from the camera.

Calibration Target: A 200x200 mm AprilTag code is placed at a fixed position.

Tag Detection: Robot determines the position of Endeffector in respect to Robot's root frame (base), while the tag's position in the camera's frame is detected via an algorithm from the AprilTag repository sourced from [7].

Data collection: The pairs of Robot and AprilTag positions, where Robot position means the Pose of Robot's end effector in respect to the Robot's root frame; and AprilTag position means the Pose of AprilTag in respect to Camera's origin (Camera's frame origin) were recorded for multiple points (40 recordings were made in this experiment) with the tool orientated in as diverse a range of positions as possible while keeping the target in-frame.

Verification: A pointer tool, calibrated with the robot so the position of its tip is known was used to establish the target's position in 3D space. The Euclidean distance between this reference point and calculated points after applying the resulting transformation matrix was used to measure the accuracy of the calibration.

DOI: https://doi.org/10.34961/researchrepository-ul.29291840.v1

1.1. Transformation Matrix Definition

The transformation matrix is essential in converting coordinates between the camera's frame of reference and the robot's frame. The matrix combines rotation and translation components as shown in Figure 1.

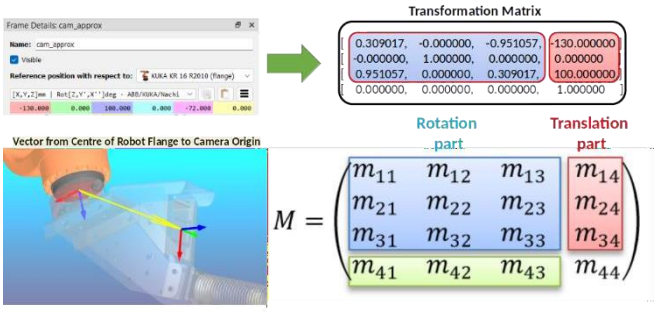

Figure 1. The transformation matrix between camera and tool.

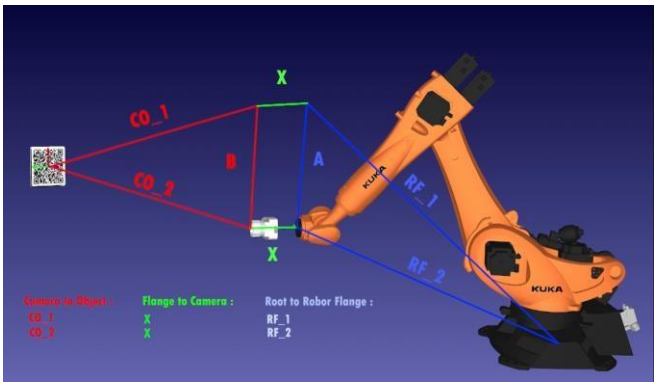

Figure 2. Vectorized View of Calibration Process

For each iteration of the calibration solver a pair of points selected at random from the calibration data are used to estimate the transformation matrix X shown in Figure 2.

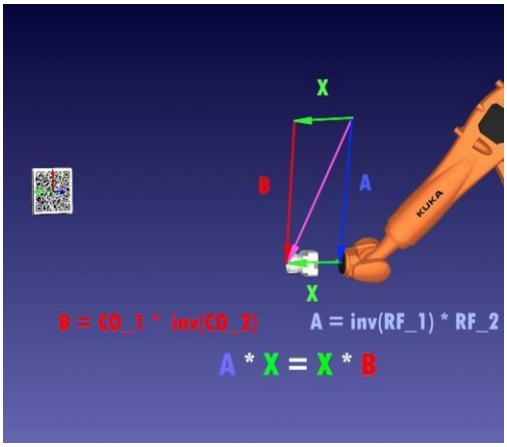

Figure 3. The AX=XB paradigm

The calibration goal is visualized as aligning the violet vectors AX and XB shown in Figure 3, which represent the transformation processes in the vectorized view. These vectors should be the same if the calibration is accurate.

1.2. Gradient Descent Algorithm

The gradient descent optimization process involves calculating the loss function and its gradient, iteratively adjusting the transformation matrix to minimize the loss in the following steps:

◦ Initialization: Initial estimates of the transformation matrix are provided. An eye matrix was used in this case.

◦ Error Minimization: The algorithm iteratively adjusts the transformation matrix to minimize the error of X. The metric used to estimate this error for the loss function was Mean Squared Error (MSE) between the vectors A*X and A*B

◦ Convergence: The process continues until the error converges to a minimal value, achieving high calibration accuracy.

1.3. Loss Function

The metric used to estimate the error for the loss function is the Mean Squared Error (MSE) between the vectors AX and BX. The MSE is defined as the average of the squares of the differences between the estimated and actual values. In our context, it measures the average squared difference between the transformed points in the robot's frame of reference and their corresponding points in the camera's frame of reference.

The loss function ***L*** can be mathematically represented as shown in Equation 1:

$$L = \frac{1}{N}\sum_{i=1}^{N} \|A_i \cdot X - X \cdot B_i\|^2 \qquad 1$$

where A_i and B_i are the known transformations, X is the transformation matrix being optimized, and N is the number of pairs of points. By minimizing this loss function, the algorithm ensures that the transformation matrix X accurately maps the camera's frame to the robot's frame, even in the presence of sensor noise.

2. Adam Optimizer Implementation:

To enhance the efficiency and stability of the gradient descent process, we employed the Adam optimizer, a popular optimization algorithm in machine learning. Adam combines the advantages of two other extensions of stochastic gradient descent: Adaptive Gradient Algorithm (AdaGrad) and Root Mean Square Propagation (RMSProp).

Algorithm Steps:

- Initialization: Initialize the first moment vector, the second moment vector, and the timestep to zero. Initialize the transformation matrix X with initial estimates.
- Hyperparameters: Set the learning rate, and a learning rate schedule for exponential decay of the moment estimates.

For each iteration:

- Compute the gradient $\nabla L_t(X)$ of the loss function with respect to the transformation matrix X.
- Gradient is a vector contains the Partial Derivatives of

the loss function.

- Applicable for the current state of X only, established for two pairs of points at a time as depicted in Figure 2, selected at random. The anti-gradient is the values for X with which the loss function will be minimised in the fastest way. As training progresses the step with which the loss will be minimised each time will be decreased.

Challenges in Optimization:

Attempts to optimize the entire transformation matrix simultaneously were unsuccessful, possibly due to the imbalance between the rotation (9 elements) and translation (3 elements) parts, which are also on different scales. This imbalance led to suboptimal solutions as the rotation and translation components impacted the optimization process differently.

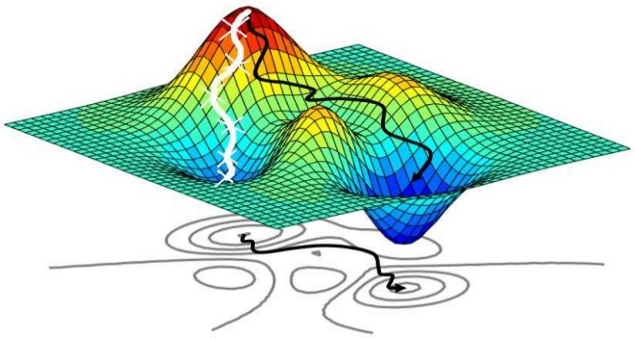

Figure 4. The problem of local minima in the loss function

Challenges such as local minima in the loss function shown in Figure 4 can be addressed by a number of approaches:

1. Adjusting hyperparameters, e.g. Learning rate, Momentum and learning schedule.

2. Change the Starting point of optimization (Initial X value)
3. Use a different function to evaluate the loss (MSE, RMSE, Euclidean distance, Cosine Similarity, etc.)
4. Optimize Rotation and Translation parts separately instead of optimizing the full matrix of [4,4]
5. A combination of the above…

From experimentation, a Two-Stage Optimization process outlined below was found to be the most effective in getting the error to converge:

1. Pose Optimization: The first stage focuses on solving the rotation part of the transformation matrix, which includes nine elements (a 3x3 matrix). This stage iteratively minimizes the rotational error to ensure accurate alignment of the robot and camera frames.

2. Translation Optimization: The second stage addresses the translation part of the transformation matrix, which includes three elements (a 1x3 matrix). By isolating the translation optimization, the algorithm can effectively minimize positional error without interference from rotational components.

3. RESULTS AND DISCUSSION

Preliminary tests using the verification method outlined above demonstrated that our gradient descent method achieves a calibration accuracy of within 15mm, even in the presence of significant sensor noise. The effectiveness of the method is validated using the KUKA KR16 robot and IFM O3D313 camera setup, with consistent results across multiple trials.

The results indicate that the proposed gradient descent method provides a robust solution for robot-camera calibration in noisy environments. This approach offers significant improvements over traditional methods, which often fail to account for sensor noise effectively. Similar calibration methods have struggled with accuracy due to sensor noise, emphasizing the importance of robust optimization techniques.

4. CONCLUSIONS

This study presents a promising gradient descent-based method for on-hand robot-camera calibration, addressing the challenges of sensor noise and achieving high accuracy. Future work will focus on refining the algorithm, exploring its application in more complex environments, and integrating it with real-time robotic systems.

By incorporating the described methodology, experimental setup, preliminary results, relevant figures, and explanations, this extended abstract provides a comprehensive overview of the proposed calibration method, setting the stage for further research and development.

ACKNOWLEDGMENTS

This work was supported with the financial support of the Science Foundation Ireland grant 13/RC/2094_P2 and co-funded under the European Regional Development Fund through the Southern & Eastern Regional Operational Programme to Lero - the Science Foundation Ireland Research Centre for Software (www.lero.ie)

REFERENCES

[1]. R. Li, S. Liu, Z. Zhang, "Robust Robot-3D Camera Calibration Using Iterative Closest Point and Robust Estimation," IEEE Transactions on Automation Science and Engineering, vol. 7, no. 2, pp. 150-160, 2010.

[2].A. Fassi, M. Mandow, A. J. Garcia-Cerezo, "Calibration of a Robot Vision System Using a Laser Tracker and Stereo Vision," IEEE Transactions on Robotics, vol. 30, no. 6, pp. 1452-1460, 2014.

[3]. Y. Zhang, J. Wang, "Adaptive On-Line Calibration for 3D Robot Vision Systems," IEEE Transactions on Industrial Electronics, vol. 64, no. 9, pp. 7238-7246, 2017.

[4].R. Y. Tsai and R. K. Lenz, "A New Technique for Fully Autonomous and Efficient 3D Robotics Hand/Eye

Calibration," IEEE Transactions on Robotics and Automation, vol. 5, no. 3, pp. 345-358, 1989.
[5].C. P. Lu and J. Chou, "Real-Time Robot-Motion Sensing by Fixating on a Target," IEEE Transactions on Robotics and Automation, vol. 11, no. 5, pp. 723-731, 1995.
[6].K. Strobl, E. Mair, T. Bodenmuller, M. Suppa, and G. Hirzinger, "RoSi: A Least-Squares Based Online Self-Calibration Approach for Vision-Based Robotic Systems," IEEE/RSJ International Conference on Intelligent Robots and Systems, pp. 5671-5678, 2011.
[7].Tinker-Twins/AprilTag, GitHub Repository, https://github.com/Tinker-Twins/AprilTag

54: AUTONOMOUS TEXTILE SORTING USING HYPERSPECTRAL IMAGING

Jessica Lo Faro[a], *Olena Lanets*[a,b], *Solomiia Liaskovska*[a,b], *Andy T. Augousti*[a,*] *and Olga Duran*[a]

[a] Department of Mechanical Engineering, Kingston University, London SW15 3DW, UK.

[b] Department of Technical Mechanics and Dynamics of Machines, Lviv Polytechnic National University, Lviv, S. Bandery Street 12 Ukraine

* Andy Augousti augousti@kingston.ac.uk

Abstract – − Textile sorting for recycling is a challenging task, currently performed manually by trained operators relying on cloth tags and on their own knowledge - a method that is highly expensive and time-consuming, and potentially unreliable. This research reports the results of material classification of fabrics using a Hyperspectral camera in the Visible Near Infrared Range (VNIR), which is a more economically viable sensor than the NIR sensor, which currently dominates research in this area. We compare the results of two methodologies that were used to classify the data, a Shallow Neural Network (NN) algorithm and a Convolutional Neural Network (CNN). Results show that NNs can quickly recognise pure materials, but difficulties arise with blended materials. CNNs are most effective in identifying small non-fabric features like buttons and zips. However, a wide range of samples and methodologies would be needed before establishing a viable, scalable system.

***Keywords*:** hyperspectral vision; textile sorting; sensors; automatic systems; textile recycling.

1. INTRODUCTION

Over the past decade, there has been a discernible increase in municipal waste across Europe, a phenomenon attributed to ongoing population growth, escalating urbanisation, and heightened per-capita buying power [1,2]. While the primary sources of waste and pollution are well-documented, certain contributors such as the textile industry often escape widespread attention: many will not be aware that the textile industry stands as the fourth-highest contributor to environmental and climate change, right after food, housing, and transportation [3].

Presently, only less than 1% of the global textile output undergoes recycling into new textiles [4]. The underlying causes of such abysmally low rates are tied to the inherent complexities of most fabrics composition and the directly proportional difficulty in approaching recycling processes.

Each material's chemical composition necessitates a distinct recycling procedure [4], demanding meticulous material sorting prior to recycling. Compounding the challenge is the removal of non-fabric elements like zippers and buttons, a preliminary step mandated before submitting fabrics to the appropriate recycling department [5]. Currently, sorting and removal of non-fabric parts are performed manually by trained operators. These are however very time-consuming activities that accounts for approximately 30% of the textile industry's recycling costs [4].

Given that materials are distinguishable through their chemical compositions, imperceptible to the naked eye [6], recent explorations into technologies for the establishment of an automated textile sorting system have focused on spectral and hyperspectral imaging (HSI) [7] a technology that has already been proven successful in diverse domains such as agriculture (for pesticide detection), biomedical engineering, and crime detection [8].

2. EXPERIMENTAL METHODS AND PROCEDURES

Twenty-two garments were selected for inspection using a hyperspectral camera and for subsequent classification using two distinct artificial neural network configurations. Of these 22 garments, 14 were made of pure materials, while the remainder consisted of blends of different materials.

The 8 materials used in these garments were

- Polyester
- Polyurethane
- Viscose
- Cotton
- Polyamide
- Elastane
- Wool and
- Acrylic.

Some of these materials were present in different colours and patterns, to enrich the diversity of the dataset.

The selection of these materials was based on their widespread popularity and their significant contribution to the prevailing production and waste streams in contemporary society.

It should be noted that due to practical constraints not all materials were scanned and tested simultaneously, and there were variations in material combinations across different training iterations.

2.1. Data Collection

The process of data collection was conducted with the following equipment and settings:

- Camera: Hinalea 4250 hyperspectral camera operating within the Visible Near Infrared (VNIR) range (450 – 1000 nm) with a 4nm interval.
- Wavelength Bands available: 299.
- Illumination of the recording area: 500W Halogen Lamp, carefully positioned approximately 80cm from the textile samples.
- Approach: To ensure uniformity in calibration across all images and mitigate the potential impact of background interference on spectral information, a consistent approach was adopted. A white background was

DOI: https://doi.org/10.34961/researchrepository-ul.29291876.v1

systematically positioned behind each textile sample during image capture, aligning with recommendations found in existing literature. This meticulous calibration process aimed at enhancing the accuracy and reliability of the spectral data collected.

- Additional Info: A total of 15 images were captured, with each image featuring 3-6 garments, encompassing both blended and pure compositions. Given the heightened sensitivity to colour of hyperspectral imaging in the Visible Near Infrared (VNIR) range, garments were frequently arranged in pairs constructed from the same materials but varying in tints, to challenge the network even further.

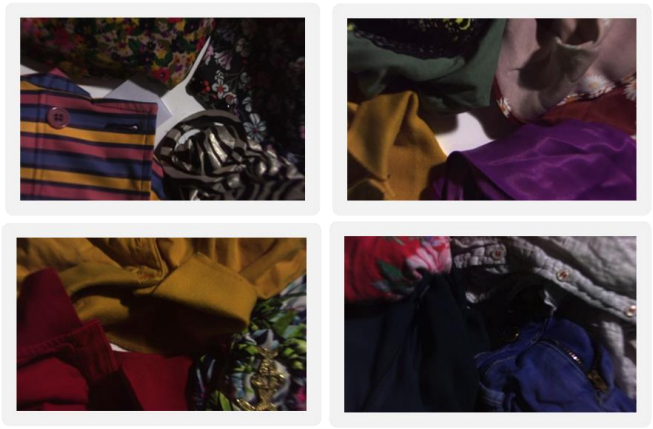

Figure 1. Typical recorded image showing a range of garments.

2.2. Training, testing and Evaluation

Two Neural Networks (NN) were used to classify images obtained from the hyperspectral camera, a shallow NN and a Convolutional NN (CNN), implemented within Matlab™.

For image classification purposes, the regions of interest (ROIs) within the garment were labelled using the Matlab app Image Labeller, as displayed in Figure 2.

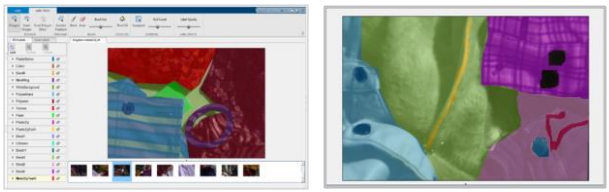

Figure 2. Use of Image Labeller in Matlab™ and ROIs labelled manually showing a range of garments.

The simple NN used was a 2-layer network used for data classification. Three built-in training algorithms were are available, namely Levenberg-Marquardt (LM), Bayesian regularization, and scaled conjugate gradient backpropagation (SCGB). Each of these results in slightly different training times and accuracy of the results. Changeable options include the number of neurons employed, the number of samples selected for training, testing and validation, and the choice of algorithm.

Although the range of options is relatively limited, the versatility of the dataset used permits a wide range of presentation formats, such as the numbers of wavelength bands selected from the hyperspectral camera, the number of pixels used in the image, and additional detailed parameter settings.

In the case of the simple NN ROIs consisting of a limited number of pixels were selected, and each of these was labelled according to the percentages of eight materials under test.

In the case of the CNN, the layers consisted of standard convolutional, Relu and Pooling layers. In this instance, pixels within each ROI were labelled manually according to the following twenty-five categories including different:

- Pure materials
- Blends
- Mixed materials (pure materials and blends)
- Mixed materials and non-fibre feature (buttons, zips and zip teeth)

There was some inevitable uncertainty introduced at border classification, including borders with regions devoid of garments.

3. RESULTS AND DISCUSSION

3.1. Shallow NN training and performance

It was found that the simple NN was able to able to achieve moderate success in identifying Pure Materials, achieving scores in the region of 49-50% for identification of real positive. The performance was lower in all of the remaining categories, partly due to the relatively limited number of samples given the relatively large number of material quantities to be recognised. Although a range of difference training approaches were employed, using between 10-100 neurons, 10-299 wavelength bands, using sample distributions for training, validation and testing varying between 50%:25%:25% to 70%:15%:15% and use of the LM or SCGB networks, the results were generally not greatly improved. It was found that better performance was generally achieved with a higher number of neurons, and the use of the SCGB network, the latter giving better results both in terms of processing time as well as accuracy.

3.2. CNN training and performance

In the case of the CNN the ground truth for categorisation is also established using Image Labeller app in Matlab™. Figure 3 shows both the classification list of 25 separate categories on the left of the figure, as well as some of the classified and colour-coded images on the right. The colour coding is referenced with a colour bar, with each colour associated with one of the categories. Although it is difficult to make out the individual colours from the colour bars, the shape of specific garments is clearly visible.

The following parameters were used in the case of training for the CNN:

- Epochs = 100
- miniBatchSize = 256
- initLearningRate = 0.001
- momentum = 0.9
- learningRateFactor = 0.01
- Wavelength Bands = 30
- Window Size = 25

- Number of Patches = 10,000

PCA was used for band selection to improve the algorithm's efficiency, reducing the number of bands to 30 of the potential 299. The number of Patches refers to the 25-pixel by 25-pixel windows that the algorithm creates from the image during the CNN training period.

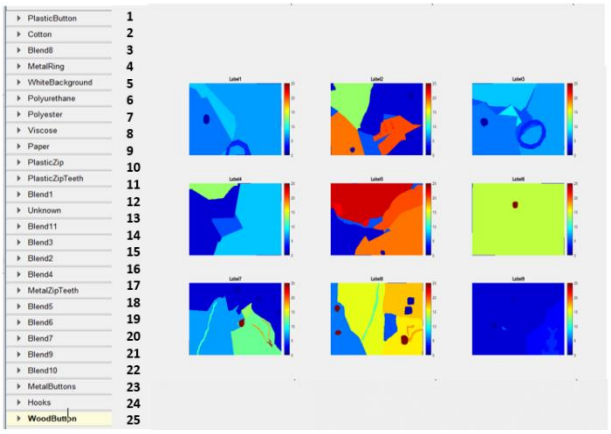

Figure 3. Classification list and colour-coded image samples, with colours attributed to ROIs in the order shown in the classification list.

Although the CNN did not succeed well in determining specific blends, it was capable of accurately recognising shapes, an outcome that is particularly useful when recognising non-fabric features.

The best classifications achieved were obtained using a higher number of patches. This is partly due to the method by which each patch is classified, which depends on the classification of the first pixel examined within the patch; the remainder of the patch is classified to be in the same category as the first pixel, which can lead to misclassification if the window overlaps other materials from other categories. This issue is reduced (although not completely eliminated) by increasing the number of patches used.

Table 1 below shows the results obtained when some of these parameters were varied. The parameters that were altered in successive rows are shown in red.

Table 1. A table showing the results obtained using different training parameters for the CNN

Training	Parameters	Val. Accuracy	Overall Accuracy	Mini Batches Accuracy
TRAINING_1	Epochs = 100; miniBatchSize = 256; initLearningRate = 0.001; momentum = 0.9; learningRateFactor = 0.01; Wavelength Bands = 30 WindowSize = 25 Number of Patches = 10,000	97.72%	96.68%	99.61%
TRAINING_2	Epochs = 100; miniBatchSize = 256; initLearningRate = 0.001; momentum = 0.9; learningRateFactor = 0.01; Wavelength Bands = 30 WindowSize = 25 Number of Patches = 1,000	89.53%	96.68%	100%
TRAINING_3	Epochs = 100; miniBatchSize = 256; initLearningRate = 0.001; momentum = 0.9; learningRateFactor = 0.01; Wavelength Bands = 100 WindowSize = 25 Number of Patches = 10,000	96.34%	96.44%	100%
TRAINING_4	Epochs = 50; miniBatchSize = 100; initLearningRate = 0.001; momentum = 0.9; learningRateFactor = 0.01; Wavelength Bands = 30 WindowSize = 25 Number of Patches = 1,000	92.86%	92.62%	100%
TRAINING_5	Epochs = 200; miniBatchSize = 256; initLearningRate = 0.001; momentum = 0.9; learningRateFactor = 0.01; Wavelength Bands = 30 WindowSize = 25 Number of Patches = 1,000	91.27%	91.77%	100%
TRAINING_6	Epochs = 100; miniBatchSize = 256; initLearningRate = 0.001; momentum = 0.9; learningRateFactor = 0.01; Wavelength Bands = 30 WindowSize = 25 Number of Patches = 500	88.54%	91.24%	100%

Better results are obtained when the number of wavelength bands are increased to 100.

4. CONCLUSIONS

The purpose of this study was to establish whether it is possible to recognise textiles accurately using a hyperspectral camera operating in the VNIR range, with the use of machine learning. Two machine learning networks were employed, a shallow NN and a CNN.

Numerous training experiments were carried out in both cases, varying the training parameters each time, with a wide range of groups of materials investigated. The results demonstrated that the shallow NN was able to identify pure materials quite well, although its performance here in distinguishing Polyester and Polyurethane was some weaker, partly due to the similarities in their composition. For the blended material samples, the NN performed best in recognising cotton and polyester within the garments, although the percentages involved were often miscalculated. Elastane was only recognised in blends at percentages higher than 15%, but not detected in cases where it was as little as 2%. On the other hand, Acrylic was often a false positive detection, being identified as present in cases where the cloth tag indicated that none was present.

The NN performed poorly when all materials were present together, or when non-fibre features were also present. This may be due to relatively limited number of training samples presented given the wide number of classes available to categorise these. Interestingly, dark or black materials did not present particular issues, as noted in the literature, although the NN often attributed the class of a sample to its adjacent one if these shared the same colour. Overall for the shallow NN, the accuracy was poor when tested on entire images, as the training occurred on limited subsets of pixels within these images. This is partly due to the fact even for specific materials the spectral variance is quite variable, depending heavily on the shade of its colour, as well as the relatively limited number of training samples available to span the possible training space.

On the other hand, the CNN performed very well in accurately recognising most classes presented, performing best when the number of patches was chosen to be high it also had reasonable success in identifying non-fabric elements too. Its performance, too, is likely to be improved with the provision of a wider range of training images, and with further exploration and optimisation of training parameters.

ACKNOWLEDGMENTS

We acknowledge the support of the British Academy's Researchers at Risk programme that has supported two of the authors (OL and SL) to be involved in this research.

REFERENCES

[1] European Commission. 2024. 'Waste Framework Directive'. https://environment.ec.europa.eu/topics/waste-and-recycling/waste-framework-directive_en#:~:text=2023%20WFD%20revision,-

Despite%20existing%20legislation&text=For%20some%20specific%20streams%2C%20such,disposed%20of%2C%20leading%20to%20pollution. [Accessed 13 June 2024].

[2] Downtoearth.org.in. 2022. 'The bane of consumerism'. Available at: https://www.downtoearth.org.in/blog/waste/the-bane-of-consumerism-61460 [Accessed 13 June 2024]

[3] European Commission. 2024. 'Press corner'. Available at: https://ec.europa.eu/commission/presscorner/detail/en/QANDA_22_2015 {Accessed 13 June 2024].

[4] Bonifazi, G., Gasbarrone, R., Palmieri, R., Serranti, S.. **End-of-Life Textile Recognition in a Circular Economy Perspective: A Methodological Approach Based on Near Infrared Spectroscopy** 2022 [Accessed 13 June 2024]. https://www.researchgate.net/publication/362799595_End-of-Life_Textile_Recognition_in_a_Circular_Economy_Perspective_A_Methodological_Approach_Based_on_Near_Infrared_Spectroscopy

[5] Afry.com. 2024. **Textile Recycling: Drivers & Challenges**. [Accessed 14 June 2024] https://afry.com/en/insight/textile-recycling-drivers-challenges

[6] Chemistry LibreTexts. 2024 Physical and Chemical Properties of Matter [Accessed 14 June 2024] https://chem.libretexts.org/Bookshelves/Inorganic_Chemistry/Supplemental_Modules_and_Websites_(Inorganic_Chemistry)/Chemical_Reactions/Properties_of_Matter

[7] Marmion, M. 2024. **Fabric recycling with NIR hyperspectral cameras - Machine Vision Technology Forum 2019** STEMMER IMAGING. [Accessed 14 June 2024] https://www.youtube.com/watch?v=rBWAjAq0EEQ

[8] Vasefi, F., Farkas, D. L. 2016. **Hyperspectral and Multispectral Imaging in Dermatology** Imaging in Dermatology. [Accessed 14 June 2024]. https://www.sciencedirect.com/topics/medicine-and-dentistry/hyperspectral-imaging

55: PIEZOELECTRICITY IN UNPOLED HYDROXYAPATITE CERAMICS

Reena Rasheed [a] **, Dinesh Barnana* [a], *Charlie O' Mahony* [a], *Syed A.M. Tofail* [a], *Ehtsham ul Haq* [a]

[a] Department of Physics, and Bernal Institute, University of Limerick, Castletroy Limerick, Ireland, V94 T9PX.

Environmental Sensing, EM010, August 13, 2024, 4:20 PM - 6:10 PM

Abstract –
Piezoelectric Sensors have gained significant importance in recent years due to conversion of mechanical stress into electrical current. Hydroxyapatite is excellent biocompatible, non-toxic and piezoelectric material for biomedical applications. In this paper, pellets of hydroxyapatite are prepared by Spark Plasma Sintering (SPS) by two different powders. The samples were characterized by the X-Ray diffractometer (XRD), Atomic Force Microscope (AFM), Piezometer and Piezo-response Microscope. Macroscopically these ceramics show weak longitudinal piezoelectricity. Local piezoelectric coefficients showed both in plane and out of plane piezoelectricity with magnitude as high as 4-5pC/N. Further improvements and tuning of piezoelectric properties are possible through thermoelectric poling and creating proper resonator structure for use as sensors and actuators.

Keywords**:** piezoelectric sensors; hydroxyapatite; Piezoelectric properties; Spark Plasma Sintering; Biomedical Applications.

1. INTRODUCTION

Piezoelectric materials have been broadly used in numerous fields such as biomedical engineering, energy, maritime, naval and aerospace industry. These materials are widely sought for energy harvesting devices, for self-powered, fit and forget type sensors and actuators. This is because piezoelectric materials can both generate the electricity from mechanical strain and vice versa. Hydroxyapatite (HAp) $(Ca_{10}(PO_4)_6(OH)_2$, belong to the family of the calcium phosphate apatite, is identified as one of the promising piezoelectric materials. It is particularly significant due to its structural similarity with mineral material present in human hard tissues such as teeth and bone. It has excellent biological properties such as biocompatibility, bioactivity, osteoconductive, nontoxicity and non-inflammatory. HAp has same chemical composition and biocompatibility with human bone. Due to the bioactive nature of the HAp desired product can be achieved because of chemical transformation. In osteoconductive process, a new bone is developed as result of chemical reaction in which HAp molecule interact with physiological fluid. In bioactivity, the change in surface of material occur subsequent to the physiological environment on HAp as biological equivalent which create a bond with the tissues of bone as it does not form fibrous tissue layer which makes is perfect for protheses and implants. The bone implants interface behaves as same as the interface of the naturally repaired tissue as it changes with time, dynamic in nature and a precise degree of reactivity is required. Bioactive properties of HAp have medical advantages which depends upon the synthetic structure, such as surface morphology, stoichiometry and crystallinity [1].

Different studies have been done by researchers for the study of piezoelectric property of HAp. Earlier experimental research showed weak piezoelectric in HAp as 2009 Tofail *et al.* noticed the piezoelectricity by direct quasistatic and ultrasonic methods. It gave strong evidence of piezoelectric property of HAp by switching the electrical polarity when mechanical loading was reversed [2].

Tofail *et al.* measured the pyroelectric constant in poled hydroxyapatite ceramics at different temperatures. At higher temperature, the constant values are similar to the common ceramics. And lower temperature, the constant values are four times greater than those calculated in tendon and bone. In 2011, Lang *et al* . studied that 500 nm films of HA were spin-coated on silicon wafers had a nonuniform polarization distribution and exhibited pyroelectricity, piezoelectricity, and photo effects. A pyroelectric coefficient of about 12 C m^{-2} K^{-1} was found. This is about 1/3 of the coefficient of fully poled PVDF.

Nishigaki *et al.* fabricated Cu/HAp/Ti or Cu/HAp/Pt structure by Plasma Laser Deposition (PLD) and measured the piezoelectricity of HAp films. The value of d_{31} constant was in order of 0.1pCN^{-1}. After two years, Nishigaki and Hontsu verified that by polling HAp films piezoelectric constant d_{31} increased by over four times. Gandhi *et.al.*, studied that by electrical poling and texturing the magnitude of the HAp piezoelectricity amplified by six orders of magnitude when compare to unpoled HAp[3].

Bystrov studied the monoclinic phase of HAp by Local Density Approximation (LDA) method and demonstrated piezoelectric coefficient is greater than 15.7pmV^{-1} which is close to the experimentally measured constant reported by the Lang *et al*. In 2017, Markham *et al.* synthesized 60µm thick films of HAp screen printed on Indium Tin Oxide (ITO)-coated glass substrates. The values of piezoelectric coefficient obtained by screen printing are higher than that obtained by in PLD method by Nishigaki [4].

In 2019, Bystrov analysed the hexagonal phase of HAp. He observed that hexagonal and monoclinic phases can coexist calculated values piezoelectric constant d33 is 6.3pm/V [12]. Recently in 2020, Katarina, *et al.* reported of Sr^{+2} doped HAp thick films which showed improved piezoelectricity. It has much larger coefficient values than the Plasma Laser Deposited (PLD) thick films screen printed.

Thick films of hydroxyapatite showed the pyroelectric behaviour and pressure sensing ability. Potential applications of hydroxyapatite in biosensing are thus indicated by its piezoelectricity, pyroelectricity, electron beam and contact poling as well as adsorption of selective proteins on the polarized domains.

DOI: https://doi.org/10.34961/researchrepository-ul.29293469.v1

Ohigashi used the piezoelectric resonance method to determine the piezoelectric and mechanical characteristics of poled polyvinylidene fluoride films at wide range of frequency from 20 kHz to 30 MHz at temperature range below the 100°C. it showed the rapid increase in piezoelectricity with increase of temperature is occurred due to change in $^{\partial \emptyset}/_{\partial T}$ of material in crystalline phase. Highest value of electromechanical coupling coefficient k_{33} of 0.2 has been reported [5].

Ando *et al.* studied the thickness-shear (TS) and thickness-extension (TE) vibration modes of $SrBi_2\ Nb_2O_9$ - based ceramics by piezoelectric resonance method. The TE2 mode, TE3 mode and TS1 mode were found for single mode resonance characteristics and not found for TE1 vibration. The advantages of TE2 mode resonator were greater than the TE3/TS1 mode for the impedance ratio, electromechanical coefficient and TSF properties. The main resonant characteristics is not affected by the spurious mode vibration in TE2 mode resonator which is showed by the measurement of impedance resonant characteristics and vibration amplitude measurement. It is concluded that the for the most of piezoelectric ceramic materials TE2 mode resonator can be obtained [6].

Zhu, Jiang, and Cao characterized the ceramic materials by resonant and ultrasonic techniques. They used length longitudinal vibrator along with ultrasonic method to attain more accurate measurements. With the combined method the piezoelectric, elastic, electrochemical coupling and dielectric constant have been determined for PZT-5H. the crystals with the symmetry of 3mm and 4mm can be analysed by this method [7].

Li *et al*. measured the dependence of piezoelectric coefficient (d_{33}, $-d_{31}$, d_{15}, g_{33}, $-g_{31}$, g_{15}) for lead zirconate titanate ceramics by Berlincourt and resonance methods. Their calculations showed d_{15}, d_{31} and d_{33} had increased with temperature whereas g_{15}, g_{31} decreased.

In 2017, de Castilla, Belanger, and Zednik measured the piezoelectricity of lithium niobate at high temperature by impedance spectroscopy method. They studied the material properties lithium niobate single crystal at temperature of 750 °C with broad range of frequency from 100 kHz to 7 MHz. They did not find the degradation piezoelectric coefficient. It is suggested that Lithium Niobate can be used for the high frequency piezoelectricity applications [8].

While low frequency broadband piezoelectricity has been reported in poled and unpoled HAp, resonance piezoelectricity has yet to be reported.

Challenges remain in creating Hap ceramics or thick films that can resonate 'freely' to allow electrically induced mechanical deformation that would be coupled with its natural oscillation. Preconditions of piezoelectricity in HAp ceramics are chemical and phase purity, texture and poling. In this paper, we report texturized HAp ceramics that would show weak piezoelectricity in unpoled condition to allow for further poling to improve piezoelectricity. Ceramic samples would allow cutting thin slices which could later be electrode to work as a resonant sensor similar to quartz crystal sensors. We elaborate ceramic preparation with Spark Plasma Sintering (SPS) technique and describe materials characterisations by complimentarity techniques to establish chemical and phase purity and texture. We will then report weak piezoelectricity in such unpoled samples.

The integration of piezoelectric properties in hydroxyapatite could open new avenues for applications in energy harvesting, biosensors, and medical devices.

2. METHODS AND PROCEDURES

2.1. Chemicals:

Phase Pure Hydroxyapatite $Ca_{10}(PO_4)_6(OH)_2$from Ceramat (India) and Hydroxyapatite $Ca_{10}(PO_4)_6(OH)_2$ from Sigma Aldrich were used for preparation of pellets by spark plasma sintering (SPS). Phase Pure Hydroxyapatite powder was prepared at ISO 13485 compliant facility. The high phase purity which makes it ideal for research and other biomedical applications. Phase purity is conformed to International Centre for Diffraction Data (ICDD) file 09-0432.

2.2. Pellets preparation:

Pellets were prepared using Spark Plasma Sintering (SPS) (Dr. Sinter, SPS-515S, SPS Syntex Inc., Kawasaki, Japan) at 900°C and 1000°C under a uniaxial pressure of 52.2MPa. The average Diameter of pellets was 10±0.05 mm with a thickness of 02±0.1mm. The sintering process utilities ~ a 0.65g HAp powder poured into a graphite die and graphite punches were used to compress and seal it. A thermocouple was inserted into graphite dies to monitor the temperature throughout the sintering process. The pressure was increased (from 40MPa to 52.2MPa) at 700°C and withholding time was 10 minutes. After the sintering process was completed, the samples were cooled under the sintering pressure down to 700°C and then pressure was released to 40MPa for further cooling down to room temperature.

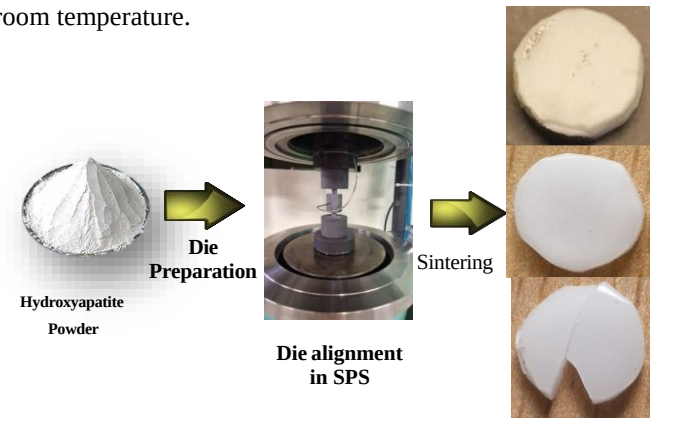

Figure 1., Schematic diagram of Pellet preparation by Spark Plasma Sintering (SPS).

The SPS process parameters are illustrated in the table 1 below.

Sr#	Diameter & Thickness	Temperature	Heating rate
1 Phase Pure Hydroxyapatite	10±0.05 mm 2±0.1mm	900°C	100°C/mint till 800°C, 800-900°C reduced by factor of 2
2 Hydroxyapatite	10±0.05 mm 2±0.1mm	900°C	100°C/mint
3 Hydroxyapatite	10±0.05 mm 2±0.1mm	1000°C	100°C/mint

3. RESULTS AND DISCUSSION

The XRD analysis of the two powders from (Phase Pure Hydroxyapatite from Ceramat and Hydroxyapatite from Sigma Aldrich) and three sintered samplesis shown in Figure 2. The diffraction peaks positions of both powders and samples were corresponded to the standard Hydroxyapatite peaks (ICDD file no. 09- 0432). The intensities of pellets were of the sintered pellets were higher than the precursor powders due to the higher volume concentration of material in the beam spot. It enhanced the signal quality. All of the samples reveal three strongest peaks at 2θ values of 31.698°, 32.161° and 32.814° which correspond to (121), (112) and (030) respectively.

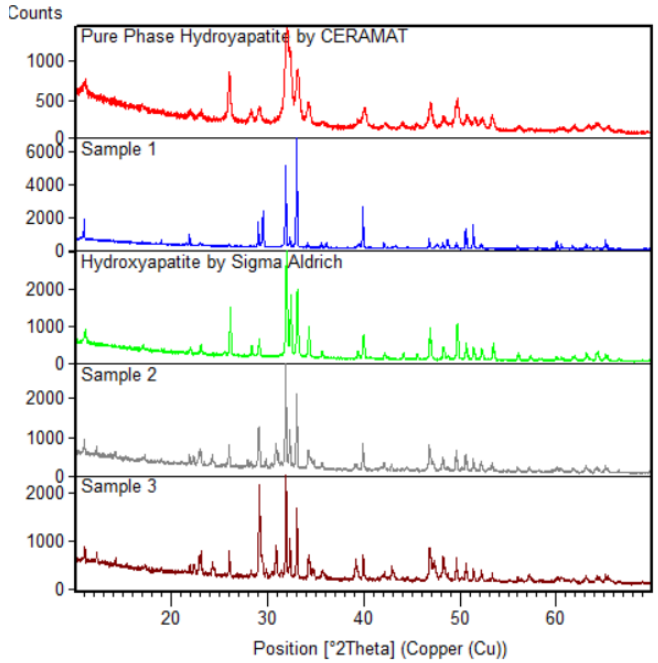

Figure 2., XRD peaks of Pure Phase Hydroxyapatite powder (red), sample 1 (blue), Hydroxyapatite powder (green), sample 2 (grey), and Sample 3 (brown).

The AFM surface roughness of the sintered pellets is shown in figure 3. The recorded images were exported to the Image Analysis software by NT-MDT. Before the analysis, the images were plane fitted and line fitted with first or second order polynomial to level and flatten them. The flatten images were then used for roughness analysis and the quantities like RMS roughness, mean roughness, maximum Z-height, maximum peak height and maximum pit depth were measured. In case the dust particle was observed on the surface, the measured quantity of Z-height or peak height was removed from the average, however, the dust particle will not alter the roughness parameters.

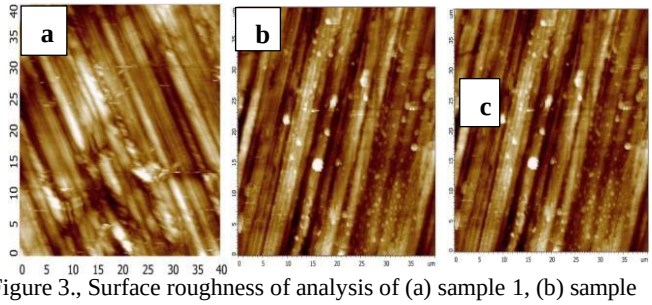

Figure 3., Surface roughness of analysis of (a) sample 1, (b) sample 2 and (c) sample 3.

The roughness is important for subsequent PFM measurements as well as the samples will later be electrode for impedance analysis.

Table 2., Measurements of roughness of samples.

Sr #	Root Mean Square (RMS) roughness (nm)	Average roughness (nm)	Maximum area peak height (nm)	Maximum area valley depth (nm)
1	39.9	31.3	181.5	167.7
2	36.5	28.8	265.8	134.8
3	24.5	19.7	138.9	120.9

The piezoelectricity d33 coefficient values were measured by the Piezometer for 3 samples without poling. Ten measurements were performed for each sample and noted the values for upright and inverted positions. Table 5 shows the change in current polarity by flipping the position which is a clear indication of piezoelectricity. The average value of positive d33 obtained from pellet was 0.05pC/N and average value of negative d33 was -0.03 pC/M. The measured values are same in order of magnitude to previously measured values published in J. American ceramic Society.

Table 3., Measured d33 values for samples of Hydroxyapatite.

Samples (without polling)	d33 measurement (pC/N)	
	Upright	Inverted
1	∼0.06	∼-0.04
2	∼0.05	∼-0.02
3	∼0.06	∼-0.03

The piezoelectric constant (d_{33} and d_{34}) of samples were measured by using PFM. Prior to the measurements to the PFM probes were calibrated for inverse optical sensitivity which converts the electrical signal from the instrument to real displacement of the cantilever in nanometres. This calibration was performed on Si sample and once IOS calibration is complete. The probe was tested on the standards samples Periodically poles Lithium Niobate. The PFM signal was converted using following equations.

$$Displacement\ (nm) = \frac{Magnitude\ (nA)}{Gain\ \times Input\ \times IOS\ (\frac{pm}{nm})}$$

$$d_{33}\ (\frac{pm}{V}) = \frac{Displacement\ (pm)}{Voltage\ applied\ (V)}$$

The PFM displacement was determined by applying ab DC biased Voltage across the sample from 0V to 10V in three steps, (1V, 5V and 10V). Fig. 5, showed that the PFM displacement with respect to the applied voltage in vertical and lateral directions which illustrate the in-plane d34 coefficient and out plane give d33 coefficient respectively indicated by Red and Black graphs. From fig. 4 (a) and (d), when bias voltage was 1V, the system noise level was high. But in fig. 4 (b), (c), (e), and (f), the both of the samples gave

almost same values for 5V and 10V. Their average slope value of sample 1 is 4.84pm/V for d34 and 1.225pm/N for d33. Similarly, sample 3 average slope value is 4.925pm/N for d34 and 1.265pm/N for d33. These observations verified there is a piezo-response is found in samples which is higher in in-plane as compare to out of plane.

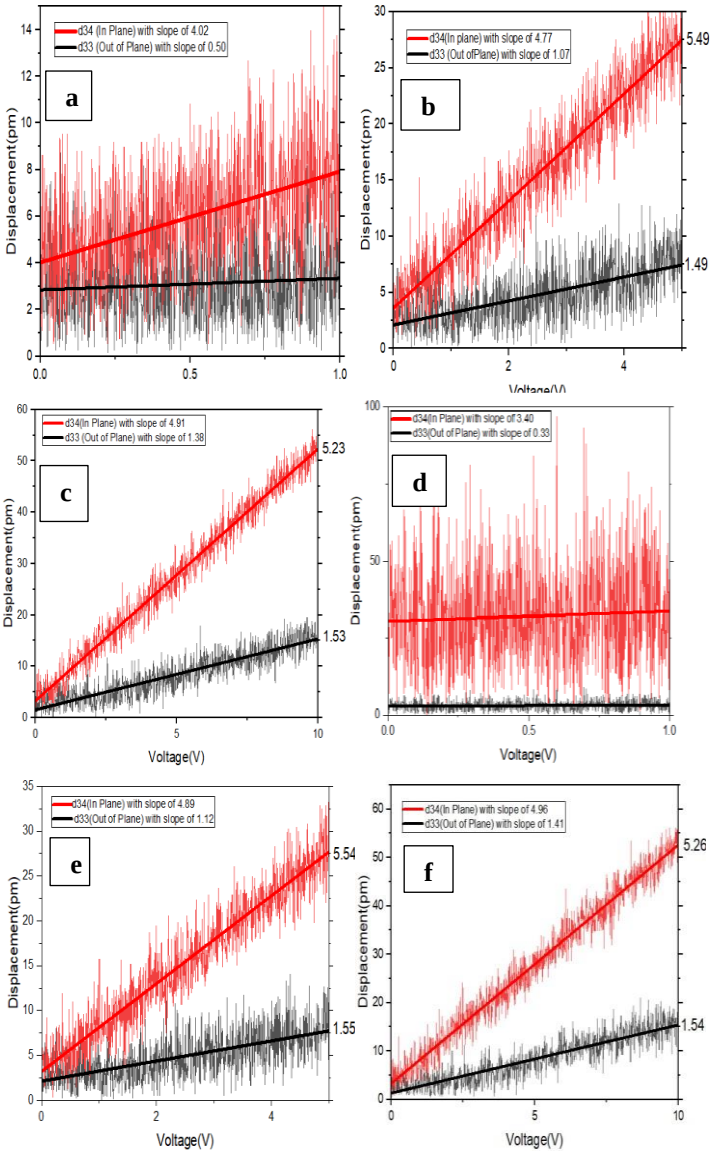

Figure 4., DC voltage dependence of displacement for sample 1 at (a) 1V, (b) 5V, (c) 10V and for sample 3 (d) 1V, (e) 5V, (f) 10V.

ACKNOWLEDGMENTS

SFI Opportunistic Fund (no. 12/RI/2345/SOF) is acknowledged for the NTEGRA Hybrid Nanoscope used in Piezoresponse Force Microscopy.

REFERENCES

[1] Kweh, S. W. K., K. A. Khor, and P. Cheang. "**The production and characterization of hydroxyapatite (HA) powders.**" *Journal of Materials Processing Technology* 89 (1999): 373-377.

[2] Tofail, S. A. M., Haverty, D., Cox, F., Erhart, J., Hána, P., & Ryzhenko, V., "**Direct and ultrasonic measurements of macroscopic piezoelectricity in sintered hydroxyapatite.**" *Journal of Applied Physics* 105.6 (2009).

[3] Gandhi, Abbasi A., Maciek Wojtas, Sidney B. Lang, Andrei L. Kholkin, and Syed AM Tofail. "**Piezoelectricity in poled hydroxyapatite ceramics**." *Journal of the American Ceramic Society* 97, no. 9 (2014): 2867-2872.

[4] Markham, S., A. Stapleton, E. U. Haq, K. Kowal, and S. A. M. Tofail. **"Piezoelectricity in screen-printed hydroxyapatite thick films."** *Ferroelectrics* 509, no. 1 (2017): 99-104.

[5] Ohigashi, Hiroji. "**Electromechanical properties of polarized polyvinylidene fluoride films as studied by the piezoelectric resonance method**." *Journal of Applied Physics* 47, no. 3 (1976): 949-955.

[6] Ando, Akira, Masahiko Kimura, and Yukio Sakabe. "**Piezoelectric resonance characteristics of SrBi2Nb2O9-based ceramics**." *Japanese journal of applied physics* 42, no. 1R (2003): 150.

[7] Zhu, Shining, Bei Jiang, and Wenwu Cao. "**Characterization of piezoelectric materials using ultrasonic and resonant techniques**." In *Medical Imaging 1998: Ultrasonic Transducer Engineering*, vol. 3341, pp. 154-162. SPIE, 1998.

[8] de Castilla, Hector, Pierre Bélanger, and Ricardo J. Zednik. "**High temperature characterization of piezoelectric lithium niobate using electrochemical impedance spectroscopy resonance method**." *Journal of Applied Physics* 122, no. 24 (2017).

56: **Stem Effect Correction Using Machine Learning Technique in Radioluminescence Sensors**

Author: MD ZUBAIR HASSAN TARIF, Faculty of Computing and Informatics (FCI), Multimedia University, Cyberjaya, Malaysia

Co-authors: Tan Yi Fei, Azmi Basaif, Adebiyi Oresegun, Chuah Kai Wei, Nor Hafizah Ishak, Hafiz M Zin, Hairul Azhar Abdul Rashid, David Bradley

Applications, EM009, August 14, 2024, 9:30 AM - 10:30 AM

Abstract-

Stem Effect has been identified as a major characteristic of fiber optic-coupled dosimetry (FOCD) systems that limits the overall accuracy of the readings. The majority of work on compensating for the stem effect has revolved around sophisticated apparatus or analog signal processing techniques. In this paper, we present the results of a software-based technique, primarily relying on machine learning algorithms, to estimate and offset stem effects in FOCDs. We obtained data from a Ge-doped silica scintillator system, comprising a PMMA channel and PMT detector. Radiation was supplied by an Elekta Synergy radiotherapy machine, providing 6MV photon radiation at dose rates between 35 to 600 MU/min (1 MU = 1 cGy). The radioluminescence signal (RL) was acquired using two in-house assembled reader units, capable of capturing data at a 50μs gate time, with a buffer capacity of 1,000,000 points, effectively allowing a data acquisition window of 50 seconds. The radiation source operates with a pulse repetition frequency (prf) of 400Hz at the highest dose rate, delivering a pulse every 2.5 seconds. Therefore, the gate time of the data acquisition system offers the ability to capture the radiation in a pulse-by-pulse mode. The pulse-by-pulse mode, or time-resolved measurements, allows for analyzing and processing individual pulses for dose information or signal correction. By reading the response of nascent PMMA optical fiber channels, we may obtain the emission from the carrier fiber alone. Pulse-by-pulse measurements allow further capability to record the individual pulses comprising the stem effect. In this study, we first used the double carrier method to capture the raw data. Initial measurements were made using two nascent PMMA optical fibers. Once their response was standardized, the Ge-doped scintillator was attached to one of the PMMA fibers.

It has been previously shown that Ge-doped silica scintillators produce an RL signal fast enough to distinguish between responses from two adjacent pulses, while being long enough for the photodetector to capture sufficient data that sustains beyond the stem effect. The data we observed were processed through a pulse detection technique

DOI: https://doi.org/10.34961/researchrepository-ul.29293601.v1

developed during the study. Once each pulse was recorded and stored separately in a database, standard regression models were applied to the data to produce prediction models for the stem effect component in the entire RL signal. Variation in the stem effect was implemented by placing various lengths (2, 3, 4, and 5 cm) of the PMMA fiber inside the field while keeping the same scintillator. It was observed that the stem effect varied greatly, fluctuating to about 300% of the smallest recorded signal, effectively creating an over-estimation of dose up to 45% in certain locations. The ground truth for the dose was established by utilizing the subtraction method at various positions of the scintillator within the 10x10 field from multiple measurements at variable gate times, and the mean RL response for a 30 MU dose solely from the scintillator was found to be 114942 counts with a standard deviation and standard error of 2850 and 1425 counts, respectively.

Our current model predicts the stem effect component on a pulse-by-pulse basis with an accuracy of 81.8%. By utilizing this stem effect prediction model, we were able to perform the data correction for stem effect within the software, obtaining mean RL counts of 124696, 117554, 110564, and 109371 for 2, 3, 4, and 5 cm of PMMA length in the field, respectively. Based on the previous mean of 114942 counts and a standard deviation of 2850 counts, the Z-scores for the predicted readings of 124696, 117554, 110564, and 109371 counts are approximately 3.42, 0.92, -1.54, and -1.95, respectively. The Z-score for 124696 counts indicates that it is an outlier, as it is more than three standard deviations above the mean. In contrast, the Z-scores for 117554, 110564, and 109371 are within the expected range of -2 to 2, suggesting these values are not outliers and are reasonably close to the mean. The exercise undertaken in this study suggests a strong case for the integration of machine learning techniques in addressing stem effect removal, especially for real-time systems without the need for additional hardware or apparatus.

58: AN OPTICAL FIBRE SENSOR PROBE FOR OXYGEN MEASUREMENT IN HYPOXIC TUMOURS DURING RADIOTHERAPY TREATMENT

Sanober Farheen Memon [a, *], *Carla McDonnell* [b], *Kevin M. Prise* [b], *Elfed Lewis* [a, *]

[a] Optical Fibre Sensors Research Centre, Department of Electronic and Computer Engineering, University of Limerick, Limerick, Ireland

[b] Patrick G. Johnston Centre for Cancer Research, Queen's University Belfast, Belfast, United Kingdom

Biomedical Sensors Session 3, EM009, August 13, 2024, 11:30 AM - 1:10 PM

Abstract – Hypoxic tumours are known to exhibit significant resistance to cancer radiotherapy treatments requiring real-time monitoring of oxygen concentration within the tumour and potentially adjusting the dose and personalising the radiotherapy treatment for better clinical outcomes. Novel optical fibre sensor probes based on the Fabry Pérot interferometric technique for real-time oxygen measurement are described The measurement is based on monitoring the refractive index changes corresponding to the changes in oxygenation levels within a hypoxic tumour. The Fabry Perot etalon is formed via an air gap cavity and a reflector located at the tip of the fibre. The sensor is fabricated based on a single-mode fibre (SMF), inserted into a glass capillary and plastic optical fibre as the reflective end cap. Results include *in-vitro* testing of the sensors in a Phosphate-Buffered Saline (PBS) solution and Bovine Serum Albumin (BSA) liquid phantom. The sensor is sufficiently small to be guided within standard Brachytherapy delivery tubes or via catheter tubes and thus can be used for future *in-vivo* testing.

Keywords**:** Hypoxic tumours; Optical fibre sensor; Fabry-Pérot; Oxygen Sensor; Radiotherapy; Clinical Oncology

1. INTRODUCTION

The World Health Organisation (WHO) estimate that the figure for global cancer cases will rise to 35 million by 2050 and the mortality rate will also significantly increase [1]. This represents a major health issue worldwide. Prostate cancer is one of the most commonly occurring cancers worldwide [1] and is often treatable at presentation, with radiotherapy being the most commonly used radical treatment modality. Among the complexities that cause the relapse of the tumour after a significant response from radiotherapy treatment is the insufficient dose at hypoxic regions of the tumour. Hypoxia is common in the majority of malignancies and leads to changes in the cellular metabolism causing quiescence and therapy treatment resistance in the cancer cells [2]. It is additionally linked with malignant advancement and unfavourable clinical results [3]. The oxygen measurements in such tumours are complex and typically performed in laboratories by biopsies and/or blood sample analysis which are invasive and time-consuming methods. A method for real-time monitoring and verification of tumour hypoxia levels would provide a major advantage in the radiotherapy treatment of cancers by enabling the real-time adaptation of radiation dose for treatment optimisation and improving the clinical outcomes.

Since the late 1980s, a computerised polarographic needle electrode system has been used to study tumour hypoxia levels and to allow the rapid and reliable collection of pO_2 (partial vapour pressure) values, enabling the identification and characterization of tumour hypoxia and assessment of its clinical relevance [4]. However, this method is biopsy-based and is not suitable for use simultaneously with treatment and repeatable measurements [4]. Currently, several techniques based on different principles are available, including fluorescence quenching, phosphorescence quenching, near-infrared, and magnetic resonance. However, their use in routine clinical applications remains limited. For example, the fluorescence sensors cannot be applied *in-vivo* to measure the oxygen of the tumour in real-time during the radiotherapy treatment. Recently, solutions based on optical fibre sensors have also emerged. Ortiz-Prado et al. have devised a method for measuring brain partial pressure of oxygen using an optical fibre U-bend sensor which proves the concept of using optical fibre sensors for oxygen measurement in tissues however, it is doubtful to be used in radiated conditions and for small tumours due to its geometry [5]. A recent evidence of optical fibre technology for oxygen measurements is available in [6] for biological applications which is Oxylite, a commercially available optical sensor for hypoxic measurement. There is little technical detail available in the literature; however, it is clear that the probe relies on measuring optical absorption due to the presence of O_2 in the tissue. However, it cannot be used *in vivo* due to FDA approval issues and this configuration is not suitable for the assessment of hypoxic tumours under irradiation conditions. This commercial model has been used in our work as a reference system to measure the oxygen level of solutions used for characterisation.

In this work, we propose novel POF end cap-based Fabry-Pérot optical fibre sensor probes to measure the oxygen level in hypoxic tumours during radiotherapy treatment. Two variations of the design differing in length of the diaphragm or end cap have been proposed and investigated for oxygen measurements in PBS solution and BSA-based liquid phantom inside a temperature-controlled hypoxia chamber. The solutions with an atmospheric pressure of approximately 21 % O_2 were used and deoxygenated inside the hypoxia chamber. The sensors were able to detect the decrease in the oxygen level of solutions due to the change in the refractive index of solutions caused by the change in the oxygen concentration. These optical fibre sensors are made of silica glass, polymer (PMMA) and a medical-grade adhesive which are biocompatible materials making them safe to come in contact with patients. This work demonstrates preliminary *in-*

DOI: https://doi.org/10.34961/researchrepository-ul.29293661.v1

vitro testing of the sensors and future work will be focused on repeatability and *in-vivo* testing of the sensors.

2. SENSING MECHANISM

The novel optical fibre sensors designed to enable the measurement of oxygen in hypoxic tissue/tumours inside the human body are based on the extrinsic Fabry-Pérot interferometric technique where a Fabry-Pérot etalon is formed by the air gap cavity and the end cap of the optical fibre. The geometry of the sensors is based on forming an air gap cavity between the input single-mode fibre and the inner face of the end-cap created using a plastic optical fibre. This creates two reflecting layers i.e., single mode fibre (SMF)/air/POF and air/POF/surrounding environment causing three reflection components, two being the most significant i.e., $R_{air\text{-}POF}$ and $R_{POF\text{-}sensing\ region}$. A schematic of the POF end cap-based optical fibre oxygen sensor using the Fabry-Pérot interference technique is shown in Figure 1.

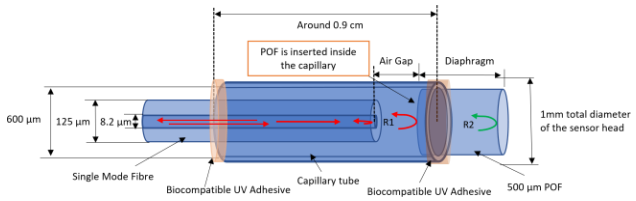

Figure 1 Schematic of the POF end cap-based Fabry-Pérot optical fibre oxygen sensor

In this sensor design, incident light of a broad wavelength range (1507 to 1592 nm wavelength range) illuminates the cavity as shown in Figure 1. There are two significant components to the reflected beam, R1 from the inner face of the end cap and R2 from the outside face. There is also a third component (not shown in the figure for clarity purposes) which is the light reflected from the end of the optical fibre directly back down the fibre. These three components (with R1 and R2 being the most significant) set up an interference pattern in the total light reflected to the detector. The signal detected is an interferogram (a graph of intensity versus wavelength which has a periodic variation of intensity) with a sinusoidal variation of intensity with wavelength in the range of interest.

The principle of operation is based on the light interaction with the surrounding medium at the outer face of the end cap or diaphragm of the sensor probe which will manipulate the spectrum properties depending on the properties of the surrounding medium. In this case, the changes in refractive index induced by oxygen changes in the liquid phantom will be detected. When light is reflected at the outer surface of the end cap, some of the light energy enters the surrounding medium and changes in the optical properties (e.g. refractive index and/or optical absorption) affect the reflected light signal and hence the received interferogram.

In this paper, two variations of the sensor designs are discussed. The variation in designs is mainly based on fabricating different lengths of end caps i.e., 900 µm and 500 µm, to create the Fabry-Pérot cavity.

3. MATERIALS AND METHODS

3.1. Materials

The sensors are fabricated using purely optical components including a standard single-mode fibre (SMF-28), a borosilicate capillary and a plastic optical fibre (POF). A medical-grade UV-cured adhesive based on Acrylic technology was used for joining the capillary with SMF and POF. Table 1 lists the parameters of the fibres, capillary and adhesive used in the sensor fabrication.

Table 1. Sensor fabrication materials

Material	Description
Single mode Fibre (SMF-28)	Corning™ SMF-28™ Ultra Fibre (bend-insensitive) Core diameter = 8.2 µm Cladding diameter = 125 µm
Plastic Optical Fibre (POF)	Fibre diameter = 500 µm
Borosilicate Glass Capillaries	Inner Diameter = 600 µm Outer Diameter = 840 µm
NovaChem OPTIMAX® Medical Grade Adhesive	OPTIMAX® UV-8967-M Conforms to ISO 10993-5 Cytotoxicity Refractive Index: 1.47

Phosphate Buffered Saline (PBS) and Bovine Serum Albumin (BSA) solution were used for the characterization of sensors in the hypoxia chamber. The BSA is the main protein present in the serum of bovine blood that can be used to mimic blood and hence was selected to prepare liquid phantom. The Phosphate buffered saline solution (PBS) was used to host the 5% BSA media. The mixing ratio was 5 % BSA and 95 % PBS. The levels of albumin in blood are normally between 3-5% w/w [7] hence only a small percentage of BSA was used in the liquid phantom preparation or to mimic human blood. One sensor was tested on 100% PBS solution as well.

3.2. Sensor Fabrication

The sensors are designed in a Fabry-Pérot configuration as shown in Figure 1. A single-mode fibre (SMF-28) is used as an input light and output reflection receiving fibre, fabricated to be housed in a borosilicate hollow glass capillary with an inner diameter (I.D.) of 600 µm and outer diameter (O.D.) of 840 µm. A POF of 500 µm diameter (matching the diameter of the capillary) is used to create the end-cap/diaphragm of the sensor. The sensors are fabricated by inserting the POF inside the capillary and splicing it using a medical-grade biocompatible UV adhesive instead of a fusion splicer. After joining the POF with the capillary, the end of the POF fibre is cut to make the end cap as small as easily possible using a sharp blade cutter and followed by polishing it until the required length. In this case, two variations of sensors were fabricated, one with 900 µm end cap and other with 500 µm end cap. The air gap between the SMF and the inner face of POF creates the Fabry-Pérot etalon. The spectrum of the sensor was monitored periodically by inserting input fibre inside the capillary and creating an air cavity. Once, the required spectrum is achieved, the capillary was cut to around 0.9 cm and single mode fibre is inserted into it and spliced

using adhesive. A photograph of the 500 µm POF end cap-based optical fibre oxygen sensor using the Fabry-Pérot interference technique is shown in Figure 2.

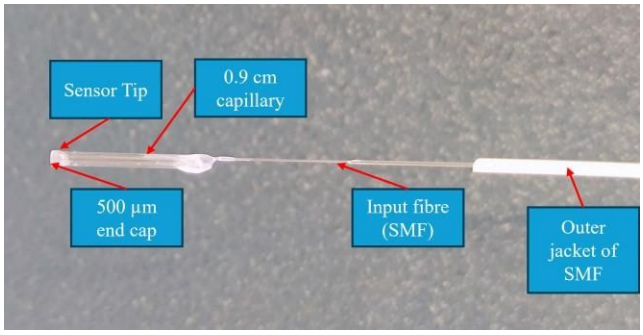

Figure 2 Photograph of the 500 µm POF end cap-based optical fibre oxygen sensor using the Fabry-Pérot interference technique

3.3. Experimental Setup

Figure 3 presents the photograph of the experimental setup for oxygen measurements using a liquid phantom in a hypoxia chamber. The sensor was connected to the BaySpec WaveCapture Fibre Bragg Grating (FBG) interrogator with an integrated super luminescent LED (SLED) producing a spectrum in the wavelength range of 1507 to 1592 nm. The spectra were monitored and recorded using the BaySpec Sense 2020 Software. A BSA liquid phantom and PBS solution were used for testing the sensors at different oxygen concentrations inside the hypoxia chamber. The OxyLite sensor (Oxford Optronix, Milton, UK) is a commercially available optical fibre sensor for measuring the partial pressure of oxygen, pO_2, and temperature in tissue or liquid samples. It was used as a reference to measure the oxygen concentration of the sample in real-time inside the Whitley H135 Hepa Hypoxystation. The OxyLite sensor's integrated thermocouple also automatically corrects the pO_2 measurement to changes in temperature and outputs both the temperature and pO_2 of the sample simultaneously on the OxyLite Pro detector.

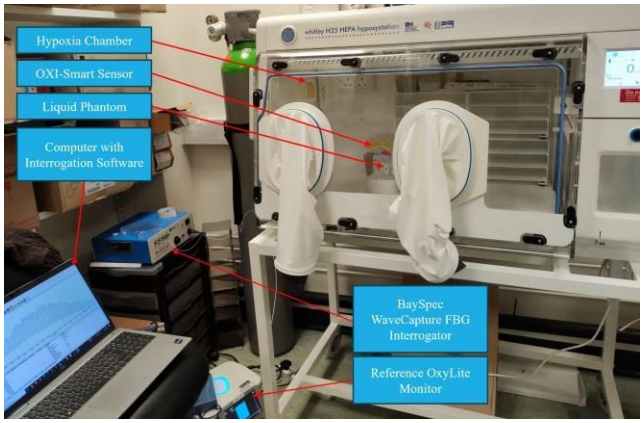

Figure 3 Experimental Setup for POF end cap-based Fabry-Pérot optical fibre oxygen sensor in the Hypoxia Chamber

4. EXPERIMENTAL RESULTS AND DISCUSSION

4.1. Characterization of 900 µm POF End Cap-based Optical Fibre Oxygen Sensor

The initial experiment was performed in 100 % PBS solution using the sensor with a 900 µm end cap. The PBS sample was initially at room temperature and atmospheric pressure of approximately 21 ◦C and 21 % O_2, respectively. This sample was placed inside the hypoxia chamber having preset oxygen concentration at 0.5 % and temperature of 37 ◦C. The temperature of the sample at first reading was noted to be at 35 ◦C and stayed in the range of 35 ±1.7 ◦C during the entire experiment. The oxygen of the sample depletes at a significantly slower rate hence the experiment continued for several hours and spectra were recorded at regular intervals. For this experiment, the range of oxygen in the sample was between 26.7-142 mmHg. The tip of the 900 µm end cap sensor was immersed in the PBS solution and the signal was detected using the FBG interrogator. The spectra were recorded in the interrogator's high-sensitive mode with an integration time of 0.05 ms. It should also be noted that the sensor remained fixed in place for all measurements to prevent any changes to the spectrum that could result from the movement or bending of the fibre. The OxyLite sensor was also inserted into the same solution and the $pO2$ and temperature were detected using the OxyLite Pro.

Figure 4 shows the spectrum of the 900 µm POF end cap-based Fabry-Pérot optical fibre oxygen sensor in 142 mmHg oxygen concentration in PBS solution. The spectrum has multiple interference peaks as expected in a Fabry-Pérot interference pattern. Figure 5 (a) presents a selection of spectra measured at various oxygen concentrations from a pO_2 value of 26.7 mmHg to 142 mmHg (equivalent to 3.51 % to 18.68 % O_2). Here, measurement at 142 mmHg is considered as a reference spectrum to compare with the following spectra. Figure 5 (b) shows the zoomed-in section of spectral peaks from 1540 nm to 1542 nm. It can be seen that there is a decrease in the intensity and shift in phase of the spectra with decreasing oxygen concentration. This phase difference or change in intensity occurs due to the refractive index of the sample varying with the oxygen level. However, on some oxygen concentrations, fluctuations are noticed which could be attributed towards temperature fluctuations and will be further analysed in future experiments using phase shift analysis with repetitive experimentation using the same sensor.

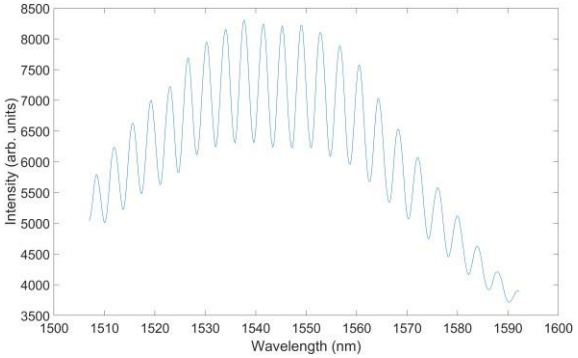

Figure 4 Spectrum of the 900 µm POF end cap-based Fabry-Pérot optical fibre oxygen sensor in 142 mmHg oxygen concentration in PBS solution

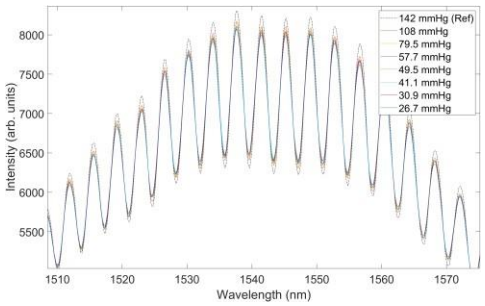

(a)

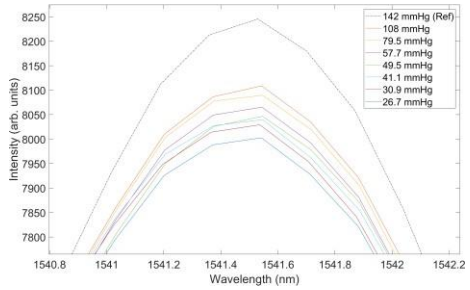

(b)

Figure 5 Spectral response of the 900 µm POF end cap-based Fabry-Pérot optical fibre oxygen sensor from 26.7 mmHg to 142 mmHg oxygen concentration inside a PBS solution (a) Full spectral response (b) Zoomed-in section of peaks from 1540 nm to 1542 nm

4.2. Characterization of 500 µm POF End Cap-based Optical Fibre Oxygen Sensor

The sensor with a 500 µm end cap was characterised in the liquid phantom prepared using 5% BSA and 95% PBS solution. The liquid phantom sample was prepared at room temperature and atmospheric pressure of approximately 21 ◦C and 21 % O_2, respectively. The sample was placed inside the hypoxia chamber with the same presetting as in measurements using the 900 µm end cap sensor. The sensor and OxyLite sensor were inserted in the liquid phantom sample and keeping in mind fluctuations in measurements with the previous sensor, no measurements were made until the sample reached a stable temperature of 36.8 ± 0.2 ◦C which took around 1 hour and stayed in this range for the remainder of the experiment. For this experiment, the spectra were recorded for an extended oxygen concentration range i.e., from 12 - 143 mmHg (equivalent to 1.58 % to 18.82 % O_2). The first measurement was taken at a pO_2 value of 143 mmHg and was used as the reference spectrum to be compared with the spectra recorded for decreasing oxygen concentration. The spectra were recorded in the interrogator's high-sensitive mode with an integration time of 0.02 ms. The integration time was changed in this experiment to avoid the saturation of the signals. The deoxygenation of the BSA sample from 142 mmHg to 12 mmHg took approximately 8 hours.

Figure 6 shows the spectrum of the 500 µm POF end cap-based Fabry-Pérot optical fibre oxygen sensor in 143 mmHg oxygen concentration in 5% BSA/PBS-based liquid phantom. Having a smaller end cap, the spectrum has less number of peaks. Figure 7 (a) shows a selection of measured spectra at decreasing oxygen concentration from 143 mmHg to 32.6 mmHg and Figure 7 (b) shows a selection of measured spectra for oxygen concentration from 29.6 mmHg to 12 mmHg. It can be seen in Figures 7 (a) and (b) that there is an increasing phase shift to the left of the reference spectrum for a decrease in oxygen concentration. The shift in the spectra is very visible in comparison to the response of the 900 µm end cap sensor which means the 500 µm end cap sensor is more sensitive to oxygen concentration changes in comparison to the 900 µm end cap sensor. The difference in sensitivity could also be attributed to different liquid solutions used for experimentation in both cases. It can be seen that the 500 µm POF end cap sensor has a significant response in phase shift at lower pO_2 values as well. This is the main requirement for an oxygen sensor for hypoxia measurements since normal tissue oxygen levels are between 3-7.4 % and oxygen levels of a hypoxic tissue normally fall below 2 % [8].

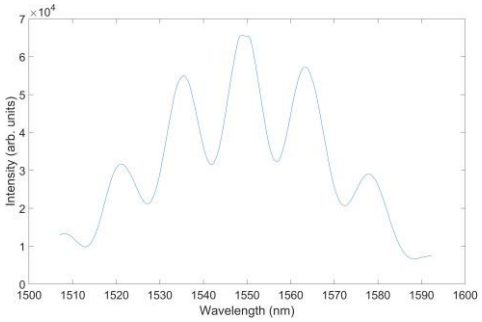

Figure 6 Spectrum of the 500 µm POF end cap-based Fabry-Pérot optical fibre oxygen sensor in 143 mmHg oxygen concentration in 5% BSA/PBS liquid phantom

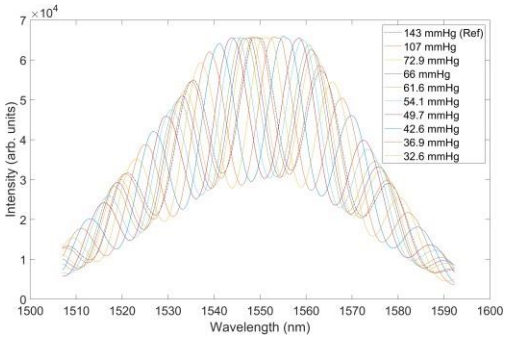

(a)

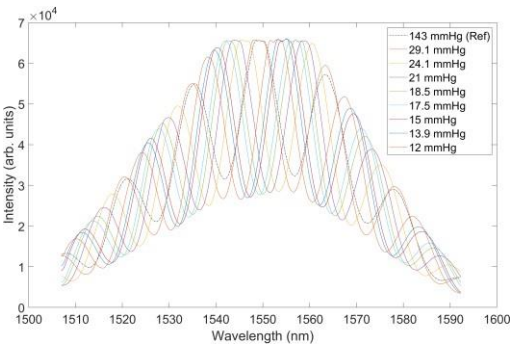

(b)

Figure 5 Spectral response of the 500 µm POF end cap-based Fabry-Pérot optical fibre oxygen sensor from 12 mmHg to 143 mmHg oxygen concentration inside a 5% BSA/PBS liquid phantom (a) Full spectral response from 143 mmHg to 32.6 mmHg (b) Full spectral response from 29.1 mmHg to 12 mmHg

The last spectrum recorded using the 900 µm POF end cap sensor was at 26.7 mmHg oxygen concentration of the PBS solution, which is equivalent to 3.57 % O_2. Further experiments are required to further validate this sensor design in the BSA or any other liquid phantom in the hypoxia region i.e., less than 2 % O_2 with proper temperature stability. The last spectrum recorded using the 500 µm POF end cap sensor was at 12 mmHg oxygen concentration of the BSA liquid phantom, which is equivalent to 1.58 % O_2 and under the hypoxia region of a tissue. The sensors demonstrate a significant response over a wide range of oxygen concentrations, especially in or near the hypoxia region of a tissue. However, these measurements are preliminary results of the *in-vitro* testing of the POF end cap-based Fabry-Pérot optical fibre oxygen sensors. After this validation of the proof of concept of these sensors, future experiments will be focused on performing the phase shift analysis and determining the repeatability of the sensors, especially in the hypoxia region using BSA and other phantom tissues.

5. CONCLUSIONS

The POF end cap-based Fabry-Pérot optical fibre oxygen concentration sensors with end cap lengths of 900 µm and 500 µm were tested *in-vitro* inside a 100 % PBS solution and 5% BSA/PBS liquid phantom. A 100 % PBS solution and blood-like liquid phantom of bovine serum albumin (5% BSA/PBS) were used as the testing media which were gradually deoxygenated within a temperature-controlled hypoxia chamber set to deliver a minimum concentration of 0.5 % O_2. A discernible shift was observed in the spectra with decreasing pO_2 in spectral responses of both variations of sensors. The 500 µm end cap sensor also exhibited a significant spectral shift in the hypoxic concentration region (i.e., < 2 % O_2). These results demonstrate the potential of these biocompatible miniature real-time optical fibre sensors to locate (localised) hypoxic regions in tumours and further enhance individualisation of radiotherapy treatments and thus improve treatment outcomes.

FUNDING STATEMENT

This work was supported by the Higher Education Authority (HEA), the Department of Further and Higher Education, Research, Innovation and Science (DFHERIS) and the Shared Island Fund for the North-South Research Programme under the OXI-SMART Project.

REFERENCES

[1] "Global cancer burden growing, amidst mounting need for services." Accessed: Jun. 02, 2024. [Online]. Available: https://www.who.int/news/item/01-02-2024-global-cancer-burden-growing--amidst-mounting-need-for-services

[2] B. Muz, P. de la Puente, F. Azab, and A. K. Azab, "The role of hypoxia in cancer progression, angiogenesis, metastasis, and resistance to therapy," *Hypoxia*, vol. 3, p. 83, Dec. 2015, doi: 10.2147/HP.S93413.

[3] P. Vaupel and A. Mayer, "Hypoxia in cancer: Significance and impact on clinical outcome," *Cancer and Metastasis Reviews*, vol. 26, no. 2, pp. 225–239, Jun. 2007, doi: 10.1007/S10555-007-9055-1/METRICS.

[4] P. Vaupel, M. Höckel, and A. Mayer, "Detection and Characterization of Tumor Hypoxia Using pO 2 Histography," *Antioxid Redox Signal*, vol. 9, no. 8, pp. 1221–1235, 2007, doi: 10.1089/ars.2007.1628.

[5] E. Ortiz-Prado, S. Natah, S. Srinivasan, and J. F. Dunn, "A method for measuring brain partial pressure of oxygen in unanesthetized unrestrained subjects: the effect of acute and chronic hypoxia on brain tissue PO2," *J Neurosci Methods*, vol. 193, no. 2, p. 217, Nov. 2010, doi: 10.1016/J.JNEUMETH.2010.08.019.

[6] J. R. Griffiths and S. P. Robinson, "The OxyLite: a fibre-optic oxygen sensor.," *British Journal of Radiology*, vol. 72, no. 859, pp. 627–630, Jul. 1999, doi: 10.1259/BJR.72.859.10624317.

[7] X. Cao *et al.*, "Quantification of oxygen depletion during FLASH irradiation in vitro and in vivo," *Int J Radiat Oncol Biol Phys*, vol. 111, no. 1, p. 240, Sep. 2021, doi: 10.1016/J.IJROBP.2021.03.056.

[8] S. R. McKeown, "Defining normoxia, physoxia and hypoxia in tumours-implications for treatment response," *Br J Radiol*, vol. 87, no. 1035, Mar. 2014, doi: 10.1259/BJR.20130676.

60: ONLINE MONITORING AND FAULT DIAGNOSIS SYSTEM FOR FILLING PIPELINE LEAKAGE BASED ON DISTRIBUTED FIBER OPTIC ACOUSTIC SENSING TECHNOLOGY

Chongqi Wei [a], *Kaizhang Lu* [b], *Xinzhong Zhang* [b], *Haifeng Zhou* [c], *Haidong Yu* [c], *Chenghao Zhang* [a], *Liang Yan* [a], *Lu Cao* [a], *Guangxian Jin* [a], *Yanong Ning* [a], *Tongyu Liu* [a, *]

[a] Shandong Micro-sensor Photonics Ltd., Jinan, Shandong China,250103:
[b] Jinxi Tai Mining Co., Ltd., Linyi, Shandong, China, 276000:
[c] Yantai Zhongjia Mining Co., Ltd., Yantai, Shandong, China, 264100:

Industrial Sensing Session 1, EM009, August 12, 2024, 11:30 AM - 12:40 PM

Abstract – With the deepening development of mineral resources, deep well mining has become an important trend in the mining industry. The filling mining method is widely used in the extraction of iron, non-ferrous metals, gold, and uranium mines due to its high safety, environmental friendliness, and high ore recovery rate. However, the failure of filling pipelines can lead to serious accidents, greatly impacting the mining operation chain. Therefore, developing an online monitoring and fault diagnosis system for detecting filling pipeline failures is of great significance. Currently, common methods such as camera surveillance and pipeline pressure monitoring have coverage limitations and environmental constraints. This paper reports a pipeline leakage monitoring system based on Distributed Acoustic Sensing (DAS) technology, utilizing fiber-optic phase-sensitive acoustic sensing technology to achieve precise location and real-time monitoring of leakage points alone the pipeline. Experimental results shows that this system can accurately capture characteristics of leakage events both in the time-domain and frequency-domain, The system provides high real-time performance, accuracy, and reliability, to effectively ensure the mining production safety.

Keywords: Filling pipeline; Leakage monitoring; Distributed Acoustic Sensing (DAS); Fault diagnosis; Mine safety

1. INTRODUCTION

In iron, non-ferrous metals, gold, and uranium mines, the filling pipeline, being the core of the filling system, can cause serious accidents such as burst pipes and blockages, which would greatly impact the mining operation chain. Therefore, developing an online monitoring and fault diagnosis system for detecting any filling pipeline failures is of great significance.

Currently, common methods for online monitoring of pipeline failures include camera surveillance and pipeline pressure monitoring. However, due to the long lengths of underground pipelines, it is difficult to comprehensively detect the entire pipeline's leakage conditions. Cameras are difficulty to deploy fully due to the harsh underground environment, inconvenient power supply that limits the number of cameras, and high humidity that also affects the image quality. Additionally, pressure monitoring methods for detecting pipeline failures may be effective for pressure transmission pipelines based on the siphon effect, but these methods are limited for self-flowing pipelines due to the lack of stable pressure.

To address these issues, this study proposes a pipeline leakage monitoring system based on Distributed Acoustic Sensing (DAS) technology. This system uses OTDR-based positioning technology and phase-sensitive fiber-optic acoustic sensing technology to achieve precise location and acoustic signal monitoring of leakage points. By analyzing and processing the acoustic signals of leaks, characteristic acoustic signals of leakage events are identified, and judgments are made based on these signals. The optical cable is laid along the pipeline, enabling distributed acoustic monitoring of the entire pipeline without the need for power supply. This system can monitor pipeline leakage in real-time, over long distances, non-intrusively, and with high precision.

1.1. Principle of Distributed Fiber Optic Acoustic Sensing System

Optical fiber DAS achieves acoustic sensing by measuring the optical phase change caused by axial strain in the optical fiber. When an acoustic wave acts on the optical fiber, it induces axial strain variation in the fiber, changing the phase of the Rayleigh scattering signal in the fiber. According to the photo elastic effect, the axial strain and the optical phase change of the optical fiber have the following linear relationship:

$$\Delta\varphi = \beta \left(1 - \frac{n^2}{2}(P_{12} + 2P_{11})\right) \Delta L \quad (1)$$

where β is the propagation constant of light, n is the refractive index of the optical fiber, p_{11} and p_{12} are the tensor coefficients of the optical fiber, and ΔL is the change in the length of the optical fiber, given by $\Delta L = \varepsilon\varepsilon_s L$, where $\varepsilon\varepsilon_s$ is the axial strain of the optical fiber and L is the length of the optical fiber. By extracting the phase difference of the detection light at different points along the optic fiber, such as points A and B in Figure 1, the axial strain change of the optical fiber segment between A and B can be determined, ultimately achieving quantitative sensing of acoustic waves and vibrations.

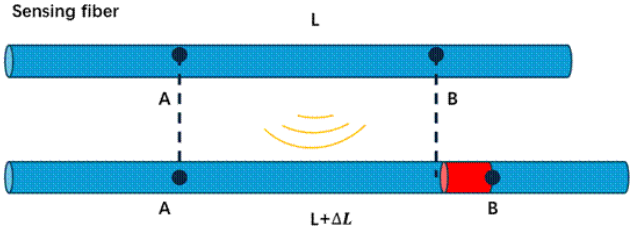

Figure 1.Principle of Acoustic Detection Based on Optical Phase

Rayleigh scattering is an elastic scattering that does not produce any nonlinear effects, and the Rayleigh scattered

DOI: https://doi.org/10.34961/researchrepository-ul.29293703.v1

light at different positions can be distinguished by the time it reflects back to the fiber emitting end. Therefore, phase-sensitive optical time-domain reflectometry (φ-OTDR), based on fiber Rayleigh scattering phase extraction technology, is widely used in DAS.

In a distributed fiber optic detection system, time information can be used to derive the corresponding distance information. By using the time difference between the pulse light output by the laser and the backscattered Rayleigh light received by the detector, the time information can be converted into distance information:

$$Z = \frac{ct}{2n} \tag{2}$$

where c is the speed of light in a vacuum, t is the time it takes for the pulse light to travel back and forth in the sensing fiber, and n is the refractive index of the optical fiber. This formula allows accurate determination of the event location along the optical fiber path.

As the optical pulse propagates forward in the sensing cable, it continuously generates backscattered Rayleigh signal light. By measuring the temporal variation of the backscattered Rayleigh light at the incident end of the sensing cable, the vibration characteristics at different positions along the sensing cable can be obtained. The backend data processing system can obtain the sound information at that location through phase demodulation of the vibration signal.

1.2. System Composition

The distributed fiber optic acoustic sensing system mainly consists of a vibration optic fiber sensing cable, a vibration demodulation host, a data processing terminal, and supporting monitoring software. The demodulation host processes the reflected scattering optical signals detected, while the data processing terminal handles digital signal processing and artificial intelligence analysis. The monitoring software includes control and display functions, visually presenting the processed data to the user. The vibration optic fiber sensing cable is laid on-site along the pipeline to detect external disturbance signals. The structure of the distributed fiber optic acoustic sensing system is shown in Figure 2.

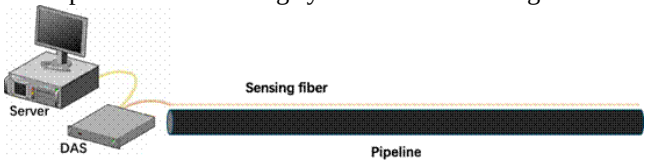

Figure 2. Distributed Fiber Optic Acoustic Sensing System

2. FIELD EXPERIMENT

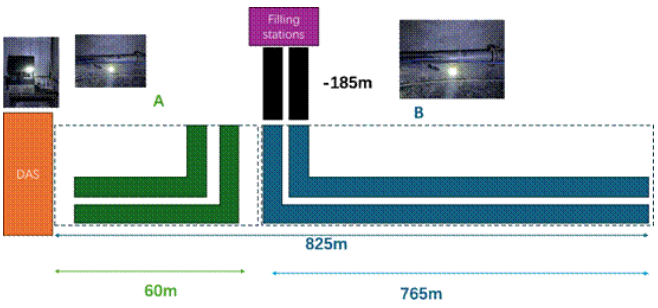

Figure 3. Experimental Site Conditions

In the filling station, two vertical filling pipelines extend from the surface through a bore hole with a depth of 185 meters. At the bottom of the bore hole, four pipelines in two groups, A and B, are connected to the vertical filling pipelines respectively, with the two groups of pipelines are directed to two opposing directions, each direction consisting of two pipelines. The underground pipelines are directly placed on the floor of the tunnel. All pipelines are connected by multiple sections with flanges, each section about 6 meters long. Group A has two pipelines approximately 60 meters long, while the Group B has two pipelines approximately 765 meters long.

Figure 4. Filling Pipeline

The distributed fiber optic acoustic monitoring system is deployed at the end of the tunnel, with the DAS demodulator being placed at the starting point of Group A. A single optical cable of 825 meters is laid from the demodulator along the pipelines of Group A and then those of Group B to monitor the signal characteristics of pipeline leakage. The optical cable is laid along the pipeline and fixed using clamps and adhesive tapes, as shown in the figure.

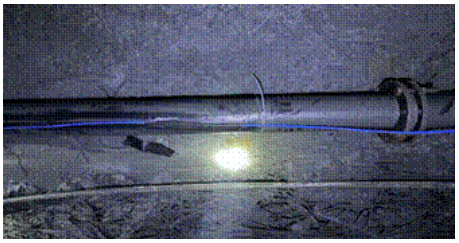

Figure 5. Fixation Method of the Sensing Fiber Optic Cable

2.1. Pipeline Global Signal Collection Experiment

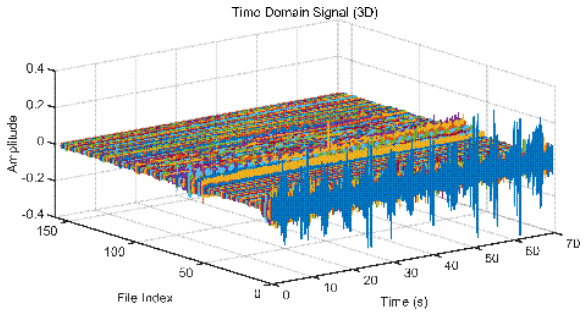

Figure 6. Distributed Acoustic Sensing Audio Recovery

The results of the distributed acoustic sensing in the pipeline signal collection experiment are shown in Figure 6. The 3D distribution of the recovered acoustic waveforms from different sensing channels is displayed. It can be observed that distinct acoustic patterns are present within the first 60 meters of the pipeline, caused by the flow of filling

materials inside the pipeline. Another noticeable acoustic waveform appears in the section around 720 meters (250 to 330 meters), caused by drilling operations in that area. In contrast, the signals detected in the sections between 60 to 330 meters and that from 330 meters to the end of the pipeline are relatively quiet due to the absence of material flow and other noise. The system's high sensitivity and fidelity allow high-quality restoration of actual sounds.

2.2. Simulated Pipeline Leakage Experiment

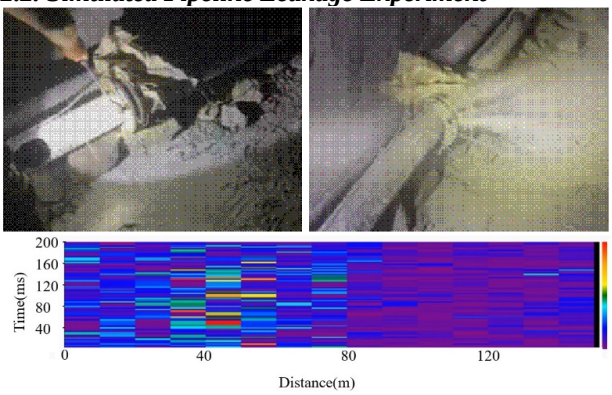

Figure 7. Pipeline Leakage Experiment

A simulated pipeline leakage experiment was conducted around the 40-meter mark of the pipeline, with flange leakage as a typical example. The experiment involved loosening the screws at the flange with a wrench, causing slurry inside the pipeline to spray out through the flange gap. The waterfall diagram in Figure 7 shows an increase in amplitude near 40 meters, with red and yellow high-amplitude signals. In contrast, areas without leakage show blue-green signals, and unfilled pipeline sections show blue-purple signals.

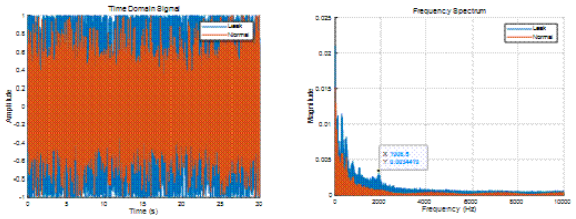

(a) (b)

Figure 8. Signal Condition during Leakage, (a) the time domain graph, (b) the frequency domain graph.

The time-domain and frequency-domain graphs of leakage and normal signals are shown in Figure 8a and 8b respectively. The time-domain graph Figure 8a shows that the signal amplitude during leakage is significantly higher than that of normal signals. The frequency-domain graph Figure 8b reveals a peak at 1908.5 Hz during leakage, which can be used to identify leakage signals.

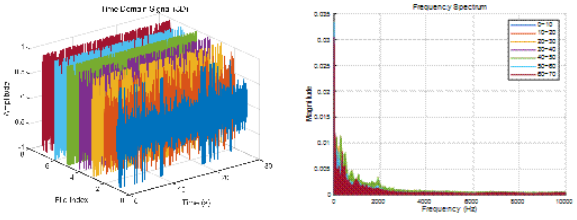

(a) (b)

Figure 9. Signals at Different Spatial Locations during Leakage

The time-domain and frequency-domain signals at different spatial locations during the same time are shown in Figure 9a and 9b respectively. Seven locations were monitored, with one having leakage and six others being normal. The time-domain signal's 3D graph shows higher signal amplitudes at the leakage location, while the frequency spectrum shows a characteristic frequency around 1908.5 Hz at the leakage location, absent in the other locations.

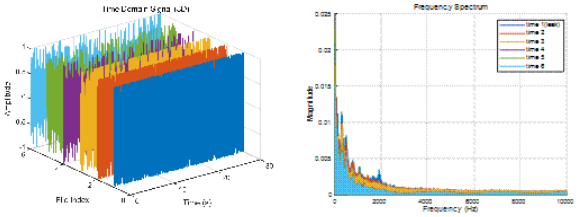

(a) (b)

Figure 10. Signals at Different Times during Leakage

The time-domain and frequency-domain signals at the same location at different times are shown in Figure 10a and 10b respectively. The time-domain graph indicates higher and more sustained signal amplitudes during leakage, while the frequency spectrum shows a characteristic frequency around 1908.5 Hz during leakage.

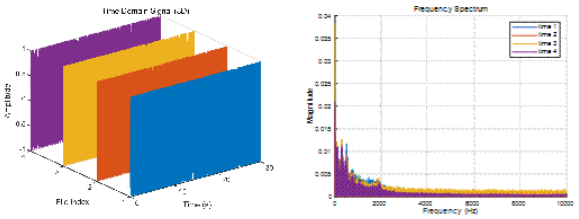

(a) (b)

Figure 11. Characteristics of the Signal during Continuous Leakage

3. RESULTS AND DISCUSSION

The distributed fiber optic acoustic sensing technology used in this work has achieved significant testing results in pipeline leakage monitoring and diagnosis. Experimental results show that this technology can accurately capture the characteristics of leakage events in both time-domain and frequency-domain. For example, in simulated experiments, leakage signal amplitudes increased, and the frequency spectrum showed a characteristic peak at 1908.5 Hz. Further spatial experiments indicated that the signal amplitude at the leakage location was significantly higher than normal, and a characteristic frequency peak appeared around 1908.5 Hz. These results verify that the system is able to provide an accurate, and reliable monitoring and diagnosis method for monitoring pipeline leakage events in real-time, ensuring the safe and efficient operation of the filling pipeline.

REFERENCES

[1] National Bureau of Statistics. China Statistical Yearbook 2018 [M]. Beijing: China Statistics Press, 2018.

[2] Zheng Jing-jing, Zhang Qin-li, Wang Xin-min, et al. Failure Mode and Effect Analysis (FMEA) and Fuzzy Evaluation of Failure Impact of Filling Pipeline Systems [J]. China Safety Science Journal, 2009, 19(06): 166-171+3.

[3] Zhang Qin-li, Wang Xin-min. Performance Study of Cemented Coal Gangue Backfill [J]. Journal of Central South University of Technology, 2007, 14(2): 216-219.

[4] Juarez J C, Maier E W, Choi K N, et al. Distributed Fiber-Optic Intrusion Sensor System [J]. Journal of Lightwave Technology, 2005, 23(6): 2081-2087.

[5] Rao Y J, Luo J, Ran Z L, et al. Long-Distance Fiber Optic Φ-OTDR Intrusion Sensing System [J]. Proceedings of SPIE, 2009, 7503: 75031O.

[6] Juarez J C, Taylor H F. Polarization Discrimination in a Phase-Sensitive Optical Time-Domain Reflectometer Intrusion Sensor System [J]. Optics Letters, 2005, 30(24): 3284-3286.

[7] Pan Z Q, Liang K Z, Ye Q, et al. Phase-Sensitive OTDR System Based on Digital Coherent Detection [J]. Proceedings of SPIE, 2011, 8311: 83110S.

[8] Han L J, Wang Q, Yang Q H, et al. Leak Detection and Localization Analysis of Underwater Gas Pipeline Based on Distributed Fiber Optic Sensing [J]. Chinese Journal of Sensors and Actuators, 2015, 33: 155-160.

[9] Zhou L, Wang F, Wang X I, et al. Distributed Strain and Vibration Sensing System Based on Phase-Sensitive OTDR [J]. IEEE Photonics Technology Letters, 2015, 27(17): 1884-1887.

[10] Wang Chen, Liu Qing-wen, Chen Dian, et al. Monitoring Pipeline Leakage Using Fiber-Optic Distributed Acoustic Sensor [J]. Acta Optica Sinica, 2019, 39(10): 1006005.

61: AN EVALUATION OF MODELLING OF PROPAGATION USING COMSOL FOR A SINGLEMODE-MULTIMODE-SINGLEMODE STRUCTURE

Thomas Freir [a,*], *Arun Kumar Mallik* [b], *Yuliya Semenova* [a], *Gerald Farrell* [a]

[a] Photonics Research Centre, Technological University Dublin, Grangegorman, Ireland:
[b] Tyndall National Institute, Lee Maltings Complex Dyke parade, T12 R5CP Cork, Ireland:

Emerging Sensing Strategies and Applications Cont., EM010, August 14, 2024, 11:00 AM - 12:10 PM

Abstract – This paper presents models developed for investigating multimode interference structures with the intention of utilising precise 3D printing to print the centre section of the structures modelled. The models allow the design of structures for use in fibre sensors, replacing the silica fibre centre section structures currently used. The paper outlines the process of evaluating and validating COMSOL propagation models by comparison to existing reported results. The proposed model shows excellent agreement in calculating self-imaging length with the other referenced models and an analytical calculation.

Keywords**:** singlemode-multimode-singlemode structures; COMSOL; Multimode Interference; 3D printing; Polymer Optical Fibre.

1. INTRODUCTION

3D printing is a powerful tool for the rapid fabrication of highly customised structures at a variety of dimensional scales, from micron level and upwards, for a wide range of applications in areas such as biomedical and rapid prototyping. Currently, state-of-the-art 3D printing can achieve a feature size as small as 100 nm and a surface roughness better than 10 nm.

Optical fibre sensors possess a range of advantages, which has resulted in their deployment in a variety of application areas which include biomedical, environmental, and structural sensing. A feature of many optical fibre sensors is the need for customisation of the sensing fibre, often to maximise sensitivity for a given measurand, for example by etching/polishing the fibre surface or by the creation of a long-period grating or other structures in the fibre. Polymer optical fibre (POF) has also been used as the basis for some fibre sensors [1] and again customisation of the POF has been used in many sensors to improve performance.

The POF light guides used in many fibre sensors [2] frequently adopt, as a starting point in the fabrication process, an off-the-shelf POF with the usual circular fibre shape. However, many sensor structures require a POF with a specific fibre diameter or some other customisation, for example, the creation of a flat surface or other feature on the side of the fibre. Such customisation can be difficult to achieve without complex equipment and ultimately customisation possibilities are limited in scope. The availability of precise 3D printing of polymer structures offers the possibility of fabricating custom POF light guides for use in sensors

However, a better understanding of the potential and challenges of 3D-printed POF elements in fibre sensors is needed. This research utilises an experimental platform based on a singlemode-multimode-singlemode (SMS) structure as the sensing structure, in which multimode interference (MMI) occurs. The centre multimode section is a POF structure, sandwiched between the two silica SMFs. An SMS structure was chosen as the basis for the experimental platform as it is well understood and has been used for sensing a wide variety of measurands [3].

Simulation of propagation in an SMS structure is necessary, to better understand its behaviour and predict the effect of POF material parameters and customisation of the POF centre section. In this work, we report on the development of a 2D model that allows for the investigation of the performance of 3D-printed POF light guides. In order to validate the COMSOL model reported here, comparisons are undertaken with a previously developed in-house Matlab model and with a COMSOL model previously reported by another group. The key metrics used for comparison are the self-imaging lengths and the transmission spectral responses. In the case of the self-imaging length, comparison with analytic results are also provided. Comparisons are undertaken for two different SMS centre section types, a step-index multimode fibre (MMF) and a no-core fibre (NCF), commonly used in simple sensors.

2. METHODS AND PROCEDURES

2.1 The 2D COMSOL Model Structure

As a starting point, a 2-dimensional model was built using the COMSOL Multiphysics Wave Optics Module, a finite element analyser, solver, and simulation software package to simulate the propagation of light through the SMS structure. This work uses COMSOL's Electromagnetic Waves, Beam Envelopes (ewbe) interface, which computes electric and magnetic field distributions where the field amplitude varies slowly on a wavelength scale. The finite elements can be multiples of the wavelength in size, which helps reduce simulation time by reducing the total number of elements.

Figure 1 illustrates the basic model structure. The model simulates a 2D cross-section of the SMS structure along its meridional axis. The model enables the simulation of propagation in a centre section, between the SMFs, which in this work is either an MMF or alternatively a NCF. Table 1. shows the dimensions and refractive indices of the well-

DOI: https://doi.org/10.34961/researchrepository-ul.29301707.v1

understood silica fibres used in the simulations for comparison.

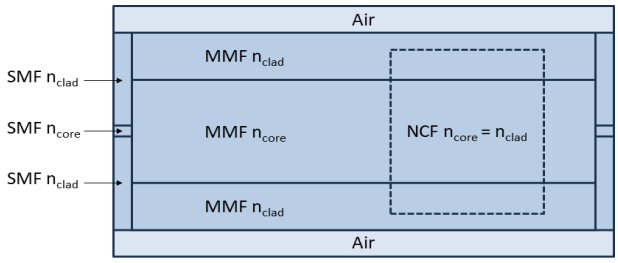

Figure 1. Structure of the 2D COMSOL Model

Table 1. Fibre parameters

	Core Diameter	Cladding Diameter	Core RI	Cladding RI
SMF	8.3µm	125µm	1.4504	1.4447
MMF	105µm	125µm	1.4446	1.4271
NCF	NA	125µm	NA	1.444

3. RESULTS OF PROPAGATION MODELLING IN SMS STRUCTURES

3.1 The 2D COMSOL Model

Two SMS structures are modelled at 1550 nm using a 105/125 multimode fibre and a NCF fibre respectively. The results of the simulation using the 2D COMSOL models are shown in Figures 2 & 3. Figure 2 shows the SMS structure based on a 105/125 multimode fibre with a 45 mm length with 1 mm input and output singlemode fibres. In practice, the SMF fibres will be considerably longer, but for the purpose of a simulation, short 1mm lengths are adequate. There is a well-defined self-imaging point at a distance circa 43 mm from the input SMF.

Figure 3 shows the SMS structure based on a 125 µm diameter NCF with a 65 mm length and 1 mm input and output singlemode fibres. There is a well-defined self-imaging point at a distance circa 59 mm from the input SMF.

The 2D models were verified by comparison with results from a COMSOL model by Younus et al [4]. There is good agreement with the work reported by Younus [4] with the self-imaging lengths for the 105/125 and NCF SMS structures showing errors of 0.60% and 0.94% respectively. Younus [4] did not report the refractive index values used in their simulation so making exact comparisons is difficult.

3.2 The 2D Matlab Model

Additionally, the 2D COMSOL models reported here were verified by comparison with results from a Matlab model by Wang et al [3]. Figures 4 and 5 show the propagation in an SMS structure using the Matlab model reported in [3], with self-imaging points again at circa 43 mm and 59 mm. The errors in the self-imaging lengths compared to the COMSOL work presented here are 0.023% and 0.19%.

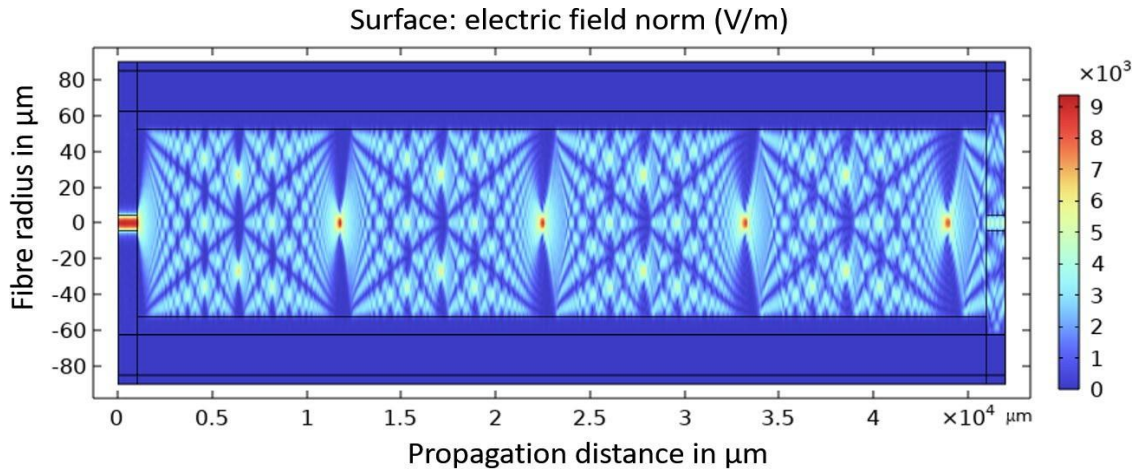

Figure 2. 105/125 centre section propagation from COMSOL Model

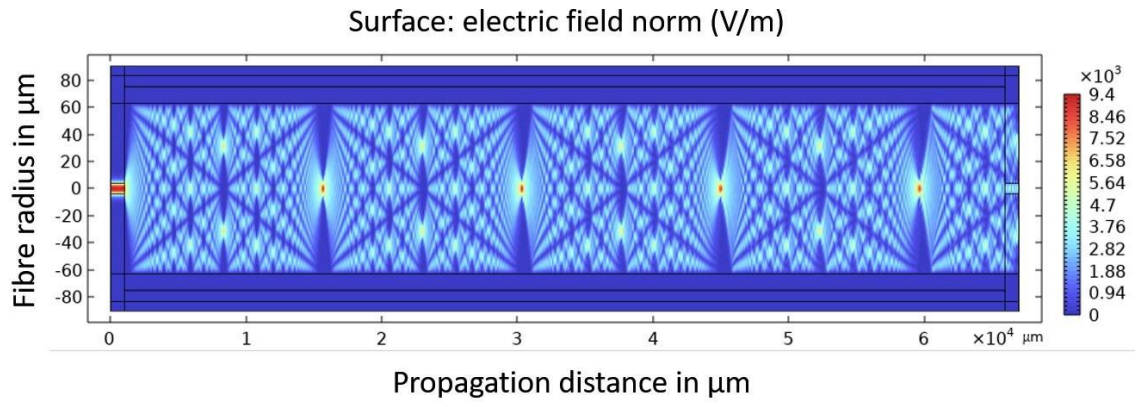

Figure 3. NCF centre section propagation from the COMSOL Model developed in this work

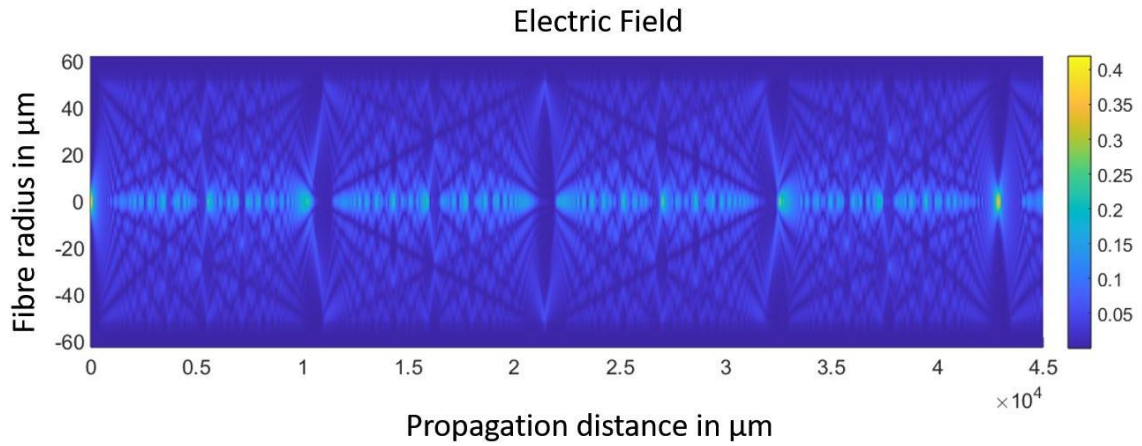

Figure 4. 105/125 centre section propagation from the Matlab Model [3]

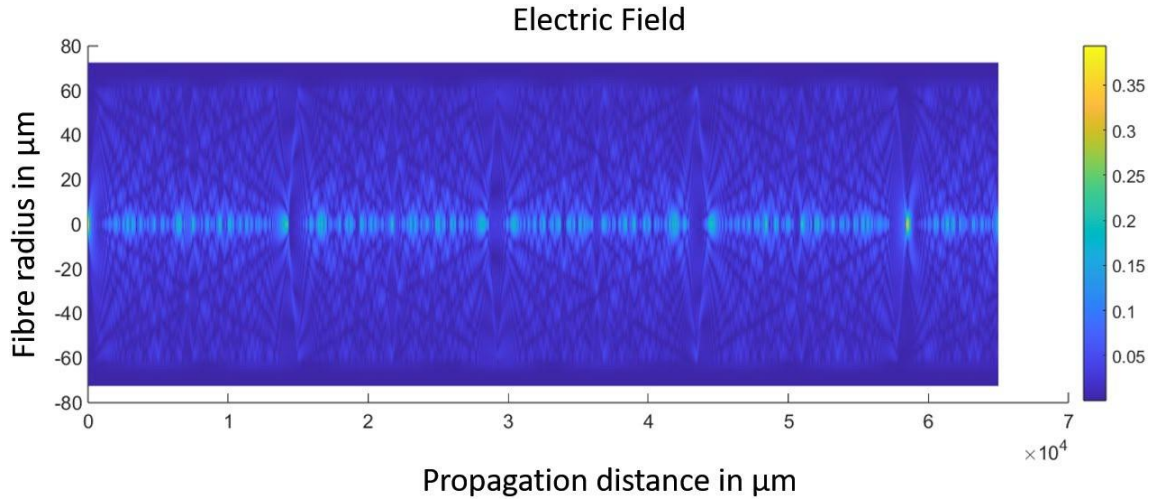

Figure 5. NCF centre section propagation from the Matlab Model [3]

3.3 Comparison with MMI Theory

The self-imaging length can also be determined analytically using (1) [4].

$$L_{MMF} = P \frac{n_1 D_{MMF}^2}{\lambda} \quad (1)$$

Where L_{MMF} is the self-imaging length, P is the self-imaging index, λ is the free-space wavelength and n_1 and D_{MMF} are the core refractive index and core diameter respectively. A value of P = 4 is typically chosen as it provides for the lowest attenuation if coupling to an output SMF at the self-imaging point. Using a wavelength of 1550 nm and a D_{MMF} value of 105 µm, for P = 4, the self-imaging length is 41,101 µm for the 105/125 MMF fibre centre section case.

However, care must be taken when using equation (1), since the underlying assumption stated in the 1995 work by Soldano et al [5] on MMI in multimode waveguides is that the waveguide width (equivalent in this case the fibre core diameter) is based not on the physical waveguide width but rather the "effective" waveguide width, which takes into account the penetration depth of the evanescent field of each mode at the edge of the waveguide. For high-contrast waveguides, the penetration depth is very small and thus the difference between the physical waveguide width and the "effective" waveguide width can be neglected. However, for the 105/125 µm MMF case, the relatively small difference between the core and cladding RI values means that the penetration depth does need to be considered. Assuming a 1/e penetration depth of 1.1 µm, the "effective" core diameter is 107.2 µm for the purpose of calculating L_{MMF} from (1). Using a value of D_{MMF} = 107.2 µm, the self-imaging length L_{MMF} is calculated as 42,842 µm at a wavelength of 1550 nm.

For the NCF case, as the cladding is effectively air, the refractive index difference between the core and the cladding RI values is much larger. The penetration depth is much smaller at 0.236 µm. Using a value of D_{MMF} = 125.472 µm as the "effective" core diameter, the self-imaging length L_{MMF} is calculated as 58,666 µm at a wavelength of 1550 nm.

Table 2 shows a comparison of the self-imaging lengths calculated by the models and the analytical approach.

Table 2. Comparison of self-imaging lengths. The percentages in brackets represent the difference with respect to the COMSOL model developed in this work.

	105/125 MMF self-imaging length in µm	125 µm NCF self-imaging length in µm
COMSOL (this work)	42,910	58,610
COMSOL, Younus et al [4]	42,650 (0.60%)	58,060 (0.94%)
Matlab, Wang et al [3]	42,900 (0.023%)	58,500 (0.19%)
Analytic using Equation 1 [5] with no adjustment for penetration depth.	41,101 (4.22%)	58,226 (0.66%)
Analytic using Equation (1) [5] with an adjustment for penetration depth.	42,842 (0.16%)	58,666 (0.1%)

From Table 2 it is clear that the COMSOL model developed in this work shows excellent agreement in the value of the self-imaging length compared to existing COMSOL [4] and Matlab [3] models. Furthermore, there is also excellent agreement with the analytically calculated self-imaging length, but only if the evanescent field penetration depth is taken account of.

3.4 Transmission Spectra Comparison

Further verification of the COMSOL model presented here was carried out by simulating the transmission spectra of the MMI devices. For an SMS device, the transmission spectrum is a bandpass response, centred on the wavelength at which the self-imaging length is calculated (in this case 1550 nm) and assuming the output SMF is attached to the MMF at the self-imaging length point.

Using a parametric sweep, COMSOL was used to repeat the field simulations such as those in Figures 2 & 3 over a range of wavelengths with the light coupled into the output SMF being calculated to calculate the transmittance at a range of wavelengths. For the sake of comparison, the self-imaging lengths for both the COMSOL and Matlab models were set to the length value shown in Table 2 specific to each model, both of which result in a spectral peak at 1550 nm.

Figure 6 shows that the transmission spectra from the models for a 105/125 SMS structure, showing good agreement. At 1550 nm the transmittance for COMSOL and Matlab are -0.55 dB and -0.35 dB respectively. The deepest notch in the spectrum at 1500 nm shows excellent wavelength alignment but there is a notable 20 dB difference in notch depth.

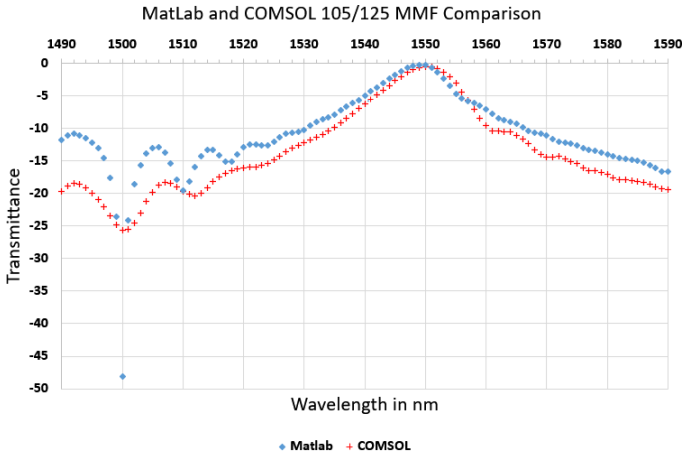

Figure 6. Simulated transmission spectrum of a 105/125 centre section with spectral peak at 1550nm

Figure 7 shows that the transmission spectra for the 125 um NCF structure, again displaying good agreement around in the wavelength region around the peak wavelength. At 1550 nm the transmittance for the COMSOL and Matlab are -0.36 dB and -1.35 dB respectively. In both models the spectra show two notches in the 1500 nm to 1520 nm region, but they are not aligned, with the first notch (leftmost) displaced by 3 nm and the second notch by 2 nm.

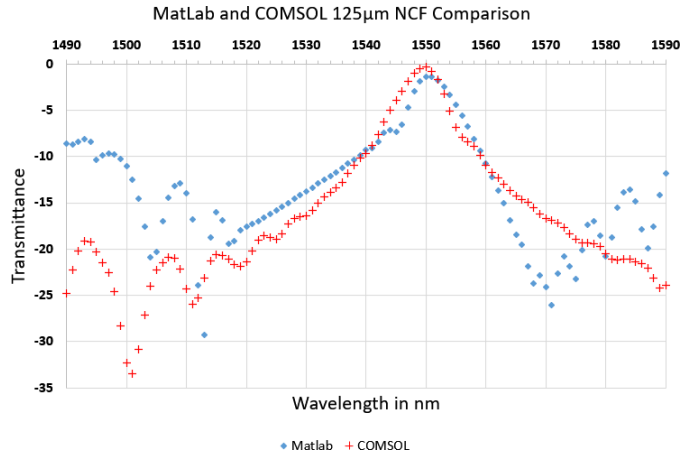

Figure 7. Simulated transmission spectrum of a 125 um NCF centre section with spectral peak at 1550nm

4 CONCLUSIONS

The COMSOL model developed here, and the Matlab model show excellent agreement in calculating the self-imaging length.

The transmission spectra show good agreement between the COMSOL and Matlab models, for both centre section types, in the wavelength region around the spectral peak. However, further work is required to investigate the inconsistencies in the spectral positions and depth of side lobe notches in the spectral responses.

Future work will consider 3D models built in COMSOL. These models will allow changes to be made to the shape of the centre section structure that cannot easily be simulated in a 2D model, e.g. a D-shaped fibre cross-section.

FUNDING STATEMENT

This research is supported by Technological University Dublin and the School of Electrical and Electronic Engineering at Technological University Dublin.

REFERENCES

[1] D. Gomez, S.P. Morgan, Barrie R.H-G, R.G. Correia, S. Korposh, **Polymeric optical fibre sensor coated by SiO2 nanoparticles for humidity sensing in the skin microenvironment**, Sensors and Actuator B, January 2018.

[2] H. Gao, G.F.R Chen, P. Xing, J.W. Choi, H.Y Low, and D.T.H Tan, **High-Resolution 3D Printed Photonic Waveguide Devices**, Advanced Optical Materials, 2020.

[3] Q. Wang, G. Farrell, and W. Yan **Investigation on Single-Mode–Multimode–Single-Mode Fiber Structure**, Journal of Lightwave Technology Vol. 26, No. 5, March 1, 2008

[4] S.I. Younus, A.A. Al-Dergazly, A.K. Abass, **Characterization of Multimode Interference Based Optical Fiber**, 2021 IOP Conf. Ser.: Mater. Sci. Eng. 1076 012060

[5] L.B. Soldano, E.C.M. Pennings, **Optical Multi-mode Interference Devices Based on Self-Imaging: Principles and Applications**, Journal of Lightwave Technology, Vol. 13, No. 4, April 1995

62: APPLICATION OF LOW-POWER FIBER OPTIC DEMODULATION TECHNOLOGY BASED ON VCSEL LASER AND WIRELESS MONITORING OF COAL MINE ROOF

Wu Zegong[a], Cao Lu[b], Deng Shijie[c], Wang Shoutao[b], Zhang Lilei[a], Jin Guangxian[b], Ning Yanong[b], Liu Tongyu[b]

[a] *Laser Institute, Qilu University of Technology (Shandong Academy of Sciences), Jinan, Shandong 250104, China*
[b] *Shandong Micro-sensor Photonics Ltd., Jinan, Shandong 250103, China*
[c] *Guilin University of Electronic Technology, Guilin, Guangxi 541004, China*
* Corresponding author

Industrial Sensing, EM009, August 13, 2024, 4:20 PM - 6:10 PM

Abstract – The report describes a VCSEL (Vertical Cavity Surface Emitting Laser) based on voltage and current wavelength modulation, along with a fiber grating demodulation technique using acetylene absorption peaks as a wavelength reference. This enables the laser to achieve a wavelength scanning range of 10.5nm, with the entire system operating normally within a temperature range of 0-40℃, and the effective wavelength scanning range of the laser being 4.5nm. Since temperature control is not applied to the laser, its operating temperature varies with ambient temperature changes, resulting in a system characterized by a wide demodulation range, low power consumption, and compact size. Additionally, the study explores self-organizing network technology based on LoRa(Long Range) wireless communication for fiber optic wireless demodulation hosts, relays, and sub-stations. Leveraging the low power consumption characteristics of the demodulation technique, this enables wireless transmission of signals.

Keywords**:** Low-power demodulator; wireless communication; fiber optic sensing

1. INTRODUCTION

In the field of coal mine roof condition monitoring, traditional electronic monitoring methods and fiber optic wired monitoring methods have played a certain role, but they also have some obvious disadvantages[1-3]. Traditional electronic monitoring methods are often limited by complex installation, data transmission interference, high cost, etc., making it difficult to meet the requirements of real-time and accurate monitoring of coal mine roof conditions. Although fiber optic based monitoring methods can solve some problems, they still suffer from difficulties in deploying, vulnerability to damage, and high maintenance costs, resulting the limitation of their applications in the coal mine environment[4]..

To overcome the shortcomings of traditional monitoring methods and further improve the efficiency and reliability of coal mine roof condition monitoring, this paper reports a new technology solution based on fiber optic wireless monitoring.

Currently, many scholars have reported wavelength demodulation schemes for fiber Bragg gratings (FBGs) using VCSELs (Vertical Cavity Surface Emitting Lasers) with current-tuned wavelength. Hu et al. [5] introduced a FBG demodulation device and method based on tunable VCSELs and acetylene absorption peaks as wavelength reference or spectral references. Due to the influence of external temperature changes on the laser emission wavelength, the laser temperature was controlled using thermoelectric cooling (TEC) to keep the emission wavelength in a region between 1527-1530nm. Meanwhile, the central wavelengths of the five absorption peaks of acetylene within this wavelength range were used as spectral references. By using the wavelengths of the 5 absorption peaks to find and detect the wavelength values of the fiber optic grating, the system achieved wavelength demodulation of the fiber optic grating using acetylene absorption peaks as references. However, to maintain the scanned wavelength of laser to cover the acetylene absorption peaks, thermoelectric cooling was used on the laser, resulting in high power consumption and a demodulation range of only 3nm. Huang et al. [6] proposed a FBG demodulation system using VCSEL as the light source. By driving VCSEL with a saw tooth wave current signal, a wavelength demodulation range of 2nm was obtained, and the number of FBGs in the system was increased using time division multiplexing. At the same time, the relationship between the wavelength tuning range of VCSEL and the scanning speed was studied.

This study aims to overcome the inability of the above-mentioned demodulation schemes using VCSELs to simultaneously meet the requirements of wide wavelength demodulation range and low power consumption. VCSEL lasers produced by BandWidth10 were used as the light source. This laser has features of voltage-tuned wavelength, current-tuned wavelength, temperature control, and temperature query. The voltage and current tuning enable the laser to scan a wavelength range of 10.5nm. Based on this laser, this paper proposes a fiber optic grating demodulation technology using voltage and current dual-wavelength modulation of VCSEL and relying on acetylene absorption peaks as references.

In addition, this study also explores the self-organizing network technology of fiber optic wireless demodulation hosts, relays, and sub-stations based on LoRa wireless communication. By fully utilizing the low power consumption characteristics of demodulation technology, wireless transmission of signals is achieved, greatly expanding the application field of fiber optic communication systems. This innovative technical solution provides new ideas and possibilities for building low-power and efficient communication systems.

This work focus on the coal mine roof condition monitoring scheme based on fiber optic wireless monitoring

DOI: https://doi.org/10.34961/researchrepository-ul.29301776.v1

technology, and analyse in depth its advantages and feasibility in practical applications.

2. Demodulation System Design

2.1 Fiber Bragg Grating Reflective Wavelength Principle Diagram

The wavelength reflection schematic diagram of the fiber Bragg grating is shown in Figure 1. When incident light passes through the core of the fiber to reach the grating region, the grating will reflect light of a specific wavelength. If there are changes in external physical quantities, such as temperature or stress applied on the gratings, the central wavelength of the reflected wave changes accordingly. The fiber Bragg grating demodulator monitors demodulates the variations of the central wavelength of the reflected wave of the fiber Bragg grating and hence monitor the changes in external physical quantities in real-time. Currently monitored physical quantities using fiber Bragg gratings mainly include temperature, pressure, displacement, and strain.

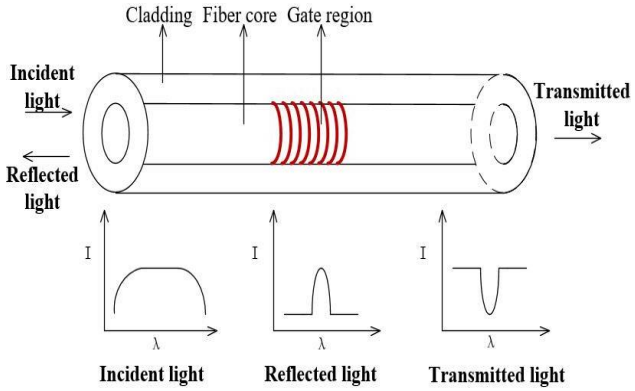

Fig.1 Schematic diagram of fiber grating sensing

2.2 Decoding System Overall Diagram and Principle

The schematic diagram of the demodulation system is shown in Figure 2. The demodulation system mainly consists of a VCSEL source, a fiber isolator, a 1X10 fiber splitter, 8 1X12 fiber couplers, a number of FBG sensors, a acetylene chamber, 10 opto-detectors, 10 amplification circuit with10 ADC, a MCU, an output interface, a DAC, current drive circuit, a voltage drive circuit, and a temperature monitoring circuit.

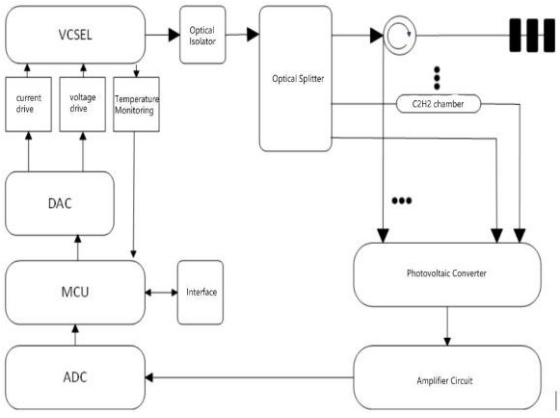

Fig.2 Block diagram of the interrogator

During the operation of the demodulation system, the MCU controls the voltage and current drive circuits respectively to ensure that the VCSEL generates a wavelength scanning range of 10.5nm. Additionally, the MCU can monitor the temperature of the laser in real-time through the internal temperature and pressure sensors.

The 1X10 fiber splitter mentioned above has one input port and ten output ports. The first fiber output is directly connected the first photo detector, while the second fiber output passes through the acetylene chamber before being linked the second photo detector. The other 8 fiber outputs are connected with 8 FBG through 8 1X2 fiber couplers respectively. The optical signals reflected from FBG are detected by the 8detectors via the 8 fiber couplers respectively. The signals from the first and second detectors are processed by the MCU, resulting in peaks as shown in Figure 3. These electronic signal peaks are correspond to the absorption peaks of acetylene, which are the fixed physical quantity and do not change with variations in external environmental factors such as temperature and pressure. Based on this characteristic, the normalized acetylene absorption peaks are used as a "wavelength scale" to measure the actual wavelength and its vaiation of the fiber Bragg grating.

The incident light reflected by each FBG is detected by the photo detector to produce the detected electronic signal. The eight electronic signals are processed by the MCU. Within the same wavelength scanning range, the demodulation system simultaneously obtains the normalized wavelength of the acetylene absorption peak and eight reflection wavelengths of the FBGs. By utilizing the known wavelength values of the acetylene absorption peaks as a "wavelength scale", the MCU performs a wavelength fitting processing, and calculates the wavelength values of each FBG after obtaining the fitting results, thereby achieving the purpose of demodulating the FBG wavelength.

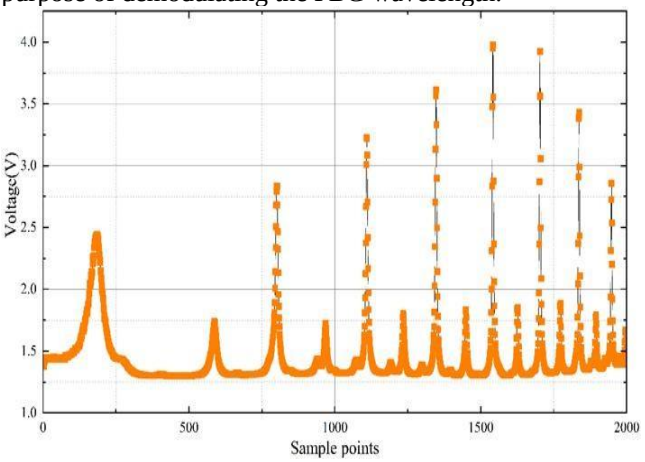

Fig.3 Normalized image of acetylene absorption peak

2.3 Voltage-Driven Characteristics of VCSEL Laser

The experimental setup for testing the spectral characteristics of VCSEL includes an Agilent 86120C multi-wavelength meter, a computer installed with customized computer software, a demodulation module equipped with a VCSEL laser, a wavelength meter and a temperature test chamber. The schematic diagram of the experimental setup is shown in Figure 4.

The specific functions of the above setup are as follows: The upper computer software can monitor the operating temperature of the laser in real-time and control and adjust the driving current and voltage of the laser through the Ethernet transmission interface. The laser is connected to the wavelength meter, which can query the emission wavelength of the laser in real-time at different currents, voltages, and temperatures. Additionally, by setting different temperatures on the temperature chamber, the setup can simulate changes in the ambient temperature during actual use of the demodulation module. The computer software can then query the temperature of the laser in real-time in order to stabilize the laser wavelength at the set value at different temperature.

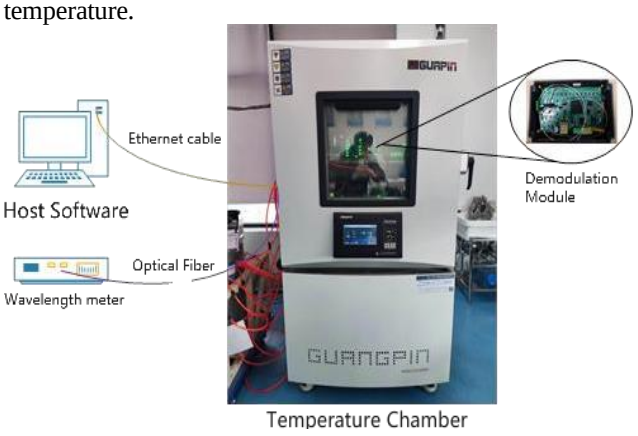

Fig.4 Diagram of the experimental setup

First, set the temperature of the temperature chamber to 0℃, and use the computer software to obtain the temperature of the laser. Once the temperature of the laser stabilizes at 0℃, to ensure that the laser has good optical power, a driving current of 16mA is applied to the laser. Then, use the computer software to scan the driving voltage of the laser within the range of 0-15V, then record the emitted wavelength of the laser, that shows about 8.6nm of wavelength tuning range. Similarly, by setting the temperature of the temperature chamber in a range of 5-40℃ respectively, the corresponding experimental data can obtained. The experimental data is shown in Figure 5, indicating an approximate quadratic relationship between the driving voltage and the emitted wavelength of the laser. The voltage tuning function can be expressed as:

$$\lambda_v = a_v V^2 + b_v V + c_v \quad (1)$$

Where, the a_v, b_v and c_v represent the coefficients of the quadratic function, V is the voltage of the saw tooth waveform used for the voltage tuning, and λ_v is the wavelength generated by the laser during the voltage tuning operation.

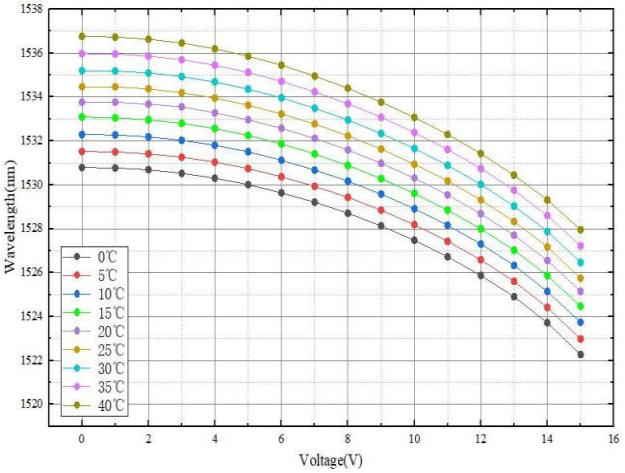

Fig.5 Drive voltage calibration experimental data of VCSEL laser

2.4 Current-Driven Characteristics of VCSEL Laser

After setting the environmental temperature to 25℃ using temperature chamber and allowing the laser temperature to stabilize at 25℃, the driving voltage of the laser is fixed at 15V. To achieve a continuous decrease in wavelength and reach a scanning range of 10.5nm, the laser's current is adjusted from 16mA to 10mA using the computer software. The emitted wavelength of the laser is recorded at each current level. The statistical data is shown in Figure 6. From Figure 6, it can be seen that the current tuning also exhibits an approximate quadratic waveform, with a wavelength tuning range of 1.8nm. The current tuning quadratic function is expressed as:

$$\lambda_i = a_i I^2 + b_i I + c_i \quad (2)$$

Where, the variables a_i, b_i and c_i represent the parameters of the quadratic function used for current tuning. Due to the small variances seen in the production process, each laser may have slightly different parameters for current tuning, thus requiring individual calibration. I represents the scanned current, and λ_i is the wavelength generated by the laser (due to the current scanning).

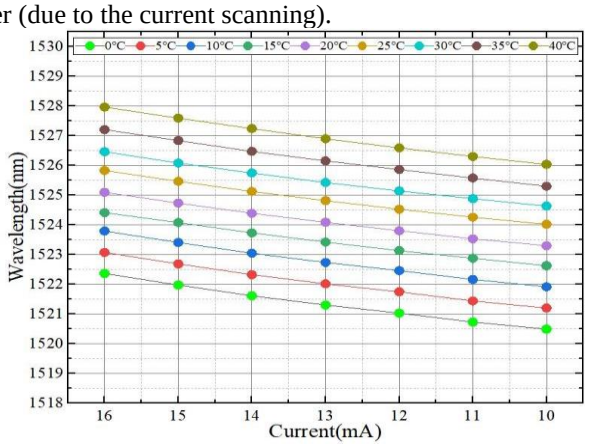

Fig.6 Drive current calibration experimental data of VCSEL laser

2.5 Temperature Characteristics of VCSEL Laser

The temperature of the temperature chamber is sequentially set from 0 to 40℃. Simultaneously, the current and voltage

of the laser are fixed using the computer software to avoid interference with the emitted light of the laser.

$$\lambda = a_i I^2 + b_i I + c_i + a_v V^2 + b_v V + c_v + kT \quad (3)$$

The equation allows determination of its emission wavelength, where, k represents the temperature tuning coefficient. Through numerous tests carried out on the laser, it was found that the temperature coefficient of the laser fell within the range of 0.1419-0.1545nm/°C and so an average value of 0.1482nm/°C was used in this work. The temperature-wavelength relationship curve for a single experiment carried out is shown in Fig. 7.

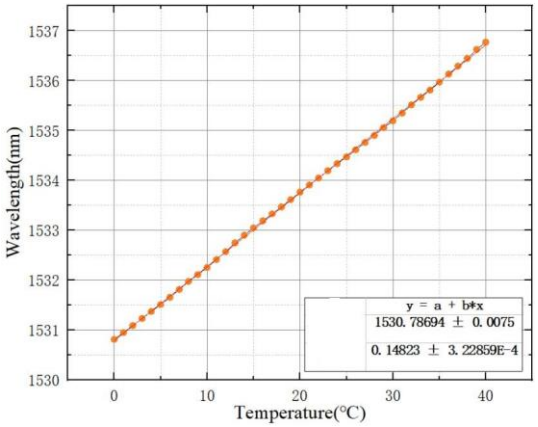

Fig.7 Temperature calibration experimental data from VCSEL

2.6 Explanation of Wavelength Overlap Region without Temperature Control

Since the entire system does not employ temperature control for the laser, the overlapping wavelength range of the laser at temperatures ranging from 0 to 40°C is studied. This facilitates the selection of FBGs within this wavelength range, ensuring that the laser can scan the FBGs at different temperatures.

By tuning the emission wavelength of the laser using a driving voltage of 0-15V and a driving current of 16-10mA, the laser can generate a wavelength scanning range of approximately 10.5nm. The 4.5nm wavelength overlapping region at different temperatures is illustrated in Figure 8. The laser test data is as follows: at 0℃, the wavelength scanning range of the laser is from 1520.2845nm to 1530.7895nm; at 20℃, it is from 1523.3365nm to 1533.7615nm; and at 40℃, it is from 1526.2945nm to 1536.7625nm. Therefore, the overlapping wavelength range is approximately 4.5nm, from 1526.2945nm to 1530.7895nm, which is the actual wavelength range used by the demodulation system.

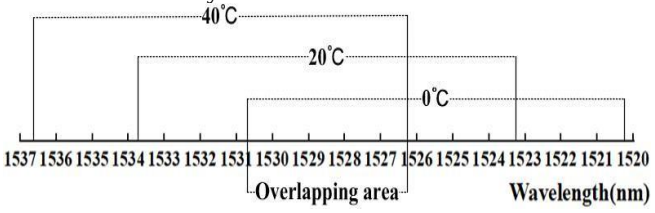

Fig.8 Schematic diagram of wavelength scanning without temperature control

2.7 Power Consumption Test

To verify the low-power characteristics of our demodulation system, conducted number of power consumption tests were conducted using an adjustable power supply. Based on the displayed current and voltage from the power supply, the overall power consumption of the system was approximately 0.189W. With such low power consumption, the demodulation system demonstrates excellent longevity when powered by portable batteries.

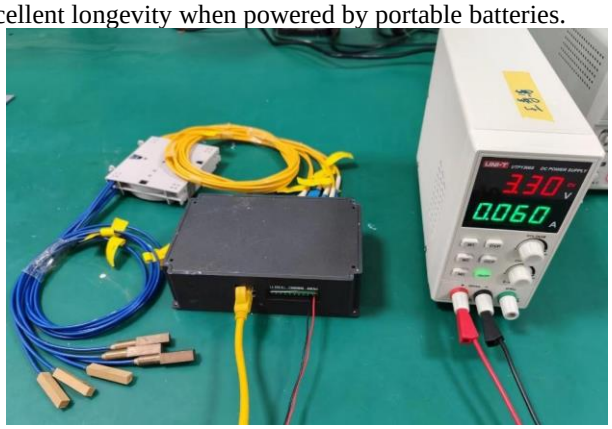

Fig. 9 Power consumption test

3. System Communication

3.1 Overview of the System Communication System

In complex environments such as mines, traditional wired communication methods face difficulties in wiring and high maintenance costs. To improve communication efficiency and safety, a mine wireless relay communication system based on LoRa technology is used. LoRa is a low-power wide-area network technology that achieves long-distance, low-power wireless communication through spread spectrum modulation techniques and optimizes communication efficiency through frequency allocation strategies.

The system consists of mine intrinsically safe wireless monitoring sub-stations, mine intrinsically safe wireless relays, and mine intrinsically safe wireless demodulation hosts. Each mine wireless monitoring sub-station can support up to 11 relays, and each relay can support up to 5 demodulation hosts. Each demodulation host can accommodate up to 5 different types of mine fiber Bragg grating sensors.

3.2 Intermittent Power Supply Communication between Relays and Demodulation Hosts

The relay adopts a dynamic frequency allocation strategy, assigning each demodulation host a non-overlapping operating frequency to enable simultaneous operation of multiple communication links. For example, one relay and five demodulation hosts mounted under the relay is used, the system communication process is as follows:

After the system is powered on, the relay initially establishes communication with all demodulation hosts at a center frequency of 470MHz. Subsequently, based on the predefined communication protocol, the relay assigns an independent working frequency to each demodulation host, these frequencies are 410MHz, 415MHz, 420MHz, 425MHz, and 430MHz, respectively. After completing signal demodulation, the demodulation hosts transmit data to the main relay using their allocated working frequencies. To

further reduce system power consumption, demodulation hosts adopt an intermittent power supply. When one demodulation host communicates with the relay to send data, the other demodulation hosts is powered off. Once all demodulation hosts finish sending data, the relay collects the data and sends it in a packaged format to the next-level relay.

3.3 Communication between Relay Stations at Each Level

Between each level of relays, LoRa communication is employed, where the relays serve to aggregate data, extend communication range, and facilitate data transmission. When a relay receives data packets sent by the upper-level relay, it internally verifies the received data to ensure its integrity and accuracy. Subsequently, the relay forwards the received data packets to the next-level relay according to predefined communication protocols and timing. Through continuous transmission via multiple levels of relays, the demodulated data is ultimately delivered to the wireless monitoring sub-station. In the event of a relay failure, where a relay becomes damaged or malfunctions, resulting in the inability to transfer data between two relays, the upper-level relay will skip the malfunctioning relay and directly send data to the next-level relay, thus achieving hierarchical data transmission and enhancing system stability and reliability.

In complex working environments, such as at corners in tunnels or obstacles obstructing signal transmission paths between two relays, the transmission and reception of relays may be hindered. In such cases, an additional relay needs to be installed at the corner of the tunnel or at the location of the obstacle to facilitate signal transmission. The overall system block diagram is shown in Figure 10, and the installation schematic of relays and demodulation hosts in the tunnel is illustrated in Figure 11.

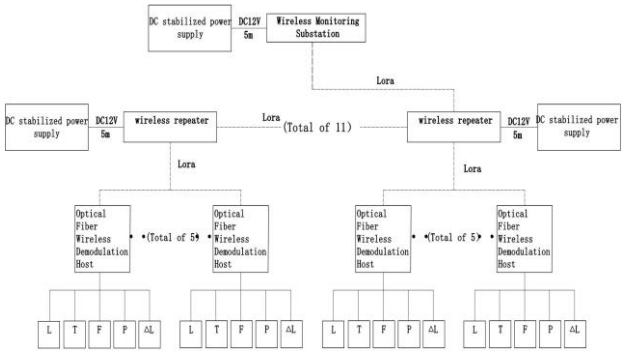

Fig. 10 Overall system diagram

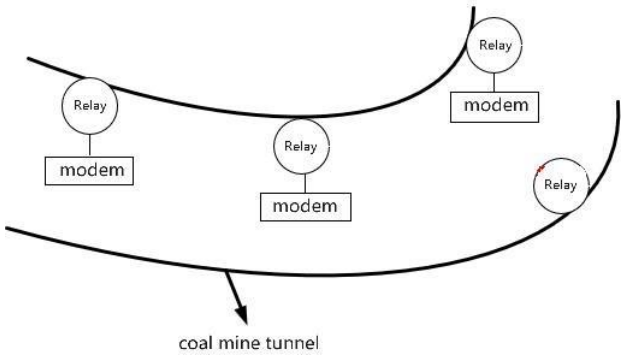

Fig. 11 Schematic diagram of repeater and demodulation host installation in the tunnel

4. Application of Wireless Demodulation Systems in Roof Monitoring of Coal Mine Roadways

Traditional fiber optic roof online monitoring systems offer advantages such as stable sensors, resilient data transmission against interference, large capacity, long-distance transmission, and passive monitoring. However, they also come with drawbacks, including complex laying of underground fiber cables, numerous fiber fusion points, and difficulties in supplying electric power through cable pulling.

To address these issues, this study proposes a low-power, wide-range demodulation wireless fiber optic grating roof separation layer detection system. This system can be powered by batteries and offers features like wireless transmission and demodulation of data. With multiple demodulation channels, the sensors can simultaneously monitor fiber optic roof separation layer sensors, fiber anchor stress sensors, and fiber drilling stress sensors, forming a comprehensive pressure and roof safety monitoring network. Figure 12 depicts the practical application of the project, with fiber optic roof separation layer sensors and anchor stress sensors shown from left to right.

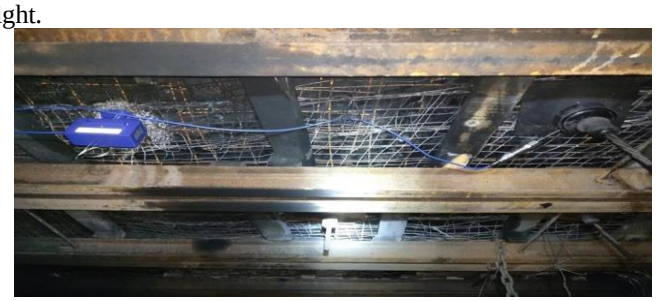

Fig.12 Practical application

5. CONCLUSION

In the coal mining industry, energy consumption and management have always been important topics. The introduction of low-power demodulation solutions is aimed at meeting this demand. Traditional monitoring systems often consume large amounts of electricity, while low-power demodulation solutions using fiber optic wireless monitoring technology can significantly reduce system energy consumption, thereby making positive contributions to energy conservation, emission reduction, and sustainable development in coal mines. A low-power demodulation solution based on fiber optic wireless monitoring technology is presented, which exhibits significant application prospects in coal mine roof separation layer monitoring. By utilizing voltage and current wavelength modulation of VCSEL and acetylene absorption peaks as wavelength reference in fiber optic grating demodulation technology, this solution achieves real-time monitoring of coal mine roof separation layer monitoring with low power consumption. The research conducted in this paper demonstrates that the demodulation system can operate at a low power consumption of 0.189W and possesses a wavelength demodulation range of 4.5nm, with a communication distance of 1000 meters.

ACKNOWLEDGMENTS

This work was supported in part by the National Key R&D Plan Project (2022YFB3207602) and Innovation Team Program of Jinan (2021GXRC037).

REFERENCES

[1] Y. Yao, Z. Li, Y. W, et al. Performance Optimization Design for a High-Speed Weak FBG Interrogation System Based on DFB Laser[J]. Sensors, 2017,17(7):1472.

[2] D. Darwich et al. “Investigation of Low-Cost Interrogation Technique Based on Modulated Distributed Feedback Laser.” IEEE Sensors Journal 20 (2020): 2460-2466.

[3] C. J. Chang-Hasnain, "Tunable VCSEL," IEEE Journal of Selected Topics in Quantum Electronics, vol. 6, no. 6, pp. 978-987 (2000).

[4] T. Mizunami, T. Yamada, and S. Tsuchiya, "Interrogation of fiber-Bragg-grating temperature and strain sensors with a temperature-stabilized VCSEL," Opt Rev 23, 703–707 (2016).

[5] B. Hu, G. Jin, T. Liu, *et al*. "A precision fiber Bragg grating interrogation system using long-wavelength vertical-cavity surface-emitting laser," Photonic Sensors, vol. 6, 09/20 (2016).

[6] Y. H. Huang, L. Chao, P. K. A. Wai, *et al*. "Fast FBG sensor interrogation system using vertical cavity surface emitting laser source," 2009 14th Opto Electronics and Communications Conference, pp. 1-2 (2009).

63: CHARACTERISATION OF THE FBGS INFINITYSCAN®, A CODE-DIVISION MULTIPLEXING INTERROGATOR FOR PRECISION AND DYNAMIC SCANNING

J. Van Roosbroeck [a*], *E. Lindner*[b], *S. Lochmann*[c], *J. Vlekken*[a*]

[a] FBGS International NV, Geel, Belgium,
[b] FBGS Technologies GmbH, Jena, Germany
[c] Hochschule Wismar, Wismar, Germany

Industrial Sensing, EM009, August 13, 2024, 4:20 PM - 6:10 PM

Abstract – A new fiber optic interrogator has been developed that relies on the principles of Code-Division Multiplexing (CDM), called the 'FBGS InfinityScan®'. It can measure the wavelengths of multiple wavelength-division multiplexed (WDM) sections of Draw Tower Gratings (DTG®s) in series. Wavelength precision measurements and wavelength accuracy estimations for dynamic measurements have been done with this interrogator and will be reported. The precision measurements show that the position of the WDM section in the fiber does not have a significant impact on the measured value. The accuracy estimations for dynamic measurements are compared with a theoretical model and good correspondence has been found. Possible system improvements are proposed to find a suitable compromise between detection accuracy and system speed for large optical sensor networks.

Keywords**:** Code Division Multiplexing, Draw Tower Gratings, InfinityScan®, precision, dynamic measurements

1. INTRODUCTION

Fiber Bragg Gratings (FBGs) attract increasing attention as alternative measurement devices [1-3]. Their key advantages are a small form factor, light weight, resistance against electromagnetic interference and the ability to be multiplexed [4]. Typical multiplexing techniques are wavelength-division multiplexing (WDM), optical frequency domain reflectometry (OFDR) or time-division multiplexing (TDM). A promising new multiplexing approach for hundreds or even thousands of serial FBGs is Code-Division Multiplexing (CDM) that uses an autocorrelation method with binary codes to discriminate between sensors with identical wavelengths. Typically, the same WDM section of gratings is repeated multiple times in the same optical fiber. In this way, the combination of CDM with WDM can be used to interrogate large arrays of sensors. Draw Tower Grating® (DTG®) arrays form the ideal sensors to be used in combination with CDM. Dense arrays of DTGs® can be produced in a reliable and cost-effective way [5]. In addition, the reflectivity can easily be tuned to the requested values of around 1% or lower to minimize shadowing. The hybrid CDM-WDM interrogation of thousands of DTG® sensors was already shown in [6]. Other examples of networks containing 4000 (50 × 80), 800 (200 × 4) and 1000 (25 × 40) serial DTGs® with different distances can be found in [7].

In this contribution, the basic principles of CDM are explained. In addition, measurements of the wavelength precision are presented that are done on an exemplary DTG® array that contains multiple WDM sections. Finally, the impact of dynamic changes during sequential reading used by CDM is investigated and experimental results are compared with a theoretical model.

1. PRINCIPLES OF CDM

The CDM setup used in the 'FBGS InfinityScan®' interrogator is depicted in Figure 1. A broadband light source is directly modulated (DM) according to a predetermined binary code. A simple on-off keying is used ('1' is on and '0' is off). Via a circulator, the modulated light enters the sensor array and is reflected by each individual DTG® according to its Bragg wavelength and its location along the fiber. Regular networks are divided into K WDM sections, each containing N DTGs at different wavelengths.

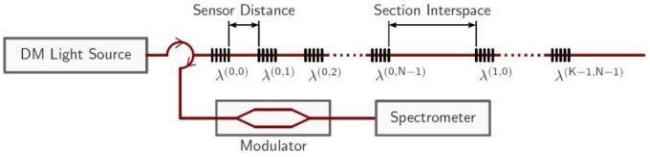

Figure 1: CDM Interrogation System (K: Number of WDM sections, N: Number of sensors per WDM section).

The reflected light is guided via the circulator to a Mach-Zehnder modulator (MZM) that is driven with the same predetermined binary code as the light source but delayed in time. The delay allows the modulation to be synchronized to a specific part of the sensor network depending on the optical path length between light source, DTG® and MZM. At synchronization, every logical '1' of the light source that is reflected at the 'synchronized' section can also pass the modulator and reach the spectrometer. During the integration time period of the spectrometer, all the light of the synchronized code is collected. The spectrum that is measured as such is called the 'direct' spectrum.

However, light from non-synchronized reflections can also coincidentally reach the spectrometer. Due to the specific nature of the code, the probability for this is 50%. Completely removing the influence of non-synchronized sections cannot be achieved with a single code. To remove these

DOI: https://doi.org/10.34961/researchrepository-ul.29301854.v1

contributions, a second spectrum is measured during which the MZM is driven with the inverted version of the predetermined binary code ('1'↔'0'), holding the same delay as for the direct spectrum. This time, light of the synchronized code is entirely blocked by the MZM due to the inversion (the MZM is closed every time reflected light from the synchronized section arrives). Non-synchronized light however again can pass the modulation stage by coincidence, with a probability of again 50%. It is collected by the spectrometer in the so-called 'inverted' spectrum. By taking the difference between the direct and the inverted spectrum, the non-synchronous light is eliminated in the difference spectrum and only the synchronized part remains.

As the synchronization is limited to one specific point within a WDM section, neighbouring sensor peaks will have reduced heights, as a small part of their light is in the inverted spectrum, which is subtracted. This leads to a triangular shaped difference spectrum, the so-called synchronization triangle, see Figure 2. It is the result of a convolution of two rectangular pulses, with its maximum in the synchronization point. The base of the triangle covers one complete WDM section.

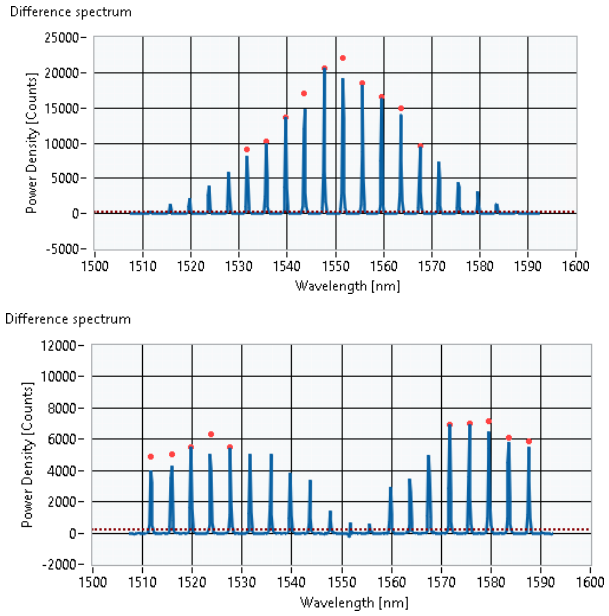

Figure 2: Triangular shaped difference spectra with the delay synchronized to the middle of a particular WDM section (top) and with the delay in between 2 adjacent sections (bottom). Only the higher power peaks are considered for peak tracking, as indicated by the bullets above the peaks.

Due to the triangular shape, the peaks at the sides are suppressed. Therefore, typically 2 delay settings are taken per WDM section: one synchronized to the middle of the section and another in between 2 sections to also measure the peaks at the borders, see also Figure 2. This CDM scheme was already used for the interrogation of 4000 (50 × 80), 800 (200 × 4) and 1000 (25 × 40) serial DTG®s with different network design parameters [6,7].

To illustrate the power of CDM, a sensor from a network containing 4000 DTG®s was strained [8], see Figure 3. The network has 50 identical WDM sections with each section containing 80 different DTG®s. The last sensor from section 50 (sensor 4000) was strained linearly and it shows a wavelength shift that corresponds to the applied strain. The last sensor from the 49th section (sensor 3920) has an identical wavelength, and this stays unaffected since it was not strained. We highlight that the strained sensor's wavelength overlaps with the Bragg wavelength of other sensors in the network during the shift, which shows no significant impact.

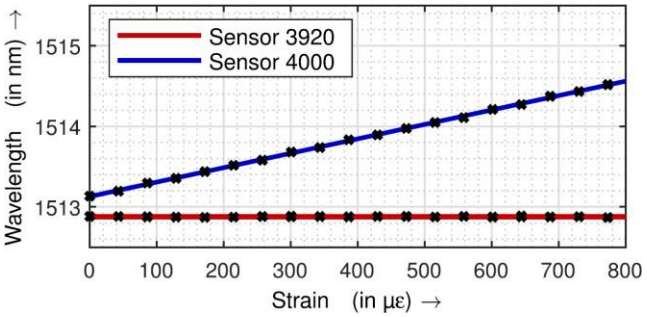

Figure 3: Strain calibration of sensor 4000 (WDM section 50) in a network containing 50 x 80 = 4000 sensors. Sensor 3920 (WDM section 49) has the same wavelength as sensor 4000 and was not strained [8].

2. PRECISION MEASUREMENT IN AN EXEMPLARY CDM SENSING NETWORK

For the precision measurement, a network with 200 DTG®s was interrogated with the 'FBGS InfinityScan®'. The network contains 10 identical WDM sections, with each 20 DTG®s distributed over the 1510 – 1590 nm bandwidth from low to high wavelengths. The interrogator takes 2 samples per delay setting (for direct and inverted spectrum), and it takes 2 delay settings per WDM section (one in the middle of the section and one at the intersection of 2 adjacent sections). For the first and last section, an additional delay setting needs to be taken. In total, 21 delay settings are chosen, see Figure 4. This is the number of sections multiplied by 2 plus one. The wavelengths from all DTG®s are pieced together from the difference spectra as measured for the 21 different delay settings.

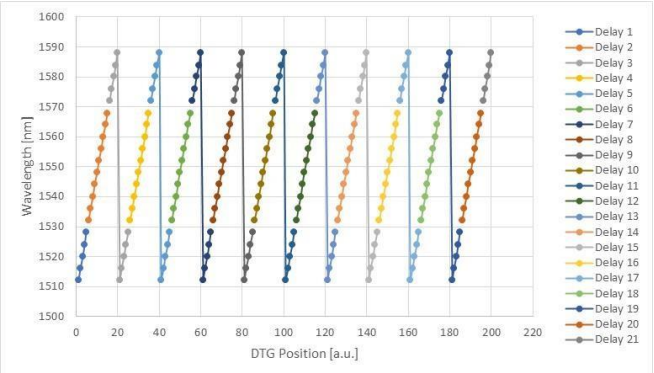

Figure 4: Gratings with their wavelengths ordered as they appear in the fiber. Gratings with the same color are measured together with a specific delay setting.

The interrogator was sampling at 1000 Hz and so every grating in the network is updated at 1000 / (2 x 21) = 23.8 Hz. The wavelengths of all DTG®s were recorded over a period

of 20 s, which yields 476 data points per grating. A simple peak detection algorithm was used to calculate the wavelength from the optical spectrum. The algorithm does a Gaussian fit of the 3 highest pixels of each peak. The standard deviation (1σ) with respect to the mean value was calculated for each peak for the complete data set. The results are shown in Figure 5: ordered as a function of the nominal wavelength or ordered as a function of the WDM section index.

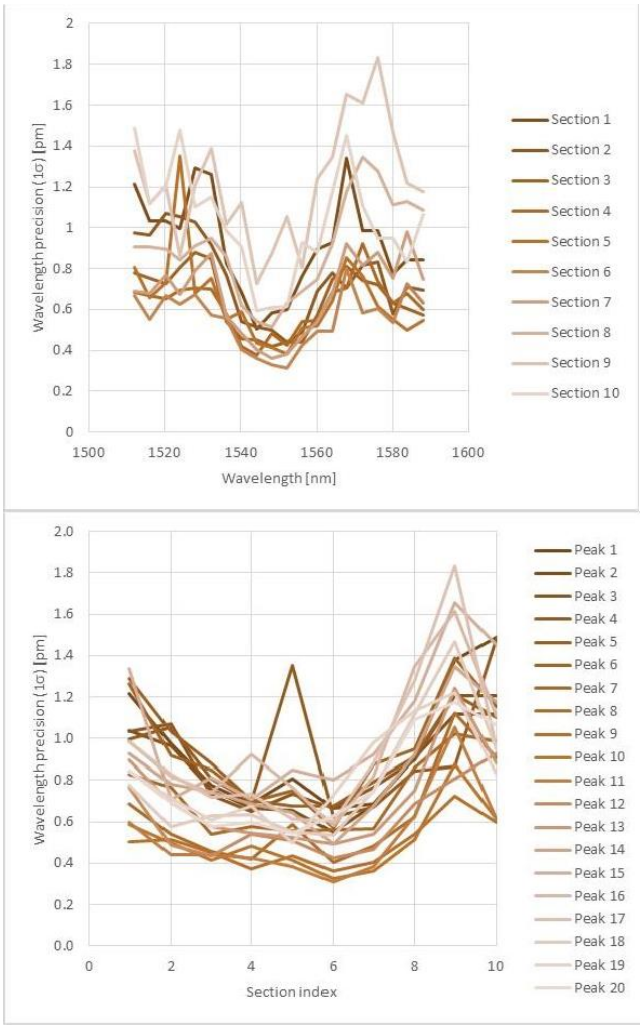

Figure 5: Wavelength precision (1σ) as measured in an exemplary CDM sensing network containing 10 x 20 = 200 DTG®s: ordered as a function of wavelength for each WDM section individually (top) or ordered as a function of the WDM section index for all wavelengths individually (bottom).

The precision is in general in the order of 1 pm. The variation is in the order of ± 0.8 pm. The graph that shows the precision as a function of wavelength indicates the peak power dependence resulting mainly from the Gaussian shaped light source: the larger the peak, the better the precision. Since the peaks from one WDM section are pieced together from 3 separate delay setting measurements, this effect is somehow masked, due to the triangular shape, but it corresponds to what can be expected. This can be understood as follows. Peaks 1-5 and 16 – 20 are measured with a delay setting in between 2 sections. Here, the lowest precision is indeed in general for the lowest and highest wavelengths, which have the highest power because they are closest to the maximum of the triangle. The peaks in the middle (6 – 15) are measured with the delay in the middle of the section. Indeed, the minimum precision for those peaks is found in the middle of the section, where the peaks are closest to the top of the triangle. So, the combination of the used CDM scheme and the shape of the optical source are the dominant parameters for the precision as a function of the wavelength.

A correlation of the precision with the position of the WDM section is less clear or even not existing. An increase in precision was initially expected since the power of the peaks is expected to decrease when advancing further down the fiber because of 'shadowing' effects from overlapping FBGs. However, the precision first seems to go down towards the middle of the fiber and then it starts to increase again, which might indicate that the variation of peak powers is not dominated by shadowing effects. This could also experimentally be verified as shown in Figure 6, where the relation between the peak power and precision for peak 11 for the different WDM sections is plotted. As can be seen in the power data, the peak power first increases when advancing further down the fiber and only starts to go down after section 6. It can also be observed that the precision is inversely proportional to the peak power, as expected. These peak power variations can be related to several effects e.g. peak power variations originating from the DTG® inscription process or the delay optimization for each WDM section. They are less affected by shadowing effects for this particular fiber configuration.

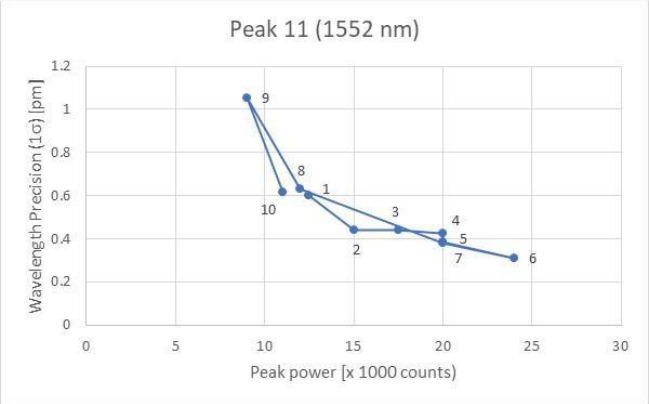

Figure 6: Precision of peak 11 versus its optical peak power for the 10 WDM sections.

3. THEORETICAL CONSIDERATIONS FOR DYNAMIC MEASUREMENTS

The difference spectrum used in CDM is calculated from 2 sequential measurements. In order for this to work properly, it is assumed that the conditions remain static during the time period between both measurements. But when dynamic effects are present, this will in general not be the case.

To investigate the influence of dynamic effects during CDM measurements, simulations were done, see Figure 7. The synchronization triangle shows the percentage of light in the inverted spectrum. To keep the Gaussian shape of the sensor peak, the reflected wavelength of these sensors must not change during the direct and the inverted spectrum acquisition. When the inverted peak is shifted towards

positive wavelengths (red dotted line), the peak in the difference spectrum will be deformed, as the subtraction diminishes the right part of the peak in the direct spectrum stronger. Therefore, the maximum of the deformed difference peak leans towards smaller wavelengths. The faster the sensing peak moves during two acquisition steps, the larger the actual wavelength shift between the direct and the inverted peak. Additionally, a slower sampling of an equal speed of wavelength shift leads as well to a larger actual wavelength shift.

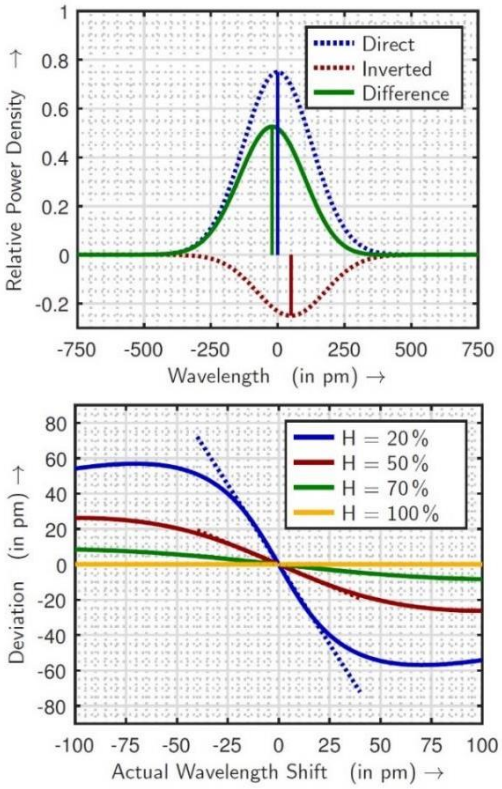

Figure 7: Theoretical approach of dynamic sensor interference: principle of spectral distortion (top) and interference at different heights of the triangle H dependent on the actual wavelength shift (bottom).

In the synchronization point, there is no light in the inverted spectrum, so no deformation of the peak occurs. The greater the distance to this point, the more light is part of the inverted spectrum and thus the larger the deformation and corresponding wavelength deviation will be. This is shown in the bottom graph in Figure 7, which shows the wavelength deviation as a function of the wavelength shift between direct and inverted peak as a function of the triangle heights H. The synchronization point (H = 100 %) serves as a reference, as no deviation occurs. The impact of actual wavelength shifts increases for smaller triangle heights, as the slope of the curves in the origin (dashed lines) indicates. The decreasing deviation for very large actual wavelength shifts can be explained by a vanishing influence of the negative peak, as it shifts outside the area where the direct peak is located.

4. EXPERIMENTAL TRACKING OF DYNAMICALLY STRAINED SENSORS

For the experimental investigation, a (4×40) serial sensor network with 160 DTGs® is used. The sensor distance equals 5 cm, and the section interspace is 80 cm. Dynamic strain is applied to the full length of section 2. The strained section is suspended vertically. Different methods are used to apply a sinusoidal strain profile. The first method uses a weight with a spring attached to the lower end of section 2. Deflecting the spring with the weight leads to large amplitudes but rather low frequency of the applied strain. For the second method, a vibration shaker is attached to the end of section 2. Thus, much higher frequencies can be obtained but with lower amplitudes.

The interrogator is synchronized to the middle of the strained section. Decreasing peak heights due to the synchronization triangle can be found towards smaller and higher wavelengths in the difference spectrum. Thus, the acquisition is identical for all investigated triangle heights in section 2. The acquisition rate is 2 kHz, the difference spectra rate is 1 kHz. Figure 8 shows two measurements where the top graph is the result of the swinging weight: applied strain of 0.5 Hz with an amplitude A of 2.1 nm. The bottom graph is the result of the vibration shaker measurement: applied strain of 40 Hz with an amplitude of 80 pm.

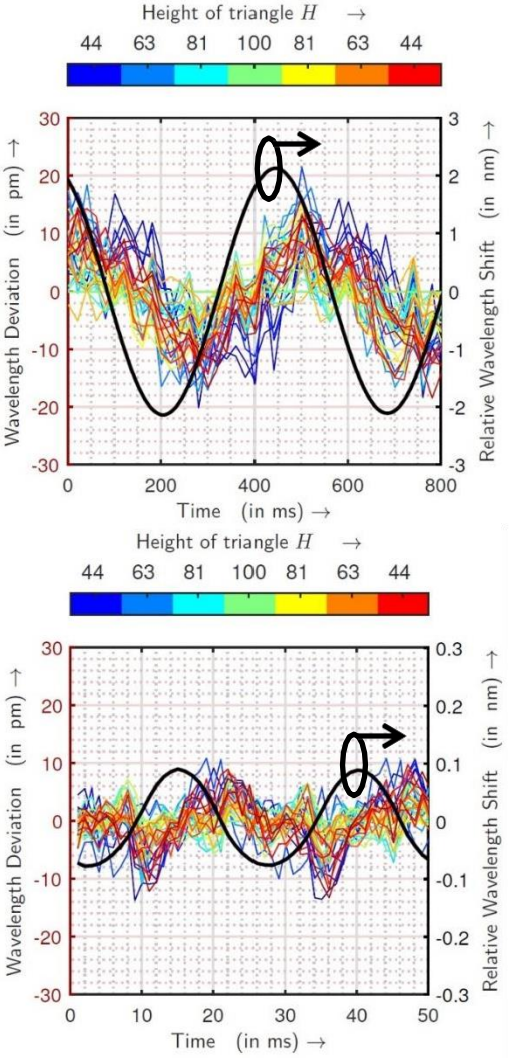

Figure 8: Measured wavelength deviation over time parameterized by the height of the synchronization triangle H in comparison with the reference wavelength shift of the synchronized sensor (H = 100%) at f = 0.5 Hz, A = ± 2.1 nm (top) and f = 40 Hz, A = ± 0.08 nm (bottom).

The obtained difference spectra are analyzed by using a three-point Gaussian fit algorithm to determine the peak wavelengths. To compare the different peaks, first the relative wavelength shift $(\lambda-\lambda_0)/\lambda_0$ is calculated with λ_0 being the mean-value of each tracked peak wavelength. Then the result is multiplied with the Bragg wavelength of the sensor in the synchronization point (H = 100 %). The sensor in the synchronization point serves as a reference for the other sensors and the subtraction leads to the shown deviation results. The triangle heights considered range from 44% to 100%. Lower heights are ignored because they will not occur in practice due to the fact that 3 synchronization points are taken for each WDM section (start, middle and end).

It can be seen that the points with the lowest triangle height (blue and red data points) reach the largest deviation, in good correspondence with the theory. The largest deviations occur where the applied strain changes the fastest, which are the inflection points of the sinusoidal curve. At the extrema, the actual wavelength shift is close to zero, which leads to the minimum of wavelength deviation. It should be noted that other influences, such as data point constellation, accuracy of the peak tracking algorithm and shading effects are also part of the wavelength deviation. The absolute deviation for slow but large sinusoidal applied strain reaches maximum 18 pm for triangle heights down to 44 %. For faster but smaller sinusoidal applied strain, the corresponding absolute deviation reaches up to 13 pm for heights down to 44 %. The corresponding actual wavelength shift between the direct and inverted spectrum can be calculated from the derivative of the curve and results in 32 pm (corresponding to a wavelength rate of 64 nm/s) and 26 pm (corresponding to a wavelength rate of 52 nm/s) for the weight and vibration shaker strain test respectively. Comparing the obtained results with Figure 7, one can see the equivalence with the theoretical approach as it states a deviation of ±15 pm for an actual wavelength shift of ±32 pm and ±12 pm for a shift of ±26 pm at a triangle height of 50 %.

5. CONCLUSIONS

In this work, the InfinityScan® has been presented. It is an interrogator used to measure dense arrays of low reflective DTG®'s. The sensing fibers are typically composed of a repeated pattern of a particular WDM section. The total number of sensors can range from several hundreds to even several thousands. The method to do so is based on Code Division Multiplexing (CDM), in combination with WDM. The operating principles of this method have been presented.

In addition, wavelength precision measurements have been done on an exemplary CDM / WDM sensing network, containing 10 identical WDM sections placed in series within the same optical fiber. Each section contains 20 different DTG®s. The wavelength information is pieced together from the measurement of 21 difference spectra with a specific delay setting. In general, all precision values (1σ) remain within the range of (1.0 ± 0.8) pm and no significant correlation with the position of the WDM section could be observed for the tested fiber configuration.

Finally, also the effect of dynamic measurements has been investigated, both theoretically and experimentally. It could be demonstrated that the sequential read-out during dynamic conditions has a limited influence on the wavelength readings. A stated deviation of ±18 pm could be observed for a wavelength rate of 64 nm/s and ±13 pm for a wavelength rate of ±52 nm/s at a triangle height of 44 %. Results were demonstrated to be in good concordance with the theoretical approach. Therefore, an analytical tool to assess accuracies of different topologies of sensor networks interrogated with the CDM-WDM scheme is established. Further possible improvements could be to have more synchronization points within a section and to use the synchronization triangle only in a narrower part. In addition, increasing the acquisition rate will reduce the wavelength shift between 2 sequential reads and hence a smaller deviation in dynamic measurements can be expected.

REFERENCES

[1] M. A. Riza, Y. I. Go, S. W. Harun, and R. R. J. Maier, **FBG Sensors for Environmental and Biochemical Applications—A Review**, IEEE Sensors Journal 20, 7614–7627, july 2020.

[2] Tochaei, E. N., Fang, Z., Taylor, T., Babanajad, S., and Ansari, F., **Structural monitoring and remaining fatigue life estimation of typical welded crack details in the Manhattan Bridge**, Engineering Structures 231, 111760, March 2021.

[3] Ma, G.-M., Zhou, H.-Y., Li, Y.-B., Zhang, H.-C., Qin, W.-Q., Li, C.-R., and Yan, C., **High-Resolution Temperature Distribution Measurement of GIL Spacer Based on OFDR and Ultraweak FBGs**, IEEE Transactions on Instrumentation and Measurement 69, 3866–3873, June 2020.

[4] Rajan, G., **Optical Fiber Sensors: Advanced Techniques and Applications**, CRC Press, Taylor & Francis Group, Boca Raton, Feb. 2015.

[5] Lindner, E., Mörbitz, J., Chojetzki, C., Becker, M., Brückner, S., Schuster, K., Rothhardt, M., and Bartelt, H., **Draw tower fiber Bragg gratings and their use in sensing technology**, in Fiber Optic Sensors and Applications VIII, Mihailov, S. J., Du, H. H., and Pickrell, G., eds., SPIE, May 2011.

[6] Götten, M., Lochmann, S., Ahrens, A., Lindner, E., and Van Roosbroeck, J., **2000 Serial FBG Sensors Interrogated With a Hybrid CDM-WDM Scheme**, Journal of Lightwave Technology 38, 2493–2503, April 2020.

[7] Götten, M., Lochmann, S., Ahrens, A., Lindner, E., Vlekken, J., and Van Roosbroeck, J., **A CDM-WDM Interrogation Scheme for Massive Serial FBG Sensor Networks**, IEEE Sensors Journal 22, 11290–11296, April 2

[8] M. Götten, S. Lochmann, A. Ahrens, E. Lindner, J. Vlekken, and J. Van Roosbroeck, **4000 Serial FBG Sensors Interrogated with a Hybrid CDM-WDM System**, 2020 IEEE SENSORS, Rotterdam, Netherlands, 2020, pp. 1-4, doi: 10.1109/SENSORS47125.2020.9278764

65: THREE-DIMENSIONAL DETECTION OF BURIED DEFECTS USING INFRARED FLASH THERMOGRAPHY: ANALYTICAL FRAMEWORK, SIMULATION AND EXPERIMENTAL VALIDATION

Charlie J. O'Mahony [a] *, *Aladin Mani* [a], *Joanna Bauer* [b], *Christophe Silien* [a], *Syed A. M. Tofail* [a]

[a] Department of Physics, and Bernal Institute, University of Limerick, Ireland
[b] Department of Bioengineering, Wroclaw University of Science and Technology, Poland
* Corresponding author

Applications Cont., EM009, August 14, 2024, 11:00 AM - 12:10 PM

Abstract – Buried defects occur below the surface of an object. Their thermal properties can lead to changes in the temperature of the surface due to non-symmetrical diffusion through the material. It is possible to detect these defects from the variation of the surface temperature even though they are buried deep inside material. In doing so, the relationship of the contrast obtained at the surface due to buried defects must be linked to the shape and the location of the defect. Initially, we tackle this by reducing a region of interest in three-dimension (3D) to a two dimensions (2D) problem with respect to peak contrast time, or positions from the surface. Both simulation and experimental thermograms were used to determine their detectability in 3D. We used known materials of known shape at known distances beneath the surface. We will start with a theoretical 2D assessment of the problem, as well as 2D simulations, operating as a cross sectioning of the 3D problem. This is a suitable simplification when considering heating along one axis, yet still leads us to a 3D-Infrared Thermography methodology using angled excitation that enables observe changes in surface temperature due to geometry and location of buried defects.

Keywords: Thermography, buried defects, non destructive testing (NDT), flash thermography.

1. INTRODUCTION

Infrared Thermography (IRT) is the process of mapping infrared radiation emitted from an object due to blackbody radiation. The usual wavelength range of detection is from 9-14 μm with temperature ranges between 225-1200 K. It gives a non-invasive method for visually measuring the surface temperature of an object. All objects of temperature above 0K emit infrared radiation, in accordance with black body radiation laws. The diffusion of heat through an object is highly dependent on the object's material properties such as heat conductivity, density of the material, etc. at and below the surface. Because of this, with the addition of a transient heat flow, surface temperature is affected by any inhomogeneity on and below the surface [1-4].

The addition of an angled excitation of heat, e.g. that by a flash, can provide qualitative information in 3D of the length and the depth of a buried geometry. The relationship of these two information must be linked to the surface contrast values seen in the thermogram. It can be difficult to consider simple variables as the measure of defects shapes, since the thermograph observed at the object surface is dependent on both the time it takes for heat to flow to the surface as well as the distance of the defect. This is explained in Figure 1 and Figure 2.

In this article, we reduce the problem to a two dimensional analytical framework to analyse the thermograph of a region of interest be it the peak contrast time or location of the defect buried under the surface. We start with a theoretical 2D assessment of the problem to carry out simulations of thermography in 2D, thus operating as a cross sectioning of the 3D problem. This is a suitable simplification when considering heating along one axis, leading to test the computational feasibility of 3D-IRT from angled excitation. [5-6]. This, in turn, allow us to determine the feasibility of the detection of buried defects in 3D both through simulation and experimental validated simulation.

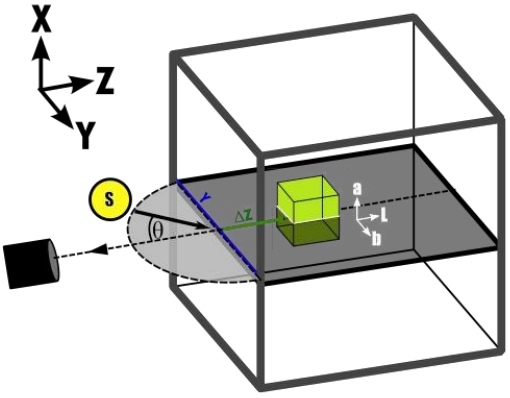

Figure 1. Defining the geometry directions, with respect to the flashed or incident face. This allows for easier explanation of "Z-direction" information, defect length and its depth.

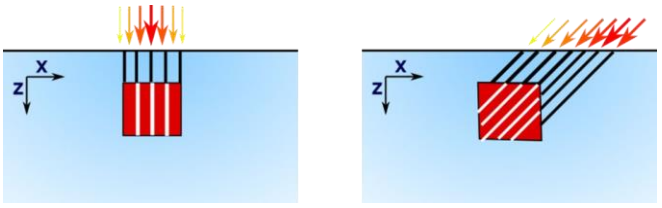

Figure 2. Schematic showing the path length of excitation and return of signal. For 0°, the distribution is symmetrical, and surface of defect is the same at all points of the defect (for this square faced defect) and for 45° the heat distributes towards the direction the heat source has been angled, the peak contrast point will be at the edge point, with the front surface and length edge appearing afterwards. Time, in flash thermography can be thought of as analogous to focusing a microscope lens through the z-axis, with reducing resolution in depth.

DOI: https://doi.org/10.34961/researchrepository-ul.29302199.v1

1. METHODS AND PROCEDURES

1.1. Experimental methodology

A list of materials used for experiments and simulation are listed in Table 1. Objects for testing were designed as 50 mm x 50 mm x 25 mm blocks containing square defects or a hollow section for the variation of defects. Materials used as objects were either paraffin wax or poly lactic acid (PLA). Defects were similarly set as 10 mm x 10 mm area with varying depth. steel nuts or thin aluminium sheets were used as defect materials. The experimental setup (Figure 3) consisted of a movable stage, an optic fibre broadband light source for excitation, a thermal camera (FLIR A655sc), and a temperature/pressure sensor (PASPORT PS-2146).

Table 1. Material properties used in experimentation and simulation obtained from literature.

	PLA	Paraffin Wax	Steel	Air	Aluminium
Density / [kg/m3]	1252	910	7900	1.225	2700
Heat Capacity / [J/kg*K]	1590	2000	480	1000	900
Thermal Conductivity / [W/(m*K)]	0.111	0.24	17	0.025	229
Surface Emissivity	0.8		0.16	-	0.04
Dimensions / L x W x B [mm]	10 x 10 x 5	50 x 50 x 30	10 x 10 x 3	-	

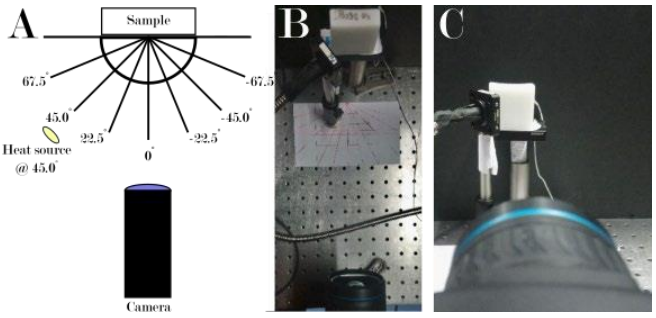

Figure 3. A: A schematic diagram of the experimental setup. B: A top-down view of the setup C: in-plane view of camera, observing the surface of interest of the defect.

1.2. Multiphysics Simulation

All finite element modelling was conducted using COMSOL™ Multiphysics, a finite element analysis, solver and Multiphysics simulation software. When considering our study, we use Multiphysics simulation to enable the use of thermal radiation in a participating medium along with the thermal conduction associated with the radiation's absorption into the object. Simulation, with validation also enables us to narrow the inverse problems variables, with the validated model describing the properties and values of relevance to 3D-IRT, while removing external, unconsidered variables such as noise. COMSOL™ specifically was used due to the use of both time dependent thermal radiation ray shooting and thermal conductivity, which this problem requires.

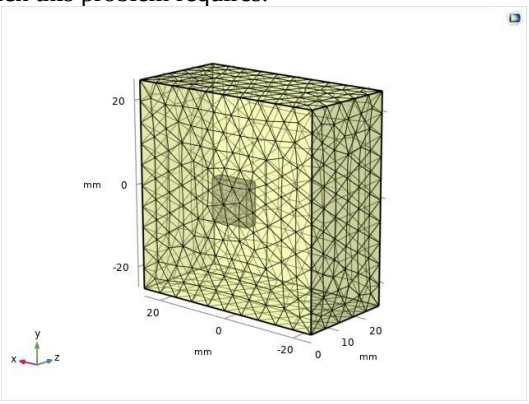

Figure 4. 3D thermal radiation simulation, 50 mm x 50 mm x 30 mm PLA block, with an aluminium defect with the example parameters 10 mm width, 10 mm height and 3 mm length defect 2 mm deep into the object. Heating angle is exemplified with a yellow rectangle, for 0° heating.

Modelling used surface-to-surface radiation heat transfer. The model setup was a wax rectangle of 50 x 50 mm^2 and a depth of 30 mm (Figure 4), with a steel square nut (3 mm width) within it. This defect was placed at 2 mm depth, to be of similar scale of the defect and allow for strong image contrast from the flash thermography method. A heat source varied between the angles of 0° and 60° was placed 20 mm away from the object. The object was heated with a single pulse, at t = 0 s for 30 s, after which the radiation source intensity reduced to zero. The objects are left to cool for 15 minutes between measurements to allow the object to return to room temperature throughout the object, minimizing thermal history in the object. The simulation was run for 60 s of cooling after this (total time 90s), to determine the highest point of contrast.

The in-plane wave propagation induced by the non-uniform heat radiation of the light source is significantly affected by the interfaces between the defects and bulk, with thermal heat propagation and hence thermal signature present on the surface.

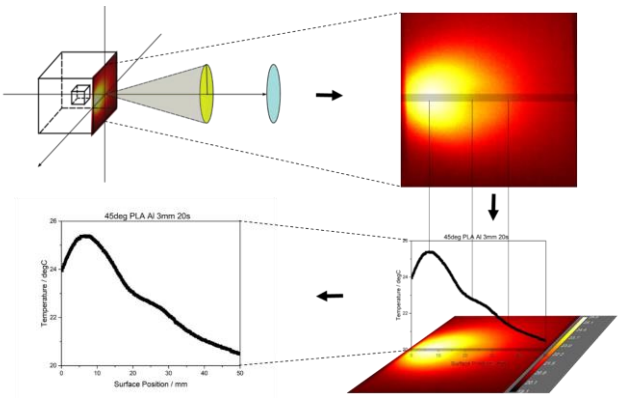

Figure 5. Image representation of "surface position" measurement. Cross profile temperature is taken at the midpoint, left to right. Reducing the surface temperature measurement to its horizontal profile temperature, the impact of defects, their material and geometries can be measured and parameterized.

1.3. Analysis methodology

Figure 5 shows the process of reducing a 2D thermogram to a 1D Temperature vs Surface position for analysis. Due to the importance of quantification in determining the effects of length and depth in angled excitation, we need to reduce the surface temperature of thermograms to a useable, quantifiable measurement. The first approach we can make is cross profiling the surface temperature of the object. This reduces the thermogram to a 1D curve of temperature vs position at a given time. This central profile is suitable, considering the angle of variation is along this axis, meaning the largest variation would be expected to be seen along this central cross profile.

For analysing defects, a simple subtraction of a thermogram with and without any defect will be standard practice to obtain defect contrast created solely by the defect to inform us of its shape. In angled thermography, surface thermograms represent non-symmetrical excitations reducing complicated surface shapes to contrasts, which informs us about the variation of defects, if any. Expanding this, due to the having possible effects in terms of thermogram surface temperatures, Furthermore, a pseudo "0 mm" aluminium defect (limiting thickness 0.0 2mm foil) was subtracted to take into account of potential contributions from optical activity of highly reflective or low emissivity defects. The subtraction of the 0 mm defect and its reflection gave consistent thermal diffusion though the object, whereas the no defect baseline subtraction presented peaks at the defect centre (seen at 22.5 mm in Figure 6).

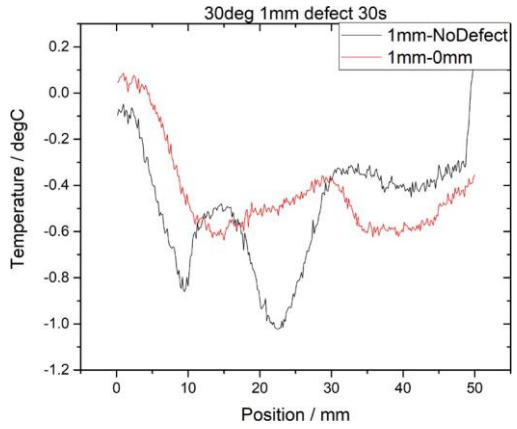

Figure 6. Comparison of subtraction methods for analysis. No defect subtracts the object without an internal defect, meaning any effects of thermal and boundary variations are presented in the surface profile. 0mm subtracts a thin layer of the defect from other lengths of the defect. This should isolate thermal variations, as boundary effects and reflection effects will occur at a "0 mm" layer similarly to an X mm defect of same material.

2. RESULTS AND DISCUSSION

2.1. 2D Simulation Results for Conduction

Despite being dependent on the diffusivity of the material, temperature increase or decrease put in the same amount of heat energy Q to a region of interest leading to a faster or a slower flow of heat through the material, which in turn effects the surface temperature. This is shown in Figure 7 and Figure 8 through simulation, where we varied the diffusivity of the defect, with an arbitrary heat applied. We used arbitrary measurements of heat and temperature of the "surface", comparing the ratio effect on ΔT from the material variation of the defect. We have, for example, measured 10 seconds of heating to allow thermal diffusion from the defect to generate contrast without any relaxation or cooling time allowed this will be determined at a later stage and is material variable, meaning delay times would bias material depending. Figure 8 shows the effect when the heat source is at 10mm left of the defect.

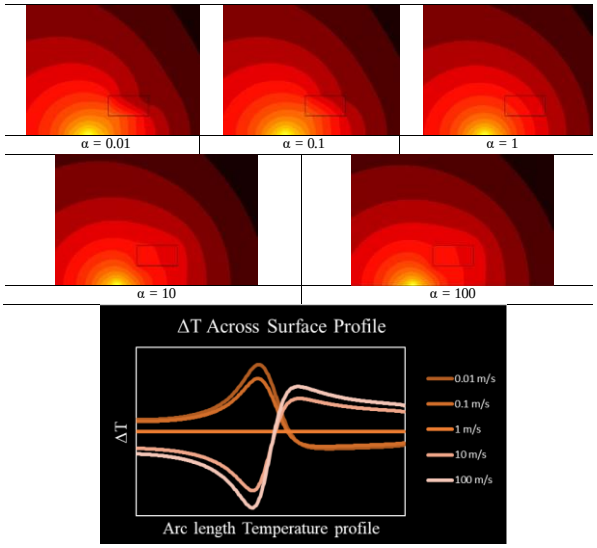

Figure 7. Temperature distribution of a point heat source on the surface of a semi-infinite region with a smaller finite region within it, though this heat source has been moved 10mm left of the centred heat source. The diffusivity, α, was varied in the finite region and compared to α=1, the same value as the semi-infinite region.

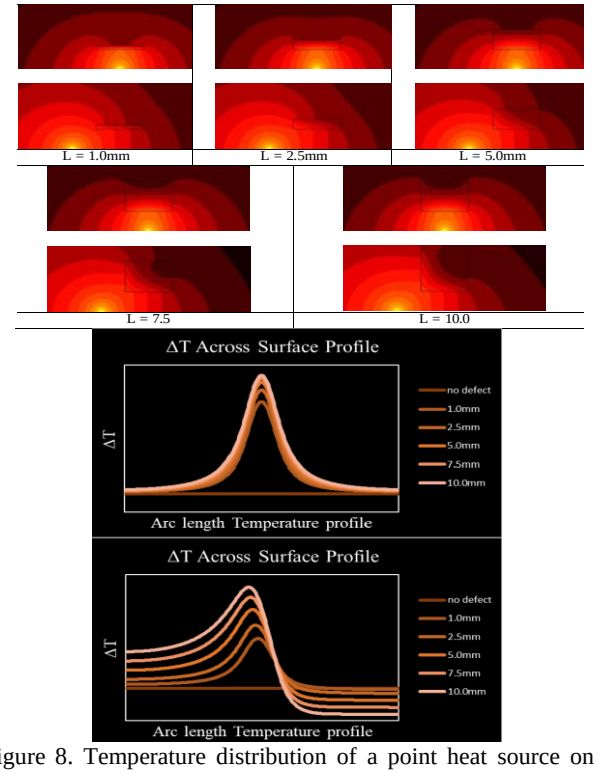

Figure 8. Temperature distribution of a point heat source on the surface of a semi-infinite region with a smaller finite region within it, though this heat source has been moved 10 mm left of the centred heat source. The diffusivity, α, was varied in the finite region and compared to α=1, the same value as the semi-infinite region.

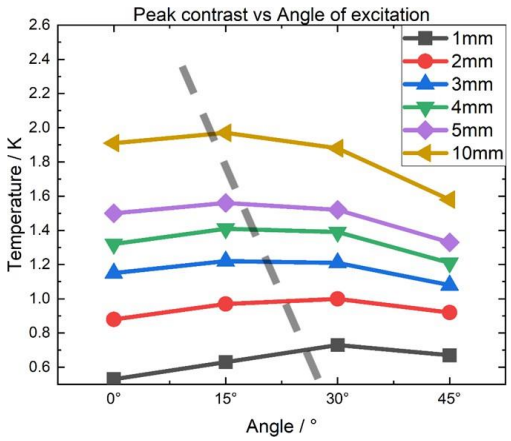

Figure 9. Peak contrasts vs the angle of excitation, for defects 1mm, 2mm, 3mm, 4mm, 5mm and 10mm. A dotted line presents the hypothetical peaks of each of these curves, although with 4 points, this assessment is limited.

Determining whether, and to what extent heat conduction alone can tell us about the location and full geometry of a defect (e.g. depth and length). By keeping the material constants (bulk material $\alpha = 1$ m/s and defect material $\alpha = 0.01$ m/s) while varying the defect depth we observe an overall increase in the temperature largely in line with an increased volume of low diffusion material. The moving of the heat source increased the contrast between 1 mm and 10 mm. We need to separate the depth from the volume, to interpret whether angled heating presents any significant contrast from conduction only heating. This can be investigated through varying the depth and width while keeping the volume constant

An important aspect for understanding the effectiveness of this method is to understand the results of defect length back behind its nearest surface to the objects surface, from angled heating. With the intentions of being able to reconstruct the 3D geometry of a defect from the heated surface of the object. Knowing the correct depth, the length determination is crucial to any reconstruction methods, as this generally is the unknown dimension for flash thermography.

Adding to this is the transmission of light through the object. When we consider the optical flash impinging on the surface of an object, more that complete symmetrical thermal conduction of the energy, reflection and transmission occur. In terms of our measurement, reflection will only affect the absolute heat applied, transmission on the other hand, gives directional shape to the thermal diffusion, through optical absorption. Allowing for this, we look at the thermal pathing of directional heat transport through the object with the use of light pulses.

From these results, we see that the smallest two defects, 1 mm and 2 mm have the highest contrast temperature at 30°. 3 mm, 4 mm, 5 mm and 10 mm have the highest contrast temperature at 45°. What these suggest is that angle has a peak contrast relative to length, meaning with a more granular angle sweep, we could detect the length and its related peak contrast. In line with this, the 3 mm length defect appears to maintain similar contrast between 15° and 30°, suggesting an optimal angle between them. These peak contrasts are shown in Figure 9.

Another approach employed in an attempt to quantify the effects of angled excitations on buried defects geometry, are temperature profile heatmaps. Temperature profile heatmaps utilize the 1D cross profile temperatures, stacked over the time frame of 60s of cooling, heat mapping the temperature or its contrast (defect profile temperature with the No defect profile temperature subtracted).

3. CONCLUSIONS

The aim of this work was to examine active thermography imaging with use of novel excitation methods so as to determine the 3D shape of buried defects. A first principles approach was taken to examine the impact of buried defects on the surface temperature of an object, after thermal excitation. In doing so the effect of defect length, defect depth, defect geometry, defect material and excitation angle were examined, with the model predictions compared to the experimental results.

This study examined the variables that effect buried defect signal with respect to active thermography. It was shown that a finite element model can exhibit similar surface thermograms to the simple experimental setup. It was found that the relationship of defect length directly effects the surface contrast, even if defect volume is maintained the same. What this tells us is that the geometry itself can be measured through thermal conduction.

The effect of defect length and depth was measured and proven to show experimental signs of defect length and depth having signature effects on the surface thermogram of an object.

ACKNOWLEDGMENTS

The work received travel support from Erasmus Bilateral Exchange Programme between the University of Limerick, Ireland and Wroclaw University of Science and Technology, Poland.

REFERENCES

[1] S. Tofail, A. Mani, J. Bauer, and C. Silien, ‘In Situ, Real-Time Infrared (IR) Imaging for Metrology in Advanced Manufacturing’, *Adv. Eng. Mater.*, vol. 20, p. 1800061, May 2018, doi: 10.1002/adem.201800061.

[2] S. M. Shepard, J. R. Lhota, and T. Ahmed, ‘Flash thermography contrast model based on IR camera noise characteristics’, *Nondestruct. Test. Eval.*, vol. 22, no. 2–3, pp. 113–126, Jun. 2007, doi: 10.1080/10589750701448662.

[3] S. Shepard, J. Lhota, and T. Ahmed, *Measurement limits in flash thermography*, vol. 7299. 2009, p. 72990T. doi: 10.1117/12.820062.

[4] J. G. Sun, ‘Quantitative Three-Dimensional Imaging of Heterogeneous Materials by Thermal Tomography’, *J. Heat Transf.*, vol. 138, no. 112004, Jul. 2016, doi: 10.1115/1.4033998.

[5] C.-Y. Chen, C.-H. Yeh, B. R. Chang, and J.-M. Pan, ‘3D Reconstruction from IR Thermal Images and Reprojective Evaluations’, *Math. Probl. Eng.*, vol. 2015, p. 520534, Aug. 2015, doi: 10.1155/2015/520534.

[6] D. Ledwon, A. Sage, J. Juszczyk, M. Rudzki, and P. Badura, ‘Tomographic reconstruction from planar thermal imaging using convolutional neural network’, *Sci. Rep.*, vol. 12, no. 1, p. 2347, Feb. 2022, doi: 10.1038/s41598-022-06076-z.

66: On-Site Rapid Detection of Ethidium Bromide Using Ultramicroelectrode Sensors

1Marcello Valente, 1Ian Seymour, 1Md Ridwan Adib, 1Tarun Narayan, 2Valentina Alessandria, 2Luca Cocolin , 3Kieran G Meade , 1Alan O'Riordan

1 Tyndall National institute, UCC, Cork, Ireland
2 DISAFA., University of Turin, Grugliasco, Italy
3 UCD School of Agriculture and Food Science, University College Dublin, Belfield, D04 V1W8, Dublin, Ireland.
UCD Conway Institute of Biomolecular and Biomedical Research, University College Dublin, Belfield, D04 V1W8, Dublin, Ireland.
Corresponding author

Abstract – Ethidium bromide (EtBr) is one of the most fluorescence-based detection of nucleic acids molecule. It also shown to be potentially dangerous due to damage at mitochondrial genome. In the last 10 years, EtBr has also been shown to be electrochemically active. In this work, we show the modification of an ultra-micro electrode sensor and subsequent detection of EtBr from Phosphate buffer on a nanomolar level (LoD of 12 nM). The sensor can detect concentrations with a higher sensitivity and reliability than the classic UV lamp in a practical manner. This novel sensor may offer a potential solution to test for and reduce potentials risks associated with both job related risk and unwanted environmental release of EtBr.

Keywords**:** Ethidium bromide, chemosensor, electrochemical detection, electrochemestry

1. INTRODUCTION

Many molecules of the phenanthridine group are used as fluorescence tags in gel electrophoresis due to their high quantum efficiencies and stability [1], [2], [3]. Ethidium bromide (EtBr) is one of the most used phenanthridine compounds, due to its ability to bind nucleic acids, and has been documented in the literature since 1964 [4]. It is typically seen as the gold standard of the florescence tags [5] used for gel electrophoresis [6], [7], [8]. More recently it is being used to assess anti-toxicity studies in bacteria [9]. The ability of EtBr to bind to DNA comes with caution since it has also been shown to stop the nucleic acids synthesis in Strigomonas oncopelti [10], damage the mitochondrial circular DNA [11], [12], [13]and cause mutations in DNA [14]. Despite these negatives, ethidium bromide is still a well-used dye [15] with it ability to bind to different sites on the dsDNA, for which it has a preference, and also to ssDNA structures [16], [17]. Recently, EtBr is also used as an electrochemical probe molecule [18]. The oxidation of EtBr has been studied using cyclic voltammetry on these, on a variety of working electrode materials such as boron-doped diamond [19] mercury drop systems [20] and large gold electrodes [21] and has been used to electrochemically detect EtBr that is bound to DNA complementing fluorescence approaches [22].

EtBr has also been used as a pest control with the toxicity of molecule gaining awareness in 1970s. EtBr was shown to cause consistent damage to mitochondrial [23], [24], [25], [26] ribosomal DNA [27] and non-nuclear DNA in different models leading to neurodegenerative disorders and higher risk of tumorigenesis [28], [29] [30]. Long term effects of EtBr induced mitochondrial DNA damage leading to rapid cellular ageing [31] for the single individual and call also lead to infertility or other reproductive problems in animal models specifically infertility or early menopause [32], [33] or spontaneous abortion [34] while damage to Male sperm's mitochondria is also possible [35]. To this end, the risk for mitochondrial has resulted in stringent Health & Safety procedures regarding EtBr use and, more specifically, concerning its disposal and detection [36]. Concerning electrochemical detection of EtBr, reports in the literature exhibit limits of detection typically in the micro molar concentrations of range. This limitation of detection may not be fit-for-purpose for on-site detection as smaller concentrations of this substance may cause damage over time; thereby highlighting the need for a more sensitive detection method [37], [38]. To date, electrochemical methods have been more successfully applied to remediation of the molecule [39], [40], [41] rather than detection.

In this work, we develop a sensitive electrochemical based sensor, incorporating solid-state ultramicroelectrode sensors, that allows detection of EtBr contamination (nanomolar) in real time and apply this to the detection of EtBr of swab samples from a microbiology laboratory. Our approach is shown schematically in Figure 1. First a cotton swab is wiped across to the area under test and then immersed in 0.5 mL of phosphate buffer and let stand for 5 minutes. The buffer is then agitated to ensure a homogeneous mixture and the placed into the sample well of a chip holder. Electrochemical analysis is then undertaken, and an EtBr concentration (time to result) obtained after 12 seconds. The approach is rapid and yields quantitative results unlike current approaches using dyes or a UV lamp [42].

DOI: https://doi.org/10.34961/researchrepository-ul.29302235.v1

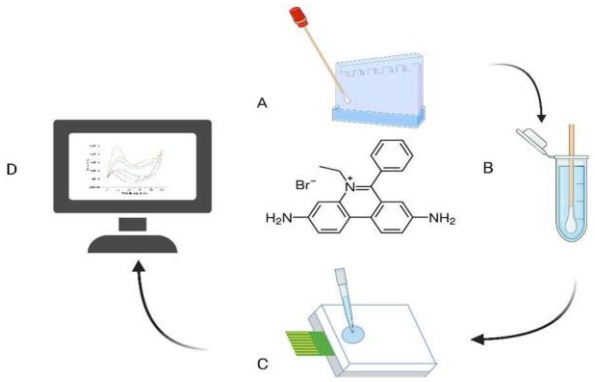

Fig. 1 schematic showing EtBr detection approach. (A) swabbing and sampling of surfaces with different potential levels of contamination risk e.g., the sample is taken from the surface where a spill or a surface where contamination is present, (B) the head of a swab is then immerse in 500 µL of phosphate buffer pH 7, (C) the liquid is transferred to the sample well of a sensor chip holder (D) analysis is undertaken and displayed visually in twelve seconds.

2. METHODS AND PROCEDURES

2.1 Chemicals

EtBr 1% solutions, sodium phosphate dibasic heptahydrate, sodium phosphate monobasic monohydrate, ferrocene carboxylic acid, PBS tablets, AuCl trihydrate, sodium acetate and acetic acid (Sigma-Aldrich) were used for XXX. 10 mM phosphate buffer (PB) was prepared by dissolving 1 tablet in 250 mL with deionized water (Elgapure, 1018 Ω). EtBr 1% solutions were then diluted with PB to prepare a stock solution of 512 nM which was then further diluted to prepare standard solutions of 256 nM, 128 nM, 64 nM, 32 nM, 16 nM and 8 nM.

2.2 Electrochemical deposition and analysis

Chronoamperometry was employed to deposit nanogold on the electrode surfaces using an optimized voltage for a set time (see results section) . Cyclic Voltammetry (CV) and electrochemical impedance spectroscopy (EIS) was employed for electrode characterization, while square wave voltammetry was used for EtBr detection. All electrochemical analysis was undertaken using a multi-autolab M101 operating under Nova 1.0.4 software control (Netherlands). Electrochemical deposition employed an off-chip Ag/AgCl reference electrode and on-chip counter electrode, while the EtBr detection was undertaken using the on-chip Pt pseudo-reference and on-chip gold counter electrodes.

2.3 Sensor Fabrication

Silicon Chip fabrication was undertaken as described in previous publications[43], [44], [45]. In brief, four-inch silicon wafer substrates bearing a 300 nm thermally grown silicon dioxide layer were used. Working electrodes were first fabricated using optical lithography, metal evaporation (Ti 10 nm /Au 50 nm Temescal FC-2000 beam evaporator) and lift-off techniques to yield well-defined, stacked metallic (Ti/Au) microband (1 µm width, 50 nm height, 45 µm length) structures. Optical lithography and metal deposition (Ti 10 nm/Ni 70 nm/Au 200 nm) process was again undertaken to define a MicroSD pin-out, on-chip metal interconnection tracks, as well as counter and reference electrodes. Finally, a passivation Si3N4 layer was deposited on the chip by PECVD, with windows opened in this layer directly above the working, reference and counter electrodes and SD pinouts. The windows defined the length of the working electrode to be 45 µm. A PCB bearing a mounted microSD port connector structure was designed and fabricated to allow facile connection between the microSD primary contact pads with the potentiostat. In this manner, the microSD electrical pin-out enabled rapid and easy electrical connection to external electronics, enabling sensors to be used as a portable field sensor. Each silicon chip comprised six independent sensors containing two interdigitated electrode (IDE) structures, a platinum counter electrode, and a platinum pseudo-reference electrode. Gold contact pads and interconnection metallisation on two sides of the chip allowed electrical connection to both interdigitated structures. Figure 2 shows an optical micrography of a fully fabricated chip (based on previous designs) the SEM image shows a high-resolution image of a typical sensor device [29] [30]. IDEs were selected due to possibility of using localized pH control of the solutions for the ethidium bromide should this be required [43]. Finally. a custom-made holder cell constructed from an aluminium base and a Teflon™ lid was fabricated to allow measurement in small electrolyte volumes (≈500 µL). The cell was included a Viton O-ring, chosen for their chemical resistance, embedded in the lid which formed a seal around the on-chip electrodes. The inner diameter of the O-ring was 7 mm with a cross section of 1.6 mm which was of sufficient size to expose all six sensors, counter, and reference electrodes on the device to the electrolyte [43], [44].

2.4 Electrochemical characterization

Cyclic voltammetry (CV) was performed in 10 mM ferrocenecarboxylic acid (FCA) in 10 mM phosphate buffered saline (PBS) in the voltage range 0 -0 .6 V @ 100 mV s-1 using a commercial Ag/AgCl (Alvateck) external reference electrode. CVs were also undertaken in Ethidium bromide solutions in the voltage range 0 to -0.6 V @ 100 mV s-1 using the on-chip platinum pseudo-reference electrode. A Square wave voltammetry protocol for detection of Ethidium bromide was developed with the conditions 22 mV/s and 10 mV amplitude versus the

platinum on-chip reference electrode.

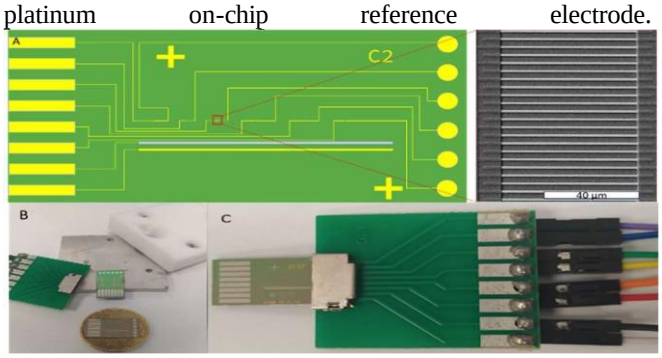

Fig. 2 (a) Structure of the sensor chip with a SEM zoom on the structure of the Working Electrode (b) Chip dimension comparison and relative holder and connector (c) Zoom on the SD chip connector.

2.5 Swabbing of contaminated surfaces

Surfaces were swabbed using a dry cotton swab over a ~20 x 20 cm area (400 cm2) for ~1 min (to ensure full loading of the swab). The head of the swab was then immersed in 500 uL of 10 mM sodium phosphate solution at pH 7 in a Eppendorf tube, closed and sealed with parafilm and stored prior to measurement. To undertake analysis, the Eppendorf tube was placed on a shaker for few seconds, then an aliquot of 500 µL was removed and pipetted directly onto a chip mounted in the chip holder and analyzed by CV.

3. RESULTS AND DISCUSSION

Initial experiments for detection of ethidium bromide were undertaken using fabricated chips. However, due to the smoothness of the gold electrode it was not possible to achieve an electrochemical response despite previous reports in the literature [46]. Following a review, it was theorized that a roughened gold surface with sufficient nucleation points was required for ethidium bromide absorption thereby allowing electron transfer to occur. To this end, electrode modification was undertaken initially using amperometry (E= -0.3 V, 80 s) in a solution of 400 ppm gold chloride in sodium phosphate buffer at pH 3. Figure 3(a) shows a SEM image of a typical gold deposition, exhibiting sharp "nanospike" structures at the edges of the electrodes. While this approach did roughen the surface, the formation of these nanospikes was stochastic and formed gold overlaps between the interdigitated electrodes resulting in short circuits with a consequent reduction in the overall yield of devices. To address this, a chronopotentiometric method was developed and the optimized protocol of applying 24 nA for 200 s resulted in a stable 0.4 um nanogold deposition on the working electrodes. All six sensors on a chip were electroplated simultaneously by temporarily electrically shorting them together. Figure 3(b) shows a typical SEM image obtained using the chronopotentiometric method. It is evident from the image that the gold deposited uniformly across the electrodes and no bridging between electrodes was observed.

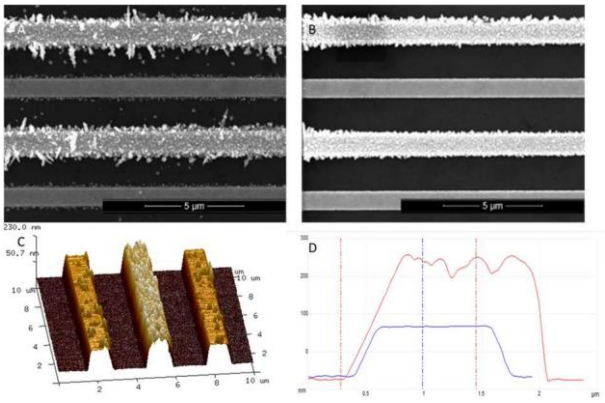

Fig. 3 SEM analysis of the working electrode interdigitated structure after the AuCl deposition. In (a) the amperometric over deposition on the interdigitated structure and the Imperfect depositions as the over deposition on the counterpart of the interdigitated working electrode. On the upper right the SEM of the deposition using chronopotentiometry in which the surface is deposited in a more coherent way and without the overdeposition in the other comb of interdigitated electrodes. In the lower images we can observe the AFM profiles of the rod deposited via chronopotentiometric protocol.

Electrochemical characterization was undertaken before and after electrode modification. Figure 4(a) shows typical CVs for both unmodified and modified electrodes. The bare gold electrodes exhibited quasi steady state behavior (black data) with a diffusion limited peak profile and increased hysteresis when compared to single microband electrodes. The nanogold modified electrode exhibited a higher peak current attributed to the increased surface area of the electrode when compared to the unmodified electrode. An increase in hysteresis was also observed. This diffusive limited behavior arose from analyte diffusion profiles at each band, in the IDE, overlapping resulting in the IDE behaving as a larger electrode. Figure 4 (a) and (b) shows typical CV from a modified and unmodified electrode undertaken at different scan rates. The near overlap of peak currents is indicative of semi-steady state behavior as occurs at low scan rates of these ultra-microelectrodes. The measure peak currents presented in Figure 4(b) following deposition of gold deposition show a significant increase when compared to the unmodified electrodes. This may be attributed to the increased surface area of the modified electrodes as agrees with previous report [47].

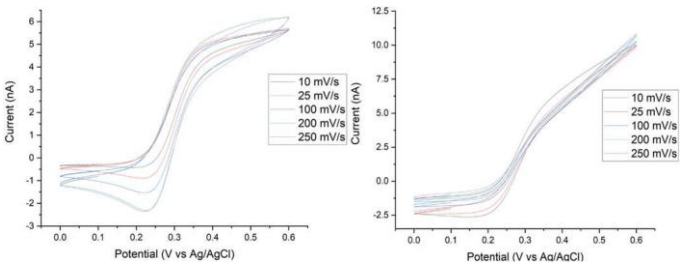

Fig.4 CV profiles of the WE using Ferrocine before (left) and after (right) the chropotentiometric deposition and the AuCl enriched WE after the detection of 256 nM of Ethidium Bromide.

We initially investigated the use CV as the electroanalytical method of choice for EtBr in the voltage range of -00.6 to 0.6 at 100 mV/s. However, no well defined

peaks were observed. To this end, square wave voltammetry 22 mV/s and 10 mV amplitude was employed. The use of a platinum on-chip reference electrode, over commercial Ag/AgCl reference electrodes, was preferred as it is solid-state and removed the need for any additional electrodes.[48]. Figure 5 (a) shows typical SWV obtained for different concentrations of EtBR. Well defined peaks, proportional to EtBr concentration, were observed at ~0.5v. Figure 5(a) shows a calibration curve plotted using the SWV peak currents presented in figure 5(b). Three different sensors were used for each concentration and, although tiny, the error bars are included in the data. Each data point represents the mean of three replicates and the error bars represent one standard deviation. The calibration curve resulted in a R2 of 0.99 with a sensitivity (slope) of 1.5 pA/pM The theoretical LOD was calculated as 12 nM using the equation 3xSD/slope which is significantly lower than the reported literature [18].

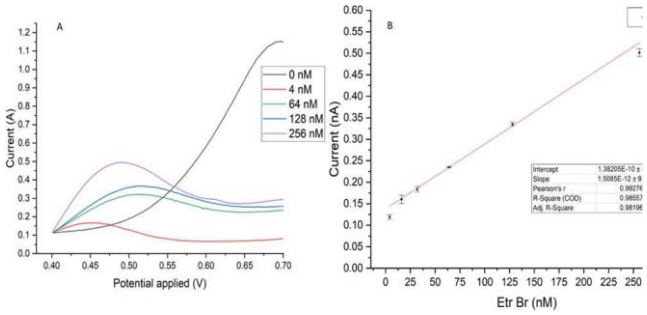

Fig.5 (a) Calibration curve for the different concentrations of EtBr (nM), with an LOD of 12 nM, (b) SWV profiles of the different concentration of [Ethidium bromide]

The SWV in figure 5 (a) exhibited a higher background current (possibly capacitive) after the EtBr oxidation event. This suggests that the redox process was influencing / modifying the electrode in some manner possibly by electrodepositing at an electrode surface. This is known to happen at commercial macroscale glassy carbon electrodes; that are typically polished between measurements to remove any bound material. To understand if this was the case with gold electrode, we undertook further AFM analysis.

Figure 6 shows AFM images of a portion of a gold electrode prior to (left), and, after (right) EtBr detection. As can be seen, there is no clear difference in the two profiles heights but there is other than a slight reduction in the root means square roughness of the electrode, suggesting that if a passivation layer is present then it is extremely thin and that the as the heights didn't change the deposited gold did not delaminate from the electrode surface.

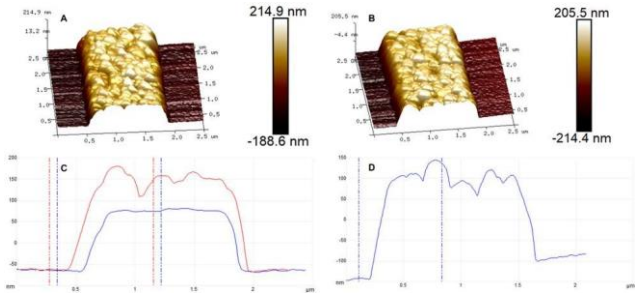

Fig.6 (A + C) AFM profile of a session of working electrode after the chronopotentiometric deposition, (B + D) profile comparison between undeposited (blue) and deposited working electrode's rode.

To confirm the presence of a passivation layer and elucidate changes in electrode behavior, CV and electrochemical impedance spectroscopy was undertaken at electrodes both pre and post EtBr detection in 5 mM FCA. The CV data presented in Figure 7(a) exhibited a significant decrease in current falling from ~12 nA to ~0.5nA following EtBr analysis. The observed hysteresis arises from capacitive charging of the electrode [44]. These results strongly suggest that a passivation layer is present. This is further supported by the EIS data presented in Figure 7(b) where the charge transfer resistance was observed to increase from ~100 kΩ for pre-ETtBR detection to 60 MΩ for post EtBr detection, which is clearly indicative of the presence of a passivation layer coating the electrode. It was observed that this passivation layer could not be removed by potentiodynamically cleaning approaches, indicating that the sensors are single use only.

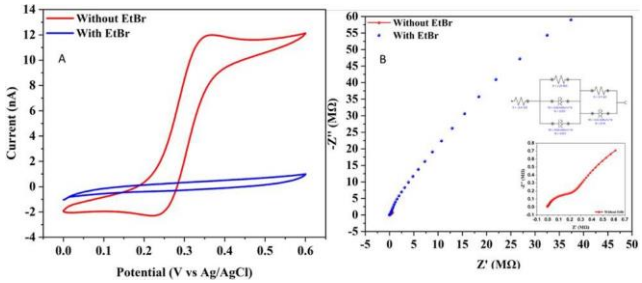

Fig. 7 Impedence profile of the sensor using Ferrocine 1 uM in PBS in different condition of deposition: after the Gold deposition using the previously described Chronopotentiometric protocol and after the detection of 256 nM of Ethidium Bromide; fig. A Use the CV using the previously protocol for Ferrocine deposition, fig. B is an impedence profile with the the circuit deduct using the potentiostat ANOVA software

To explore the applicability of the electrodes for EtBr detection, swabs were taken from different locations of a microbiology laboratory which regularly uses EtBr, a fluorescent label for nucleic acid detection. Three locations were selected where the potential for detecting EtBr was zero, low, and high, mainly: the post electrophoresis gel tray, the TAE (Tris-acetate-EDTA) buffer tray and the gel preparation fume hood and analyzed as described in the experimental section. Representative CVs with an image of the swabbed area are presented in Figure 8. As expected, zero or very low concentrations of EtBr were measured for the swabs taken from outside the fume hood. A significant concentration was measured for swabs taken inside the fume cupboard corresponding to ~250 nM of EtBr. This means that significant concentrations of EtBr remain on these surfaces despite UV and cleaning protocols. These results are important as they can inform the preparation of occupational risk assessments highlighting contaminated areas within a laboratory.

We field-tested the sensor on three different surfaces of a biotechnology lab with a long history of using EtBr for electrophoresis related activity. The first sample is the surface of the fume hood, used specifically to prepare agarose gels with EtBr, thus it has a high risk of

contamination being an area of intense activity in which the solution is used in its stock concentration. The second sample is the basin of exhausted gel, a surface which presents a moderate risk of contamination due to the leaks from the melting gel but mitigated by the UV exposure applied to the gels themselves. The last reading is an electrophoretic gel basin before use and therefore well cleaned a couple of days before.

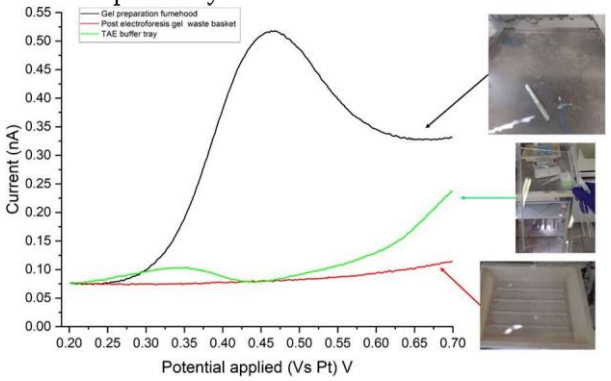

Fig. 8 Images from the surfaces of the laboratory, which samples has been taken and their relative risk of contamination due to different level of exposition and cleaning frequency. In (d) the graph with the curve together

Due to the limit of the SEM we also check the structure changes in the working electrodes before and after the exposure to Ethidium bromide, the data collected suggested a slightly decrease in roughness and volume relatable to the electrical current activity rather than a corrosion operated by the Solution or due to a potential binding between the component of the Ethidium Bromide and the surface. (Fig.8)

4. CONCLUSIONS

EtBr is commonly used in molecular biology labs and poses a risk to health and safety due to its potential mutagenic properties. In this paper we explored the possibility to develop an electrochemical sensor tailored for the reality of busy molecular biology labs in which the risk of spills related to the EtBr can still be considered a threat.

Using IDF electrochemical technology it has been proved possible to detect EtBr from an microbiology lab surface with a sensibility lower than the strict 12 nM concentration as required by the European law[27], the LoD of 12 nM represent also at the moment an important milestone to the use of EtBr as electrochemical probe for PCR-free procedures that usually operate between 10-9 and 10-8 nM of nucleic acids.

Further development will also focus on the ability to reuse the working electrode and improve the sensibility of the chip.

ACKNOWLEDGMENTS

This publication has emanated from research supported by a research grant from Science Foundation Ireland under SFi SFI-17/CDA/4717 and from Science Foundation Ireland and the Department of Agriculture, Food and Marine on behalf of the Government of Irelandunder the Grant 16/RC/3835 (VistaMilk)

REFERENCES

[1] [1] L. M. Tumir, M. R. Stojković, and I. Piantanida, ‘Come-back of phenanthridine and phenanthridinium derivatives in the 21st century’, Beilstein J. Org. Chem., vol. 10, pp. 2930–2954, Dec. 2014, doi: 10.3762/bjoc.10.312.

[2] [2] J. Matić et al., ‘DNA/RNA recognition controlled by the glycine linker and the guanidine moiety of phenanthridine peptides’, Int. J. Biol. Macromol., vol. 134, pp. 422–434, Aug. 2019, doi: 10.1016/j.ijbiomac.2019.05.063.

[3] [3] D. Saftić et al., ‘Impact of linker between triazolyluracil and phenanthridine on recognition of DNA and RNA. Recognition of uracil-containing RNA’, New J. Chem., vol. 41, no. 22, pp. 13240–13252, 2017, doi: 10.1039/c7nj02699d.

[4] [4] M. J. Waring, ‘Complex formation with DNA and inhibition of Escherichia coli RNA polymerase by ethidium bromide’, Biochim. Biophys. Acta BBA - Spec. Sect. Nucleic Acids Relat. Subj., 1964, doi: https://doi.org/10.1016/0926-6550(64)90238-5.

[5] [5] J. Olmsted III and D. R. Kearns, ‘ETHIDIUM FLUORESCENCE ENHANCEMENT MECHANISM Mechanism of Ethidium Bromide Fluorescence Enhancement on Binding to Nucleic Acids1"’, Springer-Verlag, p 21. Umezawa, H, 1972. [Online]. Available: https://pubs.acs.org/sharingguidelines

[6] [6] J. Olmsted and D. R. Kearns, ‘Biomedicine 18, 459. Umezawa, H. (1979, in Antibiotics 111’, Springer-Verlag, 1968.

[7] [7] F. Diaz, M. Pilar Bayona-Bafaluy, M. Rana, M. Mora, H. Hao, and C. T. Moraes, ‘Human mitochondrial DNA with large deletions repopulates organelles faster than full-length genomes under relaxed copy number control’.

[8] [8] K. Lalchhandama, ‘The making of modern biotechnology: how ethidium bromide made fame’. [Online]. Available: www.sciencevision.org

[9] [9] E. Rampacci et al., ‘Ethidium bromide exposure unmasks an antibiotic efflux system in Rhodococcus equi’, J. Antimicrob. Chemother., vol. 76, no. 8, pp. 2040–2048, Aug. 2021, doi: 10.1093/jac/dkab121.

[10] [10] B. B. A Newton, ‘The Mode of Action of Phenanthridines: The Effect of Ethidiurn Bromide on Cell Division and Nucleic Acid Synthesis’, 1957.

[11] [11] M. M. K. Nasst, ‘Abnormal DNA Patterns in Animal Mitochondria: Ethidium Bromide-Induced Breakdown of Closed Circular DNA and Conditions Leading to Oligomer Accumulation*’, 1970. [Online]. Available: https://www.pnas.org

[12] [12] P. Desjardins, E. Frost, and R. Morais1, ‘Ethidium Bromide-Induced Loss of Mitochondrial DNA from Primary Chicken Embryo Fibroblasts’, 1985. [Online]. Available: https://journals.asm.org/journal/mcb

[13] [13] T. Nacarelli, A. Azar, and C. Sell, ‘Inhibition of mTOR prevents ROS production initiated by ethidium bromide-induced mitochondrial DNA depletion’, Front. Endocrinol., vol. 5, no. JUL, 2014, doi: 10.3389/fendo.2014.00122.

[14] [14] L. I. Hernandez, M. Zhong, S. H. Courtney, L. A. Marky, and N. R. Kallenbach, ‘Equilibrium Analysis of Ethidium Binding to DNA Containing Base Mismatches and Branches’, Biochemistry, vol. 33, no. 44, pp. 13140–13146, Nov. 1994, doi: 10.1021/bi00248a025.

[15] [15] Y. Song et al., ‘A New Strategy to Reduce Toxicity of Ethidium Bromide by Alternating Anions: New Derivatives with Excellent Optical Performances, Convenient Synthesis, and Low Toxicity’, Small Methods, vol. 4, no. 3, Mar. 2020, doi: 10.1002/smtd.201900779.

[16] [16] R. Galindo-Murillo and T. E. Cheatham, ‘Ethidium bromide interactions with DNA: An exploration of a classic DNA-ligand complex with unbiased molecular dynamics simulations’, Nucleic Acids Res., vol. 49, no. 7, pp. 3735–3747, Apr. 2021, doi: 10.1093/nar/gkab143.

[17] [17] N. C. Garbett, N. B. Hammond, and D. E. Graves, ‘Influence of the amino substituents in the interaction of ethidium bromide with

DNA', Biophys. J., vol. 87, no. 6, pp. 3974–3981, 2004, doi: 10.1529/biophysj.104.047415.
[18] [18] S. C. B. Oliveira and V. B. Nascimento, 'Electrochemical oxidation mechanism of ethidium bromide at a glassy carbon electrode', Electroanalysis, vol. 25, no. 9, pp. 2117–2123, 2013, doi: 10.1002/elan.201300222.
[19] [19] C. Zhang, L. Liu, J. Wang, F. Rong, and D. Fu, 'Electrochemical degradation of ethidium bromide using boron-doped diamond electrode', Sep. Purif. Technol., vol. 107, pp. 91–101, 2013, doi: 10.1016/j.seppur.2013.01.033.
[20] [20] I. C. Gherghi, S. T. Girousi, A. N. Voulgaropoulos, and R. Tzimou-Tsitouridou, 'Study of interactions between DNA-ethidium bromide (EB) and DNA-acridine orange (AO), in solution, using hanging mercury drop electrode (HMDE)', Talanta, vol. 61, no. 2, pp. 103–112, Oct. 2003, doi: 10.1016/S0039-9140(03)00238-8.
[21] [21] X. Sun, P. He, S. Liu, J. Ye, and Y. Fang, 'Immobilization of single-stranded deoxyribonucleic acid on gold electrode with self-assembled aminoethanethiol monolayer for DNA electrochemical sensor applications', 1998.
[22] [22] R. A. M. S. Corrêa, F. S. Da Cruz, C. C. Santos, T. C. Pimenta, D. L. Franco, and L. F. Ferreira, 'Optimization and application of electrochemical transducer for detection of specific oligonucleotide sequence for mycobacterium tuberculosis', Biosensors, vol. 8, no. 3, 2018, doi: 10.3390/bios8030084.
[23] [23] A. E.-D. Salah El-Din, S. Abdullah, and A. E.-D. H. Sayed, 'Antioxidant capacity and DNA damage in Nile tilapia (Oreochromis niloticus) exposed to Ethidium bromide: A protective role for Spirulina Platensis', Sci. Afr., vol. 13, p. e00961, Sep. 2021, doi: 10.1016/j.sciaf.2021.e00961.
[24] [24] N. Von Wurmb-Schwark, L. Cavelier, and G. A. Cortopassi, 'A low dose of ethidium bromide leads to an increase of total mitochondrial DNA while higher concentrations induce the mtDNA 4997 deletion in a human neuronal cell line', Mutat. Res. Mol. Mech. Mutagen., vol. 596, no. 1–2, pp. 57–63, Apr. 2006, doi: 10.1016/j.mrfmmm.2005.12.003.
[25] [25] R. B. Uera, A. M. Paz-Alberto, and G. C. Sigua, 'Phytoremediation potentials of selected tropical plants for Ethidium bromide', Environ. Sci. Pollut. Res. - Int., vol. 14, no. 7, pp. 505–509, Nov. 2007, doi: 10.1065/espr2007.02.391.
[26] [26] M. Miko and B. Chance, 'Ethidium bromide as an uncoupler of oxidative phosphorylation', FEBS Lett., vol. 54, no. 3, pp. 347–352, Jul. 1975, doi: 10.1016/0014-5793(75)80937-9.
[27] [27] M. Lange and P. May, 'Effects of ethidium bromide on the production of ribosomal RNA in cultured mouse cells', Nucleic Acids Res., vol. 6, no. 8, pp. 2863–2877, 1979, doi: 10.1093/nar/6.8.2863.
[28] [28] F. M. Yakes and B. Van Houten, 'Mitochondrial DNA damage is more extensive and persists longer than nuclear DNA damage in human cells following oxidative stress', Proc. Natl. Acad. Sci., vol. 94, no. 2, pp. 514–519, Jan. 1997, doi: 10.1073/pnas.94.2.514.
[29] [29] A. S. Bess, T. L. Crocker, I. T. Ryde, and J. N. Meyer, 'Mitochondrial dynamics and autophagy aid in removal of persistent mitochondrial DNA damage in Caenorhabditis elegans', Nucleic Acids Res., vol. 40, no. 16, pp. 7916–7931, Sep. 2012, doi: 10.1093/nar/gks532.
[30] [30] Z. Rong et al., 'The Mitochondrial Response to DNA Damage', Front. Cell Dev. Biol., vol. 9, p. 669379, May 2021, doi: 10.3389/fcell.2021.669379.
[31] [31] L. J. Niedernhofer, A. U. Gurkar, Y. Wang, J. Vijg, J. H. J. Hoeijmakers, and P. D. Robbins, 'Nuclear Genomic Instability and Aging', Annu. Rev. Biochem., vol. 87, no. 1, pp. 295–322, Jun. 2018, doi: 10.1146/annurev-biochem-062917-012239.
[32] [32] E. Seli, T. Wang, and T. L. Horvath, 'Mitochondrial unfolded protein response: a stress response with implications for fertility and reproductive aging', Fertil. Steril., vol. 111, no. 2, pp. 197–204, Feb. 2019, doi: 10.1016/j.fertnstert.2018.11.048.
[33] [33] G. N. Cecchino, E. Seli, E. L. Alves Da Motta, and J. A. García-Velasco, 'The role of mitochondrial activity in female fertility and assisted reproductive technologies: overview and current insights', Reprod. Biomed. Online, vol. 36, no. 6, pp. 686–697, Jun. 2018, doi: 10.1016/j.rbmo.2018.02.007.
[34] [34] X.-L. Wang et al., 'Mitophagy, a Form of Selective Autophagy, Plays an Essential Role in Mitochondrial Dynamics of Parkinson's Disease', Cell. Mol. Neurobiol., vol. 42, no. 5, pp. 1321–1339, Jul. 2022, doi: 10.1007/s10571-021-01039-w.
[35] [35] M. Boguenet, P.-E. Bouet, A. Spiers, P. Reynier, and P. May-Panloup, 'Mitochondria: their role in spermatozoa and in male infertility', Hum. Reprod. Update, vol. 27, no. 4, pp. 697–719, Jun. 2021, doi: 10.1093/humupd/dmab001.
[36] [36] G. Lunn and E. B. Sansone, 'Ethidium Bromide: Destruction and Decontamination of Solutions1v2', 1987.
[37] [37] S. Singh, N. Singh, and A. N. Singh, 'Ethidium bromide: Is a stain turning into a pollutant? A synthesis on its status, waste management, monitoring challenges and ecological risks to the environment', Int. J. Res. Anal. Rev., vol. 5, 2018, [Online]. Available: https://www.researchgate.net/publication/341524958
[38] [38] A. Debroy, M. Yadav, R. Dhawan, S. Dey, and N. George, 'DNA dyes: toxicity, remediation strategies and alternatives', Folia Microbiol. (Praha), vol. 67, no. 4, pp. 555–571, Aug. 2022, doi: 10.1007/s12223-022-00963-8.
[39] [39] R. Sulthana, S. N. Taqui, F. Zameer, U. T. Syed, and A. A. Syed, 'Adsorption of ethidium bromide from aqueous solution onto nutraceutical industrial fennel seed spent: Kinetics and thermodynamics modeling studies', Int. J. Phytoremediation, vol. 20, no. 11, pp. 1075–1086, Sep. 2018, doi: 10.1080/15226514.2017.1365331.
[40] [40] Saruchi, R. Verma, V. Kumar, and A. A. ALOthman, 'Comparison between removal of Ethidium bromide and eosin by synthesized manganese (II) doped zinc (II) sulphide nanoparticles: kinetic, isotherms and thermodynamic studies', J. Environ. Health Sci. Eng., vol. 18, no. 2, pp. 1175–1187, 2020, doi: 10.1007/s40201-020-00536-2.
[41] [41] C. Weeraphan et al., 'Application of the Magnetic Fraction of Fly Ash as a Low-Cost Heterogeneous Fenton Catalyst for Degrading Ethidium Bromide', Anal. Lett., vol. 55, no. 6, pp. 965–979, Apr. 2022, doi: 10.1080/00032719.2021.1977313.
[42] [42] D. Lowe, 'The Myth of Ethidium Bromide', 2016. [Online]. Available: http://blogs.sciencemag.org/pipeline/archives/2016/04/18/the-myth-of-ethidium-bromide
[43] [43] B. O'Sullivan et al., 'A simulation and experimental study of electrochemical pH control at gold interdigitated electrode arrays', Electrochimica Acta, vol. 395, Nov. 2021, doi: 10.1016/j.electacta.2021.139113.
[44] [44] I. Seymour, B. O'Sullivan, P. Lovera, J. F. Rohan, and A. O'Riordan, 'Electrochemical detection of free-chlorine in Water samples facilitated by in-situ pH control using interdigitated microelectrodes', Sens. Actuators B Chem., vol. 325, Dec. 2020, doi: 10.1016/j.snb.2020.128774.
[45] [45] N. Moukri, B. Patella, C. Cipollina, E. Pace, A. O'Riordan, and R. Inguanta, 'Electrochemical detection of human Immunoglobulin-G using Gold Nanowires Immunosensor', in 2023 IEEE BioSensors Conference, BioSensors 2023 - Proceedings, Institute of Electrical and Electronics Engineers Inc., 2023. doi: 10.1109/BioSensors58001.2023.10281025.
[46] [46] G. Wang, J. Zhang, and R. W. Murray, 'DNA binding of an ethidium intercalator attached to a monolayer-protected gold cluster', Anal. Chem., vol. 74, no. 17, pp. 4320–4327, 2002.
[47] [47] L. A. Wasiewska et al., 'Reagent free electrochemical-based detection of silver ions at interdigitated microelectrodes using in-situ pH control', Sens. Actuators B Chem., vol. 333, p. 129531, Apr. 2021, doi: 10.1016/j.snb.2021.129531.
[48] [48] Y. Seguí Femenias, U. Angst, F. Caruso, and B. Elsener, 'Ag/AgCl ion-selective electrodes in neutral and alkaline environments containing interfering ions', Mater. Struct. Constr., vol. 49, no. 7, pp. 2637–2651, Jul. 2016, doi: 10.1617/s11527-015-0673-8.
DOI: https://doi.org/10.17632/xwj98nb39r.1

68: Bent optical microfibre sensor and its application for nanonewton force measurement (invited talk by Dr. Tongyu Liu)

Qiang Wu
Faculty of Engineering and Environment, Northumbria University at Newcastle, United Kingdom

Optical Fibre Sensors Session Three, EM010, August 13, 2024, 11:30 AM - 1:10 PM

Abstract:

Optical fibre interferometers are instruments that can make very precise measurements of objects using the interference pattern of two waves of light, which are one of the promising candidates for next generation photonics sensors for applications in military navigation and tactical surveillance, security, environmental and structural health monitoring and life health/medical diagnostics. A bent Singlemode-multimode-singlemode (SMS) microfibre structure is a typical type of fibre interferometer, where a short length of tapered multimode fibre (MMF) is fusion spliced between two singlemode fibres. The bent SMS microfiber sensor is more sensitive than traditional straight SMS fibre structure, which can be used for vibration and biochemical measurement. By properly design the bent SMS microfiber sensor device, it can be used for ultra-low force detection (in the order of nanonewton). This talk will give a review of a bent SMS microfiber sensor for biochemical and nanonewton force detection.

DOI: https://doi.org/10.34961/researchrepository-ul.29302310.v1

69: Advancement of Low-power Microwave Sensors for Non-invasive Lactate Monitoring

Alex Mason*

Norwegian University of Life Sciences, Aas, Norway.

Microwave and Photonic Sensors, EM010, August 13, 2024, 2:50 PM - 4:00 PM

Abstract

Lactate is an important biological marker in sports, clinical and agrifood settings. Work to develop novel sensors to detect it non-invasively has been ongoing for over a decade, but still there are no suitable solutions on the market. The gold standard remains to be blood gas analysis – a highly accurate method which is also labour intensive, invasive, and requires relatively large blood volumes. Handheld electrochemical analysers have become more widely available, but they too require blood extraction, and overall acceptance has been poor due to variation in results and the lack of true real-time monitoring capabilities in most realistic settings. This work presents the advancement of a low-power microwave sensor for real-time non-invasive monitoring of blood lactate by presenting the latest results from a proof of concept device which is now in wearable form-factor, and is shown to provide adequate performance (0.6721 mmol/L 95% mean error). The sensor is currently able to provide a lactate measurement every 10s with no measurement latency. Further, the sensor eliminates single-use waste resulting from current commercial devices.

DOI: https://doi.org/10.34961/researchrepository-ul.29302397.v1

70: A MULTIMODAL ADAPTIVE DETECTION ALGORITHM FOR OPTICAL FIBER MEMS FABRY-PEROT SENSOR

Guoxiu Wu [a], *Zhen Li* [a], *Lu Cao* [b], *Lin Zhao* [a], *Jiqiang Wang* [a, *]

[a] Laser Institute, Qilu University of Technology (Shandong Academy of Sciences), Jinan, Shandong China ,250104;
[b] Shandong Micro-sensor Photonics Ltd, Jinan, Shandong, China, 250103;
* Corresponding author

Industrial Sensing, EM009, August 13, 2024, 4:20 PM - 6:10 PM

Abstract – Considering about the problem of distorted spectrum of optical fiber MEMS Fabry-Perot sensors which cannot be solved by the traditional peak finding algorithm, we have proposed an adaptive algorithm for peak finding to resolve the problem of spectral distortion. The multimodal signal is divided into a single-peak signal by the Hilbert transform, and a number of independent interference peak spectra with only one peak are obtained, and the number of data points on the left and right sides of the peak point is used as the basis to determine whether the distortion is determined. For the distortion spectrum, a distortion spectrum correction algorithm based on Gaussian fitting was proposed by constructing a correction function to achieve accurate peak finding of the interference spectrum.The simulation results based on MATLAB show that compared to traditional peak finding methods such as centroid algorithm, polynomial fitting method, Gaussian algorithm, etc., the algorithm is more suitable for different degrees of distorted spectrum, and the accuracy of which is higher with an average error of ±3pm. We have carried out experiments and the result shows that the algorithm error is less than 0.0051MPa within the pressure range of 0-3MPa.

Keywords: optical fiber MEMS sensor; distorted spectrum; adaptive algorithm; interferometric interrogator

1. INTRODUCTION

The sensor is a type of optical fiber sensor based on MEMS technology. The cavity are manufactured using MEMS technology, and then optical fiber is used as transmission media to inject light into the Fabry Perot microcavity and receive reflected signals through a optical fiber interrogator. It has the advantages of high sensitivity, small size, high temperature and corrosion resistance, high reliability, low cost, and mass production, and has a wide range of applications, mostly used in medical, chemical, mining, transportation and other fields.The stability and measurement accuracy of the sensor directly constrain its application and engineering development. Based on the previous research we have found that the interference spectrum wavelength directly affects the measurement accuracy of the sensor[1-2]. The excellent peak-finding algorithm can ensure that the demodulation accuracy meets the requirements to the greatest extent. The common peak-finding algorithm is not able to perform high-precision peak-finding for the distorted signal, and the interference spectrum of the sensor is easy to be distorted due to the interference of the light source, the distortion of the arithmetic amplification circuit, and the external noise[3-4]. Improving algorithms have been proposed for the distorted spectrum in many papers. Such as Liao et al. found that the spectra have asymmetric conditions[5]; Jiang Hao et al. proposed a distributed estimation algorithm for distorted spectrum with the average error controlled within 1 pm[6]; Chen Y et al. proposed an exponentially modified Gaussian fitting peak-finding algorithm with detection error within 1 pm[7]. However, the above distortion correction algorithms are more complex, delay in real-time, and difficult to apply in embedded system.

In this paper, a distortion spectrum correction algorithm based on Gaussian fitting is proposed, which judges whether the spectrum is distorted according to the number of data points on the left and right sides of the center of the peak point, and corrects the distorted spectrum, which is suitable for both normal and asymmetric spectrum, and the principle is simple and easy to implement.

2. PRINCIPLE OF FIBER MEMS INTERFEROMETRY

As shown in Figure 1(a), the light from the light source is transmitted to the sensor Faper cavity through the fiber, because the Faper cavity is affected by external pressure, temperature, pressure and other parameters, a part of the light is reflected on the end face of the optical fiber, and the other part is transmitted through the end face of the optical fiber into the cavity, and the reflection and transmission occur again on the pressure-sensitive diaphragm. The principle of optical interference is shown in Figure 1(b), where the A_{r1} and A_{r2} have a stable phase difference, which are superimposed on each other to form optical interference.

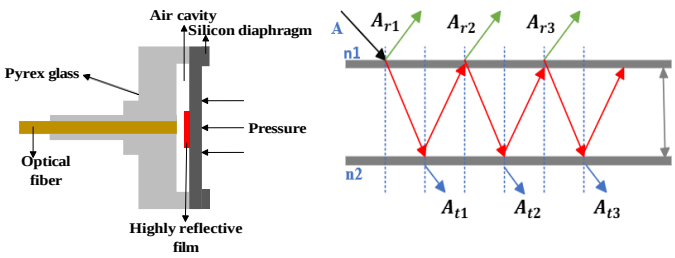

(a) (b)

Figure1. Optical fiber MEMS Faper sensor (a) Schematic diagram of sensor structure (b) Interferometric principle

According to the principle of multi-beam interferometry, the intensity distribution formula of the reflected beam

DOI: https://doi.org/10.34961/researchrepository-ul.29302448.v1

$$I_r = I_0 \frac{2R(1-\cos\frac{4\pi}{\lambda}L)}{1+R^2-2R\cos\frac{4\pi}{\lambda}L} \quad (1)$$

The I_0 is the intensity of the incident light; R is the end-face reflectivity; is the wavelength of the light wave; L is the cavity length of Fabry-Perot cavity. When the reflectivity of the two end faces of the Fabry-Perot cavity is small and equal, the light intensity of the reflected light can be reduced to equation (2).

$$I \approx 2R[1-\cos(\frac{4\pi}{\lambda}L)]I_0 \quad (2)$$

In order to better describe the sharpness and spectral characteristics of the interference spectrum of the fiber MEMS Faper cavity, the fineness of the Faper cavity is usually expressed, and the relationship between the reflectance R and the fineness coefficient F is equation (3). The relationship between the intensity of the reflected light and the reflectance R of the end face is simulated in Figure 2.

$$F = \frac{4R}{(1-R)^2} \quad (3)$$

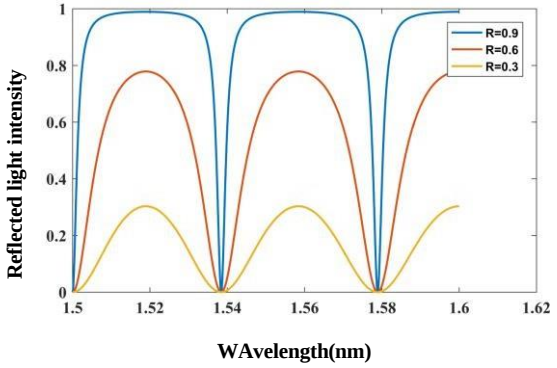

Figure 2. Simulation of the reflection spectrum of the sensor at different reflectance

Through the simulation, it can be seen that with the larger the R, the higher the fineness F of the Faper cavity, and the greater the sharpness of the fringes. However, the reflection curve of the low-precision Faper cavity is cosine-shaped.

The individual interfering peaks in the interference spectrum can be represented by the standard Gaussian function model as equation (4):

$$f(x) = A\exp[-4\ln 2(\frac{\lambda-\lambda_B}{\Delta\lambda_B})^2] \quad (4)$$

Where λ is the wavelength, λ_B is the center coordinate of the single peak obtained after Gaussian fitting, and $\Delta\ \lambda_B$ is the 3 dB bandwidth after Gaussian fitting. For practical interference signals, due to the influence of optical noise, environmental noise, and nonlinearity of equipment such as optical detectors and optical connectors, the spectrum may exhibit broadening and distortion. Therefore, an improved hyper-Gaussian function is adopted as the model for the fiber MEMS interference peak, namely:

$$g(\lambda,\lambda_B) = \varepsilon I_r \begin{cases} exp\ [-2^v \ln 2\ (\frac{\lambda-\lambda_B}{\Delta\lambda_B})^{\ v}\ ] & \lambda < \lambda_B \\ exp\ [-2^v \ln 2\ (\frac{\lambda-\lambda_B}{\alpha\Delta\lambda_B})^{\ v}\ ] & \lambda \approx \lambda_B \end{cases} \quad (5)$$

In the equation: λ represents the interval point value within the wavelength setting range of the MEMS; λ_B denotes the center wavelength; α is the asymmetry parameter of the waveform; $\Delta\lambda_B$ is set to 0.2 nm theoretically to maintain consistency with the 3dB bandwidth of the actual interference signal.

3. DISTORTED SPECTRUM PEAK-FINDING ALGORITHM

The wavelength correction algorithm of multi-peak distortion interference spectral signal mainly includes signal spectrum acquisition, spectral filtering and noise reduction, multi-peak region segmentation, construction of distortion function, and peak wavelength detection

3.1 Peak segmentation

The multimodal signal is divided into multiple subspectra by Hilbert transform, and the redundant data is removed to reduce the amount of subspectral data, which is conducive to improving the peak finding efficiency and speeding up the demodulation speed.

$$x(\lambda) = H[x(\lambda)] = \frac{1}{\pi}\int_{-\infty}^{\infty} x(\tau)\frac{1}{\lambda-\tau}d\tau \quad (6)$$

As shown in Figure 3, the results of the Hilbert transform of the analog signal of the MEMS interference spectrum can be seen that the inflection points on both sides of the original signal correspond to the poles on both sides of the Hilbert transform signal, and the extreme points on both sides are the segmentation thresholds of the multimodal spectrum, so as to achieve the purpose of multimodal segmentation, as shown in Figure 4.

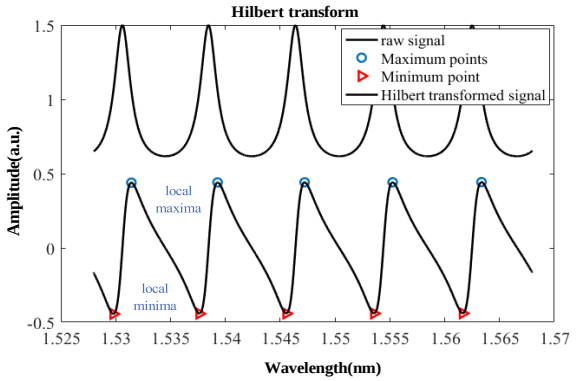

Figure 3. Hilbert Transform Plot of Simulated Interference Signal.

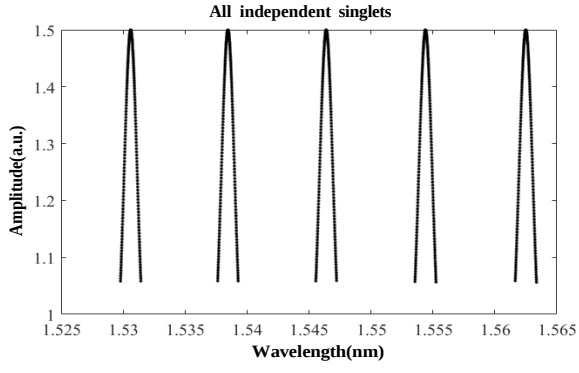

Figure 4. Independent unimodal after Hilbert transformation.

3.2 Determination of Distortion Correction Function

After the spectrum undergoes Hilbert transform, Gaussian fitting is applied to perform peak-finding in the segmented sub-spectral regions, yielding peak wavelength values λ_B. Subsequently, the number of sampling points in the left and right intervals can be obtained using Equations (7) and (8):

$$D_r = (X_r - \lambda_B)/k \tag{7}$$

$$D_l = (\lambda_B - X_l)/k \tag{8}$$

Where D_r and D_l represent the number of sampling points on the right and left sides, respectively, X_l and X_r are the left and right coordinate sampling points, k is the sampling interval. If the spectrum is symmetrical, $D_l - D_r = 0$; if the spectrum is distorted towards the right, $D_l - D_r < 0$; if the spectrum is distorted towards the left, $D_l - D_r > 0$. Additionally, the total number of sampling points is defined as D_z.

$$\mathrm{D}_z = \mathrm{D}_1 + \mathrm{D}_\mathrm{r} \tag{9}$$

For distorted spectra, a distortion correction function is constructed as Equation (10):

$$\lambda_\mathrm{c} = \begin{cases} \lambda_\mathrm{B} + (\mathrm{a}D_z^2 + \mathrm{b}D_z + \mathrm{c})\Delta\lambda_\mathrm{B} & D_\mathrm{r} < D_l \\ \lambda_l & D_\mathrm{r} = D_l \\ \lambda_\mathrm{B} - (\mathrm{a}D_z^2 + \mathrm{b}D_z + \mathrm{c})\Delta\lambda_\mathrm{B} & D_\mathrm{r} > D_l \end{cases} \tag{10}$$

The determination of parameters a, b, and c is done based on the actual conditions of the interference spectrum. The specific steps are as follows: simulated generation of a standard Gaussian signal with known center wavelength and 3 dB bandwidth, modification of the distortion factor for this signal, obtaining λ_B through Gaussian fitting The simulation is shown in Figure 5(a). Based on the actual characteristics of the interference spectrum parameters, set the 3 dB bandwidth $\Delta\lambda_B$ to 0.2 nm, with a sampling interval of 0.079 pm. Multiple sets of data are statistically analyzed by varying the distortion coefficient α. The results of multiple statistical analyses of parameters D_z and ($\lambda_B - \lambda_c$)/ c_i are used to perform a second-order fitting curve, as shown in Figure 5, to predict the region where future data may fall. The confidence band, a statistical measure used during the curve fitting process, indicates the confidence level of the fitting results. It reflects the range in which the data points may exist at a certain confidence level. From Figure 5(b). it can be observed that all data points fall within the 95% confidence band, indicating good fitting accuracy of the curve.

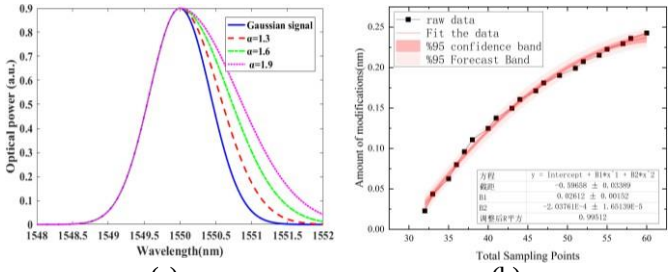

(a) (b)

Figure 5. Construct distortion equations (a) Distortion on the right side of the spectrum (b) Correction Function and Fitting Equation.

Therefore, we obtain:

$$\lambda_c = \begin{cases} \lambda_\mathrm{B} + (0.000204D_z^2 + 0.002612D_z - 0.596580)\Delta\lambda_\mathrm{B} \\ \lambda_\mathrm{B} \\ \lambda_\mathrm{B} - (0.000204D_z^2 + 0.002612D_z - 0.596580)\Delta\lambda_\mathrm{B} \end{cases} \tag{11}$$

4. SIMULATION ANALYSIS AND EXPERIMENTAL VERIFICATION

4.1 Simulation Analysis

Using distortion correction algorithm, centroid algorithm, general polynomial fitting, Gaussian fitting, and other peak-finding algorithms to find peaks in noisy distorted signals and comparing peak-finding errors. Through simulation, interference peak signals with the center wavelength of 1550nm are generated. Distortion coefficients α are set to 1.1, 1.3, 1.5, and 1.7, respectively. Then, the above-mentioned common peak-finding algorithms are used to find peaks. Under each distortion coefficient, there are 10 simulation experiments are conducted to calculate the average, and the errors are respectively counted. The experimental results are shown in Figure 6. It can be observed that the peak-finding errors of the three traditional peak-finding algorithms are relatively large, and they cannot accurately find the wavelength values of distorted spectra. However, the distortion correction algorithm has higher accuracy, with an error of ±3pm.

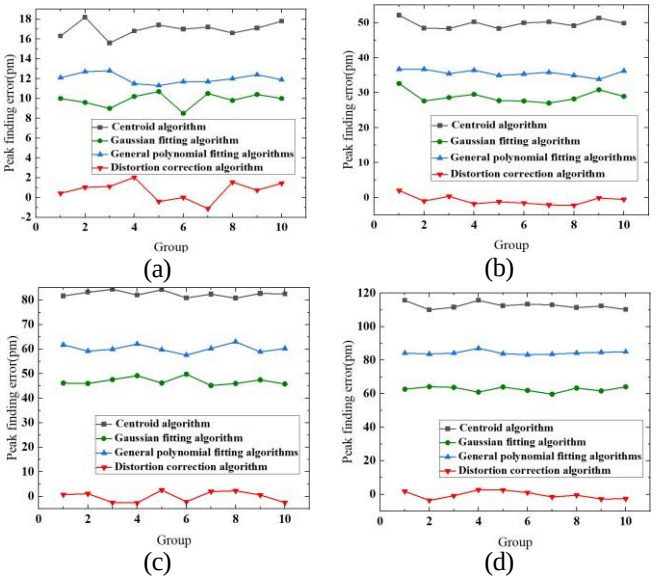

Figure 6. Errors of Four Peak Detection Algorithms (a) Distortion coefficient α =1.1 (b) Distortion coefficient α =1.3 (c) Distortion coefficient α =1.5 (d) Distortion coefficient α =1.7

4.2. Experimental Verification

The optical fiber MEMS wavelength demodulation system is shown in Figure 7, and the light source reaches the optical fiber MEMS through the optical isolator and the optical circulator. The optical signal interferes in the optical fiber, and then the interference light passes through the optical circulator to the interrogator to convert the optical signal into an electrical signal, and finally transmits the interference spectral data to the computer to achieve wavelength demodulation.

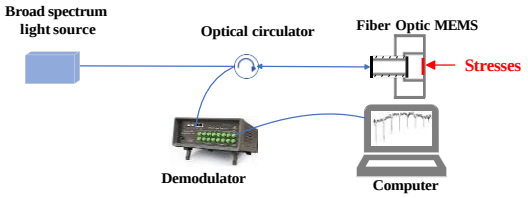

Figure 7. Optical fiber MEMS wavelength demodulation system

Firstly, the multimodal spectral signal voltage is negated and normalized, and the multimodal is divided into single peaks by using the Hilbert transform, as shown in Figure 8. The number of coordinate points on the left and right of the center wavelength is used to determine whether it is distorted, and then the Gaussian fitting results are corrected.

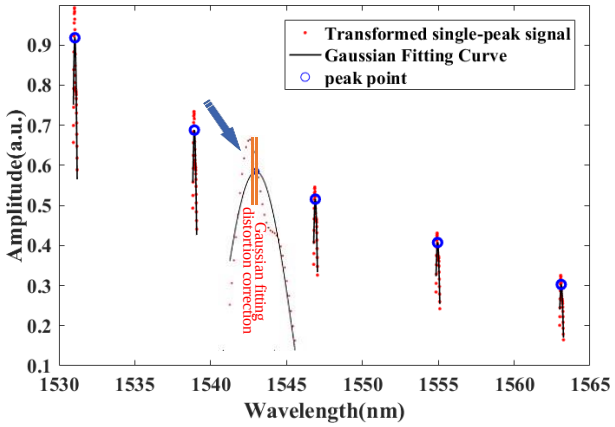

Figure 8. Single Peak Fitting and Gaussian Fitting

In order to compare the accuracy of the above four algorithms, the pressure gauge is pressurized from 0MPa to 3MPa at room temperature, with an interval of 0.2MPa at each pressurization, and the pressure is kept stable for 3 minutes after each pressurization, and finally the corresponding output spectrum is derived. Figure 9 shows the voltage and wavelength fitting curves during the pressurization experiment of the spectral adaptive peak finding algorithm, and the pressure coefficient of the fiber MEMS pressure sensor is determined to be -0.24515MPa/nm, and the fitting coefficient can reach 0.99994.

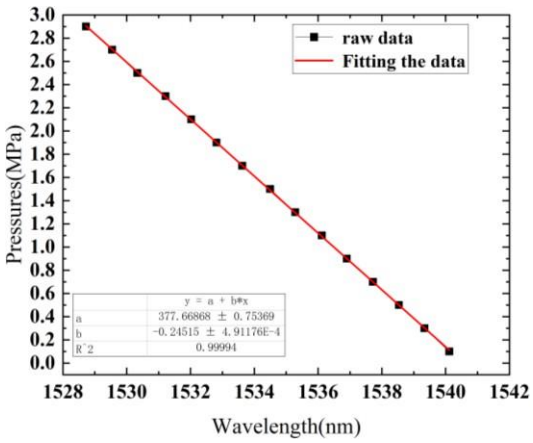

Figure 9. Relationship between Peak Wavelength of Sub-spectrum and Pressure

The fitting coefficients obtained from the first pressure increase are used to calculate the pressure values sensed by the sensor. The calculation formula is as follows:

$$F_1 = (\lambda_1 - \lambda_0)K + F_0 \quad (12)$$

In the formula, F_1 represents the calculated pressure value, λ_1 is the current wavelength value of the target interference peak, λ_0 is the initial wavelength value of the target interference peak, and F_0 is the initial pressure value. In order to verify the pressure demodulation accuracy of the sensor, five sets of pressurization experiments were carried out, and the peak finding was processed by the above four common peak finding algorithms, and the comparative pressure error is shown in Figure 10.

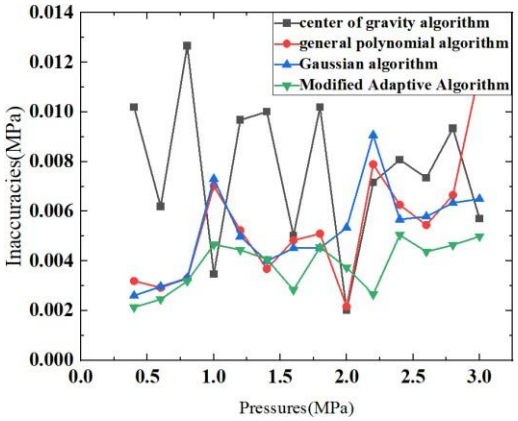

Figure 10. Comparison of Peak Detection Algorithm Errors

5. CONCLUSION

In this paper, a distortion spectrum correction algorithm based on Gaussian fitting is proposed, firstly, the distortion spectrum model is constructed according to the interference spectrum characteristics to simulate the left and right trailing distortion and broadened distortion spectra, the multimodal signal is transformed into a single-peak signal by Hilbert transform, and the total number of sampling points and 3dB bandwidth are used as parameters to construct the distortion correction function, and the simulation results show that the peak finding error of the algorithm is controlled within ±3pm, which has obvious advantages compared with common peak-finding algorithms. The actual pressure (0-3MPa) test results show that the average demodulation error of the algorithm is controlled within 0.0051MPa.

ACKNOWLEDGMENTS

This work was supported in part by the National Key R&D Plan Project (2022YFB3207602) and Innovation Team Program of Jinan (2021GXRC037)

FUNDING STATEMENT

This work was supported in part by the National Key R&D Plan Project (2022YFB3207602) and Innovation Team Program of Jinan (2021GXRC037).

REFERENCES

[1] Yang, H., Tong, X., Cui, Z., Deng, C., Guo, Q., & Hu, P. (2017). Demodulation algorithm for optical fiber F–P sensor. *Applied Optics*, *56*(26), 7450-7453.

[2] Wang, Y., Ni, X., Wang, M., Cui, Y., & Shi, Q. (2017). Demodulation of an optical fiber MEMS pressure sensor based on single bandpass microwave photonic filter. *Optics express*, *25*(2), 644-653.

[3] Zhang, X., Max, J. J., Jiang, X., Yu, L., & Kassi, H. (2007, February). Experimental investigation on optical spectral deformation of embedded FBG sensors. In *Photonics Packaging, Integration, and Interconnects VII* (Vol. 6478, pp. 104-110). SPIE.

[4] Cai, L. J., Li, Z. Y., Tang, Z. H., Meng, W., & Liu, Q. (2012). A novel peak-seek algorithm used in FBG sensor demodulation system for vibration monitoring. *Applied Mechanics and Materials*, *160*, 135-139.

[5] Liao Y, Austin E, Nash P J, et al. Highly scalable amplified hybrid TDM/DWDM array architecture for interferometric fiber-optic sensor systems[J]. Journal of Lightwave Technology, 2012, 31(6): 882-888.Ang J, Li H C H, Herszberg I, et al. Tensile fatigue properties of fibre Bragg grating optical fibre sensors[J]. International Journal of Fatigue, 2010, 32(4): 762-768.

[6] Jiang H, Zhou Q, Chen J, Miao X, Wavelength Detection Optimization of Fiber Bragg Grating Sensing Networks Based on Distortion Spectrum.Acta[J] Optica Sinica 2019,39(10),92-101.

[7] Chen Y, Yang X, Liu H, Yang K, Zhang Y. Processing FBG Sensing Signals with Exponent Modified Gaussian Curve FittingPeak Detection Method. Spectroscopy and Spectral Analysis[J]. 2016,36(05),1526-1531

73: AN INTELLIGENT OPTICAL FIBER DEVICE INTEGRATING SENSING, STORAGE, AND COMPUTING FUNCTIONS

Yiran Feng [a, b], *Zhihai Liu* [a, b *], Yu Zhang [a, b *], Siying Cheng [a, b], Xiang Li [a, b], Yaru Li [a, b], Wei Jin [a, b]

[a] Key Laboratory of In-Fiber Integrated Optics, Ministry of Education, Harbin Engineering University, Harbin, 150001, P. R. China

[b] Key Laboratory of Photonic Materials and Device Physics for Oceanic Applications, Ministry of Industry and Information Technology of China, Harbin Engineering University, Harbin, 150001, P. R. China

Optical Fibre Sensors Session 2, EM010, August 13, 2024, 10:05 AM - 11:15 AM

Abstract – Future neuromorphic computing seeks to transcend the limitations inherent in von Neumann architectures by integrating sensing, storage, and computation. Emerging as the preferred framework for advanced AI systems, non-von Neumann architectures present a viable alternative. Moreover, all-optical modulated memristors are a promising avenue for the evolution of innovative memory computing technologies. This study introduces and validates an all-optical, controllable, high-density memory element embedded within a vanadium dioxide (VO_2)-based seven-core optical fiber. By utilizing a pulsed laser with an average power requirement of merely 0.5 mW, our optical modulation scheme ensures stable, repeatable switching operations and achieves eight distinct levels of data storage (21 bits). This optical fiber memory device exhibits substantial optical contrast (~45%) and facilitates all-optical logic functions, including "AND" and "OR" operations. The advanced optical fiber showcased in this research holds significant potential for optical network applications, heralding a new paradigm in bio-inspired sensing and computational processes.

1. INTRODUCTION

The rapid advancement in big data and artificial intelligence necessitates higher standards for data transmission and storage [1]. Facing the data explosion, with Moore's law approaching its limits and traditional von Neumann architectures encountering significant obstacles, computing stands at a critical juncture [2]. Photonics emerges as a promising solution for the next generation of computing systems, offering capabilities for data storage and processing through optical methods[3]. Photonic memory is essential to photonic computing[4], integrating sensing, storage and computing functions to provide highly efficient sensing, dense storage and computation within a unified system, significantly reducing power consumption[5].

Traditional platforms for optical storage are predominantly silicon-based[6], relying on III-V compound semiconductors[7], ferroelectric materials[8], and two-dimensional materials[9]. These materials undergo thermal, electrical, photo-excitation, and stress-induced changes in optical properties[10]. Despite benefits such as high integration density, rapid memory access, and low energy use, these designs require costly growth conditions and intricate integration techniques[11]. Additionally, the necessity of coupling silicon-based chips to transmission fibers with external devices creates a bottleneck in transmission efficiency[12]. Fiber-optic integrated memory addresses compatibility issues between silicon waveguides and transmission systems[13]. Mature fiber optic devices are more straightforward to process and less expensive to produce, especially those using functional materials, achieving high-capacity, ultra-high-speed transmission while integrating storage and computational intelligence[14].

Phase change materials (PCMs) are prime candidates for device fabrication due to their ability to switch between two stable phases with high reproducibility and long-term stability. Vanadium dioxide (VO_2) is particularly attractive because of its broad range of electronic and optical properties, which can be altered through thermal, electrical, optical excitation, and stress[15]. VO_2 undergoes a reversible insulator (monoclinic, m-VO_2) to metal (rutile, r-VO_2) phase transition (IMT), leading to significant changes in its optical constants[16]. By leveraging the large variations in the complex refractive index ($\Delta n > 1$, $\Delta k > 2$) across the IMT, VO_2-fiber devices, particularly for optical switches and memory, have been extensively studied[17]. However, many modulation methods rely on thermal or electrical manipulation, requiring additional equipment, which leads to high power consumption and delays in transmission. All-optical modulation is essential for achieving simple and efficient operation[18].

In this study, we demonstrate an all-fiber memory by integrating a seven-core optical fiber with VO_2 and indium-tin-oxide (ITO) as the capping layer. VO_2 exhibits a significant contrast in optical reflectivity between its monoclinic state (logic high-reflectivity state, or state 1) and rutile state (logic low-reflectivity state, or state 0), allowing information to be encoded based on its reflectivity. We employ pump pulses to switch the state of VO_2, achieving an average switching power as low as 0.5 mW. The emergent optical field, rather than the evanescent field, significantly promotes phase transition, reducing power requirements. Continuous light, with energy much lower than the switching energy, is used for data reading. We achieved eight levels of storage (3-bit) in a single core, demonstrating high repeatability and excellent reversibility with an optical contrast ratio of about 45%. With seven cores in a memory cell, 21-bit dense storage is possible. Additionally, we explored its application in a logical fiber calculator within one core, achieving "AND" and "OR" computations. This all-fiber memory opens new pathways toward intelligent fiber net systems

DOI: https://doi.org/10.34961/researchrepository-ul.29302505.v1

2. METHODS AND PROCEDURES

2.1. Structure preparation

We fabricated an all-fiber memory by integrating a standard seven-core optical fiber with phase-change materials (PCMs), specifically vanadium dioxide (VO_2), to fully utilize the photosensitive and storage properties of the materials. The PCM layer has a thickness of approximately 100 nm, and the indium-tin-oxide (ITO) layer is about 50 nm thick. The structure is grown on the fiber end face using a magnetron radio-frequency (RF) sputtering system. Specifically, VO_2 is deposited using RF sputtering at 300 watts of RF power in a 2 Torr argon atmosphere with a base pressure of 9×10^{-4} Torr, while ITO is deposited at 200 watts RF power under the same atmospheric and pressure conditions. The structure of our all-optical fiber memory is shown in Fig.1.

Optimal thickness of the PCM film is crucial to prevent ablation from high-energy pulse trains. Increasing the film thickness avoids such ablation risks[19]. The stability of the film's structure and its properties remain largely unchanged with increased thickness. However, excessively thick films lead to unnecessary material wastage. Hence, we set the PCM thickness at 50 nm, ensuring enough light transmission and accurate reproduction of light patterns in the film without surplus material.

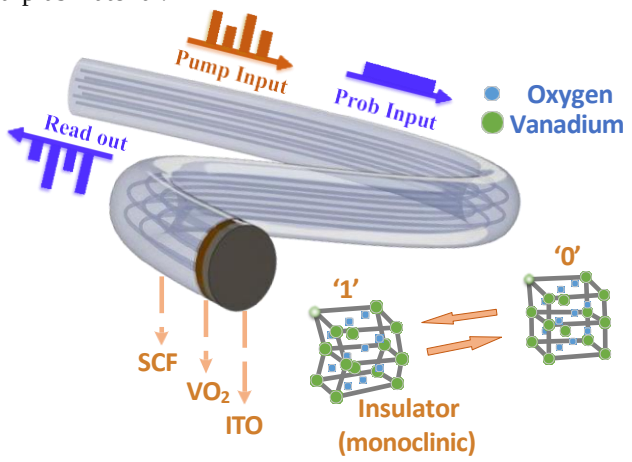

Figure 1. The all-fiber memory device. The all-fiber memory device comprises a seven-core fiber, VO_2, and ITO. Information is stored in VO_2, encoded by its reflectivity. To read or write information, a pump pulse at $\lambda = 1550$ nm and probe light at $\lambda = 1530$ nm are introduced into the optical fiber storage unit.".

As a unique material, optical PCMs exhibit significant changes in optical properties in response to external stimuli such as electrical or optical excitation[20]. These tuneable optical properties occur on sub-nanosecond time scales. Phase transitions in these materials can generate a broadband change in the refractive index and extinction coefficient, triggered by thermal, electrical, or optical means. VO_2 is widely used as an optical PCM due to its compositionally tuneable optical properties, including strong light reflection properties and nonlinear optical effects.

The properties of VO_2 are intrinsically linked to its geometric structure. In the rutile state, VO_2 adopts a cubic lattice configuration, with oxygen atoms occupying specific lattice sites while vanadium atoms are randomly distributed across the remaining sites. Conversely, in the monoclinic state, this cubic lattice becomes locally distorted. This structural alteration is directly related to the two-state transitions of VO_2, which can be reversibly switched between states by suitable optical stimuli.

Generally, by heating VO_2 above the phase transition temperature, it will become metal (rutile) phase. Whereas heating materials can obtain r- VO_2 until the temperature remove from the phase transition temperature and then materials quickly restore to the initial state.

In our experiments, we precisely control the pulse energy of the pump pulses to adjust the various states of the PCMs. This approach enables us to fabricate a reflective multilevel optical memory device tailored for the telecom C + L bands. By using this method, we can achieve high-performance optical memory suitable for advanced telecommunications applications

2.2. METHODS

Fiber Probe Fabrication.

Fabrication of the fiber probe was by introducing the seven-core fiber and a seven-core fiber optic fan-in coupler. The core diameter of the SCF is 8 μm, and the cladding diameter is 150 μm. The inter-core distance is 41.5μm. We cleaned the end face of the fibre probe using the of the fibre optic welding machine

Measurement.

The glass substrate was cleaned sequentially with acetone, isopropanol and deionised water. The cleaned glass substrate was coated with VO_2 and ITO of the same thickness as above. The thickness of the VO_2 was measured at 120 nm using a morphology analyser.

Experimental Instruments

The low-power probe laser source we use is 'VLSP-C-B-TL-20-FA, CONNET' and the pump laser source is 'VFLS-1550-M-DTS-1-FA, CONNET'.

The photodetector (PD) is '2051-FC-M, Newport'

2.3. Experimental setup

In Fig. 2, the measurement setup involves several steps: first, the one-part-N fiber coupler averages the energy of the continuous laser detected by the readout system and feeds it into an array of one-part-two in Fig. 2, the measurement setup involves several steps: first, the one-part-N fiber coupler averages the energy of the continuous laser detected by the readout system and feeds it into an array of one-part-two fiber couplers. These couplers then combine the averaged continuous laser with optical pulse signals directed at specific wavelength channels, which are subsequently directed into a fiber optic circulator array. Within this array, optical energy from each wavelength channel is transmitted from port 1 to port 2, while energy reflected by the backend device travels from port 2 to port 3. Finally, a seven-core fiber optic fan-in coupler distributes optical signals from each wavelength channel to corresponding cores within the seven-core fibres.

Using a pump laser source induces the state change to write or stored "information", the pulse width of the pump laser source is on the order of nanoseconds (10 ns). The low-power probe laser source to monitor the state change to read the "information". power is controlled by the probe laser source and the optical attenuator to ensure that the phase change is not affected. Two light beams from a pump laser source (λ=1550 nm) and a probe laser source (λ=1530 nm) are coupled into a single beam through a 90:10 coupler. The light beam exiting through the coupler enters port of the circulator and is then transmitted to port, which is directly

connected to the seven-core fiber optic fan-in/fan-out device, acts directly on the material at the end face through the fiber. Using the emergent light field instead of the evanescent light field can make the transmitted pulse in the fiber act directly on the VO_2 and this is significantly improving efficiency of action and reduces power consumption

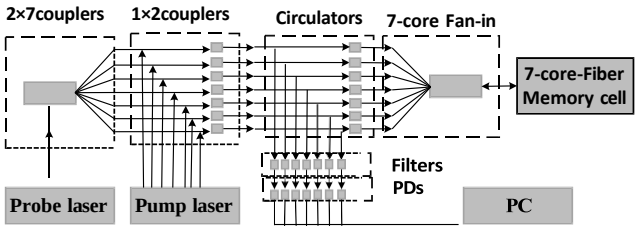

Figure 2. The control system for the reflective seven-core fiber-optic memristor involves core-welding it to the output of a seven-core fiber-optic fan-in, enabling transmission of optical signals from each wavelength channel to corresponding cores within the memristor. A fiber optic filter array selectively permits continuous laser wavelength optical signals to pass through. A photodetector array monitors real-time optical signal sizes reflected from each core of the seven-core fiber-optic memristor, thereby reading stored information from each core

3. RESULTS AND DISCUSSION

All experimental step of our all-fiber memory device are performed at room temperature. we change the state of the optical switch by switching the VO_2 film between its low reflective state and high reflective state. The optical reflection of the device without laser is defined as the 'OFF', and when there is light reflection it is defined as 'on'. Moreover, the reflectivity contrast is about 45% between 'on' and 'off'. Different levels of reflectivity form our storage hierarchy. Therefore, our device design implements optical switching as well as optical storage. Take one of the cores as an example. We use 1550 nm pulsed laser to switch the open state of the fiber memory, the pulse train with 1 kHz repetition rate and with a fixed width of 10 ns. Different average power can switch the state of fiber memory and the different relative reflectivity presents the different levels. Here the powers of different optical pump pulses are 50mW-100 mW in the experiment. For example, levels 1 up to 8 are sequentially achieved by decreasing the power from P7 to P0[Fig. 3(a)]. In a similar way, we can also achieve an 8 to 1 level shift. Here the powers of different optical pump pulses are P0 =95mW, Pi =95,90,85,80,75,70,65,60,55,50 mW (i =0,1, 2, 3, 4, 5, 6, 7) in the experiment. When the low energy p7 acts on the material, the PCMs are in the room temperature state, currently the optical constant of the material is n=3.24[21], the reflectivity is high, we define it as levle8; when p0 acts on the material, currently the material belongs to the rutile state, the reflectivity is low, we define it as levle1.

Importantly, we can use a pulse sequence with a power of Pi to switch to any energy level i, and this switching does not consider the state of VO_2, as shown in Figure 3(c). The same level has the same corresponding P1 and Pi, and each level is unaffected by the previous state. For example, we can go from level 0 to level 2 and then back from level 2 to level 1, or we can go directly from level 2 to level 4 and then from level 4 to level 7. To check the stability of the memory, we switched the device back and forth between level 1 and level 8, as shown in Figure 3(b), we performed 30 cycles of cyclic switching and the data storage has a high stability. This means that each level can be accessed from all the others, with accurate reflection levels and remarkable repeatability. The result shows that our all-fibre memory cell has good reversibility and high contrast in optical reflection

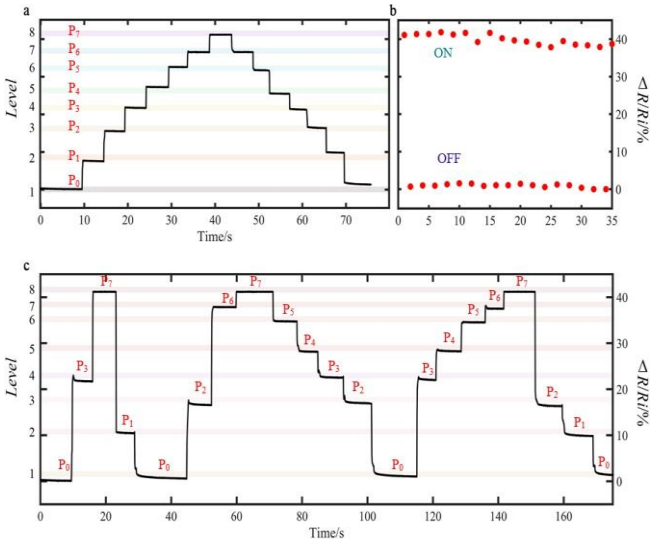

Figure 3. Measurements of multi-level operation. (a) Experimental demonstration of eight different levels in in a single core with the relative change in reflection recorded. A single pulse is implemented to switch the photonic memory, and each level is reached by a determined optical power, from 50 to 100 mW. Moreover, the 40 cycles verified. (c) Accessing same levels but in random order featuring intra-level switching.

As integrated electrical logic devices incorporating PCMs have been developed to tackle complex computational tasks, we have fabricated full fiber-optic logic gates ('AND' and 'OR') on memory cells. In our design, logic '0' and logic '1' correspond to reflective strengths at level 1 and level 8, respectively, which we denote as '0' and '1'. Our approach utilizes PCM-based fiber-optic integrated devices, merging storage elements with logic gates such as 'AND' and 'OR' gates (see Figure 4).

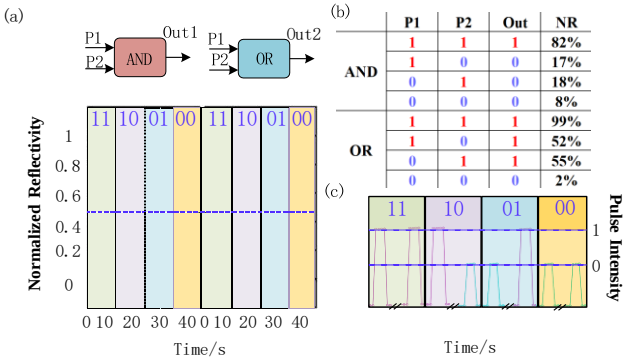

	P1	P2	Out	NR
AND	1	1	1	82%
	1	0	0	17%
	0	1	0	18%
	0	0	0	8%
OR	1	1	1	99%
	1	0	1	52%
	0	1	1	55%
	0	0	0	2%

Figure 4. Results from the logical operation experiment are presented as follows: (a) The schematic of the optical logic device based on fiber memory features two signal inputs, P1 and P2. An 'AND' gate is realized using two storage logic units in series, while an 'OR' gate combines output signals from parallel-connected units using a coupler. (b) Normalized reflectivity outputs for various input combinations are shown, with logic '1' defined above a reference value. The left diagram illustrates the input-output relationship of the 'AND' gate, while the right diagram depicts that of the 'OR' gate. (c), (d) Truth tables for basic 'AND' and 'OR' logic

operations display outputs corresponding to input states ('1', '1'), ('1', '0'), ('0', '1'), and ('0', '0').

To perform an AND logic operation, two memory cells are connected in series, while to perform an OR logic operation, they are connected in parallel and their outputs are combined using a coupler. Each memory cell interfaces with the CIR as our all-fibre memory is based on fibre reflection measurements. Input information is stored and read using continuous wave light. Prior to logic calculations, lasers are held back to maintain initial conditions. For example, in a series 'OR' gate setup, two independent optical pulses (P1, P2) with fixed pulse widths (10 ns) are used as inputs, corresponding to digital inputs '0' and '1' with pulse amplitudes of 50 mW and 95 mW, respectively, as shown in Figure 4(c). These inputs are applied to the memory cells. Figure 6(a) shows how different combinations of P1 and P2 give different NR values. Comparisons with a reference value of 0.5 (purple line) determine the optical memory's logic outputs (out1 and out2), which can be '0' or '1' relative to this line. Specifically, inputs '00', '01', '10' and '11' produce 'OR' gate outputs of 0.02, 0.55, 0.52 and 0.99 respectively, and 'AND' gate outputs of 0.08, 0.18, 0.17 and 0.82 respectively, with the reference line set to 0.5. Thus, the logic outputs for 'AND' and 'OR' operations are '0', '1', '1', '1' and '0', '0', '0', '1' respectively. Corresponding truth tables for the memory cells are shown in Figure 4(b), corresponding to conventional electronic 'AND' and 'OR' gates. Differences in NR values result from different reflectivity contrasts between the memory cells, further increasing the output differences.

The application of this memory element could be of benefit to the field of all-optical signal processing and data processing.

4. CONCLUSIONS

In this study, we have successfully demonstrated 3-bit data storage using an all-fibre memory cell within one core of a seven-core fibre. Using all-optical modulation, we achieve state changes in the PCM memory cell by controlling the reflectivity by varying the pulse power. Our results highlight the ability to switch between multiple memory levels with ease and precision, ensuring high accuracy in signal readout and excellent repeatability. In addition, basic logic operations ('AND' and 'OR') have been implemented, paving the way for more complex logic operations using additional fibre optic memory cells. These results represent a significant step forward in the development of fast, low-power fibre memory solutions for a wide range of applications. The all-fibre non-volatile multi-level memory holds promise for applications in neuromorphic computing and in-memory computing. In addition, the integration of memory and computing units into optical networks is expected to drive innovation in optical network applications, heralding a new paradigm in bio-inspired sensing and computational processes.

ACKNOWLEDGMENTS

Yiran Feng: Data curation, Investigation, Methods. **Zhihai Liu**: Writing – original draft, Investigation, Formal analysis, Data curation, Conceptualization. **Yu Zhang**: Investigation, Data curation, Conceptualization. **Siying Cheng**: Supervision, Resources, Funding acquisition. **Xiang Li**: Supervision, Resources, Methods, Funding acquisition. **Yaru Li**: Validation, Supervision, Resources, Funding acquisition. **Wei Jin:** Data curation, Conceptualization, Methods.

FUNDING STATEMENT

The Basic Research Support Program for Excellent Young Teachers of Heilongjiang Province (YQJH2023281); Fundamental Research Funds of Harbin Engineering University.

REFERENCES

[1] J.S. Wey, and J. Zhang, **Passive optical networks for 5G transport: technology and standards**. *Journal of Lightwave Technology*, *37*(12), pp.2830-2837.

[2] Z. Cheng, C. Ríos, N. Youngblood, C.D. Wright, W.H. Pernice, and H. Bhaskaran, **Device-level photonic memories and logic applications using phase-change materials**. *Advanced Materials*, *30*(32), p.1802435.

[3] Y.Chai, **In-sensor computing for machine vision**. Nature. 2020 Mar;579(7797):32-33.

[4] Y. Chen, Y. Wang, Z. Wang, Y. Gu, Y. Ye, X. (+ another 7 authors), **Unipolar barrier photodetectors based on van der Waals heterostructures**, J. Nature Electronics, 2021, 4(5): 357-363.

[5] K. J. Miller, R. F. Haglund, S. M. Weiss, **Optical phase change materials in integrated silicon photonic devices**, J. Optical Materials Express, 2018, 8(8): 2415-2429.

[6] Y.Jung, H. Han, A. Sharma, J. Jeong, S. S. P. Parkin, and J. K. S. Poon, Integrated Hybrid VO_2–Silicon Optical Memory ACS Photonics, 2022, 9 (1), 217-223

[7] Y. Ge, F. Zhao, L. Wang, X.Wang, **A novel perspective on the design of thermochromic VO2 films: combining ab initio calculations with FDTD simulations**, J. Surface and Coatings Technology, 2020, 402: 126493.

[8] H.Coy, R.Cabrera, N.Sepúlveda,F.E.Fernández ,**Optoelectronic and all-optical multiple memory states in vanadium dioxide**,J . Journal of Applied Physics, 2010, 108(11).

[9] H.M.K.Wong, Z.Yan, K.A.Hallman, R.E. Marvel, R.P. Prasankumar, R.F.Haglund, A.S.Helmy. **Broadband, integrated, micron-scale, all-optical Si3N4/VO2 modulators with pJ switching energy**,J . ACS Photonics, 2019, 6(11): 2734-2740.

[10] Y. Kim, P. C. Wu, R. Sokhoyan, K. Mauser, R. Glaudell, G. K. Shirmanesh, H.A. Atwater, **Phase modulation with electrically tunable vanadium dioxide phase-change metasurfaces**,J . Nano letters, 2019, 19(6): 3961-3968

[11] T. Alexoudi, G.T. Kanellos, N. Pleros, **Optical RAM and integrated optical memories: a survey**, J. Light: Science & Applications, 2020, 9(1): 91.

[12] J. Sun, M. Jiang, Q. Zhou, C. Wang, Y.Sun. **Memristive cluster based compact high-density nonvolatile memory design and application for image storage**, J. Micromachines, 2022, 13(6): 844.

[13] X.Q.Cai, Z.T.Zhou, T.H.Tao, **Programmable Vanishing Multifunctional Optics**. Adv Sci. 2018 Dec 27;6(4):1801746.

[14] Z. Fang, R. Chen, B. Tossoun, S. Cheung, D. Liang, A. Majumdar,I. Vassalini, I. Alessandri, D. D. D. Ceglia, **Stimuli-responsive phase change materials: optical and optoelectronic applications.** Materials, 14(12), 3396.

[15] C.X. Wu, Y. B. Xue, H.Bao, L.Yang, J. C.Li, J.Tian, S. G. Ren, Y.Li, X. S.Miao, **Forward stage wise regression with multilevel memristor for sparse coding,** J. Semicond, 2023, 44(10): 104101.

[16] B. Jiang, Y. Hou, H. Wang, X. Gan, A. Li, Z. Hao, K. Zhou, L. Zhang, J. Zhao, **Few-layer graphene integrated tilted fiber grating for all-optical switching**, J. Journal of Lightwave Technology, 2021, 39(5): 1477-1482.

[17] J.D.Ryckman, K.A. Hallman, R.E. Marvel, R.F. Haglund, S.M. Weiss, **Ultra-compact silicon photonic devices reconfigured by an optically induced semiconductor-to-metal transition**, J. Optics express, 2013, 21(9): 10753-10763.

[18] J. F. Song, X. S. Luo, A. E. J. Lim, C. Li, Q. Fang, T.Y. Liow, L.X. Jia, X.G. Tu, Y. Huang, H.F. Zhou, G.Q. Lo, **Integrated photonics with programmable non-volatile memory**, J. Scientific reports, 2016, 6(1): 22616.

[19] M.Wuttig, H.Bhaskaran, T.Taubner, **Phase-change materials for non-volatile photonic applications**, J. Nature photonics, 2017, 11(8): 465-476.

[20] J. Zheng, A. Khanolkar, P. Xu, S. Colburn, S. Deshmukh, J. Myers, J. Frantz, E. Pop, J. Hendrickson, J. Doylend, N. Boechler, and A.Majumdar. **GST-on-silicon hybrid nanophotonic integrated circuits: a non-volatile quasi-continuously reprogrammable platform**, J. Optical Materials Express, 2018, 8(6): 1551-1561.

[21] Y.Ge, F. Zhao, L. Wang, and X. Wang, **A novel perspective on the design of thermochromic VO2 films: combining ab initio calculations with FDTD simulations**. *Surface and Coatings Technology*, *402*, p.126493.

78: Innovative MIR LASER-, LED- and PD-cascade technologies for sensing
Dr Lars Hildebrandt

The growing demand for monitoring of specific molecules in environmental, health, and security applications has created a need for inexpensive and power-efficient light sources. In particular, the mid-infrared (MIR) wavelength ranges from 3 µm to 6 µm is of high interest for gas-sensing. Many trace gases ubiquitous to industrial sites have their strongest absorption bands in this region, e.g. carbon dioxide, nitric oxide, water, and various important hydrocarbons. They show absorption strengths that are several orders of magnitude higher than those in other spectral areas.

Aiming at providing reliable broadband and cost-effective alternatives to standard optical gas analysis, nanoplus has developed light-emitting diodes (LEDs) in the MIR. The novel substrate-side-emitting devices rely on the innovative nanoplus technology for distributed feedback (DFB) interband cascade lasers (ICL) and are available at customized wavelengths between 2800 nm and 6500 nm. They display higher wall-plug efficiencies and maximum output powers than previous MIR LEDs, operating in continuous-wave (cw) at room temperature.

nanoplus has specialized in designing DFB lasers for high-precision gas sensing in industry and research. Based on a ridge waveguide structure, which is independent of the material system, nanoplus designs CW DFB lasers at any wavelength between 760 nm and 14 µm. The nanoplus flagship product is a DFB ICL with target wavelengths from 2800 nm to 6500 nm and an extremely narrow linewidth of below 3 MHz. At top-rated wavelengths, the laser shows output powers above 15 mW and is hence perfectly suitable for highly sensitive gas detection. In this talk we will present various applications which utilize DFB ICLs or MIR LEDs and give a general overview of this technology including latest results from interband cascade photodiodes (PD) and LED-arrays in the MIR or up to 10 µm.

DOI: https://doi.org/10.34961/researchrepository-ul.29304419.v1

79: DEVELOPMENT OF CHINA'S SMART MINES AND UNDERGROUND SPATIOTEMPORAL PERCEPTION DETECTION TECHNOLOGY

WANG Guofa[a,*]

[a] China Coal Technology & Engineering Group, Beijing 100013, China,

Welcome Session/Plenary Session One, Jean Monnet Theatre, August 12, 2024, 9:00 AM - 11:10 AM

Abstract – The development of smart coal mining in China has gone through the process of "from single machine to group", "from on site operation to remote centralized control", and "from process automation to perception decision adaptation". Currently, 1922 smart coal mining faces and 2154 smart excavation faces have been built. With the development and application of basic technologies such as artificial intelligence, blockchain, cloud computing, big data, and 5G, further breakthroughs have been made in the theoretical research of digital coal mines and smart mining. A digital coal mine intelligent logic model based on intelligent perception is constructed; an intelligent control method for mining systems under the framework of intelligent logic models is proposed; methods for evaluating the health status, predicting lifespan, and making maintenance decisions of mining systems are innovated. The underground spatiotemporal perception and detection technology in coal mines, as well as the mining machine vision measurement and equipment posture control technology, are key technologies in the perception process of smart coal mine development. A theoretical and technical system for dynamic three-dimensional reconstruction and precise real-time positioning of underground spaces is established, targeting the basic problem of visual computability in underground spaces, and solving the core technical difficulties of holographic perception and calculation of global physical space underground, intelligent equipment groups, and operator targets. Technologies that integrate vision for equipment full pose monitoring, edge vision AI monitoring, multi camera panoramic video splicing, dual spectral thermal infrared imaging, and image enhancement are proposed to achieve functions such as collision prevention warning for fully mechanized mining cutting, straightness monitoring for fully mechanized mining, posture monitoring for protective panels, hydraulic support posture monitoring, intelligent monitoring of tunnel deformation, posture monitoring for tunneling machines, spatial positioning and orientation of tunneling machines, and monitoring of coal face spalling. The relevant technologies have been applied in the Zhangjiamao Coal Mine and Huangling No.1 Coal Mine of Shaanxi Coal Mine, and a cross domain integrated intelligent comprehensive control platform has been built for the coal mine. A comprehensive spatiotemporal information perception and real-time interconnection mechanism have been constructed, bridging the business data barriers of multiple systems, levels, and departments. Normalized production has been realized with one person patrolling the working face, the shearer independently planning and cutting, and two people on the surface for remote auxiliary control.

Keywords**:** smart coal mine; digital coal mine; detection technology; data logic model; multi-source data fusion

DOI: https://doi.org/10.34961/researchrepository-ul.29304500.v1

80: Intelligent Long Wall Top Coal Caving Mining

Jiachen Wang, Yang Li
China University of Mining and Technology-Beijing, China

Abstract:

Longwall Top Coal Caving (LTCC) mining technology is an effective method for mining thick and extra thick coal seams in China. Since its application in China in 1982, significant progress has been made, forming a variety of mining modes such as LTCC with large mining height, LTCC in extra thick coal seams and LTCC in steeply inclined thick coal seams. Caving door is an essential part of the support in LTCC face, which determines the beginning and end of coal caving. But the control of caving door is still high labor intensity and low working efficiency. There are technical problems in intelligent control of the caving door, such as difficulty in adapting to the complex underground environment, monitoring the migration state of top coal, and estimating the rock mixed ratio. Based on BBR theory, an image-based intelligent control technology of caving door was introduced in this paper. The third-generation top coal migration tracing marker is developed to realize multiple rounds of coal caving. The effect of illuminance on the image features of coal and rock is analyzed. An improved Retinex enhancement algorithm is proposed to remove dust and fog. A lightweight multi-scale rock boundary detection model and the rock volume estimation model are established to estimate the rock mixed ratio in real-time. The hardware and software of image-based intelligent caving door control technology are developed and tested in both the laboratory and in-site. The results show that the features between coal and rock can be enlarged when considering optimal illuminance. The dust and fog can be effectively removed using the proposed algorithm and the developed hardware. The research results have been successfully applied in many coal mines, and the working efficiency and top coal recovery ratio have been improved.

DOI: https://doi.org/10.34961/researchrepository-ul.29304599.v1

81. EARLY DETECTION OF PIPELINE FRACTURES IN AGED INFRASTRUCTURE IN THE WATER INDUSTRY

Matthias Fabian[1],*, Shailendra Singh[1], Richard Scott[1], Tong Sun[1], Kenneth T V Grattan[1], Heriberto Bustamante[2], Timothy Hill[2], James McCulloch[2]

[1] City St George's, University of London, London, EC1V 0HB, UK
[2] Sydney Water Corporation, Parramatta, NSW 2124, Australia
* matthias.fabian.1@city.ac.uk

Abstract – This paper introduces a ruggedised, highly sensitive optical fibre-based pressure sensor for use in pumped sewer mains. Tests reported were carried out for different leak sizes on a plant scale test rig using water. The pressure drop resolution achieved is better than 100Pa (1mbar) which corresponds to a leak size of 2mm (in a pipe of 100mm in diameter and a flow rate of 16 litres per second).

Keywords: optical fibre sensors, pressure sensor, leak detection, pipeline, water industry

1. INTRODUCTION

Ageing infrastructure is still in operation in the water industry world-wide, which raises an ever-increasing demand for improved sensing technology that requires no expensive excavation. Both potable water and wastewater pipelines are often buried deep underground with few access points over long distances. Sometimes wastewater leaks can potentially go undetected for months and cause serious impacts on the surrounding environment.

Considerable effort has been made to develop suitable sensing solutions ranging from acoustic [1] to temperature-based [2] sensors. The most promising approach appears to be the detection of negative pressure waves caused by a leak-induced pressure drop and travelling in both directions of a pipe [3]. When distributing multiple such pressure sensors along a pipeline, an estimate can be derived for the leak location based on when the negative pressure wave is detected by the individual sensors [4].

The limiting factor is the sensitivity of commercially available pressure sensors, which is directly linked to how small a leak they are capable of detecting. The latter is important because of the need of early detection to prevent catastrophic failures, particularly in hot-spot areas.

This report builds on an original proposed sensor design previously reported by the authors [5] with improvements in sensitivity and leak detection analysis.

2. METHODS AND PROCEDURES

The sensing mechanism is based on fibre Bragg grating (FBG) technology (the fibre-optic equivalent of an electric strain gauge). The fundamental principle of using FBGs for strain monitoring has been widely reported, e.g. in [6], and will not be repeated here.

2.1. Sensor design

The sensor comprises of a well machined into a sensor substrate made of aluminium 6061-T6 (referred to here as a sensor coupon). The FBG is placed across the well and both are covered by a stainless-steel diaphragm (50µm thick) as depicted in Figure 1. Deformation in the diaphragm induced by pressure applies strain to the FBG underneath it which causes a shift in its characteristic reflected peak wavelength. An additional FBG is embedded in the sensor coupon, isolated from the pressure-sensitive area, allowing for compensation of the temperature effect on the pressure-sensing FBG. A spacer attached to the diaphragm and sitting across the sensing fibre ensures reliable contact between the two.

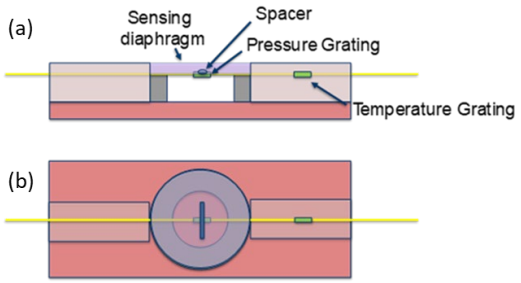

Figure 1. Schematic diagram of the pressure transducer design. A diaphragm deflects under pressure inducing strain in the optical fibre located beneath it. (a) cross-sectional view; (b) top view.

For the purposes of attaching the sensor to a pipeline, a stainless-steel flange is attached to the top of the membrane as shown in Figure 2. Both ends of the sensing fibre are terminated within the sensor housing to avoid damage during the installation process.

Figure 2. Schematic diagram of the sensor assembly and photograph of the fully assembled sensor. The sensing fibre and diaphragm are sandwiched between a flange and the connector housing, which holds the terminated fibres.

2.2. Test setup

Large scale tests were carried out at the National Distributed Water Infrastructure Facility based within the Integrated Civil and Infrastructure Research Centre (ICAIR) at the University of Sheffield, UK. The facility provides a

DOI: https://doi.org/10.34961/researchrepository-ul.29304674.v1

constant head tank system capable of delivering flow rates of up to 100 litres per second.

Figure 3 schematically shows the 37m long high-density polyethylene pipeline (HDPE, 100mm dia.) connected to the head tank as used in this investigation. At approximately the half-way point, an access point allowed for 'simulating' leaks using disks of varying holes sizes. Four pressure sensors were connected to additional access points, two on either side of the leak position and approximately 5.6m apart.

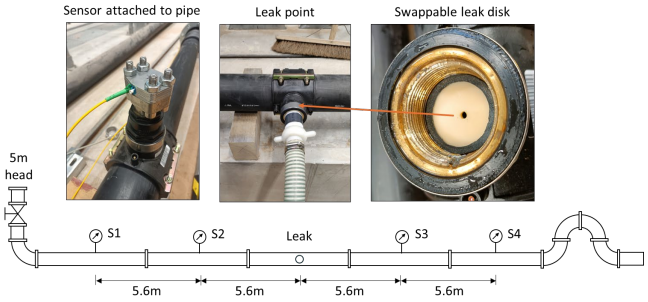

Figure 3. Leak and sensor locations along the 100mm HDPE pipe used in this investigation. Water is supplied by a 5m head tank at a flow rate of 16 litres per second.

The ultimate purpose of having multiple sensors distributed along the pipe is to estimate the location of a detected leak by determination of the time a negative pressure wave arrives at those different locations, however this is beyond the scope of the present study. Here the focus is on the minimum detectable leak size through monitoring of the pressure drop induced by leaks.

2.3. Sensor interrogation

Throughout this investigation, the sensor data was acquired using a Luna optical sensing instrument (si155, Hyperion) with a maximum sampling rate of 5kHz.

3. RESULTS AND DISCUSSION

This section covers the sensor calibration followed by an analysis of the results obtained from the large-scale tests.

3.1. Sensor calibration

The calibration setup comprised of an air compressor, an electronically adjustable valve and an electronic reference sensor sitting between the fibre-optic sensors and the valve. The recorded sensor responses are shown in Figure 4 highlighting the effect of the diaphragm thickness on the sensitivity of the sensors (50µm for sensors 1 and 2; 100µm for sensors 3 and 4). The pressure range of up to 5 meters (0.5 bar) corresponds to the maximum pressure of the head tank system used to evaluate the sensor performance described in the following sections.

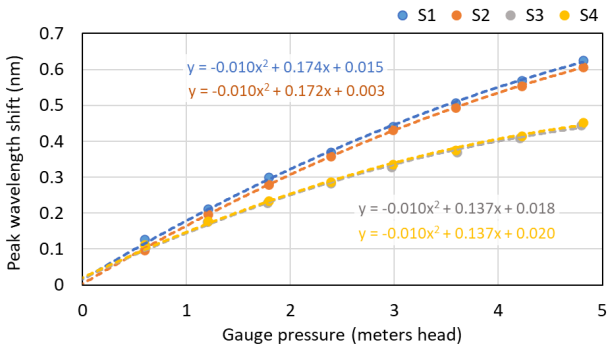

Figure 4. Sensor response vs pressure for different diaphragm thicknesses, i.e., 50µm (S1, S2) and 100µm (S3, S4).

Figure 4 highlights the consistency of the calibration resulting in almost identical calibration coefficients for the two pairs of sensors. The diaphragm thickness could be further reduced but at the expense of robustness, i.e., the dynamic range of the sensor.

3.2. Large-scale testing

The schedule for the pipeline test started with approximately one minute of the pipe being empty to establish a clear baseline in the sensor signals. The main valve connecting the head tank to the pipeline was then opened causing water to flow at a rate of 16 litres per second through the pipe. Two minutes were allowed for the flow to stabilize before the valve on the outlet hose connected to the leak point was opened to simulate a leak. The leak was kept 'active' for one minute followed by another two minutes of steady flow with the leak closed. Finally, the main valve was shut cutting off flow from the head tank, and data was recorded for another minute. The individual sensor responses (after calibration) to the above test schedule are shown in Figure 5.

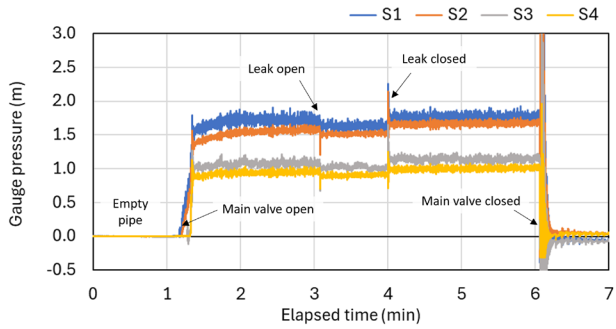

Figure 5. Pipe pressure at the different sensing locations for an exemplary test cycle.

It is clear from Figure 5 that the static pipe pressure drops along its length verifying the calibration of the sensors. It is also clear that the leak (in this case a 12mm leak) causes a sudden drop in pressure as well as certain transient signatures when the leak is opened and closed. All subsequent figures are based on the sensor 1 trace in Figure 5.

Figure 6 shows a magnified view of the response of sensor 1 for the duration of the leak being open. The low-pass filtered trace (2nd order Butterworth, 0.1Hz) clearly highlights the pressure drop.

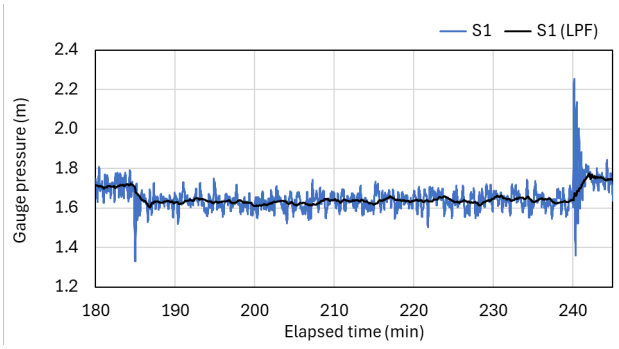

Figure 6. Exemplary pressure drop and transient signatures caused by a leak of 12mm in diameter. Blue line (raw data); Grey line (low-pass filtered data).

The above test sequence was repeated for ever smaller leak sizes. However, detecting the point or time at which a drop in pressure occurs in turbulent flow data becomes increasingly difficult as the leak size is reduced. For that reason, a second approach was used, looking at the spectral features contained in the real-time data. For that purpose, the raw data was high-pass filtered (2nd order Butterworth, 0.125Hz) to remove the static pressure (avoiding large spectral features at very low frequency). Figure 7 shows both plots, the filtered raw data and spectrogram corresponding to the sensor 1 signal in Figure 5.

It is apparent in Figure 7 that the turbulent flow of water in the pipe results in persistent low-frequency features (<30Hz) captured by the sensor. They are, however, overshadowed by the closing event of the main valve and the end of the cycle which causes a water hammer of very low frequency (<1Hz) but much larger amplitude than the leak events which are therefore hardly detectable in the plot.

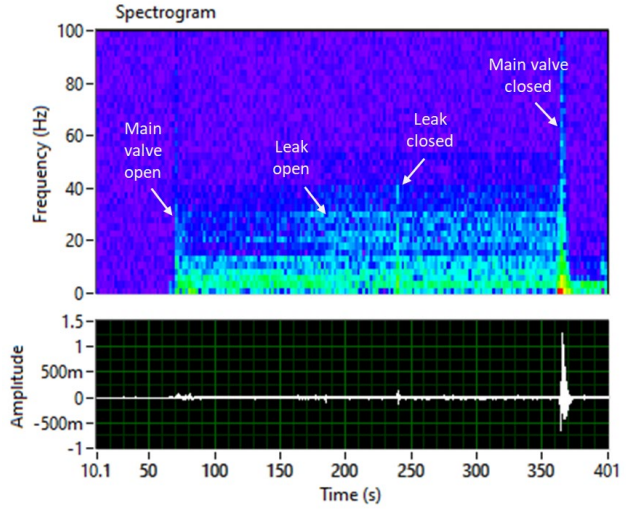

Figure 7. Spectral features extracted from the data of sensor 1. Bottom graph: High-pass filtered data of sensor 1. Top graph: Spectrogram of the high-pass filtered signal revealing the spectral components contained in the real-time signal.

Knowing the frequency bands of those unwanted effects, it is possible to disregard them using optimised filtering which eventually reveals the leak event to be clearly detectable in the spectrogram of Figure 8.

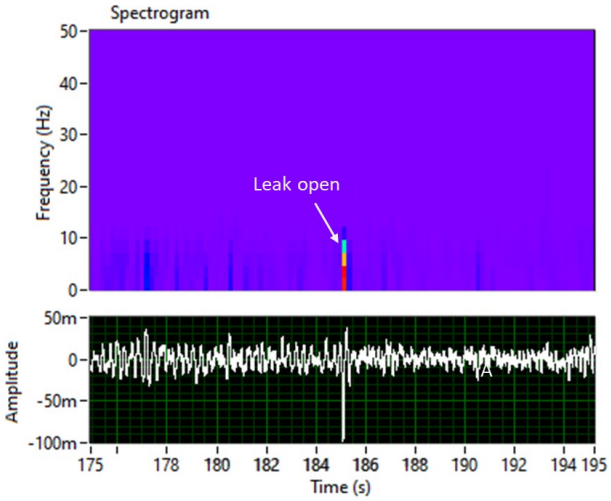

Figure 8. Spectral features of sensor 1 around the 'leak open' event after optimised filtering has been applied, clearly revealing the event as a distinct feature.

Using this approach of detecting leaks by their spectral features and then looking at the pressure drop at that point allowed for the identification of leaks down to 2mm in diameter (pressure drop <100Pa, 1mbar) as depicted in Figure 9.

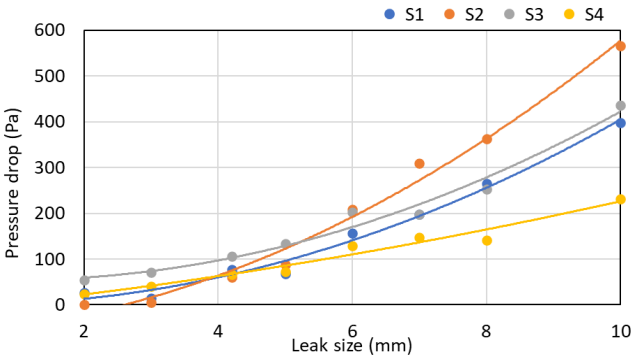

Figure 9. Pressure drop vs leak size. Leaks down to 2mm in diameter were successfully identified.

Figure 9 also confirms the expected relative pressure drops to be greater in magnitude closer to the leak than further away from it, i.e., sensor 2 registering a larger drop than sensor 1 and sensor 3 a larger drop than sensor 4.

4. CONCLUSIONS AND FUTURE WORK

It has been shown that the proposed FBG-based fibre-optic sensor design can detect minute pressure drops in pressurized water pipes. The combined use of spectral analysis and adaptive filtering allowed for the detection of the 'onset' of leaks as small as **2mm** in diameter.

Future work will focus on leak location identification and on the design of cascaded sensor arrays each operating at high sensitivity over a limited pressure range. Such arrays combined with pattern recognition of real-time transients as well as spectral features will provide a highly sensitive monitoring platform over a large pressure range.

ACKNOWLEDGMENTS

The authors acknowledge the funding support of Sydney Water and the material assistance provided by Integrated Civil and Infrastructure Research Centre, which was part funded by EPSRC Grant EP/R010420/1. This project is funded through an enforceable undertaking with the Australian New South Wales Environment Protection Authority (NSW EPA) following a discharge of untreated sewage from a Sydney Water rising main in Shellharbour in July 2020. As part of this undertaking, Sydney Water will contribute funds towards environmental projects.

FUNDING STATEMENT

This work was supported by Sydney Water Corporation.

REFERENCES

[1] W. Liang, L. Zhang, Q. Xu, C. Yan, **Gas pipeline leakage detection based on acoustic technology**, Eng. Fail. Anal., vol. 31, 2013, pp. 1–7.

[2] S. Großwig, A. Graupner, E. Hurtig, K. Kühn, A. Trostel, **Distributed Fibre Optical Temperature Sensing Technique - A Variable Tool for Monitoring Tasks**, TEMPMEKO, Vol. 1, 2001, pp. 9–18.

[3] C. X. Hou, E. H. Zhang, **Pipeline Leak Detection Based on Double Sensor Negative Pressure Wave**, Appl. Mech. Mater., vol. 313–314, 2013, pp. 1225–1228.

[4] J. Wang, L. Ren, Z. Jia, T. Jiang, G. Wang, **A novel pipeline leak detection and localization method based on the FBG pipe-fixture sensor array and compressed sensing theory**, Mech. Syst. Signal Process., vol. 169, 2022, p. 108669.

[5] J. A. A. Bremner, M. Fabian, R. Scott, J. Carlton, T. Sun, (+another 6 authors), **Using Novel Fibre Bragg Grating Based Pressure Sensor for Early Detection of Pipeline Leaks,** 28th International Conference on Optical Fiber Sensors, Hamamatsu, Japan, 20-24 Nov., 2023, paper Tu3.93.

[6] Y.-J. Rao, **In-fibre Bragg grating sensors**, Meas. Sci. Technol., vol. 8, 1997, pp. 355–375.

82. FIBER OPTIC-BASED THERMOMETRY: EVOLUTION AND DEVELOPMENT SPANNING FIVE DECADES

Kenneth T V Grattan[1,2], Tong Sun [1,2], Matthias Fabian [1,2]

[1] Sensors & Instrumentation Centre, City St George's, University of London, London, EC1V 0HB, United Kingdom;
[2] City Optotech Ltd, London, United Kingdom
* Corresponding author: k.t.v.grattan@city.ac.uk

Abstract – Fiber Optic Sensors (FOS) have been developed since the late 1970s and amongst the earliest devices produced have been transducers for the measurement of temperature, in particular as a result of its critical importance to many industrial processes. Moving on from the original simplistic devices reported, the 1980s saw both the first use of non-linear optical techniques for distributed temperature sensing and the success of the (initially longitudinally-written) Fiber Bragg Grating – this opened up the potential of this important in-fiber device for quasi-distributed temperature sensors. Research in the field has continued now for nearly five decades and the main driver continues to be to produce a wide range optical-fiber based techniques, which can be suited to a variety of different sensor purposes, providing techniques that represent the most effective temperature measurement technology for use by industry world-wide. All this points to the value of a closer examination of the variety of approaches taken to such measurements, building on the different principles discussed. It is important to see the way those have either gone on to further success – or been largely discarded – and how the continuing need for better temperature monitoring for a number of different industries is met – and thus best served by using fiber optic techniques. This paper aims to provide such a brief overview and to point to future directions.

Keywords: Fibre Optic Sensors; temperature measurement; thermometry

1. INTRODUCTION

Fiber Optic Sensors (OFS) have been developed since the late 1970s and amongst the earliest devices produced have been transducers for the measurement of temperature, as a result of the critical importance of that measurement to a wide variety of industries world-wide. That period saw some of the first experiments on low-loss optical fibers being used, not for telecommunications — as had been the prime motivation for their development — but for sensor purposes and success to measure temperature in a new and important way. Many of the original suite of sensors mirrored non-fibre based optical techniques, taking advantage of the convenience of fibre-based light transmission in the devices. The suite of optical fiber sensors thus developed from the 1970s, including those for temperature measurement, which owes its existence to two of the most important scientific advances made in the previous decade — the laser (1960) and the modern low-loss optical fiber (1966). In addition, following the initial development of several simple devices, the 1980s saw the first use of non-linear optical techniques for distributed temperature sensing. A major leap forward resulted from the success of the side-written Fiber Bragg Grating in the late 1980s – this opened up the potential of this important in-fiber device for quasi-distributed temperature sensors, especially when phase mask-based techniques were introduced to the grating writing process.

The Global Optical Fiber Sensor (OFS) market size is significant and growing well – it was valued at ~$3 billion in 2024. The Optical Fiber Sensor market industry has been projected to grow from that ~$3 billion in 2024 to ~$7.7 billion by 2034 and to exhibit an impressive compound annual growth rate (CAGR) of ~10% from 2024 to 2032 [1]. Figure 1 illustrates this from published data.

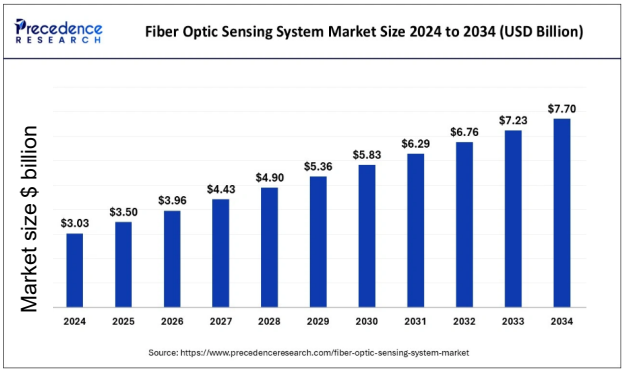

Figure 1: Global *Fiber Optic Sensor* Market – prediction by year to 2032

Research in the field has continued now for nearly five decades since the 1970s – and as shown above is planned to continue at a rapid pace to keep up with the demand, which is the main driver of such research. This continues to produce a range optical-fiber based techniques which can be used for a variety of different sensor purposes – with temperature an important parameter amongst several others key measurands. Thus the global fiber optic temperature sensor market is projected to grow significantly in the coming years, driven by increasing demand across various industries and technological advancements. Given the market is expected to see substantial growth (as noted, a CAGR ~10% over the next few years), the key market trends and growth drivers which fuel this include:

- Rising demand for sensors: the need for precise and reliable temperature measurement in diverse applications, including industrial automation, energy, healthcare, and infrastructure, is fuelling market growth.

DOI: https://doi.org/10.34961/researchrepository-ul.29304770.v1

- Exploiting technological advancements: these include such familiar aspects as Fiber Bragg grating (FBG) technology, Raman-based sensing, and other advancements are enhancing the capabilities of fiber optic temperature sensors, leading to wider use.
- Distributed sensing: distributed fiber optic sensors (DFOS) offer the ability to measure temperature along the full length of the fiber, making them ideal for monitoring large structures or complex systems.
- The breadth and diversity of industrial applications continues to increase: industries mentioned such as oil and gas, power generation, and manufacturing are increasingly utilizing fiber optic temperature sensors for process monitoring, safety, and efficiency.
- Real-time Monitoring: the ability to provide real-time temperature data allows for proactive maintenance and optimization of systems.
- Artificial Intelligence (AI): AI techniques will support the better use of OFS devices and analysis of data.

Within the global optical fiber sensor market lies the global optical fiber ***temperature*** sensor market, whose size has gone from being worth $0.42 billion in 2024, to be expected to achieve $0.83 billion by 2033 (with a CAGR of 8% during the forecast period from 2025 to 2033) [2], as illustrated in Figure 2. Thus this market is about 10% of the global optical fiber sensor market overall, and shares its high predicted growth in the 8 – 10% range.

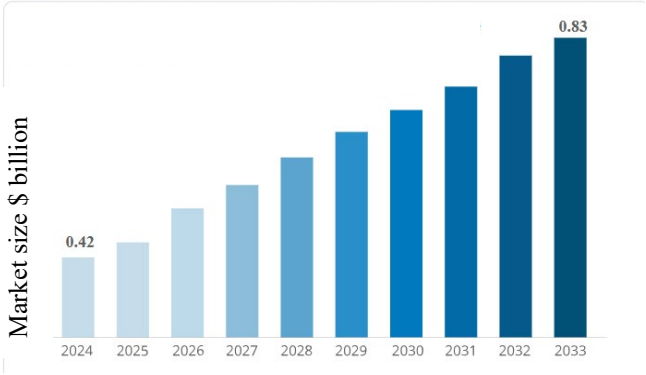

Figure 2: Global Optical Fiber *Temperature Sensor Market* size – prediction by year to 2033 [2]

2. BETTER TEMPERATURE MEASUREMENT FOR INDUSTRY

The reliable measurement of temperatures over a very wide range, from low to high temperatures, is critically important for many industries world-wide – it plays a key role in fields such as aerospace (for example in the combustion chambers and turbines of an aircraft engine), in raw production engineering (especially of metals for industry e.g. steel production) and in the nuclear power industry, to give just a few, diverse examples. In the latter case the possibility of real-time monitoring of internal temperatures of boilers links strongly to combustion efficiency and the use of better safety measures, taking advantage of the inertness of the optical fibre-based measurement technique. It is clear that reliable measurement of temperature continues to be important for an even wider range of applications, including the oil and gas, materials engineering and renewable energy production, amongst many others. Temperature monitoring of wind turbines play a key role in today's society and fiber optic temperature sensors enable measurements in harsh environments, for example those where high temperatures, pressures, and strong electromagnetic fields make more conventional techniques either inappropriate or difficult.

Thus providing a foundation for an effective temperature measurement technology for industry and which can complete with conventional methods, especially in niche areas is critically important. Therein lies the recipe for the success of optical fiber sensors — in tackling effectively difficult measurement situations where conventional sensors are not well suited to use, in a particular environment. Fiber optic sensors are typically compact, lightweight and inert and have moved on from the initial single point sensors seen in early models to offer multiple measurements from a single fiber network, whether in a quasi-distributed or fully distributed mode.

Importantly, all OFS devices are designed to be immune to electromagnetic interference (EMI) as there are no electrical currents flowing at the sensing point. There is, however, the expectation that they should be able to be produced at relatively low or competitive cost, often using a range of the technologies that have been 'spun-off' from research in the optical communications field. Investigations which have been conducted by several groups have confirmed that fiber sensors can survive in difficult environments — for example, even stringent radiation tests, and this is especially true of the rapidly developing field of Fiber Bragg Grating (FBG) and other grating-based sensors such as those based on Long Period Gratings (LPGs). In this field, one of the most important technological developments in the sensor and optical telecommunications fields in recent years, the width, amplitude and temperature sensitivity of the grating resonance had been shown to remain unaltered even with under high temperature exposure or, for example, high radiation doses. This is an important characteristic for this type of device, pointing to potential applications not just in the nuclear industry, but more widely. In addition, a technology such as the use of plastic fiber in sensors is undergoing rapid growth, and this, again, is driven by new developments in telecommunications systems. Equally important, such in-fiber gratings can be produced even in polymer and crystal fiber, opening up new possibilities in sensor applications. A number of useful reviews of the subject have been produced over the years [3].

3. FIBER OPTICS AND THE INTERNET OF THINGS (IOT)

The development of the field over the period and the wide range of techniques and applications offers a fascinating insight into technological innovation, as new applications are opening up, especially for challenging environments. One significant trend in the optical fiber temperature sensor market is the integration of these sensors with the Internet of Things (IoT) technology. Fiber optic devices are a perfect fit for IoT applications and the most common types of IoT sensors include temperature sensors, motion sensors, proximity sensors, light sensors and gas sensors.

IoT comprises large networks, potentially spanning vast geographical distances, and has several connected devices, sensors, actuators, and more as required. Thus the combination of the Internet of Things (IoT) and fiber optic sensors offers significant benefits, especially in applications

demanding high-speed data transmission, real-time monitoring, and distributed sensing. Fiber optic sensors, with their ability to withstand electromagnetic interference and transmit data at high speeds, are well-suited for IoT applications requiring minimal latency and reliable data transfer. Key features in the interplay between IoT and fiber optic sensors include the following.

Fiber Optic Temperature Sensors as IoT nodes:

- Fiber optic sensors can be integrated into IoT devices to collect data on various parameters including temperature, pressure, strain, vibration, and even chemical or biological changes.
- These sensors can be designed to be compact and non-electrical, making them suitable for integration into various IoT devices and applications.
- They can be used in distributed sensing setups, allowing for widespread real-time monitoring and data collection at a lower cost.

Advantages of Fiber Optic Sensors in IoT applications include:

- High-Speed Data Transmission: Fiber optics provide significantly faster data transmission speeds compared to traditional methods, enabling real-time data processing and analysis in IoT applications.
- Minimal latency: The low latency of fiber optic networks is crucial for critical IoT applications like industrial automation and autonomous vehicles, ensuring timely data transmission and action.
- Greater security and reliability: Fiber optic cables are immune to electromagnetic interference and offer strong security, making them ideal for applications where data integrity and confidentiality are critical.
- Potential for fully and quasi-distributed sensing: Fiber optic sensors can be deployed across large areas, enabling comprehensive monitoring and data collection from diverse locations.
- Overall system cost-effectiveness: fiber optic sensors are cost-effective IoT solutions.
- Full compatibility with Artificial Intelligence.

Broader applications of Fiber Optic Sensors in IoT:

- 'Smart cities': fiber optics can support various smart city applications like traffic monitoring, smart public lighting, and waste management by providing reliable and high-speed data transmission.
- Industrial Automation: fiber optic sensors can be used in industrial settings to monitor machinery, process parameters, and ensure optimal performance.
- Precision Agriculture: in agriculture, fiber optics can support remote monitoring systems and real-time tracking of environmental conditions, enabling more precise management of agricultural resources.
- 'Smart Healthcare': fiber optic sensors can be used in connected medical devices to enable fast and secure data transmission from remote patient monitoring systems and more 'personalized, patient-focused healthcare.
- Infrastructure Monitoring: fiber optics can be used to monitor the structural integrity of bridges, pipelines, tunnels and other infrastructure, providing real-time data and early warning of potential issues.
- 'Smart Security Systems': fiber optic sensors can be integrated into intrusion detection systems, providing real-time alerts and enabling rapid response to security breaches.

The Future of Fiber Optic Sensors in IoT is encouraging as:

- As noted, the enormous potential with the integration of fiber optic sensors with AI and machine learning will further enhance their capabilities, allowing for real-time data analysis and actionable insights without human intervention.
- AI-powered fiber optic sensors will likely streamline processes, enabling devices to learn from their environments and adapt to changes occurring.

This integration enables real-time and remote temperature monitoring, data collection, and analysis. As industries strive for enhanced efficiency and predictive maintenance, IoT-enabled optical fiber temperature sensors have become a vital tool. These sensors can be seamlessly integrated into existing IoT platforms, allowing businesses to optimize their operations based on accurate temperature insights [3].

All this points to the importance of a closer examination of the different techniques proposed, the way those have either gone on to success or been largely discarded and the continuing need for better temperature monitoring for a number of different industries which can be best served by using fiber optic techniques.

This work thus links to the outputs of a recent **Euramet** project bringing together some 27 European Universities, National Measurement Institutes and industries to investigate the area more fully. The project recognizes that the measurement and control of temperature plays a key role in achieving the goals of the European Green Deal for a low-carbon energy system. The project exploits the fact that fiber-optic thermometry is a developing technology offering advantages, such as distributed sensing and immunity to electromagnetic fields, in many applications. A key feature is that since fibre optic thermometers exhibit cross-sensitivities to other quantities, these must be investigated, minimised, and quantified to obtain traceable and reliable. The focus has been to overcome limitations that prevent their widespread use by creating a dedicated European metrological infrastructure addressing research, testing, calibration, and training and undertaking 'real-time' *in situ* testing.

4. SUMMARY OF TECHNOLOGY UNDERPINNING CURRENT AND FUTURE SENSING TRENDS

The field of optical fiber temperature sensors is dominated by several key technologies – and to these are linked the potential use of different types of optical fiber [4] . The six main technologies include optical fiber interferometry, rare earth (and other material) fluorescence, intensity-based sensors, and black-body radiation based sensor (especially for high temperatures). Two major categories of optical fiber temperature sensor illustrated are the Fiber Bragg Grating (and indeed as well Long Period Grating sensors) and fully distributed temperature sensors, using non-linear effects.

This is shown schematically in Figure 3, which illustrates both the main six technologies and the linkages to the different optical fiber types used in such sensors. The center of the diagram shows these different optical fiber types which may be employed, from pure silica fiber (used widely in optical fiber temperature sensors) to crystal fibre (used especially in high temperature sensors), through doped silica fiber (exploited in fluorescence lifetime decay and

fluorescence intensity ration sensors) and microstructured fiber, of which there are many different types, and which enables the exploitation of different optical effects.

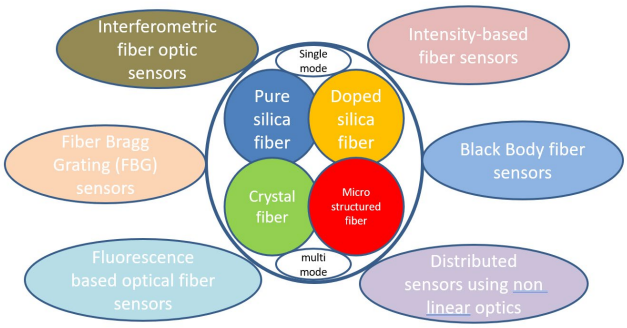

Figure 3: schematic of key optical fiber temperature sensor techniques and optical fibre types involved in sensor design

A simple way to show the comparative cost the sensors based on each of these technologies is shown in Figure 4, where '$' represents devices that can be sources at prices typically <$1k; '$$' devices in the $1k to $10k range typically and '$$$' represents devices at prices above that. This is of course a generalization and approximation, but illustrates the trend for *sensor systems* based on the above different illustrative technologies.

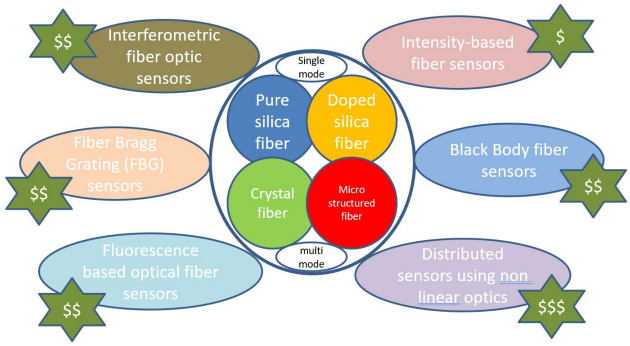

Figure 4: As above, with illustrative technology costs

5. REGIONAL TRENDS

North America stands out as a significant and dynamic market for optical fiber temperature sensors. This prominence can be attributed to the advanced industrial infrastructure, technological monitored in aircraft engines, critical components, and cabin environments exploiting their ability to withstand extreme conditions and provide real-time data – invaluable for ensuring the safety, efficiency, and reliability of aviation systems. Additionally, the automotive industry in North America has embraced these sensors for thermal management, engine monitoring, and battery temperature control in electric vehicles. As the automotive sector there transitions toward electrification and autonomous technologies, the demand for accurate and efficient temperature sensing solutions continues to rise.

The Asia Pacific region is currently witnessing a remarkable surge in the adoption of optical fiber temperature sensors, driven by a combination of factors including the expansion of manufacturing activities, infrastructural development, and the increasing recognition of sensor technologies' benefits. In that region, countries such as China, Japan, and South Korea are at the forefront of this growth, actively investing in various industries that require accurate temperature monitoring solutions. China, with its massive manufacturing ecosystem, is a primary driver of the optical fiber temperature sensor market in Asia Pacific. The rapid industrial expansion, especially in sectors like electronics, automotive, and energy, creates a strong demand for temperature sensors that can withstand harsh conditions and provide real-time insights. Optical fiber temperature sensors find applications in manufacturing processes, quality control, and predictive maintenance, all contributing to increased operational efficiency [5].

6. FUTURE TRENDS AND GROWTH

Key Future Trends and important growth elements in the field can be deduced from the above and summarized as:

- increased demand for sensors – in harsh environments like oil and gas, aerospace, and automotive industries.
- driving forward technological advancements leading to more compact and cost-effective fiber optic sensors.
- addressing the growing demand for real-time temperature monitoring in industrial automation.
- exploiting advances in materials used for fiber optic sensors, improving their durability and sensitivity.
- enhanced sensor integration with smart systems and IoT/AI technology for predictive maintenance.
- integrating the new directions in fiber optic technology which are reported, improving accuracy and reliability
- encouraging industry leaders to invest in expanding production capabilities to meet the rising demand for temperature sensors employed across various sectors.

All this can lead to increased partnerships and collaborations between sensor manufacturers and automation solution providers to enhance sensor functionalities and broaden applications. [5 - 7]

FUNDING STATEMENT

This work was supported by the Euramet project the Royal Academy of Engineering for Grattan and Sun.

REFERENCES

[1] https://www.marketresearchfuture.com/reports/fiber-optic-sensor-market-2514 and https://www.precedenceresearch.com/fiber-optic-sensing-system-market)
[2] https://www.businessresearchinsights.com/market-reports/optical-fiber-temperature-sensor-market-107899
[3] Grattan, K. T. V. and Sun, T. "Fiber optic sensor technology: an overview", Sensors and Actuators A: Physical 82, 40-61 (2000). Elsevier BV. doi:10.1016/s0924-4247(99)00368-4
[4] https://www.businessresearchinsights.com/market-reports/optical-fiber-temperature-sensor-market-107899
[5] https://www.linkedin.com/pulse/industrial-fiber-optic-temperature-sensors-2ecuc/
[6] https://www.ruggedmonitoring.com/
[7] Ma, Y. Xu, Y. Pang, X. Zhao, Y. Li, Z. Qin, Z. Liu, P. Lu, P and X. Bao, "Optical Fiber Sensors for High-Temperature Monitoring: A Review", Sensors 2022, 22, 5722. https://doi.org/10.3390/s22155722